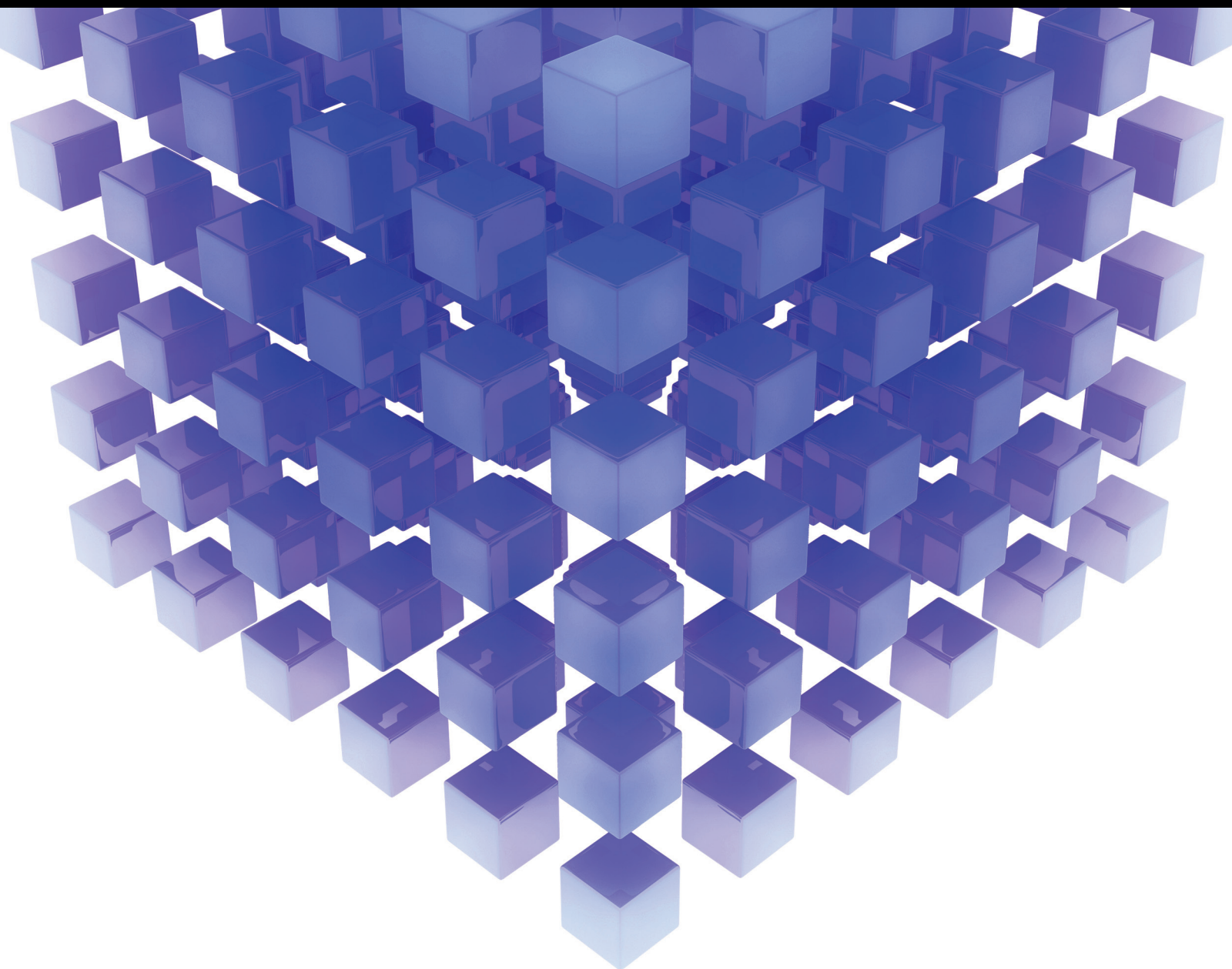


Mathematical Problems in Engineering

Recent Advances in the Application of Differential Equations in Mechanical Engineering Problems

Lead Guest Editor: Rahmat Ellahi

Guest Editors: Constantin Fetecau and Mohsen Sheikholeslami





**Recent Advances in the Application
of Differential Equations in
Mechanical Engineering Problems**

Mathematical Problems in Engineering

**Recent Advances in the Application
of Differential Equations in
Mechanical Engineering Problems**

Lead Guest Editor: Rahmat Ellahi

Guest Editors: Constantin Fetecau and Mohsen Sheikholeslami



Copyright © 2018 Hindawi. All rights reserved.

This is a special issue published in “Mathematical Problems in Engineering.” All articles are open access articles distributed under the Creative Commons Attribution License, which permits unrestricted use, distribution, and reproduction in any medium, provided the original work is properly cited.

Editorial Board

- Mohamed Abd El Aziz, Egypt
José Ángel Acosta, Spain
Paolo Addresso, Italy
Claudia Adduce, Italy
Ramesh Agarwal, USA
Francesco Aggogeri, Italy
Juan C. Agüero, Australia
R Aguilar-López, Mexico
Tarek Ahmed-Ali, France
Muhammad N. Akram, Norway
Guido Ala, Italy
Reza Alam, USA
Salvatore Alfonzetti, Italy
Mohammad D. Aliyu, Canada
Juan A. Almendral, Spain
Cláudio Alves, Portugal
Lionel Amodeo, France
Sebastian Anita, Romania
Renata Archetti, Italy
Felice Arena, Italy
Sabri Arik, Turkey
Alessandro Arsie, USA
Edoardo Artioli, Italy
Fumihiro Ashida, Japan
Mohsen Asle Zaeem, USA
Romain Aubry, USA
Matteo Aureli, USA
Viktor Avrutin, Germany
Francesco Aymerich, Italy
Michele Bacciocchi, Italy
Seungik Baek, USA
Khaled Bahlali, France
Laurent Bako, France
Stefan Balint, Romania
Ines Tejado Balsera, Spain
Alfonso Banos, Spain
Roberto Baratti, Italy
Azeddine Beghdadi, France
Denis Benasciutti, Italy
Ivano Benedetti, Italy
Elena Benvenuti, Italy
Michele Betti, Italy
Jean-Charles Beugnot, France
Carlo Bianca, France
- Simone Bianco, Italy
Gennaro N. Bifulco, Italy
David Bigaud, France
Antonio Bilotta, Italy
Paul Bogdan, USA
Alberto Borboni, Italy
Paolo Boscariol, Italy
Daniela Boso, Italy
Guillermo Botella-Juan, Spain
Fabio Bovenga, Italy
Francesco Braghin, Italy
Maurizio Brocchini, Italy
Julien Bruchon, France
Matteo Bruggi, Italy
Michele Brun, Italy
Tito Busani, USA
Raquel Caballero-Águila, Spain
Filippo Cacace, Italy
Pierfrancesco Cacciola, UK
Salvatore Caddemi, Italy
Roberto Caldelli, Italy
Eric Campos-Canton, Mexico
Salvatore Cannella, Italy
Francesco Cannizzaro, Italy
Javier Cara, Spain
Ana Carpio, Spain
Sara Casciati, Italy
Federica Caselli, Italy
Fernando Castanos, Mexico
Carmen Castillo, Spain
Inmaculada T. Castro, Spain
Nicola Caterino, Italy
Gabriele Cazzulani, Italy
Luis Cea, Spain
Miguel Cerrolaza, Venezuela
M. Chadli, France
Gregory Chagnon, France
Ludovic Chamoin, France
Ching-Ter Chang, Taiwan
Michael J. Chappell, UK
Kacem Chehdi, France
Peter N. Cheimets, USA
Xinkai Chen, Japan
Francisco Chicano, Spain
- Hung-Yuan Chung, Taiwan
Simone Cinquemani, Italy
Joaquim Ciurana, Spain
John D. Clayton, USA
Giuseppina Colicchio, Italy
Mario Cools, Belgium
Sara Coppola, Italy
Jean-Pierre Corriou, France
J.-C. Cortés, Spain
Carlo Cosentino, Italy
Paolo Crippa, Italy
Andrea Crivellini, Italy
Erik Cuevas, Mexico
Maria C. Cunha, Portugal
Peter Dabnichki, Australia
Luca D'Acerno, Italy
Weizhong Dai, USA
Andrea Dall'Asta, Italy
Purushothaman Damodaran, USA
Farhang Daneshmand, Canada
Fabio De Angelis, Italy
Samuele De Bartolo, Italy
Pietro De Lellis, Italy
Stefano de Miranda, Italy
Filippo de Monte, Italy
Maria do Rosário de Pinho, Portugal
Michael Defoort, France
Xavier Delorme, France
Angelo Di Egidio, Italy
Ramón I. Diego, Spain
Yannis Dimakopoulos, Greece
Zhengtao Ding, UK
M. Djemai, France
Alexandre B. Dolgui, France
Florent Duchaine, France
George S. Dulikravich, USA
Bogdan Dumitrescu, Romania
Horst Ecker, Austria
Ahmed El Hajjaji, France
Antonio Elipe, Spain
Fouad Erchiqui, Canada
Anders Eriksson, Sweden
R. Emre Erkmen, Australia
Andrea L. Facci, Italy

Giovanni Falsone, Italy
Hua Fan, China
Nicholas Fantuzzi, Italy
Yann Favennec, France
Julien Favier, France
Fiorenzo A. Fazzolari, UK
Giuseppe Fedele, Italy
Roberto Fedele, Italy
Jesus M. Fernandez Oro, Spain
Massimiliano Ferrara, Italy
Francesco Ferrise, Italy
Eric Feulvarch, France
Barak Fishbain, Israel
S. Douwe Flapper, Netherlands
Thierry Floquet, France
Eric Florentin, France
Alessandro Formisano, Italy
Francesco Franco, Italy
Elisa Francomano, Italy
Tomonari Furukawa, USA
Mohamed Gadala, Canada
Matteo Gaeta, Italy
Mauro Gaggero, Italy
Zoran Gajic, Iraq
Erez Gal, Israel
Jaime Gallardo-Alvarado, Mexico
Ugo Galvanetto, Italy
Akemi Gálvez, Spain
Rita Gamberini, Italy
Maria L. Gandarias, Spain
Arman Ganji, Canada
Zhong-Ke Gao, China
Giovanni Garcea, Italy
Jose M. Garcia-Aznar, Spain
Akhil GARG, China
Alessandro Gasparetto, Italy
Oleg V. Gendelman, Israel
Mergen H. Ghayesh, Australia
Agathoklis Giaralis, UK
Anna M. Gil-Lafuente, Spain
Ivan Giorgio, Italy
Gaetano Giunta, Luxembourg
Alessio Gizzi, Italy
Emilio Gómez-Déniz, Spain
David González, Spain
Rama S. R. Gorla, USA
Oded Gottlieb, Israel

Nicolas Gourdain, France
Kannan Govindan, Denmark
Antoine Grall, France
Fabrizio Greco, Italy
Jason Gu, Canada
Federico Guarracino, Italy
José L. Guzmán, Spain
Quang Phuc Ha, Australia
Petr Hájek, Czech Republic
Zhen-Lai Han, China
Thomas Hanne, Switzerland
Xiao-Qiao He, China
Sebastian Heidenreich, Germany
Luca Heltai, Italy
Alfredo G. Hernández-Díaz, Spain
M.I. Herreros, Spain
Eckhard Hitzer, Japan
Paul Honeine, France
Jaromir Horacek, Czech Republic
Muneo Hori, Japan
András Horváth, Italy
Gordon Huang, Canada
Sajid Hussain, Canada
Asier Ibeas, Spain
Orest V. Iftime, Netherlands
Giacomo Innocenti, Italy
Emilio Insfran Pelozo, Spain
Nazrul Islam, USA
Benoit Iung, France
Benjamin Ivorra, Spain
Payman Jalali, Finland
Mahdi Jalili, Australia
Łukasz Jankowski, Poland
Samuel N. Jator, USA
Reza Jazar, Australia
Khalide Jbilou, France
Linni Jian, China
Bin Jiang, China
Zhongping Jiang, USA
Emilio Jiménez Macías, Spain
Ningde Jin, China
Dylan F. Jones, UK
Tamas Kalmar-Nagy, Hungary
Tomasz Kapitaniak, Poland
Julius Kaplunov, UK
Haranath Kar, India
Konstantinos Karamanos, Belgium

Jean-Pierre Kenne, Canada
Chaudry M. Khalique, South Africa
Do Wan Kim, Republic of Korea
Nam-Il Kim, Republic of Korea
Sotiris B. Kotsiantis, Greece
Manfred Krafczyk, Germany
Frederic Kratz, France
Petr Krysl, USA
Jurgen Kurths, Germany
Kyandoghere Kyamakya, Austria
Davide La Torre, Italy
Risto Lahdelma, Finland
Hak-Keung Lam, UK
Jimmy Lauber, France
Antonino Laudani, Italy
Aimé Lay-Ekuakille, Italy
Nicolas J. Leconte, France
Marek Lefik, Poland
Yaguo Lei, China
Kauko Leiviskä, Finland
Thibault Lemaire, France
Stefano Lenci, Italy
Roman Lewandowski, Poland
Panos Liatsis, UAE
Peide Liu, China
Peter Liu, Taiwan
Wanquan Liu, Australia
Alessandro Lo Schiavo, Italy
Jean Jacques Loiseau, France
Paolo Lonetti, Italy
Sandro Longo, Italy
Sebastian López, Spain
Luis M. López-Ochoa, Spain
Ezequiel López-Rubio, Spain
Vassilios C. Loukopoulos, Greece
Gabriel Luque, Spain
Valentin Lychagin, Norway
Antonio Madeo, Italy
José María Maestre, Spain
Fazal M. Mahomed, South Africa
Noureddine Manamanni, France
Didier Maquin, France
Giuseppe Carlo Marano, Italy
Damijan Markovic, France
Francesco Marotti de Sciarra, Italy
Rodrigo Martinez-Bejar, Spain
Benoit Marx, France

Franck Massa, France	Alejandro Ortega-Moñux, Spain	Gerasimos Rigatos, Greece
Paolo Massioni, France	Sergio Ortobelli, Italy	Francesco Ripamonti, Italy
Alessandro Mauro, Italy	Naohisa Otsuka, Japan	Eugenio Roanes-Lozano, Spain
Fabio Mazza, Italy	Erika Ottaviano, Italy	Bruno G. M. Robert, France
Laura Mazzola, Italy	Arturo Pagano, Italy	Ana Maria A. C. Rocha, Portugal
Driss Mehdi, France	Alkis S. Paipetis, Greece	José Rodellar, Spain
Roderick Melnik, Canada	Alessandro Palmeri, UK	Rosana Rodríguez López, Spain
Pasquale Memmolo, Italy	Pasquale Palumbo, Italy	Ignacio Rojas, Spain
Xiangyu Meng, USA	Elena Panteley, France	Alessandra Romolo, Italy
Jose Merodio, Spain	Achille Paolone, Italy	Debasish Roy, India
Alessio Merola, Italy	George A. Papakostas, Greece	Gianluigi Rozza, Italy
Luciano Mescia, Italy	Xosé M. Pardo, Spain	Rubén Ruiz García, Spain
Laurent Mevel, France	Vicente Parra-Vega, Mexico	Antonio Ruiz-Cortes, Spain
Aki Mikkola, Finland	Manuel Pastor, Spain	Ivan D. Rukhlenko, Australia
Giovanni Minafò, Italy	Pubudu N. Pathirana, Australia	Mazen Saad, France
Hiroyuki Mino, Japan	Luis Payá, Spain	Kishin Sadarangani, Spain
Pablo Mira, Spain	Francesco Pellicano, Italy	Andrés Sáez, Spain
Vito Mocella, Italy	Marcello Pellicciari, Italy	Mehrdad Saif, Canada
Roberto Montanini, Italy	Haipeng Peng, China	Salvatore Salamone, USA
Francisco J. Montáns, Spain	Mingshu Peng, China	Nunzio Salerno, Italy
Luiz H. A. Monteiro, Brazil	Zhi-ke Peng, China	Miguel A. Salido, Spain
Gisele Mophou, France	Marzio Pennisi, Italy	Roque J. Saltarén, Spain
Rafael Morales, Spain	Maria Patrizia Pera, Italy	Alessandro Salvini, Italy
Marco Morandini, Italy	Matjaz Perc, Slovenia	Giuseppe Sanfilippo, Italy
Javier Moreno-Valenzuela, Mexico	Francesco Pesavento, Italy	Miguel A. F. Sanjuan, Spain
Simone Morganti, Italy	Dario Piga, Switzerland	Vittorio Sansalone, France
Caroline Mota, Brazil	Antonina Pirrotta, Italy	José A. Sanz-Herrera, Spain
Aziz Moukrim, France	Marco Pizzarelli, Italy	Nickolas S. Sapidis, Greece
Emiliano Mucchi, Italy	Vicent Pla, Spain	Evangelos J. Sapountzakis, Greece
Josefa Mula, Spain	Javier Plaza, Spain	Andrey V. Savkin, Australia
Jose J. Muñoz, Spain	Sébastien Poncet, Canada	Thomas Schuster, Germany
Giuseppe Muscolino, Italy	Jean-Christophe Ponsart, France	Lotfi Senhadji, France
Marco Mussetta, Italy	Mauro Pontani, Italy	Joan Serra-Sagrasta, Spain
Hakim Naceur, France	Radu-Emil Precup, Romania	Gerardo Severino, Italy
Hassane Naji, France	Christopher Pretty, New Zealand	Ruben Sevilla, UK
Mariko Nakano-Miyatake, Mexico	Luca Pugi, Italy	Leonid Shaikhet, Israel
Keivan Navaie, UK	Giuseppe Quaranta, Italy	Hassan M. Shanechi, USA
Dong Ngoduy, New Zealand	Vitomir Racic, Italy	Bo Shen, Germany
Tatsushi Nishi, Japan	Jose Ragot, France	Suzanne M. Shontz, USA
Xesús Nogueira, Spain	Carlo Rainieri, Italy	Babak Shotorban, USA
Ben T. Nohara, Japan	K. Ramamani Rajagopal, USA	Zhan Shu, UK
Mohammed Nouari, France	Alain Rassineux, France	Christos H. Skiadas, Greece
Mustapha Nourelfath, Canada	S.S. Ravindran, USA	Neale R. Smith, Mexico
Roger Ohayon, France	Alessandro Reali, Italy	Delfim Soares Jr., Brazil
Krzysztof Okarma, Poland	Oscar Reinoso, Spain	Alba Sofi, Italy
Mitsuhiro Okayasu, Japan	Nidhal Rezg, France	Francesco Soldovieri, Italy
Calogero Orlando, Italy	Ricardo Riaza, Spain	Raffaele Solimene, Italy

Jussi Sopanen, Finland
Marco Spadini, Italy
Bernardo Spagnolo, Italy
Ruben Specogna, Italy
Vasilios Spitas, Greece
Sri Sridharan, USA
Ivanka Stamova, USA
Salvatore Strano, Italy
Yakov Strelniker, Israel
Sergey A. Suslov, Australia
Thomas Svensson, Sweden
Andrzej Swierniak, Poland
Andras Szekrenyes, Hungary
Yang Tang, Germany
Alessandro Tasora, Italy
Sergio Teggi, Italy
Alexander Timokha, Norway
Gisella Tomasini, Italy
Francesco Tornabene, Italy
Antonio Tornambe, Italy
Javier Martinez Torres, Spain
George Tsiatas, Greece
Antonios Tsourdos, UK
Federica Tubino, Italy
Emilio Turco, Italy
Vladimir Turetsky, Israel

Mustafa Tutar, Spain
Ilhan Tuzcu, USA
Efstratios Tzirtzilakis, Greece
Filippo Ubertini, Italy
Francesco Ubertini, Italy
Hassan Ugail, UK
Giuseppe Vairo, Italy
Eusebio Valero, Spain
Pandian Vasant, Malaysia
Marcello Vasta, Italy
Miguel E. Vázquez-Méndez, Spain
Josep Vehi, Spain
Martin Velasco Villa, Mexico
K. C. Veluvolu, Republic of Korea
Fons J. Verbeek, Netherlands
Franck J. Vernerey, USA
Georgios Veronis, USA
Vincenzo Vespri, Italy
Anna Vila, Spain
Rafael J. Villanueva, Spain
Francisco R. Villatoro, Spain
Uchekukwu E. Vincent, UK
Francesca Vipiana, Italy
Mirko Viroli, Italy
Michael Vynnycky, Sweden
Shuming Wang, China

Yongqi Wang, Germany
Roman Wendner, Austria
Desheng D. Wu, Sweden
Yuqiang Wu, China
Guangming Xie, China
Xuejun Xie, China
Gen Q. Xu, China
Hang Xu, China
Joseph J. Yame, France
Xinggang Yan, UK
Luis J. Yebra, Spain
Peng-Yeng Yin, Taiwan
Qin Yuming, China
Elena Zaitseva, Slovakia
Daniel Zaldivar, Mexico
Vittorio Zampoli, Italy
Ibrahim Zeid, USA
Huaguang Zhang, China
Qingling Zhang, China
Zhao Zhang, China
Jian G. Zhou, UK
Quanxin Zhu, China
Mustapha Zidi, France
Gaetano Zizzo, Italy

Contents

Recent Advances in the Application of Differential Equations in Mechanical Engineering Problems

Rahmat Ellahi , Constantin Fetecau, and Mohsen Sheikholeslami

Volume 2018, Article ID 1584920, 3 pages

Applications of Group Theoretical Methods to Non-Newtonian Fluid Flow Models: Survey of Results

Taha Aziz and F. M. Mahomed

Volume 2017, Article ID 6847647, 43 pages

CuO–Water Nanofluid Magneto-hydrodynamic Natural Convection inside a Sinusoidal Annulus in Presence of Melting Heat Transfer

M. Sheikholeslami, R. Ellahi, and C. Fetecau

Volume 2017, Article ID 5830279, 9 pages

Mathematical Model for Electric Field Sensor Based on Whispering Gallery Modes Using Navier's Equation for Linear Elasticity

Amir R. Ali and Mohamed A. Kamel

Volume 2017, Article ID 9649524, 8 pages

A Comparative Study on Evaluation Methods of Fluid Forces on Cartesian Grids

Taku Nonomura and Junya Onishi

Volume 2017, Article ID 8314615, 15 pages

An Improved Finite Element Meshing Strategy for Dynamic Optimization Problems

Minliang Gong, Aipeng Jiang, Quannan Zhang, Haokun Wang, Junjie Hu, and Yinghui Lin

Volume 2017, Article ID 4829195, 10 pages

A Self-Adaptive Numerical Method to Solve Convection-Dominated Diffusion Problems

Zhi-Wei Cao, Zhi-Fan Liu, Zhi-Feng Liu, and Xiao-Hong Wang

Volume 2017, Article ID 8379609, 13 pages

Finite Element Model for Linear Elastic Thick Shells Using Gradient Recovery Method

Achille Germain Feumo, Robert Nzengwa, and Joseph Nkongho Anyi

Volume 2017, Article ID 5903503, 14 pages

Global Attractor of Thermoelastic Coupled Beam Equations with Structural Damping

Peirong Shi, Danxia Wang, and Weiyi Chen

Volume 2017, Article ID 2908964, 13 pages

Frequency Equation of Flexural Vibrating Cantilever Beam Considering the Rotary Inertial Moment of an Attached Mass

Binghui Wang, Zhihua Wang, and Xi Zuo

Volume 2017, Article ID 1568019, 5 pages

Unsteady Bioconvection Squeezing Flow in a Horizontal Channel with Chemical Reaction and Magnetic Field Effects

Qingkai Zhao, Hang Xu, and Longbin Tao

Volume 2017, Article ID 2541413, 9 pages

Level-of-Service Based Hierarchical Feedback Control Method of Network-Wide Pedestrian Flow

Zhe Zhang, Limin Jia, and Yong Qin

Volume 2016, Article ID 9617890, 14 pages

Editorial

Recent Advances in the Application of Differential Equations in Mechanical Engineering Problems

Rahmat Ellahi ^{1,2} **Constantin Fetecau**³ and **Mohsen Sheikholeslami**⁴

¹*Department of Mathematics & Statistics, IIUI, Islamabad, Pakistan*

²*University of California, Riverside, CA, USA*

³*Academy of Romanian Scientists, 050094 Bucuresti, Romania*

⁴*Department of Mechanical Engineering, Babol Noshirvani University of Technology, Babol, Iran*

Correspondence should be addressed to Rahmat Ellahi; rahmatellahi@yahoo.com

Received 9 January 2018; Accepted 9 January 2018; Published 5 March 2018

Copyright © 2018 Rahmat Ellahi et al. This is an open access article distributed under the Creative Commons Attribution License, which permits unrestricted use, distribution, and reproduction in any medium, provided the original work is properly cited.

Differential equations arising in mechanics, physics, engineering, biological sciences, economics, and other fields of sciences are classified as either linear or nonlinear and formulated as initial and/or boundary value problems. For nonlinear problems, it is mostly difficult to obtain closed-form solutions. However, recent advances made by the guest editors in the application of differential equations in the simulation and modeling of fluids, and particularly in the rheological characteristics of fluids, have motivated us to consider this special issue. Such models are described by several constitutive relations as opposed to one, and as a result they have found wide range of applications in many areas of engineering and sciences, such as mechanical engineering, for example, in solid mechanics; aerospace engineering, for example, in aerodynamics; geophysical/astrophysical phenomena, for example, in weather-forecasting and space-exploration; and biomedical and health sciences, for example, in infectious disease control.

At present, there exist several theoretical and experimental problems in engineering which are still unsolved. The aim of the special issue was to present recent advances at attempts to extend exact, semianalytic, and computational methods for mathematical models in science and engineering, in both the theoretical and applied aspects. In addition, it was also hoped that it will serve as a forum for presenting new and novel developments in the application of differential equations in several branches of science and engineering. Due to vast range of application the investigations on this special issue were still scant. In order to fill this gap, researchers were invited to contribute original research and review articles.

We received a total of 35 submissions for possible publication. We tried to focus on material that either advances the state-of-the-art of experimental, numerical, and theoretical methodologies or extends the bounds of existing methodologies to new contributions in mechanical sciences. After comprehensive peer review only 11 out of 35 submitted papers have been accepted for final publication where the authors are from geographically distributed countries (USA, China, UK, Japan, South Africa, Egypt, Romania, Iran, Pakistan, Cameroon, and Saudi Arabia). This reflects the high impact of the proposed topic, the academic standings of guest editors, and well organization of journal's Editorial Board of this special issue.

In the paper "Mathematical Model for Electric Field Sensor Based on Whispering Gallery Modes Using Navier's Equation for Linear Elasticity," A. R. Ali and M. A. Kamel presented a mathematical model of an electric field sensor based on the whispering gallery mode (WGM). A microsphere is used to measure the applied electric field due to the electrostriction effect. Generally, this electric field induces body or surface forces which deform the sphere changing its size and causing shifts in its WGM transmission spectrum. The applied electric field can be obtained by calculating these shifts. For some dielectric materials the volumetric body force is zero and the deformation due to the pressure forces is obtained using Navier's equation for the linear elasticity at steady state. The sensor characteristics and behavior have been verified by numerical finite element studies.

In the paper "Applications of Group Theoretical Methods to Non-Newtonian Fluid Flow Models: Survey of Results,"

T. Aziz and F. M. Mahomed offered a comprehensive survey of the studies which deal with flow models of non-Newtonian fluids using the Lie group method and conditional symmetries. This method is used to solve differential equations having a sufficient number of symmetries and its application does not depend of the type of equation or the number of variables. Moreover, it can be applied to any class of differential equations. Recently, the Lie symmetry analysis has been widely applied in different areas of mathematics, mechanics, physics, and applied sciences. It became an efficient tool for solving nonlinear problems which are formulated in terms of ordinary or partial differential equations. In order to prove this, the authors illustrated the use of this method on well-known Korteweg-de Vries equation and different motion problems of power-law, Sisko, Jeffrey, Williamson, second grade, modified second grade, power law of second grade, Maxwell, micropolar, Eyring-Powell, Oldroyd-B, third-grade, fourth-grade, couple stress, Phan-Tien-Taner, and Casson fluids or nanofluids. A brief version of the nonclassical symmetry method for partial differential equations is also included and the present survey provides a platform for researchers to apply this method to tackle nonlinear problems of Fluid Mechanics.

In the paper "A Self-Adaptive Numerical Method to Solve Convection-Dominated Diffusion Problems," Z.-W. Cao et al. reported new numerical approach to solve convection-dominated diffusion problems. Common adaptive mesh approaches involve complex adaptive operations but this method was developed as an adaptive mesh method which is free from complex adaptive operations. To solve the time-dependent problem, movement of mesh points is tracked according to the governing equation, while their values are fixed. Adaptivity of the mesh points is automatically achieved during the course of solving the discretized equation. Several verifications have been applied. All of them indicate good agreement.

In the paper "Finite Element Model for Linear Elastic Thick Shells Using Gradient Recovery Method," A. G. Feumo et al. investigated linear elastic thick shells. They employed Finite Element Model (FEM). Simulation on increasing values of the ratio of the shell shows impact of the N-T model especially on transverse stresses because of the significant energy contribution due to the third fundamental form tensor present in the kinematics of this model. The analysis of the thickness ratio shows difference between the classical K-L theory and N-T model when the ratio is greater than 0.099.

In the paper "Unsteady Bioconvection Squeezing Flow in a Horizontal Channel with Chemical Reaction and Magnetic Field Effects," Q. Zhao et al. reported the transient squeezing flow in a channel in existence of magnetic field and chemical reaction. The fully coupled nonlinear systems describing the total mass, momentum, thermal energy, mass diffusion, and microorganisms equations are reduced to a set of ordinary differential equations via a set of new similarity transformations. The detailed analysis illustrating the influences of various physical parameters such as the magnetic, squeezing, and chemical reaction parameters and the Schmidt and Prandtl numbers on the distributions of

temperature and microorganisms as well as the skin friction and the Nusselt number was presented. They found that flow field, temperature, and chemical reaction profiles are significantly influenced by magnetic parameter, heat generation/absorption parameter, and chemical parameter.

In the paper "Level-of-Service Based Hierarchical Feedback Control Method of Network-Wide Pedestrian Flow," Z. Zhang et al. introduced a network-wide pedestrian flow model based on the modified cell transmission model which describes the link flow as ordinary differential equations. Level-of-Service Based Hierarchical Feedback Control Method was applied to control the crowd of a hall and the comparison of the simulation results in the controlled and uncontrolled scenarios shows that the proposed HFCM has the capability to suggest the optimal link inflows and walking speeds in real time to meet the LOS requirement.

In the paper "A Comparative Study on Evaluation Methods of Fluid Forces on Cartesian Grids," T. Nonomura and J. Onishi proposed a simple method for evaluating the forces acting on flows around bodies in the immersed boundary scenario. This method has been developed by employing a novel mesh-face integration method and an extrapolation method for evaluating pressure and shear stresses at the mesh faces, such as the first-order, ghost-cell, or ghost-fluid methods. The present method is, in principle, advantageous over the conventional methods based on control volumes in that pressure and shear stress can be evaluated separately. Moreover, authors have applied the present method to the computation of the drag force acting on a sphere in Stokes flow and have investigated the effects of grid spacing and extrapolation methods on the errors originating from the present force estimation method by using the existing analytical solutions. In addition, we have addressed the computational costs. As a result, the accuracy of the proposed mesh-based scheme has been proven to be comparable to that of the polygon-based scheme, which is commonly adopted in straightforward implementation. This indicates that the proposed scheme works better than the polygon-based one when complex geometries are involved, since its implementation is simple and its computational cost is low. The error sources in the proposed implementation are sourced from (1) the surface area vector of the staircase body shape and (2) the approximated shear stress. Of these, error in the evaluated shear stress dominates and is significant. If the shear stress is appropriately evaluated, the fluid force can be accurately obtained by summing over the mesh faces, because the surface area vector components converge with increasing grid density while the surface area does not. The shear stress is adequately evaluated by the second-order finite differencing scheme with the ghost-cell or ghost-fluid method. Sometimes, it is difficult to estimate the shear stress accurately with this method by its complex shape. It should be noted that this difficulty is caused by the immersed boundary methods themselves and the present idea using the staircase integration does not have difficulty.

In the paper "An Improved Finite Element Meshing Strategy for Dynamic Optimization Problems," M. Gong et al. have studied a finite element mesh-partitioning strategy based on the direct transcription method to solve the optimal

control problem with error estimation on noncollocation point. Firstly, the simultaneous strategy based on the finite element is used to transform the differential and algebraic optimization problems (DAOPs) into large scale nonlinear programming problems. Then, the state variables of the reaction process are obtained by simulating with fixed control variables. The noncollocation points are introduced to compute the error estimates of the state variables at noncollocation points. Finally, in order to improve the computational accuracy with less finite element, moving finite element strategy was used for dynamically adjusting the length of finite element appropriately to satisfy the set margin of error. The proposed strategy is applied to two classical control problems and a large scale reverse osmosis seawater desalination process. Computing result shows that the proposed strategy can effectively reduce the computing effort with satisfied accuracy for dynamic optimization problems.

In the paper “CuO–Water Nanofluid Magnetohydrodynamic Natural Convection inside a Sinusoidal Annulus in Presence of Melting Heat Transfer,” M. Sheikholeslami et al. examined the impact of nanofluid natural convection due to magnetic field in existence of melting heat transfer by means of CVFEM. The KKL model is taken into account to obtain properties of CuO–H₂O nanofluid. Roles of melting parameter (δ), CuO–H₂O volume fraction (ϕ), Hartmann number (Ha), and Rayleigh (Ra) number are depicted in outputs. Results depict that temperature gradient improves with rise of Rayleigh number and melting parameter. Nusselt number detracts with rise of Ha. At the end, a comparison as a limiting case of the considered problem with the existing studies is made and found in good agreement. It is observed that adding magnetic field makes the temperature gradient reduce due to domination of conduction mechanism in high Hartmann number.

In the paper “Global Attractor of Thermoelastic Coupled Beam Equations with Structural Damping,” P. Shi et al. have inspected the existence of a global attractor for a class of n -dimension thermoelastic coupled beam equations with structural damping within bounded domain of both continuous nonnegative nonlinear real functions. They used classical Galerkin method to establish the existence and uniqueness of regular solution to problem. Obtained results have been validated by several examples.

In the paper “Frequency Equation of Flexural Vibrating Cantilever Beam Considering the Rotary Inertial Moment of an Attached Mass,” B. Wang et al. addressed the derivation of the frequency equation of flexural vibrating cantilever beam considering the bending moment generated by an additional mass at the free end of beam, not just the shear force. It is a transcendental equation with two unambiguous physical meaning parameters which can be defined as the ratio of rotary mass moment of inertia and the ratio of the mass, respectively. It is found that as the ratio of rotary mass moment of inertia increases, the natural frequency climbs. Even a little increment of the ratio may cause higher variance between considering and not considering the rotary mass moment of inertia, especially for the high natural frequency. The results show that the inertial moment of the mass has the significant effect on the natural frequency and the shape

mode. And it is more reasonable to use this frequency equation to analyze vibration and measure modulus.

Acknowledgments

The guest editorial team would like to thank all authors for contributing their original work to this special issue. A large number of papers could not be accommodated: while the submission was technically correct, they were inappropriate for the scope of this special issue. The editorial team would also like to thank all anonymous reviewers for their valuable input, efforts, and cooperation during review process. We also acknowledge the entire staff of journal’s Editorial Board for providing us with their support regarding this special issue. We hope that the scientists who are working in the same regime not only will enjoy this special issue but would also appreciate the efforts devoted to it by the entire team.

*Rahmat Ellahi
Constantin Fetecau
Mohsen Sheikholeslami*

Review Article

Applications of Group Theoretical Methods to Non-Newtonian Fluid Flow Models: Survey of Results

Taha Aziz¹ and F. M. Mahomed^{2,3}

¹*School of Computer, Statistical and Mathematical Sciences, North-West University, Potchefstroom Campus, Private Bag X6001, Potchefstroom 2531, South Africa*

²*DST-NRF Centre of Excellence in Mathematical and Statistical Sciences, Johannesburg, South Africa*

³*School of Computer Science and Applied Mathematics, University of the Witwatersrand, Johannesburg, Wits 2050, South Africa*

Correspondence should be addressed to Taha Aziz; tahaaziz77@yahoo.com

Received 27 February 2017; Revised 2 May 2017; Accepted 29 May 2017; Published 30 August 2017

Academic Editor: Constantin Fetecau

Copyright © 2017 Taha Aziz and F. M. Mahomed. This is an open access article distributed under the Creative Commons Attribution License, which permits unrestricted use, distribution, and reproduction in any medium, provided the original work is properly cited.

The present review is intended to encompass the applications of symmetry based approaches for solving non-Newtonian fluid flow problems in various physical situations. Works which deal with the fundamental science of non-Newtonian fluids that are analyzed using the Lie group method and conditional symmetries are reviewed. We provide the mathematical modelling, the symmetries deduced, and the solutions obtained for all the models considered. This survey includes, as far as possible, all the articles published until 2015. Only papers published by a process of peer review in archival journals are reviewed and are grouped together according to the specific non-Newtonian models under investigation.

1. Introduction

The scientific and applications appeal of non-Newtonian fluid mechanics has necessitated a deeper study of its theory. There has been considerable focus in the study of the physical behavior and properties of non-Newtonian fluids over the past several decades. One particular reason for this interest is the wide range of applications of such models, both natural and industrial. These applications range from the extraction of crude oil from petroleum products to the polymer industry. Spin coating is a classic example where the coating fluids are typically non-Newtonian. A non-Newtonian fluid is one whose flow curve (shear stress versus shear rate) is nonlinear or does not pass through the origin, that is, where the apparent viscosity, shear stress divided by shear rate, is not constant at a given temperature and pressure but is dependent on flow conditions such as flow geometry and shear rate and sometimes even on the kinematic history of the fluid element under consideration. Such fluids may be conveniently grouped into three general classes as follows:

(1) Fluids for which the rate of shear at any point is determined only by the value of the shear stress at that

point at that instant: these fluids are variously known as *time independent*, *purely viscous*, *inelastic*, or *generalized Newtonian fluids* (GNF).

(2) More complex fluids on which the relation between shear stress and shear rate depends: in addition, based upon the duration of shearing and their kinematic history, they are known as *time-dependent fluids*.

(3) Those substances exhibiting characteristics of both ideal fluids and elastic solids and showing partial elastic recovery, after deformation, are categorized as *viscoelastic fluids*.

Due to the complex physical structure of non-Newtonian fluids, there is not a single constitutive expression which describes the physical and mathematical properties of all nonlinear fluids. For this reason, many non-Newtonian fluid models for constitutive equations are available with most of them being empirical and semiempirical.

There are three diverse motivations for analyzing the flow behavior of non-Newtonian fluids: firstly, to extend the results of the flow models of Newtonian fluids to various classes of non-Newtonian fluids; secondly, to study the flow structure of non-Newtonian fluids as they occur in industry

under conditions which arise there; thirdly, to construct solutions of complicated nonlinear equations as exact solutions: these, when reported, facilitate the verification of complicated numerical codes and are also helpful in stability analysis. Consequently, the exact (closed-form) solutions of the flow models of non-Newtonian fluids are physically very significant. The most challenging task that we need to address when dealing with flow problems of non-Newtonian fluids is that the governing equations of these models are of a high order, nonlinear, and complicated in nature. Such fluids are modelled by constitutive equations which vary greatly in complexity. Thus, the resulting nonlinear equations are not easy to solve exactly. Several methods have been developed in recent years to obtain the solutions of these fluid models. Some of the techniques are the variational iteration method, Adomian decomposition method, homotopy analysis method, homotopy perturbation method, simplest equation method, semi-inverse variational method, and the exponential function method, amongst others. There are also the Lie symmetry and conditional symmetry group methods which are the main focus of this review.

Lie symmetry methods for differential equation were originated in the 1870s and were introduced by the Norwegian mathematician Marius Sophus Lie. Lie's theory is useful for solving differential equations that admit sufficient number of symmetries in a systematic way. Lie group methods are capable of handling a large number of equations. The application of this method neither depends on the type of the equation nor on the number of variables involved in the equations. Lie's theory is a general procedure which can be applied to any class of differential equations. However, if one peruses the literature on Lie's methods, we observe that this method and its extensions have rarely been applied in comparison with the wealth of differential equations in practical and theoretical problems.

The Lie symmetries of differential equations naturally form a group. Such groups are called Lie groups and are invertible point transformations of both the dependent and independent variables of the differential equations. Lie pointed out in his work that these groups are of great importance in understanding and constructing solutions of differential equations. Lie demonstrated that many techniques for finding solutions can be unified and extended by considering symmetry groups. Today, the Lie symmetry approach to differential equations is widely applied in various fields of mathematics, mechanics, physics, and the applied sciences and many results published in these areas demonstrate that Lie's theory is an efficient tool for solving nonlinear problems formulated in terms of differential equations. The primary objective of the Lie symmetry analysis advocated by Lie is to find one or several parameters of local continuous transformations leaving the equations invariant and then exploit them to obtain reductions and the so-called invariant or similarity solutions, and the usefulness of this approach has been widely illustrated by several researchers in different contexts. An extension of this approach is the conditional symmetry approach which is also very useful.

Motivated by the above-mentioned facts, the purpose of the present survey is to provide a detailed review of those

studies which deal with the flow models of non-Newtonian fluids and solved using the group theoretic approaches. We have presented the mathematical modelling of each of the problem under review together with the symmetries deduced and the solutions obtained for that particular problem.

2. Symmetry Methods for Differential Equations

In this section, we briefly discuss the main aspects of the Lie symmetry method for differential equations with some words on conditional or nonclassical symmetries.

2.1. Symmetry Transformations of Differential Equations. A transformation under which a differential equation remains invariant (unchanged) is called a symmetry transformation of the differential equation.

Consider a k th order ($k \geq 1$) system of differential equations

$$F^\sigma(x, u, u_{(1)}, \dots, u_{(k)}) = 0, \quad \sigma = 1, \dots, m, \quad (1)$$

where $u = (u^1, \dots, u^m)$, called the dependent variable, is a function of the independent variable $x = (x^1, \dots, x^n)$ and $u_{(1)}, u_{(2)}$ up to $u_{(k)}$ are the collection of all first-order and second-order up to k th order derivatives of u .

A transformation of the variables x and u , namely,

$$\begin{aligned} \bar{x}^i &= f^i(x, u), \\ \bar{u}^\alpha &= g^\alpha(x, u), \end{aligned} \quad (2)$$

$$i = 1, \dots, n; \quad \alpha = 1, \dots, m,$$

is called a symmetry transformation of system (1) if (1) is form-invariant in the new variables \bar{x} and \bar{u} ; that is,

$$F^\sigma(\bar{x}, \bar{u}, \bar{u}_{(1)}, \dots, \bar{u}_{(k)}) = 0, \quad \sigma = 1, \dots, m, \quad (3)$$

whenever

$$G^\sigma(x, u, u_{(1)}, \dots, u_{(k)}) = 0, \quad \sigma = 1, \dots, m. \quad (4)$$

For example, the first-order Abel equation of the second kind

$$f \frac{df}{dy} = y^3 + yf \quad (5)$$

has symmetry transformations

$$\begin{aligned} \bar{y} &= ay, \\ \bar{f} &= a^2 f, \end{aligned} \quad (6)$$

$$a \in \mathbb{R}^+.$$

2.2. Lie Symmetry Method for Partial Differential Equations. Here we discuss the classical Lie symmetry method to obtain all possible symmetries of a system of partial differential equations.

Let us consider a p th order system of partial differential equations in n independent variables $x = (x_1, \dots, x_n)$ and m dependent variable $u = (u_1, \dots, u_m)$, namely.

$$E(x, u, u_{(1)}, \dots, u_{(p)}) = 0, \quad (7)$$

where $u_{(k)}^\alpha$, $1 \leq k \leq p$, denotes the set of all k th order derivative of u , with respect to the independent variables defined by

$$u_{(k)}^\alpha = \left\{ \frac{\partial^k u}{\partial x_{i_1} \dots \partial x_{i_k}} \right\}, \quad (8)$$

with

$$1 \leq i_1, i_2, \dots, i_k \leq n. \quad (9)$$

For finding the symmetries of (7), we first construct the group of invertible transformations depending on the real parameter a , which leaves (7) invariant; namely,

$$\begin{aligned} \bar{x}_1 &= f^1(x, u, a), \\ &\vdots \\ \bar{x}_n &= f^n(x, u, a), \\ \bar{u}^\alpha &= g^\alpha(x, u, a). \end{aligned} \quad (10)$$

The above transformations have the closure property, are associative, admit inverses and identity transformation, and are said to form a one-parameter group.

Since a is a small parameter, transformations (10) can be expanded in terms of a series expansion as

$$\begin{aligned} \bar{x}_1 &= x_1 + a\xi_1(x, u) + O(a^2), \\ &\vdots \\ \bar{x}_n &= x_n + a\xi_n(x, u) + O(a^2), \\ \bar{u}_1 &= u_1 + a\eta_1(x, u) + O(a^2), \\ &\vdots \\ \bar{u}_m &= u_m + a\eta_m(x, u) + O(a^2). \end{aligned} \quad (11)$$

Transformations (11) are the infinitesimal transformations and the finite transformations are found by solving the Lie equations

$$\begin{aligned} \xi_1(\bar{x}, \bar{u}) &= \frac{d\bar{x}_1}{da}, \\ &\vdots \\ \xi_n(\bar{x}, \bar{u}) &= \frac{d\bar{x}_n}{da}, \\ \eta(\bar{x}, \bar{u}) &= \frac{d\bar{u}}{da}, \end{aligned} \quad (12)$$

with the initial conditions

$$\begin{aligned} \bar{x}_1(\bar{x}, \bar{u}, a)|_{a=0} &= x_1, \\ &\vdots \\ \bar{x}_n(\bar{x}, \bar{u}, a)|_{a=0} &= x_n, \\ \bar{u}_1(\bar{x}, \bar{u}, a)|_{a=0} &= u_1, \\ &\vdots \\ \bar{u}_m(\bar{x}, \bar{u}, a)|_{a=0} &= u_m, \end{aligned} \quad (13)$$

where $\bar{x} = (\bar{x}_1, \dots, \bar{x}_n)$ and $\bar{u} = (\bar{u}_1, \dots, \bar{u}_m)$.

Transformations (10) can be denoted by the Lie symmetry generator

$$X = \xi^i(x, u) \frac{\partial}{\partial x^i} + \eta^\alpha(x, u) \frac{\partial}{\partial u^\alpha}, \quad (14)$$

where the functions ξ^i ($i = 1, \dots, n$) and η^α ($\alpha = 1, \dots, m$) are the coefficient functions of the operator X .

Operator (14) is a symmetry generator of (7) if

$$X^{[p]}E|_{E=0} = 0, \quad (15)$$

where $X^{[p]}$ represents the p th prolongation of the operator X and is given by

$$\begin{aligned} X^{[1]} &= X + \sum_{i=1}^n \zeta_{x_i}^\alpha \frac{\partial}{\partial u_{x_i}}, \\ X^{[2]} &= X^{[1]} + \sum_{i=1}^n \sum_{j=1}^n \zeta_{x_i x_j}^\alpha \frac{\partial^2}{\partial u_{x_i x_j}}, \\ &\vdots \\ X^{[p]} &= X^{[1]} + \dots + X^{[p-1]} \\ &\quad + \sum_{i_1=1}^n \dots \sum_{i_p=1}^n \zeta_{x_{i_1} \dots x_{i_p}}^\alpha \frac{\partial^p}{\partial u_{x_{i_1} \dots x_{i_p}}}, \end{aligned} \quad (16)$$

with

$$\begin{aligned} u_{x_i} &= \frac{\partial u}{\partial x_i}, \\ u_{x_{i_1} \dots x_{i_k}} &= \frac{\partial^k u}{\partial x_{i_1} \dots \partial x_{i_k}}. \end{aligned} \quad (17)$$

In the above equations, the additional coefficient functions satisfy the following relations:

$$\begin{aligned} \zeta_{x_i}^\alpha &= D_{x_i}(\eta) - \sum_{j=1}^n u_{x_j} D_{x_i}(\xi^j), \\ \zeta_{x_i x_j}^\alpha &= D_{x_j}(\eta^{x_i}) - \sum_{k=1}^n u_{x_i x_k} D_{x_j}(\xi^k), \\ &\vdots \\ \zeta_{x_{i_1} \dots x_{i_p}}^\alpha &= D_{x_{i_p}}(\eta^{x_{i_1} \dots x_{i_{p-1}}}) - \sum_{j=1}^n u_{x_{i_1} \dots x_{i_{p-1}} x_j} D_{x_{i_p}}(\xi^j), \end{aligned} \tag{18}$$

where D_{x_i} denotes the total derivative operator and is given by

$$D_{x_i} = \frac{\partial}{\partial x_i} + u_{x_i} \frac{\partial}{\partial u} + \sum_{j=1}^n u_{x_i x_j} \frac{\partial}{\partial x_j} + \dots \tag{19}$$

The determining equation (15) results in a polynomial in terms of the derivatives of the dependent variable u . After separation of (15) with respect to the partial derivatives of u and their powers, one obtains an overdetermined system of linear homogeneous partial differential equations for the coefficient functions ξ^i 's and η^α 's. By solving the overdetermined system, one has the following cases:

- (i) There is no symmetry, which means that the Lie point symmetry generators given by ξ^i and η^α are all zero.
- (ii) The point symmetry has $r \neq 0$ arbitrary constants; in this case, we obtain r generators of symmetry which forms an r -dimensional Lie algebra of point symmetries.
- (iii) The point symmetry admits some finite number of arbitrary constants and arbitrary functions, in which case we obtain an infinite-dimensional Lie algebra.

2.3. Example on the Lie Symmetry Method. Here we illustrate the use of the Lie symmetry method on the well-known Korteweg-de Vries equation given by

$$f_t + f_{xxx} + ff_x = 0. \tag{20}$$

We seek for an operator of the form

$$X = \xi^1(t, x, f) \frac{\partial}{\partial t} + \xi^2(t, x, f) \frac{\partial}{\partial x} + \eta(t, x, f) \frac{\partial}{\partial f}. \tag{21}$$

Equation (21) is a symmetry generator of (20) if

$$X^{[3]}(f_t + f_{xxx} + ff_x)|_{f_t = -f_{xxx} - ff_x} = 0. \tag{22}$$

The third prolongation in this case is

$$X^{[3]} = X + \zeta^t \frac{\partial}{\partial f_t} + \zeta^x \frac{\partial}{\partial f_x} + \zeta^{xxx} \frac{\partial}{\partial f_{xxx}}. \tag{23}$$

Therefore, the determining equation (22) becomes

$$\left(\zeta^t + \zeta^{xxx} + f_x \zeta + f \zeta^x \right) \Big|_{f_t = -f_{xxx} - ff_x} = 0. \tag{24}$$

Using the definitions of ζ^t , ζ^x , and ζ^{xxx} into (24) lead to an overdetermined system of linear homogenous system of partial differential equations given by

$$\begin{aligned} f_{txx} f_x : \xi_f^1 &= 0, \\ f_{txx} : \xi_x^1 &= 0, \\ f_{xx}^2 : \xi_f^2 &= 0, \\ f_{xx} f_x : \eta_{ff} &= 0, \\ f_{xx} : 3\eta_{xf} - 3\xi_{xx}^2 &= 0, \\ f_t : -3\xi_x^2 + \xi_t^1 &= 0, \\ f_x : \eta - f\xi_x^2 + 3\eta_{xxf} - \xi_{xxf}^2 + f\xi_t^1 - \xi_t^2 &= 0, \\ I : f\eta_x + \eta_{xxx} + \eta_t &= 0. \end{aligned} \tag{25}$$

By solving system (25), we find four Lie point symmetries which are generated by the following generators:

$$\begin{aligned} X_1 &= \frac{\partial}{\partial t}, \\ X_2 &= \frac{\partial}{\partial x}, \\ X_3 &= t \frac{\partial}{\partial x} + \frac{\partial}{\partial f}, \\ X_4 &= -3t \frac{\partial}{\partial t} - x \frac{\partial}{\partial x} + 2f \frac{\partial}{\partial f}. \end{aligned} \tag{26}$$

2.4. Nonclassical Symmetry Method for Partial Differential Equations. Here we present a brief version of the nonclassical symmetry method for partial differential equations. In last few years, the interest in nonclassical group method has increased. There are mathematical problems appearing in applications that do not admit Lie point symmetries but have nonclassical symmetries. Therefore, this approach is helpful in obtaining exact solutions.

We begin by considering a k th order partial differential equation

$$G(x, u, u^{(1)}, \dots, u^{(k)}) = 0, \tag{27}$$

in n independent variables $x = (x_1, \dots, x_n)$ and one dependent variable u , with $u^{(k)}$ denoting the derivatives of the u with respect to x up to order k defined by

$$u^{(k)} = \left[\frac{\partial^k u}{\partial x_{i_1} \dots \partial x_{i_k}} \right], \tag{28}$$

with

$$1 \leq i_1, \dots, i_k \leq n. \tag{29}$$

Suppose that \mathbf{X} is a field of vectors which consists of dependent and independent variables:

$$\mathbf{X} = \xi^1(x, u) \frac{\partial}{\partial x_1} + \dots + \xi^n(x, u) \frac{\partial}{\partial x_n} + \eta(x, u) \frac{\partial}{\partial u}, \quad (30)$$

where ξ^i and η are the coefficient functions of the vector field \mathbf{X} .

Suppose that the vector field \mathbf{X} is the nonclassical symmetry generator of (27). Then the solution

$$u = f(x_1, x_2, \dots, x_n) \quad (31)$$

of (27) is an invariant solution of (27) under a one-parameter subgroup generated by \mathbf{X} if the condition

$$\Phi(x, u) = \eta(x, u) - \sum_{i=1}^n \xi^i(x, u) \frac{\partial u^\alpha}{\partial x_i} = 0 \quad (32)$$

holds together with (27). The condition given in (32) is known as an *invariant surface condition*. Thus, the invariant solution of (27) is obtained by solving the invariant surface condition (32) together with (27).

For (27) and (32) to be compatible, the k th prolongation $\mathbf{X}^{[k]}$ of the generator \mathbf{X} must be tangent to the intersection of G and the surface Φ ; that is,

$$\mathbf{X}^{[k]}(G)|_{G \cap \Phi} = 0. \quad (33)$$

If (32) is satisfied, then the operator \mathbf{X} is called a nonclassical infinitesimal symmetry of the k th order partial differential equation (27).

For the case of two independent variables, t and y , two cases arise, namely, when $\xi^1 \neq 0$ and $\xi^1 = 0$.

When $\xi^1 \neq 0$, the operator is

$$\mathbf{X} = \frac{\partial}{\partial t} + \xi^2(t, y, u) \frac{\partial}{\partial y} + \eta(t, y, u) \frac{\partial}{\partial u}, \quad (34)$$

and thus

$$\Phi = u_t - \eta + \xi^2 u_y = 0 \quad (35)$$

is the invariant surface condition.

When $\xi^1 = 0$, the operator is

$$\mathbf{X} = \frac{\partial}{\partial y} + \eta(t, y, u) \frac{\partial}{\partial u}, \quad (36)$$

and hence

$$\Phi = u_y - \eta = 0 \quad (37)$$

is the invariant surface condition.

2.5. Example on the Nonclassical Symmetry Method. We illustrate the use of the nonclassical symmetry method on the well-known heat equation

$$u_t = u_{xx}. \quad (38)$$

Consider the infinitesimal operator

$$X = \xi(t, x, u) \frac{\partial}{\partial x} + \tau(t, x, u) \frac{\partial}{\partial t} + \eta(t, x, u) \frac{\partial}{\partial u}. \quad (39)$$

The invariant surface condition is

$$\begin{aligned} \Phi(t, x, u) &= \eta(t, x, u) - \xi(t, x, u) \frac{\partial u}{\partial x} - \tau(t, x, u) \frac{\partial u}{\partial t} \\ &= 0. \end{aligned} \quad (40)$$

One can assume without loss of generality that $\tau = 1$, so that (40) takes the form

$$\Phi(t, x, u) = \eta(t, x, u) - \xi(t, x, u) \frac{\partial u}{\partial x} - \frac{\partial u}{\partial t} = 0. \quad (41)$$

The nonclassical symmetries determining equations are

$$X^{[2]}u_t - u_{xx}|_{\text{Eq.(38)=0,}\Phi=0} = 0, \quad (42)$$

where $X^{[2]}$ is the usual third prolongation of operator X .

Applying the method to the heat PDE (38) with $\tau = 1$ yields

$$\begin{aligned} \xi &= \xi(x, t), \\ \eta &= A(x, t)u + B(x, t), \end{aligned} \quad (43)$$

where

$$\begin{aligned} A_t + 2A\xi_x - A_{xx} &= 0, \\ B_t + 2B\xi_x - B_{xx} &= 0, \\ \xi_t + 2\xi\xi_x - \xi_{xx} + 2A_x &= 0. \end{aligned} \quad (44)$$

The solution of system of (44) gives the following nonclassical infinitesimals:

$$\begin{aligned} \xi &= -\frac{w_t v - w v_t}{w_x v - w v_x}, \\ \tau &= 1, \end{aligned} \quad (45)$$

$$\eta = \frac{v_t w_x - v_x w_t}{w_x v - w v_x} (u - u_0) + \xi f_x + f_t,$$

where w , v , and f satisfy the heat equation.

3. Power-Law Fluid Flow Problems

In this section, all those problems dealing with the flow of a power-law fluid and solved by using the Lie symmetry approach are discussed.

The Cauchy stress tensor for a power-law fluid is written as

$$\mathbf{T} = -p\mathbf{I} + \mu \left(\left| \sqrt{\frac{1}{2} \text{tr} \mathbf{A}_1^2} \right|^{n-1} \right) \mathbf{A}_1, \quad (46)$$

where p is the fluid pressure, \mathbf{I} is the identity tensor, μ is the dynamic viscosity of the fluid, tr is the trace, and the first Rivlin-Ericksen tensor \mathbf{A}_1 is given by

$$\mathbf{A}_1 = (\text{grad } \mathbf{V}) + (\text{grad } \mathbf{V})^T, \quad (47)$$

in which \mathbf{V} is the fluid velocity. It should be noted that n is the power-law index. If $n = 1$, (46) represents a viscous fluid. Furthermore, (46) represents shear thinning behavior when $n < 1$ and shear thickening for $n > 1$.

3.1. Solution of the Rayleigh Problem for a Power-Law Non-Newtonian Conducting Fluid via Group Method [1]. Abdel-Malek et al. [1] studied the magnetic Rayleigh problem where a semi-infinite plate is given an impulsive motion and thereafter moves with constant velocity in a non-Newtonian power-law fluid of infinite extent. The governing nonlinear model was solved by means of the Lie group approach.

The governing problem describing the flow model [1] is given by

$$\frac{\partial u}{\partial t} - \gamma \frac{\partial}{\partial y} \left\{ \left[\left(\frac{\partial u}{\partial y} \right)^2 \right]^{(n-1)/2} \frac{\partial u}{\partial y} \right\} + MH^2 u = 0, \quad (48)$$

with the boundary and initial conditions

$$\begin{aligned} u(0, t) &= V, \\ u(\infty, t) &= 0, \\ t &> 0, \\ u(y, 0) &= 0, \quad y > 0. \end{aligned} \quad (49)$$

The method of solution employed in [1] depends on the application of a one-parameter group of transformations to the partial differential equation (48). The one-parameter group, which transforms the PDE (48) and the boundary conditions (49), is of the form [1]

$$\begin{aligned} \bar{y} &= (h^t)^{1/(n+1)} y, \\ \bar{t} &= h^t t, \\ \bar{u} &= u, \\ \bar{H} &= \left(\frac{1}{\sqrt{h^t}} \right) H. \end{aligned} \quad (50)$$

Under transformations (50), the two independent variables reduce by one and the partial differential equation (48) is transformed into an ordinary differential equation. The reduced ordinary differential equation was then solved numerically.

3.2. Invariant Solutions of the Unidirectional Flow of an Electrically Charged Power-Law Non-Newtonian Fluid over a Flat Plate in Presence of a Transverse Magnetic Field [2]. Wafo Soh [2] investigated a boundary value problem for a nonlinear diffusion equation arising in the study of a charged power-law non-Newtonian fluid through a time-dependent transverse

magnetic field. Two families of exact invariant solutions were obtained by use of the Lie symmetry method.

The governing equation describing the flow model is given by [2]

$$\frac{\partial u}{\partial t} - n\gamma \left(\frac{\partial u}{\partial y} \right)^{n-1} \frac{\partial^2 u}{\partial y^2} + MH^2(t) u = 0. \quad (51)$$

The relevant boundary and initial conditions are

$$\begin{aligned} u(0, t) &= V(t), \quad t > 0, \\ u(\infty, t) &= 0, \quad t > 0, \\ u(y, 0) &= 0, \quad y > 0. \end{aligned} \quad (52)$$

The symmetry Lie algebra of PDE (51) is five-dimensional and is spanned by the operators [2]

$$\begin{aligned} X_1 &= \frac{\partial}{\partial y}, \\ X_2 &= y \frac{\partial}{\partial y} + \frac{n+1}{n-1} u \frac{\partial}{\partial u}, \quad n \neq 1, \\ X_3 &= L'_2(t) \frac{\partial}{\partial u}, \\ X_4 &= \frac{1}{L'_n(t)} \frac{\partial}{\partial t} - \frac{MH^2}{L'_n(t)} u \frac{\partial}{\partial u}, \\ X_5 &= \frac{L_n(t)}{L'_n(t)} \frac{\partial}{\partial t} - \left[MH^2 \frac{L_n(t)}{L'_n(t)} + \frac{1}{n-1} \right] u \frac{\partial}{\partial u}, \end{aligned} \quad (53)$$

$n \neq 1,$

where

$$L_n(t) = \int_0^t d\tau e^{(1-n)M \int_0^\tau H^2(\lambda) d\lambda}. \quad (54)$$

With the use of the above symmetries, the group invariant solution for the PDE (51) found in [2] is

$$u(y, t) = L_n^{1/(1-n)}(t) L'_2(t) \psi(y), \quad (55)$$

with $\psi(y)$ given by

$$\begin{aligned} \psi(y) &= \left[\left(\frac{n-1}{n+1} \right) \left(\frac{1+n}{2\gamma n(1-n)} \right)^{1/(1+n)} y + 1 \right]^{(n+1)/(n-1)}. \end{aligned} \quad (56)$$

3.3. Unsteady Boundary Layer Flow of Power-Law Fluid on Stretching Sheet Surface [3]. Yürüsoy [3] treated the unsteady boundary layer equations of a power-law fluid over a stretching sheet. By the use of similarity transformations, the governing system of partial differential equations reduced to a nonlinear ordinary differential equation system. Finally, the resulting system of reduced ordinary differential equations was solved using a combination of the Runge-Kutta algorithm and shooting technique.

The governing equations describing the flow model [3] are

$$\begin{aligned} \frac{\partial u}{\partial x} + \frac{\partial v}{\partial y} &= 0, \\ \frac{\partial u}{\partial t} + u \frac{\partial u}{\partial x} + v \frac{\partial u}{\partial y} &= (2m + 1) 2^m \left| \frac{\partial u}{\partial y} \right|^{2m} \frac{\partial^2 u}{\partial y^2} + \frac{\partial U}{\partial t} \\ &+ U \frac{\partial U}{\partial x}, \end{aligned} \quad (57)$$

where u and v are the velocity components inside the boundary layer and $U(x, t)$ is the velocity outside the boundary layer.

The boundary conditions for flow over a stretching sheet are

$$\begin{aligned} u(x, 0, t) &= A(x, t), \\ v(x, 0, t) &= 0, \\ u(x, \infty, t) &= 0. \end{aligned} \quad (58)$$

By use of the Lie group method, the similarity transformations for the reduction of the above system of PDEs are given by [3]

$$\begin{aligned} \xi &= yt^{(2m-1)/(2m+2)} x^{-m/(m+1)}, \\ v &= x^{m/(m+1)} t^{-(4m+1)/(2m+2)} g(\xi), \\ u &= \frac{x}{t} f(\xi), \\ A(x, t) &= \lambda \frac{x}{t}. \end{aligned} \quad (59)$$

Transformation (59) transforms the two-dimensional unsteady boundary layer equation problem into ordinary differential equations. The reduced ordinary differential equations have been solved numerically using a variable step size Runge-Kutta subroutine combined with a shooting technique.

3.4. Axisymmetric Spreading of a Thin Power-Law Fluid under Gravity on a Horizontal Plane [4]. Nguetchue and Momoniat [4] studied a nonlinear PDE modelling the axisymmetric spreading under gravity of a thin power-law fluid on a horizontal surface. The model equation was reduced to a nonlinear second-order ordinary differential equation for the spatial variable. Then Lie symmetry analysis applied to the nonlinear ordinary differential equation enabled its linearization and solution.

The equation modelling the height of a thin power-law fluid film on a horizontal plane in presence of gravity is given by [4]

$$\frac{\partial h}{\partial t} = \frac{1}{(\beta + 1)x} \frac{\partial}{\partial x} \left[xh^{\beta+1} \left(\frac{\partial h}{\partial x} \right)^{\beta-1} \right]. \quad (60)$$

Here $h(x, t)$ is the film height and β is the power-law fluid parameter. The Lie point symmetry generator for the PDE (60) is [4]

$$X = [(1 - \beta)At + B] \frac{\partial}{\partial t} + Ah \frac{\partial}{\partial h}. \quad (61)$$

The invariant solution of PDE (60) corresponding to the symmetry generator (61) found in [4] is

$$h(x, t) = \frac{3A^{1/3}x^{2/3}}{2(3At - B)^{1/3}}. \quad (62)$$

3.5. Symmetry Reductions of a Flow with Power-Law Fluid and Contaminant-Modified Viscosity [5]. Moitsheki et al. [5] have analyzed a system dealing with nonreactive pollutant transport along a single channel. Constitutive equations obeying a power-law fluid are utilized in the description of the mathematical problem. Invariant solutions which satisfy physical boundary conditions have been constructed using the Lie group approach.

The dimensionless governing equations that describe the flow model are [5]

$$\begin{aligned} \frac{\partial u}{\partial t} &= K + M \frac{\partial}{\partial y} \left[c^\lambda \left(\frac{\partial u}{\partial y} \right)^{n-1} \frac{\partial u}{\partial y} \right], \\ \frac{\partial c}{\partial t} &= \frac{1}{R} \frac{\partial}{\partial y} \left(c^\lambda \frac{\partial c}{\partial y} \right) + S(y, t). \end{aligned} \quad (63)$$

Here R is the Schmidt number and K is the imposed constant pressure axial gradient. The Lie point symmetries of the above system corresponding to different forms of the source term $S(y, t)$ are given in Table 1 of [5]. The invariant solutions of system (63) found in [5] are of the form

$$\begin{aligned} u(y, t) &= Kt + 4\gamma_1 R \gamma_3 \left[\frac{1}{2} \cos \left(\frac{y + c_2}{2c_1} \right) \sin \left(\frac{y + c_2}{2c_1} \right) \right. \\ &\quad \left. + \left(\frac{y + c_2}{4c_1} \right) \right] + c_3, \\ c(y, t) &= \frac{t}{2\gamma_2 R} \sec^2 \left(\frac{y + c_2}{2c_1} \right). \end{aligned} \quad (64)$$

3.6. Scaling Group Transformation under the Effect of Thermal Radiation Heat Transfer of a Non-Newtonian Power-Law Fluid over a Vertical Stretching Sheet with Momentum Slip Boundary Condition [6]. An analysis has been conducted to study the problem of heat transfer of a power-law fluid over a vertical stretching sheet with slip boundary condition by Mutlag et al. [6]. The partial differential equations governing the physical model have been converted into a set of nonlinear coupled ordinary differential equations using scaling group of transformations. These reduced equations are then solved numerically using the Runge-Kutta-Fehlberg fourth-fifth order numerical method.

The dimensionless forms of the governing equations of the flow model [6] are

$$\begin{aligned} \frac{\partial u}{\partial x} + \frac{\partial v}{\partial y} &= 0, \\ u \frac{\partial u}{\partial x} + v \frac{\partial u}{\partial y} &= -\frac{\partial}{\partial y} \left| \frac{\partial u}{\partial y} \right|^n \frac{\partial^2 u}{\partial y^2} \pm \lambda x \theta, \\ \frac{\theta}{x} u + u \frac{\partial \theta}{\partial x} + v \frac{\partial \theta}{\partial y} &= \frac{R_e^{2/(1+n)}}{LU_r} \left[\alpha + \frac{16\sigma_1 T_\infty^3}{3\rho c_p k_1} \right] \frac{\partial^2 \theta}{\partial y^2}. \end{aligned} \quad (65)$$

The boundary conditions specified to solve the above system of PDEs are

$$\begin{aligned} u &= x + \frac{aU_r^{n-2}R_e^{1/(1+n)}}{L^n} \left| \frac{\partial u}{\partial y} \right|^n \frac{\partial u}{\partial y}, \\ v &= 0, \\ \theta &= 1 \end{aligned} \quad \text{at } y = 0, \quad (66)$$

$$\begin{aligned} u &= 0, \\ \theta &= 0 \end{aligned} \quad \text{as } y \rightarrow \infty.$$

The scaling symmetry operator for the system of PDEs (65) is calculated as [6]

$$X = \left(\frac{n+1}{2n} \right) \frac{\partial}{\partial x} + \left(\frac{n-1}{2n} \right) \frac{\partial}{\partial y} + u \frac{\partial}{\partial u}. \quad (67)$$

The corresponding similarity transformations are

$$\begin{aligned} \eta &= yx^{(1-n)/(1+n)}, \\ \psi &= x^{2n/(1+n)} f(\eta), \\ \theta &= \theta(\eta). \end{aligned} \quad (68)$$

Transformation (67) transforms the system of PDEs (65) into a nonlinear system of ODEs. The reduced ordinary differential equations are solved numerically.

3.7. Lie Group Analysis of a Non-Newtonian Fluid Flow over a Porous Surface [7]. Akgül and Pakdemirli [7] investigated the two-dimensional unsteady squeezed flow over a porous surface for a power-law non-Newtonian fluid. Lie Group theory was applied on the model equations. Then, a partial differential system with three independent variables was converted into an ordinary differential system, via application of two successive symmetry generators. The ordinary differential equations were then solved numerically.

The problem describing the flow model [7] is given by

$$\begin{aligned} \frac{\partial u}{\partial x} + \frac{\partial v}{\partial y} &= 0, \\ \frac{\partial u}{\partial t} + u \frac{\partial u}{\partial x} + v \frac{\partial u}{\partial y} &= F(x, t) + n \left| \frac{\partial u}{\partial y} \right|^{n-1} \frac{\partial^2 u}{\partial y^2}, \\ \frac{\partial T}{\partial t} + u \frac{\partial T}{\partial x} + v \frac{\partial T}{\partial y} &= \frac{1}{P_r} \frac{\partial^2 \theta}{\partial y^2}, \end{aligned} \quad (69)$$

with

$$\begin{aligned} u(x, 0, t) &= S(x, t), \\ v(x, 0, t) &= V, \\ T(x, 0, t) &= 1, \\ u(x, \infty, t) &= U(x, t), \\ T(x, \infty, t) &= 0. \end{aligned} \quad (70)$$

The symmetries for the system of PDEs (69) found in [7] are

$$\begin{aligned} \xi_1 &= \frac{3}{2}ax + b(t), \\ \xi_2 &= \frac{a}{2}y, \\ \xi_3 &= at + d, \\ \eta_1 &= \frac{a}{2}u + b', \\ \eta_2 &= -\frac{a}{2}v, \\ \eta_3 &= 0. \end{aligned} \quad (71)$$

Symmetries (71) are used to reduce the nonlinear system of PDEs (69) to a nonlinear system of ODEs which was then solved using a numerical approach.

3.8. Flow of Power-Law Fluid over a Stretching Surface: A Lie Group Analysis [8]. The investigation of the boundary layer flow of power-law fluid over a permeable stretching surface was made by Jalil and Asghar [8]. The use of Lie group analysis reveals all possible similarity transformations of the problem. The similarity transformations have been utilized to reduce the governing system of nonlinear PDEs to a nonlinear boundary value problem.

The governing equations of the flow model [8] are

$$\begin{aligned} \frac{\partial u}{\partial x} + \frac{\partial v}{\partial y} &= 0, \\ u \frac{\partial u}{\partial x} + v \frac{\partial u}{\partial y} &= -\frac{\partial}{\partial y} \left| \left(-\frac{\partial u}{\partial y} \right) \right|^n. \end{aligned} \quad (72)$$

The boundary conditions are

$$\begin{aligned}
 u &= u_x(x), \\
 v &= \frac{V_0 v_w(x)}{U_0} \left(\frac{\rho U_0^{2-n} L^n}{K} \right)^{1/(n+1)} \\
 &\text{at } y = 0, \\
 u &= 0 \quad \text{as } y \rightarrow \infty.
 \end{aligned} \tag{73}$$

The form of the infinitesimals is found to be [8]

$$\begin{aligned}
 \xi_1 &= a + b(x), \\
 \xi_2 &= \frac{b + (n-2)c}{(n+1)} y + \gamma(x), \\
 \varphi_1 &= cu, \\
 \varphi_2 &= \frac{(2n-1)c - nb}{(n+1)} v + uy'(x).
 \end{aligned} \tag{74}$$

Symmetries (74) are used to compute the appropriate similarity transformations which were then used to reduce the nonlinear system of the above PDEs to a nonlinear boundary value problem. The reduced boundary value problem was solved numerically.

3.9. Group Invariant Solution for a Preexisting Fracture Driven by a Power-Law Fluid in Impermeable Rock [9]. The effect of power-law rheology on hydraulic fracturing has been studied by Fareo and Mason [9]. With the aid of lubrication theory and the PKN approximation, a partial differential equation for the fracture half-width was derived. By using a linear combination of the Lie symmetry generators of the governing equation, the group invariant solution was obtained and the problem was reduced to a boundary value problem for an ordinary differential equation.

The mathematical problem describing the preexisting fracture driven by a power-law fluid in impermeable rock [9] is given by

$$\frac{\partial h}{\partial t} + \frac{\partial}{\partial x} \left[h^{(2n+1)/n} \left(-\frac{\partial h}{\partial x} \right)^{1/n} \right] = 0, \tag{75}$$

with

$$\begin{aligned}
 \frac{dV}{dt} &= 2 \left(-\frac{\partial h(0,t)}{\partial x} \right)^{1/n} h^{(2n+1)/n}(0,t), \\
 h(L(t), t) &= 0.
 \end{aligned} \tag{76}$$

The symmetry Lie algebra of (75) is spanned by the operators [9]

$$\begin{aligned}
 X_1 &= \frac{\partial}{\partial x}, \\
 X_2 &= \frac{\partial}{\partial t}, \\
 X_3 &= t \frac{\partial}{\partial t} - \left(\frac{n}{n+2} \right) h \frac{\partial}{\partial h}, \\
 X_4 &= x \frac{\partial}{\partial x} + \left(\frac{n+1}{n+2} \right) h \frac{\partial}{\partial h}.
 \end{aligned} \tag{77}$$

The group invariant solutions of the PDE (75) found in [9] are of the form

$$\begin{aligned}
 h(x,t) &= \frac{1}{L(t)} \left[1 - u^{n+1} \right]^{1/(n+2)}, \\
 h(x,t) &= L(t)^{1/(n+2)} \left[1 - u \right]^{1/(n+2)},
 \end{aligned} \tag{78}$$

where the particular values of $L(t)$ are given in [9]. The Lie symmetries given in (77) were also utilized to perform various reductions of PDE (75) which was then solved numerically.

4. Sisko Fluid Flow Problems

In this section, we investigate all those models which deal with the flow of a Sisko fluid and solved with the aid of the Lie group approach.

The Cauchy stress tensor \mathbf{T} for a Sisko fluid model is given by

$$\mathbf{T} = -p\mathbf{I} + \left[a + b \left| \sqrt{\frac{1}{2} \text{tr} \mathbf{A}_1^2} \right|^{n-1} \right] \mathbf{A}_1, \tag{79}$$

where \mathbf{V} is the velocity vector, \mathbf{A}_1 is the first Rivlin-Ericksen tensor, and a and b are the material constants. The model is a combination of viscous and power-law models. For $a = 0$, the model exhibits power-law behavior whereas for $b = 0$, the flow is Newtonian and $n > 0$ is a characteristic of the non-Newtonian behavior of the fluid.

4.1. Rayleigh Problem for a MHD Sisko Fluid [10]. Molati et al. [10] studied the problem of unsteady unidirectional flow of an incompressible Sisko fluid bounded by a suddenly moved plate. The fluid is magnetohydrodynamic (MHD) in the presence of a time-dependent magnetic field applied in the transverse direction of the flow. The nonlinear governing flow model was solved analytically using the Lie symmetry approach.

The problem describing the flow model [10] is given by

$$\frac{\partial u}{\partial t} = \frac{\partial^2 u}{\partial y^2} + L \frac{\partial}{\partial y} \left[\left(\frac{\partial u}{\partial y} \right)^{n-1} \frac{\partial u}{\partial y} \right] - M^2 H^2(t) u, \tag{80}$$

with

$$\begin{aligned} u(t, 0) &= g(t), \quad t > 0, \\ u(t, y) &\longrightarrow 0 \quad \text{as } y \longrightarrow \infty, \quad t > 0, \\ u(0, y) &= 0, \quad y > 0. \end{aligned} \quad (81)$$

The symmetry Lie algebra of the PDE (80) is three-dimensional and spanned by the operators [10]

$$\begin{aligned} X_1 &= \frac{\partial}{\partial y}, \\ X_2 &= (2t + \beta) \frac{\partial}{\partial t} + y \frac{\partial}{\partial y} + u \frac{\partial}{\partial u}, \\ X_3 &= \left(\frac{2t + \beta}{2 + \beta} \right)^{-M^2 H_0^2 / 2} \frac{\partial}{\partial u}, \end{aligned} \quad (82)$$

where

$$H_0 = \sqrt{2t + \beta} H(t). \quad (83)$$

The similarity solution from the invariants of X_2 assumes the form [10]

$$\begin{aligned} u(t, y) &= (2t + \beta)^{1/2} F(\gamma) \\ &\quad \text{with } \gamma = y(2t + \beta)^{-1/2}. \end{aligned} \quad (84)$$

Invariant (84) is used to reduce the PDE (80) into a nonlinear ODE. The reduced ODE together with suitable boundary conditions was solved by employing a numerical approach.

4.2. Reduction and Solutions for MHD Flow of a Sisko Fluid in a Porous Medium [11]. Mamboundou et al. [11] obtained the analytical solutions for magnetohydrodynamic (MHD) flow of a Sisko fluid in a semi-infinite porous medium. The governing nonlinear differential equation was solved by employing the symmetry method.

The governing equation of the flow model [11] is

$$\begin{aligned} \frac{\partial u}{\partial t} &= \frac{\partial}{\partial y} \left[\left(1 + b \left(\frac{\partial u}{\partial y} \right)^{n-1} \right) \frac{\partial u}{\partial y} \right] \\ &\quad - \frac{1}{K} \left[1 + b \left(\frac{\partial u}{\partial y} \right)^{n-1} \right] - M^2 u. \end{aligned} \quad (85)$$

The relevant boundary and initial conditions are

$$\begin{aligned} u(0, t) &= V(t), \quad t > 0, \\ u(\infty, t) &= 0, \quad t > 0, \\ u(y, 0) &= h(y), \quad y > 0. \end{aligned} \quad (86)$$

The above PDE admits the Lie point symmetry generators [11]

$$\begin{aligned} X_1 &= \frac{\partial}{\partial t}, \\ X_2 &= \frac{\partial}{\partial y}. \end{aligned} \quad (87)$$

The travelling wave solutions of the PDE (85) were constructed corresponding to the symmetry generators (87) and is given by [11]

$$u(y, t) = \exp \left[\frac{1}{nK} \left(1 - n - nKM^2 \right) t - \frac{1}{\sqrt{nK}} y \right]. \quad (88)$$

4.3. Stokes' First Problem for Sisko Fluid over a Porous Wall [12]. The study of time-dependent flow of an incompressible Sisko fluid over a wall with suction or blowing was performed by Hayat et al. [12]. The magnetohydrodynamic nature of the fluid was taken into account by applying a variable magnetic field. The resulting nonlinear problem was solved by invoking the symmetry approach.

The problem governing the flow model [12] in a non-dimensional form is given by

$$\frac{\partial u}{\partial t} - S \frac{\partial u}{\partial y} = \frac{\partial}{\partial y} \left[\left(1 + L \left| \frac{\partial u}{\partial y} \right|^{n-1} \right) \frac{\partial u}{\partial y} \right] \quad (89)$$

$$- M^2 H^2(t) u,$$

$$u(t, 0) = 1, \quad t > 0, \quad (90)$$

$$\lim_{y \rightarrow \infty} u(t, y) = 0, \quad t > 0, \quad (91)$$

$$u(y, 0) = 0, \quad y > 0. \quad (92)$$

The symmetry analysis of (89) revealed that extra symmetries are admitted for the cases

$$H = 0,$$

$$H = \text{Constant},$$

$$H = \frac{h_0}{\sqrt{t}},$$

$$H = \frac{h_0}{\sqrt{\alpha t + t_0}}, \quad (93)$$

$$H = \frac{h_0}{\sqrt{2t + t_0}}, \quad \text{where } h_0, t_0 \in \mathfrak{R}.$$

The reductions of PDE (89) for these cases lead to nonlinear ordinary differential equations. However, the imposed boundary conditions are not invariant under the admitted Lie point symmetries. Hence, the governing model was then solved by making use of numerical techniques.

4.4. Boundary Layer Equations and Lie Group Analysis of a Sisko Fluid [13]. Sari et al. [13] recently derived the boundary layer equations for a Sisko fluid. Using Lie group theory, a symmetry analysis of the equations was performed. A partial differential system is transferred to an ordinary differential system using symmetries and the resulting reduced equations were numerically solved.

The dimensionless form of the boundary layer equations for a Sisko fluid is [13]

$$\begin{aligned} \frac{\partial u}{\partial x} + \frac{\partial v}{\partial y} &= 0, \\ u \frac{\partial u}{\partial x} + v \frac{\partial u}{\partial y} &= U \frac{dU}{dx} + \varepsilon_1 \frac{\partial^2 u}{\partial y^2} + \varepsilon_2 \left(\frac{\partial u}{\partial y} \right)^{n-1} \frac{\partial^2 u}{\partial y^2}. \end{aligned} \quad (94)$$

The classical boundary conditions for the problem are [13]

$$\begin{aligned} u(x, 0) &= 0, \\ v(x, 0) &= 0, \\ u(x, \infty) &= U(x). \end{aligned} \quad (95)$$

The infinitesimals of the above system of PDEs are [13]

$$\begin{aligned} \xi_1 &= 3ax + b, \\ \xi_2 &= ay, \\ \eta_1 &= au, \\ \eta_2 &= -av. \end{aligned} \quad (96)$$

The corresponding similarity transformations are

$$\begin{aligned} \xi &= \frac{y}{x^{1/3}}, \\ u &= x^{1/3} f(\xi), \\ v &= \frac{g(\xi)}{x^{1/3}}. \end{aligned} \quad (97)$$

Transformations (97) are used to reduce the above PDE system to an ordinary differential system. The reduced ordinary differential system was solved by using a numerical method.

4.5. Analytic Approximate Solutions for Time-Dependent Flow and Heat Transfer of a Sisko Fluid [14]. The purpose of this study was to find analytic approximate solutions for unsteady flow and heat transfer of a Sisko fluid. Translational symmetries were utilized in [14] to find a family of travelling wave solutions of the governing nonlinear problem.

In dimensionless form, the governing problem takes the form [14]

$$\frac{\partial u}{\partial t} = \frac{\partial}{\partial y} \left[\left(1 + b \left(-\frac{\partial u}{\partial y} \right)^{n-1} \right) \frac{\partial u}{\partial y} \right], \quad (98)$$

$$\frac{\partial \theta}{\partial t} = \frac{1}{Pr} \frac{\partial^2 \theta}{\partial t^2} + Ec \left[1 + b \left(-\frac{\partial u}{\partial y} \right)^{n-1} \right] \left(\frac{\partial u}{\partial y} \right)^2, \quad (99)$$

with the boundary conditions

$$\begin{aligned} u(0, t) &= V_1(t), \\ \theta(0, t) &= V_2(t), \\ t &> 0, \\ u(\infty, t) &= 0, \\ \theta(\infty, t) &= 0, \\ t &> 0, \\ u(y, 0) &= h_1(y), \\ \theta(y, 0) &= h_2(y), \\ y &> 0. \end{aligned} \quad (100)$$

Equation (98) admits the Lie point symmetry generators $X = \partial/\partial t$ and $Y = \partial/\partial y$. The generator $X - cY$ which represents a family of travelling wave with constant wave speed c has been used in [14] to perform reduction of the above system of PDEs into nonlinear system of ODEs. The reduced system of ODEs was solved by homotopy analysis method.

4.6. Self-Similar Unsteady Flow of a Sisko Fluid in a Cylindrical Tube Undergoing Translation [15]. The governing equation for unsteady flow of a Sisko fluid in a cylindrical tube due to translation of the tube wall is modelled in [15]. The reduction of the nonlinear problem was carried out by using Lie group approach. The partial differential equation is transformed into an ordinary differential equation, which was integrated numerically.

The unsteady flow of a Sisko fluid in a cylindrical tube due to impulsive motion of tube is governed by [15]

$$\begin{aligned} \frac{\partial w}{\partial t} &= \frac{\partial^2 w}{\partial r^2} + bn \frac{\partial^2 w}{\partial r^2} \left(\frac{\partial w}{\partial r} \right)^{n-1} \\ &+ \frac{1}{r} \left[\frac{\partial w}{\partial r} + b \left(\frac{\partial w}{\partial r} \right)^n \right], \end{aligned} \quad (101)$$

subject to the boundary conditions

$$\begin{aligned} w(1, t) &= V(t), \quad t > 0, \\ \frac{\partial w}{\partial r}(0, t) &= 0, \quad t > 0, \\ W(r, 0) &= W(r), \quad y > 0. \end{aligned} \quad (102)$$

The Lie point symmetries for the PDE (101) are spanned by the operators [15]

$$\begin{aligned} X_1 &= \frac{\partial}{\partial t}, \\ X_2 &= w \frac{\partial}{\partial w}, \\ X_3 &= 2t \frac{\partial}{\partial t} + r \frac{\partial}{\partial r} + w \frac{\partial}{\partial w}, \\ X_4 &= (w + br) \frac{\partial}{\partial w}, \\ X_5 &= d(t, r) \frac{\partial}{\partial w}, \end{aligned} \quad (103)$$

where $d(t, r)$ satisfies the linear partial differential equation (101). The operator X_3 has been used in [15] to deduce the similarity transformations

$$w(r, t) = rf(\zeta), \quad \zeta = \frac{r}{\sqrt{t}}. \quad (104)$$

The similarity transformations (104) are employed to reduce the partial differential equation (101) into a nonlinear ordinary differential equation. The reduced ordinary differential together with suitable boundary and initial conditions was solved by shooting method.

5. Jeffrey Fluid Flow Problems

Here we discuss the problems dealing with the flow of a Jeffrey fluid that are solved using the Lie group approach.

The constitutive equations for an incompressible Jeffrey fluid model are

$$\mathbf{T} = -p\mathbf{I} + \mathbf{S}, \quad (105)$$

with

$$\mathbf{S} = \frac{\mu}{1 + \lambda_1} [\dot{\gamma} + \lambda_2 \ddot{\gamma}], \quad (106)$$

where \mathbf{T} and \mathbf{S} are the Cauchy stress tensor and the extra stress tensor, respectively, p is the pressure, \mathbf{I} is the identity tensor, λ_1 is the ratio of relaxation to retardation times, λ_2 is the retardation time, $\dot{\gamma}$ is the shear rate, and the dots over the quantities indicate differentiation with respect to time.

5.1. Lie Point Symmetries and Similarity Solutions for an Electrically Conducting Jeffrey Fluid [16]. The only model available in the literature dealing with the flow of a Jeffrey fluid and solved by employing the Lie symmetry approach was studied by Mekheimer et al. [16]. In their work, the equations for the two-dimensional incompressible fluid flow of an electrically conducting Jeffrey fluid are studied. A Lie symmetry analysis was performed and the group invariant solutions were derived.

The governing equations of the model [16] are

$$\begin{aligned} \frac{\partial u}{\partial x} + \frac{\partial v}{\partial y} &= 0, \\ \frac{\partial u}{\partial t} + u \frac{\partial u}{\partial x} + v \frac{\partial u}{\partial y} + \frac{\partial p}{\partial x} &= \epsilon_1 \left(\frac{\partial S_{xx}}{\partial x} + \frac{\partial S_{xy}}{\partial y} \right) - \epsilon_2 u, \\ \frac{\partial v}{\partial t} + u \frac{\partial v}{\partial x} + v \frac{\partial v}{\partial y} + \frac{\partial p}{\partial y} &= \epsilon_1 \left(\frac{\partial S_{xy}}{\partial x} + \frac{\partial S_{yy}}{\partial y} \right), \end{aligned} \quad (107)$$

with

$$\begin{aligned} S_{xx} &= \frac{2}{1 + \lambda_1} \left[1 + \lambda_2 \left(\frac{\partial}{\partial t} + u \frac{\partial}{\partial x} + v \frac{\partial}{\partial y} \right) \right] \frac{\partial u}{\partial x}, \\ S_{xy} &= \frac{1}{1 + \lambda_1} \left[1 + \lambda_2 \left(\frac{\partial}{\partial t} + u \frac{\partial}{\partial x} + v \frac{\partial}{\partial y} \right) \right] \\ &\quad \cdot \left(\frac{\partial u}{\partial y} + \frac{\partial v}{\partial x} \right), \\ S_{yy} &= \frac{2}{1 + \lambda_1} \left[1 + \lambda_2 \left(\frac{\partial}{\partial t} + u \frac{\partial}{\partial x} + v \frac{\partial}{\partial y} \right) \right] \frac{\partial v}{\partial y}. \end{aligned} \quad (108)$$

The relevant boundary conditions are of the form [16]

$$\begin{aligned} u(x, 0, 0) &= U_0, \\ u(x, \infty, t) &= 0, \\ \frac{\partial u(x, 0, 0)}{\partial y} &= 0, \\ v(x, 0, 0) &= -V_0, \\ p(x, \infty, 0) &= P_0, \end{aligned} \quad (109)$$

where U_0 is the velocity of the plate, V_0 is the magnetic fluid penetrating into the plate, and P_0 is the pressure deep in the magnetic fluid. The symmetries of the system of PDEs (107) found in [16] are

$$\begin{aligned} \xi_1 &= \gamma(t), \\ \xi_2 &= a_1, \\ \xi_3 &= a_2, \\ \eta_1 &= \gamma'(t), \\ \eta_2 &= 0, \\ \eta_3 &= \delta(t) - x(\gamma''(t)' + \epsilon_2 \gamma'(t)), \end{aligned} \quad (110)$$

where a_1 and a_2 are the arbitrary constants and $\gamma(t)$ and $\delta(t)$ are the arbitrary functions of the variable t only. With the use

of symmetries given in (110), the group invariant solutions for the system of PDEs (107) are [16]

$$\begin{aligned}
 u(x, y, t) &= \frac{U_0}{(\alpha_2 - \alpha_1)} [\alpha_2 \exp[\alpha_1 (y - Ct)] \\
 &\quad - \alpha_1 \exp[\alpha_2 (y - Ct)]], \\
 v(x, y, t) &= \frac{U_0}{(\alpha_2 - \alpha_1)} [\alpha_2 \exp[\alpha_1 (y - Ct)] \\
 &\quad - \alpha_1 \exp[\alpha_2 (y - Ct)]] - (U_0 + P_0), \\
 p(x, y, t) &= \frac{U_0}{(\alpha_2 - \alpha_1)(1 + \lambda_1)} \alpha_1 \epsilon_1 + (1 + \lambda_1 \\
 &\quad - 2\epsilon_1 \alpha_1^2 \lambda_2) (C + U_0 + V_0) \times \alpha_2 \exp[\alpha_1 (y - Ct)] \\
 &\quad - [\alpha_2 \epsilon_1 + (1 + \lambda_1 - 2\epsilon_1 \alpha_1^2 \lambda_2) (C + U_0 + V_0) \\
 &\quad \times \alpha_1 \exp[\alpha_2 (y - Ct)]] + P_0.
 \end{aligned} \tag{111}$$

6. Williamson Fluid Flow Problems

In this section, we investigate the problems which deal with the flow of a Williamson fluid which are solved using the Lie symmetry approach.

The Cauchy stress tensor \mathbf{T} for a Williamson fluid model is given by

$$\mathbf{T} = \left[\mu_\infty + \frac{\mu_0 - \mu_\infty}{1 + \lambda |\dot{\gamma}|} \right] \dot{\gamma}, \tag{112}$$

where

$$\dot{\gamma} = \begin{bmatrix} 2 \frac{\partial u}{\partial x} & \frac{\partial u}{\partial y} + \frac{\partial v}{\partial x} \\ \frac{\partial u}{\partial y} + \frac{\partial v}{\partial x} & 2 \frac{\partial v}{\partial y} \end{bmatrix}, \tag{113}$$

$$|\dot{\gamma}| = \left[2 \left(\frac{\partial u}{\partial x} \right)^2 + 2 \left(\frac{\partial v}{\partial y} \right)^2 + \left(\frac{\partial u}{\partial y} + \frac{\partial v}{\partial x} \right)^2 \right]^{1/2}.$$

Here μ_0 and μ_∞ are the limiting viscosities at zero and at infinite shear rate, respectively, and λ is a rheological parameter.

6.1. Boundary Layer Theory and Symmetry Analysis of a Williamson Fluid [17]. The first study available in the literature dealing with the flow of a Williamson fluid and solved by employing the Lie group approach was performed by Aksoy et al. [17]. In [17], the boundary layer equations for a Williamson fluid are derived for the first time. Using Lie group theory, a symmetry analysis of the equations was performed. The partial differential system was converted to an ordinary differential system via symmetries and the resulting equations were numerically solved.

The governing problem of the flow model [17] is

$$\begin{aligned}
 \frac{\partial u}{\partial x} + \frac{\partial v}{\partial y} &= 0, \\
 u \frac{\partial u}{\partial x} + v \frac{\partial u}{\partial y} &= U \frac{dU}{dx} + k_2 \frac{\partial^2 u}{\partial y^2} \\
 &\quad + (k_1 - k_2) \left[1 + k_3 \left| \frac{\partial u}{\partial y} \right| \right]^{-1} \frac{\partial^2 u}{\partial y^2} \\
 &\quad - (k_1 - k_2) k_3 \left[1 + k_3 \left| \frac{\partial u}{\partial y} \right| \right]^{-2} \frac{\partial^2 u}{\partial y^2} \frac{\partial u}{\partial y},
 \end{aligned} \tag{114}$$

where $\epsilon_1 = k_1 \delta^2$, $\epsilon_2 = k_2 \delta^2$, and $\epsilon_3 = k_1 \delta$. The classical boundary conditions for the problem are

$$\begin{aligned}
 u(x, 0) &= 0, \\
 v(x, 0) &= 0, \\
 u(x, \infty) &= U(x).
 \end{aligned} \tag{115}$$

The infinitesimals of the above system of PDEs are [17]

$$\begin{aligned}
 \xi_1 &= 3ax + b, \\
 \xi_2 &= ay, \\
 \eta_1 &= au, \\
 \eta_2 &= -av.
 \end{aligned} \tag{116}$$

The corresponding similarity transformations are

$$\begin{aligned}
 \xi &= \frac{y}{x^{1/3}}, \\
 u &= x^{1/3} f(\xi), \\
 v &= \frac{g(\xi)}{x^{1/3}}.
 \end{aligned} \tag{117}$$

The similarity transformations (117) are used to reduce the above PDE system into a system of nonlinear ordinary differential equations. The reduced ordinary differential system was solved by using numerical techniques.

6.2. Boundary Layer Flow of Williamson Fluid with Chemically Reactive Species Using Scaling Transformation and Homotopy Analysis Method [18]. The study of Williamson fluid flow with a chemically reactive species was made recently by Khan et al. [18]. The governing equations of Williamson model in two-dimensional flows were constructed by using scaling group transformation. The series solution of the system of reduced nonlinear ordinary differential equations (ODEs) was obtained by using homotopy analysis method.

The equations governing the model [18] are

$$\begin{aligned} \frac{\partial u}{\partial x} + \frac{\partial v}{\partial y} &= 0, \\ u \frac{\partial u}{\partial x} + v \frac{\partial u}{\partial y} &= -\frac{dp}{dx} + \frac{1}{R_e} \frac{\partial^2 u}{\partial y^2} + 2 \frac{R_e}{W_e} \left(\frac{\partial u}{\partial y} \right) \frac{\partial^2 u}{\partial y^2}, \\ u \frac{\partial C}{\partial x} + v \frac{\partial C}{\partial y} &= \gamma \frac{\partial^2 C}{\partial y^2}, \end{aligned} \quad (118)$$

where W_e is the Weissenberg number and R_e is a Reynolds number. The boundary conditions for the problem are

$$\begin{aligned} u(x, 0) &= 0, \\ v(x, 0) &= 0, \\ u(x, \infty) &= U(x), \\ C(x, 0) &= 1, \\ C(x, \infty) &= 0. \end{aligned} \quad (119)$$

The Lie point symmetries of the system of PDEs (118) are [18]

$$\begin{aligned} \xi_1 &= 3ax + b, \\ \xi_2 &= ay, \\ \eta_1 &= au, \\ \eta_2 &= -av, \\ \eta_3 &= aU, \\ \eta_4 &= aC. \end{aligned} \quad (120)$$

The corresponding similarity transformations are

$$\begin{aligned} \eta &= \frac{y}{x^{1/3}}, \\ u &= x^{1/3} f(\eta), \\ v &= \frac{g(\eta)}{x^{1/3}}, \\ U &= x^{1/3}, \\ C &= \phi(\eta). \end{aligned} \quad (121)$$

The similarity transformations (121) are utilized in [18] to reduce the above PDE system into a system of nonlinear ordinary differential equations. The reduced ordinary differential system was solved analytically by homotopy analysis method.

7. Second-Grade Fluid Flow Problems

In this section, we present the studies related to flow of a second-grade fluid model that are solved by the Lie symmetry reduction method.

The constitutive equation for an incompressible homogeneous Rivlin-Ericksen fluid of second grade is given by the following relation:

$$\mathbf{T} = -p\mathbf{I} + \mu\mathbf{A}_1 + \alpha_1\mathbf{A}_2 + \alpha_2\mathbf{A}_1^2, \quad (122)$$

where p is the pressure of the fluid, \mathbf{I} is the identity tensor, μ is the dynamic viscosity, and α_i ($i = 1, 2$) are the material moduli and denote the first and second normal stress coefficients which are not always constants.

7.1. Lie Group Analysis of Creeping Flow of a Second-Grade Fluid [19]. Yürüsoy et al. [19] considered the steady plane creeping flow equations of a second-grade fluid in Cartesian coordinates. Lie group theory was applied to the equations of motion. The symmetries of the equations were found. Two different types of exact solutions were constructed for the model equation.

The equations governing the creeping flow of a second-grade fluid are [19]

$$\begin{aligned} \frac{\partial u}{\partial x} + \frac{\partial v}{\partial y} &= 0, \\ -\frac{\partial p}{\partial x} + \epsilon \left(\frac{\partial^2 u}{\partial x^2} + \frac{\partial^2 u}{\partial y^2} \right) + \epsilon_1 \left[5 \frac{\partial u}{\partial x} \frac{\partial^2 u}{\partial x^2} + \frac{\partial u}{\partial x} \frac{\partial^2 u}{\partial y^2} \right. \\ &+ u \frac{\partial^3 u}{\partial x^3} + v \frac{\partial^3 u}{\partial y^3} + u \frac{\partial^3 u}{\partial y^2 \partial x} + 2 \frac{\partial v}{\partial x} \frac{\partial^2 v}{\partial x^2} \\ &+ \left. \frac{\partial u}{\partial y} \frac{\partial^2 u}{\partial y \partial x} + \frac{\partial u}{\partial y} \frac{\partial^2 v}{\partial x^2} + v \frac{\partial^3 u}{\partial x^2 \partial y} \right] = 0, \\ -\frac{\partial p}{\partial y} + \epsilon \left(\frac{\partial^2 v}{\partial x^2} - \frac{\partial^2 u}{\partial x \partial y} \right) + \epsilon_1 \left[5 \frac{\partial u}{\partial x} \frac{\partial^2 u}{\partial x \partial y} - \frac{\partial u}{\partial x} \frac{\partial^2 v}{\partial x^2} \right. \\ &- v \frac{\partial^3 u}{\partial x \partial y^2} + u \frac{\partial^3 v}{\partial x^3} - v \frac{\partial^3 u}{\partial x^3} + 2 \frac{\partial u}{\partial y} \frac{\partial^2 u}{\partial y^2} - \frac{\partial v}{\partial x} \frac{\partial^2 u}{\partial x^2} \\ &+ \left. \frac{\partial v}{\partial x} \frac{\partial^2 u}{\partial y^2} - u \frac{\partial^3 u}{\partial x^2 \partial y} \right] = 0, \end{aligned} \quad (123)$$

where

$$\begin{aligned} \epsilon &= \frac{1}{R_e} = \frac{\mu}{\rho UL}, \\ \epsilon_1 &= \frac{\alpha_1}{\rho L^2}. \end{aligned} \quad (124)$$

The Lie point symmetries of the above system of PDEs (123) are [19]

$$\begin{aligned} \xi_1 &= ax + b, \\ \xi_2 &= ay + c, \\ \eta_1 &= au, \\ \eta_2 &= av, \\ \eta_3 &= d. \end{aligned} \quad (125)$$

With the use of Lie point symmetries (125), the group invariant solutions for the system of PDEs (123) are [19]

$$\begin{aligned}
 u(x, y) &= c_1 \left(\frac{\alpha \epsilon_1}{\epsilon} \right)^2 \exp \left[- \left(\frac{\epsilon}{\alpha \epsilon_1} \right) (y - mx) \right] \\
 &\quad + c_2 (y - mx) + c_3, \\
 v(x, y) &= m \left[c_1 \left(\frac{\alpha \epsilon_1}{\epsilon} \right)^2 \exp \left[- \left(\frac{\epsilon}{\alpha \epsilon_1} \right) (y - mx) \right] \right. \\
 &\quad \left. + c_2 (y - mx) + c_3 \right] + \alpha,
 \end{aligned} \tag{126}$$

$$\begin{aligned}
 p(x, y) &= 2(1 + m^2)^2 \epsilon_1 c_1 \left(\frac{\alpha \epsilon_1}{\epsilon} \right) \\
 &\quad \cdot \left(\frac{1}{2} \frac{\alpha \epsilon_1}{\epsilon} c_1 \exp \left[- \left(\frac{\epsilon}{\alpha \epsilon_1} \right) (y - mx) \right] \right. \\
 &\quad \left. - c_2 \exp \left[- \left(\frac{\epsilon}{\alpha \epsilon_1} \right) (y - mx) \right] \right) + c_4.
 \end{aligned}$$

7.2. Similarity Solutions for Creeping Flow and Heat Transfer in Second-Grade Fluids [20]. The steady plane creeping flow and heat transfer equations of a second-grade fluid in Cartesian coordinates are modelled by Yürüsoy [20]. Lie group theory was employed for the equations of motion. The symmetries of the equations were deduced. The equations admit a scaling symmetry, translation symmetries, and an infinite parameter dependent symmetry. New exact analytical solutions are found for the model equations.

The equations of the flow model [20] are

$$\begin{aligned}
 0 &= \frac{\partial u}{\partial x} + \frac{\partial v}{\partial y}, \\
 0 &= -\frac{\partial p}{\partial x} + \left(\frac{\partial^2 u}{\partial x^2} + \frac{\partial^2 u}{\partial y^2} \right) + \delta \left[5 \frac{\partial u}{\partial x} \frac{\partial^2 u}{\partial x^2} + \frac{\partial u}{\partial x} \frac{\partial^2 u}{\partial y^2} \right. \\
 &\quad + u \frac{\partial^3 u}{\partial x^3} + v \frac{\partial^3 u}{\partial y^3} + u \frac{\partial^3 u}{\partial y^2 \partial x} + 2 \frac{\partial v}{\partial x} \frac{\partial^2 v}{\partial x^2} \\
 &\quad \left. + \frac{\partial u}{\partial y} \frac{\partial^2 u}{\partial y \partial x} + \frac{\partial u}{\partial y} \frac{\partial^2 v}{\partial x^2} + v \frac{\partial^3 u}{\partial x^2 \partial y} \right], \\
 0 &= -\frac{\partial p}{\partial y} + \left(\frac{\partial^2 v}{\partial x^2} - \frac{\partial^2 u}{\partial x \partial y} \right) + \delta \left[5 \frac{\partial u}{\partial x} \frac{\partial^2 u}{\partial x \partial y} \right. \\
 &\quad - \frac{\partial u}{\partial x} \frac{\partial^2 v}{\partial x^2} - v \frac{\partial^3 u}{\partial x \partial y^2} + u \frac{\partial^3 v}{\partial x^3} - v \frac{\partial^3 u}{\partial x^3} + 2 \frac{\partial u}{\partial y} \frac{\partial^2 u}{\partial y^2} \\
 &\quad \left. - \frac{\partial v}{\partial x} \frac{\partial^2 u}{\partial x^2} + \frac{\partial v}{\partial x} \frac{\partial^2 u}{\partial y^2} - u \frac{\partial^3 u}{\partial x^2 \partial y} \right], \\
 0 &= \frac{\partial^2 \theta}{\partial x^2} + \frac{\partial^2 \theta}{\partial y^2} + \delta_1^* \left[4 \left(\frac{\partial u}{\partial x} \right)^2 + \left(\frac{\partial u}{\partial y} + \frac{\partial v}{\partial x} \right)^2 \right] \\
 &\quad + \delta_2^* \left[\frac{\partial^2 u}{\partial x^2} \left(4u \frac{\partial u}{\partial x} - v \frac{\partial v}{\partial x} - v \frac{\partial u}{\partial y} \right) \right. \\
 &\quad + \frac{\partial^2 u}{\partial y^2} \left(v \frac{\partial v}{\partial x} + v \frac{\partial u}{\partial y} \right) + \frac{\partial^2 v}{\partial x^2} \left(u \frac{\partial u}{\partial y} + u \frac{\partial v}{\partial x} \right) \\
 &\quad \left. + \frac{\partial^2 u}{\partial x \partial y} \left(4v \frac{\partial u}{\partial x} + u \frac{\partial v}{\partial x} + u \frac{\partial u}{\partial y} \right) \right].
 \end{aligned} \tag{127}$$

The infinitesimals for the system of PDEs (127) are [20]

$$\begin{aligned}
 \xi_1 &= ax + b, \\
 \xi_2 &= ay + c, \\
 \eta_1 &= au, \\
 \eta_2 &= av, \\
 \eta_3 &= d, \\
 \eta_4 &= 2a\theta + \gamma(x, y), \quad \text{with } \frac{\partial^2 \gamma}{\partial x^2} + \frac{\partial^2 \gamma}{\partial y^2} = 0.
 \end{aligned} \tag{128}$$

The invariant solutions for the system of PDEs (127) deduced in [20] are

$$\begin{aligned}
 u(x, y) &= (a\delta)^2 \exp \left[- \frac{(y - mx)}{a\delta} \right] + c_2 (y - mx) \\
 &\quad + c_3, \\
 v(x, y) &= m \left[c_1 (a\delta)^2 \exp \left[- \frac{(y - mx)}{a\delta} \right] + c_2 (y - mx) + c_3 \right] + \alpha, \\
 p(x, y) &= 2(1 + m^2)^2 \delta c_1 (a\delta) \left[\frac{1}{2} (a\delta) c_1 \right. \\
 &\quad \cdot \exp \left[- \frac{2(y - mx)}{a\delta} \right] - c_2 \exp \left[- \frac{(y - mx)}{a\delta} \right] \left. \right] \\
 &\quad + c_4, \\
 \theta(x, y) &= -\frac{m^4 + 2m^2 + 1}{1 + m^2} \left[\delta_1^* \left\{ c_1 \frac{(a\delta)^4}{4} \right. \right. \\
 &\quad \cdot \exp \left[- \frac{2(y - mx)}{a\delta} \right] - 2c_1 c_2 (a\delta)^3 \\
 &\quad \cdot \exp \left[- \frac{(y - mx)}{a\delta} \right] + c_2^2 \frac{(y - mx)^2}{2} \left. \right\} \\
 &\quad + \alpha \delta_2^* \left\{ c_1 c_2 (a\delta)^2 \exp \left[- \frac{(y - mx)}{a\delta} \right] - c_1^2 \frac{(a\delta)^3}{4} \right. \\
 &\quad \left. \left. \cdot \exp \left[- \frac{2(y - mx)}{a\delta} \right] \right\} \right] + c_5 (y - mx) + c_6.
 \end{aligned} \tag{129}$$

7.3. Lie Symmetry Analysis and Some New Exact Solutions for Rotating Flow of a Second-Order Fluid on a Porous Plate [21]. The Lie symmetry analysis and the basic similarity reductions are performed for the rotating flow of a second-order fluid on a porous plate by Fakhari et al. [21]. Two new exact solutions to these equations were generated from the similarity transformations.

The equations governing the rotating flow of a second-order fluid on a porous plate are [21]

$$\begin{aligned} & \frac{\partial^2 u}{\partial t \partial z} - W_0 \frac{\partial^2 u}{\partial z^2} - 2\Omega \frac{\partial v}{\partial z} \\ &= v \frac{\partial^3 u}{\partial z^3} + \beta \left(\frac{\partial^4 u}{\partial t \partial z^3} - W_0 \frac{\partial^4 u}{\partial z^4} \right), \\ & \frac{\partial^2 v}{\partial t \partial z} - W_0 \frac{\partial^2 v}{\partial z^2} + 2\Omega \frac{\partial u}{\partial z} \\ &= v \frac{\partial^3 v}{\partial z^3} + \beta \left(\frac{\partial^4 v}{\partial t \partial z^3} - W_0 \frac{\partial^4 v}{\partial z^4} \right), \end{aligned} \tag{130}$$

where u and v are the velocity components.

The Lie point symmetries for the above system of PDEs are spanned by the operators [21]

$$\begin{aligned} X_1 &= \frac{\partial}{\partial t}, \\ X_2 &= \frac{\partial}{\partial z}, \\ X_3 &= u \frac{\partial}{\partial u} + v \frac{\partial}{\partial v}, \\ X_4 &= v \frac{\partial}{\partial u} - u \frac{\partial}{\partial v}, \\ X_5 &= f_1(t, z) \frac{\partial}{\partial u}, \\ X_6 &= f_2(t, z) \frac{\partial}{\partial v}. \end{aligned} \tag{131}$$

With the use of symmetries (131), two different types of exact solutions were deduced and these are given by

$$\begin{aligned} u(t, z) &= 2ic_1 e^{\lambda_1(t-z)} \sin[\mu_1(t-z)], \\ v(t, z) &= 2ic'_1 e^{\lambda_1(t-z)} \sin[\mu_1(t-z)], \\ u(t, z) &= e^{t-z} [A_1 \sin(z-2t-\theta_1) + A_0 \sin(z-\theta_0)], \\ v(t, z) &= e^{t-z} [-\{A_1 \cos(z-2t-\theta_1) + A_0 \cos(z-\theta_0)\}]. \end{aligned} \tag{132}$$

7.4. Some New Exact Solutions for MHD Aligned Creeping Flow and Heat Transfer in Second-Grade Fluids by Using Lie Group Analysis [22]. Afify [22] carried out the Lie group analysis and the basic similarity reductions for the MHD aligned flow and heat transfer in a second-grade fluid. Two new exact solutions were constructed for the model equations.

The equations governing the model [22] are

$$\begin{aligned} 0 &= \frac{\partial u}{\partial x} + \frac{\partial v}{\partial y}, \\ 0 &= -\frac{\partial p}{\partial x} + \left(\frac{\partial^2 u}{\partial x^2} + \frac{\partial^2 u}{\partial y^2} \right) + \delta \left[5 \frac{\partial u}{\partial x} \frac{\partial^2 u}{\partial x^2} + \frac{\partial u}{\partial x} \frac{\partial^2 u}{\partial y^2} \right. \\ &+ u \frac{\partial^3 u}{\partial x^3} + v \frac{\partial^3 u}{\partial y^3} + u \frac{\partial^3 u}{\partial y^2 \partial x} + 2 \frac{\partial v}{\partial x} \frac{\partial^2 v}{\partial x^2} + \frac{\partial u}{\partial y} \frac{\partial^2 u}{\partial y \partial x} \\ &+ \frac{\partial u}{\partial y} \frac{\partial^2 v}{\partial x^2} + v \frac{\partial^3 u}{\partial x^2 \partial y} \left. \right] - \delta_3 \left(\frac{\partial H_2}{\partial x} - \frac{\partial H_1}{\partial y} \right), \\ 0 &= -\frac{\partial p}{\partial y} + \left(\frac{\partial^2 v}{\partial x^2} - \frac{\partial^2 u}{\partial x \partial y} \right) + \delta \left[5 \frac{\partial u}{\partial x} \frac{\partial^2 u}{\partial x \partial y} \right. \\ &- \frac{\partial u}{\partial x} \frac{\partial^2 v}{\partial x^2} - v \frac{\partial^3 u}{\partial x \partial y^2} + u \frac{\partial^3 v}{\partial x^3} - v \frac{\partial^3 u}{\partial x^3} + 2 \frac{\partial u}{\partial y} \frac{\partial^2 u}{\partial y^2} \\ &- \frac{\partial v}{\partial x} \frac{\partial^2 u}{\partial x^2} + \frac{\partial v}{\partial x} \frac{\partial^2 u}{\partial y^2} - u \frac{\partial^3 u}{\partial x^2 \partial y} \left. \right] - \delta_3 H_1 \left(\frac{\partial H_2}{\partial x} \right. \\ &\left. - \frac{\partial H_1}{\partial y} \right), \\ 0 &= \frac{\partial H_1}{\partial x} + \frac{\partial H_2}{\partial y}, \\ 0 &= \frac{\partial^2 \theta}{\partial x^2} + \frac{\partial^2 \theta}{\partial y^2} + \delta_1^* \left[4 \left(\frac{\partial u}{\partial x} \right)^2 + \left(\frac{\partial u}{\partial y} + \frac{\partial v}{\partial x} \right)^2 \right] \\ &+ \delta_2^* \left[\frac{\partial^2 u}{\partial x^2} \left(4u \frac{\partial u}{\partial x} - v \frac{\partial v}{\partial x} - v \frac{\partial u}{\partial y} \right) \right. \\ &+ \frac{\partial^2 u}{\partial y^2} \left(v \frac{\partial v}{\partial x} + v \frac{\partial u}{\partial y} \right) + \frac{\partial^2 v}{\partial x^2} \left(u \frac{\partial u}{\partial y} + u \frac{\partial v}{\partial x} \right) \\ &+ \frac{\partial^2 u}{\partial x \partial y} \left(4v \frac{\partial u}{\partial x} + u \frac{\partial v}{\partial x} + u \frac{\partial u}{\partial y} \right) \left. \right], \\ \frac{\partial^3 H_1}{\partial x^2 \partial y} + \frac{\partial^3 H_1}{\partial y^3} - \frac{\partial^3 H_1}{\partial x^3} - \frac{\partial^3 H_2}{\partial x \partial y^2} &= \delta_4 \left[v \frac{\partial H_1}{\partial x^2} \right. \\ &+ \frac{\partial^2 v}{\partial x^2} H_1 + v \frac{\partial^2 H_1}{\partial y^2} + \frac{\partial^2 v}{\partial y^2} H_1 - u \frac{\partial H_2}{\partial x^2} - \frac{\partial^2 u}{\partial x^2} H_2 \\ &\left. - u \frac{\partial^2 H_2}{\partial y^2} - \frac{\partial^2 u}{\partial y^2} H_2 \right]. \end{aligned} \tag{133}$$

The symmetries for the system of PDEs (133) are [22]

$$\begin{aligned} \xi_1 &= ax + b, \\ \xi_2 &= ay + c, \\ \eta_1 &= au, \\ \eta_2 &= av, \\ \eta_3 &= d, \end{aligned}$$

$$\begin{aligned} \eta_4 &= 2a\theta + \gamma(x, y), \quad \text{with } \frac{\partial^2 \gamma}{\partial x^2} + \frac{\partial^2 \gamma}{\partial y^2} = 0, \\ \eta_5 &= aH_1 + n, \\ \eta_6 &= aH_2 + s. \end{aligned} \tag{134}$$

With the use of the symmetries given in (134), the invariant solutions for the system of PDEs (133) are [22]

$$\begin{aligned} u(x, y) &= a_1(y - mx) + a_2, \\ v(x, y) &= m[a_1(y - mx) + a_2], \\ H_1(x, y) &= a_3(y - mx)^2 + a_4(y - mx) + a_5, \\ H_2(x, y) &= m[a_3(y - mx)^2 + a_4(y - mx) + a_5], \\ p(x, y) &= \frac{-\delta_3}{2}(1 + m^2) \\ &\quad \cdot (a_3(y - mx)^2 + a_4(y - mx) + a_5)^2 + a_6, \\ \theta(x, y) &= - \left[\frac{\delta_1^* a_1^2 (1 + m^2) (y - mx)^2}{2} \right] \\ &\quad + a_7(y - mx) + a_8. \end{aligned} \tag{135}$$

The same model was investigated again very recently by Khan et al. [23]. The travelling wave symmetry reduction was performed in [23] to reduce the governing system of PDEs (133) and thereafter the same family of exact solutions was found as in [22].

7.5. *Symmetry Analysis for Steady Boundary Layer Stagnation-Point Flow of Rivlin-Ericksen Fluid of Second-Grade Subject to Suction* [24]. Abd-el-Malek and Hassan [24] studied the steady two-dimensional boundary layer stagnation-point flow of Rivlin-Ericksen fluid of second grade with a uniform suction that is carried out via symmetry approach. By using the Lie group method for the given system of nonlinear partial differential equations, the symmetries of the equations were obtained. Using these symmetries, the solution of the given equations was constructed.

The dimensionless form of the governing equations is [24]

$$\begin{aligned} \frac{\partial u}{\partial x} + \frac{\partial v}{\partial y} &= 0, \\ u \frac{\partial u}{\partial x} + v \frac{\partial u}{\partial y} &= U \frac{dU}{dx} + \frac{\partial^2 u}{\partial y^2} \\ &\quad + k \left[\frac{\partial}{\partial x} \left(u \frac{\partial^2 u}{\partial y^2} \right) + \frac{\partial u}{\partial y} \frac{\partial^2 v}{\partial y^2} + v \frac{\partial^3 u}{\partial y^3} \right], \\ u \frac{\partial T}{\partial x} + v \frac{\partial T}{\partial y} &= \frac{1}{Pr} \frac{\partial^2 T}{\partial y^2}. \end{aligned} \tag{136}$$

The relevant boundary conditions are

$$\begin{aligned} u &= 0, \\ v &= \frac{-v_0}{\sqrt{av}}, \\ T &= 1 \\ &\quad \text{at } y = 0, \\ u &\rightarrow x, \\ \frac{\partial u}{\partial y} &= 0, \\ T &\rightarrow 0 \\ &\quad \text{as } y \rightarrow \infty. \end{aligned} \tag{137}$$

The system of nonlinear partial differential equations (136) has the three-parameter Lie group of point symmetries generated by [24]

$$\begin{aligned} X_1 &= x \frac{\partial}{\partial x} + \Psi \frac{\partial}{\partial \Psi} + U \frac{\partial}{\partial U}, \\ X_2 &= \frac{\partial}{\partial \Psi}, \\ X_3 &= \frac{\partial}{\partial y}, \end{aligned} \tag{138}$$

where Ψ denotes the stream function. The symmetries given in (138) are used to reduce the nonlinear system of PDEs (136) to a nonlinear system of ODEs. The resulting system of nonlinear differential equations was solved numerically using a shooting method coupled with a Runge-Kutta scheme.

7.6. *Application of the Lie Groups of Transformations for an Approximate Solution of MHD Flow of a Second-Grade Fluid* [25]. Islam et al. [25] investigated the problem of steady boundary layer flow of a viscous incompressible electrically conducting second-grade fluid over a stretching sheet. The Lie symmetry method was utilized to reduce the governing partial differential equation into an ordinary differential equation and then numerical solutions were obtained.

The governing equations of the model [25] are

$$\begin{aligned} \frac{\partial u}{\partial x} + \frac{\partial v}{\partial y} &= 0, \\ u \frac{\partial u}{\partial x} + v \frac{\partial u}{\partial y} &= \frac{\partial^2 u}{\partial y^2} - k \left[\frac{\partial}{\partial x} \left(u \frac{\partial^2 u}{\partial y^2} \right) + \frac{\partial u}{\partial y} \frac{\partial^2 v}{\partial y^2} + v \frac{\partial^3 u}{\partial y^3} \right] \\ &\quad - Mu, \end{aligned} \tag{139}$$

where M is known as a Hartman number. The imposed boundary conditions are

$$\begin{aligned} u &= 0, \\ v &= 0, \\ &\text{at } y = 0, \\ u &\longrightarrow 0, \quad \text{as } y \longrightarrow \infty. \end{aligned} \quad (141)$$

The generator of the one-parameter infinitesimal Lie group of point transformations found in [25] is

$$X_1 = x \frac{\partial}{\partial x} + \psi \frac{\partial}{\partial \psi}, \quad (142)$$

where ψ is the stream function. The Lie point symmetry has been utilized to reduce the above nonlinear system of PDEs to a nonlinear boundary value problem. The resulting nonlinear boundary value problem was solved numerically.

8. Modified Second-Grade Fluid Flow Problems

In this section, we analyze the problems dealing with the flow of a modified second-grade fluid which are solved using the Lie symmetry approach.

The Cauchy stress tensor for a modified second-grade fluid model is given by

$$\mathbf{T} = -p\mathbf{I} + \mu\Pi^{m/2}\mathbf{A}_1 + \alpha_1\mathbf{A}_2 + \alpha_2\mathbf{A}_1^2, \quad (143)$$

where p is the pressure, \mathbf{I} is the identity matrix, \mathbf{A}_1 and \mathbf{A}_2 are the first and second Rivlin-Ericksen tensors, respectively, and μ, m, α_1 , and α_2 are material moduli that may be constants or temperature dependent. For both the models, when $m = 0$, $\alpha_1 = \alpha_2 = 0$, the fluid is Newtonian and hence μ represents the usual viscosity. The situation when $m = 0$ corresponds to the second-grade fluid and that of $\alpha_1 = \alpha_2 = 0$ to the power-law fluid. The tensor Π is defined as

$$\Pi = \frac{1}{2} \text{tr} \mathbf{A}_1^2. \quad (144)$$

8.1. Boundary Layer Equations and Stretching Sheet Solutions for the Modified Second-Grade Fluid [26]. The boundary layer equations for a modified second-grade fluid model were derived by Aksoy et al. [26]. The symmetries of the boundary layer equations were calculated using the Lie group approach. With the use of one of the symmetries, the partial differential system was transferred to an ordinary differential system. The ordinary differential equations were then numerically integrated for the stretching sheet boundary conditions.

The boundary layer equations for a modified second-grade fluid model are [26]

$$\begin{aligned} \frac{\partial u}{\partial x} + \frac{\partial v}{\partial y} &= 0, \\ u \frac{\partial u}{\partial x} + v \frac{\partial u}{\partial y} &= U \frac{dU}{dx} + (m+1) \left(\frac{\partial u}{\partial y} \right)^m \frac{\partial^2 u}{\partial y^2} \\ &+ k_1 \left[v \frac{\partial^3 u}{\partial y^3} + u \frac{\partial^3 u}{\partial x \partial y^2} + \frac{\partial u}{\partial x} \frac{\partial^2 u}{\partial y^2} - \frac{\partial u}{\partial y} \frac{\partial^2 u}{\partial x \partial y} \right], \end{aligned} \quad (145)$$

For $m = 0$, the equations represent the boundary layers of a standard second-grade fluid and for $k_1 = 0$, the equations represent the boundary layers of a power-law fluid.

The Lie point symmetries for the above system of PDEs are spanned by the operators [26]

$$\begin{aligned} \xi_1 &= (1-m)ax + b, \\ \xi_2 &= c(x), \\ \eta_1 &= au, \\ \eta_2 &= c'(x)u + amv. \end{aligned} \quad (146)$$

The symmetry operators (146) are used to reduce the above PDE system into a system of nonlinear ODEs. The reduced ordinary differential systems were solved by using a numerical approach for the specific boundary conditions.

9. Power-Law Second-Grade Fluid Flow Problems

Here we discuss the problems dealing with the flow of a power-law second-grade fluid model solved using the Lie symmetry method.

The Cauchy stress tensor for a modified second-grade fluid model is given by

$$\mathbf{T} = -p\mathbf{I} + \Pi^{m/2} (\mu\mathbf{A}_1 + \alpha_1\mathbf{A}_2 + \alpha_2\mathbf{A}_1^2), \quad (147)$$

where p is the pressure, \mathbf{I} is the identity matrix, \mathbf{A}_1 and \mathbf{A}_2 are the first and second Rivlin-Ericksen tensors, respectively, and μ, m, α_1 , and α_2 are the material constants.

9.1. Symmetries of Boundary Layer Equations of Power-Law Fluids of Second Grade [27]. The only model available dealing with the flow of a power-law second-grade fluid and solved by employing the Lie group method was investigated by Pakdemirli et al. [27]. They derived the boundary layer equations for an incompressible power-law second-grade fluid. Symmetries of the boundary layer equations are found by using Lie theory. By using one of the symmetries, namely, the scaling symmetry, the partial differential system was transformed into an ordinary differential system, which was then numerically integrated under the classical boundary layer conditions.

The equations governing the flow model [27] are

$$\begin{aligned} \frac{\partial u}{\partial x} + \frac{\partial v}{\partial y} &= 0, \\ u \frac{\partial u}{\partial x} + v \frac{\partial u}{\partial y} &= U \frac{dU}{dx} + (m+1) \left(\frac{\partial u}{\partial y} \right)^m \frac{\partial^2 u}{\partial y^2} \\ &+ k_1 \left(\frac{\partial u}{\partial y} \right)^{m-1} \left\{ m \left[\frac{\partial^2 u}{\partial y^2} \left(u \frac{\partial u}{\partial x \partial y} + v \frac{\partial^2 u}{\partial y^2} \right) \right. \right. \\ &+ 2 \frac{\partial u}{\partial x} \frac{\partial u}{\partial y} - 2 \left(\frac{\partial u}{\partial y} \right)^2 \frac{\partial^2 u}{\partial x \partial y} \left. \right] + \frac{\partial u}{\partial y} \left(v \frac{\partial^3 u}{\partial y^3} \right. \\ &\left. \left. + u \frac{\partial^3 u}{\partial x \partial y^2} + \frac{\partial u}{\partial x} \frac{\partial^2 u}{\partial y^2} - \frac{\partial u}{\partial y} \frac{\partial^2 u}{\partial x \partial y} \right) \right\}. \end{aligned} \quad (148)$$

For $m = 0$, the equations represent the boundary layers of a second-grade fluid and for $k_1 = 0$, the equations represent the boundary layers of a power-law fluid.

The symmetries for the system of PDEs (148) are [27]

$$\begin{aligned} \xi_1 &= \frac{m+2}{m} a_1 x + a_3, \\ \xi_2 &= a_1 y + a_2(x), \\ \eta_1 &= \frac{m+2}{m} a_1 u, \\ \eta_2 &= a_2'(x) u + a_1 v. \end{aligned} \quad (149)$$

The infinitesimals given in (149) are used to reduce the above system of PDEs into a system of nonlinear ODEs. The reduced ordinary differential system was solved by using a numerical approach for the classical boundary conditions.

10. Maxwell Fluid Flow Problems

In this section, we present those problems which are related to flow of a Maxwell fluid and solved by using the Lie group method.

The Cauchy stress tensor \mathbf{T} in an incompressible Maxwell fluid is given by

$$\begin{aligned} \mathbf{T} &= -p\mathbf{I} + \mathbf{S}, \\ \mathbf{S} + \lambda (\dot{\mathbf{S}} - \mathbf{L}\mathbf{S} - \mathbf{S}\mathbf{L}^T) &= \mu\mathbf{A}, \end{aligned} \quad (150)$$

where $-p\mathbf{I}$ is the indeterminate part of the stress due to the constraint of incompressibility, \mathbf{S} is the extra stress tensor, \mathbf{A} is the first Rivlin-Ericksen tensor, \mathbf{L} is the velocity gradient, μ is the dynamic viscosity, λ is the relaxation time, and the dot denotes the material time differentiation.

10.1. Lie Group Analysis and Similarity Solutions for Hydro-magnetic Maxwell Fluid through a Porous Medium [28]. The only model available dealing with the flow of a Maxwell fluid and solved by employing the Lie group approach was studied by Mekheimer et al. [28]. The equations of a two-dimensional incompressible fluid flow for hydromagnetic Maxwell fluid through a porous medium were investigated in [28]. Lie

group analysis was employed and group invariant solutions were obtained.

The equations governing the two-dimensional motion of an incompressible hydromagnetic Maxwell fluid through a porous medium are written as [28]

$$\begin{aligned} \frac{\partial u}{\partial x} + \frac{\partial v}{\partial y} &= 0, \\ \left(1 + \lambda \frac{\partial}{\partial t} \right) \left[\frac{\partial u}{\partial t} + u \frac{\partial u}{\partial x} + v \frac{\partial u}{\partial y} \right] &+ \left(1 + \lambda \frac{\partial}{\partial t} \right) \frac{\partial p}{\partial x} \\ &- \frac{1}{R} \nabla^2 u + \left(1 + \lambda \frac{\partial}{\partial t} \right) [M\theta(u - mv)] + \frac{1}{Rk} u = 0, \\ \left(1 + \lambda \frac{\partial}{\partial t} \right) \left[\frac{\partial v}{\partial t} + u \frac{\partial v}{\partial x} + v \frac{\partial v}{\partial y} \right] &+ \left(1 + \lambda \frac{\partial}{\partial t} \right) \frac{\partial p}{\partial y} \\ &- \frac{1}{R} \nabla^2 v + \left(1 + \lambda \frac{\partial}{\partial t} \right) [M\theta(v + mu)] + \frac{1}{Rk} v = 0, \end{aligned} \quad (151)$$

where $R = \rho LU/\mu$ is the Reynolds number, $M = \sigma B_0^2/\rho U$ is the Hartmann number, and L, U are the dimensionless length and velocity, respectively.

The infinitesimals for the system of PDEs (151) calculated in [28] are

$$\begin{aligned} \xi_1 &= a_2 - a_1 y, \\ \xi_2 &= a_3 + a_1 x, \\ \xi_3 &= a_4, \\ \eta_1 &= -a_1 v, \\ \eta_2 &= a_2 u, \\ \eta_3 &= \delta(t), \end{aligned} \quad (152)$$

where a_i ($i = 1, \dots, 5$) are arbitrary constants and $\delta(t)$ is an arbitrary function of the variable t only.

With the use of symmetries given in (152), the group invariant solutions for the above system of PDEs with suitable choice of boundary conditions found in [28] are

$$\begin{aligned} u(x, y, t) &= \frac{U_0}{(\alpha_2 - \alpha_1)} \left[\alpha_2 \exp[\alpha_1(y + Wt)] \right. \\ &\left. - \alpha_1 \exp[\alpha_2(y + Wt)] \right], \\ v(x, y, t) &= \frac{V_0}{(\alpha_2 - \alpha_1)} \left[\alpha_2 \exp[\alpha_1(y + Wt)] \right. \\ &\left. - \alpha_1 \exp[\alpha_2(y + Wt)] \right], \\ p(x, y, t) &= \frac{mM\theta U_0}{\alpha_1 \alpha_2 (\alpha_2 - \alpha_1)} \left[-\alpha_1^2 \exp[\alpha_2(y + Wt)] \right. \\ &+ \alpha_2^2 \exp[\alpha_1(y + Wt)] \left. \right] - \left[p_0 - P_a \right. \\ &\left. + \frac{mM\theta U_0}{\alpha_1 \alpha_2} (\alpha_1 + \alpha_2) \right] \exp \left[-\frac{(y + Wt)}{C\lambda} \right] + P_0. \end{aligned} \quad (153)$$

11. Micropolar Fluid Flow Problems

In this section, we recall the flow problems of micropolar fluid solved by the Lie group approach.

The field equations of the micropolar fluid dynamics are

$$\begin{aligned} \operatorname{div} \mathbf{V} &= 0, \\ \rho \frac{d\mathbf{V}}{dt} &= -\operatorname{grad} p - k \operatorname{curl} \mathbf{v} - (\mu + k) \operatorname{curl} \operatorname{curl} \mathbf{v}, \\ \rho j \frac{\partial \mathbf{v}}{\partial t} &= 2k\mathbf{v} + k \operatorname{curl} \mathbf{V} - \gamma \operatorname{curl} \operatorname{curl} \mathbf{v} \\ &\quad + (\alpha + \beta + \gamma) \operatorname{grad} (\operatorname{div} \mathbf{v}), \end{aligned} \quad (154)$$

where \mathbf{V} is the velocity vector, \mathbf{v} is the microrotation vector, p is the pressure of the fluid, ρ and j are the fluid density and the microgyration parameter, and (μ, k) and (α, β, γ) are the viscosity and gyroviscosity coefficients, respectively.

The stress tensor τ_{ij} and the couple stress tensor M_{ij} are given by

$$\begin{aligned} \tau_{ij} &= -p\delta_{ij} + (2\mu + k) e_{ij} + k\varepsilon_{ijm} (\omega_m - v_m), \\ M_{ij} &= \alpha v_{k,k} \delta_{ij} + \beta v_{i,j} + \gamma v_{j,i}, \end{aligned} \quad (155)$$

where ω is the vorticity vector, δ_{ij} is the Kronecker delta, and ε_{ijm} is the alternating symbol.

11.1. Symmetries and Solution of a Micropolar Fluid Flow through a Cylinder [29]. Calmelet-Eluhu and Rosenhaus [29] considered the system of equations of motion for a micropolar fluid inside a cylinder. Classical Lie symmetries of the system of equations are studied and various classes of invariant solutions corresponding to different symmetry subgroups were obtained.

The equations governing the flow of a micropolar fluid inside a cylinder subject to longitudinal and rotational motion are [29]

$$\begin{aligned} \frac{1}{r} U_\theta^2 &= P_r, \\ U_{\theta,t} &= -KW_{z,r} + (1 + K) \left(U_{\theta,rr} + \frac{1}{r} U_{\theta,r} - \frac{1}{r^2} U_\theta \right), \\ U_{z,t} &= K \left(\frac{1}{r} W_\theta + W_{\theta,r} \right) + (1 + K) \left(U_{z,rr} + \frac{1}{r} U_{z,r} \right), \\ JW_{r,t} - J \frac{U_\theta W_\theta}{r} &= -2KW_r + C \left(W_{r,rr} + \frac{1}{r} W_{r,r} - \frac{1}{r^2} W_r \right), \\ JW_{\theta,t} + J \frac{U_\theta W_r}{r} &= -2KW_\theta - KU_{r,z} + \Gamma \left(W_{\theta,rr} + \frac{1}{r} W_{\theta,r} - \frac{1}{r^2} W_\theta \right), \\ JW_{z,t} &= -2KW_z + K \left(U_{\theta,r} + \frac{1}{r} U_\theta \right) \\ &\quad + \Gamma \left(W_{z,rr} + \frac{1}{r} W_{z,r} \right), \end{aligned} \quad (156)$$

where the dimensionless micropolar parameters are

$$\begin{aligned} G &= \frac{\alpha + \beta}{\mu R^2}, \\ J &= \frac{j}{R^2}, \\ K &= \frac{k}{\mu}, \\ \Gamma &= \frac{\gamma}{\mu R^2}, \\ C &= \Gamma + G. \end{aligned} \quad (157)$$

The system of PDEs (156)-(157) is invariant under the algebra of the following operators [29]:

$$\begin{aligned} X_1 &= \frac{\partial}{\partial t}, \\ X_2 &= W_r \frac{\partial}{\partial W_r} + W_\theta \frac{\partial}{\partial W_\theta} + U_z \frac{\partial}{\partial U_z}. \end{aligned} \quad (158)$$

The symmetries given in (158) have been employed to construct the group invariant solutions given by [29]

$$\begin{aligned} W_r &= \sum_{n=1}^{\infty} \frac{a_n l_n}{b_n} J_1(p_n r) e^{-\lambda_n t}, \\ W_\theta &= \sum_{n=1}^{\infty} a_n l_n J_1(p_n r) e^{-\lambda_n t}, \\ U_z &= V + \sum_{n=1}^{\infty} l_n \frac{J_0(p_n) - J_0(p_n r)}{p_n} e^{-\lambda_n t}, \\ U_\theta &= wr, \\ W_z &= w \left(1 - e^{(-2K/r)t} \right). \end{aligned} \quad (159)$$

11.2. Analytic Solution for Flow of a Micropolar Fluid [30]. Shahzad et al. [30] discussed the time-independent equations for the two-dimensional incompressible micropolar fluid. Using group methods, the equations are reduced to ordinary differential equations and then solved analytically.

The governing problem of the flow model [30] is

$$\begin{aligned} \frac{\partial u}{\partial x} + \frac{\partial v}{\partial y} &= 0, \\ u \frac{\partial u}{\partial x} + v \frac{\partial u}{\partial y} &= (\epsilon_1 + \epsilon_2) \left(\frac{\partial^2 u}{\partial x^2} + \frac{\partial^2 u}{\partial y^2} \right) + \epsilon_3 \frac{\partial \sigma}{\partial y} \\ &\quad - \epsilon_4 \frac{\partial p}{\partial x}, \end{aligned}$$

$$\begin{aligned}
 u \frac{\partial u}{\partial x} + v \frac{\partial u}{\partial y} &= (\epsilon_1 + \epsilon_2) \left(\frac{\partial^2 v}{\partial x^2} + \frac{\partial^2 v}{\partial y^2} \right) - \epsilon_3 \frac{\partial \sigma}{\partial x} \\
 &\quad - \epsilon_4 \frac{\partial p}{\partial y}, \\
 u \frac{\partial \sigma}{\partial x} + v \frac{\partial \sigma}{\partial y} &= \epsilon_5 \left(\frac{\partial^2 \sigma}{\partial x^2} + \frac{\partial^2 \sigma}{\partial y^2} \right) - \epsilon_6 \sigma \\
 &\quad + \epsilon_7 \left(\frac{\partial v}{\partial x} - \frac{\partial u}{\partial y} \right),
 \end{aligned}
 \tag{160}$$

with

$$\begin{aligned}
 u(x, 0) &= U_0, \\
 u(x, \infty) &= 0, \\
 \frac{\partial u}{\partial x}(0, y) &= 0, \\
 v(x, 0) &= -V_0, \\
 \sigma(x, 0) &= 0, \\
 \sigma(x, \infty) &= 0, \\
 p(x, \infty) &= p_0,
 \end{aligned}
 \tag{161}$$

where U_0 is the velocity of the plate, V_0 is the magnetic fluid penetrating into the plate, and p_0 is the pressure deep in the magmatic fluid. The infinitesimals for the system of PDEs (160) are [26]

$$\begin{aligned}
 \xi_1 &= b, \\
 \xi_2 &= c, \\
 \eta_1 &= 0, \\
 \eta_2 &= 0, \\
 \eta_3 &= d, \\
 \eta_4 &= e.
 \end{aligned}
 \tag{162}$$

The infinitesimals given in (162) have been used to construct the group invariant solutions given as [30]

$$\begin{aligned}
 u(x, y) &= \frac{-U_0}{(\gamma_2 - \gamma_1)} (\gamma_1 e^{-\alpha y} - \gamma_2 e^{-\beta y}), \\
 v(x, y) &= m \left[\frac{-U_0}{(\gamma_2 - \gamma_1)} (\gamma_1 e^{-\alpha y} - \gamma_2 e^{-\beta y}) \right] - mU_0 \\
 &\quad - V_0, \\
 \sigma(x, y) &= \frac{U_0}{(\gamma_2 - \gamma_1)} (e^{-\alpha y} - e^{-\beta y}), \\
 p(x, y) &= p_0,
 \end{aligned}
 \tag{163}$$

where

$$\begin{aligned}
 \gamma_1 &= \frac{\epsilon_5 (1 + m^2) \alpha^2 - \epsilon_6 + C_1 \alpha}{-\epsilon_7 (1 + m^2) \alpha}, \\
 \gamma_2 &= \frac{\epsilon_5 (1 + m^2) \beta^2 - \epsilon_6 + C_1 \beta}{-\epsilon_7 (1 + m^2) \beta}.
 \end{aligned}
 \tag{164}$$

11.3. Lie Group Analysis of Unsteady MHD Mixed Convection Boundary Layer Flow of a Micropolar Fluid along a Symmetric Wedge with Variable Surface Temperature Saturated Porous Medium [31]. The problem of unsteady mixed convection along a symmetric wedge in the presence of magnetic field was investigated by Mansour et al. [31]. Lie group theory was employed to reduce the governing system of nonlinear partial differential equations. The family of reduced ordinary differential equations was solved numerically using a fourth-order Runge-Kutta algorithm with a shooting technique.

The equations governing the unsteady MHD mixed convection boundary layer flow of a micropolar fluid along a symmetric wedge with variable surface temperature saturated porous medium are [31]

$$\begin{aligned}
 \frac{\partial u}{\partial x} + \frac{\partial v}{\partial y} &= 0, \\
 \frac{\partial u}{\partial t} + u \frac{\partial u}{\partial x} + v \frac{\partial u}{\partial y} &= mx^{2m-1} + (1 + \Delta) \frac{\partial^2 u}{\partial y^2} + \Omega \theta \\
 &\quad + \Delta \frac{\partial N}{\partial y} \\
 &\quad - \left[M + \frac{1}{Da} \right] (u - x^m), \\
 \frac{\partial N}{\partial t} + u \frac{\partial N}{\partial x} + v \frac{\partial N}{\partial y} &= \lambda \frac{\partial^2 N}{\partial y^2} - \Delta B \left[\frac{\partial u}{\partial y} + 2N \right], \\
 \frac{\partial \theta}{\partial t} + u \frac{\partial \theta}{\partial x} + v \frac{\partial \theta}{\partial y} &= \frac{1}{Pr} \frac{\partial^2 \theta}{\partial y^2}.
 \end{aligned}
 \tag{165}$$

In the above equations, Pr is the Prandtl number, Ω is the mixed convection parameter, λ is the microrotation parameter, M is the magnetic parameter, Δ is the vortex-viscosity parameter, and Da is the permeability parameter.

The relevant boundary conditions are

$$\begin{aligned}
 u = v = 0, \\
 N = -n \frac{\partial u}{\partial y}, \\
 T = x^{2m-1} \\
 \text{at } y = 0, \\
 u = x^m, \\
 N \rightarrow 0, \\
 T \rightarrow T_\infty \\
 \text{as } y \rightarrow \infty.
 \end{aligned}
 \tag{166}$$

The system of PDEs (165) is invariant under the algebra spanned by the following generators [31]:

$$\begin{aligned}
 X_1 &= x \frac{\partial}{\partial x}, \\
 X_2 &= x \frac{\partial}{\partial y} + u \frac{\partial}{\partial v}, \\
 X_3 &= y \frac{\partial}{\partial y}, \\
 X_4 &= t \frac{\partial}{\partial t}, \\
 X_5 &= \frac{\partial}{\partial t}, \\
 X_6 &= u \frac{\partial}{\partial u}, \\
 X_7 &= v \frac{\partial}{\partial v}, \\
 X_8 &= N \frac{\partial}{\partial N}, \\
 X_9 &= \theta \frac{\partial}{\partial \theta}, \\
 X_{h_1(t)} &= h_1(t) \frac{\partial}{\partial x} + h_1'(t) \frac{\partial}{\partial u}.
 \end{aligned} \tag{167}$$

The operators given in (167) are used to reduce the above system of PDEs into a system of nonlinear ODEs. The reduced ordinary differential system was solved numerically using a fourth-order Runge-Kutta algorithm and the shooting technique.

11.4. Group Properties and Invariant Solutions of Plane Micropolar Flows [32]. The study dealing with the plane micropolar flows from the viewpoint of Lie groups was made by Saccomandi [32]. An exact steady state solution for the plane flow of an incompressible micropolar fluid was deduced by employing the theory of Lie groups.

The equations governing the motion of an incompressible two-dimensional micropolar fluid are

$$\begin{aligned}
 \frac{\partial u}{\partial x} + \frac{\partial v}{\partial y} &= 0, \\
 \rho \left(\frac{\partial u}{\partial t} + u \frac{\partial u}{\partial x} + v \frac{\partial u}{\partial y} \right) - (\mu + k) \left(\frac{\partial^2 u}{\partial x^2} + \frac{\partial^2 u}{\partial y^2} \right) \\
 - k \frac{\partial b}{\partial y} + \frac{\partial p}{\partial x} &= 0, \\
 \rho \left(\frac{\partial v}{\partial t} + u \frac{\partial v}{\partial x} + v \frac{\partial v}{\partial y} \right) - (\mu + k) \left(\frac{\partial^2 v}{\partial x^2} + \frac{\partial^2 v}{\partial y^2} \right) \\
 + k \frac{\partial b}{\partial x} + \frac{\partial p}{\partial y} &= 0,
 \end{aligned}$$

$$\begin{aligned}
 pI \left(\frac{\partial b}{\partial t} + u \frac{\partial b}{\partial x} + v \frac{\partial b}{\partial y} \right) + 2kb - k \left(\frac{\partial v}{\partial x} - \frac{\partial u}{\partial y} \right) \\
 - \alpha \left(\frac{\partial^2 b}{\partial x^2} + \frac{\partial^2 b}{\partial y^2} \right) = 0.
 \end{aligned} \tag{168}$$

The infinitesimals for the system of PDEs (168) are [32]

$$\begin{aligned}
 \xi_1 &= \alpha, \\
 \xi_2 &= -\gamma y + f(t), \\
 \xi_3 &= \gamma x + g(t), \\
 \eta_1 &= -\gamma v + f'(t), \\
 \eta_2 &= \gamma u + g'(t), \\
 \eta_3 &= j(t) - x f''(t) - y g''(t), \\
 \eta_4 &= \lambda \exp \left(-\frac{2k}{pI} t \right),
 \end{aligned} \tag{169}$$

where, γ , and λ are three arbitrary parameters and $f(t)$, $g(t)$, and $j(t)$ are arbitrary smooth functions of t .

With the use of symmetries given in (169), the group invariant solutions for the above system of PDEs are [32]

$$\begin{aligned}
 u &= f(t) - (y - G(t)) (c_1 \zeta^{-1} + c_7 \ln(\zeta) + c_8), \\
 v &= g(t) + (x - F(t)) (c_1 \zeta^{-1} + c_7 \ln(\zeta) + c_8), \\
 p &= p \left(-x f'(t) - y g'(t) - \frac{1}{2} c_1 \zeta^{-1} \right. \\
 &\quad \left. + (c_7^2 - c_7 c_8 + \frac{1}{2} c_8^2) \zeta + c_1 c_6 \ln(\zeta) \right. \\
 &\quad \left. - (c_7^2 - c_7 c_8) \zeta \ln(\zeta) + \frac{1}{2} c_1 c_7 [\ln(\zeta)]^2 \right. \\
 &\quad \left. + \frac{1}{2} c_7^2 \zeta [\ln(\zeta)]^2 \right) - 4(\mu + k) \tan^{-1} \left[\frac{x - F(t)}{y - G(t)} \right] \\
 &\quad + 2k c_5 \left(\tan^{-1} \left[\frac{x - F(t)}{y - G(t)} \right] + \tan^{-1} \left[\frac{y - G(t)}{x - F(t)} \right] \right) \\
 &\quad + K(t),
 \end{aligned} \tag{170}$$

where

$$\zeta = [x - F(t)]^2 + [y - G(t)]^2. \tag{171}$$

12. Eyring-Powell Fluid Flow Problems

Here, we review the flow models of Eyring-Powell fluid which are solved using the Lie symmetry method.

The stress tensor of the Eyring-Powell non-Newtonian fluid model is

$$\tau_{ij} = \mu \frac{\partial V_i}{\partial x_j} + \frac{1}{\beta} \sinh^{-1} \left[\frac{1}{c} \left(\frac{\partial V_i}{\partial x_j} \right) \right], \tag{172}$$

where

$$\sinh^{-1} \left[\frac{1}{c} \left(\frac{\partial V_i}{\partial x_j} \right) \right] \approx \frac{1}{c} \left(\frac{\partial V_i}{\partial x_j} \right) - \frac{1}{6} \left(\frac{1}{c} \frac{\partial V_i}{\partial x_j} \right)^3; \tag{173}$$

$$\left| \frac{1}{c} \frac{\partial V_i}{\partial x_j} \right| \ll 1.$$

In the above equations, μ is the dynamic viscosity, x_j is the number of space variables on which the velocity components depend, and β and c are the Eyring-Powell fluid parameters.

12.1. Similarity Solutions for Boundary Layer Equations of a Powell-Eyring Fluid [33]. A study is available in the literature dealing with the flow of Eyring-Powell fluid and solved by employing the Lie symmetry approach which is very recent by Hayat et al. [33]. They derived the boundary layer equations for the first time for the Eyring-Powell fluid model. Using a scaling symmetry of the equations, the partial differential system was transformed to an ordinary differential system. The resulting equations were numerically solved using a finite difference algorithm.

The dimensionless form of the boundary layer equations for Eyring-Powell fluid is [33]

$$\frac{\partial u}{\partial x} + \frac{\partial v}{\partial y} = 0,$$

$$u \frac{\partial u}{\partial x} + v \frac{\partial u}{\partial y} = -\frac{\partial p}{\partial x} + (\varepsilon_1 + \varepsilon_2 \varepsilon_3) \frac{\partial^2 u}{\partial y^2} - \frac{1}{2} \varepsilon_2 \varepsilon_3^2 \left(\frac{\partial u}{\partial y} \right)^2 \frac{\partial^2 u}{\partial y^2}. \tag{174}$$

The classical boundary conditions for the problem are

$$\begin{aligned} u(x, 0) &= 0, \\ v(x, 0) &= 0, \\ u(x, \infty) &= U(x). \end{aligned} \tag{175}$$

By the use of the Lie group method, the similarity transformation used for the reduction of the above system of PDEs is [33]

$$\begin{aligned} \xi &= \frac{y}{x^{1/3}}, \\ u &= x^{1/3} f(\xi), \\ v &= \frac{g(\xi)}{x^{1/3}}, \\ U &= x^{1/3}. \end{aligned} \tag{176}$$

The transformation given in (176) transforms the two-dimensional unsteady boundary layer equation problem of Eyring-Powell fluid to ordinary differential equations. The reduced ordinary differential equations were solved numerically by using a finite difference method.

12.2. Flow and Heat Transfer of Powell-Eyring Fluid over a Stretching Surface: A Lie Group Analysis [34]. The flow and heat transfer analysis of Powell-Eyring fluid over a permeable stretching surface was studied by Jalil and Asghar [34]. By using the Lie group analysis, the symmetries of the equations were obtained. Four finite parameter and one infinite parameter Lie group of transformations were found. Similarity transformations for the model were derived with the help of these symmetries. The governing system of partial differential equations was transformed to a system of ordinary differential equations by using the similarity transformations. The reduced equations were solved numerically using the Keller-box method.

The two-dimensional laminar flow of a steady, incompressible Powell-Eyring fluid over a semi-infinite surface stretching is governed by [34]

$$\frac{\partial u}{\partial x} + \frac{\partial v}{\partial y} = 0,$$

$$u \frac{\partial u}{\partial x} + v \frac{\partial u}{\partial y} = (1 + \varepsilon) \frac{\partial^2 u}{\partial y^2} - \varepsilon \delta \left(\frac{\partial u}{\partial y} \right)^2 \frac{\partial^2 u}{\partial y^2}, \tag{177}$$

$$u \frac{\partial T}{\partial x} + v \frac{\partial T}{\partial y} = \frac{1}{Pr} \frac{\partial^2 T}{\partial y^2}.$$

The corresponding boundary conditions are

$$\begin{aligned} u &= u_w(x), \\ v &= v_w(x), \\ T &= T_w(x) \end{aligned} \quad \text{at } y = 0, \tag{178}$$

$$\begin{aligned} u &= 0, \\ T &= 0 \end{aligned} \quad \text{as } y \rightarrow \infty.$$

The infinitesimals for the system of PDEs (177) are [34]

$$\begin{aligned} \xi_1 &= a + bx, \\ \xi_2 &= \frac{b}{3}y + \gamma(x), \\ \eta_1 &= \frac{b}{3}u, \\ \eta_2 &= -\frac{b}{3}v + u\gamma'(x), \\ \eta_3 &= c + mT. \end{aligned} \tag{179}$$

With the use of the symmetries given in (179), the similarity transformations used for the reduction of above system of PDEs are [34]

$$\begin{aligned} \eta &= \frac{yx^{-1/3}}{(a+bx)^{1/3}}, \\ u &= u_w(x) f'(\eta), \\ v &= v_w(x) h(\eta), \\ T &= T_w(x) \theta(\eta). \end{aligned} \tag{180}$$

The similarity transformation given in (180) transforms the above system of PDEs into nonlinear system of ODEs. The reduced ordinary differential equations were solved numerically by using a Keller-box method.

12.3. Self-Similar Solutions for the Flow and Heat Transfer of Powell-Eyring Fluid over a Moving Surface in a Parallel Free Stream [35]. The boundary layer flow and heat transfer of Powell-Eyring fluid over a continuously moving permeable surface were studied by Jalil et al. [35]. The boundary layer equations were transformed to self-similar nonlinear ordinary differential equations using group of transformations. Numerical results of the resulting equations were obtained using the Keller-box method.

The dimensionless form of the boundary layer equations is [35]

$$\begin{aligned} \frac{\partial u}{\partial x} + \frac{\partial v}{\partial y} &= 0, \\ u \frac{\partial u}{\partial x} + v \frac{\partial u}{\partial y} &= u_e \frac{du_e}{dx} + (1 + \varepsilon) \frac{\partial^2 u}{\partial y^2} \\ &\quad - \varepsilon \delta \left(\frac{\partial u}{\partial y} \right)^2 \frac{\partial^2 u}{\partial y^2}, \\ u \frac{\partial T}{\partial x} + v \frac{\partial T}{\partial y} &= \frac{1}{Pr} \frac{\partial^2 T}{\partial y^2}. \end{aligned} \tag{181}$$

The boundary conditions for the problem are

$$\begin{aligned} u &= \gamma u_w(x), \\ v &= s v_w(x), \\ T &= T_w(x) \\ &\text{at } y = 0, \\ u &= u_e(x), \\ T &= 0 \\ &\text{as } y \rightarrow \infty, \end{aligned} \tag{182}$$

where ε and δ are the fluid parameters, γ is the velocity ratio, and s is a nondimensional constant. The symmetries for the system of PDEs (181) are [35]

$$\begin{aligned} \xi_1 &= ax, \\ \xi_2 &= \frac{a}{3}y, \\ \eta_1 &= \frac{a}{3}u, \\ \eta_2 &= -\frac{a}{3}v, \\ \eta_3 &= \frac{a}{3}u_e + mT. \end{aligned} \tag{183}$$

Using the symmetries given in (183), the transformations used for the reduction of above system of PDEs are [35]

$$\begin{aligned} \eta &= \gamma x^{-1/3}, \\ u &= x^{1/3} f'(\eta), \\ v &= x^{-1/3} h(\eta), \\ T &= x^m \theta(\eta), \\ u_e &= kx^{1/3}. \end{aligned} \tag{184}$$

The above system of PDEs is transformed into nonlinear system of ODEs under the transformation given in (184). The reduced ODEs system was solved numerically by using a Keller-box method.

13. Oldroyd-B Fluid Flow Problems

In this section, we discuss the studies related to flow of an Oldroyd-B fluid that are solved with the aid of the Lie group method.

The constitutive equation of Oldroyd-B fluid is written as

$$\mathbf{S} + \lambda_1 \frac{\delta \mathbf{S}}{\delta t} = \mu \left(1 + \lambda_1 \frac{\delta}{\delta t} \right) \mathbf{A}_1, \tag{185}$$

where μ is the viscosity and λ_1 and λ_2 are material time constants referred to the characteristic relaxation and characteristic retardation times. It is assumed that $\lambda_1 \geq \lambda_2 \geq 0$. The tensor \mathbf{A}_1 and L are defined as

$$\begin{aligned} \mathbf{A}_1 &= L + L^T, \\ L &= \text{grad } \mathbf{V}. \end{aligned} \tag{186}$$

The operator $\delta/\delta t$ operating on any tensor \mathbf{S} is defined by

$$\frac{\delta \mathbf{S}}{\delta t} = \frac{\partial \mathbf{S}}{\partial t} + \mathbf{V} \cdot \nabla \mathbf{S} - \mathbf{S} L - L^T \mathbf{S}. \tag{187}$$

13.1. Similarity Solutions and Conservation Laws for Rotating Flows of an Oldroyd-B Fluid [36]. The similarity reduction arising from the classical Lie point symmetries of the

unsteady hydromagnetic flows of a rotating Oldroyd-B fluid under influence of Hall currents is carried out by Fakhar et al. [36]. They employed different combinations of translation and rotational symmetries and obtained a class of new exact solutions under certain initial and boundary conditions.

The unsteady hydromagnetic flow of a rotating Oldroyd-B fluid under influence of a Hall current is governed by the following system [36]:

$$\begin{aligned}
 u_{zt} &= 2\Omega v_z - \lambda_1 (u_{ztt} - 2\Omega v_{zt}) \\
 &\quad - \frac{M}{1+m^2} (u_z + \lambda_1 u_{zt}) \\
 &\quad + \frac{mM}{1+m^2} (v_z + \lambda_1 v_{zt}) + v u_{zzz} + v \lambda_2 u_{zzzt}, \\
 v_{zt} &= -2\Omega u_z - \lambda_1 (v_{ztt} + 2\Omega u_{zt}) \\
 &\quad - \frac{M}{1+m^2} (v_z + \lambda_1 v_{zt}) \\
 &\quad - \frac{mM}{1+m^2} (u_z + \lambda_1 u_{zt}) + v v_{zzz} + v \lambda_2 v_{zzzt}.
 \end{aligned} \tag{188}$$

The symmetry Lie algebra for the above system of PDEs is spanned by the following operators [36]:

$$\begin{aligned}
 X_1 &= \frac{\partial}{\partial t}, \\
 X_2 &= \frac{\partial}{\partial z}, \\
 X_3 &= u \frac{\partial}{\partial u} + v \frac{\partial}{\partial v}, \\
 X_4 &= v \frac{\partial}{\partial u} - u \frac{\partial}{\partial v}, \\
 X_5(f_1) &= f_1(z, t) \frac{\partial}{\partial u}, \\
 X_6(f_2) &= f_2(z, t) \frac{\partial}{\partial v}.
 \end{aligned} \tag{189}$$

The symmetry Lie operators given in (189) were employed to construct the group invariant solutions given by [36]

$$\begin{pmatrix} u \\ v \end{pmatrix} = \begin{pmatrix} \gamma_{01} \\ \gamma_{02} \end{pmatrix} + \begin{pmatrix} \gamma_{11} \\ \gamma_{12} \end{pmatrix} e^{(1/b\lambda_1)(az-bt)} + \begin{bmatrix} \cos \frac{a\beta}{b} \left(z - \frac{b}{a} t \right) & -\sin \frac{a\beta}{b} \left(z - \frac{b}{a} t \right) \\ \sin \frac{a\beta}{b} \left(z - \frac{b}{a} t \right) & \cos \frac{a\beta}{b} \left(z - \frac{b}{a} t \right) \end{bmatrix} \begin{pmatrix} \gamma_{21} \\ \gamma_{22} \end{pmatrix} e^{(a\alpha/b)(z-(b/a)t)}, \tag{190}$$

where $c_j = \gamma_{j1} + i\gamma_{j2}$ ($j = 0, 1, 2$) and

$$\begin{aligned}
 \lambda_1 &= \frac{1}{bk_1}, \\
 b &= \frac{\alpha + i\beta}{k_2}, \\
 \alpha &= \frac{M}{1+m^2}, \\
 \beta &= m\alpha + 2\Omega.
 \end{aligned} \tag{191}$$

14. Third-Grade Fluid Flow Problems

In this section, we provide a review of those problems which are related to the flow of a third-grade fluid model.

The constitutive relation for an incompressible third-grade fluid is

$$\begin{aligned}
 \mathbf{T} &= -p\mathbf{I} + \mu\mathbf{A}_1 + \alpha_1\mathbf{A}_2 + \alpha_2\mathbf{A}_1^2 + \beta_1\mathbf{A}_3 \\
 &\quad + \beta_2(\mathbf{A}_1\mathbf{A}_2 + \mathbf{A}_2\mathbf{A}_1) + \beta_3(\text{tr } \mathbf{A}_1^2)\mathbf{A}_1.
 \end{aligned} \tag{192}$$

In the above relation, p is the pressure, \mathbf{I} is the identity tensor, μ is the dynamic viscosity, α_i ($i = 1, 2$) and β_i ($i = 1-3$) are the material constants, and \mathbf{A}_i ($i = 1-3$) are the Rivlin-Ericksen tensors.

Moreover, the Clausius-Duhem inequality and the result that the Helmholtz free energy is minimum in equilibrium provide the following restrictions:

$$\begin{aligned}
 \mu &\geq 0, \\
 \alpha_1 &\geq 0, \\
 |\alpha_1 + \alpha_2| &\leq \sqrt{24\mu\beta_3}, \\
 \beta_1 = \beta_2 &= 0, \\
 \beta_3 &\geq 0.
 \end{aligned} \tag{193}$$

Therefore, the constitutive relation for a thermodynamically compatible fluid of grade three becomes

$$\mathbf{T} = -p\mathbf{I} + \mu\mathbf{A}_1 + \alpha_1\mathbf{A}_2 + \alpha_2\mathbf{A}_1^2 + \beta_3(\text{tr } \mathbf{A}_1^2)\mathbf{A}_1. \tag{194}$$

14.1. Exact Flow of a Third-Grade Fluid on a Porous Wall [37]. The flow of a third-grade fluid occupying the space over a wall was studied by Hayat et al. [37]. The governing nonlinear partial differential equation was solved analytically using the Lie group method.

The equation governing the flow model [37] is

$$\rho \left[\frac{\partial u}{\partial t} - W_0 \frac{\partial u}{\partial y} \right] = \mu \frac{\partial^2 u}{\partial y^2} + \alpha_1 \frac{\partial^3 u}{\partial y^2 \partial t} - \alpha_1 W_0 \frac{\partial^3 u}{\partial y^3} + 6\beta_3 \left(\frac{\partial u}{\partial y} \right)^2 \frac{\partial^2 u}{\partial y^2}. \tag{195}$$

We know that from basics of Lie symmetry methods that if a differential equation is explicitly independent of any dependent or independent variable, then this differential equation remains invariant under the translation symmetry corresponding to that particular variable. The above PDE (195) admits Lie point symmetry generators, $\partial/\partial t$ (time translation) and $\partial/\partial y$ (space-translation in y). Thus, a travelling wave solution was obtained in [37] corresponding to the generator $\partial/\partial t + M\partial/\partial y$. After performing the successive symmetry reductions, the governing PDE (195) admits exact solution of the form [37]

$$u(y, t) = \frac{1}{\Delta} 2\alpha_1 \left[(M + W_0) \exp \left(\frac{\Delta(Mt - y)}{2\alpha_1(M + W_0)} \right) \right] \times \left[-A_1 + \frac{\varepsilon(2\Delta + 3\mu)A_1^3 \exp(\Delta(Mt - y)/2\alpha_1(M + W_0))}{3\mu^2 + 16\alpha_1\rho(M + W_0)^2} - \varepsilon A_3 \right], \tag{196}$$

where

$$\Delta = \mu + \sqrt{\mu^2 + 4\alpha_1\rho(M + W_0)^2}. \tag{197}$$

The same problem was investigated later by Fakhar [38]. In [38], translational type symmetries were utilized to perform the travelling wave reduction on the governing model and the reduced model was solved using a power series method. Fakhar et al. [39] investigated the same model again. They made use of translational symmetries to reduce the governing model and presented some numerical solutions for a particular choice of boundary conditions.

14.2. Similarity Solutions of Boundary Layer Equations for a Special Non-Newtonian Fluid in a Special Coordinate System [40]. Yürüsoy [40] derived the boundary layer equations for a third-grade non-Newtonian fluid. By using Lie group methods, infinitesimal generators of the boundary layer equations were calculated. The equations were transformed into an ordinary differential system and then the numerical solutions of the resultant nonlinear differential equations were found by using a combination of a Runge-Kutta algorithm and a shooting technique.

The governing problem describing the flow model [40] is

$$\frac{\partial W_\phi}{\partial \phi} + \frac{\partial W_\psi}{\partial \psi} = 0, \tag{198}$$

$$W_\phi \frac{\partial W_\phi}{\partial \phi} + W_\psi \frac{\partial W_\phi}{\partial \psi} + (W_\phi^2 - 1) \frac{dQ_B}{d\phi} = \frac{\partial^2 W_\phi}{\partial \psi^2} + 6k_{q_B}^4 \phi \frac{\partial^2 W_\phi}{\partial \psi^2} \left(\frac{\partial W_\phi}{\partial \psi} \right)^2,$$

with

$$W_\phi(\phi, 0) = W_\psi(\psi, 0) = 0, \tag{199}$$

$$W_\phi(\phi, \infty) = 1,$$

where $Q'_B = q'_B/q_B$ and k is a third-grade fluid parameter.

The infinitesimals for the system of PDEs (198) are [40]

$$\xi_1 = 2a\phi + b, \tag{200}$$

$$\xi_2 = a\psi, \tag{200}$$

$$\eta_1 = 0, \tag{200}$$

$$\eta_2 = -aW'_\psi.$$

The infinitesimals given in (200) were used to reduce the above system of PDEs to a system of nonlinear ODEs. The reduced ordinary differential system was solved by using a numerical approach for the classical boundary conditions given in (199).

14.3. Couette Flow of a Third-Grade Fluid with Variable Magnetic Field [41]. The study dealing with the analytic solution for the time-dependent flow of an incompressible third-grade fluid under the influence of a magnetic field of variable strength was made by Jalil et al. [35]. Group theoretic methods were employed to analyze the nonlinear problem and a solution for the velocity field was obtained analytically.

The governing equation of the problem [41] is

$$\frac{\partial u}{\partial t} = \frac{\nu}{r} \frac{\partial}{\partial r} (ru_r) + \frac{\alpha}{r} \frac{\partial}{\partial r} (ru_{tr}) + \frac{2\Gamma}{r} \frac{\partial}{\partial r} (ru_r^3) - H^2(t) + k, \tag{201}$$

where $\alpha = \alpha_1/\rho$, $\Gamma = \beta_3/\rho$, $M = \sigma\mu^2/\rho$, and ν is the kinematic viscosity.

The Lie point symmetries for the PDE (201) are [41]

$$X_1 = \frac{\partial}{\partial u}, \tag{202}$$

$$X_2 = \frac{\partial}{\partial t} - H^2(t) \frac{\partial}{\partial u}.$$

With the use of the symmetries in (202), the group invariant solution for the PDE (201) was calculated in [41] and is given by

$$u(x, t) = \int \frac{54cx + 6 \sqrt[2]{(48 + 81c^2x^2)} - 12}{6 \left(54cx + 6 \sqrt[1]{(48 + 81c^2x^2)} \right)} dx + c1 - 2ct - \int H^2(t) dt. \tag{203}$$

14.4. *Hall Effects on Unsteady Magnetohydrodynamic Flow of a Third-Grade Fluid [42].* The model of unsteady MHD flow of an incompressible third-grade fluid bounded by an infinite porous plate in the presence of Hall current was investigated by Fakhar et al. [42]. Similarity transformations were employed to reduce the governing partial differential equation into two nonlinear ordinary differential equations. The numerical solutions of the reduced equations were presented by the use of finite difference schemes.

The equation governing the unsteady MHD flow of an incompressible electrically conducting third-grade fluid in the presence of Hall current is written as [42]

$$\frac{\partial F}{\partial t} - \frac{\partial F}{\partial y} = \frac{\partial^2 F}{\partial y^2} + \alpha \left(\frac{\partial^3 u}{\partial y^2 \partial t} - \frac{\partial^3 F}{\partial y^3} \right) + \varepsilon \left(\frac{\partial F}{\partial y} \right)^2 \frac{\partial^2 F}{\partial y^2} - \kappa F, \tag{204}$$

where $\kappa = (k/(1 - i\psi))$ and $F = u + iw$.

In [42], the travelling wave symmetries were utilized to reduce the above PDE into two nonlinear ODEs. The reduced ODEs were solved for the particular choice of boundary conditions using the finite difference method.

Fakhar et al. [43] recently revisited the above problem. In [43], they performed the complete Lie group analysis of (204). The Lie point symmetries of PDE (204) found in [43] are

$$\begin{aligned} X_1 &= \frac{\partial}{\partial y}, \\ X_2 &= \frac{\partial}{\partial t}, \\ X_3 &= e^{(-\kappa/(1+\psi^2))t} \left[e^{-i((\kappa\psi/(1+\psi^2))t)} \frac{\partial}{\partial F} + e^{i((\kappa\psi/(1+\psi^2))t)} \frac{\partial}{\partial \bar{F}} \right], \\ X_4 &= -e^{(-\kappa/(1+\psi^2))t} \left[e^{-i((\kappa\psi/(1+\psi^2))t)} \frac{\partial}{\partial F} + e^{i((\kappa\psi/(1+\psi^2))t)} \frac{\partial}{\partial \bar{F}} \right]. \end{aligned} \tag{205}$$

The symmetry Lie generators given in (205) were used to reduce the above PDE into two nonlinear ODEs. The reduced ODEs were solved by making use of the homotopy analysis method.

14.5. *Unsteady Solutions in a Third-Grade Fluid Filling the Porous Space [44].* An analysis was made of the unsteady flow of a third-grade fluid in a porous medium by Hayat et al. [44]. Reduction and exact solutions of the governing model were obtained by employing the Lie group theoretic approach.

The problem governing the model [44] is

$$\frac{\partial u}{\partial t} = \mu_* \frac{\partial^2 u}{\partial y^2} + \alpha \frac{\partial^3 u}{\partial y^2 \partial t} + \gamma_1 \left(\frac{\partial u}{\partial y} \right)^2 \frac{\partial^2 u}{\partial y^2} - \gamma_2 u \left(\frac{\partial u}{\partial y} \right)^2 - \phi_1 u. \tag{206}$$

The relevant boundary and initial conditions are

$$\begin{aligned} u(0, t) &= u_0 V(t), \quad t > 0, \\ u(\infty, t) &= 0, \quad t > 0, \\ u(y, 0) &= g(y), \quad y > 0, \end{aligned} \tag{207}$$

where

$$\begin{aligned} \mu_* &= \frac{\mu}{\rho + \alpha_1 (\phi/k)}, \\ \alpha &= \frac{\alpha_1}{\rho + \alpha_1 (\phi/k)}, \\ \gamma_1 &= \frac{6\beta_3}{\rho + \alpha_1 (\phi/k)}, \\ \beta_* &= \frac{2\beta_3 (\phi/k)}{\rho + \alpha_1 (\phi/k)}, \\ \phi_1 &= \frac{\mu (\phi/k)}{\rho + \alpha_1 (\phi/k)}. \end{aligned} \tag{208}$$

The complete Lie symmetry analysis of (206) resulted in [44].

Case 1 ($\phi_1 \neq \mu_*/\alpha$). For this case, a two-dimensional Lie algebra is generated by

$$\begin{aligned} X_1 &= \frac{\partial}{\partial t}, \\ X_2 &= \frac{\partial}{\partial y}. \end{aligned} \tag{209}$$

Case 2 ($\phi_1 = \mu_*/\alpha$). Here a three-dimensional Lie algebra is generated by

$$\begin{aligned} X_1 &= \frac{\partial}{\partial t}, \\ X_2 &= \frac{\partial}{\partial y}, \\ X_3 &= e^{2(\mu_*/\alpha)t} \frac{\partial}{\partial t} - \frac{\mu_*}{\alpha} u e^{2(\mu_*/\alpha)t} \frac{\partial}{\partial u}. \end{aligned} \tag{210}$$

With the use of the symmetries given above, two types of group invariant solutions have been found in [44] and are

$$u(y, t) = u_0 \exp\left(\frac{\sqrt{\gamma_2}(y + ct)}{-\sqrt{\gamma_1}}\right),$$

$$u(y, t) = \exp\left[-\left\{\left(\frac{\mu_*}{\alpha}\right)t + \left(\sqrt{\frac{\gamma_2}{\gamma_1}}\right)y\right\}\right]. \tag{211}$$

14.6. *The Rayleigh Problem for a Third-Grade Electrically Conducting Fluid in a Magnetic Field* [45]. The influence of a magnetic field on the flow of an incompressible third-grade electrically conducting fluid bounded by a rigid plate was investigated by Hayat et al. [45]. The Lie group approach was employed to perform the reduction of the model equation and thereafter numerical solutions were obtained.

The governing problem describing the flow model [45] is

$$\frac{\partial u}{\partial t} = \nu \frac{\partial^2 u}{\partial y^2} + \alpha \frac{\partial^3 u}{\partial y^2 \partial t} + \epsilon \left(\frac{\partial u}{\partial y}\right)^2 \frac{\partial^2 u}{\partial y^2} - MH^2(t)u, \tag{212}$$

with

$$u(0, t) = u_0 V(t), \quad t > 0,$$

$$u(y, t) \rightarrow 0 \quad \text{as } y \rightarrow \infty, \quad t > 0, \tag{213}$$

$$u(y, 0) = g(y), \quad y > 0.$$

The symmetry Lie algebra of the PDE (212) is spanned by the following operators [45]:

$$X_1 = \frac{\partial}{\partial y},$$

$$X_2 = e^{2\beta t} \frac{\partial}{\partial t} - \beta u e^{2\beta t} \frac{\partial}{\partial u}, \tag{214}$$

$$X_3 = L(t) \frac{\partial}{\partial u},$$

where

$$L(t) = \exp\left(-M \int_0^t H^2(s) ds\right). \tag{215}$$

The point symmetries given in (214) were used to reduce the PDE (212) into a nonlinear ODE. The reduced ODE was solved numerically with suitable invariant boundary conditions.

14.7. *A Note on the Interplay between Symmetries, Reduction, and Conservation Laws of Stokes' First Problem for Third-Grade Rotating Fluids* [46]. Fakhar et al. [46] studied the equations governing the Stokes' first problem for a third-grade rotating fluid. Lie symmetry formulation was used to perform various reductions of the governing system.

The system of equations describing the Stokes' first problem for a third-grade rotating fluid is [46]

$$u_t - 2Cv = u_{xx} + au_{txx} + 2b \frac{\partial}{\partial x} (u_x^3 + u_x v_x^2),$$

$$v_t + 2Cu = v_{xx} + av_{txx} + 2b \frac{\partial}{\partial x} (v_x^3 + v_x u_x^2). \tag{216}$$

The symmetries for the above system of PDEs were calculated in [46] and are given by

$$X_1 = \frac{\partial}{\partial x},$$

$$X_2 = \frac{\partial}{\partial t},$$

$$X_3 = u \frac{\partial}{\partial v} - v \frac{\partial}{\partial u}, \tag{217}$$

$$X_4 = -\sin(2Ct) \frac{\partial}{\partial v} + \cos(2Ct) \frac{\partial}{\partial u},$$

$$X_5 = \cos(2Ct) \frac{\partial}{\partial v} + \sin(2Ct) \frac{\partial}{\partial u}.$$

The five Lie symmetries given in (217) were used to reduce the PDE system (216) to a system of ODEs.

14.8. *Group Invariant Solutions for the Unsteady MHD Flow of a Third-Grade Fluid in a Porous Medium* [47]. Aziz et al. [47] investigated the governing nonlinear partial differential equation for the unidirectional flow of a third-grade fluid by using the symmetry approach. Three types of analytical solutions were obtained for the governing model by employing the Lie symmetry method.

The problem governing the unsteady magnetohydrodynamic flow of a third-grade fluid in a porous medium is [47]

$$\frac{\partial u}{\partial t} = \mu_* \frac{\partial^2 u}{\partial y^2} + \alpha_* \frac{\partial^3 u}{\partial y^2 \partial t} + \beta \left(\frac{\partial u}{\partial y}\right)^2 \frac{\partial^2 u}{\partial y^2}$$

$$- \beta_* u \left(\frac{\partial u}{\partial y}\right)^2 - \phi_* u - M_*^2 u. \tag{218}$$

The relevant time and space dependent velocity boundary conditions are

$$u(y, 0) = g(y), \quad y > 0,$$

$$u(0, t) = V(t), \quad t > 0, \tag{219}$$

$$u(\infty, t) = 0, \quad t > 0,$$

where

$$\mu_* = \frac{\mu}{1 + \alpha_1 \phi},$$

$$\alpha_* = \frac{\alpha_1}{1 + \alpha_1 \phi},$$

$$\beta = \frac{3\beta_3}{1 + \alpha_1 \phi},$$

$$\beta_* = \frac{\beta_3 \phi}{1 + \alpha_1 \phi}, \tag{220}$$

$$\phi_* = \frac{\phi}{1 + \alpha_1 \phi},$$

$$M_*^2 = \frac{M^2}{1 + \alpha_1 \phi}.$$

The Lie point symmetries for the PDE (218) are [47]

$$\begin{aligned}
 X_1 &= \frac{\partial}{\partial t}, \\
 X_2 &= \frac{\partial}{\partial y}, \\
 X_3 &= -\left(\frac{1}{\phi_* + M_*^2}\right) e^{2(\phi_* + M_*^2)t} \frac{\partial}{\partial t} + u e^{2(\phi_* + M_*^2)t} \frac{\partial}{\partial u}, \\
 &\text{where } \phi_* + M_*^2 = \frac{\mu_*}{\alpha_*}.
 \end{aligned}
 \tag{221}$$

With the use of the symmetries given in (221), three types of invariant solutions were obtained in [47] for PDE (218) and are given by

$$\begin{aligned}
 u(y, t) &= \exp\left(\frac{\sqrt{\beta_*}(y - ct)}{-\sqrt{\beta}}\right), \\
 u(y, t) &= \exp\left[-\left\{(\phi_* + M_*^2)t + \sqrt{\frac{\beta_*}{\beta}}y\right\}\right], \\
 u(y) &= v_0 \exp\left(-\frac{\sqrt{\beta_*}}{\sqrt{\beta}}y\right).
 \end{aligned}
 \tag{222}$$

14.9. MHD Flow of a Third-Grade Fluid in a Porous Half Space with Plate Suction or Injection [48]. The modelling and solution of the unsteady flow of an incompressible third-grade fluid over a porous plate within a porous medium were performed by A. Aziz and T. Aziz [48]. Lie group theory was employed to find the symmetries of the model equation. These symmetries were applied to transform the original third-order partial differential equation to third-order ordinary differential equations. These third-order ordinary differential equations were solved analytically.

The governing problem describing the flow model [48] is

$$\begin{aligned}
 \frac{\partial u}{\partial t} &= \mu_* \frac{\partial^2 u}{\partial y^2} + \alpha_* \frac{\partial^3 u}{\partial y^2 \partial t} - \alpha_* W_0 \frac{\partial^3 u}{\partial y^3} \\
 &+ \gamma \left(\frac{\partial u}{\partial y}\right)^2 \frac{\partial^2 u}{\partial y^2} - \gamma_* u \left(\frac{\partial u}{\partial y}\right)^2 \\
 &+ W_0 \frac{\partial u}{\partial y} - \phi_* u - M_*^2 u,
 \end{aligned}
 \tag{223}$$

$$u(0, t) = V(t), \quad t > 0, \tag{224}$$

$$u(y, t) \rightarrow 0 \quad \text{as } y \rightarrow \infty, \quad t > 0, \tag{225}$$

$$u(y, 0) = f(y), \quad y > 0, \tag{226}$$

where

$$\begin{aligned}
 \mu_* &= \frac{1}{(1 + \alpha\phi)}, \\
 \alpha_* &= \frac{\alpha}{(1 + \alpha\phi)}, \\
 \gamma &= \frac{3\beta}{(1 + \alpha\phi)}, \\
 \gamma_* &= \frac{\beta\phi}{(1 + \alpha\phi)}, \\
 \phi_* &= \frac{\phi}{(1 + \alpha\phi)}, \\
 M_*^2 &= \frac{M^2}{(1 + \alpha\phi)}.
 \end{aligned}
 \tag{227}$$

The symmetry Lie algebra of the PDE (225) is spanned by the following generators [48].

Case 1 (when $(\phi_* + M_*^2) \neq \mu_*/\alpha_*$). For this case, we find a two-dimensional Lie algebra generated by

$$\begin{aligned}
 X_1 &= \frac{\partial}{\partial t}, \\
 X_2 &= \frac{\partial}{\partial y}.
 \end{aligned}
 \tag{228}$$

Case 2 (when $(\phi_* + M_*^2) = \mu_*/\alpha_*$). Here we obtain a three-dimensional Lie algebra generated by

$$\begin{aligned}
 X_1 &= \frac{\partial}{\partial t}, \\
 X_2 &= \frac{\partial}{\partial y}, \\
 X_3 &= -e^{2(\phi_* + M_*^2)t} \frac{\partial}{\partial t} + W_0 e^{2(\phi_* + M_*^2)t} \frac{\partial}{\partial y} \\
 &+ u(\phi_* + M_*^2) e^{2(\phi_* + M_*^2)t} \frac{\partial}{\partial u}.
 \end{aligned}
 \tag{229}$$

The generators given above were utilized to obtain three different types of group invariant solutions [48]

$$\begin{aligned}
 u(y, t) &= \exp\left(-\frac{\sqrt{\gamma_*}(y - ct)}{\sqrt{\gamma}}\right), \\
 u(y, t) &= \exp\left(-\frac{\sqrt{\gamma_*}(y + ct)}{\sqrt{\gamma}}\right), \\
 u(y, t) &= u_0 \\
 &\cdot \exp\left[-\left\{\left(\sqrt{\frac{\gamma_*}{\gamma}}W_0 + \phi_* + M_*^2\right)t + \sqrt{\frac{\gamma_*}{\gamma}}y\right\}\right].
 \end{aligned}
 \tag{230}$$

Remark 1. A revisit has been made by Aziz et al. [49] for three flow problems [44, 47, 48] related to a third-grade fluid model and discussed earlier. A conditional symmetry approach was employed in [49] to construct some new exact solutions of these models. All possible nonclassical symmetry generators were calculated in [49] for these problems. The concept of conditional/nonclassical symmetry was not previously used to find conditionally invariant solutions of non-Newtonian fluid flow problems. This is the first time that a complete nonclassical symmetry analysis was performed to tackle a nonlinear problem dealing with the flow models of non-Newtonian fluids.

For the flow model [44], the following nonclassical symmetry generators were found in [49]

$$\begin{aligned} X_1 &= \left[\exp\left(-\frac{2}{K_*}t\right) - K_* \right] \frac{\partial}{\partial t} + u \frac{\partial}{\partial u}, \\ X_2 &= -K_* \frac{\partial}{\partial t} + \exp\left(-\frac{2}{K_*}t\right) \frac{\partial}{\partial y} + u \frac{\partial}{\partial u}, \\ X_3 &= \frac{\partial}{\partial t} + \theta u \frac{\partial}{\partial u}, \\ X_4 &= \frac{\partial}{\partial t} + \lambda(t) u \frac{\partial}{\partial u}, \end{aligned} \tag{231}$$

where $\lambda(t)$ is any function of time t . Thus, infinitely many nonclassical symmetry generators were obtained for any arbitrary value of the function $\lambda(t)$. With the use of the nonclassical symmetries given in (231), the following new invariant solutions were obtained in [49] for the model [44]

$$\begin{aligned} u(t) &= u_0 \exp\left[-\frac{t}{(\kappa/\phi\nu + \alpha_1/\mu)}\right], \\ u(y, t) &= \exp\left[-\left\{\left(\frac{\beta - \mu_*\beta_*K_*}{K_*\beta - \alpha_*K_*\beta_*}\right)t + \sqrt{\frac{\beta_*}{\beta}}y\right\}\right], \\ u(y, t) &= \exp\left[\gamma(t) - \sqrt{\frac{1}{K_*\mu_*}}y\right] \end{aligned} \tag{232}$$

$$\text{where } \gamma(t) = \int \lambda(t) dt,$$

$$u(y, t) = \left[a_3 \exp\left(\frac{2}{K_*}t\right) \right]^{-1/2} \exp\left(-\frac{\sqrt{\beta_*}}{\sqrt{\beta}}y\right).$$

For the model [46], the following nonclassical symmetry generators were found in [49]

$$\begin{aligned} X_1 &= \left[\exp\left(-\left(\frac{1}{K_*} + M_*^2\right)2t\right) - (K_* + M_*^2) \right] \frac{\partial}{\partial t} \\ &\quad + u \frac{\partial}{\partial u}, \\ X_2 &= -(K_* + M_*^2) \frac{\partial}{\partial t} \\ &\quad + \exp\left(-\left(\frac{1}{K_*} + M_*^2\right)2t\right) \frac{\partial}{\partial y} + u \frac{\partial}{\partial u}, \end{aligned}$$

$$\begin{aligned} X_3 &= \frac{\partial}{\partial t} + \lambda u \frac{\partial}{\partial u}, \\ X_4 &= \frac{\partial}{\partial t} + \delta(t) u \frac{\partial}{\partial u}, \end{aligned} \tag{233}$$

where $\delta(t)$ is any arbitrary function of time. With the use of the symmetries given in (233), the following new exact solutions were found in [49] for the model [46]

$$\begin{aligned} u(y, t) &= \exp\left[-\left(\frac{1 + KM^2}{K + \alpha}\right)t\right], \\ u(y, t) &= \exp\left[-\left\{\left(\frac{\beta + K_*\beta M_*^2 - \mu_*\beta_*K_*}{K_*\beta - \alpha_*K_*\beta_*}\right)t\right.\right. \\ &\quad \left.\left.+ \left(\sqrt{\frac{\beta_*}{\beta}}\right)y\right\}\right], \\ u(y, t) &= \exp\left[\zeta(t) - \sqrt{\left(\frac{1}{K_*\mu_*} + \frac{M_*^2}{\mu_*}\right)}y\right] \end{aligned} \tag{234}$$

$$\text{where } \zeta(t) = \int \delta(t) dt,$$

$$u(y, t) = \left[b_3 \exp\left(\frac{1}{K_*} + M_*^2\right)2t \right]^{-1/2} \exp\left(-\frac{\sqrt{\beta_*}}{\sqrt{\beta}}y\right).$$

For the flow model [48], the only nonclassical symmetry operator found in [49] is

$$\chi = \frac{\partial}{\partial t} + \epsilon u \frac{\partial}{\partial u}. \tag{235}$$

With the use of the symmetry given above, the new group invariant solution of the flow model [48] found in [49] is given by

$$\begin{aligned} u(y, t) &= \exp\left[-\left\{\left(\frac{1}{\beta - \alpha_*\beta_*}\right)\right.\right. \\ &\quad \cdot \left(\frac{\beta}{K_*} + \beta M_*^2 - \mu_*\beta_* + W\sqrt{\frac{\beta_*}{\beta}}(\beta - \alpha_*\beta_*)\right)t \\ &\quad \left.\left.+ \sqrt{\frac{\beta_*}{\beta}}y\right\}\right]. \end{aligned} \tag{236}$$

15. Fourth-Grade Fluid Flow Problems

In this section, all those problems dealing with the flow of a fourth-grade non-Newtonian fluid model investigated by using Lie symmetry approach are revisited.

For a fourth-grade fluid model, the Cauchy stress tensor satisfies the constitutive equations

$$\mathbf{T} = -p\mathbf{I} + \sum_{j=1}^n \mathbf{S}_j \quad \text{with } n = 4, \quad (237)$$

where p is the pressure, \mathbf{I} is the identity tensor, and \mathbf{S}_j is the extra stress tensor with components

$$\begin{aligned} \mathbf{S}_1 &= \mu \mathbf{A}_1, \\ \mathbf{S}_2 &= \alpha_1 \mathbf{A}_2 + \alpha_2 \mathbf{A}_1^2, \\ \mathbf{S}_3 &= \beta_1 \mathbf{A}_3 + \beta_2 (\mathbf{A}_1 \mathbf{A}_2 + \mathbf{A}_2 \mathbf{A}_1) + \beta_3 (\text{tr } \mathbf{A}_1^2) \mathbf{A}_1, \\ \mathbf{S}_4 &= \gamma_1 \mathbf{A}_4 + \gamma_2 (\mathbf{A}_3 \mathbf{A}_1 + \mathbf{A}_1 \mathbf{A}_3) + \gamma_3 \mathbf{A}_2^2 \\ &\quad + \gamma_4 (\mathbf{A}_2 \mathbf{A}_1^2 + \mathbf{A}_1^2 \mathbf{A}_2) \gamma_5 (\text{tr } \mathbf{A}_2) \mathbf{A}_2 \\ &\quad + \gamma_6 (\text{tr } \mathbf{A}_2) \mathbf{A}_1^2 \\ &\quad + [\gamma_7 \text{tr } \mathbf{A}_3 + \gamma_8 \text{tr } (\mathbf{A}_2 \mathbf{A}_1)] \mathbf{A}_1. \end{aligned} \quad (238)$$

Here μ is the dynamic viscosity, α_i ($i = 1, 2$), β_i ($i = 1, 2, 3$), and γ_i ($i = 1, 2, \dots, 8$) are the material constants, and \mathbf{A}_1 to \mathbf{A}_4 are the Rivlin-Ericksen tensors.

15.1. *The Unsteady Flow of a Fourth-Grade Fluid Past a Porous Plate* [50]. Hayat et al. [50] examined the unsteady flow of a hydrodynamic fluid past a porous plate. The solution of the governing nonlinear problem was obtained by the implementation of the Lie group method.

The problem governing the unsteady flow model of a fourth-grade fluid past a porous plate is [50]

$$\begin{aligned} \rho \left[\frac{\partial u}{\partial t} - W \frac{\partial u}{\partial y} \right] &= \mu \frac{\partial^2 u}{\partial y^2} + \alpha_1 \left[\frac{\partial^3 u}{\partial y^2 \partial t} - W \frac{\partial^3 u}{\partial y^3} \right] \\ &\quad + \beta_1 \left[\frac{\partial^4 u}{\partial y^2 \partial t^2} - 2W \frac{\partial^4 u}{\partial y^3 \partial t} + W_0^2 \frac{\partial^4 u}{\partial y^4} \right] + 6(\beta_2 \\ &\quad + \beta_3) \left(\frac{\partial u}{\partial y} \right)^2 \frac{\partial^2 u}{\partial y^2} + \gamma_1 \left[\frac{\partial^5 u}{\partial y^2 \partial t^3} - 3W \frac{\partial^5 u}{\partial y^3 \partial t^2} \right. \\ &\quad \left. + 3W^2 \frac{\partial^5 u}{\partial y^4 \partial t} - W^3 \frac{\partial^5 u}{\partial y^5} \right] + \Gamma \frac{\partial}{\partial y} \left[\left(\frac{\partial u}{\partial y} \right)^2 \frac{\partial^2 u}{\partial y \partial t} \right] \\ &\quad - \Gamma W \frac{\partial}{\partial y} \left[\left(\frac{\partial u}{\partial y} \right)^2 \frac{\partial^2 u}{\partial y^2} \right], \end{aligned} \quad (239)$$

where $\Gamma = 2(3\gamma_2 + \gamma_3 + \gamma_4 + \gamma_5 + 3\gamma_7 + \gamma_8)$. The relevant initial and boundary conditions are

$$\begin{aligned} u(0, t) &= 0, \\ u(y, t) &\rightarrow U \quad \text{as } y \rightarrow \infty, \\ \frac{\partial u^n}{\partial y^n} &\rightarrow 0 \quad \text{as } y \rightarrow \infty \quad (n = 1, 2, 3). \end{aligned} \quad (240)$$

Equation (239) admits the Lie point symmetry generators $G = \partial/\partial t$ (time translation) and $X = \partial/\partial y$ (translation in y). The invariant solution corresponding to the generator $G + cX$ which represents a travelling wave solution with constant wave speed c has been considered in [50]. The final form of the travelling wave solution found in [50] is

$$\begin{aligned} u(y, t) &= -U \exp \left(\frac{-2c(\beta_2 + \beta_3)(t - T)}{\Gamma(c + W)} \right) \\ &\quad \cdot \left[\exp \left(\frac{2(\beta_2 + \beta_3)y}{\Gamma(c + W)} \right) - 1 \right]. \end{aligned} \quad (241)$$

The same model was recently discussed by Aziz and Mahomed [51] by considering a different set of boundary and initial conditions and they found some more physically meaningful exact solutions. The closed-form travelling wave and the steady state solutions found in [51] are

$$\begin{aligned} u(y, t) &= \exp \left[\frac{-\beta(y + ct)}{6\Gamma(c - W_0)} \right], \quad \text{with } c > W_0, \\ u = H(y) &= \exp \left(\frac{\beta y}{3\Gamma W_0} \right). \end{aligned} \quad (242)$$

15.2. *Travelling Wave Solutions to Stokes' Problem for a Fourth-Grade Fluid* [52]. A nonlinear partial differential equation modelling the flow of a fourth-grade fluid was derived by Hayat et al. [52]. Travelling wave solutions admitted by the model equation were deduced by employing the Lie symmetry approach.

The nonlinear governing PDE for the unsteady flow of a fourth-grade fluid over a flat rigid plate is [52]

$$\begin{aligned} \rho \frac{\partial u}{\partial t} &= \mu \frac{\partial^2 u}{\partial y^2} + \alpha \frac{\partial^3 u}{\partial y^2 \partial t} + \beta \frac{\partial^4 u}{\partial y^2 \partial t^2} \\ &\quad + \beta_* \left(\frac{\partial u}{\partial y} \right)^2 \frac{\partial^2 u}{\partial y^2} + \gamma \frac{\partial^5 u}{\partial y^2 \partial t^3} \\ &\quad + \Gamma \frac{\partial}{\partial y} \left[\left(\frac{\partial u}{\partial y} \right)^2 \frac{\partial^2 u}{\partial y \partial t} \right], \end{aligned} \quad (243)$$

where $\beta_* = (\beta_2 + \beta_3)$ and $\Gamma = 2(3\gamma_2 + \gamma_3 + \gamma_4 + \gamma_5 + 3\gamma_7 + \gamma_8)$.

It can be seen that the PDE (243) admits Lie point symmetry generators

$$\begin{aligned} X_1 &= \frac{\partial}{\partial t}, \\ X_2 &= \frac{\partial}{\partial y}. \end{aligned} \quad (244)$$

With the use of symmetry generators given in (244), the exact travelling wave solutions found in [52] are given by

$$u(y, t) = \exp \left[\frac{\beta_*(y - ct)}{6c\Gamma} \right]. \quad (245)$$

The same PDE (243) was investigated recently by Aziz and Mahomed [53] with a suitable choice of physically realistic

boundary conditions. Both forward and the backward wave front type travelling wave solutions were found in [53] with the aid of the Lie group approach and are given by

$$\begin{aligned} u(y, t) &= \exp\left[\frac{-\beta(y+ct)}{6c\gamma}\right] \quad \text{with } c > 0, \\ u(y, t) &= \exp\left[\frac{\beta(y-ct)}{6c\gamma}\right] \quad \text{with } c > 0. \end{aligned} \quad (246)$$

A conditional/nonclassical symmetry solution of PDE (243) was also found by Aziz and Mahomed [53] and is given by

$$\begin{aligned} u(y, t) &= \exp\left[-\left\{\left(\frac{\beta}{6\gamma}\right)t\right.\right. \\ &\left.\left. + \sqrt{\left(\frac{-\beta/6\gamma}{1-\alpha(\beta/6\gamma)+\beta_1(\beta/6\gamma)^2-\gamma_1(\beta/6\gamma)^3}\right)y}\right\}\right]. \end{aligned} \quad (247)$$

15.3. Effect of Magnetic Field on the Flow of a Fourth-Order Fluid [54]. A study was conducted by Hayat et al. [54] to examine the flow engendered in a semi-infinite expanse of an incompressible non-Newtonian fluid by an infinite rigid plate moving with an arbitrary velocity in its own plane. The fluid was considered to be fourth-order and electrically conducting. A magnetic field was applied in the transverse direction to the flow. The nonlinear problem was solved for a constant magnetic field analytically using Lie reduction methods.

The governing problem describing the flow model [54] is given by

$$\begin{aligned} \frac{\partial u}{\partial t} &= \frac{\partial^2 u}{\partial y^2} + \alpha_1 \frac{\partial^3 u}{\partial y^2 \partial t} + \beta_1 \frac{\partial^4 u}{\partial y^2 \partial t^2} + \beta \left(\frac{\partial u}{\partial y}\right)^2 \frac{\partial^2 u}{\partial y^2} \\ &+ \gamma_1 \frac{\partial^5 u}{\partial y^2 \partial t^3} + \gamma \frac{\partial}{\partial y} \left[\left(\frac{\partial u}{\partial y}\right)^2 \frac{\partial^2 u}{\partial y \partial t} \right] \\ &- \rho M H^2 u, \end{aligned} \quad (248)$$

with

$$\begin{aligned} u(0, t) &= u_0 V(t), \quad t > 0, \\ u(\infty, t) &= 0, \quad t > 0, \\ u(y, 0) &= g(y), \quad y > 0, \end{aligned} \quad (249)$$

where u_0 is the reference velocity.

Note that (248) has two translation symmetry generators: namely,

$$\begin{aligned} X_1 &= \frac{\partial}{\partial t}, \\ X_2 &= \frac{\partial}{\partial y}. \end{aligned} \quad (250)$$

Thus, a travelling wave solution was obtained in [54] for the above problem using the translational symmetries and is

given by

$$u(y, t) = u_0 \exp\left[\frac{\beta y}{3c\gamma} - \frac{\beta t}{3\gamma}\right], \quad (251)$$

provided that

$$\begin{aligned} -c\rho \left(\frac{\beta}{3c\gamma}\right) &= \mu \left(\frac{\beta}{3c\gamma}\right)^2 - \alpha_1 c \left(\frac{\beta}{3c\gamma}\right)^3 \\ &+ \beta_1 c^2 \left(\frac{\beta}{3c\gamma}\right)^4 - \gamma_1 c^3 \left(\frac{\beta}{3c\gamma}\right)^5 \\ &- \rho M H^2 = 0. \end{aligned} \quad (252)$$

15.4. A Note on Some Solutions for the Flow of a Fourth-Grade Fluid in a Porous Space [55]. Hayat et al. [55] investigated the time-independent unidirectional flow of a fourth-grade fluid filling the porous half space. Flow modelling was based upon a modified Darcy's law. Travelling wave and conditional symmetry solutions were developed for the governing model.

The flow problem governing the time-dependent flow of a fourth-grade fluid in a porous space is given by [55]

$$\begin{aligned} \frac{\partial u}{\partial t} &= \mu_* \frac{\partial^2 u}{\partial y^2} + \alpha_* \frac{\partial^3 u}{\partial y^2 \partial t} + \beta \frac{\partial^4 u}{\partial y^2 \partial t^2} \\ &+ \beta_* \left(\frac{\partial u}{\partial y}\right)^2 \frac{\partial^2 u}{\partial y^2} + \gamma \frac{\partial^5 u}{\partial y^2 \partial t^3} \\ &+ \gamma_* \frac{\partial}{\partial y} \left[\left(\frac{\partial u}{\partial y}\right)^2 \frac{\partial^2 u}{\partial y \partial t} \right] - \phi_1 u - \phi_2 u \frac{\partial^2 u}{\partial t^2} \\ &- \phi_3 u \left(\frac{\partial u}{\partial y}\right)^2 - \phi_4 u \frac{\partial^3 u}{\partial t^3} \\ &- \phi_5 u \left(\frac{\partial u}{\partial y}\right) \left(\frac{\partial^2 u}{\partial y \partial t}\right), \end{aligned} \quad (253)$$

where

$$\mu_* = \frac{\mu}{(\rho + \alpha(\phi/\kappa))},$$

$$\alpha_* = \frac{\alpha_1}{(\rho + \alpha(\phi/\kappa))},$$

$$\beta = \frac{\beta_1}{(\rho + \alpha(\phi/\kappa))},$$

$$\beta_* = \frac{6(\beta_2 + \beta_3)}{(\rho + \alpha(\phi/\kappa))},$$

$$\gamma = \frac{\gamma_1(\phi/\kappa)}{(\rho + \alpha(\phi/\kappa))},$$

$$\gamma_* = \frac{\Gamma}{(\rho + \alpha(\phi/\kappa))},$$

$$\gamma_* = \frac{2(3\gamma_2 + \gamma_3 + \gamma_4 + \gamma_5 + 3\gamma_7 + \gamma_8)}{(\rho + \alpha(\phi/\kappa))},$$

$$\begin{aligned} \phi_1 &= \frac{\mu\varphi(\phi/\kappa)}{(\rho + \alpha(\phi/\kappa))}, \\ \phi_2 &= \frac{\beta_1(\phi/\kappa)}{(\rho + \alpha(\phi/\kappa))}, \\ \phi_3 &= \frac{2(\beta_2 + \beta_3)(\phi/\kappa)}{(\rho + \alpha(\phi/\kappa))}, \\ \phi_4 &= \frac{\gamma_1(\phi/\kappa)}{(\rho + \alpha(\phi/\kappa))}, \\ \phi_5 &= \frac{2(3\gamma_2 + \gamma_3 + \gamma_4 + \gamma_5 + 3\gamma_7 + \gamma_8)(\phi/\kappa)}{(\rho + \alpha(\phi/\kappa))}. \end{aligned} \tag{254}$$

The relevant initial and boundary conditions are

$$\begin{aligned} u(0, t) &= u_0 V(t), \quad t > 0, \\ u(\infty, t) &= 0, \quad t > 0, \\ u(y, 0) &= f(y), \quad y > 0, \\ \frac{\partial u(y, 0)}{\partial t} &= g(y), \quad y > 0, \\ \frac{\partial^2 u(y, 0)}{\partial t^2} &= h(y), \quad y > 0. \end{aligned} \tag{255}$$

With the use of translational symmetry generators, the travelling wave solution for the PDE (253) found in [55] is given by

$$u(y, t) = u_0 \exp\left[-\frac{\phi_2}{c\phi_4}(y + ct)\right]. \tag{256}$$

The nonclassical symmetry generator for the PDE (253) found in [55] is given by

$$X = \frac{\partial}{\partial t} - \frac{\phi_2}{\phi_4} u \frac{\partial}{\partial u}. \tag{257}$$

With the use of nonclassical symmetry operator (257), the conditionally invariant solution found in [55] is given by

$$u(y, t) = \exp\left(-\frac{\phi_2}{\phi_4} t\right) B(y), \tag{258}$$

where

$$B(y) \left(\phi_1 - \frac{\phi_2}{\phi_4}\right) = \left(\frac{-\gamma_1 \phi_2^3}{\phi_4^3} + \frac{\beta_2 \phi_2^2}{\phi_4^2} - \frac{\alpha \phi_2}{\phi_4}\right), \tag{259}$$

with

$$\begin{aligned} B(0) &= 1, \\ B(l) &= 0, \quad l > 0. \end{aligned} \tag{260}$$

15.5. *Invariant Solutions for the Unsteady Magneto hydrodynamics (MHD) Flow of a Fourth-Grade Fluid Induced due to the Impulsive Motion of a Flat Porous Plate* [56]. An analysis is carried out recently by Aziz et al. [56] to investigate the time-dependent flow of an incompressible electrically conducting fourth-grade fluid over an infinite porous plate. The governing nonlinear problem was solved by invoking the Lie group theoretic approach and a numerical technique. Travelling wave solutions of the forward and backward type, together with a steady state solution, were obtained in [56].

The governing PDE for the flow model [56] is given by

$$\begin{aligned} \frac{\partial u}{\partial t} &= W \frac{\partial u}{\partial y} + \frac{\partial^2 u}{\partial y^2} + \alpha_1 \left[\frac{\partial^3 u}{\partial y^2 \partial t} - W \frac{\partial^3 u}{\partial y^3} \right] \\ &+ \beta_1 \left[\frac{\partial^4 u}{\partial y^2 \partial t^2} - 2W \frac{\partial^4 u}{\partial y^3 \partial t} + W_0^2 \frac{\partial^4 u}{\partial y^4} \right] \\ &+ \beta \left(\frac{\partial u}{\partial y} \right)^2 \frac{\partial^2 u}{\partial y^2} + \gamma \left[\frac{\partial^5 u}{\partial y^2 \partial t^3} - 3W \frac{\partial^5 u}{\partial y^3 \partial t^2} \right. \\ &+ 3W^2 \frac{\partial^5 u}{\partial y^4 \partial t} - W^3 \frac{\partial^5 u}{\partial y^5} \left. \right] \\ &+ 2\Gamma \frac{\partial}{\partial y} \left[\left(\frac{\partial u}{\partial y} \right)^2 \frac{\partial^2 u}{\partial y \partial t} \right] \\ &- 2\Gamma W \frac{\partial}{\partial y} \left[\left(\frac{\partial u}{\partial y} \right)^2 \frac{\partial^2 u}{\partial y^2} \right] - M^2 u. \end{aligned} \tag{261}$$

The relevant boundary and initial conditions are [56]

$$\begin{aligned} u(0, t) &= V(t), \quad t > 0, \\ u(\infty, t) &= 0, \quad t > 0, \\ u(y, 0) &= f(y), \quad y > 0, \\ \frac{\partial u}{\partial t}(y, 0) &= g(y), \quad y > 0, \\ \frac{\partial^2 u}{\partial t^2}(y, 0) &= h(y), \quad y > 0. \end{aligned} \tag{262}$$

With the use of translational symmetry generators, the backward type travelling wave solution for the PDE (261) found in [56] is given by

$$\begin{aligned} u(y, t) &= \exp \left[\left(-\frac{M^2}{(m - W)} + \frac{\gamma \beta^5}{(6\Gamma)^5 (m - W)^3} \right. \right. \\ &- \frac{\beta_1 \beta^4}{(6\Gamma)^4 (m - W)^3} + \frac{\alpha \beta^3}{(6\Gamma)^3 (m - W)^3} \\ &\left. \left. - \frac{\beta^2}{(6\Gamma)^2 (m - W)^3} \right) (y + mt) \right]. \end{aligned} \tag{263}$$

The forward type travelling wave solution for the PDE (261) is given by

$$u(y, t) = \exp \left[\frac{\beta(y - mt)}{6\Gamma(m + W)} \right]. \tag{264}$$

Finally the steady-state solution of the problem found in [56] is

$$u = R(y) = \exp\left(\frac{\beta y}{6\Gamma W}\right). \tag{265}$$

15.6. Group Theoretical Analysis and Invariant Solutions for Unsteady Flow of a Fourth-Grade Fluid over an Infinite Plate Undergoing Impulsive Motion in a Darcy Porous Medium [57]. An incompressible time-dependent flow of a fourth-grade fluid in a porous half space has been investigated very recently by Aziz et al. [57]. The partial differential equation governing the motion was reduced to ordinary differential equations by means of Lie group theoretic analysis. Various new classes of group invariant solutions were developed for the model problem by employing the classical and nonclassical symmetry methods. Travelling wave solutions, steady state solution, and conditional symmetry solutions were obtained in [57] as closed-form exponential functions.

The governing PDE for the flow model [57] is given by

$$\begin{aligned} \frac{\partial u}{\partial t} = & \mu_* \frac{\partial^2 u}{\partial y^2} + \alpha_* \frac{\partial^3 u}{\partial y^2 \partial t} + \beta \frac{\partial^4 u}{\partial y^2 \partial t^2} \\ & + \beta_* \left(\frac{\partial u}{\partial y}\right)^2 \frac{\partial^2 u}{\partial y^2} + \gamma_* \frac{\partial^5 u}{\partial y^2 \partial t^3} \\ & + 2\Gamma_* \frac{\partial}{\partial y} \left[\left(\frac{\partial u}{\partial y}\right)^2 \frac{\partial^2 u}{\partial y \partial t} \right] - \kappa_1 u - \kappa_2 \frac{\partial^2 u}{\partial t^2} \\ & - \kappa_3 u \left(\frac{\partial u}{\partial y}\right)^2 - \kappa_4 \frac{\partial^3 u}{\partial t^3} \\ & - \kappa_5 u \left(\frac{\partial u}{\partial y}\right) \left(\frac{\partial^2 u}{\partial y \partial t}\right). \end{aligned} \tag{266}$$

The relevant space and time-dependent velocity boundary and initial conditions are [57]

$$\begin{aligned} u(0, t) &= V(t), \quad t > 0, \\ u(\infty, t) &= 0, \quad t > 0, \\ u(y, 0) &= f(y), \quad y > 0, \\ \frac{\partial u(y, 0)}{\partial t} &= g(y), \quad y > 0, \\ \frac{\partial^2 u(y, 0)}{\partial t^2} &= h(y), \quad y > 0, \end{aligned} \tag{267}$$

where $f(y) = I(y)/U_0$, $g(y) = J(y)/U_0$, and $h(y) = K(y)/U_0$. The Lie point symmetries for the PDE (266) are [57]

$$\begin{aligned} X_1 &= \frac{\partial}{\partial t}, \\ X_2 &= \frac{\partial}{\partial y}, \\ X_3 &= -\exp\left(\frac{\kappa_3 t}{\kappa_5}\right) \frac{\partial}{\partial t} + \left(\frac{\kappa_3}{\kappa_5}\right) \exp\left(\frac{\kappa_3 t}{\kappa_5}\right) u \frac{\partial}{\partial u}, \end{aligned} \tag{268}$$

provided that

$$\begin{aligned} 3\Gamma_* \left(\frac{\kappa_3}{\kappa_5}\right) - \beta_* &= 0, \\ 6\kappa_4 \left(\frac{\kappa_3}{\kappa_5}\right) - \kappa_2 &= 0, \\ 6\gamma_* \left(\frac{\kappa_3}{\kappa_5}\right) - \beta &= 0, \\ \kappa_4 \left(\frac{\kappa_3}{\kappa_5}\right)^3 + \kappa_2 \left(\frac{\kappa_3}{\kappa_5}\right)^2 + \left(\frac{\kappa_3}{\kappa_5}\right) - 3\kappa_1 &= 0, \\ 4\kappa_4 \left(\frac{\kappa_3}{\kappa_5}\right)^2 + 3\kappa_2 \left(\frac{\kappa_3}{\kappa_5}\right) - 2 &= 0, \\ 4\gamma_* \left(\frac{\kappa_3}{\kappa_5}\right)^2 + 3\beta \left(\frac{\kappa_3}{\kappa_5}\right) - 2\alpha_* &= 0, \\ \gamma_* \left(\frac{\kappa_3}{\kappa_5}\right)^3 + \beta \left(\frac{\kappa_3}{\kappa_5}\right)^2 + \alpha_* \left(\frac{\kappa_3}{\kappa_5}\right) - 3\mu_* &= 0. \end{aligned} \tag{269}$$

Here X_1 is translation in time, X_2 is translation in space, and X_3 has path curves which are equivalent to a combination of translations in t and scaling in u . With the use of the symmetries given in (268), the following exact solutions were found in [57] for the model [57]

$$\begin{aligned} u(y, t) &= \exp \left[- \left\{ \left(\frac{\kappa_3}{\kappa_5}\right) t + \sqrt{\frac{(\kappa_1 - \kappa_2 \beta_*^2 / 9\Gamma_*^2)}{(\mu_* - \beta^3 / 36\gamma_*^2)}} y \right\} \right], \\ u(y) &= \exp \left(- \sqrt{\frac{\kappa_3}{\beta_*}} y \right), \\ u(y, t) &= \exp \left[- \left\{ \frac{\beta_* + \sqrt{\beta_*^2 + 12m\Gamma_* (\kappa_3 + \kappa_5 m)}}{6\Gamma_* m} \right\} \cdot (y + mt) \right], \quad m > 0. \end{aligned} \tag{270}$$

The nonclassical symmetry generator for the PDE (266) found in [57] is given by

$$\chi = \frac{\partial}{\partial t} - u \frac{\partial}{\partial u}. \tag{271}$$

With the use of nonclassical symmetry operator (271), the conditionally invariant solutions found in [57] are given by

$$u(y, t) = \exp \left[- \left\{ t + \sqrt{\left(\frac{\kappa_3 - \kappa_5}{\beta_* - 6\Gamma_*} \right) y} \right\} \right],$$

$$u(y, t) = \exp \left[- \left\{ t + \sqrt{\left(\frac{\kappa_1 + \kappa_2 - \kappa_4 - 1}{\mu_* - \alpha_* + \beta - \gamma_*} \right) y} \right\} \right]. \quad (272)$$

16. Couple Stress Fluid Flow Problems

In this section, we provide a review of those problems which deal with the flow of non-Newtonian couple stress fluid and solved using the classical Lie group approach.

The governing equations for the flow of an incompressible couple stress fluid are

$$\bar{\nabla} \cdot \bar{\mathbf{q}} = 0,$$

$$\rho \left[\frac{\partial}{\partial t} + (\bar{\mathbf{q}} \cdot \bar{\nabla}) \bar{\mathbf{q}} \right] = -\bar{\nabla} p - \mu \bar{\nabla} \times \bar{\nabla} \times \bar{\mathbf{q}} - \eta \bar{\nabla} \times \bar{\nabla} \times \bar{\nabla} \times \bar{\mathbf{q}}, \quad (273)$$

where ρ is the density, $\bar{\mathbf{q}}$ is the velocity vector, p is the fluid pressure, μ is the fluid viscosity, and η is the couple stress fluid parameter.

The force stress tensor \mathbf{T} and the couple stress tensor \mathbf{M} that arise in the theory of couple stress fluids are given by

$$\mathbf{T} = (-p + \lambda_1 \text{div } \bar{\mathbf{q}}) \mathbf{I} + \mu \left[\text{grad } \bar{\mathbf{q}} + (\text{grad } \bar{\mathbf{q}})^T \right] + \frac{1}{2} \mathbf{I} \times [\text{div } \mathbf{M} + \rho C], \quad (274)$$

$$\mathbf{M} = m \mathbf{I} + 2\eta \text{grad} (\text{curl } \bar{\mathbf{q}}) + 2\eta^l (\text{grad} (\text{curl } \bar{\mathbf{q}}))^T,$$

where m is 1/3 trace of \mathbf{M} and ρC is the body couple tensor. The quantity λ_1 is the material constant and η^l is the constant associated with couple stresses. These material constants satisfy the inequalities

$$\begin{aligned} \mu &\geq 0, \\ 3\lambda + 2\mu &\geq 0, \\ \eta &\geq 0, \\ \eta^l &\leq \eta. \end{aligned} \quad (275)$$

16.1. Flow and Heat Transfer of Couple Stress Fluid in a Porous Channel with Expanding and Contracting Walls [58]. The study related to an incompressible laminar flow of a couple stress fluid in a porous channel with expanding or contracting walls was considered by Srinivasacharya et al. [58]. With the use of similarity transformations, the governing equations were reduced to nonlinear ordinary differential equations. The resulting equations were solved numerically using a quasi-linearization technique.

The equations governing the flow model [58] are

$$\begin{aligned} \frac{\partial u}{\partial x} + \frac{\partial v}{\partial y} &= 0, \\ \rho \left[u \frac{\partial u}{\partial x} + v \frac{\partial u}{\partial y} \right] &= -\frac{\partial p}{\partial x} + \mu \nabla^2 u - \eta \nabla^4 u, \\ \rho \left[u \frac{\partial v}{\partial x} + v \frac{\partial v}{\partial y} \right] &= -\frac{\partial p}{\partial y} + \mu \nabla^2 v - \eta \nabla^4 v, \\ \rho C \left[u \frac{\partial T}{\partial x} + v \frac{\partial T}{\partial y} \right] &= \mu \left[2 \left(\frac{\partial u}{\partial x} \right)^2 + 2 \left(\frac{\partial v}{\partial y} \right)^2 + \left(\frac{\partial u}{\partial y} + \frac{\partial v}{\partial x} \right)^2 \right] \\ &+ \eta \left[(\nabla^2 v)^2 + (\nabla^2 u)^2 \right] + k \nabla^2 T. \end{aligned} \quad (276)$$

The boundary conditions on the velocity profile and temperature are

$$\begin{aligned} u(x, y) &= 0, \\ v(x, y) &= v_w = -A\alpha, \\ \nabla \times q &= 0, \\ T(x, y) &= T_1, \\ &\text{at } y = a(t), \\ u(x, y) &= 0, \\ v(x, y) &= 0, \\ \nabla \times q &= 0, \\ T(x, y) &= T_2, \\ &\text{at } y = 0. \end{aligned} \quad (277)$$

With the use of classical Lie similarity approach, the solution for the above system of PDEs is written as [58]

$$\begin{aligned} u &= \frac{ux}{\rho a^2} F^1(\eta, t), \\ v &= -\frac{ux}{\rho a} F(\eta, t), \\ &\text{where } \eta = \frac{y}{a}. \end{aligned} \quad (278)$$

The similarity transformation given in (278) was used to reduce the above system of PDEs into a system of nonlinear ODEs. The reduced ordinary differential system was solved by using numerical methods for the boundary conditions given in (277).

17. Upper Convected Maxwell (UCM) Fluid Flow Problems

In this section, we discuss the studies related to flow of an upper convected Maxwell fluid and solved with the use of the Lie symmetry method.

The normalized momentum equation for unsteady flow is

$$\frac{\partial u}{\partial t} + v_w \frac{\partial u}{\partial y} = \frac{1}{R_e} \frac{\partial \tau_{xy,p}}{\partial y}, \quad (279)$$

with the polymer shear stress ($\tau_{xy} = \tau_{yx}$) given by the UCM differential constitutive equation having a relaxation time λ and a viscosity coefficient η_p , as mentioned above.

For a UCM fluid, the polymer extra stress tensor is written in index notation and in nondimensional form as

$$\begin{aligned} \tau_{ij,p} + D_e \left[\frac{\partial \tau_{ij,p}}{\partial t} + u_k \frac{\partial \tau_{ij,p}}{\partial x_k} - \tau_{ik,p} \frac{\partial u_i}{\partial x_k} - \tau_{ik,p} \frac{\partial u_j}{\partial x_k} \right] \\ = \frac{\partial u_i}{\partial x_j} + \frac{\partial u_j}{\partial x_k}. \end{aligned} \quad (280)$$

17.1. Group Theoretical Analysis and Similarity Solutions for Stress Boundary Layers in Viscoelastic Flows [59]. Atalık [59] employed the Lie group theory to obtain the point symmetries of the boundary layer equations derived in the literature for the high Weissenberg number flow of an upper convected Maxwell (UCM) fluid. The equations were reduced to ordinary differential equation systems with the use of scaling and spiral transformation groups.

The boundary layer equations for the UCM fluid in stream function formulation are [59]

$$\begin{aligned} \frac{\partial^2 T_{xx}}{\partial x \partial y} + \frac{\partial^2 T_{xy}}{\partial y^2} &= 0, \\ \frac{\partial \psi}{\partial y} \frac{\partial T_{xx}}{\partial x} - \frac{\partial \psi}{\partial x} \frac{\partial T_{xx}}{\partial y} - 2 \frac{\partial^2 \psi}{\partial x \partial y} T_{xx} - 2 \frac{\partial^2 \psi}{\partial y^2} T_{xy} \\ + T_{xx} &= 0, \\ \frac{\partial \psi}{\partial y} \frac{\partial T_{xy}}{\partial x} - \frac{\partial \psi}{\partial x} \frac{\partial T_{xy}}{\partial y} - \frac{\partial^2 \psi}{\partial y^2} T_{yy} + \frac{\partial^2 \psi}{\partial x^2} T_{xx} + T_{xy} \\ - \frac{\partial^2 \psi}{\partial y^2} &= 0, \\ \frac{\partial \psi}{\partial y} \frac{\partial T_{yy}}{\partial x} - \frac{\partial \psi}{\partial x} \frac{\partial T_{yy}}{\partial y} + 2 \frac{\partial^2 \psi}{\partial x^2} T_{xy} + 2 \frac{\partial^2 \psi}{\partial x \partial y} T_{yy} + T_{yy} \\ + 2 \frac{\partial^2 \psi}{\partial x \partial y} &= 0. \end{aligned} \quad (281)$$

The symmetry Lie algebra for the above system of PDEs is spanned by the following generators [59]:

$$\begin{aligned} X_1 &= \frac{\partial}{\partial x}, \\ X_2 &= \frac{\partial}{\partial \psi}, \\ X_3 &= f(x) \frac{\partial}{\partial y} + T_{xx} f'(x) \frac{\partial}{\partial T_{xy}} \\ &\quad + 2T_{xy} f'(x) \frac{\partial}{\partial T_{yy}}, \\ X_4 &= x \frac{\partial}{\partial x} + y \frac{\partial}{\partial y} + 2\psi \frac{\partial}{\partial \psi}, \\ X_5 &= -\frac{y}{2} \frac{\partial}{\partial y} - \frac{\psi}{2} \frac{\partial}{\partial \psi} + T_{xx} \frac{\partial}{\partial T_{xx}} + \frac{T_{xy}}{2} \frac{\partial}{\partial T_{xy}}, \end{aligned} \quad (282)$$

where $f(x)$ is an arbitrary function.

The generators given in (282) were utilized to reduce the PDE system (281) to a nonlinear system of ODEs which was then solved numerically.

18. Phan-Tien-Tanner (PTT) Fluid Flow Problems

In this section, we provide a review of those studies which deal with the flow of a Phan-Tien-Tanner fluid and solved using the classical Lie similarity approach.

The constitutive equation for Phan-Tien-Tanner fluid model is

$$\begin{aligned} W_e \left[(\mathbf{V} \cdot \nabla) \mathbf{T} - (\nabla \mathbf{V}) \mathbf{T} - \mathbf{T} (\nabla \mathbf{V})^T + k \text{trace}(\mathbf{T}) \mathbf{T} \right] \\ + \mathbf{T} = \nabla \mathbf{V} + (\nabla \mathbf{V})^T, \end{aligned} \quad (283)$$

where W_e is the Weissenberg number characterizing elastic effects.

Atalık [59] also used Lie group theory to unveil point symmetry groups of the equations of stress boundary layers for creeping flow of a PTT type non-Newtonian fluid. Similarity transformations were obtained for the boundary layer equations to reduce the governing partial differential equations into nonlinear system of ordinary differential equations. Numerical integration of the reduced ordinary differential equation systems was performed thereafter.

The boundary layer equations for the PTT fluid in the form of stream function are [59]

$$\begin{aligned} \frac{\partial^2 T_{xx}}{\partial x \partial y} + \frac{\partial^2 T_{xy}}{\partial y^2} &= 0, \\ \frac{\partial \psi}{\partial y} \frac{\partial T_{xx}}{\partial x} - \frac{\partial \psi}{\partial x} \frac{\partial T_{xx}}{\partial y} - 2 \frac{\partial^2 \psi}{\partial x \partial y} T_{xx} - 2 \frac{\partial^2 \psi}{\partial y^2} T_{xy} \\ + T_{xx} &= 0, \end{aligned}$$

$$\begin{aligned} & \frac{\partial \psi}{\partial y} \frac{\partial T_{xy}}{\partial x} - \frac{\partial \psi}{\partial x} \frac{\partial T_{xy}}{\partial y} - \frac{\partial^2 \psi}{\partial y^2} T_{yy} + \frac{\partial^2 \psi}{\partial x^2} T_{xx} + T_{xx} T_{xy} \\ & - \frac{\partial^2 \psi}{\partial y^2} = 0, \\ & \frac{\partial \psi}{\partial y} \frac{\partial T_{yy}}{\partial x} - \frac{\partial \psi}{\partial x} \frac{\partial T_{yy}}{\partial y} + 2 \frac{\partial^2 \psi}{\partial x^2} T_{xy} + 2 \frac{\partial^2 \psi}{\partial x \partial y} T_{yy} \\ & + T_{xx} T_{yy} + 2 \frac{\partial^2 \psi}{\partial x \partial y} = 0. \end{aligned} \tag{284}$$

The Lie point symmetries for the PDE system (284) are [59]

$$\begin{aligned} X_1 &= \frac{\partial}{\partial x}, \\ X_2 &= \frac{\partial}{\partial \psi}, \\ X_3 &= f(x) \frac{\partial}{\partial y} + T_{xx} f'(x) \frac{\partial}{\partial T_{xy}} \\ & + 2 T_{xy} f'(x) \frac{\partial}{\partial T_{yy}}, \\ X_4 &= x \frac{\partial}{\partial x} + y \frac{\partial}{\partial y} + 2 \psi \frac{\partial}{\partial \psi}, \\ X_5 &= -\frac{y}{2} \frac{\partial}{\partial y} + \frac{\psi}{2} \frac{\partial}{\partial \psi} + T_{xx} \frac{\partial}{\partial T_{xx}} + \frac{T_{xy}}{2} \frac{\partial}{\partial T_{xy}}. \end{aligned} \tag{285}$$

The operators given in (285) were employed to reduce the above nonlinear system of PDEs to a nonlinear system of ODEs. The reduced nonlinear ODE system was solved by using a numerical approach.

19. Nanofluid Flow Problems

In this section, we present the problems related to the flow of a non-Newtonian nanofluid and solved by employing the Lie group approach.

The governing equations of the flow of an incompressible nanofluid are

$$\nabla \cdot \mathbf{V} = 0, \tag{286}$$

$$\begin{aligned} & \rho_f \left[\frac{\partial \mathbf{V}}{\partial t} + \mathbf{V} \cdot \nabla \mathbf{V} \right] \\ & = -\nabla p + \mu \nabla^2 \mathbf{V} \\ & + [C \rho_p + (1 - C) \{ \rho_f (1 - \beta (T - T_\infty)) \}] \mathbf{g}, \end{aligned} \tag{287}$$

$$\begin{aligned} & (C \rho)_f \left[\frac{\partial T}{\partial t} + \mathbf{V} \cdot \nabla T \right] \\ & = k \nabla^2 T + (C \rho)_p D_B \nabla C \cdot \nabla T + \left(\frac{\nabla_T}{T_\infty} \right) \nabla T \cdot \nabla T, \end{aligned} \tag{288}$$

$$\frac{\partial C}{\partial t} + \mathbf{V} \cdot \nabla C = D_B \nabla^2 C + \left(\frac{\nabla_T}{T_\infty} \right) \nabla^2 T. \tag{289}$$

Equation (286) is the conservation of total mass, (287) is the conservation of momentum, (288) is the conservation of thermal energy, and (289) is the equation of nanoparticles, respectively. In the above equations, ρ_f is the density of the base fluid, and μ , k , and β are the viscosity, thermal conductivity, and volumetric volume expansion coefficient of the nanofluid, while ρ_p is the density of the particles. The gravitational acceleration is denoted by \mathbf{g} .

19.1. *Scaling Transformations for Boundary Layer Flow Near the Stagnation-Point on a Heated Permeable Stretching Surface with a Nanofluid* [60]. Hamad and Pop [60] obtained the similarity solution of the steady boundary layer flow near the stagnation-point flow on a permeable stretching sheet in a porous medium saturated with a nanofluid and in the presence of internal heat generation/absorption. The governing partial differential equations with the corresponding boundary conditions were reduced to a set of ordinary differential equations with the appropriate boundary conditions via Lie group analysis and thereafter a numerical approach was utilized.

The problem governing the boundary layer flow near the stagnation-point on a heated permeable stretching surface in a porous medium saturated with a nanofluid and heat generation/absorption effects in the form of stream function is [60]

$$\begin{aligned} & \frac{\partial \psi}{\partial y} \frac{\partial^2 \psi}{\partial x \partial y} - \frac{\partial \psi}{\partial x} \frac{\partial^2 \psi}{\partial y^2} \\ & = U \frac{dU}{dx} + \frac{1}{(1 - \phi)^{2.5} [1 - \phi + \phi (\rho_s / \rho_f)]} \frac{\partial^3 \psi}{\partial y^3} \\ & + \frac{1}{(1 - \phi)^{2.5} [1 - \phi + \phi (\rho_s / \rho_f)]} K_1 \left(U - \frac{\partial \psi}{\partial y} \right), \end{aligned} \tag{290}$$

$$\begin{aligned} & \frac{\partial \psi}{\partial y} \frac{\partial \theta}{\partial x} - \frac{\partial \psi}{\partial x} \frac{\partial \theta}{\partial y} \\ & = \frac{1}{Pr} \left(\frac{\alpha_n}{\alpha_f} \right) + \left[\frac{\lambda}{1 - \phi + \phi (\rho C_p)_s / (\rho C_p)_f} \right] \theta, \end{aligned}$$

with the boundary conditions

$$\begin{aligned} & \frac{\partial \psi}{\partial y} = x, \\ & \frac{\partial \psi}{\partial x} = S, \\ & \theta = 1 \end{aligned} \tag{291}$$

at $y = 0$,

$$\begin{aligned} & \frac{\partial \psi}{\partial y} \rightarrow U = \frac{a}{c} x, \\ & \theta \rightarrow 0 \end{aligned}$$

as $y \rightarrow \infty$.

With the use of the Lie symmetry method, the scaling transformation for the above system of PDEs found in [60] is given by

$$\begin{aligned} y &= \eta, \\ \psi &= xF(\eta), \\ \theta &= \theta(\eta). \end{aligned} \tag{292}$$

The transformation given in (292) reduces the above PDE into ordinary differential equations. The reduced ordinary differential equations were solved numerically.

19.2. Scaling Group Transformation for MHD Boundary Layer Flow of a Nanofluid Past a Vertical Stretching Surface in the Presence of Suction/Injection [61]. The problem of laminar fluid flow which results from the stretching of a vertical surface with variable stream conditions in a nanofluid was investigated numerically by Kandasamy et al. [61]. The symmetry groups admitted by the corresponding boundary value problem were obtained by using a special form of Lie group transformations, namely. the scaling group of transformations.

The governing problem describing the flow model [61] is given by

$$\begin{aligned} \frac{\partial \psi}{\partial y} \frac{\partial^2 \psi}{\partial x \partial y} - \frac{\partial \psi}{\partial x} \frac{\partial^2 \psi}{\partial y^2} - \nu \frac{\partial^3 \psi}{\partial y^3} &= -\frac{\sigma B_0^2}{\rho_f} \frac{\partial \psi}{\partial y} + (1 - \phi_\infty) \rho_f \infty \beta g \theta \Delta \theta \\ &\quad - (\rho_p - \rho_f \infty) g \phi \Delta \phi, \\ \frac{\partial \psi}{\partial y} \frac{\partial \theta}{\partial x} - \frac{\partial \psi}{\partial x} \frac{\partial \theta}{\partial y} &= \alpha \frac{\partial^2 \theta}{\partial y^2} + \tau D_B \frac{\partial \phi}{\partial y} \frac{\partial \theta}{\partial y} + \frac{D_T}{T_\infty} \left(\frac{\partial \theta}{\partial y} \right)^2, \\ \frac{\partial \psi}{\partial y} \frac{\partial \phi}{\partial x} - \frac{\partial \psi}{\partial x} \frac{\partial \phi}{\partial y} &= D_B \frac{\partial^2 \phi}{\partial y^2} + \frac{D_T}{T_\infty} \frac{\partial^2 \theta}{\partial y^2}, \end{aligned} \tag{293}$$

where $\Delta \theta = T_w - T_\infty$, $\Delta \phi = C_w - C_\infty$. The appropriate boundary conditions are

$$\begin{aligned} \frac{\partial \psi}{\partial y} &= x^m, \\ \frac{\partial \psi}{\partial x} &= -V_0 x^{(m-1)/2}, \\ \theta &= \phi = 1 \\ &\text{at } y = 0, \\ \frac{\partial \psi}{\partial y} &\rightarrow 0, \\ \theta &\rightarrow 0, \\ \phi &\rightarrow 0 \\ &\text{as } y \rightarrow \infty. \end{aligned} \tag{294}$$

The similarity transformation used to reduce the PDE system (293) of [61] is given by

$$\begin{aligned} yx^{-1/4} &= \eta, \\ \psi &= x^{3/4} f(\eta), \\ \theta &= \theta(\eta), \\ \phi &= \phi(\eta). \end{aligned} \tag{295}$$

With the use of transformations (295), the above system of PDEs was reduced to a nonlinear system of ODEs which was then solved using a numerical method.

19.3. Magnetic Field Effects on Free Convection Flow of a Nanofluid Past a Vertical Semi-Infinite Flat Plate [62]. The similarity reductions for problems of magnetic field effects on free convection flow of a nanofluid past a semi-infinite vertical flat plate were studied by Hamad et al. [62]. The application of a one-parameter group reduced the number of independent variables by one and consequently the governing partial differential equation with the auxiliary conditions to an ordinary differential equation with the appropriate corresponding conditions. The differential equations obtained were solved numerically.

The governing problem describing the flow model [62] is

$$\begin{aligned} \frac{\partial \psi}{\partial y} \frac{\partial^2 \psi}{\partial x \partial y} - \frac{\partial \psi}{\partial x} \frac{\partial^2 \psi}{\partial y^2} &= \frac{1}{(1 - \phi + \phi(\rho_s/\rho_f))} \left[\frac{1}{(1 - \phi)^{2.5}} \frac{\partial^3 \psi}{\partial y^3} \right] \\ &\quad + \frac{1}{(1 - \phi + \phi(\rho_s/\rho_f))} [(1 - \phi)] \\ &\quad + \frac{1}{(1 - \phi + \phi(\rho_s/\rho_f))} \left[\phi \frac{(\rho\beta)_s}{(\rho\beta)_f} \theta - M \frac{\partial \psi}{\partial y} \right], \\ \frac{\partial \psi}{\partial y} \frac{\partial \theta}{\partial x} - \frac{\partial \psi}{\partial x} \frac{\partial \theta}{\partial y} &= \frac{1}{P_r} \left(\frac{k_{nf}}{k_f} \right) \\ &\quad + \left[\frac{1}{1 - \phi + \phi(\rho C_p)_s / (\rho C_p)_f} \right] \frac{\partial^2 \theta}{\partial y^2}, \end{aligned} \tag{296}$$

with

$$\begin{aligned} \frac{\partial \psi}{\partial y} = \frac{\partial \psi}{\partial x} = 0, \\ \theta = 1 \end{aligned} \quad \text{at } y = 0, \tag{297}$$

$$\begin{aligned} \frac{\partial \psi}{\partial y} \rightarrow 0, \\ \theta \rightarrow 0 \end{aligned} \quad \text{as } y \rightarrow \infty.$$

With the use Lie symmetry method, the generators for the above PDE system obtained in [62] are given by

$$\begin{aligned} X_1 &= x \frac{\partial}{\partial x} + g(x) \frac{\partial}{\partial y} + \psi \frac{\partial}{\partial \psi} + \theta \frac{\partial}{\partial \theta}, \\ X_2 &= \frac{\partial}{\partial x} + g(x) \frac{\partial}{\partial y}, \\ X_3 &= g(x) \frac{\partial}{\partial y} + \frac{\partial}{\partial \psi}. \end{aligned} \tag{298}$$

The operators given in (298) are used to find the similarity transformations

$$\begin{aligned} y &= \eta, \\ \psi &= xF_1(\eta), \\ \theta &= xF_2(\eta). \end{aligned} \tag{299}$$

The similarity transformations (299) are utilized to reduce the above PDE system to a nonlinear ODE system which was solved numerically.

19.4. Unsteady Hiemenz Flow of Cu-Nanofluid over a Porous Wedge in the Presence of Thermal Stratification due to Solar Energy Radiation: Lie Group Transformation [63]. The unsteady Hiemenz flow of an incompressible viscous Cu-nanofluid past a porous wedge due to incident radiation was investigated by Kandasamy et al. [63]. The partial differential equations governing the model under investigation were transformed into a system of ordinary differential equations by utilizing one-parameter Lie group of transformation. The reduced ODE system was solved numerically using Runge-Kutta Gill based shooting method.

The nondimensional form of governing equations in terms of stream function is [63]

$$\begin{aligned} \frac{\partial^2 \psi}{\partial t \partial y} + \frac{\partial \psi}{\partial y} \frac{\partial^2 \psi}{\partial x \partial y} - \frac{\partial \psi}{\partial x} \frac{\partial^2 \psi}{\partial y^2} \\ = \frac{1}{(1 - \varsigma + \varsigma(\rho_s/\rho_f))} \left[\left\{ \left(1 - \varsigma + \varsigma \frac{(\rho\beta)_s}{(\rho\beta)_f} \right) \gamma \right. \right. \\ \cdot \cos \frac{\Omega}{2} \theta \left. \left. \right\} + \frac{1}{(1 - \varsigma)^{2.5}} \frac{\partial^3 \psi}{\partial y^3} + \left\{ \frac{\partial U}{\partial t} + U \frac{dU}{dx} \right\} \right. \\ \left. \cdot \frac{\rho_{fn}}{\rho_f} - \frac{\nu_f}{K(1 - \varsigma)^{2.5}} \left(\frac{\partial \psi}{\partial y} - U \right) \right], \end{aligned} \tag{300}$$

$$\begin{aligned} \frac{\partial T}{\partial t} + \frac{\partial \psi}{\partial y} \frac{\partial T}{\partial x} - \frac{\partial \psi}{\partial x} \frac{\partial T}{\partial y} \\ = \left[\frac{1}{1 - \varsigma + \varsigma(\rho C_p)_s / (\rho C_p)_f} \right] \times \left[\frac{1}{P_r} \left\{ \frac{k_{fn}}{k_f} \right. \right. \\ \left. \left. \cdot \frac{\partial^2 T}{\partial y^2} + \frac{4}{3} ((c_T + T)^3 T') T' \right\} \right], \end{aligned}$$

with the boundary conditions

$$\begin{aligned} \frac{\partial \psi}{\partial y} = 0, \\ \frac{\partial \psi}{\partial x} = -V_0, \\ T = T_w \end{aligned} \quad \text{at } y = 0, \tag{301}$$

$$\begin{aligned} \frac{\partial \psi}{\partial y} \rightarrow \frac{\nu x^m}{\delta^{m+1}}, \\ T \rightarrow T_\infty \rightarrow (1 - n) T_0 + n T_w \end{aligned} \quad \text{as } y \rightarrow \infty.$$

Using Lie groups, the symmetry generators for the above PDE system obtained in [63] are

$$\begin{aligned} X_1 &= x \frac{\partial}{\partial x} + g(x) \frac{\partial}{\partial y} + \psi \frac{\partial}{\partial \psi} + T \frac{\partial}{\partial T}, \\ X_2 &= \frac{\partial}{\partial x} + g(x) \frac{\partial}{\partial y}, \\ X_3 &= g(x) \frac{\partial}{\partial y} + \frac{\partial}{\partial \psi}. \end{aligned} \tag{302}$$

The corresponding similarity transformations are given by [63]

$$\begin{aligned}y &= \eta, \\ \psi &= xf\eta, \\ T &= xT(\eta).\end{aligned}\quad (303)$$

Transformations (302) are employed to reduce the PDE system (300) to a nonlinear ODE system which was solved numerically by Runge-Kutta Gill based shooting technique.

Rosmila et al. [64] studied the magnetohydrodynamics convection flow and heat transfer of an incompressible viscous nanofluid past a semi-infinite vertical stretching. The partial differential equations governing the problem under consideration were transformed by a special form of the Lie symmetry group transformations, that is, a one-parameter group of transformations into a system of ordinary differential equations which was numerically solved using the Runge-Kutta-Gill-based shooting method.

Recently, Das [65] has numerically investigated the steady MHD boundary layer flow of an electrically conducting nanofluid past a vertical convectively heated permeable stretching surface with variable stream conditions. The symmetry groups admitted by the corresponding boundary value problem were obtained by using scaling group of transformations which have been utilized to reduce the governing PDE system to a nonlinear ODE system.

20. Casson Fluid Flow Problems

Here we discuss the problems dealing with the flow of a Casson fluid that are solved using the Lie group approach.

The constitutive equations for Casson fluid are presented as follows:

$$\tau^{1/n} = \tau_0^{1/n} + \mu\dot{\gamma}^{1/n}, \quad (304)$$

or

$$\tau_{ij} = \left[\mu_B + \left(\frac{P_y}{\sqrt{2\pi}} \right)^{1/n} \right]^n 2e_{ij}, \quad (305)$$

where μ is the dynamic viscosity, $\pi = e_{ij}e_{ij}$ is the product of the component of deformation rate with e_{ij} being the (i, j) th component of the deformation rate, μ_B is plastic dynamic viscosity of the non-Newtonian fluid, and P_y is the yield stress of fluid, with $n \gg 1$.

20.1. Heat Source/Sink Effects on Non-Newtonian MHD Fluid Flow and Heat Transfer over a Permeable Stretching Surface: Lie Group Analysis [66]. The only study available in the literature dealing with the flow of a Casson fluid and solved by using the Lie symmetry method was performed by Tufail et al. [66]. In [66], an analysis is carried out for flow and heat transfer of a Casson fluid over a permeable stretching surface through a porous medium. Lie symmetry analysis was used to reduce the governing partial differential equations to nonlinear ordinary differential equations. These reduced ordinary

differential equations were solved exactly and solutions were obtained in terms of Kummer's function.

The dimensionless form of the equations governing for flow and heat transfer of Casson model is

$$\begin{aligned}\frac{\partial u}{\partial x} + \frac{\partial v}{\partial y} &= 0, \\ u \frac{\partial u}{\partial x} + v \frac{\partial u}{\partial y} &= \left(1 + \frac{1}{\beta}\right) \frac{\partial^2 u}{\partial y^2} - \left(\frac{1}{K} + K\right) u, \\ u \frac{\partial \theta}{\partial x} + v \frac{\partial \theta}{\partial y} &= \frac{1}{P_r} \frac{\partial^2 \theta}{\partial y^2} + Q\theta.\end{aligned}\quad (306)$$

The boundary conditions on the velocity profile and temperature are

$$\begin{aligned}u(x, y) &= x, \\ v(x, y) &= \frac{v_w}{\sqrt{by}}, \\ \theta(x, y) &= 1, \\ &\text{at } y = 0, \\ u(x, y) &= 0, \\ v(x, y) &= 0, \\ \theta(x, y) &= 1, \\ &\text{at } y \rightarrow \infty.\end{aligned}\quad (307)$$

In the above equations, K is the porous medium permeability parameter, M is the magnetic field parameter, P_r is the Prandtl number, and Q is the dimensionless heat source or sink parameter.

The infinitesimals for the system of PDEs (306) are [66]

$$\begin{aligned}\xi_1 &= c_3 + c_4 x, \\ \xi_2 &= g(x), \\ \eta_1 &= c_1 + c_4 \psi, \\ \eta_2 &= c_2 \theta.\end{aligned}\quad (308)$$

The infinitesimals given in (308) were used to reduce the above system of PDEs to a system of nonlinear ODEs. The reduced ordinary differential system was solved exactly in the closed-form Kummer's function.

21. Concluding Remarks

In this topical survey, we have classified all those studies which are related to the flow models of different non-Newtonian fluids and solved using Lie symmetry and conditional symmetry approaches. The mathematical modelling, the symmetries found, and the solutions obtained for each of the studies under investigation were presented. We have

observed that the symmetry methods used to solve different non-Newtonian fluid flow models are useful for a wide range of nonlinear problems in fluids given the paucity of known exact solutions especially in non-Newtonian fluids. In the majority of the models that we have reviewed, the Lie symmetry methods have been successfully applied to obtain exact solutions. Another notable significant feature of the Lie theory analysis that we have observed is that it has been used to construct the similarity transformations which are used for the reductions of the governing equations into reduced (these reduced equations are sometimes solved numerically) or exactly solvable equations. The Lie approach is not only applicable to many nonlinear and complicated scalar ODEs and PDEs but also to a nonlinear system of ODEs and PDEs in the context of non-Newtonian fluid mechanics.

In recent years, the ansatz method has been used to construct exact solutions of nonlinear differential equations arising in the study of non-Newtonian fluids. In the ansatz method, different forms of the solution are assumed and different techniques are used to develop analytical results. We pinpoint one of the central points of this survey which is the usefulness of systematic group theoretic approach. Other methods such as homotopy approach, Adomian method, and similar iterative methods have been applied for number of times for similar class of problems discussed in this survey. However, their precise application is still unclear and the results they produce are not dictated by the physical problem at hand. The applications of Lie symmetry methods for non-Newtonian fluid flow models as discussed here are more systematic, rigorous, and general treatment for such type of problems. In other words, the group theoretical methods provide a unified treatment to classify exact solutions of models of Newtonian and non-Newtonian fluids which are solved in the literature using different techniques.

Another important aspect of this survey we have observed is that many researchers have employed Lie group methods to investigate different interesting features of non-Newtonian fluids in different situations but very limited studies have been reported in the literature in which researchers have utilized the nonclassical symmetry method to solve non-Newtonian fluid flow models. In particular, only a single study [49] has been found in which the authors have performed the nonclassical symmetry analysis of a particular model of a non-Newtonian third-grade fluid. Thus, the concept of nonclassical symmetry has not been widely used to find conditionally invariant solutions of non-Newtonian fluid flow problems. This also applies to the use of weak and higher symmetries in the context of fluids. We believe that these deserve further importance in tackling non-Newtonian fluid flow problems. Since the problems dealing with the flow of non-Newtonian fluids have received much attention in recent years, the present survey is intended to provide a platform for researchers to apply group methods to tackle nonlinear problems in the fertile field of fluid mechanics.

Moreover, we did not focus on symmetry associated with conservation law works such as that of [67–69]. This necessitated giving notions on conservation laws of partial differential equations and the group approaches related to these which are extensive.

Conflicts of Interest

The authors declare that there are no conflicts of interest regarding the publication of this paper.

References

- [1] M. B. Abd-el-Malek, N. A. Badran, and H. . Hassan, "Solution of the Rayleigh problem for a power law non-Newtonian conducting fluid via group method," *International Journal of Engineering Science*, vol. 40, no. 14, pp. 1599–1609, 2002.
- [2] C. Wafo Soh, "Invariant solutions of the unidirectional flow of an electrically charged power-law non-Newtonian fluid over a flat plate in presence of a transverse magnetic field," *Communications in Nonlinear Science and Numerical Simulation*, vol. 10, no. 5, pp. 537–548, 2005.
- [3] M. Yürüsoy, "Unsteady boundary layer flow of power-law fluid on stretching sheet surface," *International Journal of Engineering Science*, vol. 44, no. 5-6, pp. 325–332, 2006.
- [4] N. N. Nguetchue and E. Momoniat, "Axisymmetric spreading of a thin power-law fluid under gravity on a horizontal plane," *Nonlinear Dynamics. An International Journal of Nonlinear Dynamics and Chaos in Engineering Systems*, vol. 52, no. 4, pp. 361–366, 2008.
- [5] R. J. Moitsheki, S. Abelman, and T. Hayat, "Symmetry reductions of a flow with power law fluid and contaminant-modified viscosity," *Mathematical and Computational Applications*, vol. 15, no. 4, pp. 685–696, 2010.
- [6] A. A. Mutlag, M. J. Uddin, A. I. Md. Ismail, and M. A. A. Hamad, "Scaling group transformation under the effect of thermal radiation heat transfer of a non newtonian power-law fluid over a vertical stretching sheet with momentum slip boundary condition," *Applied Mathematical Sciences*, vol. 6, no. 121-124, pp. 6035–6052, 2012.
- [7] M. B. Akgül and M. Pakdemirli, "Lie group analysis of a non-Newtonian fluid flow over a porous surface," *Scientia Iranica*, vol. 19, no. 6, pp. 1534–1540, 2012.
- [8] M. Jalil and S. Asghar, "Flow of power-law fluid over a stretching surface: a Lie group analysis," *International Journal of Non-Linear Mechanics*, vol. 48, pp. 65–71, 2013.
- [9] A. G. Fareo and D. P. Mason, "Group invariant solution for a pre-existing fracture driven by a power-law fluid in impermeable rock," *Communications in Nonlinear Science and Numerical Simulation*, vol. 18, no. 12, pp. 3298–3316, 2013.
- [10] M. Molati, T. Hayat, and F. Mahomed, "Rayleigh problem for a MHD Sisko fluid," *Nonlinear Analysis. Real World Applications. An International Multidisciplinary Journal*, vol. 10, no. 6, pp. 3428–3434, 2009.
- [11] H. M. Mamboundou, M. Khan, T. Hayat, and F. Mahomed, "Reduction and solutions for magnetohydrodynamic flow of a sisko fluid in a porous medium," *Journal of Porous Media*, vol. 12, no. 7, pp. 695–714, 2009.
- [12] T. Hayat, R. J. Moitsheki, and S. Abelman, "Stokes' first problem for Sisko fluid over a porous wall," *Applied Mathematics and Computation*, vol. 217, no. 2, pp. 622–628, 2010.
- [13] G. Sari, M. Pakdemirli, T. Hayat, and Y. Aksoy, "Boundary layer equations and lie group analysis of a sisko fluid," *Journal of Applied Mathematics*, vol. 2012, Article ID 259608, 2012.
- [14] M. Khan, A. Shahzad, A. Anjum, and F. M. Mahomed, "Analytic approximate solutions for time-dependent flow and heat transfer of a Sisko fluid," *International Journal of Numerical Methods*

- for *Heat Fluid Flow*, vol. 24, no. 5, Article ID 17111470, pp. 1005–1019, 2014.
- [15] M. Khan, S. Abelman, D. P. Mason, and F. M. Mahomed, “Self-similar unsteady flow of a Sisko fluid in a cylindrical tube undergoing translation,” *Mathematical Problems in Engineering*, Article ID 135424, Art. ID 135424, 14 pages, 2015.
 - [16] K. S. Mekheimer, S. Z.-A. Husseny, A. T. Ali, and A. E. Abo-Elkhair, “Lie point symmetries and similarity solutions for an electrically conducting Jeffrey fluid,” *Physica Scripta*, vol. 83, no. 1, Article ID 015017, 2011.
 - [17] Y. Aksoy, T. Hayat, and M. Pakdemirli, “Boundary layer theory and symmetry analysis of a Williamson fluid,” *Zeitschrift fur Naturforschung - Section A Journal of Physical Sciences*, vol. 67, no. 6-7, pp. 363–368, 2012.
 - [18] N. A. Khan, S. Khan, and F. Riaz, “Boundary Layer Flow of Williamson Fluid with Chemically Reactive Species using Scaling Transformation and Homotopy Analysis Method,” *Mathematical Sciences Letters*, vol. 3, no. 3, pp. 199–205, 2014.
 - [19] M. Yürüsoy, M. Pakdemirli, and O. F. Noyan, “Lie group analysis of creeping flow of a second grade fluid,” *International Journal of Non-Linear Mechanics*, vol. 36, no. 6, pp. 955–960, 2001.
 - [20] M. Yürüsoy, “Similarity solutions for creeping flow and heat transfer in second grade fluids,” *International Journal of Non-Linear Mechanics*, vol. 39, no. 4, pp. 665–672, 2004.
 - [21] K. Fakhar, C. Yi, J. Xiaoda, and L. Xiaodong, “Lie symmetry analysis and some new exact solutions for rotating flow of a second-order fluid on a porous plate,” *International Journal of Engineering Science*, vol. 44, no. 13-14, pp. 889–896, 2006.
 - [22] A. A. Afify, “Some new exact solutions for MHD aligned creeping flow and heat transfer in second grade fluids by using Lie group analysis,” *Nonlinear Analysis. Theory, Methods and Applications. An International Multidisciplinary Journal*, vol. 70, no. 9, pp. 3298–3306, 2009.
 - [23] N. A. Khan, A. Ara, M. Jamil, and A. Yildirim, “Travelling waves solution for MHD aligned flow of a second grade fluid with heat transfer: A symmetry independent approach,” *Journal of King Saud University - Science*, vol. 24, no. 1, pp. 63–67, 2012.
 - [24] M. B. Abd-el-Malek and H. S. Hassan, “Symmetry analysis for steady boundary-layer stagnation-point flow of Rivlin-Ericksen fluid of second grade subject to suction,” *Lithuanian Association of Nonlinear Analysts (LANA). Nonlinear Analysis. Modelling and Control*, vol. 15, no. 4, pp. 379–396, 2010.
 - [25] N. Islam, B. Islam, H. P. Mazumdar, and J. Lahiri, “Application of the Lie groups of transformations for an approximate solution of MHD flow of a visco-elastic second grade fluid,” *APPS. Applied Sciences*, vol. 13, pp. 65–73, 2011.
 - [26] Y. Aksoy, M. Pakdemirli, and C. M. Khalique, “Boundary layer equations and stretching sheet solutions for the modified second grade fluid,” *International Journal of Engineering Science*, vol. 45, no. 10, pp. 829–841, 2007.
 - [27] M. Pakdemirli, Y. g. Aksoy, M. Yürüsoy, and C. M. Khalique, “Symmetries of boundary layer equations of power-law fluids of second grade,” *Acta Mechanica Sinica*, vol. 24, no. 6, pp. 661–670, 2008.
 - [28] K. S. Mekheimer, M. F. El-Sabbagh, and R. E. Abo-Elkhair, “Lie group analysis and similarity solutions for hydro-magnetic Maxwell fluid through a porous medium,” *Boundary Value Problems*, 2012:15, 18 pages, 2012.
 - [29] C. Calmelet-Eluhu and V. Rosenhaus, “Symmetries and solution of a micropolar fluid flow through a cylinder,” *Acta Mechanica*, vol. 147, no. 1-4, pp. 59–72, 2001.
 - [30] F. Shahzad, M. Sajid, T. Hayat, and M. Ayub, “Analytic solution for flow of a micropolar fluid,” *Acta Mechanica*, vol. 188, no. 1-2, pp. 93–102, 2007.
 - [31] M. A. Mansour, R. A. Mohamed, M. M. Abd-Elaziz, and S. E. Ahmed, “Lie group Analysis of unsteady MHD mixed convection boundary layer flow of a micropolar fluid along a symmetric wedge with variable surface temperature saturated porous medium,” *Int. J. Appl. Math and Mech*, vol. 5, no. 2, pp. 97–114, 2009.
 - [32] G. Saccomandi, “Group properties and invariant solutions of plane micropolar flows,” *International Journal of Engineering Science*, vol. 29, no. 5, pp. 645–648, 1991.
 - [33] T. Hayat, M. Pakdemirli, and Y. g. Aksoy, “Similarity solutions for boundary layer equations of a Powell-Eyring fluid,” *Mathematical and Computational Applications*, vol. 18, no. 1, pp. 62–70, 2013.
 - [34] M. Jalil and S. Asghar, “Flow and heat transfer of powell-eyring fluid over a stretching surface: A lie group analysis,” *Journal of Fluids Engineering, Transactions of the ASME*, vol. 135, no. 12, Article ID 121201, 2013.
 - [35] M. Jalil, S. Asghar, and S. M. Imran, “Self similar solutions for the flow and heat transfer of Powell-Eyring fluid over a moving surface in a parallel free stream,” *International Journal of Heat and Mass Transfer*, vol. 65, pp. 73–79, 2013.
 - [36] K. Fakhar, A. H. Kara, R. Morris, and T. Hayat, “Similarity solutions and conservation laws for rotating flows of an Oldroyd-B fluid,” *Indian Journal of Physics*, vol. 87, no. 10, pp. 1035–1040, 2013.
 - [37] T. Hayat, A. H. Kara, and E. Momoniat, “Exact flow of a third-grade fluid on a porous wall,” *International Journal of Non-Linear Mechanics*, vol. 38, no. 10, pp. 1533–1537, 2003.
 - [38] K. Fakhar, “Exact solutions for nonlinear partial differential equation arising in third grade fluid flows,” *Southeast Asian Bulletin of Mathematics*, vol. 32, no. 1, pp. 65–70, 2008.
 - [39] K. Fakhar, Z. Xu, and C. Yi, “Exact solutions of a third grade fluid flow on a porous plate,” *Applied Mathematics and Computation*, vol. 202, no. 1, pp. 376–382, 2008.
 - [40] M. Yürüsoy, “Similarity solutions of boundary layer equations for a special non-Newtonian fluid in a special coordinate system,” *Applied Mathematics and Mechanics. English Edition*, vol. 25, no. 5, pp. 587–594, 2004.
 - [41] T. Hayat and A. H. Kara, “Couette flow of a third-grade fluid with variable magnetic field,” *Mathematical and Computer Modelling*, vol. 43, no. 1-2, pp. 132–137, 2006.
 - [42] K. Fakhar, Z.-L. Xu, and Y. Cheng, “Hall effects on unsteady magnetohydrodynamic flow of a third grade fluid,” *Chinese Physics Letters*, vol. 24, no. 5, article no. 001, pp. 1129–1132, 2007.
 - [43] K. Fakhar, A. H. Kara, I. Khan, and M. Sajid, “On the computation of analytical solutions of an unsteady magnetohydrodynamics flow of a third grade fluid with Hall effects,” *Computers and Mathematics with Applications. An International Journal*, vol. 61, no. 4, pp. 980–987, 2011.
 - [44] T. Hayat, H. Mambili-Mamboundou, and F. M. Mahomed, “Unsteady solutions in a third-grade fluid filling the porous space,” *Mathematical Problems in Engineering*, Article ID 139560, Art. ID 139560, 12 pages, 2008.
 - [45] T. Hayat, H. Mambili-Mamboundou, E. Momoniat, and F. M. Mahomed, “The Rayleigh problem for a third grade electrically conducting fluid in a magnetic field,” *Journal of Nonlinear Mathematical Physics*, vol. 15, no. suppl. 1, pp. 77–90, 2008.

- [46] K. Fakhar, A. A. Zainal, and A. H. Kara, "A note on the interplay between symmetries, reduction and conservation laws of Stokes' first problem for third-grade rotating fluids," *Pramana - Journal of Physics*, vol. 77, no. 3, pp. 439–445, 2011.
- [47] T. Aziz, F. M. Mahomed, and A. Aziz, "Group invariant solutions for the unsteady MHD flow of a third grade fluid in a porous medium," *International Journal of Non-Linear Mechanics*, vol. 47, no. 7, pp. 792–798, 2012.
- [48] A. Aziz and T. Aziz, "MHD flow of a third grade fluid in a porous half space with plate suction or injection: an analytical approach," *Applied Mathematics and Computation*, vol. 218, no. 21, pp. 10443–10453, 2012.
- [49] T. Aziz, F. M. Mahomed, M. Ayub, and D. P. Mason, "Non-linear time-dependent flow models of third grade fluids: a conditional symmetry approach," *International Journal of Non-Linear Mechanics*, vol. 54, pp. 55–65, 2013.
- [50] T. Hayat, A. H. Kara, and E. Momoniat, "The unsteady flow of a fourth-grade fluid past a porous plate," *Mathematical and Computer Modelling*, vol. 41, no. 11-12, pp. 1347–1353, 2005.
- [51] T. Aziz and F. M. Mahomed, "Reductions and solutions for the unsteady flow of a fourth grade fluid on a porous plate," *Applied Mathematics and Computation*, vol. 219, no. 17, pp. 9187–9195, 2013.
- [52] T. Hayat, A. H. Kara, and E. Momoniat, "Travelling wave solutions to Stokes' problem for a fourth grade fluid," *Applied Mathematical Modelling. Simulation and Computation for Engineering and Environmental Systems*, vol. 33, no. 3, pp. 1613–1619, 2009.
- [53] T. Aziz and F. M. Mahomed, "Closed-form solutions for a nonlinear partial differential equation arising in the study of a fourth grade fluid model," *Journal of Applied Mathematics*, vol. 2012, Article ID 931587, 2012.
- [54] T. Hayat, H. Mambili-Mamoundou, C. M. Khaliq, and F. M. Mahomed, "Effect of magnetic field on the flow of a fourth order fluid," *Nonlinear Analysis. Real World Applications. An International Multidisciplinary Journal*, vol. 10, no. 6, pp. 3413–3419, 2009.
- [55] T. Hayat, H. Mambili-Mamoundou, and F. M. Mahomed, "A note on some solutions for the flow of a fourth grade fluid in a porous space," *Nonlinear Analysis. Real World Applications. An International Multidisciplinary Journal*, vol. 10, no. 1, pp. 368–374, 2009.
- [56] T. Aziz, A. B. Magan, and F. M. Mahomed, "Invariant Solutions for the Unsteady Magnetohydrodynamics (MHD) Flow of a Fourth-Grade Fluid Induced Due to the Impulsive Motion of a Flat Porous Plate," *Brazilian Journal of Physics*, vol. 45, no. 1, pp. 120–131, 2014.
- [57] T. Aziz, A. Fatima, A. Aziz, and F. M. Mahomed, "Group theoretical analysis and invariant solutions for unsteady flow of a fourth-grade fluid over an infinite plate undergoing impulsive motion in a darcy porous medium," *Zeitschrift fur Naturforschung - Section A Journal of Physical Sciences*, vol. 70, no. 7, pp. 483–498, 2015.
- [58] D. Srinivasacharya, N. Srinivasacharyulu, and O. Odelu, "Flow and heat transfer of couple stress fluid in a porous channel with expanding and contracting walls," *International Communications in Heat and Mass Transfer*, vol. 36, no. 2, pp. 180–185, 2009.
- [59] K. Atalik, "Group theoretical analysis and similarity solutions for stress boundary layers in viscoelastic flows," *Journal of Non-Newtonian Fluid Mechanics*, vol. 153, no. 1, pp. 62–71, 2008.
- [60] M. A. Hamad and I. Pop, "Scaling transformations for boundary layer flow near the stagnation-point on a heated permeable stretching surface in a porous medium saturated with a nanofluid and heat generation/absorption effects," *Transport in Porous Media*, vol. 87, no. 1, pp. 25–39, 2011.
- [61] R. Kandasamy, P. Loganathan, and P. P. P. Arasu, "Scaling group transformation for MHD boundary-layer flow of a nanofluid past a vertical stretching surface in the presence of suction/injection," *Nuclear Engineering and Design*, vol. 241, no. 6, pp. 2053–2059, 2011.
- [62] M. A. Hamad, I. Pop, and A. I. Ismail, "Magnetic field effects on free convection flow of a nanofluid past a vertical semi-infinite flat plate," *Nonlinear Analysis. Real World Applications. An International Multidisciplinary Journal*, vol. 12, no. 3, pp. 1338–1346, 2011.
- [63] R. Kandasamy, I. Muhaimin, A. B. Khamis, and R. B. Roslan, "Unsteady Hiemenz flow of Cu-nanofluid over a porous wedge in the presence of thermal stratification due to solar energy radiation: Lie group transformation," *International Journal of Thermal Sciences*, vol. 65, pp. 196–205, 2013.
- [64] A. B. Rosmila, R. Kandasamy, and I. Muhaimin, "Lie symmetry group transformation for MHD natural convection flow of nanofluid over linearly porous stretching sheet in presence of thermal stratification," *Applied Mathematics and Mechanics. English Edition*, vol. 33, no. 5, pp. 593–604, 2012.
- [65] K. Das, "Lie group analysis for nanofluid flow past a convectively heated stretching surface," *Applied Mathematics and Computation*, vol. 221, pp. 547–557, 2013.
- [66] M. N. Tufail, A. S. Butt, and A. Ali, "Heat source/sink effects on non-Newtonian MHD fluid flow and heat transfer over a permeable stretching surface: lie group analysis," *Indian Journal of Physics*, vol. 88, no. 1, pp. 75–82, 2014.
- [67] R. Naz, F. M. Mahomed, and D. P. Mason, "Comparison of different approaches to conservation laws for some partial differential equations in fluid mechanics," *Applied Mathematics and Computation*, vol. 205, no. 1, pp. 212–230, 2008.
- [68] R. Naz, D. P. Mason, and F. M. Mahomed, "Conservation laws and conserved quantities for laminar two-dimensional and radial jets," *Nonlinear Analysis. Real World Applications. An International Multidisciplinary Journal*, vol. 10, no. 5, pp. 2641–2651, 2009.
- [69] R. Naz, F. M. Mahomed, and D. P. Mason, "Conservation laws via the partial Lagrangian and group invariant solutions for radial and two-dimensional free jets," *Nonlinear Analysis. Real World Applications. An International Multidisciplinary Journal*, vol. 10, no. 6, pp. 3457–3465, 2009.

Research Article

CuO–Water Nanofluid Magnetohydrodynamic Natural Convection inside a Sinusoidal Annulus in Presence of Melting Heat Transfer

M. Sheikholeslami,¹ R. Ellahi,² and C. Fetecau³

¹Department of Mechanical Engineering, Babol Noshirvani University of Technology, Babol, Iran

²Department of Mathematics & Statistics, FBAS, IIUI, H-10 Sector, Islamabad, Pakistan

³Academy of Romanian Scientists, 050094 Bucharest, Romania

Correspondence should be addressed to R. Ellahi; rahmatellahi@yahoo.com

Received 23 April 2017; Accepted 3 July 2017; Published 31 July 2017

Academic Editor: Efstratios Tzirtzilakis

Copyright © 2017 M. Sheikholeslami et al. This is an open access article distributed under the Creative Commons Attribution License, which permits unrestricted use, distribution, and reproduction in any medium, provided the original work is properly cited.

Impact of nanofluid natural convection due to magnetic field in existence of melting heat transfer is simulated using CVFEM in this research. KKL model is taken into account to obtain properties of CuO–H₂O nanofluid. Roles of melting parameter (δ), CuO–H₂O volume fraction (ϕ), Hartmann number (Ha), and Rayleigh (Ra) number are depicted in outputs. Results depict that temperature gradient improves with rise of Rayleigh number and melting parameter. Nusselt number detracts with rise of Ha. At the end, a comparison as a limiting case of the considered problem with the existing studies is made and found in good agreement.

1. Introduction

Melting process has various uses such as application like in thermocouple, heat exchangers, and heat engines. Chamkha and Ismael [1] examined the Cu-H₂O nanofluid mixed convection in an enclosure with lid wall. Also, Ellahi et al. [2] reported the similar study for nanofluid over permeable wedge in mixed convection. Harikrishnan et al. [3] investigated melting behavior of composite PCM for heating application. Nanofluid melting in a pipe with external fins has been studied by Mat et al. [4]. Manikandan and Rajan [5] utilized hybrid nanofluid for heat transfer augmentation. Koca et al. [6] utilized Ag-H₂O nanofluid for natural circulation loops. Shyam and Tiwari [7] investigated the coiled heat exchanger by means of nanofluid. Das [8] reported the radiative flow in existence of melting heat.

Sheremet et al. [9] illustrated the free convective flow of ferrofluid in a rotating enclosure. Wavy duct in existence of Brownian forces has been examined by Shehzad et al. [10]. Sheikholeslami et al. [11] illustrated different uses of nanotechnology in their article paper. Abbas et al. [12] demonstrated the nanofluid flow through a horizontal Riga

plate. Chamkha and Rashad [13] reported the nanoparticle migration on porous cone. Ellahi et al. [14] analyzed particle shape effects on Marangoni convection boundary layer flow of a nanofluid. They considered the Lorentz forces impact in governing equations. Malvandi et al. [15] reported nanofluid flow inside a channel in existence of Lorentz forces. Garoosi et al. [16] investigated performance of heat exchanger via nanofluid. They indicated that optimum volume fraction of nanoparticle exists to obtain maximum Nusselt number. Mesoscopic method has been utilized by Sheikholeslami and Ellahi [17] for a three-dimensional problem.

This research intends to present the impact of melting heat transfer on free convection of ferrofluid in the presence of Lorentz forces. CVFEM is selected to find the outputs. Roles of melting parameter, CuO–water volume fraction, and Hartmann and Rayleigh numbers are presented.

2. Problem Statement

Figure 1 depicts the geometry, boundary condition, and sample element. The inner wall is hot wall ($T = T_h$) and

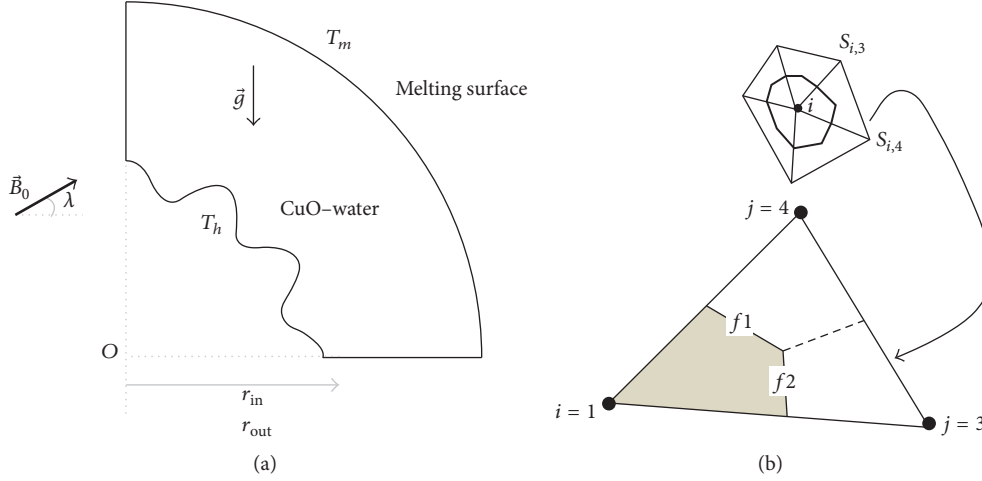


FIGURE 1: (a) Geometry; (b) sample element.

the outer one is melting surface ($T = T_m$). Other walls are adiabatic. Horizontal magnetic field has been applied. The enclosure is field with nanofluid.

3. Governing Equation and Simulation

3.1. Governing Formulation. 2D steady convective nanofluid flow is considered in existence of constant magnetic field. The fluid flow is laminar and incompressible. The flow is steady and Newtonian. The viscous dissipation is negligible in this study. The effects of Brownian force and thermophoretic force are not taken into condition. The flow also follows the Boussinesq assumption. The prevailing equations under these constraints can be written as [20]

$$\begin{aligned}
 \frac{\partial v}{\partial y} + \frac{\partial u}{\partial x} &= 0, \\
 (\rho_{nf}) \left(v \frac{\partial u}{\partial y} + u \frac{\partial u}{\partial x} \right) \\
 &= \left[B_y \sigma_{nf} \nu B_x - B_y^2 \sigma_{nf} u + \mu_{nf} \left(\frac{\partial^2 u}{\partial y^2} + \frac{\partial^2 u}{\partial x^2} \right) - \frac{\partial P}{\partial x} \right], \\
 \rho_{nf} \left(\frac{\partial v}{\partial y} v + \frac{\partial v}{\partial x} u \right) \\
 &= u B_y \sigma_{nf} B_x + (T - T_c) \beta_{nf} g \rho_{nf} - \nu B_x \sigma_{nf} B_x \\
 &\quad + \left(\frac{\partial^2 v}{\partial x^2} + \frac{\partial^2 v}{\partial y^2} \right) \mu_{nf} - \frac{\partial P}{\partial y}, \\
 B_x &= B_0 \cos \lambda, \\
 B_y &= B_0 \sin \lambda, \\
 (\rho C_p)_{nf} \left(v \frac{\partial T}{\partial y} + u \frac{\partial T}{\partial x} \right) &= k_{nf} \left(\frac{\partial^2 T}{\partial x^2} + \frac{\partial^2 T}{\partial y^2} \right),
 \end{aligned} \tag{1}$$

$(\rho C_p)_{nf}$, ρ_{nf} , $(\rho \beta)_{nf}$, and σ_{nf} are calculated as [17, 18]

$$\begin{aligned}
 (\rho C_p)_{nf} &= \phi (\rho C_p)_s + (1 - \phi) (\rho C_p)_f, \\
 \rho_{nf} &= \rho_f (1 - \phi) + \phi \rho_s, \\
 (\rho \beta)_{nf} &= \phi (\rho \beta)_s + (1 - \phi) (\rho \beta)_f,
 \end{aligned} \tag{2}$$

$$\begin{aligned}
 \sigma_{nf} \\
 &= \sigma_f \left[\left(\frac{+(2 + \sigma_s/\sigma_f) - \phi(-1 + \sigma_s/\sigma_f)}{3\phi(-1 + \sigma_s/\sigma_f)} \right)^{-1} + 1 \right].
 \end{aligned}$$

k_{nf} , μ_{nf} are calculated via KKL model [19]:

$$\begin{aligned}
 \frac{k_{nf}}{k_f} &= 1 + \frac{3(k_p/k_f - 1)\phi}{(k_p/k_f + 2) - (k_p/k_f - 1)\phi} + 5 \\
 &\quad \times 10^4 g'(\phi, T, d_p) \phi \rho_f c_{p,f} \sqrt{\frac{\kappa_b T}{d_p \rho_p}}, \\
 R_f &= 4 \times 10^{-8} \text{ km}^2/\text{W}, \\
 R_f &= -d_p (1/k_p - 1/k_{p,\text{eff}}), \\
 g'(\phi, d_p, T) &= \ln(T) (a_1 + a_3 \ln(\phi) + a_2 \ln(d_p)) \\
 &\quad + a_5 \ln(d_p)^2 + a_4 \ln(d_p) \ln(\phi) + (a_6 + a_8 \ln(\phi) \\
 &\quad + a_7 \ln(d_p) + a_{10} \ln(d_p)^2 + a_9 \ln(\phi) \ln(d_p)), \\
 \mu_{nf} &= \frac{\mu_f}{(1 - \phi)^{2.5}} + \frac{k_{\text{Brownian}}}{k_f} \times \frac{\mu_f}{\text{Pr}}.
 \end{aligned} \tag{3}$$

Properties and needed parameters are provided in Tables 1 and 2 [19].

TABLE 1: Coefficient values of CuO–H₂O [19].

Coefficient values	CuO–water
a_1	-26.5933108
a_2	-0.403818333
a_3	-33.3516805
a_4	-1.915825591
a_5	6.421858E - 02
a_6	48.40336955
a_7	-9.787756683
a_8	190.245610009
a_9	10.9285386565
a_{10}	-0.72009983664

Vorticity and stream function should be used to eliminate pressure source terms:

$$\begin{aligned}\omega + \frac{\partial u}{\partial y} - \frac{\partial v}{\partial x} &= 0, \\ \frac{\partial \Psi}{\partial x} &= -v, \\ \frac{\partial \Psi}{\partial y} &= u.\end{aligned}\quad (4)$$

Dimensionless quantities are introduced as follows:

$$\begin{aligned}P &= \frac{P}{\rho_{nf} (\alpha_{nf}/L)^2}, \\ U &= \frac{uL}{\alpha_{nf}}, \\ V &= \frac{vL}{\alpha_{nf}}, \\ \theta &= \frac{T - T_m}{T_h - T_m}, \\ (X, Y) &= \frac{(x, y)}{L}, \\ \Psi &= \frac{\Psi}{\alpha_{nf}}, \\ \Omega &= \frac{\omega L^2}{\alpha_{nf}}.\end{aligned}\quad (5)$$

The final formulae are

$$\begin{aligned}\Omega + \frac{\partial^2 \Psi}{\partial Y^2} + \frac{\partial^2 \Psi}{\partial X^2} &= 0, \\ \frac{\partial \Omega}{\partial X} U + V \frac{\partial \Omega}{\partial Y} &= \text{Pr} \frac{A_5}{A_1} \frac{A_2}{A_4} \left(\frac{\partial^2 \Omega}{\partial Y^2} + \frac{\partial^2 \Omega}{\partial X^2} \right) + \text{PrHa}^2 \\ &\cdot \frac{A_6}{A_1} \frac{A_2}{A_4} \left(-\frac{\partial V}{\partial X} B_x B_x + B_y \frac{\partial U}{\partial X} B_x - \frac{\partial V}{\partial Y} B_y B_x \right. \\ &\left. + B_y \frac{\partial U}{\partial Y} B_y \right) + \text{PrRa} \frac{A_3 A_2^2}{A_1 A_4^2} \frac{\partial \theta}{\partial X},\end{aligned}$$

$$\frac{\partial \theta}{\partial X} U + \frac{\partial \theta}{\partial Y} V = \left(\frac{\partial^2 \theta}{\partial X^2} + \frac{\partial^2 \theta}{\partial Y^2} \right).\quad (6)$$

Boundary conditions are

$$\begin{aligned}\frac{\partial \theta}{\partial n} &= 0 \quad \text{on other walls,} \\ \theta &= 0 \quad \text{on outer wall,} \\ \theta &= 1.0 \quad \text{on inner wall,} \\ \Psi &= 0.0 \quad \text{on all walls except melting surface}\end{aligned}\quad (7)$$

and in melting surface, we have

$$\frac{\partial \theta}{\partial n} = \frac{A_2}{A_1} \frac{1}{\delta} (L + c_s (T_m - T_0)) \frac{\partial \Psi}{\partial n},\quad (8)$$

where dimensionless and constants parameters are illustrated as

$$\begin{aligned}\text{Pr} &= \frac{\nu_f}{\alpha_f}, \\ \text{Ra} &= \frac{g \beta_f \Delta T L^3}{(\nu_f \alpha_f)}, \\ \text{Ha} &= LB_0 \sqrt{\frac{\sigma_f}{\mu_f}}, \\ \delta &= \frac{(\rho C_p)_f}{\rho_f} \frac{(T_h - T_m)}{1 + c_s (T_m - T_0)}, \\ A_1 &= \frac{\rho_{nf}}{\rho_f}, \\ A_5 &= \frac{\mu_{nf}}{\mu_f}, \\ A_2 &= \frac{(\rho C_p)_{nf}}{(\rho C_p)_f}, \\ A_6 &= \frac{\sigma_{nf}}{\sigma_f}, \\ A_4 &= \frac{k_{nf}}{k_f}, \\ A_3 &= \frac{(\rho \beta)_{nf}}{(\rho \beta)_f}.\end{aligned}\quad (9)$$

It should be mentioned that δ is related to Stefan numbers.

Local and average Nusselt over the cold wall can be calculated as follows:

$$\begin{aligned}\text{Nu}_{\text{loc}} &= \left(\frac{k_{nf}}{k_f} \right) \frac{\partial \theta}{\partial r}, \\ \text{Nu}_{\text{ave}} &= \frac{1}{0.5\pi} \int_0^{0.5\pi} \text{Nu}_{\text{loc}} d\xi.\end{aligned}\quad (10)$$

TABLE 2: Properties of H₂O and CuO [19].

	ρ (kg/m ³)	C_p (j/kgk)	k (W/m·k)	$\beta \times 10^5$ (K ⁻¹)	d_p (nm)	σ ($\Omega \cdot m$) ⁻¹
Water	997.1	4179	0.613	21	—	0.05
CuO	6500	540	18	29	45	10 ⁻¹⁰

TABLE 3: Mesh independency analysis when Ra = 10000, $\delta = 0.2$, Ha = 40, and $\phi = 0.04$.

Mesh size	51 × 151	61 × 181	71 × 211	81 × 241	91 × 271
Nu _{ave}	0.890241	0.895531	0.907145	0.908743	0.909166

TABLE 4: Nu_{ave} for various Gr and Ha at Pr = 0.733.

Ha	Gr = 2 × 10 ⁴		Gr = 2 × 10 ⁵	
	Present work	Rudraiah et al. [20]	Present work	Rudraiah et al. [20]
0	2.5665	2.5188	5.093205	4.9198
10	2.26626	2.2234	4.9047	4.8053
50	1.09954	1.0856	2.67911	2.8442
100	1.02218	1.011	1.46048	1.4317

3.2. Numerical Procedure. CVFEM uses both benefits of two common CFD methods. This method uses triangular element (see Figure 1(b)). Upwind approach is utilized for advection term. Gauss-Seidel approach is applied to solve the algebraic equations. Further notes can be found in [21].

4. Grid Independency and Validation

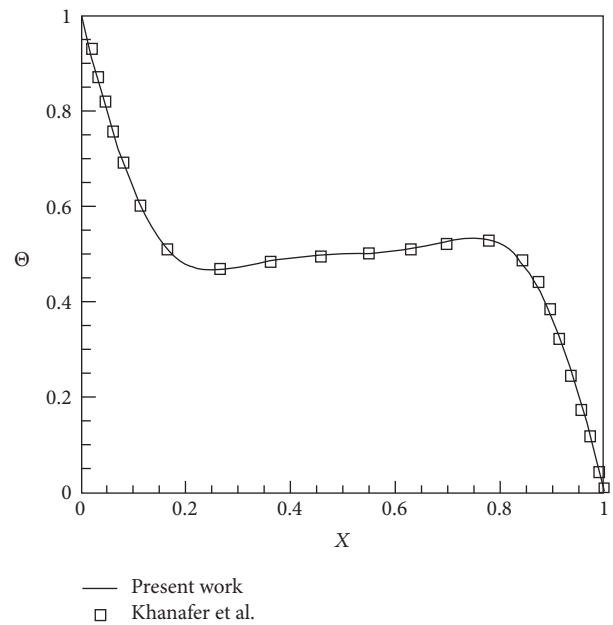
Outputs should not rely on mesh size. Therefore, several grids should be tested. For example, as shown in Table 3, a grid size of 71 × 211 can be selected. The correctness of CVFEM code for nanofluid natural convective heat transfer is demonstrated in Figure 2 ([18]). This CVFEM code has good accuracy for magnetohydrodynamic flow as depicted in Table 4 [20].

5. Results and Discussion

Nanofluid flow in a half sinusoidal annulus due to magnetic field in presence of melting surface is examined. μ_{nf} , k_{nf} of CuO–water nanofluid are estimated by means of KKL model. Graphs and tables are depicted for different amounts of CuO–H₂O volume fraction ($\phi = 0$ to 0.04), melting parameter ($\delta = 0$ to 0.2), Rayleigh number (Ra = 500 to 5000), and Hartmann number (Ha = 0 to 40).

Impact of adding CuO nanoparticles in water on velocity and temperature contours is depicted in Figure 3. Temperature gradient decreases with augment of ϕ . $|\Psi_{max}|$ augments with adding nanoparticles because of increment in the solid movements. In presence of melting heat transfer and magnetic field, effect of adding nanoparticles on isotherms becomes negligible.

Figures 4 and 5 depict the impact of Rayleigh and Hartmann numbers in absence of melting heat transfer. There

FIGURE 2: Validation of present code (Khanafar et al. [18]) when Gr = 10⁴, $\phi = 0.1$, and Pr = 6.8 (Cu–water).

is only one eddy in streamline. In low Rayleigh number, conduction mechanism is dominant. As Ra increases, the distortion of isotherms is enhanced close to the hot wall. Adding magnetic field makes isotherms become parallel. In presence of melting heat transfer the primary eddy diminishes and increasing Lorentz forces generates three layers for streamline. Increasing melting parameter augments the bottom eddy.

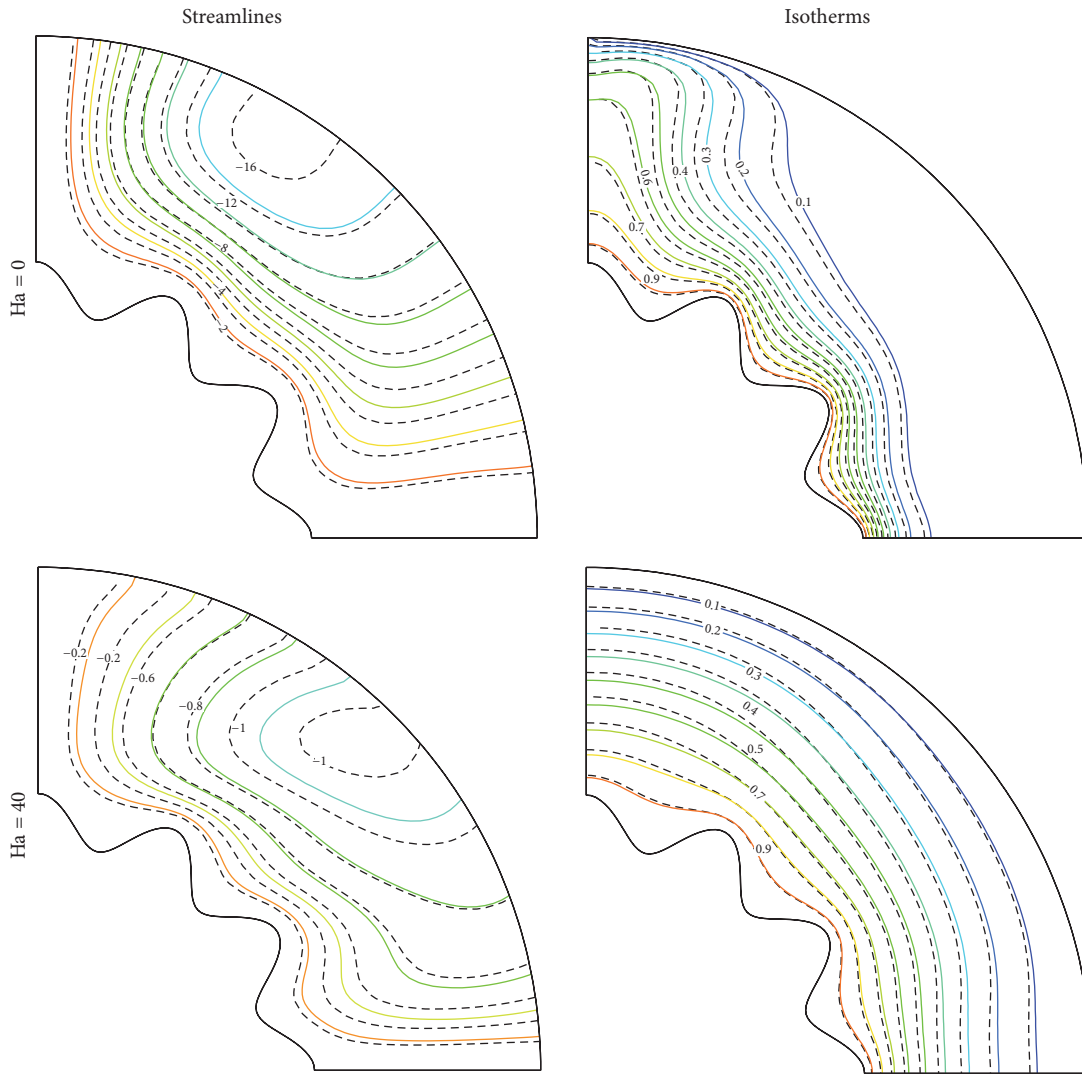


FIGURE 3: Impact of adding CuO in water on streamlines and isotherms (nanofluid ($\phi = 0.04$) (—) and pure fluid ($\phi = 0$) (- - -)) when $Ra = 5000$ and $\delta = 0.2$.

Figure 6 illustrates the impact of δ , Ra , and Ha on Nu_{ave} . The formula for Nu_{ave} corresponding to active parameters is

$$Nu_{ave} = 0.799 + 0.305\delta + 0.19Ra^* - 0.16Ha^* + 0.003Ra^*\delta - 0.0039\delta Ha^* - 0.028Ra^*Ha^* + 0.058\delta^2 - 0.012Ra^{*2} + 0.039Ha^{*2}, \quad (11)$$

where $Ha^* = 0.1Ha$ and $Ra^* = 0.001Ra$. As melting parameter augments, temperature gradient is enhanced and in turn Nusselt number is enhanced. Increasing buoyancy forces leads the thermal boundary layer thickness to reduce. So Nusselt number increases with enhancement of Ra . As Hartmann number augments, isotherms become parallel. Therefore Nusselt number has opposite relationship with Ha .

6. Conclusions

Nanofluid free convection due to Lorentz force in existence of melting surface is reported. Combination of FEM and FVM is utilized to solve the PDEs. KKL model is considered for nanofluid. Roles of Hartmann number, CuO–water volume fraction, Rayleigh number, and melting parameter are presented. Outputs depict that temperature gradient improves with augment of melting parameter and Rayleigh number. Adding magnetic field makes the temperature gradient reduce due to domination of conduction mechanism in high Hartmann number.

Nomenclature

B : Magnetic field
 T : Fluid temperature
 Nu : Nusselt number

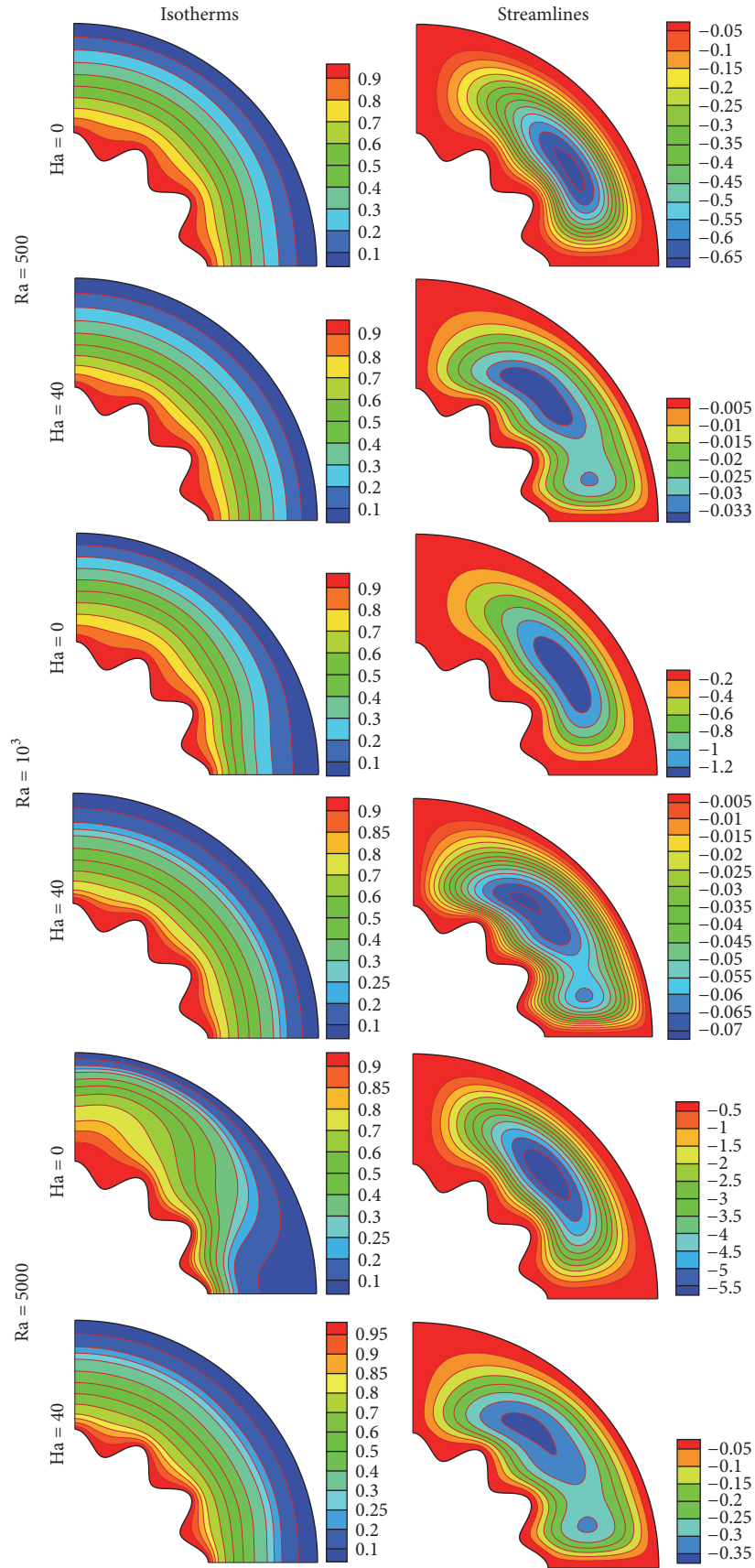


FIGURE 4: Isotherms and streamlines for various Ha, Ra when $\delta = 0$ and $\phi = 0.04$.

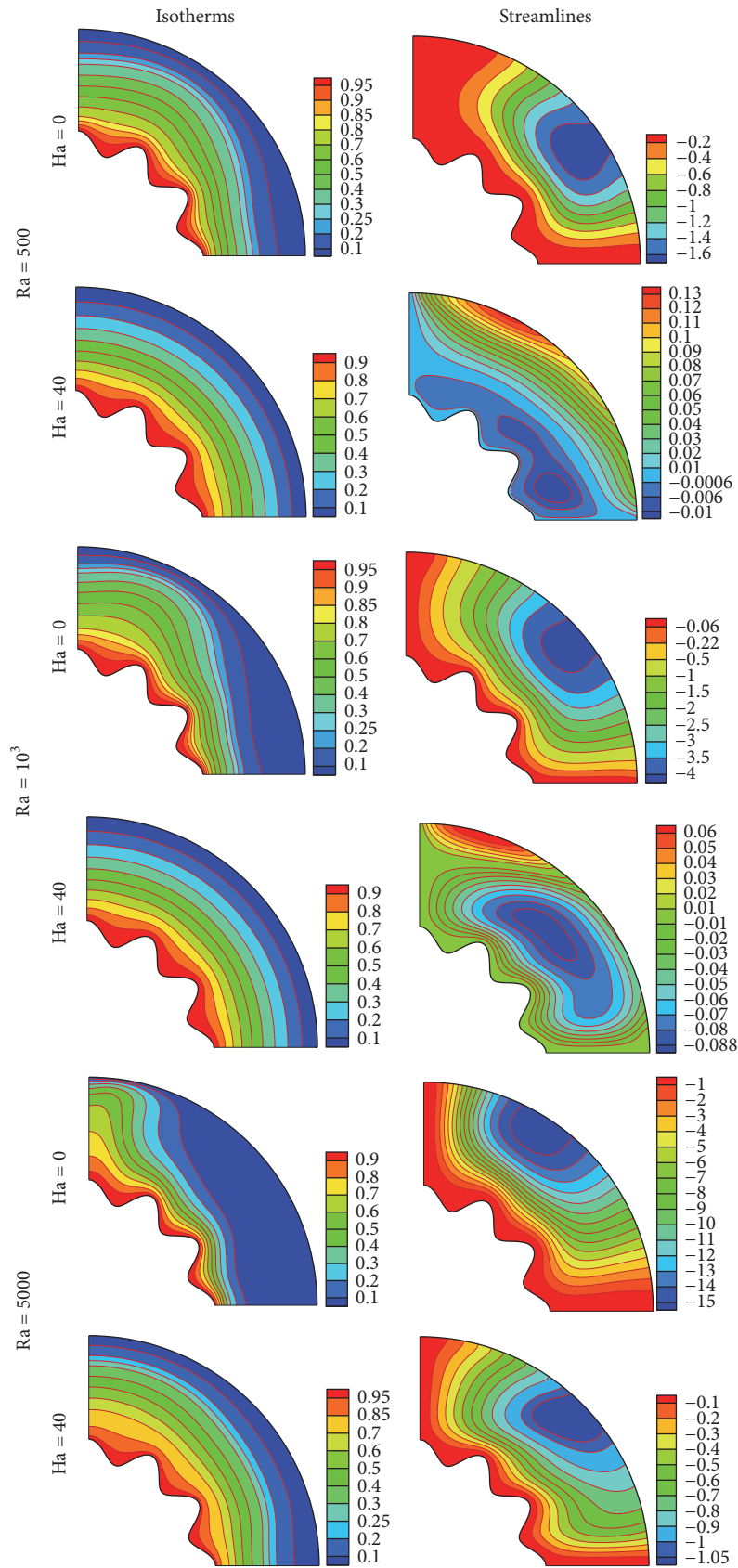


FIGURE 5: Isotherms and streamlines for various Ha, Ra when $\delta = 0.2$ and $\phi = 0.04$.

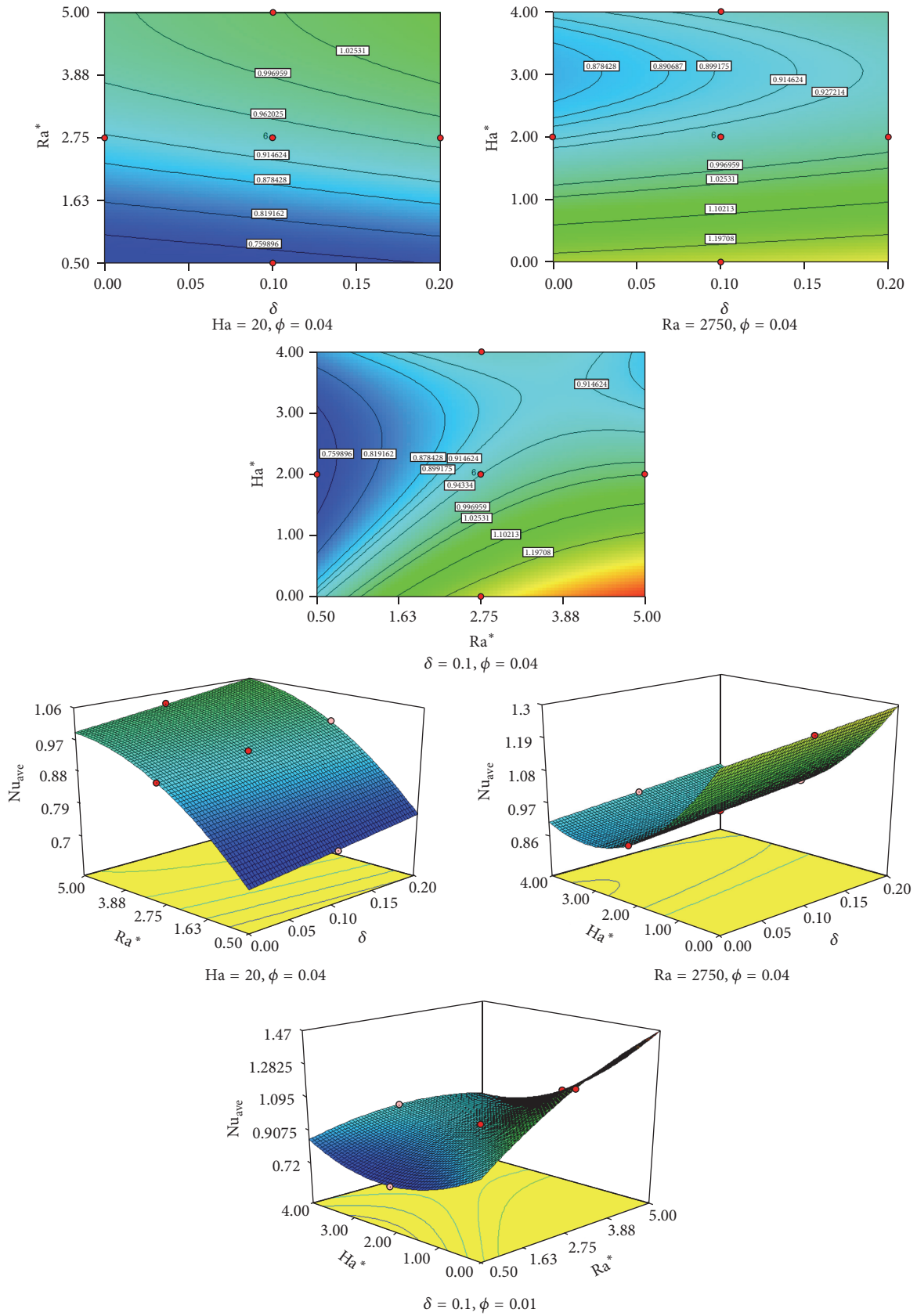


FIGURE 6: Impacts of δ , Ha , and Ra on Nu_{ave} .

Ra: Rayleigh number

\vec{g} : Gravitational acceleration vector

Ha: Hartmann number.

Greek Symbols

Θ :	Dimensionless temperature
α :	Thermal diffusivity
Ω and Ψ :	Dimensionless vorticity and stream function
δ :	Melting parameter
β :	Thermal expansion coefficient
σ :	Electrical conductivity
μ :	Dynamic viscosity.

Subscripts

f :	Base fluid
loc:	Local
nf:	Nanofluid.

Conflicts of Interest

The authors declare that there are no conflicts of interest regarding the publication of this paper.

References

- [1] A. J. Chamkha and M. A. Ismael, "Magnetic field effect on mixed convection in lid-driven trapezoidal cavities filled with a Cu-Water nanofluid with an aiding or opposing side wall," *Journal of Thermal Science and Engineering Applications*, vol. 8, no. 3, Article ID 031009, 2016.
- [2] R. Ellahi, M. Hassan, and A. Zeeshan, "Aggregation effects on water base Al₂O₃ - Nanofluid over permeable wedge in mixed convection," *Asia-Pacific Journal of Chemical Engineering*, vol. 11, no. 2, pp. 179–186, 2016.
- [3] S. Harikrishnan, M. Deenadhayalan, and S. Kalaiselvam, "Experimental investigation of solidification and melting characteristics of composite PCMs for building heating application," *Energy Conversion and Management*, vol. 86, pp. 864–872, 2014.
- [4] S. Mat, A. A. Al-Abidi, K. Sopian, M. Y. Sulaiman, and A. T. Mohammad, "Enhance heat transfer for PCM melting in triplex tube with internal-external fins," *Energy Conversion and Management*, vol. 74, pp. 223–236, 2013.
- [5] S. Manikandan and K. Rajan, "New hybrid nanofluid containing encapsulated paraffin wax and sand nanoparticles in propylene glycol-water mixture: Potential heat transfer fluid for energy management," *Energy Conversion and Management*, vol. 137, pp. 74–85, 2017.
- [6] H. D. Koca, S. Doganay, and A. Turgut, "Thermal characteristics and performance of Ag-water nanofluid: Application to natural circulation loops," *Energy Conversion and Management*, vol. 135, pp. 9–20, 2017.
- [7] L. S. Shyam and G. N. Tiwari, "Analytical characteristic equation of nanofluid loaded active double slope solar still coupled with helically coiled heat exchanger," *Energy Conversion and Management*, vol. 135, pp. 308–326, 2017.
- [8] K. Das, "Radiation and melting effects on MHD boundary layer flow over a moving surface," *Ain Shams Engineering Journal*, vol. 5, no. 4, pp. 1207–1214, 2014.
- [9] M. A. Sheremet, H. F. Oztop, and I. Pop, "MHD natural convection in an inclined wavy cavity with corner heater filled with a nanofluid," *Journal of Magnetism and Magnetic Materials*, vol. 416, pp. 37–47, 2016.
- [10] N. Shehzad, A. Zeeshan, R. Ellahi, and K. Vafai, "Convective heat transfer of nanofluid in a wavy channel: Buongiorno's mathematical model," *Journal of Molecular Liquids*, vol. 222, pp. 446–455, 2016.
- [11] M. Sheikholeslami, Q. M. Z. Zia, and R. Ellahi, "Influence of Induced Magnetic Field on Free Convection of Nanofluid Considering Koo-Kleinstreuer-Li (KKL) Correlation," *Applied Sciences (Switzerland)*, vol. 6, no. 11, article no. 324, 2016.
- [12] T. Abbas, M. Ayub, M. . Bhatti, M. M. Rashidi, and M. . Ali, "Entropy generation on nanofluid flow through a horizontal Riga plate," *Entropy. An International and Interdisciplinary Journal of Entropy and Information Studies*, vol. 18, no. 6, Paper No. 223, 11 pages, 2016.
- [13] A. J. Chamkha and A. M. Rashad, "Natural convection from a vertical permeable cone in a nanofluid saturated porous media for uniform heat and nanoparticles volume fraction fluxes," *International Journal of Numerical Methods for Heat and Fluid Flow*, vol. 22, no. 8, pp. 1073–1085, 2012.
- [14] R. Ellahi, A. Zeeshan, and M. Hassan, "Particle shape effects on marangoni convection boundary layer flow of a nanofluid," *International Journal of Numerical Methods for Heat and Fluid Flow*, vol. 26, no. 7, pp. 2160–2174, 2016.
- [15] A. Malvandi, M. H. Kaffash, and D. D. Ganji, "Nanoparticles migration effects on magnetohydrodynamic (MHD) laminar mixed convection of alumina/water nanofluid inside microchannels," *Journal of the Taiwan Institute of Chemical Engineers*, vol. 52, pp. 40–56, 2015.
- [16] F. Garoosi, F. Hoseininejad, and M. M. Rashidi, "Numerical study of natural convection heat transfer in a heat exchanger filled with nanofluids," *Energy*, vol. 109, pp. 664–678, 2016.
- [17] M. Sheikholeslami and R. Ellahi, "Three dimensional mesoscopic simulation of magnetic field effect on natural convection of nanofluid," *International Journal of Heat and Mass Transfer*, vol. 89, Article ID 12118, pp. 799–808, 2015.
- [18] K. Khanafer, K. Vafai, and M. Lightstone, "Buoyancy-driven heat transfer enhancement in a two-dimensional enclosure utilizing nanofluids," *International Journal of Heat and Mass Transfer*, vol. 46, no. 19, pp. 3639–3653, 2003.
- [19] M. S. Kandelousi and R. Ellahi, "Simulation of ferrofluid flow for magnetic drug targeting using the lattice boltzmann method," *Zeitschrift fur Naturforschung - Section A Journal of Physical Sciences*, vol. 70, no. 2, pp. 115–124, 2015.
- [20] N. Rudraiah, R. M. Barron, M. Venkatachalappa, and C. K. Subbaraya, "Effect of a magnetic field on free convection in a rectangular enclosure," *International Journal of Engineering Science*, vol. 33, no. 8, pp. 1075–1084, 1995.
- [21] V. R. Voller, *Basic control volume finite element methods for fluids and solids*, vol. 1 of *IISc Research Monographs Series*, World Scientific Publishing Co. Pte. Ltd., Hackensack, NJ; IISc Press, Bangalore, 2009.

Research Article

Mathematical Model for Electric Field Sensor Based on Whispering Gallery Modes Using Navier's Equation for Linear Elasticity

Amir R. Ali^{1,2} and Mohamed A. Kamel¹

¹Applied-Science & Robotics Laboratory for Applied-Mechatronics (ARATronics Lab.), Mechatronics Engineering Department, German University in Cairo, New Cairo, Cairo 11835, Egypt

²Micro-Sensor Laboratory, Mechanical Engineering Department, Southern Methodist University, Dallas, TX 75275, USA

Correspondence should be addressed to Amir R. Ali; arahmed@mail.smu.edu

Received 30 March 2017; Revised 5 June 2017; Accepted 18 June 2017; Published 25 July 2017

Academic Editor: Constantin Fetecau

Copyright © 2017 Amir R. Ali and Mohamed A. Kamel. This is an open access article distributed under the Creative Commons Attribution License, which permits unrestricted use, distribution, and reproduction in any medium, provided the original work is properly cited.

This paper presents and verifies the mathematical model of an electric field sensor based on the whispering gallery mode (WGM). The sensing element is a dielectric microsphere, where the light is used to tune the optical modes of the microsphere. The light undergoes total internal reflection along the circumference of the sphere; then it experiences optical resonance. The WGM are monitored as sharp dips on the transmission spectrum. These modes are very sensitive to morphology changes of the sphere, such that, for every minute change in the sphere's morphology, a shift in the transmission spectrum will happen and that is known as WGM shifts. Due to the electrostriction effect, the applied electric field will induce forces acting on the surface of the dielectric sphere. In turn, these forces will deform the sphere causing shifts in its WGM spectrum. The applied electric field can be obtained by calculating these shifts. Navier's equation for linear elasticity is used to model the deformation of the sphere to find the WGM shift. The finite element numerical studies are performed to verify the introduced model and to study the behavior of the sensor at different values of microspheres' Young's modulus and dielectric constant. Furthermore, the sensitivity and resolution of the developed WGM electric field sensor model will be presented in this paper.

1. Introduction

Recently, optical cavities have been used for many sensory applications due their high quality factor and resolution [1, 2]. These applications include wall shear stress calculation [3, 4]; temperature measurement [5–7]; biosensing [8–13]; hemozoin nanocrystals detection in aquatic environment [14]; nanoparticle detection [15]; and acceleration measurement [16–18]. In this paper, WGM based optical cavities are used to detect and measure the applied electric field. These cavities come in different shapes such as sphere, toroid, disk, and cylinder. The optical modes of these cavities can be excited using tunable laser. A single mode optical fiber is utilized to couple the incoming laser light into the cavity. When resonance occurs, the WGM modes are monitored as sharp dips on the transmission. WGM modes are highly responsive

to changes in the morphology of the cavity and the outer medium; consequently, they are also called morphology dependent resonances (MDR) modes. Any minute external disturbance on the sphere or its surrounding environment will be detected as shift in its transmission spectrum. Consequently, these cavities are used in many sensory applications by measuring the WGM shifts corresponding to the change in the measured phenomenon.

Figure 1 presents a microsphere WGM cavity of an outer radius b subjected to an applied electric field of strength E_0 . The sphere is usually fabricated from dielectric polymeric material, like polydimethylsiloxane (PDMS). At the beginning, an optical fiber (~5 cm long) was stripped of its plastic cladding and then subjected to heat while stretching. The final diameter size after stretching is ~50 μm . Afterwards, the fiber is dipped into the PDMS polymer pool. Then, a sphere

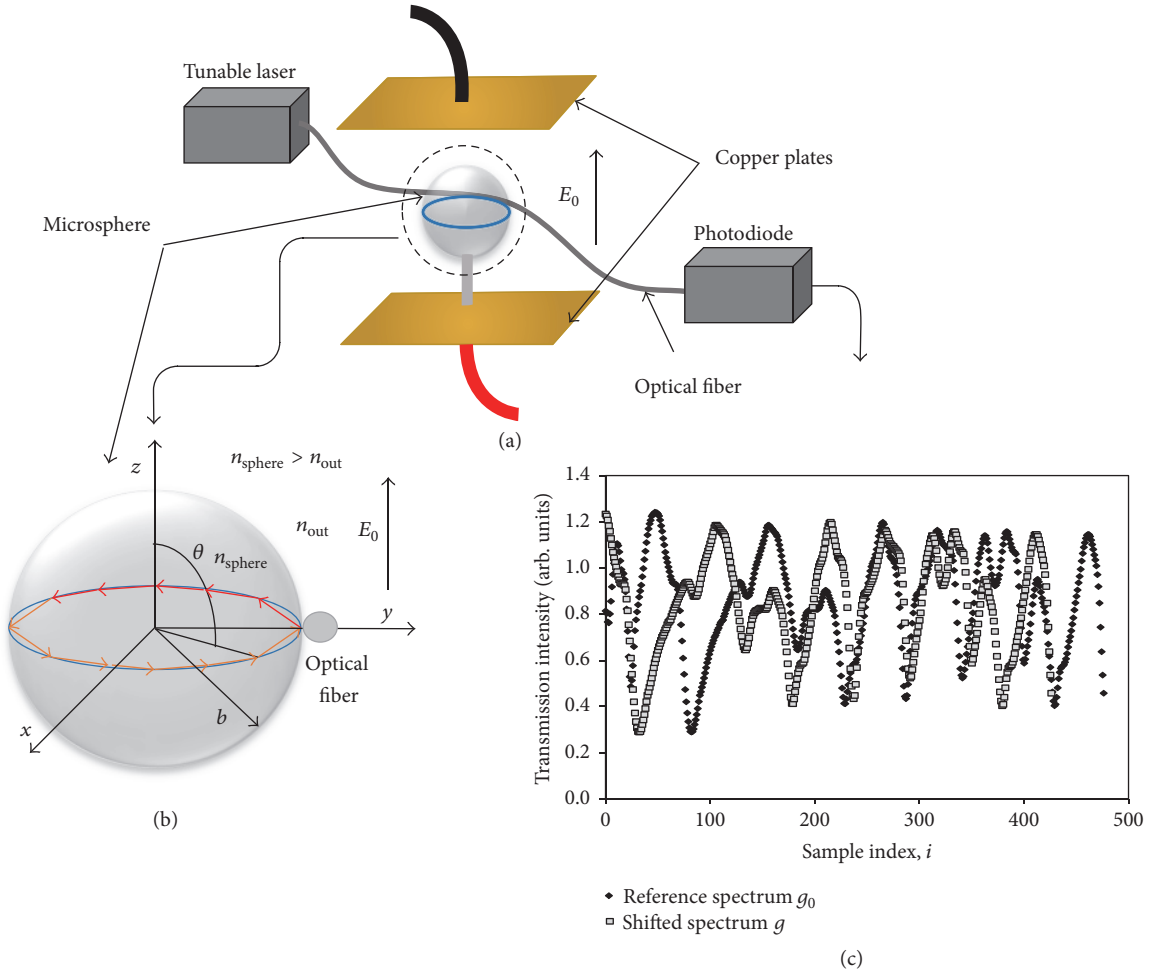


FIGURE 1: (a) Schematic diagram of the WGM based electric field sensor, (b) WGM microsphere, and (c) transmission spectrum for a microsphere before and after morphology changes.

of PDMS will form at the end of the fiber due to the surface tension and the gravitational forces. The fiber and sphere assembly is heated to cure of the polymeric material as reported in [19].

The microsphere is coupled to a single mode optical fiber. A tunable laser is utilized to supply the light traveling through the optical fiber. The light is coupled to a microsphere cavity through the tapered section of the optical fiber; then it circumnavigates the microsphere undergoing total internal reflection. The condition of total internal reflection must be fulfilled, such that the refractive index of the cavity n_{sphere} is greater than the surrounding n_{out} . A photodiode is placed on the other side of the optical fiber to monitor the intensity of the transmitted light.

The optical resonance will only happen when the total distance traveled by the light (round trip) is almost equal to a multiple integer k of the light's wavelength as seen in 1st-order approximation of (1). Then the WGM would be presented as a sharp dips on the transmission spectrum as shown in Figure 1(c).

$$2\pi n_{\text{sphere}} b \approx k\lambda, \quad b \gg \lambda, \quad (1)$$

where n_{sphere} is the refractive index the microsphere; λ is the wavelength of the light; and b is the radius of the sphere. The change in the morphology (size or the refractive index) of the cavity will induce a shift $d\lambda$ in the resonance wavelength as follows:

$$\frac{d\lambda}{\lambda} = \frac{db}{b} + \frac{dn_{\text{sphere}}}{n_{\text{sphere}}}. \quad (2)$$

In this paper, the microsphere is used to measure the applied electric field due to the electrostriction effect. When an electric field is applied on a dielectric microsphere, it induces surface and body forces across its body. In turn, these forces will deform the sphere changing its size, causing shifts in its WGM transmission spectrum, thus creating a WGM based electric field sensor. The induced electrostrictive volumetric body force \vec{f} can be written as follows [20]:

$$\vec{f} = -\frac{1}{2}E^2\nabla\epsilon_{\text{sphere}} - \frac{1}{4}(a_1 + a_2)\nabla E^2, \quad (3)$$

where ϵ_{sphere} is the dielectric constant of the microsphere's material; E is the applied electric field inside the sphere; and

a_1 and a_2 are coefficients describing the strain of the dielectric material due to the applied electric field in the directions parallel and perpendicular to the field. \vec{f} is the summation of the gradients of E^2 and ϵ_{sphere} . For a homogenous dielectric material under a static uniform applied electric field, both gradients of (3) are equal to zero; thus \vec{f} is also zero. However, at the interface separating the microsphere and the surrounding, a surface pressure force \vec{P} exists. It exists due to the discontinuity of the dielectric constant along the media and given by

$$\vec{P} = [\alpha \vec{E} (\vec{E} \cdot \vec{n})]_o + [\alpha \vec{E} (\vec{E} \cdot \vec{n})]_s - [\beta E^2 \vec{n}]_o - [\beta E^2 \vec{n}]_s. \quad (4)$$

α and β are coefficients that depend on the electrostrictive properties of the microsphere's material. \vec{n} is the unit surface normal vector and the subscripts indicate the values to be taken on either side of the interface (s denotes the sphere's and o denotes the outer medium). The induced deformation due to the pressure forces can be obtained by solving Navier's equation for linear elasticity at steady state, which is given by

$$\nabla^2 \vec{u} + \frac{1}{1-2\nu} \nabla (\nabla \cdot \vec{u}) + \frac{\vec{f}}{G} = 0, \quad (5)$$

where \vec{u} is the deformation of the cavity, ν is Poisson's ratio, and G is the shear modulus of the cavity's material. Thus the deformation of the microsphere needs to be calculated to get the WGM shift due to the applied electric field.

2. Analysis

2.1. Electric Field and Pressure Force Calculation. To solve Navier's equation, the pressure forces must be obtained first; so the first step is to calculate the electric field composing the pressure forces. The applied electric field is obtained by differentiating the electric potential. When a dielectric microsphere is placed under an applied static axisymmetric electric field, the potential is defined by Laplace's equation in spherical coordinates (r, θ, φ) [21].

$$\nabla^2 D = 0, \quad (6)$$

where D is the electric potential. Due to the symmetry of the applied electric field, the solution of Laplace's equation is also independent of the azimuthal angle φ . Separation of variables method is used to obtain the solution $D(r, \theta)$.

$$D(r, \theta) = \sum_{m=0} r^m \left(A_m + \frac{B_m}{r} \right) P_m(\cos \theta), \quad (7)$$

where r is radius of the microsphere, θ is the azimuthal angle between the position vector and the z axis, P_m is the associated Legendre polynomial of the m th order, and A_m, B_m are coefficients. The boundary conditions enforced on the microsphere, due to the continuity of the potential and electric

field lines at the interface (where the value of the radius r is equal to b), are

$$D_{\text{sphere}}(b) = D_{\text{out}}(b), \quad (8)$$

$$\epsilon_{\text{sphere}} \frac{\partial D_{\text{sphere}}}{\partial r} = \epsilon_{\text{out}} \frac{\partial D_{\text{out}}}{\partial r} \Big|_{r=b}.$$

D_{sphere} and D_{out} are the electric potential inside and outside the microsphere, respectively. ϵ_{out} is the dielectric constant of material outside the sphere. After the application of the boundary conditions, the coefficients are A_m and B_m are obtained. The gradient of the potential is applied to find the radial E_r and azimuthal E_θ components of the applied electric field inside and outside the cavity. The electric field components are

$$E_r = \begin{cases} \frac{-3E_0 \epsilon_{\text{out}}}{2\epsilon_{\text{out}} + \epsilon_{\text{sphere}}} \cos \theta & r < b \\ -E_0 \left(\frac{2b^3 (\epsilon_{\text{out}} - \epsilon_{\text{sphere}})}{r^3 (2\epsilon_{\text{out}} + \epsilon_{\text{sphere}})} - 1 \right) \cos \theta & r > b, \end{cases} \quad (9)$$

$$E_\theta = \begin{cases} \frac{3E_0 \epsilon_{\text{out}}}{\epsilon_{\text{sphere}} + 2\epsilon_{\text{out}}} \sin \theta & r < b \\ E_0 \left(\frac{b^3 (\epsilon_{\text{out}} - \epsilon_{\text{sphere}}) + r^3 (2\epsilon_{\text{out}} + \epsilon_{\text{sphere}})}{r^3 (2\epsilon_{\text{out}} + \epsilon_{\text{sphere}})} \right) \cos \theta & r > b. \end{cases}$$

E_0 is the applied electric field strength. The acting radial and azimuthal components of the pressure force (P_r and P_θ) on the interface are

$$P_r = \frac{9E_0^2}{4(2\epsilon_{\text{out}} + \epsilon_{\text{sphere}})^2} \left((a_1 + a_2 + 2\epsilon_0 - \epsilon_{\text{out}}) (\epsilon_{\text{sphere}} - \epsilon_{\text{out}})^2 + ((a_1 + a_2 + 2\epsilon_0) \epsilon_{\text{sphere}} + (a_1 + a_2 + 2\epsilon_0 - \epsilon_{\text{out}}) \epsilon_{\text{out}} + \epsilon_{\text{out}}^2) (\epsilon_{\text{sphere}} - \epsilon_{\text{out}}) \cdot \cos 2\theta \right), \quad (10)$$

$$P_\theta = \frac{-9E_0^2 (a_1 + 2\epsilon_0) (\epsilon_{\text{sphere}} - \epsilon_{\text{out}}) \epsilon_{\text{out}} \sin 2\theta}{4(2\epsilon_{\text{out}} + \epsilon_{\text{sphere}})^2}.$$

ϵ_0 is the dielectric permittivity of vacuum ($8.854 \times 10^{-12} \text{ F}\cdot\text{m}^{-1}$). The boundary stresses acting on the sphere will be equated to the pressure forces. These forces will deform the microsphere; and the deformation is calculated using Navier's equation.

2.2. Solution of Navier's Equation. Due to the absence of the body force, Navier's equation can be written as follows:

$$\nabla^2 \vec{u} + \frac{1}{1-2\nu} \nabla (\nabla \cdot \vec{u}) = 0. \quad (11)$$

Using Helmholtz theory, \vec{u} can be expressed as follows [24]:

$$\vec{u} = \vec{u}_s + \vec{u}_{ir}, \quad (12)$$

where \vec{u}_s and \vec{u}_{ir} are solenoidal and irrotational vectors, respectively; these vectors satisfy the following relations:

$$\begin{aligned}\nabla \times \vec{u}_{ir} &= 0, \\ \nabla \cdot \vec{u}_s &= 0.\end{aligned}\quad (13)$$

Thus \vec{u} can be written as follows:

$$\vec{u} = \vec{B} + \nabla\Gamma, \quad (14)$$

where \vec{B} is a harmonic vector; and Γ is a scalar potential function. Substitution of (14) in (11) yields

$$\nabla^2\Gamma = \frac{-1}{2(1-\nu)}\nabla \cdot \nabla\vec{B}. \quad (15)$$

Γ is chosen to satisfy the previous equation and given by

$$\Gamma = \frac{-1}{4(1-\nu)}\left(\vec{R} \cdot \vec{B} + B_0\right), \quad (16)$$

where B_0 is harmonic and satisfying the boundary conditions; and \vec{R} is the position vector. After substitution of Γ in (11), the solution to Navier's equation in spherical coordinates can be written as follows:

$$\vec{u} = 4(1-\nu)\vec{B} - \nabla\left(\vec{R} \cdot \vec{B} + B_0\right). \quad (17)$$

Laplace's equation is solved again to find the harmonic vector \vec{B} , where the components of \vec{B} and B_0 are represented as a series of Legendre polynomials. Thus, the radial deformation of the sphere due to the applied electric field can be written as follows:

$$u_r = \sum_n \left[A_n (n+1)(n-2+4\nu)R^{n+1} + B_n nR^{n-1} \right] P_n(\xi) \quad (18)$$

$$\xi = \cos(\theta).$$

u_r is series of the associated Legendre polynomials $P_n(\xi)$ of the n th order. The polynomials are multiplied by the coefficients A_n and B_n . These coefficients are also obtained using the boundary conditions imposed on the sphere. Finally the boundary stresses in the radial σ_{rr} and azimuthal $\sigma_{r\theta}$ directions derived from the deformations are represented as follows:

$$\begin{aligned}\sigma_{rr} &= 2G \sum_n \left[A_n (n+1)(n^2 - n - 2 - 2\nu)R^n \right. \\ &\quad \left. + B_n n(n-1)R^{n-2} \right] P_n(\xi), \\ \sigma_{r\theta} &= 2G \sum_n \left[A_n (n^2 + 2n - 1 + 2\nu)R^n \right. \\ &\quad \left. + B_n (n-1)R^{n-2} \right] \frac{d}{d\theta} P_n(\xi).\end{aligned}\quad (19)$$

In electrostriction, the pressure forces are the applied boundary stresses on the microsphere and satisfy

$$\begin{aligned}\sigma_{rr} &= P_r|_{r=b} \\ \sigma_{r\theta} &= P_\theta|_{r=b}.\end{aligned}\quad (20)$$

In this case the solution \vec{u} can be presented as follows:

$$\begin{aligned}u_r &= \frac{3bE_0^2(\epsilon_{\text{sphere}} - \epsilon_{\text{out}})}{4E_e(\epsilon_{\text{sphere}} + 2\epsilon_{\text{out}})^2(1+\nu)^2} \left((a_1 + a_2 + 2\epsilon_0) \right. \\ &\quad \cdot \epsilon_{\text{sphere}} + (a_1 + a_2 + 2\epsilon_0 - \epsilon_{\text{sphere}})\epsilon_{\text{out}} - 2\epsilon_{\text{out}}^2) (4 \\ &\quad - 2\nu) + \frac{(1+\nu)}{7+5\nu} (-7(a_1 + a_2 + 2\epsilon_0)\epsilon_{\text{sphere}} - 7(a_1 \\ &\quad + a_2 + 2\epsilon_0 - \epsilon_{\text{sphere}})\epsilon_{\text{out}} - 7\epsilon_{\text{out}}^2 \\ &\quad + 2\nu(2(a_1 + a_2 + 2\epsilon_0)\epsilon_{\text{sphere}} \\ &\quad - (25a_1 - 2a_2 + 50\epsilon_0 + 2\epsilon_{\text{sphere}})\epsilon_{\text{out}} + 2\epsilon_{\text{out}}^2) (1 \\ &\quad \left. + 3\cos(2\theta)) \right).\end{aligned}\quad (21)$$

E_e is Young's modulus of the material of the microsphere. The radial deformation u_r is directly proportional to the square of the electric field strength; inversely proportional to E_e ; and dependent on the dielectric constants ϵ_{sphere} and ϵ_{out} . Navier's equation is solved at the equator (θ is $\pi/2$); thus, the calculated u_r is the same change dr in the optical path of the circumnavigating light:

$$\begin{aligned}u_r &= \frac{9bE_0^2(\epsilon_{\text{sphere}} - \epsilon_{\text{out}})}{2E_e(\epsilon_{\text{sphere}} + 2\epsilon_{\text{out}})^2(1+\nu)^2(7+5\nu)} \left(2\nu(a_1 \right. \\ &\quad \left. + a_2 + 2\epsilon_0)(2+\nu)\epsilon_{\text{sphere}} + 2\nu\epsilon_{\text{out}}(11a_1 + 2a_2 \right. \\ &\quad \left. + 22\epsilon_0 - 2\epsilon_{\text{sphere}} + \nu(10a_1 + a_2 + 20\epsilon_0 - \epsilon_{\text{sphere}})) \right. \\ &\quad \left. + \epsilon_{\text{out}}^2(7-\nu(5+8\nu)) \right).\end{aligned}\quad (22)$$

The $d\lambda$ is independent of the outer radius b and can be written using (2) as follows:

$$\begin{aligned}d\lambda &= \frac{9\lambda_L E_0^2(\epsilon_{\text{sphere}} - \epsilon_{\text{out}})}{2E_e(\epsilon_{\text{sphere}} + 2\epsilon_{\text{out}})^2(1+\nu)^2(7+5\nu)} \left(2\nu(a_1 \right. \\ &\quad \left. + a_2 + 2\epsilon_0)(2+\nu)\epsilon_{\text{sphere}} + 2\nu\epsilon_{\text{out}}(11a_1 + 2a_2 \right. \\ &\quad \left. + 22\epsilon_0 - 2\epsilon_{\text{sphere}} + \nu(10a_1 + a_2 + 20\epsilon_0 - \epsilon_{\text{sphere}})) \right. \\ &\quad \left. + \epsilon_{\text{out}}^2(7-\nu(5+8\nu)) \right).\end{aligned}\quad (23)$$

λ_L is the wavelength of the light provided by the tunable laser. Using Navier's equation, an optical WGM based electric field sensor can be constructed. The relation between the microsphere's WGM shift and the applied electric field is investigated extensively by means of numerical studies using finite element simulation software.

TABLE 1: Simulation parameters for the 1st numerical study.

Parameter	Magnitude
Microsphere (PDMS 60 : 1)	
Diameter	600 μm
Poisson's ratio	0.49
Density	1030 kg/m^3
Dielectric constant	$2.7 \times \epsilon_0$
Young's modulus	3 kpa
Outer medium (air)	
Dielectric constant	$1 \times \epsilon_0$
Laser light (infrared)	
Wavelength	1.312 μm

2.3. Numerical Studies. Three numerical studies are done to investigate the relation between $d\lambda$ and the applied electric field. The studies calculate $d\lambda$ using the deformation of the sphere due to the electrostriction effect. The purpose of the first two studies is to confirm the quadratic dependence of sphere's WGM shift on the applied electric field strength and the inverse proportionality between the sphere's WGM shift and Young's modulus of the sphere's material, while the third one aims to see the effect varying the dielectric constant of the sphere on its WGM shift. During the studies, the electric field is supplied by means of 2 copper electrodes. The microsphere is situated at the center between the plates as seen in Figure 1.

For the first study, cured PDMS [25] is used as the construction material of the microsphere. The mixture has an elastomer to curing agent ratio of 60:1. Under steady-state conditions, $d\lambda$ is measured against an increasing applied electric field. The simulation parameters during the first study are presented in Table 1.

As for the second study, the inverse proportionality between the sphere's WGM shift and Young's modulus of the sphere's material is investigated. The study measures $d\lambda$ of several microspheres with different Young's moduli under the same applied electric field strength. The simulation parameters of the second study is similar to the first one, except for the varying Young's modulus value. Finally, the third study investigates the effect of varying the sphere's dielectric constant on its WGM shift. The 3rd study subjects several microspheres with different values of dielectric constant to the same applied electric field input; then it measures the value of $d\lambda$ of the several microspheres. Also, the simulation parameters of the 3rd study is similar to the first one, except for the changing dielectric constant. The strength of the applied electric field for the 2nd and 3rd studies is 5 kV/m.

3. Results and Discussion

Results of the 1st numerical studies are shown in Figure 2. $d\lambda$ is plotted against the increasing electric field strength up to 1300 kV/m. The increasing electric field will be met by the increasing shift. It can be seen that the quadratic relation

between $d\lambda$ and the electric field strength is confirmed. In Figure 2, the numerical range under study was split to three main regions (0–200 kV/m, 200–500 kV/m, and 500–1300 kV/m). It is clear that the nonlinear behavior in the response was linearized per each region to be able to find the linear relation between the output $d\lambda$ and the input E_0 . Since the proposed sensor is a linear optical sensor, so we will find out the sensitivity and the resolution for that sensor per each region. Table 2 summarized sensitivity and resolution values for each mentioned region.

Figure 3 shows the results of the second study, where the WGM shift $d\lambda$ is modeled against the varying Young's modulus (E_e) of microsphere for different values of applied electric field strength (0.5 kV/m, 1 kV/m, 1.5 kV/m, 2 kV/m, and 5 kV/m). Decreasing Young's modulus of the sphere will lead to the increase of the shift. It is clear that the WGM shift is inversely proportional with respect to Young's modulus of the sensing element material.

Finally, Figure 4 shows the results of the 3rd study, which is the WGM shift of the microsphere is directly proportional to the relative dielectric constant (ϵ_R) of the microsphere. In this study, we do find the sensor response for the same applied electric field strength mentioned in the 2nd study (0.5 kV/m, 1 kV/m, 1.5 kV/m, 2 kV/m, and 5 kV/m).

Up to now, several sensor technologies for electric field detection have been implemented. Table 3 summarizes the sensitivities of electric field from various techniques. In this paper, we show that our new modeling technique will be promising to be used in a complex sensor structure like multilayered composite sphere as reported in [26].

4. Conclusion

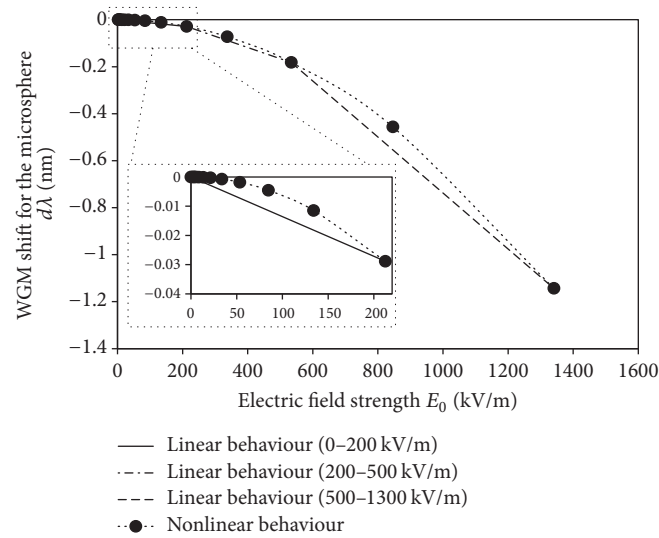
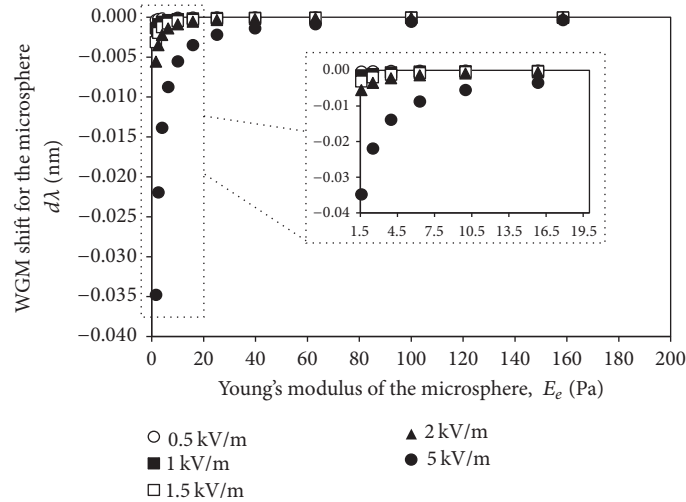
In this paper, the mathematical model of a WGM based electric field sensor is presented. Navier's equation for linear elasticity is solved to find the deformation of the seeing element upon application of the electric field strength with different values (0.5 kV/m, 1 kV/m, 1.5 kV/m, 2 kV/m, and 5 kV/m). The response indicates that the WGM shift in the transmission spectrum has a quadratic dependence on the applied electric field strength. However, the linearization behavior for the sensor is needed for the practical usage. That was the reason to split the sensing range into three main regions (0–200 kV/m, 200–500 kV/m, and 500–1300 kV/m). Results show that the WGM shift is inversely proportional to Young's modulus of the microsphere's material under different electric field strength values (0.5 kV/m, 1 kV/m, 1.5 kV/m, 2 kV/m, and 5 kV/m). Furthermore, the studies also show that the WGM shift is directly proportional to the dielectric constant of the microsphere's material under the same electric field strength values that were mentioned before. The sensor behavior and characteristics were verified by numerical finite element studies. Finally, in this paper, we show that our new promising modeling technique will be easily used in a complex sensor structure like multilayered composite sphere.

TABLE 2: Sensitivity and resolution along the different detection regions.

	0–200 kV/m	200–500 kV/m	500–1300 kV/m
Sensitivity $ d\lambda/dE_0 $ nm/(kV/m)	0.00014	0.00048	0.00119
Resolution kV/m	28.64	23.17	57.88

TABLE 3: Electric field sensor's sensitivity with different techniques.

Electric field detection technique	Sensitivity achieved	Reference	Year
Unpolarized PDMS sphere	8×10^{-4} pm/(V/m)	[22]	2012
Polarized PDMS sphere	6×10^{-3} pm/(V/m)	[22]	2012
Beam coupled PDMS cavity	0.01 pm/(V/m)	[22]	2012
PDMS homogenous sphere	0.0017 pm/(V/m)	[23]	2014
Composite sphere	0.027 pm/(V/m)	[23]	2014

FIGURE 2: WGM shifts $d\lambda$ against the applied electric field strength during the 1st study.FIGURE 3: WGM shifts $d\lambda$ against Young's modulus during the 2nd study.

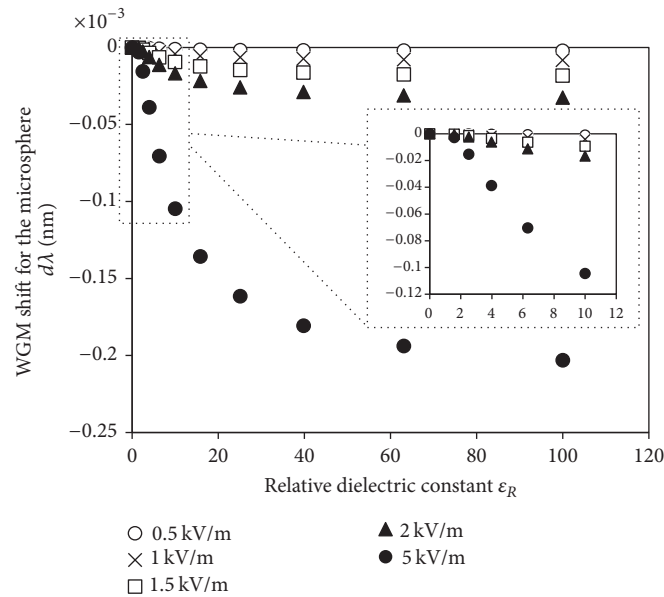


FIGURE 4: WGM shifts $d\lambda$ against relative dielectric constant during the 3rd study.

Conflicts of Interest

The authors declare that there are no conflicts of interest regarding the publication of this paper.

References

- [1] M. L. Gorodetsky, A. A. Savchenkov, and V. S. Ilchenko, "Ultimate Q of optical microsphere resonators," *Optics Letters*, vol. 21, no. 7, pp. 453–455, 1996.
- [2] F. Monifi, Ş. Kaya Özdemir, and L. Yang, "Tunable add-drop filter using an active whispering gallery mode microcavity," *Applied Physics Letters*, vol. 103, no. 18, Article ID 181103, 2013.
- [3] U. K. Ayaz, T. Ioppolo, and M. V. Ötügen, "Direct measurement of wall shear stress in a reattaching flow with a photonic sensor," *Measurement Science and Technology*, vol. 24, no. 12, Article ID 124001, 2013.
- [4] U. K. Ayaz, T. Ioppolo, and M. V. Ötügen, "Wall shear stress sensor based on the optical resonances of dielectric microspheres," *Measurement Science and Technology*, vol. 22, no. 7, Article ID 075203, 2011.
- [5] B. Özel, R. Nett, T. Weigel, G. Schweiger, and A. Ostendorf, "Temperature sensing by using whispering gallery modes with hollow core fibers," *Measurement Science and Technology*, vol. 21, no. 9, Article ID 094015, 2010.
- [6] G. Guan, S. Arnold, and M. V. Otugen, "Temperature measurements using a microoptical sensor based on whispering gallery modes," *AIAA Journal*, vol. 44, no. 10, pp. 2385–2389, 2006.
- [7] C. H. Dong, L. He, Y. F. Xiao et al., "Fabrication of high-Q polydimethylsiloxane optical microspheres for thermal sensing," *Applied Physics Letters*, vol. 94, no. 23, pp. 1–3, 2009.
- [8] L. He, Ş. K. Özdemir, J. Zhu, W. Kim, and L. Yang, "Detecting single viruses and nanoparticles using whispering gallery microlasers," *Nature Nanotechnology*, vol. 6, no. 7, pp. 428–432, 2011.
- [9] F. Vollmer, S. Arnold, D. Braun, I. Teraoka, and A. Libchaber, "Multiplexed DNA quantification by spectroscopic shift of two microsphere cavities," *Biophysical Journal*, vol. 85, no. 3, pp. 1974–1979, 2003.
- [10] K. Schult, A. Katerkamp, D. Trau, F. Grawe, K. Cammann, and M. Meusel, "Disposable optical sensor chip for medical diagnostics: New ways in bioanalysis," *Analytical Chemistry*, vol. 71, no. 23, pp. 5430–5435, 1999.
- [11] S. Arnold and S. I. Shopova, "Whispering Gallery Mode Biosensor," in *Biophotonics: Spectroscopy, Imaging, Sensing, and Manipulation*, NATO Science for Peace and Security Series B: Physics and Biophysics, pp. 237–259, Springer, Dordrecht, The Netherlands, 2011.
- [12] F. Vollmer and S. Arnold, "Whispering-gallery-mode biosensing: label-free detection down to single molecules," *Nature Methods*, vol. 5, no. 7, pp. 591–596, 2008.
- [13] W. Lukosz, "Integrated optical chemical and direct biochemical sensors," *Sensors and Actuators B: Chemical*, vol. 29, no. 1-3, pp. 37–50, 1995.
- [14] W. Kim, S. K. Ozdemir, J. Zhu, M. Faraz, C. Coban, and L. Yang, "Detection and size measurement of individual hemozoin nanocrystals in aquatic environment using a whispering gallery mode resonator," *Optics Express*, vol. 20, no. 28, pp. 29426–29446, 2012.
- [15] Ş. K. Özdemir, J. Zhu, X. Yang et al., "Highly sensitive detection of nanoparticles with a self-referenced and self-heterodyned whispering-gallery Raman microlaser," *Proceedings of the National Academy of Sciences of the United States of America*, vol. 111, no. 37, pp. E3836–E3844, 2014.
- [16] A. B. Matsko, A. A. Savchenkov, V. S. Ilchenko, and L. Maleki, "Optical gyroscope with whispering gallery mode optical cavities," *Optics Communications*, vol. 233, no. 1-3, pp. 107–112, 2004.
- [17] T. Ioppolo, V. Ötügen, D. Fourquette, and L. Laroque, "Effect of acceleration on the morphology-dependent optical resonances of spherical resonators," *Journal of the Optical Society of America B: Optical Physics*, vol. 28, no. 2, pp. 225–227, 2011.
- [18] J.-P. Laine, C. Tapalian, B. Little, and H. Haus, "Acceleration sensor based on high-Q optical microsphere resonator and

- pedestal antiresonant reflecting waveguide coupler,” *Sensors and Actuators A: Physical*, vol. 93, no. 1, pp. 1–7, 2001.
- [19] T. Ioppolo, V. Ötügen, and U. Ayaz, “Development of whispering gallery mode polymeric micro-optical electric field sensors,” *Journal of Visualized Experiments*, vol. 71, no. e50199, 2013.
- [20] J. A. Stratton, *Electromagnetic Theory*, McGraw-Hill Book Company, New York and London, 1941.
- [21] P. Lorrain, D. R. Corson, and F. Lorrain, *Electromagnetic Fields and Waves Including Electric Circuits*, Freeman and Company, 1988.
- [22] A. R. Ali, T. Ioppolo, and M. V. Otugen, “High-resolution electric field sensor based on whispering gallery modes of a beam-coupled dielectric resonator,” in *Proceedings of the 1st International Conference on Engineering and Technology, ICET 2012*, Cairo, Egypt, October 2012.
- [23] A. R. Ali, T. Ioppolo, V. Ötügen, M. Christensen, and D. MacFarlane, “Photonic electric field sensor based on polymeric microspheres,” *Journal of Polymer Science, Part B: Polymer Physics*, vol. 52, no. 3, pp. 276–279, 2014.
- [24] R. W. Soutas-Little, *Elasticity*, Dover Publications, 1999.
- [25] Dow Corning, “Sylgard®184 Silicone Elastomer,” 1-3184B-01 data sheet, April 2014.
- [26] A. R. Ali and M. A. Kamel, “Novel techniques for optical sensor using single core multilayer structures for electric field detection,” in *Proceedings of SPIE 10231*, Prague, Czech Republic, May 2017.

Research Article

A Comparative Study on Evaluation Methods of Fluid Forces on Cartesian Grids

Taku Nonomura^{1,2} and Junya Onishi³

¹*Institute of Space and Astronautical Science, Japan Aerospace Exploration Agency, Yoshinodai 3-1-1 1816, Sagami-hara, Kanagawa, Japan*

²*Department of Aerospace Engineering, Tohoku University, Sendai, Miyagi, Japan*

³*Institute of Industrial Science, The University of Tokyo, 7-1-26, Minatojima-minimi-machi, Chuo-ku, Kobe, Hyogo, Japan*

Correspondence should be addressed to Taku Nonomura; nonomura@aero.mech.tohoku.ac.jp

Received 7 April 2017; Revised 31 May 2017; Accepted 14 June 2017; Published 19 July 2017

Academic Editor: Rahmat Ellahi

Copyright © 2017 Taku Nonomura and Junya Onishi. This is an open access article distributed under the Creative Commons Attribution License, which permits unrestricted use, distribution, and reproduction in any medium, provided the original work is properly cited.

We investigate the accuracy and the computational efficiency of the numerical schemes for evaluating fluid forces in Cartesian grid systems. A comparison is made between two different types of schemes, namely, polygon-based methods and mesh-based methods, which differ in the discretization of the surface of the object. The present assessment is intended to investigate the effects of the Reynolds number, the object motion, and the complexity of the object surface. The results show that the mesh-based methods work as well as the polygon-based methods, even if the object surface is discretized in a staircase manner. In addition, the results also show that the accuracy of the mesh-based methods is strongly dependent on the evaluation of shear stresses, and thus they must be evaluated by using a reliable method, such as the ghost-cell or ghost-fluid method.

1. Introduction

In recent years, Cartesian grids have been widely used in computational fluid dynamics applications. This is not only because of the simplicity of data structure and algorithms, but also because of the fast, automatic, and robust grid generation for complex geometries. The latter reason is particularly important for industrial applications, since grid generation is one of the most time-consuming tasks. Cartesian grids have potential to overcome this difficulty.

However, flow simulation using Cartesian grids still has some issues to be addressed before being put into practice. A key issue is the development of accurate methods for evaluating physical quantities and fluxes at the surface of solid objects. This issue comes from the fact that Cartesian grids do not necessarily align with the surface of the objects. As a result, there arises some arbitrariness in the location and the orientation of the object surfaces, and thus the evaluation of physical quantities and fluxes at the object surface is highly dependent on the numerical schemes used. To improve the

numerical evaluation described above, many efforts have been already devoted since the pioneering work by Peskin [1]. An extensive review of the methods developed in the literatures is given by Mittal and Iaccarino [2].

Despite these efforts, however, there has been no established method that can be applied to any problems. This is partly due to the lack of the systematic investigation on the accuracy of the numerical schemes used in these methods. In this study, we assess and compare the accuracy and the computational efficiency of the numerical schemes for evaluating physical quantities and fluxes in Cartesian grid systems. In particular, we focus on the evaluation of the local fluid stresses at the surface of an object and on the evaluation of the total fluid forces acting on the object body, as the integration of the local stresses.

The fluid force acting on a solid body is evaluated by integrating the fluid stresses over the body surface:

$$F_j = \int_{\Gamma_s} \sigma_{ij} n_i dS, \quad (1)$$

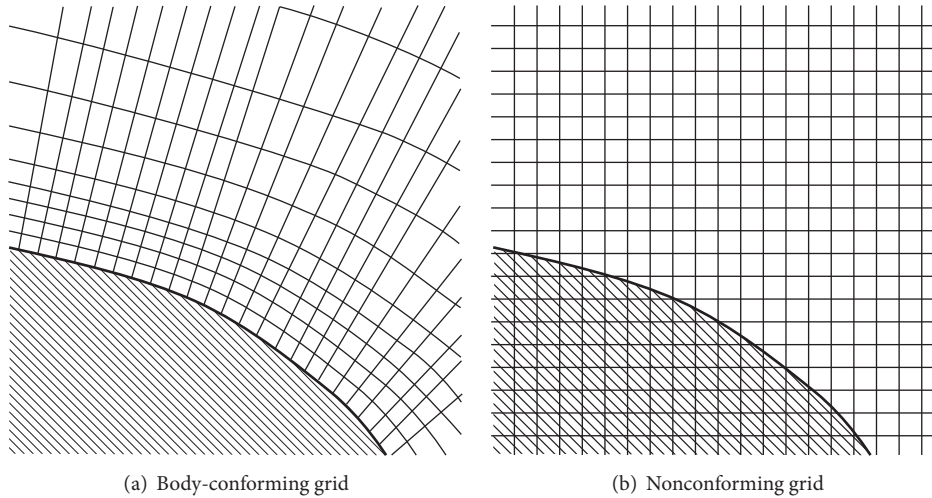


FIGURE 1: Examples of body-conforming and nonconforming grids.

where σ_{ij} is the stress tensor and n_j is the unit outward normal of the surface element. The stress tensor σ_{ij} of Newtonian fluids is given by

$$\sigma_{ij} = -p\delta_{ij} + \mu \left(\frac{\partial u_j}{\partial x_i} + \frac{\partial u_i}{\partial x_j} \right), \quad (2)$$

where p is the pressure, u_i is the velocity, and μ is the viscosity.

In numerical computations, the surface integral defined by (1) is evaluated in two steps:

- (i) discretization of the surface,
- (ii) estimation of the physical quantities at the surface.

The numerical procedures to conduct these steps depend on the grid system used in the simulation. In body-conforming curvilinear grid systems, shown in Figure 1(a), both steps can be implemented on the specified grids in a straightforward manner. However, in nonconforming grid systems, shown in Figure 1(b), some special treatment is required since the grids do not exactly match the body surface. To the best of our knowledge, there are two different ways which have been adopted in nonconforming grid systems, namely, the control volume method and the direct calculation.

The control volume method introduces a virtual volume which encompasses the body and estimates the fluid forces from the net momentum flux through the surface of this virtual volume. This method was firstly applied to steady forces by Lai and Peskin [3], and later, it was extended to unsteady forces by Balaras [4] and to moving body problems by Shen et al. [5]. The control volume method has an advantage that it is unnecessary to directly handle the complex geometries expressed by the immersed boundaries. On the other hand, it has a severe disadvantage that local stresses cannot be computed; that is, only the total force acting on the body can be evaluated. Moreover, the contributions from pressure and viscous forces cannot be evaluated separately.

In the direct calculation, the body surface is usually discretized by a set of polygons, and the local stresses on these

surface elements are estimated. Then, the local stresses are integrated over the body surfaces to obtain the total force, as in body-conforming grid systems. However, unlike the cases of body-conforming grid systems, the estimation of the flow variables on the surface elements is not straightforward and requires elaborate interpolation and/or extrapolation methods in order to accurately take into account the location (and orientation if necessary) of the surface. Moreover, the computational cost of the stress integration may become prohibitive when the body shape is complex, since it depends on the number of the polygons used to express the body surface. Such a dependency is undesirable, in particular, in engineering applications. For example, the number of the polygons reaches up to the order of 10^7 for an aerodynamic simulation using a detailed car model with both exterior and interior parts [6].

In this study, we discuss numerical schemes that are suitable for evaluating fluid forces in nonconforming grid systems. In particular, we propose a simple and computationally efficient method for calculating the surface integral in (1). The proposed method is a kind of direct calculation described above. Therefore, it has inherited an advantage over the control volume method in that the contributions from pressure and viscous forces can be evaluated locally and separately. Moreover, in the present method, the fluid stresses are integrated over the mesh faces (staircase surfaces) in the grid system used, not over the discretized surface elements of the original body. Therefore, the undesirable dependency on quality or numbers of surface polygons can be removed. Hereafter, the present method is referred to as a “mesh-based scheme (MS),” whereas the method based on the integration over surface polygons is called a “polygon-based scheme (PS).” We present a comparative study of the accuracy of these methods.

It is worth noting here that, in both mesh-based and polygon-based schemes, the physical quantities at the discretized surfaces must be estimated by interpolation or extrapolation, and the accuracy of this estimation would

influence the final results of the fluid forces. For the PS, we have employed the ghost-cell approach described by Mittal et al. [7]. For the MSs, we have tested three approaches that are often used in the studies of immersed boundary methods: a staircase approach, a ghost-cell approach, and a ghost-fluid approach, the details of which are described in Section 2.

The rest of the paper is organized as follows. Section 2 describes the details of the computational procedures of a polygon-based scheme and three mesh-based schemes. The computational grid, the discretization of the body surface, and the extrapolation method used in these schemes are fully discussed. In Section 3, both polygon-based and mesh-based schemes are applied to evaluate the drag force acting on a sphere in Stokes flow. The obtained results are compared with the analytical solution. The grid convergence test is also performed to investigate the numerical accuracy of the schemes. Stokes flow is used here because analytical solutions are available not only for the fluid forces but also for the flow fields, that is, pressure and velocity fields. By using the analytical solutions of the flow fields, the error associated with the force evaluation schemes can be assessed separately from the error in the computation of the flow fields themselves. In contrast, in higher Reynolds number flows, the flow fields must be numerically computed. Therefore, these errors are hardly evaluated separately. In Section 4, the extension to the moving body problem and the computational efficiency of the force evaluation schemes are discussed. In addition, to show the applicability of the present mesh-based scheme in higher Reynolds number flows, the results for the case of the Reynolds number of 100 are presented in Section 5. In Section 6, the discussion on the applicability to the complex body problem is conducted. Finally, the last section summarizes this study.

2. Numerical Methods

Herein, Section 2.1 describes the computational grid and defines the cell types. The polygon-based force evaluation scheme, which seems to be commonly used in the immersed boundary method, and the mesh-based force evaluation scheme proposed in this paper are described in Sections 2.2 and 2.3, respectively.

2.1. Computational Grids and Definition of Cell Type. The grid system used in this work is illustrated in Figure 2. In this figure, the entire domain is divided into equally sized cubic cells. These cells are classified into two groups according to their locations:

- (i) fluid cells (cells whose center is in the fluid region),
- (ii) solid cells (cells whose center is in the solid region).

Within these categories, special cells close to the interface are defined as follows:

- (i) boundary cells (fluid cells adjacent to at least one solid cell).

The flow properties used to evaluate (1), namely, the pressure and the velocity, are assumed to be available only at the

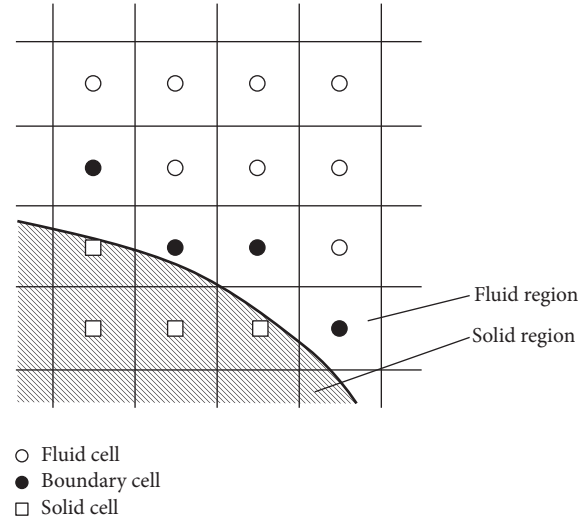


FIGURE 2: Classification of the computational cells.

center of the fluid cells, including the boundary cells. When the values at the solid cells are needed, they must be interpolated or extrapolated by some methods considering a body shape. In the following, we call such solid cells ghost cells.

Note that, although we use collocated layout of variables throughout this study, the extension to staggered layout of variables is trivial. The accuracy of mesh-face integration, which is key idea of this paper, does not seem to be affected by the layout of variables. Note also that the above cell classification is not trivial, especially when the solid region has a complicated shape. This issue, however, is beyond the scope of the present study and is not further discussed here.

2.2. Polygon-Based Scheme. The polygon-based scheme (PS) appears to be most commonly implemented in the immersed boundary method [8]. This scheme divides three-dimensional body surfaces into sets of polygons or two-dimensional surfaces into series of lines. Hereafter, to avoid confusion, these surface elements will be referred to as “facets.” A schematic of this approach is shown in Figure 3(a).

In PS, the surface integral defined by (1) is conveniently evaluated by summing over the facets:

$$F_j = \sum_{\text{facet}} (\sigma_{ij} n_i \Delta S)_{\text{facet}}, \quad (3)$$

where ΔS is the surface area of the facet, and the normal stresses are summed over all facets. The remaining task is to estimate the bracketed quantities at the center of each facet, which requires the geometric properties (the surface normal and the area of the facet) and the physical properties (the pressure and the velocity). The former quantities can be computed from the coordinates of the polygon vertexes. In this paper, the latter are estimated by an approach using the normal, which is described in the following.

As shown in Figure 3(a), a normal probe is extended from the center of the facet (indicated by I), and two markers

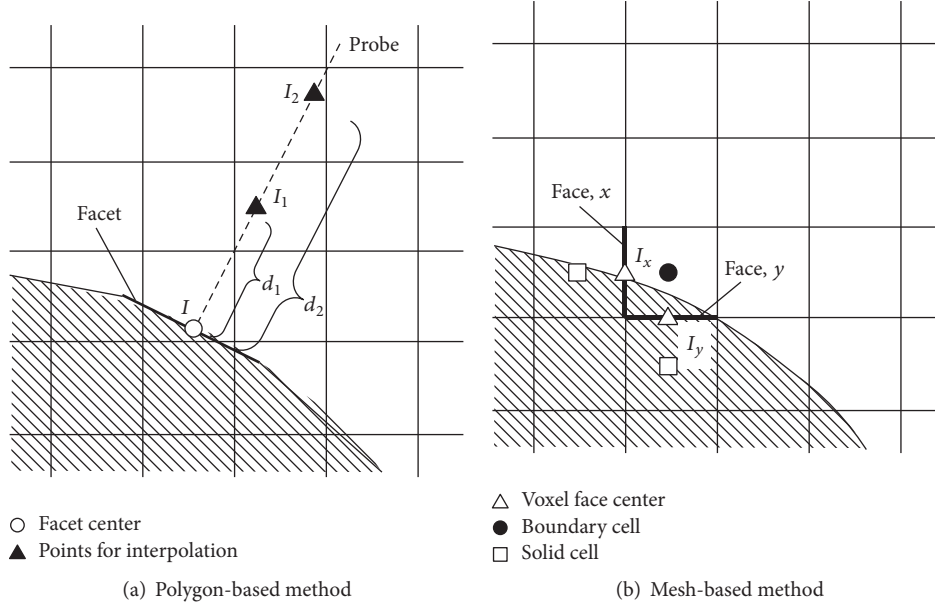


FIGURE 3: Polygon and mesh-based methods.

(indicated by I_1 and I_2) are placed at distances d_1 and d_2 , respectively, along the normal probe. These markers are used as reference points for interpolating the value at the center of the facet. The pressure field assumes a linear distribution along the probe:

$$p(d) = C_1 d + C_0. \quad (4)$$

The coefficients C_1 and C_0 are determined such that

$$p(d_1) = p_1, \quad (5)$$

$$p(d_2) = p_2,$$

where p_1 and p_2 are the values at the reference points I_1 and I_2 , respectively. From this linear extrapolation, the value at the point I is obtained as

$$p_I = p(0) = p_1 - \frac{d_1}{d_2 - d_1} (p_2 - p_1). \quad (6)$$

The velocity components are computed from a quadratic function. For example, the x -component of the velocity is fitted to

$$u(d) = C_2 d^2 + C_1 d + C_0, \quad (7)$$

where the coefficients are determined by the values at both reference points and the center of the facet:

$$u(d_1) = u_1, \quad (8)$$

$$u(d_2) = u_2,$$

$$u(0) = u_B,$$

where u_1 and u_2 are the velocities at the reference points I_1 and I_2 , respectively, and u_B is the velocity at the center of the

facet. Note that u_B is the velocity of the object because no-slip and no-penetration conditions are imposed. Differentiating this obtained function yields the components of the velocity gradient tensor at the point I

$$\frac{\partial u}{\partial n} \Big|_I = \frac{u_1 d_2^2 - u_2 d_1^2}{d_1 d_2 (d_2 - d_1)}, \quad (9)$$

$$\frac{\partial u}{\partial s} \Big|_I = 0,$$

$$\frac{\partial u}{\partial t} \Big|_I = 0,$$

where the coordinates n , s , and t are defined along the normal and the tangential directions at the facet, respectively. The other components are computed similarly.

In the above extrapolation, the values at the reference points should be estimated in advance. In this paper, the reference values are computed by trilinear interpolation from the quantities in the surrounding fluid cells. If the reference points are not carefully chosen, the interpolation involves a quantity in a solid cell that must also be extrapolated. To avoid such recursive interpolations and extrapolations, the distances to the reference points are simply selected to be long enough. In this paper, d_1 and d_2 are set to $1.75\Delta x$ and $3.5\Delta x$, respectively. Note that the value $1.75\Delta x$ comes from the possible largest distance between neighboring cell centers, namely, $\sqrt{3}\Delta x$ for a three-dimensional case, and the value $3.5\Delta x$ is twice as long as it. This method is called a simplified ghost-cell method in this paper.

2.3. Mesh-Based Scheme. The PS described above is simple in algorithm, but it seems to be prohibitive for practical applications where complex geometries must be handled. This is

because the PS requires operations of $O(N_S)$, where N_S is the number of the polygons used to represent the geometries. For example, N_S is of the order of 10^7 for a detailed car model with both exterior and interior parts [6]. This problem becomes significant, in particular, on distributed memory platform, since the operations are intensive only in the small area of the computational domain and thus the work load is not balanced well.

As an alternative to the PS, we propose mesh-based schemes (MSs), in which the body is simplified by mesh faces between boundary and solid cells, and the surface integral defined by (1) is discretized over the mesh faces. A schematic illustration of this approach is shown in Figure 3(b).

In MSs, the surface integral defined by (1) is decomposed into its directional components, each approximated from the mesh face in its corresponding direction:

$$\begin{aligned} F_x &= \int \sigma_{xx} n_x dS + \int \sigma_{yx} n_y dS + \int \sigma_{zx} n_z dS \\ &\approx \sum_{\text{face},x} (\sigma_{xx} n_x \Delta S)_{\text{face},x} + \sum_{\text{face},y} (\sigma_{yx} n_y \Delta S)_{\text{face},y} \\ &\quad + \sum_{\text{face},z} (\sigma_{zx} n_z \Delta S)_{\text{face},z}. \end{aligned} \quad (10)$$

Here, since the directional components can be independently summed, the surface normal and the area are easily evaluated from the geometrical characteristics of the mesh face. For example, $n_x = \pm 1$ and $\Delta S = \Delta y \Delta z$ are held for the mesh faces in the x -direction. The surface normal and the areas of mesh faces in other orientations can be similarly evaluated. Note also that the summations involve only the faces of the boundary cells, which simplifies the computational implementation.

The stress at the center point of the mesh face (I_x and I_y in Figure 3(b)) can be computed in several ways. In the following, three methods, which seem to be used widely in the studies of immersed boundary methods, are discussed.

2.3.1. MS1: A Staircase Approach. In MS1, the pressure is simply extrapolated using the cell-centered value:

$$\begin{aligned} p_{I,x} &= p_{b.c.}, \\ p_{I,y} &= p_{b.c.}, \end{aligned} \quad (11)$$

where $p_{I,x}$ and $p_{I,y}$ are, respectively, the pressures at I_x and I_y and $p_{b.c.}$ is the pressure at the related boundary cell. To approximate the shear stress, the velocities at I_x and I_y are assumed to correspond to that of the object $u_I = 0$:

$$\begin{aligned} \left. \frac{\partial u}{\partial x} \right|_{I,x} &= \frac{u_{i,j} - u_I}{\Delta x/2}, \\ \left. \frac{\partial u}{\partial y} \right|_{I,x} &= \frac{u_{i,j+1} - u_{i,j-1}}{2\Delta x}, \end{aligned} \quad (12)$$

where the computational stencil used for these derivatives is depicted in Figure 4.

Although the above staircase approach may be used less often nowadays, it is introduced in order to show its inaccuracy and to clearly demonstrate the important aspects of the other schemes introduced later.

2.3.2. MS2: A Ghost-Cell Approach. In MS2, the assumed pressure at I_x is the average of the pressures at the centers of the adjacent boundary cell and the solid cell.

$$p_{I,x} = \frac{p_{i,j} + p_{i-1,j}}{2}. \quad (13)$$

The shear stress is approximated by a second-order central difference scheme. The x - and y -derivatives of the x component of the velocity at the point I_x are estimated as follows:

$$\begin{aligned} \left. \frac{\partial u}{\partial x} \right|_{I,x} &= \frac{u_{i,j} - u_{i-1,j}}{\Delta x}, \\ \left. \frac{\partial u}{\partial y} \right|_{I,x} &= \frac{1}{2} \left[\frac{u_{i,j+1} - u_{i,j-1}}{2\Delta x} + \frac{u_{i-1,j+1} - u_{i-1,j-1}}{2\Delta x} \right]. \end{aligned} \quad (14)$$

The computational stencil used to compute these derivatives is also depicted in Figure 4(a).

Note that the computation of both x - and y -derivatives requires quantities inside the solid region, in other words, in the ghost cells. For MS2, these quantities are estimated by the simplified version (avoiding recursive interpolation and extrapolation) of the ghost-cell method [7]. Concretely, the quantities in solid cells are computed by the fitting functions (see (6) and (7)) constructed in the normal probe approach illustrated in Figure 4(b):

$$\begin{aligned} p_s &= p(-d_0), \\ u_s &= u(-d_0), \end{aligned} \quad (15)$$

where d_0 is the distance between the solid cell and the closest point on the body surface.

2.3.3. MS3: A Ghost-Fluid Approach. In MS3, the ghost-fluid method described by Gibou et al. [9] is applied to estimate the quantities in the ghost cells.

For example, in order to estimate a quantity at the solid cell $(i-1, j)$ in Figure 4(a), a quadratic function along the x -axis is introduced and is fitted to the two points at the fluid cells (i, j) and $(i+1, j)$ and the interface point:

$$f(x) = C_2 x^2 + C_1 x + C_0, \quad (16)$$

where f denotes the pressure or a component of the flow velocity, x is the coordinate of the x -axis, and C_i ($i = 0, 1, 2$) is the fitting coefficients to be determined. Note that the interface point is defined as the intersection between the solid surface and the line segment connecting (i, j) and $(i-1, j)$. Here, the origin is set to (i, j) , and the distance from the origin to the interface point is assumed to be $\theta \Delta x$, without loss of generality. For the x -component of the flow velocity, three coefficients in (16) are uniquely determined by solving the following system of equations:

$$\begin{aligned} u(0) &= u_{i,j}, \\ u(\Delta x) &= u_{i+1,j}, \\ u(-\theta \Delta x) &= u_B, \end{aligned} \quad (17)$$

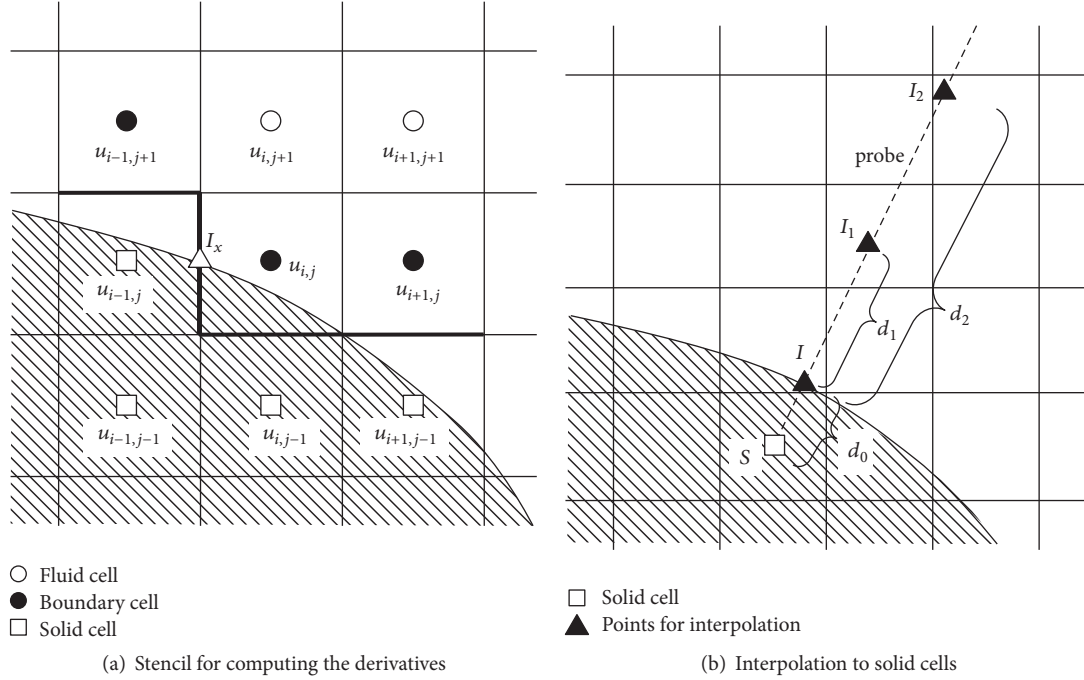


FIGURE 4: Stencils for stress evaluation and extrapolation to the solid cell.

where u_B is the prescribed boundary value for u . As a result, the target value at the solid cell is estimated as follows:

$$u_{i-1,j} = u(-\Delta x). \quad (18)$$

The values for the other components can be calculated in a similar manner. The pressure can be also estimated in a similar manner, but it is necessary to replace one of the conditions by the Neumann boundary condition:

$$\begin{aligned} p(0) &= p_{i,j}, \\ p(\Delta x) &= p_{i+1,j}, \\ \frac{\partial p}{\partial x}(-\theta \Delta x) &= \left. \frac{\partial p}{\partial x} \right|_B, \end{aligned} \quad (19)$$

where $(\partial p / \partial x)_B$ is the x -component of the pressure gradient at the boundary, which is assumed to be 0 in this study.

3. Force Estimation for Stokes Flows

In this section, the accuracies of PS, MS1, MS2, and MS3 are assessed by comparison with analytical solutions of Stokes flow past a sphere.

3.1. Stokes Flow Past a Sphere. Analytical solutions to the pressure and velocity of Stokes flow around a sphere are given by [10]:

$$\begin{aligned} p &= p_\infty - \frac{3\mu}{2\rho} u_\infty \frac{ax}{r^3}, \\ u &= u_\infty - \frac{1}{4} u_\infty \frac{a}{r} \left(3 + \frac{a^2}{r^2} \right) - \frac{3}{4} u_\infty \frac{ax^2}{r^3} \left(1 - \frac{a^2}{r^2} \right), \end{aligned}$$

$$\begin{aligned} v &= -\frac{3}{4} u_\infty \frac{axy}{r^3} \left(1 - \frac{a^2}{r^2} \right), \\ w &= -\frac{3}{4} u_\infty \frac{axz}{r^3} \left(1 - \frac{a^2}{r^2} \right), \end{aligned} \quad (20)$$

where a is the radius of the sphere, ρ is the mass density, μ is the viscosity, u_∞ is the freestream velocity, p_∞ is the reference pressure, x , y , and z are the Cartesian coordinates, and r is the distance from the origin (where the origin is the center of the sphere).

The fluid is assumed to flow parallel to the x -axis; therefore, the drag force acting on the sphere is the x -component of the force defined in (1). Substituting the analytical solutions (20) into this definition, the pressure drag and the frictional drag are, respectively, obtained as

$$\begin{aligned} C_{Dp} &= \frac{F_x^p}{(1/2) \rho u_\infty^2 A} = \frac{2\pi a \mu u_\infty}{(\rho u_\infty^2 / 2) (\pi a^2)} = \frac{8\mu}{\rho u_\infty D} \\ &= \frac{8}{\text{Re}}, \\ C_{Df} &= \frac{F_x^v}{(1/2) \rho u_\infty^2 A} = \frac{4\pi a \mu u_\infty}{(\rho u_\infty^2 / 2) (\pi a^2)} = \frac{16\mu}{\rho u_\infty D} \\ &= \frac{16}{\text{Re}}, \end{aligned} \quad (21)$$

where C_{Dp} and C_{Df} are the coefficients of the pressure drag and frictional drag, respectively, and $\text{Re} = \rho u_\infty D / \mu$ is the Reynolds number. $D = 2a$ and $A = \pi a^2$ define the diameter and the projected area of the sphere, respectively.

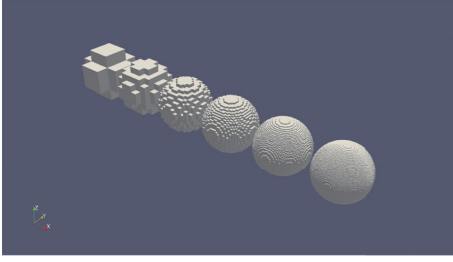


FIGURE 5: Spheres constructed on meshes with different resolutions. From left to right, a sphere of diameter D is constructed on mesh resolved to $\Delta x = a/4, a/8, a/16, a/32, a/64,$ and $a/128$.

3.2. Computational Settings and Data. The drag force is now computed by the numerical methods described in Section 2. To compute the drag forces, a sphere of the diameter D is centralized within a cubic domain of the side length L . The value of L is arbitrary but must be sufficiently large to encompass the sphere. The present study selects $L = 2D$. The computational cells are generated by dividing the cubic domain into $2N$ equally sized cells in each direction. The fineness of the sphere is altered by setting the number of grid points N occupied by the sphere in each direction to $N = 4, 8, 16, 32, 64, 128, 256, 512, 1024, 2048$. The solid cells constituting the sphere of grid points less than 128 are illustrated in Figure 5. The PS requires an additional polygon mesh. The force computed on each Cartesian mesh properly converges with that on a spherical equally distributed polygon mesh with $3,200 \times 3,200$ points. Therefore, this polygon mesh is adopted in the remainder of the study. The analytical solutions (20) are assumed to be available only at the centers of the fluid cells, including the boundary cells.

3.3. Results

3.3.1. Total Drag Forces. The forces estimated by PS, MS1, MS2, and MS3 at different mesh resolutions are plotted in Figure 6. Here, the Reynolds number is $Re = 0.01$ for all the cases. Correspondingly, the pressure and friction drags are, respectively, solved as $C_{Dp,exact} = 800$ and $C_{Df,exact} = 1600$, using the analytical solutions. The result shows that the convergence rate for the pressure drag is first order in MS1 and second order in PS and MS2 and that the convergence rate for the friction drag is zeroth order in MS1 and first to second order in PS, MS2, and MS3. These results indicate that the proposed MS2 and MS3 can evaluate the fluid force as accurately as PS, but at much smaller computational cost and using a much simpler computational code. Thus, fluid forces can be simply and efficiently evaluated by MS2 and MS3 in the immersed boundary method. Comparing MS2 and MS3, it interestingly shows that MS2 has fewer errors than MS3. This clarifies that the MS2 based on the ghost-cell method is better for the force estimation than MS1 based on the ghost-fluid method. Apart from the success of MS2 and MS3, MS1 is shown to be unacceptable for practical use since the friction drag is not converged even when a very fine mesh is used. At $\Delta x = 0.06$, sudden decrease in friction drag of PS is observed and this might be caused by canceling out two different error sources which is not clarified well in this study.

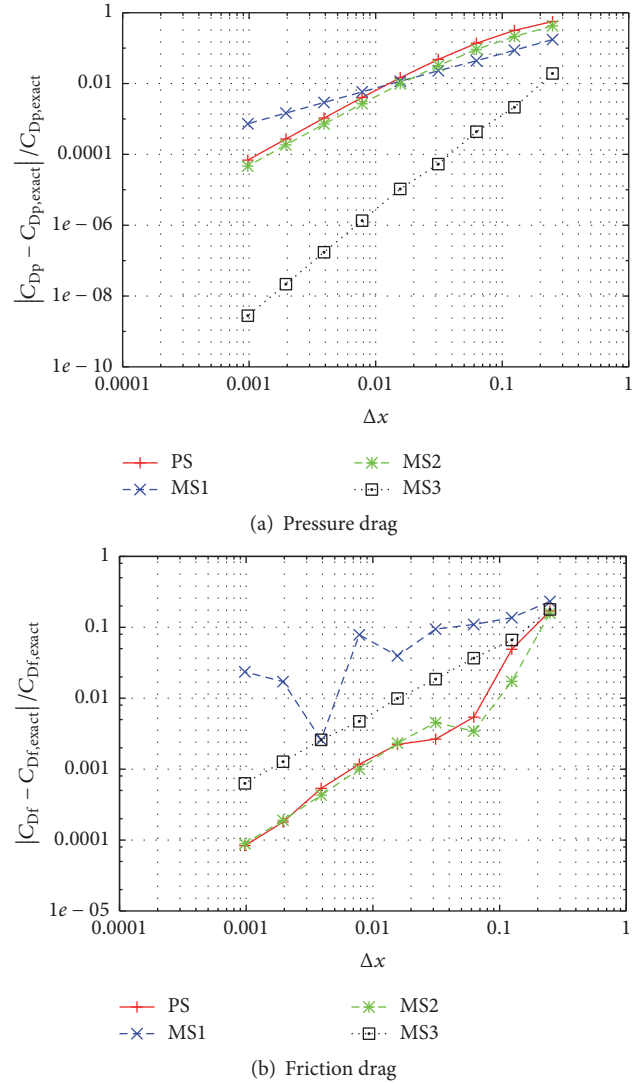


FIGURE 6: Estimated drag in Stokes flow around a sphere as functions of mesh spacing. Analytical pressure and friction drag are $C_{Dp,exact} = 800$ and $C_{Df,exact} = 1600$, respectively.

It is worth noting that the PS results are sensitive to the density of the polygon mesh at coarser polygon mesh resolutions, whereas we use a very fine polygon mesh in this study to eliminate the error introduced by coarse polygon mesh. This implies that the polygon density requires special attention in the PS method.

3.3.2. Force Distributions. Then, we visualized the force distributions on the each cell projected on $x, y,$ and z plane. The partial drag coefficients for each projected cell are defined as follows:

$$\begin{aligned}
 C_{d_{p,x}} &= \frac{\int_{\text{cell}} p \, dy \, dz}{(1/2) \rho u_{\infty}^2 \Delta y \Delta z} \\
 C_{d_{f,y}} &= \frac{\int_{\text{cell}} \tau_{xy} + \tau_{yz} \, dx \, dz}{(1/2) \rho u_{\infty}^2 \Delta x \Delta z} \\
 &\vdots
 \end{aligned} \tag{22}$$

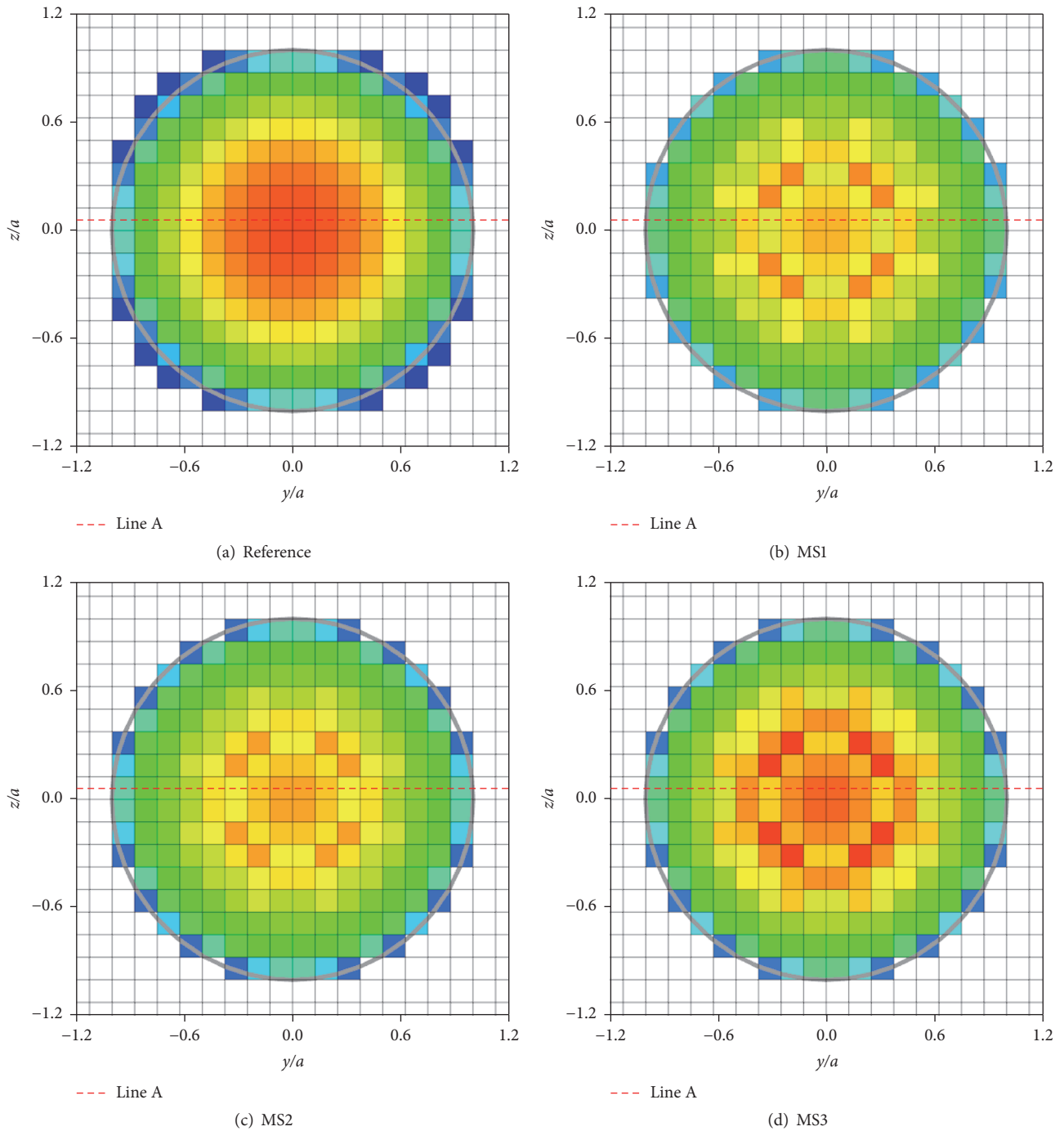


FIGURE 7: Distribution of partial pressure drag for each cell front-projected on x plane. Contour range is set to be $-0.1 < C_{dp,x}/C_{Dp,exact} < 0.8$. Analytical pressure drag is $C_{Dp,exact} = 800$.

Here, integration is conducted for the surface in each projected cell. In the case of a sphere, there are two projections: front and rear projections. In this definition, the reference solution can be obtained with very fine discretization. On the other hand, MSs evaluate them in simplified ways as in the inside summation of (10). The distributions of reference solutions and MSs are shown in Figures 7 and 8. Here, the reference solution is obtained with the ten times finer

submesh. The results of MS1 have strong oscillation in friction drag because this method does not compute shear stress correctly. On the other hand, MS2 and MS3 can predict them quantitatively, though they have weak oscillation. This behavior is illustrated in Figures 9 and 10, which shows the partial drag on the line indicated in Figures 7 and 8. These figures show the same trend more quantitatively. Figure 8 shows that the MS2 predict partial friction drag more

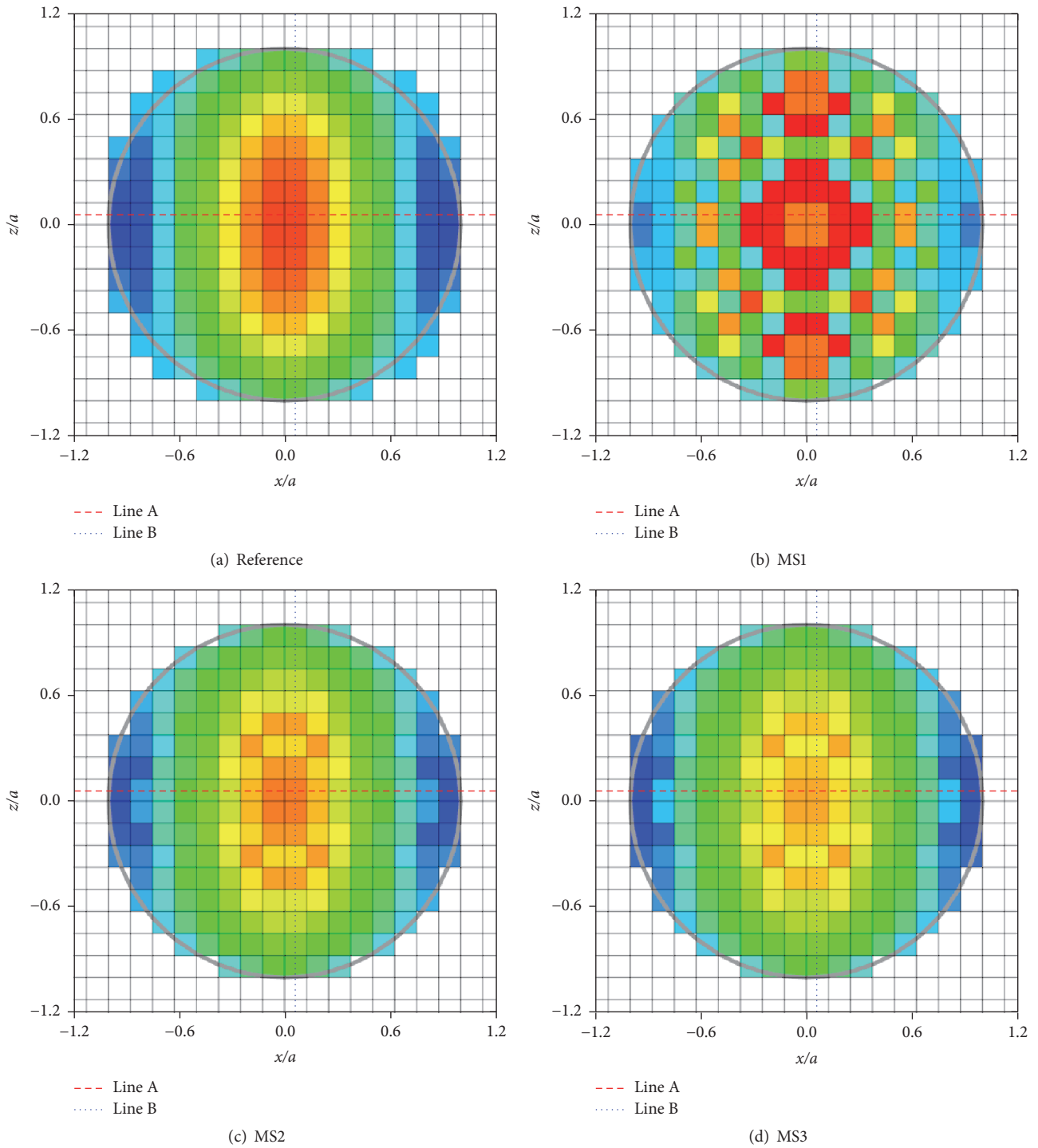


FIGURE 8: Distribution of partial friction drag for each cell front-projected on y plane. Contour range is set to be $-0.1 < C_{df,y}/C_{Df,exact} < 0.4$. Analytical pressure drag is $C_{Df,exact} = 1600$.

accurately than MS3, as discussed above for total friction drag.

3.3.3. *Effects of Estimation Methods for Ghost Cells.* In MS, the error in the friction drag appears to arise from two sources: (1) the estimated shear stress and (2) the estimated surface area vector. These error sources are distinguished for clarity.

The error in the estimated shear stress at the interface of the staircase body can be completely removed by analytically computing the shear stress in the Stokes flow, rather than approximating it by a finite difference scheme. The estimated drag with analytical shear stress at the boundary is plotted in Figure 11. This solution is labeled as “MS with the analytical shear stress” in the figure. Clearly, the analytical shear stress

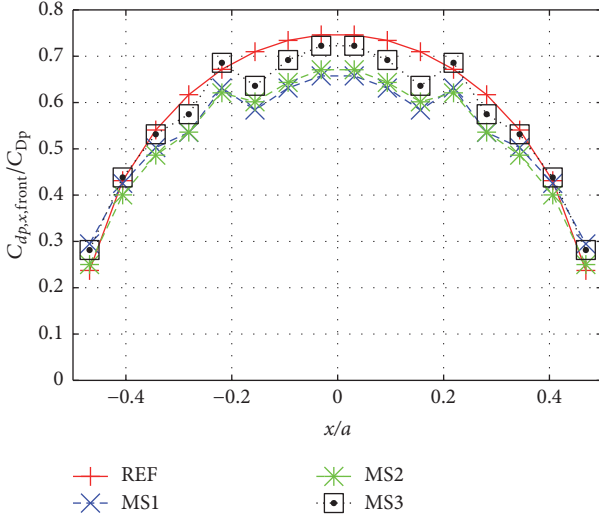


FIGURE 9: Distribution of partial pressure drag for each cell front-projected on x plane on line A in Figure 7. Analytical pressure drag is $C_{Dp,exact} = 800$.

yields much more accurate results than MS1, MS2, and MS3, in which the shear stress is numerically computed. This result illustrates that (1) the error in the estimated shear stress is significant and prevents the numerically computed force from converging, and (2) the error in the surface area vector is probably insignificant.

Also note that, according to Figure 11, the error in shear stress for MS2 depends on the accuracy of the ghost-cell method. Therefore, the order of accuracy in MS2 (shown in Figure 6) seems to be determined by the formal order of accuracy in the ghost-cell method.

3.3.4. Surface Area Vector Estimation. We now discuss the error in the estimated surface area vector. The surface area vectors ($x > 0$, $y > 0$, and $z > 0$ of the staircase body represented by the mesh faces) are summed in Figure 12. The sum converges to the exact integral over the surface area as the mesh density increases. It should be noted that the surfaces of the staircase body never exactly sum to the area of the body surface, even on very fine meshes. The estimated force acting on the body depends on the surface area vector, rather than on the surface area itself. This may explain why the staircase body approximation for integration does not matter.

3.3.5. Computational Costs. The computational costs for PS and MS2 for $N = 4$ to 128 are discussed in this subsection. Here, costs for MS1 and MS3 are almost the same as MS2. The computation is measured by a core of the computer process unit of Xeon X5450 3.0 GHz. For the PS computation, computational costs strongly depend on the number of polygon meshes. In this study, numbers of polygon mesh for each grid resolutions are determined with increasing it twice until the drag coefficient is firstly converged with 10% error. The results are shown in Table 1. The number of

TABLE 1: Computational costs for body force estimation of Stokes flow around a sphere.

N	PS		MS2
	Computational costs [s]	Number of polygons	Computational costs [s]
4	0.0006043	64×64	0.0001197
8	0.002353	128×128	0.0003260
16	0.04947	512×512	0.001319
32	0.1955	1024×1024	0.00677
64	0.6897	2048×2048	0.05297
128	2.939	4096×4096	0.3567

polygon meshes for convergence is larger than we expected, and resulting computational costs of PS are much higher than that of MS2. The computational cost of MS2 is 5–30 times lower than that of PS, and table shows that the MS2 is much more efficient than PS. This is because MS2 only requires the mesh-face loop to compute the body force while PS requires the polygon mesh loop, the number of which is much larger than that of the mesh face.

4. Evaluation of Force on a Moving Sphere: Various Alignment of Body and Grid

Then, the Stokes flow around a moving sphere is considered because the immersed boundary method is often used for the moving body problems. In the moving body problems, we should consider following additional two points:

- (i) change in the evaluation of the shear stress,
- (ii) the various locations of the body compared with the grid.

If we consider the exact solution of the Stokes flow around a moving sphere, it is exactly corresponding to the superimposition of the exact solution of the Stokes flow and the uniform velocity of moving body. If we use the MS1, MS2, MS3, and PS for the evaluation of the shear stress, it exactly corresponds to that in the static case because the uniform velocity added in the flow fields is perfectly canceled out by the boundary velocity imposed on the moving body. Therefore, the first point, that is, change in evaluation of the shear stress, does not appear for MS1, MS2, MS3, and PS, in the case we considered. On the other hand, the second point seems to be more important for moving body problems. The smaller force variation due to the alignment of the body and the grid is preferred. In this section, force variation due to the alignment of the body and the grid for each method is investigated.

In this test case, the center of the sphere is shifted by $(c_x \Delta x, c_y \Delta y, c_z \Delta z)$ from the original location used in the previous section, where $-0.5 < c_x \leq 0.5$, $-0.5 < c_y \leq 0.5$, and $-0.5 < c_z \leq 0.5$. We set $c_y = c_z = 0$ for simplicity and force is evaluated with changing c_x , assuming flow around the moving sphere through the quiescent air.

The force is evaluated with the grid resolutions of $N = 4, 8, 16, 32$, and 64 in this section. The results of $N = 16$ are

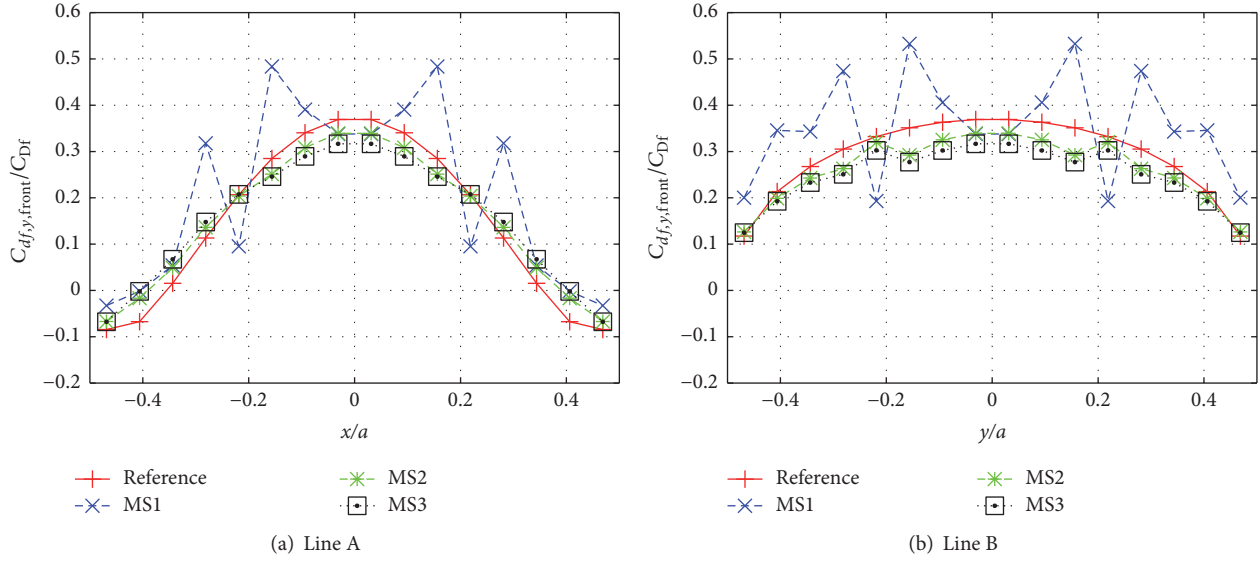


FIGURE 10: Distribution of partial pressure drag for each cell front-projected on x plane on lines A and B in Figure 8. Analytical friction drag is $C_{Df,exact} = 1600$.

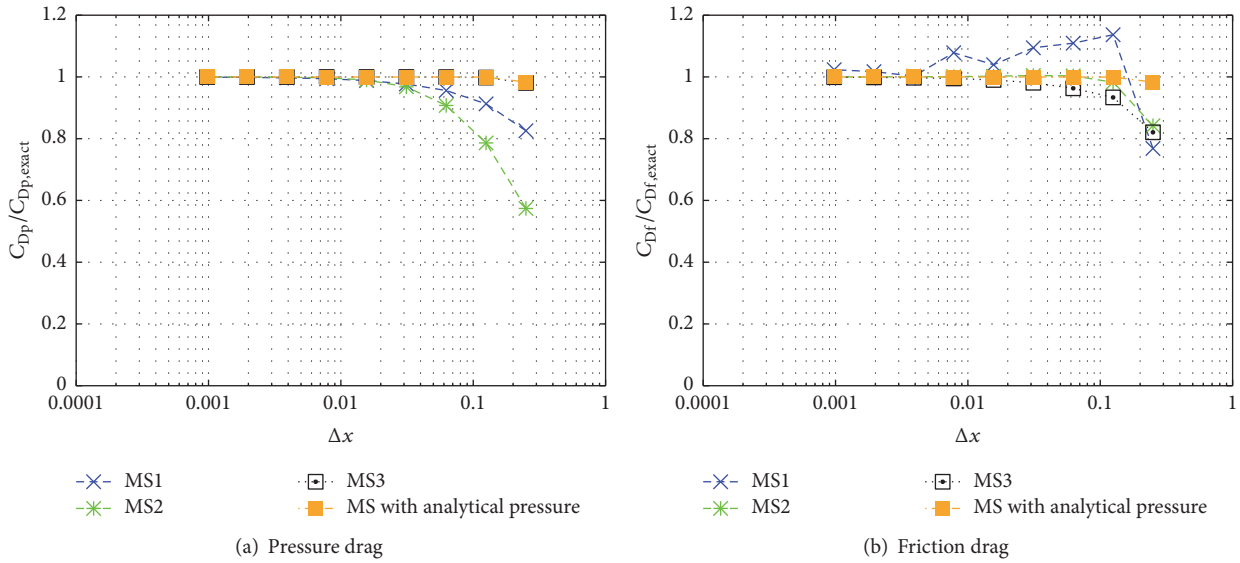


FIGURE 11: Estimated drag in Stokes flow around a sphere as functions of mesh spacing using a mesh-base scheme with analytical shear stress. Analytical estimates of pressure and friction drag are $C_{Dp,exact} = 800$ and $C_{Df,exact} = 1600$, respectively.

shown in Figure 13. The results show that the friction drag of MS1 has large oscillations depending on the alignment of the body and the grid, while the other results have much smaller oscillations. Interestingly, the oscillation is significantly suppressed by PS, though the accuracy of its averaged value is worse than MS2 in this case.

In order to quantitatively evaluate the force oscillation by the alignment of the body and the grid, the root mean square value is introduced in Figure 14, where the bracket represents the averaging operator for $-0.5 < c_x \leq 0.5$. The root mean square of the force oscillation normalized by the analytical force for each case is shown by the thin lines in Figure 14, together with the error of averaged force compared with the

analytical force by the thick lines. Here, MS1 has very large oscillations due to the alignment as well as very large errors in averaged value as discussed in the previous section. MS2 and MS3 have similar or smaller oscillations than the errors in averaged value and their oscillations are considered to be acceptable. Besides, PS has very small oscillation and shows the best characteristics for the grid alignment.

The test case shown in this section illustrates that the proposed MS2 and MS3 methods have similar or smaller oscillation than error and can be used for the moving body problems, though PS shows the best characteristics for the grid alignment of the body and the grid.

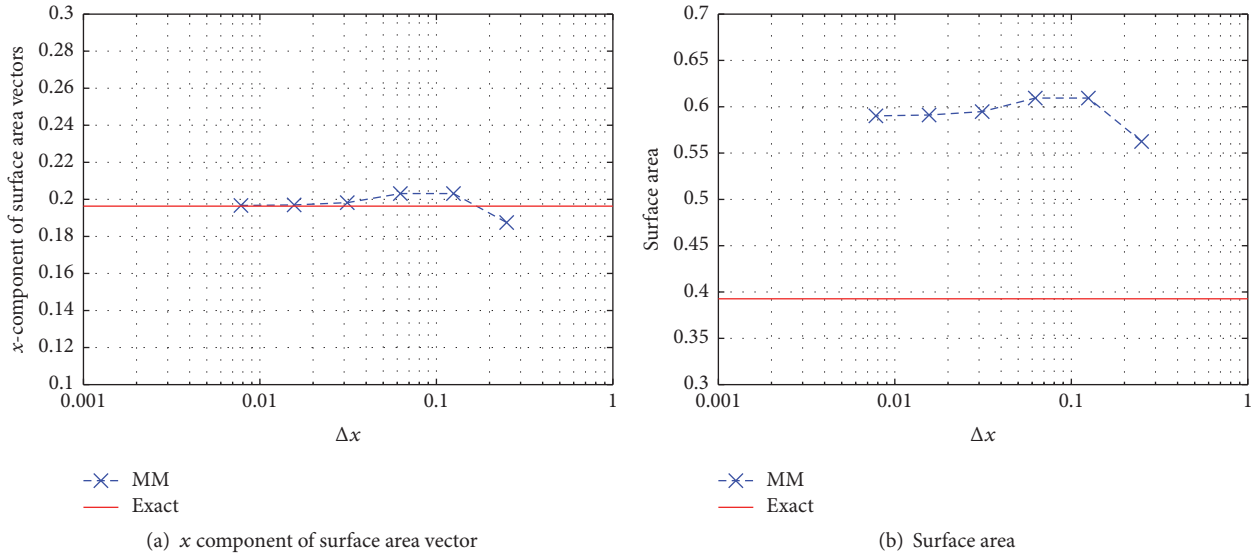


FIGURE 12: Evaluation of summation of surface area vectors and surface areas in MS.

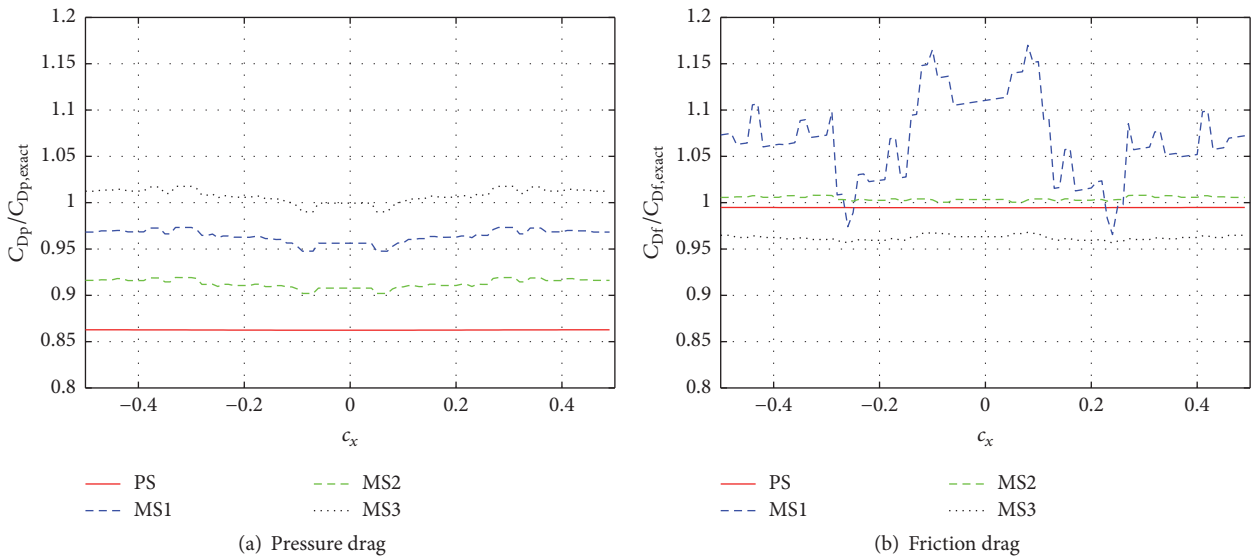


FIGURE 13: Effects of alignment of body and grid on estimated drag for $N = 16$. Analytical estimates of pressure and friction drag are $C_{Dp,exact} = 800$ and $C_{Df,exact} = 1600$, respectively.

5. Estimating the Force in the Flow around a Sphere at the Reynolds Number 100

To evaluate MS at the higher Reynolds number, the force was estimated in fluid flowing around a sphere at the Reynolds number 100. Since no analytical solution was available for such higher Reynolds number flows, numerical solution was obtained by using an incompressible flow solver developed by Onishi et al. [11]. This solver adopts a simple marker and cell algorithm with collocated variable layout. The grid system is based on the building cube method proposed by Nakahashi [12]. Space is discretized by a second-order finite difference scheme [13] and the simple immersed boundary method based on the ghost-fluid based method proposed

by Sato et al. [14]. This test case includes the errors in the computed flow fields, and therefore the result does not directly indicate the performance of the force estimation method.

The forces evaluated by PS, MS1, MS2, and MS3 are shown in Figure 15. The result shows that the forces estimated by PS, MS2, and MS3 seem to converge to 1.09, which is consistent with the existing data obtained by the empirical relation derived from a number of experiments [15] and the numerical computations [7, 16].

Interestingly, MS3 has less error in a coarse grid. This might be because fluid dynamic computation and force evaluation methods are consistent. On the other hand, the magnitudes of the errors in PS and MS2 are almost identical

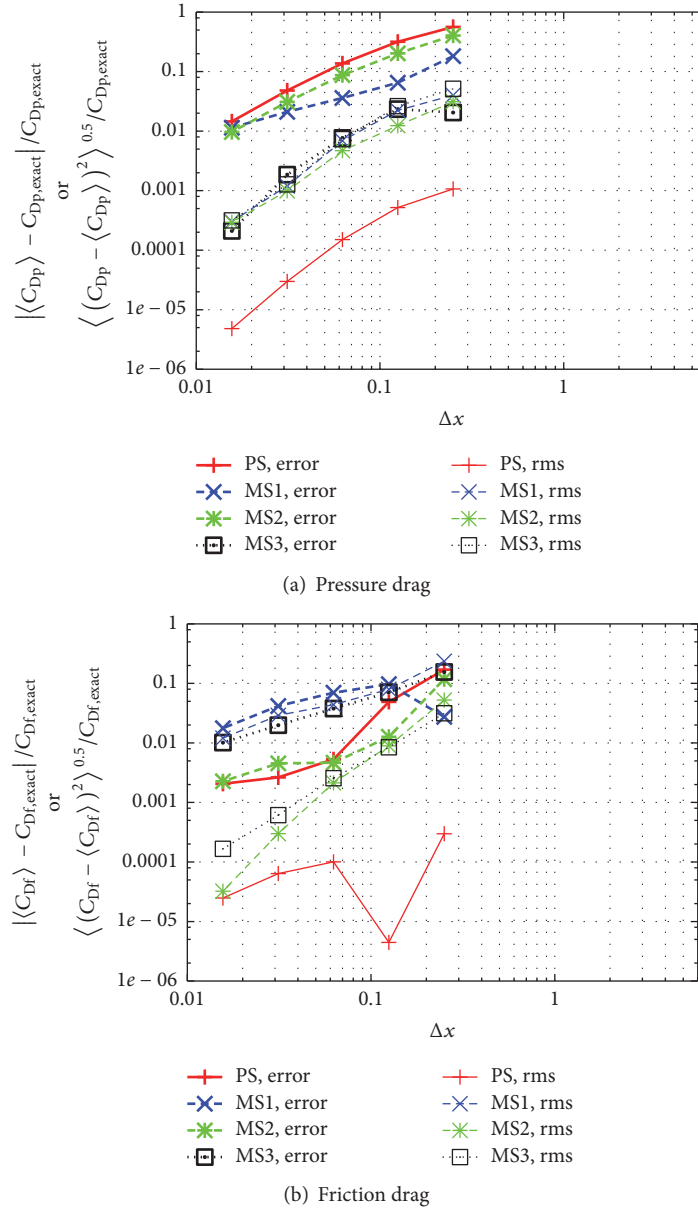


FIGURE 14: Estimated averaged drag and oscillation due to alignment of body and grid in Stokes flow around a moving sphere as functions of mesh spacing. Analytical estimates of pressure and friction drag are $C_{Dp,exact} = 800$ and $C_{Df,exact} = 1600$, respectively.

on the coarser and finer meshes. This result illustrates that MS2 and MS3 are adequate methods for evaluating forces acting on flows around objects in the immersed boundary method, although only the information of mesh and flow variables is used in the flow and boundary cell computations.

6. Applicability to More Complex Problems: Body with Sharp Edges, Multibody Treatment, and Compressibility

In this paper, we introduced the mesh-based force evaluation methods in the immersed boundary methods. When it is applied to the complex body problems, there are the sharp

edge problems or other multiple body problems. However, this method can be applied to such complex body problems, as far as the base immersed boundary method can treat such bodies. This is because the proposed method just uses the cell-face value which is given by the base immersed boundary method, regardless of whichever method, such as a ghost-cell method or a ghost-fluid method, is used as the base immersed boundary method. Therefore, the applicability of this method to the complex body problem is highly depending on the base immersed boundary methods and the further discussion is left for the other papers which discuss applicability of the base immersed boundary method to the complex body problems.

In addition, it is worth emphasizing that the present method can be applied to compressible flows as well as

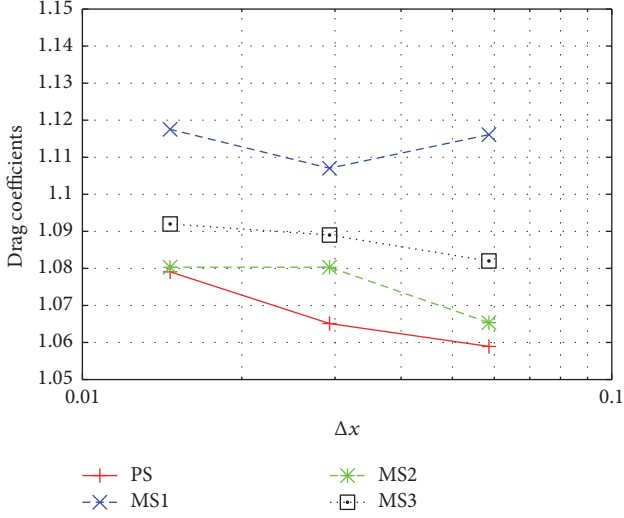


FIGURE 15: Estimated drags in flow around a sphere at the Reynolds number 100 as functions of mesh spacing.

incompressible flows. This is because the present method does not rely on the details of fluid flows (i.e., the divergence of velocity field). Although all the numerical results shown in this paper have been obtained by incompressible flows, several studies can be found in the literature on this subject [17, 18].

7. Conclusions

We have proposed a simple method for evaluating the forces acting on flows around bodies in the immersed boundary scenario. This method has been developed by employing a novel mesh-face integration method and an extrapolation method for evaluating pressure and shear stresses at the mesh faces, such as the first-order, ghost-cell, or ghost-fluid methods. The present method is, in principle, advantageous over the conventional methods based on control volumes in that pressure and shear stress can be evaluated separately.

Moreover, we have applied the present method to the computation of the drag force acting on a sphere in Stokes flow and have investigated the effects of grid spacing and extrapolation methods on the errors originating from the present force estimation method by using the existing analytical solutions. In addition, we have addressed the computational costs. As a result, the accuracy of the proposed mesh-based scheme has been proven to be comparable to that of the polygon-based scheme, which is commonly adopted in straightforward implementation. This indicates that the proposed scheme works better than the polygon-based one when complex geometries are involved, since its implementation is simple and its computational cost is low.

The error sources in the proposed implementation are sourced from (1) the surface area vector of the staircase body shape and (2) the approximated shear stress. Of these, error in the evaluated shear stress dominates and is significant. If the shear stress is appropriately evaluated, the fluid force

can be accurately obtained by summing over the mesh faces, because the surface area vector components converge with increasing grid density while the surface area does not. The shear stress is adequately evaluated by the second-order finite differencing scheme with the ghost-cell or ghost-fluid method. Sometimes, it is difficult to estimate the shear stress accurately with this method by its complex shape. It should be noted that this difficulty is caused by the immersed boundary methods themselves and the present idea using the staircase integration does not have difficulty.

Nomenclature

ΔS :	Surface area of a facet [m ²]
Δx :	Grid spacing [m]
δ_{ij} :	Kronecker's delta function
Γ_S :	Surface of a solid object
μ :	Dynamic viscosity [Pa·s]
ρ :	Mass density [kg/m ³]
σ_{ij} :	Fluid stress tensor [Pa]
a :	Radius of a sphere [m]
C_{D_f} :	The coefficient of frictional drag
C_{D_p} :	The coefficient of pressure drag
d :	Distance from an interface [m]
d_1, d_2 :	Distance of a marker 1 (or 2) from an interface [m]
F_j :	Hydrodynamic force [N]
n_i :	Unit normal vector
p :	Pressure [Pa]
p_∞ :	Reference pressure [Pa]
r :	Distance from the center of a sphere [m]
Re:	Reynolds number
S :	Area of surface [m ²]
u_∞ :	Free stream velocity [m/s]
u_1, u_2 :	Velocity at a marker 1 (or 2) [m]
u_B :	Velocity at an interface [m/s]
u_i :	Velocity [m/s]
x_i :	Coordinate [m].

Conflicts of Interest

The authors declare that they have no conflicts of interest.

Authors' Contributions

Taku Nonomura and Junya Onishi equally contributed to this paper.

Acknowledgments

A portion of this research was supported by the grant for "Strategic Programs for Innovative Research" Field no. 4, Industrial Innovations from the Ministry of Education, Culture, Sports, Science, and Technology's (MEXT's) "Development and Use of Advanced, High-Performance, General-Purpose Supercomputers Project," and JSPS KAKENHI Grant no. 17K06167. And a part of the results was obtained by using the K computer at the RIKEN Advanced Institute for Computational Science and by pursuing HPCI Systems

Research Projects (Proposals nos. hp130001 and hp130018). The authors express their thanks to all parties involved.

References

- [1] C. S. Peskin, "Fluid dynamics of heart valves: experimental, theoretical, and computational methods," *Annual Review of Fluid Mechanics*, vol. 14, pp. 235–259, 1982.
- [2] R. Mittal and G. Iaccarino, "Immersed boundary methods," in *Annual review of fluid mechanics*. Vol. 37, vol. 37 of *Annu. Rev. Fluid Mech.*, pp. 239–261, Annual Reviews, Palo Alto, CA, 2005.
- [3] M.-C. Lai and C. S. Peskin, "An immersed boundary method with formal second-order accuracy and reduced numerical viscosity," *Journal of Computational Physics*, vol. 160, no. 2, pp. 705–719, 2000.
- [4] E. Balaras, "Modeling complex boundaries using an external force field on fixed Cartesian grids in large-eddy simulations," *Computers and Fluids*, vol. 33, no. 3, pp. 375–404, 2004.
- [5] L. Shen, E.-S. Chan, and P. Lin, "Calculation of hydrodynamic forces acting on a submerged moving object using immersed boundary method," *Computers and Fluids*, vol. 38, no. 3, pp. 691–702, 2009.
- [6] K. Ono and J. Onishi, "A challenge to large-scale simulation of fluid flows around a car using ten billions cells," *Supercomputing News*, vol. 15, pp. 59–69, 2013 (Japanese).
- [7] R. Mittal, H. Dong, M. Bozkurttas, F. M. Najjar, A. Vargas, and A. von Loebbecke, "A versatile sharp interface immersed boundary method for incompressible flows with complex boundaries," *Journal of Computational Physics*, vol. 227, no. 10, pp. 4825–4852, 2008.
- [8] Y. Takahashi and T. Imamura, "Force calculation and wall boundary treatment for viscous flow simulation using cartesian grid methods in," in *Proceedings of the 26th (Japanese) Computational Fluid Dynamics Symposium*, 2012.
- [9] F. Gibou, R. P. Fedkiw, L.-T. Cheng, and M. Kang, "A second-order-accurate symmetric discretization of the Poisson equation on irregular domains," *Journal of Computational Physics*, vol. 176, no. 1, pp. 205–227, 2002.
- [10] F. M. White, "Visous fluid flows," 1991.
- [11] J. Onishi, K. Ono, and S. Suzuki, "Development of a CFD software for large-scale computation: An approach to grid generation for arbitrary complex geometries using hierarchical blocks," in *Proceedings of the 12th International Symposium on Fluid Control, Measurement and Visualization (FLUCOME '13)*, 2013.
- [12] K. Nakahashi, "High-Density Mesh Flow Computations with Pre-/Post-Data Compressions," in *Proceedings of the 17th AIAA Computational Fluid Dynamics Conference*, Toronto, Ontario, Canada.
- [13] Y. Morinishi, T. S. Lund, O. V. Vasilyev, and P. Moin, "Fully conservative higher order finite difference schemes for incompressible flow," *Journal of Computational Physics*, vol. 143, no. 1, pp. 90–124, 1998.
- [14] N. Sato, S. Takeuchi, T. Kajishima, M. Inagaki, and N. Hori-nouchi, "A cartesian grid method using a direct discretization approach for simulations of heat transfer and fluid flow," *Joint EUROMECH/ERCOTAC Colloquium 549—Immersed Boundary Methods: Current Status and Future Research Directions*, 2013.
- [15] M. W. R. Clift and J. Grace, *Bubbles, Drops, and Particles*, Dover Publications, 2005.
- [16] M. Tabata and K. Itakura, "A precise computation of drag coefficients of a sphere," *International Journal of Computational Fluid Dynamics*, vol. 9, no. 3-4, pp. 303–311, 1998.
- [17] S. Takahashi, T. Nonomura, and K. Fukuda, "A numerical scheme based on an immersed boundary method for compressible turbulent flows with shocks: application to two-dimensional flows around cylinders," *Journal of Applied Mathematics*, Article ID 252478, Art. ID 252478, 21 pages, 2014.
- [18] Y. Mizuno, S. Takahashi, T. Nonomura, T. Nagata, and K. Fukuda, "A simple immersed boundary method for compressible flow simulation around a stationary and moving sphere," *Mathematical Problems in Engineering*, Article ID 438086, Art. ID 438086, 17 pages, 2015.

Research Article

An Improved Finite Element Meshing Strategy for Dynamic Optimization Problems

Minliang Gong, Aipeng Jiang, Quannan Zhang, Haokun Wang, Junjie Hu, and Yinghui Lin

School of Automation, Hangzhou Dianzi University, Hangzhou 310018, China

Correspondence should be addressed to Aipeng Jiang; jiangaipeng@163.com

Received 7 April 2017; Accepted 11 June 2017; Published 19 July 2017

Academic Editor: Rahmat Ellahi

Copyright © 2017 Minliang Gong et al. This is an open access article distributed under the Creative Commons Attribution License, which permits unrestricted use, distribution, and reproduction in any medium, provided the original work is properly cited.

The finite element orthogonal collocation method is widely used in the discretization of differential algebraic equations (DAEs), while the discrete strategy significantly affects the accuracy and efficiency of the results. In this work, a finite element meshing method with error estimation on noncollocation point is proposed and several cases were studied. Firstly, the simultaneous strategy based on the finite element is used to transform the differential and algebraic optimization problems (DAOPs) into large scale nonlinear programming problems. Then, the state variables of the reaction process are obtained by simulating with fixed control variables. The noncollocation points are introduced to compute the error estimates of the state variables at noncollocation points. Finally, in order to improve the computational accuracy with less finite element, moving finite element strategy was used for dynamically adjusting the length of finite element appropriately to satisfy the set margin of error. The proposed strategy is applied to two classical control problems and a large scale reverse osmosis seawater desalination process. Computing result shows that the proposed strategy can effectively reduce the computing effort with satisfied accuracy for dynamic optimization problems.

1. Introduction

The direct transcription method is an important method to solve the problem of optimal control. By discretization of differential and algebraic optimization problems (DAOPs), the state variables and control variables are completely discretized. The discrete method uses the finite element orthogonal collocation, and generally the number of finite elements is empirically selected and the length of each finite element is equally divided. This results in low discretization accuracy for state and control variables, and to guarantee the satisfactory accuracy for some problems, the calculation time is too long to accept. Moving finite element strategy is a good idea for the solution. With the need of discrete differential algebraic equations, moving finite element is becoming the popular and practical technique for chemical process.

At present, we are concerned with calculation accuracy not only of the material, but also of the time in the process parameters for the chemical process attention. Modeling methods based on first principle and data-driven are used for practical control. With the development of solving technology, we can better understand the changes of state variables in the whole process of chemical reaction.

Betts and Kolmanovsky proposed a refinement procedure for nonlinear programming for discrete processes and estimating the discretization error for state variables [1]. Liu et al. used a novel penalty method to deal with nonlinear dynamic optimization problems with inequality path constraints [2]. Paiva and Fontes studied the adaptive mesh refinement algorithms which allow a nonuniform node collocation and apply a time mesh refinement strategy based on the local error into practical problems [3]. Zhao and Tsiotras introduced an efficient and simple method based on density (or monitor) functions, which have been used extensively for grid refinement. The accuracy and stability of the method were improved by choosing the appropriate density function. [4]. When using the discrete method to solve the nonlinear problem, iterative programming (IDP) algorithm is rather vulnerable to the stage of time in several aspects such as accuracy and the convergence rate. Li et al. introduce a self-adaptive variable-step IDP algorithm, taking account of the performance and control variables [5]. Zhang et al. presented an adaptive variable-step-size RKF method based on norm control. The method automatically adjusts the step size and the case where the local error norm value

is 0 or the minimum value is discussed [6]. In view of the optimization of biochemical processes, some researchers have proposed adaptive parameterization methods to solve such problems [7, 8].

The above work is quite helpful to quick and stable solution of the dynamic optimization problem, but most of them put emphasis on method of choice and do not propose a specific operational process. As we know, the results of the optimization problem are often dependent on the specific algorithm.

This paper is a mesh refinement strategy based on the variable finite element mesh method [9–11]. Prior to optimization, a suitable initial mesh and length are obtained by GAMS platform simulation. Then, to optimize the objective function, the finite element is moved appropriately under the condition that the set error is satisfied. The method is applied to the chemical reaction of simple ODE equation [12, 13] and large scale reverse osmosis seawater desalination process, which proves its validity and feasibility.

2. Finite Element Discrete Method for Equation Model

According to the whole chemical reaction process, we want to know the changes in the material. Discrete solution of the model is the key part for computing process. Here, we introduce the orthogonal polynomials based on Lagrange's use of the Radau collocation points on the finite element [14] and use of simultaneous method to the entire time domain $[0, t_f]$. The simplified model can be written as the following equations:

$$\begin{aligned}
 & \min_{z_{ik}, u_{ik}} \phi(z(t_f)) \\
 & \text{s.t.} \quad z_{ik} = z_i + h_i \sum_{j=1}^{N_c} \Omega(\tau_k) f(z_{ij}, y_{ij}, p) \\
 & \quad 0 = g(z_{ik}, y_{ik}, u_{ik}, p) \\
 & \quad z_{i+1} = z_{i, N_c} \\
 & \quad z_0 = \bar{z}_0 \\
 & \quad z_L \leq z_{ik} \leq z_U \\
 & \quad y_L \leq y_{ik} \leq y_U \\
 & \quad P_L \leq P \leq P_U \\
 & \quad u_L \leq u_{ik} \leq u_U \\
 & \quad i = 0, \dots, N-1, \quad k = 1, \dots, N_c,
 \end{aligned} \tag{1}$$

where ϕ is the scalar objective function, $z(t) \in R^{N_z}$ and $y(t) \in R^{N_y}$ as differential and algebraic variables, respectively; g is the constraint equation for the state variables and the control variables, $u(t) \in R^{N_u}$ and $p \in R^{N_p}$ as a control variable and time independent optimization variable. $\Omega_j(\tau_k)$ is a polynomial of order $N_c + 1$ in collocation τ_k . h_i denotes the length of element i . z_{ik} is value of its first derivative in element i at the collocation point k . The advantage of the Lagrange interpolation polynomial over other interpolation methods

is that the value of the variable at each collocation point is exactly equal to its coefficient

$$\begin{aligned}
 t_{ik} &= t_{i-1} + (t_i - t_{i-1}) \tau_k, \\
 z^k(t_{ik}) &= z_{ik}, \\
 u^k(t_{ik}) &= u_{ik}.
 \end{aligned} \tag{2}$$

3. Error Calculation at Noncollocation Point

On the selection of collocation points on finite elements, if the mathematical expression is configured according to the Gauss point, the algebraic precision of the numerical integration is the highest. k Gauss points can achieve the algebraic precision of $2k - 1$ order. When using k Radau points to configure, the algebraic precision is lower than the Gauss point, $2k - 2$. The discretization proposition based on Radau point has better stability [15]. Therefore, this paper uses Radau points to configure.

In order to improve the accuracy of the solution, Vasantharajan and Biegler [16] inserted the noncollocation points on the finite element to determine the increase and decrease of the finite element by the error of the noncollocation point.

Generally, in the solution of problem (1), it will cause compute error on state or control profiles due to finite mesh. In this study, the error of collocation finite elements can be estimated from

$$T_i(t_{nc}) = \frac{dz(t_{nc})}{d\tau} - h_i f_{nc}, \tag{3}$$

$$\text{error}(i) = \bar{C} T_i(t_{nc}). \tag{4}$$

Here \bar{C} is constant depending on collocation points. f_{nc} is differential state equation at t_{nc}

$$\bar{C} = \frac{1}{A} \int_0^{\tau_{nc}} \prod_{j=1}^K (s - \tau_j) ds, \tag{5}$$

$$A = \prod_{j=1}^K (\tau_{nc} - \tau_j).$$

From (3), T_i will be zero at the collocations. So we need to select a noncollocation point τ_{nc} ; that is, $t_{nc} = t_i + h_i \tau_{nc}$. Specifically, $dz(t_{nc})/d\tau$ can be stated as

$$\frac{dz(t_{nc})}{d\tau} = h_i \sum_{j=1}^{N_c} \hat{\Omega}(\tau_{nc}) f, \tag{6}$$

where $\hat{\Omega}(\tau_{nc})$ is the differential of $\Omega_j(\tau_k)$. Then we add (3)-(4) to problem (1) and then resolve the OPC problem.

4. Finite Element Method

As the error estimation gotten with (3) and (4), we can divide the finite elements mesh. Generally, equally spaced method was widely used in many research, due to its simply operation. The flow chart of calculation is shown in Figure 1.

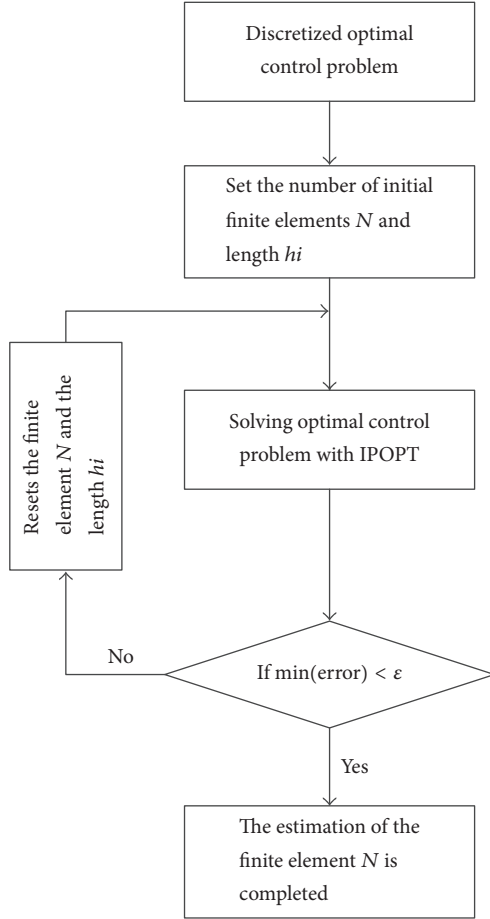


FIGURE 1: Equally spaced method for finite element mesh.

On the contrary, this approach will take more time and get larger N after the mesh divided. Now we take an idea of adaptive mesh and obtain algorithm of mesh initialization.

Step 1. Divide the time domain $[t_0, t_f]$ equally with a coarse mesh and compute the error at every location of element by solving problem (1).

Step 2. When each finite element error $\text{radio}_i = \log(|\text{error}_i/\epsilon|) < 0.5$, end the initialization of the finite element. If the requirement of less than 0.5 is not met, turn to Step 3.

Step 3. Once the error of each finite element $\text{radio}_i \geq 0.5$, add R finite element; here R rounds up from radio_i . Then resolve problem (1).

However, the finite element mesh gotten above has not satisfied accuracy yet. So we first fix the mesh h_i and suitable control profile and take simulate calculation by solving problem (1) without objective function. After that, relax h_i and add constraint (7) as follows:

$$\sum_{i=1}^N h_i = t_f \quad h_i \in [0.6\bar{h}_i, 1.4\bar{h}_i]. \quad (7)$$

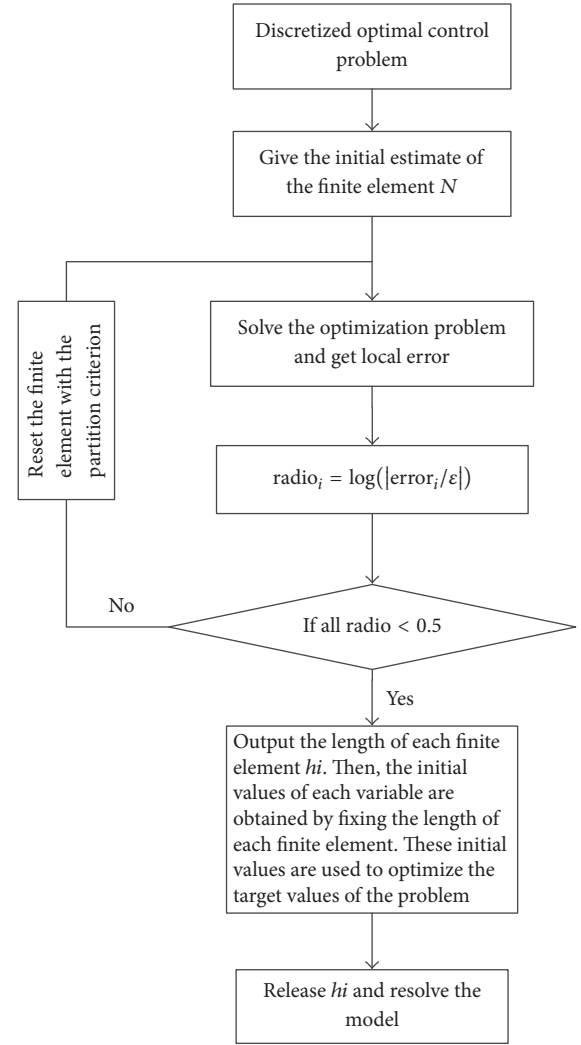


FIGURE 2: Finite element mesh refinement algorithm chart.

Through this way, reasonable initial values for optimization are provided. What is more, it also offers some freedom to search the breakpoint of control profiles.

From now on, we can summarize the approach described with program flow chart in Figure 2.

Through the above grid division and GAMS platform simulation and optimization, the optimized result is obtained finally. However, the optimality of the above result should be verified. According to the optimal control theory, the value of the Hamiltonian function comprising the objective function and the constraints should be kept as constant along the time axis. According to the optimal control theory, the discrete Hamiltonian function is denoted as

$$\begin{aligned} H_{i,j} = & \lambda_{i,j}^T f(z_{i,j}, y_{i,j}, u_{i,j}, p) \\ & + \mu_{i,j}^T g_E(z_{i,j}, y_{i,j}, u_{i,j}, p) \\ & + \gamma_{i,j}^T g_i(z_{i,j}, y_{i,j}, u_{i,j}, p). \end{aligned} \quad (8)$$

When the solution is optimal, the last two terms of the Hamiltonian are zero. According to the optimal control theory, when a system is optimal, the Hamiltonian must be a constant:

$$H_{i,j} = \text{Constant} \quad \forall i, j. \quad (9)$$

Therefore, if the finite element and the configuration point are not constant, the result is not optimal, and the meshing needs to read the finite element. Here we use method of Tanartkit and Biegler [11], who put forward a Hamilton function criterion:

$$\left\| \frac{dH(t_{i,j})}{dt} \right\| \leq \text{tol}. \quad (10)$$

When tol is set to allowable errors, it is set as $\max_{i,j}(0.001, 0.001\|H_{i,j}\|)$. If the meshing method proposed by us can not satisfy the above Hamilton function error requirement, we must read the finite element mesh quantity.

5. Case Study

This numerical experiment is based on Intel (R) Core (TM) i3-2350M 2.3 GHz processor with 4 GB RAM; the nonlinear programming solver IPOPT [17, 18] is developed by Carnegie Mellon University.

To illustrate the above strategies, we consider two classical process dynamic optimization problems and a large scale reverse osmosis seawater (SWRO) desalination process. At the same time, we use the error analysis based on the equipartition finite element method for comparison. For the following example, we use the 3-order Radau collocation points; each finite element has a noncollocation point. Three of these collocation points are $\tau_1 = 0.155051$, $\tau_2 = 0.644949$, and $\tau_3 = 1$, noncollocation point is $\tau_{nc} = 0.5$, finite element tolerance error is $\varepsilon = 1.0e - 5$, and default set point error estimation limit is $\varepsilon = 1.0e - 5$.

5.1. Batch Temperature Profile with Parallel Reactions. This example is a chemical process, considering a nonisothermal reactor with first order $A \rightarrow B$, $A \rightarrow C$, where A is reaction material, B is target product, and C is by-product. Now the goal is to find a feasible temperature profile that maximizes the final amount of product B after one hour. The optimal control problem can be stated as

$$\begin{aligned} \min \quad & -b(1) \\ \text{s.t.} \quad & \frac{da}{dt} = -a(t) \left(u(t) + \frac{u(t)^2}{2} \right) \\ & \frac{db}{dt} = a(t) u(t) \\ & a(0) = 1 \\ & b(0) = 0 \\ & 0 \leq t \leq 1, \quad u(t) \in [0, 5]. \end{aligned} \quad (11)$$

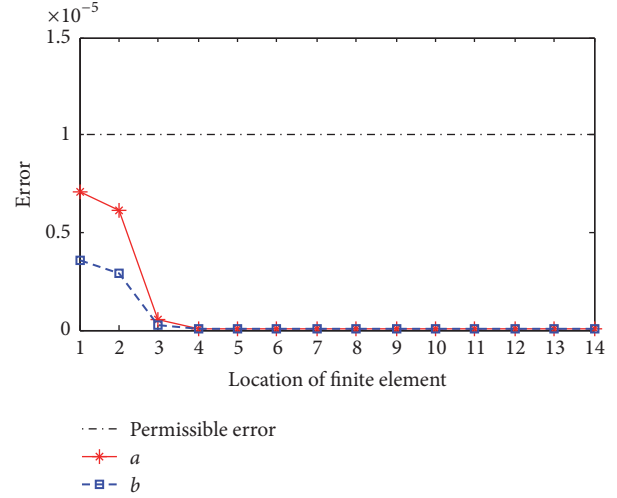


FIGURE 3: Error of differential profiles at finite elements with equally spaced method.

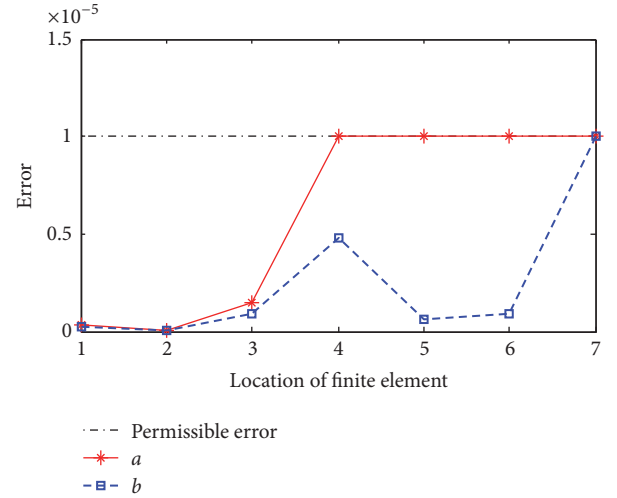


FIGURE 4: Error of differential profiles at finite elements with new method.

The problem has been solved in many pieces of literature. In [19], adaptive iterative dynamic programming leads to 50 time steps and needs more than 60 CPUs. Here we first adopt equally spaced elements method, which leads to 14 finite elements. Local errors for all finite elements are shown in Figure 3.

As shown in Figure 3, we can see that the first- and second-finite element errors are large, and other places have to meet the set error tolerance. This means that we can use fewer finite elements to calculate the problem. In Figure 4, when using our proposed meshing method, only 7 finite elements are needed. In the use of the equally finite element method, the posterior finite element error is very small, so that when we use a partitioning method, the error is close to the set error tolerance.

In Figure 5, fixed finite element length is gotten from the simulation. After adding the boundary constraint (7), a new

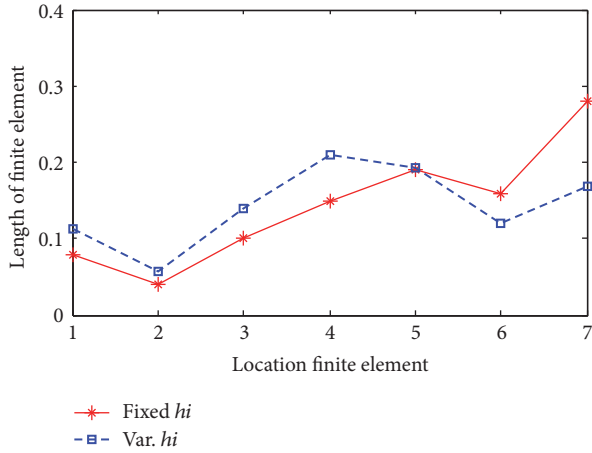


FIGURE 5: Size of finite element in simulation and optimization.

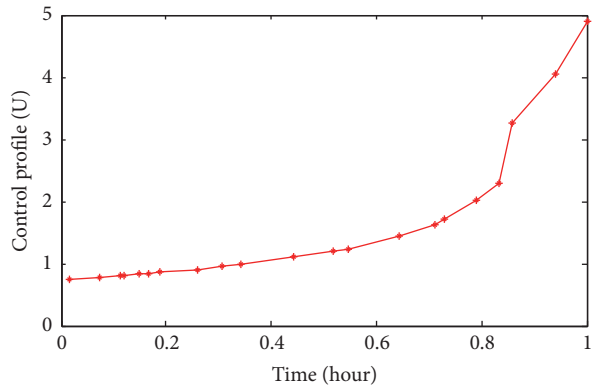


FIGURE 6: Optimal control for the batch reaction problem.

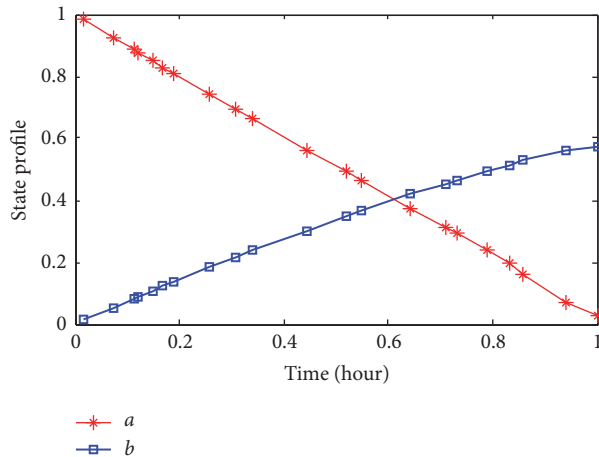


FIGURE 7: State profiles for the batch reaction problem.

finite element length is obtained (blue line). This can also help for locating breakpoints into specific problems.

Figures 6 and 7 show the optimal control image and the state variable change image, respectively. These changes are close to those obtained by previous researchers. This fully proves the feasibility of the proposed method.

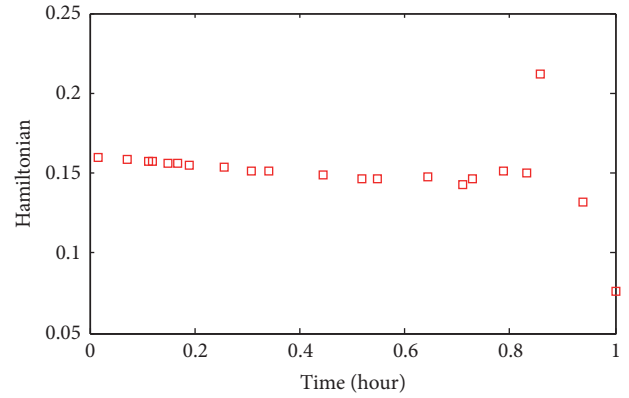


FIGURE 8: Profile of Hamiltonian function.

TABLE 1: Batch reaction numerical results.

Strategy	N	Var	Eq	Iter	Accuracy	CPU(s)
ESM	14	294	252	11	$1e-5$	9.841
MFE	7	217	190	39	$1e-5$	5.330

Figure 8 shows that the Hamiltonian function is a constant and the derivative of Hamiltonian function satisfies the above error that the problem has been the optimal solution.

From Table 1, we can see that, by using an improved finite element method we propose, the finite element number can be reduced by half. The calculation time can be reduced by 4.5 s under the same precision.

5.2. *Rayleigh Problem.* Here we consider another optimal control problem which can be described as

$$\begin{aligned}
 \min \quad & \int_0^{t_f=2.5} (x_1^2 + u^2) dt \\
 \text{s.t.} \quad & \frac{dx_1}{dt} = x_2 \\
 & \frac{dx_2}{dt} = -x_1 + (1.4 - 0.14x_2^2)x_2 + 4u \\
 & x_1(0) = -5, \\
 & x_2(0) = -5.
 \end{aligned} \tag{12}$$

In this example, the number of finite elements is often estimated by trial and error. Here, we use 104 equally spaced finite elements to make the two differential equations meet the error requirements, as shown in Figure 9.

As can be seen from Figure 9, most of the finite elements have been early to meet the error requirements. Here we use the new method we propose. Only 8 finite elements are required to satisfy the error requirements, as shown in Figure 10.

Figure 11 shows the length of each finite element position. It can be seen from the figure that the length of the 6, 7, and 8th finite element position is greater than the length of the simulation (red line), which indicates that the addition

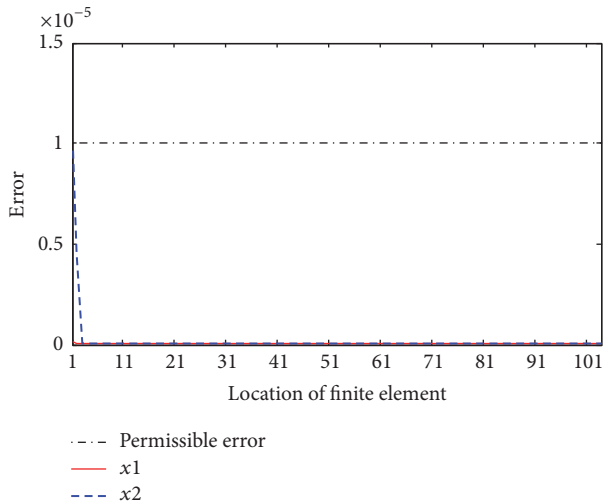


FIGURE 9: Error of differential profiles at finite elements with equally spaced method.

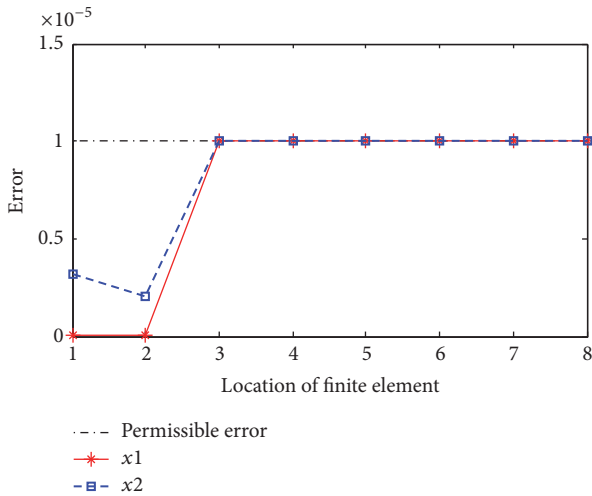


FIGURE 10: Error of differential profiles at finite elements with new method.

TABLE 2: Rayleigh reaction numerical results.

Strategy	N	Var	Eq	Iter	Accuracy	CPU(s)
ESM	104	36	31	8	$1e-5$	67.277
MFE	8	248	217	71	$1e-5$	5.352

of the boundary constraint is effective when optimizing the objective function and finding the boundary breakpoint.

Figures 12 and 13 show the optimal control image and the state variable change image in process.

The Hamiltonian function image of Figure 14 indicates that the objective function has been optimized.

In Table 2, when using the finite element method, the total number of variables is 36, and the computer time is 67.277 s. But using our new method, the total number of discrete variables is 8, and the calculation time is 5.352 s. In terms of

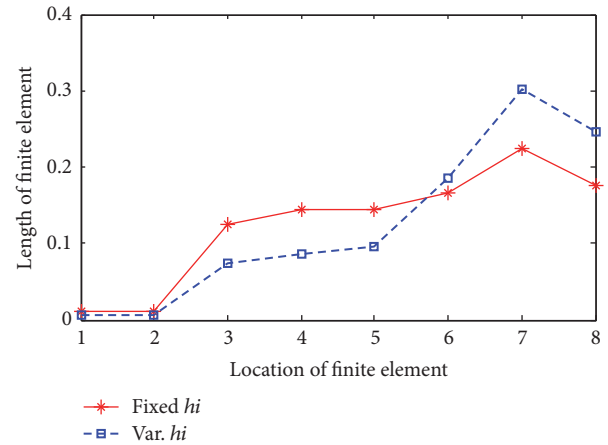


FIGURE 11: Size of finite element in simulation and optimization.

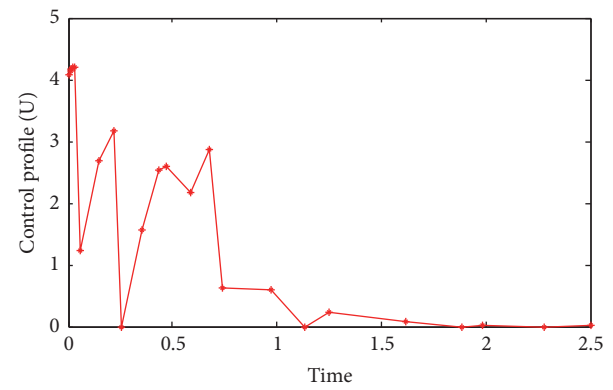


FIGURE 12: Optimal control for Rayleigh problem.

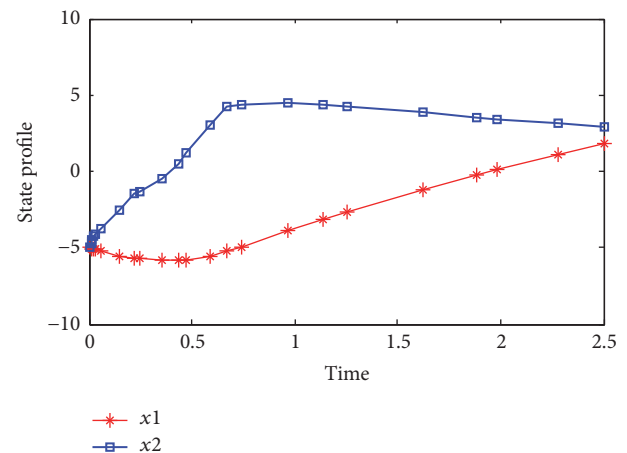


FIGURE 13: State profiles for Rayleigh problem.

the number of finite elements and the computation time, the new method presented in this paper has some advantages.

5.3. Reverse Osmosis Sweater Desalination Process. The feasibility of the proposed method is illustrated by two classical chemical reaction control problems. The following is an operational optimization study of a large scale reverse osmosis

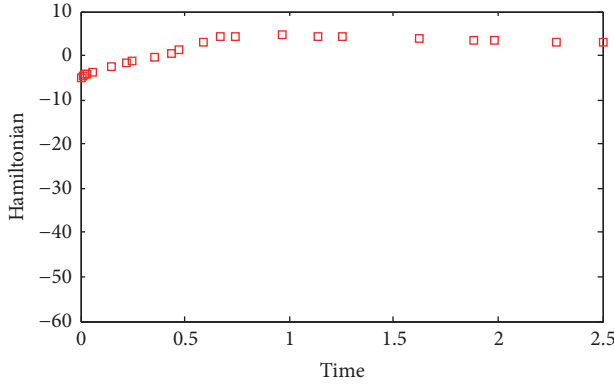


FIGURE 14: Profile of Hamiltonian function.

seawater (SWRO) desalination process. The model equation can be expressed as

$$\begin{aligned}
 A_w(i, j) &= A_{w0} \cdot FA \cdot MFA \\
 &\quad \cdot e^{(\alpha_1((T-273)/273) - \alpha_2(P_f - P_d(i, j)))}, \\
 B_s &= B_{s0} \cdot FB \cdot MFB \cdot e^{(\beta_1((T-273)/273))}, \\
 Jv_{i,j} &= A_w (P_f - P_{di,j} - \Delta\pi_{i,j}), \\
 Js_{i,j} &= B_w (C_{mi,j} - C_{pi,j}), \\
 C_{pi,j} &= \frac{Js_{i,j}}{Jv_{i,j}}, \\
 \Delta\pi_{i,j} &= RT (C_{mi,j} - C_{pi,j}), \\
 C_{mi,j} &= \left[(C_{bi,j} - C_{pi,j}) \exp\left(\frac{Jv_{i,j}}{k_{ci,j}}\right) \right] + C_{pi,j}, \\
 k_{ci,j} &= 0.065 \text{Re}_{i,j}^{0.875} \text{Sc}_{i,j}^{0.25} \cdot \frac{d_e}{D_{AB}}, \\
 \text{Sc}_{i,j} &= \frac{\mu_{i,j}}{(\rho D_{AB})}, \\
 \lambda_{i,j} &= 6.23 K_\lambda \text{Re}_{i,j}^{-0.3}, \\
 \text{Re}_{i,j} &= \frac{\rho V_{i,j} d_e}{\mu_{i,j}}, \\
 \frac{dV_{i,j}}{dz} &= -\frac{2Jv_{i,j}}{h_{sp}}, \\
 \frac{dC_{bi,j}}{dz} &= \frac{2Jv_{i,j}}{h_{sp} V_{i,j}} (C_{bi,j} - C_{pi,j}), \\
 \frac{dP_{di,j}}{dz} &= -\lambda_{i,j} \frac{\rho}{d_e} \frac{V_{i,j}^2}{2}.
 \end{aligned} \tag{13}$$

And then according to the objective function of the cost of water production,

$$\min_{Q_f, P_f, H_t, T} \text{OC} = \text{OC}_{\text{IP}} + \text{OC}_{\text{EN}} + \text{OC}_{\text{CH}} + \text{OC}_{\text{OTR}}. \tag{14}$$

Here OC_{IP} and OC_{EN} are reverse osmosis process water intake and RO energy costs; OC_{CH} is the cost of system chemicals; OC_{OTR} indicates other costs, including labor costs and maintenance costs.

The optimization proposition also needs to satisfy the RO process model, the reservoir model, the operation cost model, and the inequality constraint equation. The system cost model is shown as follows:

$$\text{OC}_{\text{EN}} = \text{SEC} \cdot Q_p \cdot P_{\text{elc}},$$

$$\text{OC}_{\text{IP}} = P_{\text{in}} \cdot Q_f \cdot P_{\text{elc}} \cdot \frac{\text{PLF}}{\eta_{\text{IP}}}, \tag{15}$$

$$\text{OC}_{\text{CH}} = 0.0225 Q_f.$$

Here, P_{elc} is the unit price; η_{IP} is the motor energy efficiency; PLF represents the load factor; P_{in} is the outlet pressure of the pump.

From the optimization program mainly to the day, there are peaks and valleys of electricity prices, resulting in different periods of water production costs. The system can be done through the cistern reservoir volume, regulating the water system and the user's demand for water to reduce the overall cost.

The reverse osmosis process model mainly includes three differential variables: membrane concentration, flow rate, and pressure. In this paper, the number of finite elements is divided into discrete errors based on the steady-state simulation process, so as to reduce the computational complexity of the optimization model.

Figure 15 shows three differential variables and the error of velocity, concentration, and pressure can only meet the error tolerance when the 22 finite elements are divided equally. Since the error of velocity and pressure is much smaller than that of channel concentration, the discrete error analysis was mainly focused on the channel concentration. Figure 16 is the finite element error analysis using the new method.

Figure 17 shows that after the initial finite element length is obtained by simulation, the constraint equation is added to obtain a more suitable finite element length.

Figures 18, 19, and 20 represent the flow rate, concentration, and pressure at the feed of the membrane module, respectively. It can be seen from these figures that adding boundary constraints to each curve is more smoothly and more responsive to changes in the variables within the actual membrane module.

Table 3 shows the use of a method proposed in this paper, both from the number of variables, the number of iterations, and computing time above a great upgrade.

It can be seen that the number of finite elements required for the model discretization is reduced to 14 when using the moving finite element method. Due to the finite element method, the finite element length can be adjusted to a small extent, which greatly increases the accuracy of the solution.

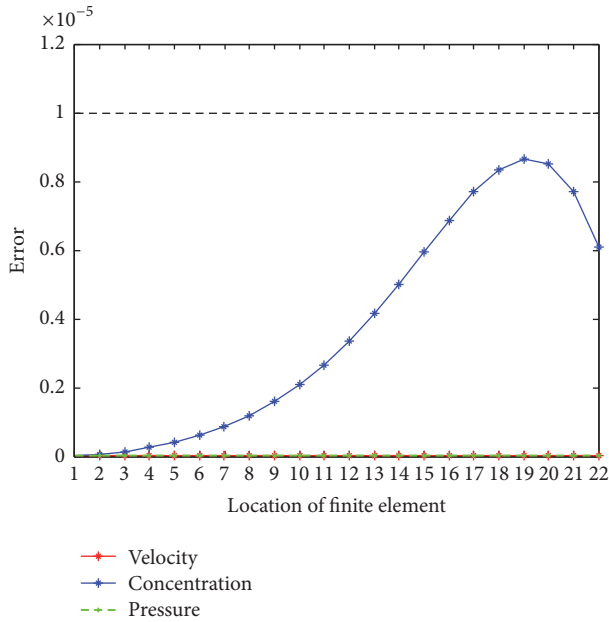


FIGURE 15: Error of differential profiles at finite elements with equally spaced method. The black dotted line represents the maximum error of each finite element at the noncollocation point.

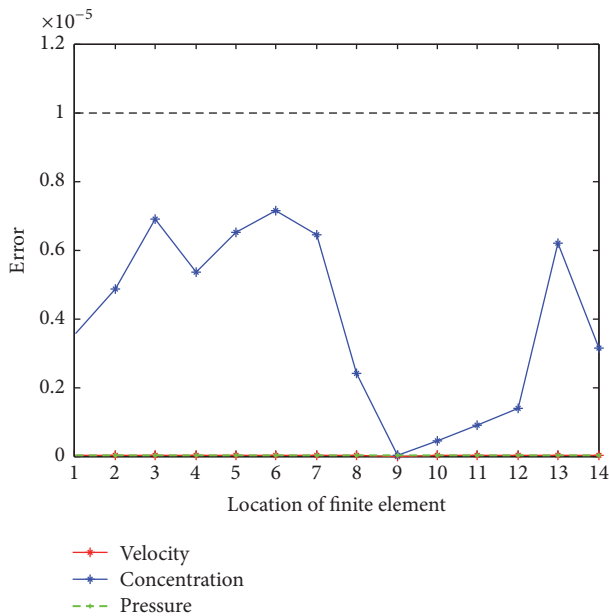


FIGURE 16: Error of differential profiles at finite elements with new method. The black dotted line represents the maximum error of each finite element at the noncollocation point.

6. Conclusion

In this paper, we proposed a mesh-partitioning strategy based on the direct transcription method to solve the optimal control problem. This method discretizes the differential algebraic equation (DAE) using the Radau collocation point based on the variable finite element and finally transforms

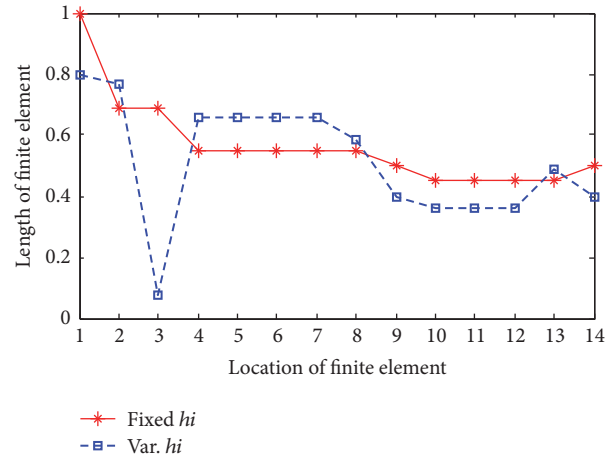


FIGURE 17: Size of finite element in simulation and optimization.

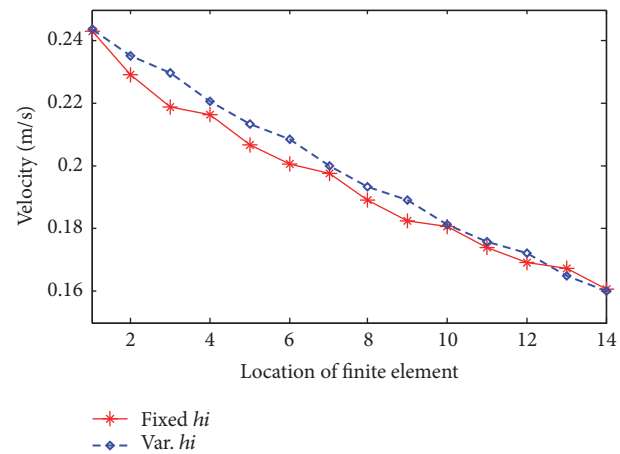


FIGURE 18: Membrane channel within one hour of the velocity changes.

TABLE 3: SWRO numerical results.

Strategy	N	Var	Eq	Iter	Accuracy	CPU(s)
ESM	22	44044	43996	42	$1e-5$	163.775
MFE	14	23836	23778	33	$1e-5$	154.924

into a nonlinear programming problem. Here, the initialization variable finite element uses a valid termination criterion. At the same time, the computation time can be saved under the condition of satisfying certain precision.

Cases study of two classical control problems and a large scale reverse osmosis process optimization problem was carried with our proposed method and conventional method. The computing results show that the proposed method can effectively reduce the number of finite element and thus reduce the computing efforts with permitted discrete accuracy.

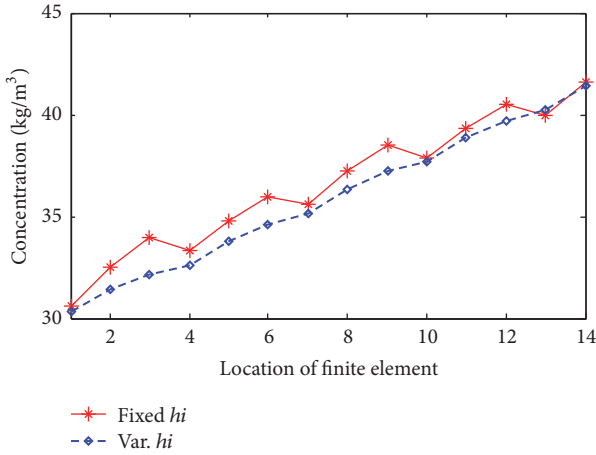


FIGURE 19: Membrane channel within one hour of the concentration changes.

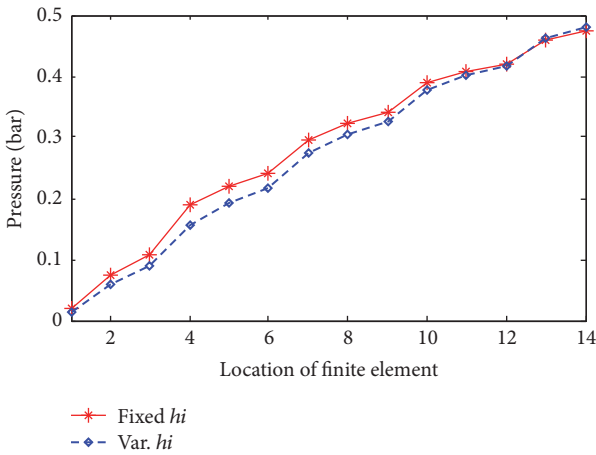


FIGURE 20: Membrane channel within one hour of the pressure changes.

Nomenclature

- t_f : Terminal time (s)
- ϕ : The scalar objective function
- $z(t)$: Differential state variables
- $y(t)$: Algebraic state variables
- g : Constraint equation for the state and control variables
- $u(t)$: Control variable
- p : Time independent optimization variable
- h_i : The length of element i
- k : Number of collocation points
- z_{ik} : First derivative in element i at the collocation point k
- \bar{c} : Constant depending on collocation points
- f_{nc} : Differential state equation at t_{nc}
- ε : Default set point error estimation limit
- tol: The setting error
- N : Number of finite elements
- Var: Number of variables
- Eq: Number of equations

- Iter: The number of iterations calculated
- ESM: Equally spaced method
- MFE: Moving finite elements
- A_w : Membrane water permeability ($m \cdot s^{-1} \cdot Pa^{-1}$)
- A_{w0} : Intrinsic membrane water permeability ($m \cdot s^{-1} \cdot Pa^{-1}$)
- B_s : Membrane TDS permeability (m/s)
- B_{s0} : Intrinsic membrane TDS permeability (m/s)
- α_1 : Constant parameter
- α_2 : Constant parameter
- β_1 : Constant parameter
- T : Feed (operational) temperature (K)
- P_f : Feed pressure (bar)
- P_d : Pressure drop along RO spiral wound module (bar)
- J_v : Solvent flux ($kg/m^2 \cdot s$)
- $\Delta\pi$: Pressure loss of osmosis pressure (bar)
- J_s : Solute flux ($kg/m^2 \cdot s$)
- C_m : Salt concentration of membrane surface (kg/m^3)
- C_p : Permeate concentration of RO unit (kg/m^3)
- C_b : Bulk concentration along feed channel (kg/m^3)
- k_c : Mass transfer coefficient (m/s)
- Re: Reynolds number (dimensionless)
- Sc: Schmidt number (dimensionless)
- d_e : Hydraulic diameter of the feed spacer channel (m)
- D_{AB} : Dynamic viscosity (m^2/s)
- μ : Kinematic viscosity
- ρ : Density of permeate water (kg/m^3)
- λ : Friction factor
- K_λ : Empirical parameters
- V : Axial velocity in feed channel (m/s)
- h_{sp} : Height of the feed spacer channel (m)
- OC: Operational cost of entire process
- OC_{EN}: Energy cost of RO process
- OC_{IP}: Energy cost for intake and pretreatment
- OC_{CH}: Cost for chemicals
- OC_{OTR}: Other costs
- SEC: Specific energy consumption ($kw \cdot h/m^3$)
- Q_p : Permeate flow rate (m^3/h)
- P_{elc} : Electricity price (CNY/ $kw \cdot h$)
- P_{in} : Output pressure of the intake pump (bar)
- PLF: Load coefficient
- η_{IP} : Mechanical efficiency of intake pump.

Conflicts of Interest

The authors declare no conflicts of interest.

Acknowledgments

This work is supported by National Natural Science Foundation (NNSF) of China (no. 61374142), the Natural Science Foundation of Zhejiang (LY16F030006), the Public Projects of Zhejiang Province, China (no. 2017C31065), Research and Innovation Fund of Hangzhou Dianzi University (CXJJ2016043), and Hangzhou Dianzi University Graduate Core Curriculum Construction Project (GK168800299024-012).

References

- [1] J. T. Betts and I. Kolmanovskiy, *Practical methods for optimal control using nonlinear programming [M.S. thesis]*, Society for Industrial and Applied Mathematics (SIAM), Philadelphia, PA, USA, 2001.
- [2] X. Liu, Y. Hu, J. Feng, and K. Liu, "A novel penalty approach for nonlinear dynamic optimization problems with inequality path constraints," *Institute of Electrical and Electronics Engineers. Transactions on Automatic Control*, vol. 59, no. 10, pp. 2863–2867, 2014.
- [3] L. T. Paiva and F. A. C. C. Fontes, "Time—mesh Refinement in Optimal Control Problems for Nonholonomic Vehicles," *Procedia Technology*, vol. 17, pp. 178–185, 2014.
- [4] Y. Zhao and P. Tsiotras, "Density functions for mesh refinement in numerical optimal control," *Journal of Guidance, Control, and Dynamics*, vol. 34, no. 1, pp. 271–277, 2011.
- [5] H.-G. Li, J.-P. Liu, and J.-W. Huang, "Self-adaptive variable-step approach for iterative dynamic programming with applications in batch process optimization," *Control and Decision*, vol. 30, no. 11, pp. 2048–2054, 2015.
- [6] Z. Zhang, Y. Liao, and Y. Wen, "An adaptive variable step-size RKF method and its application in satellite orbit prediction," *Computer Engineering and Science*, vol. 37, no. 4, pp. 842–846, 2015.
- [7] P. Liu, G. Li, X. Liu, and Z. Zhang, "Novel non-uniform adaptive grid refinement control parameterization approach for biochemical processes optimization," *Biochemical Engineering Journal*, vol. 111, pp. 63–74, 2016.
- [8] L. Wang, X. Liu, and Z. Zhang, "A new sensitivity-based adaptive control vector parameterization approach for dynamic optimization of bioprocesses," *Bioprocess and Biosystems Engineering*, vol. 40, no. 2, pp. 181–189, 2017.
- [9] L. T. Biegler, *Nonlinear programming: concepts, algorithms, and applications to chemical processes [M.S. thesis]*, Society for Industrial and Applied Mathematics, Pittsburgh, Pa, USA, 2010.
- [10] W. F. Chen, K. X. Wang, Z. J. Shao, and L. T. Biegler, "Moving finite elements for dynamic optimization with direct transcription formulations," in *Control and Optimization with Differential-Algebraic Constraints*, L. T. Biegler, S. L. Campbell, and V. Mehrmann, Eds., SIAM, Philadelphia, PA, USA, 2011.
- [11] P. Tanartkit and L. T. Biegler, "A nested, simultaneous approach for dynamic optimization problems—II: the outer problem," *Computers and Chemical Engineering*, vol. 21, no. 12, pp. 735–741, 1997.
- [12] G. A. Hicks and W. H. Ray, "Approximation methods for optimal control synthesis," *The Canadian Journal of Chemical Engineering*, vol. 49, no. 4, pp. 522–528, 1971.
- [13] J. S. Logsdon and L. T. Biegler, "Accurate solution of differential-algebraic optimization problems," *Industrial and Engineering Chemistry Research*, vol. 28, no. 11, pp. 1628–1639, 1989.
- [14] V. M. Zavala, *Computational strategies for the optimal operation of large-scale chemical processes [Ph.D. thesis]*, Carnegie Mellon University, Pennsylvania, Pa, USA, 2008.
- [15] J. Bausa, "Dynamic optimization of startup and load-increasing processes in power plants—part I: method," *Journal of Engineering for Gas Turbines and Power*, vol. 123, no. 1, pp. 251–254, 2001.
- [16] S. Vasantharajan and L. T. Biegler, "Simultaneous strategies for optimization of differential-algebraic systems with enforcement of error criteria," *Computers and Chemical Engineering*, vol. 14, no. 10, pp. 1083–1100, 1990.
- [17] A. Wächter and L. T. Biegler, "Line search filter methods for nonlinear programming: motivation and global convergence," *SIAM Journal on Optimization*, vol. 16, no. 1, pp. 1–31, 2005.
- [18] A. Chter and L. T. Biegler, "Line search filter methods for nonlinear programming: local convergence," *SIAM Journal on Optimization*, vol. 16, no. 1, pp. 32–48, 2005.
- [19] L. I. Qianxing, X. Liu, and W. U. Gaohui, "An adaptive step-size approach to iterative dynamic programming," *Bulletin of Science and Technology*, vol. 26, no. 5, pp. 666–669, 2010.

Research Article

A Self-Adaptive Numerical Method to Solve Convection-Dominated Diffusion Problems

Zhi-Wei Cao, Zhi-Fan Liu, Zhi-Feng Liu, and Xiao-Hong Wang

Department of Thermal Science and Energy Engineering, University of Science and Technology of China, Hefei, Anhui 230026, China

Correspondence should be addressed to Zhi-Fan Liu; zfliu13@ustc.edu.cn

Received 5 April 2017; Accepted 11 June 2017; Published 17 July 2017

Academic Editor: Mohsen Sheikholeslami

Copyright © 2017 Zhi-Wei Cao et al. This is an open access article distributed under the Creative Commons Attribution License, which permits unrestricted use, distribution, and reproduction in any medium, provided the original work is properly cited.

Convection-dominated diffusion problems usually develop multiscaled solutions and adaptive mesh is popular to approach high resolution numerical solutions. Most adaptive mesh methods involve complex adaptive operations that not only increase algorithmic complexity but also may introduce numerical dissipation. Hence, it is motivated in this paper to develop an adaptive mesh method which is free from complex adaptive operations. The method is developed based on a range-discrete mesh, which is uniformly distributed in the value domain and has a desirable property of self-adaptivity in the spatial domain. To solve the time-dependent problem, movement of mesh points is tracked according to the governing equation, while their values are fixed. Adaptivity of the mesh points is automatically achieved during the course of solving the discretized equation. Moreover, a singular point resulting from a nonlinear diffusive term can be maintained by treating it as a special boundary condition. Several numerical tests are performed. Residual errors are found to be independent of the magnitude of diffusive term. The proposed method can serve as a fast and accuracy tool for assessment of propagation of steep fronts in various flow problems.

1. Introduction

It is well known that convection-diffusion equations arise in a variety of important science and engineering fields, for example, thermodynamics, fluid mechanics, and chemical reactions [1, 2]. In many applications recognized as convection-dominated problems, diffusion may be quite small in contrast to convection, so that the solution will develop steep moving fronts that are nearly shocks. Efficient and accurate assessment of propagations of moving fronts is important. However, standard Finite Difference Methods (FDM) tend to introduce spurious oscillations and stabilized methods often resort to upwind schemes, which introduce excessive numerical dissipations that will oversmooth the fronts [3, 4]. Consequently, an extremely fine mesh is needed to increase the resolution, making the convection-diffusion equation a most challenging one to be solved numerically.

There are mainly two lines of research in numerical methods for achieving higher resolution with limited computation cost. One is the development of higher-order methods trying to reduce the numerical diffusion, such as high-order FDM

with flux limiters [5–10] and the method of characteristics [3, 11–14]. The other important approach is using adaptive meshes. That is, mesh points are concentrated in the region where the solution varies steeply and is less concentrated in slowly varying regions.

Different adaptive strategies, for example, Adaptive Mesh Refinement method and moving mesh methods, have shown success in solving convection-diffusion problems [15–22]. As an adaptive scheme is designed to yield highly nonuniform mesh, discretization of the governing equation on general meshes should be settled first [23]. As for how to locate mesh points adaptively, such methods often appeal to equidistributing a monitor function or solving mesh equations [19]. As a whole, adaptive methods generally consist of two parts: one is to locate mesh points adaptively and the other is to solve the governing equation on the nonuniform mesh. As a result, computation complexity is certainly increased. Moreover, a local interpolation is usually needed to project the information to new meshes. Such a remeshing operation often brings numerical diffusion. So, it is desirable to develop a numerical

method that solves the problem adaptively but without complex adaptive operations.

In this paper, we propose a self-adaptive numerical method to capture the steep fronts accurately. We first consider the following convection-diffusion equation to illustrate the main ideas of our method [1, 2]:

$$\frac{\partial S}{\partial t} + \frac{\partial f(S)}{\partial x} = \frac{\partial}{\partial x} \left(\epsilon(S) \frac{\partial S}{\partial x} \right), \quad (1)$$

where the diffusive coefficient $\epsilon(S)$ is positive. Instead of a traditional spatial-discretized mesh, the proposed method is based on a “range-discrete mesh” which is uniformly distributed in the value domain [24]. It is found that the range-discrete mesh has an adaptive nature because the density of mesh points is proportionate to the spatial gradient of the solution. During the computation process, positions of the mesh points are determined by the governing equation, while their values are fixed. In this way, movement of the mesh points not only solves the equation but also locates mesh points adaptively. In other words, the proposed method combines the two parts of an adaptive method, the adaptive strategy and solving the equation, in one procedure. Therefore, neither complex adaptive operations nor any interpolations are involved in the proposed method, leading to a simple and efficient method for convection-diffusion problems.

It must be emphasized that, with a linear diffusive coefficient, the solution of (1) is smooth, though there exist steep gradients, which is the most concerned situation in the literature. However, with a nonlinear diffusive coefficient, though small, spatial gradient of the solution can be discontinuous or even infinite [25–27]. This singularity phenomenon is common in many applications but often smeared out by traditional methods. By simply treating it as a boundary condition, such a singular point can be maintained in our method.

It should be noted that, for monotone solutions, the proposed method is similar to the method of Fayers and Sheldon [25]. Unfortunately, as the unknown is no longer single valued in their Lagrangian form, their method does not work for nonmonotone solutions. The proposed method overcomes this disadvantage by discretizing the governing equation over dynamic control volumes. Furthermore, how to deal with different kinds of boundary conditions with the proposed method is discussed.

This paper is organized as follows. Section 2 introduces the range-discrete strategy to obtain an adaptive mesh. Next, the numerical scheme based on the range-discrete mesh, including boundary conditions, will be illustrated in detail in Sections 3, 4, and 5. Several numerical tests are conducted to validate the numerical method in Section 6 and conclusions are drawn in Section 7.

2. Range-Discrete Mesh

Considering that the unknown in (1) has bounded value, that is, $S(x, t) \in [m, M]$, a series of discrete values can be obtained as $m \leq S_0 < S_1 < \dots < S_j < \dots < S_k \leq M$, where $S_{j+1} = S_j + \Delta S_j$. Then, one can get a series of intersection points of the line sets $S = S_j$ ($j = 0, 1, \dots, k$) and the curve $S = S(x, t)$,

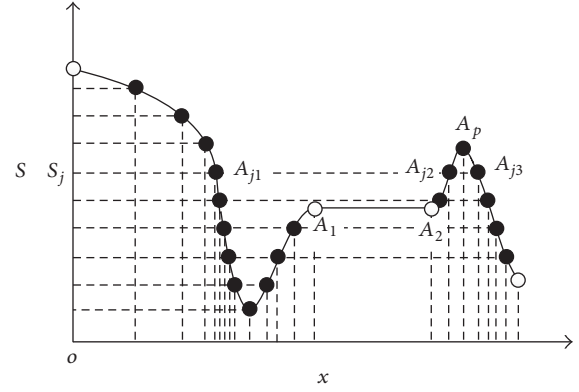


FIGURE 1: Description of the range-discrete mesh.

namely, A_i ($i = 0, 1, \dots$) as graphed in Figure 1. Then, with the location of each intersection known, approximation of $S(x, t)$ is obtained. Thus, a mesh can be formed by treating each intersection as a mesh point.

For a constant piece in the solution curve, the governing equation is satisfied trivially. The solutions on both sides of this constant piece do not interact with each other until the constant piece disappears. Consequently, each endpoint of the constant piece can be treated as a boundary condition for each side, respectively. With two adjacent mesh points assigned to the same value and marked as boundary points, for example, A_1 and A_2 shown in Figure 1, a constant piece is sufficiently described.

If $S = S(x)$ is nonmonotone, several intersections of the line $S = S_j$ and the curve $S = S(x)$ exist, for example, points A_{j1}, A_{j2}, A_{j3} shown in Figure 1. It is intuitive to employ all these intersections, assigned with the same discrete value S_j , as different mesh points to describe the nonmonotone feature. Moreover, a mesh point should also be set at the position of an extremum of $S = S(x)$, for example, point A_p in Figure 1, because, without it, the solution between A_{j2} and A_{j3} will be identified as a constant piece.

In contrast to spatial-discrete mesh used by FDM and many other methods, the discrete mesh obtained using the rules above is named as a “range-discrete” mesh. We should state that, though ΔS_j can be different from each other, we focus our attention on the equidistance situation for the sake of simplicity.

If there exist n mesh points in the spatial area $[x_a, x_b]$, the density of mesh points can be defined as $\rho = n/|x_b - x_a|$. For a range-discrete mesh, variation of the solution over the area $[x_a, x_b]$ can be defined as $TV_{[x_a, x_b]}(S) = \sum_{j=1}^{n-1} |S(x_{j+1}) - S(x_j)| = (n - 1)\Delta S$. Thus, we can obtain

$$\rho \propto \frac{TV(S)_{[x_a, x_b]}}{|x_a - x_b|}, \quad (2)$$

where $TV(S)_{[x_a, x_b]}/|x_a - x_b|$ can be interpreted as the spatial variation speed of the solution. Thus, we can conclude from (2) that ρ is proportionate to the spatial variation speed of the solution, so that the density of mesh points is large where the solution varies quickly and vice versa, indicating an adaptive nature, which can also be seen from Figure 1. As a special case,

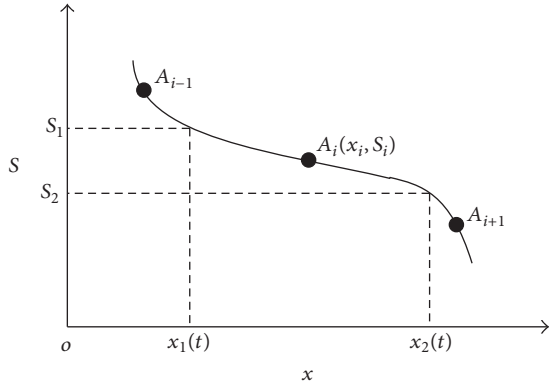


FIGURE 2: A dynamic control volume around a mesh point.

the density of mesh points for a constant piece is actually zero, being quite computational effort saving.

In fact, as $\lim_{|x_a - x_b| \rightarrow 0} TV(S)_{[x_a, x_b]} / |x_a - x_b| = |S_x(x)|$, we can observe an equidistribution of the solution gradient $|S_x(x)|$ in the range-discrete grid. This is an obvious adaptive criterion widely used in many adaptive mesh methods [19, 28, 29]. While complex adaptive operations have to be involved in these methods, it is done by the range-discrete mesh simply via an equidistance discretization in value domain.

With the technique illustrated above, a range-discrete mesh can be obtained for general solutions. Next, the numerical scheme based on the range-discrete mesh for solving (1) will be present.

3. Numerical Scheme Based on the Range-Discrete Mesh

For the initial-boundary value problem of (1), one can get an initial range-discrete mesh using the technique illustrated in Section 2. Once a range-discrete mesh is obtained, a dynamic control volume can be formed around each mesh point. Take $[x_1(t), x_2(t)]$ in Figure 2 as an example, and let $S(x_1(t), t) \equiv S_1 = (S_i + S_{i-1})/2$ and $S(x_2(t), t) \equiv S_2 = (S_{i+1} + S_i)/2$, making the control volume moving with the flow. Integrating (1) on this control volume and a small time interval $[t_0, t_1]$ where $t_1 - t_0 = \Delta t$, one can get

$$\begin{aligned} & \int_{t_0}^{t_1} \int_{x_1(t)}^{x_2(t)} \frac{\partial S}{\partial t} dx dt + \int_{t_0}^{t_1} \int_{x_1(t)}^{x_2(t)} \frac{\partial f(S)}{\partial x} dx dt \\ &= \int_{t_0}^{t_1} \int_{x_1(t)}^{x_2(t)} \frac{\partial}{\partial x} \left(\epsilon(S) \frac{\partial S}{\partial x} \right) dx dt, \end{aligned} \quad (3)$$

where the integration of the convective and diffusive term can be done directly as

$$\begin{aligned} & \int_{t_0}^{t_1} \int_{x_1(t)}^{x_2(t)} \frac{\partial f(S)}{\partial x} dx dt \\ &= \int_{t_0}^{t_1} [f(S(x_2(t), t)) - f(S(x_1(t), t))] dt \\ &= \int_{t_0}^{t_1} [f(S_2) - f(S_1)] dt, \end{aligned}$$

$$\begin{aligned} & \int_{t_0}^{t_1} \int_{x_1(t)}^{x_2(t)} \frac{\partial}{\partial x} \left(\epsilon(S) \frac{\partial S}{\partial x} \right) dx dt \\ &= \int_{t_0}^{t_1} [(\epsilon(S) S_x)|_{x_2(t)} - (\epsilon(S) S_x)|_{x_1(t)}] dt \\ &= \int_{t_0}^{t_1} [\epsilon(S_2) S_{x_2} - \epsilon(S_1) S_{x_1}] dt. \end{aligned} \quad (4)$$

As for the transient term, according to Appendix A, if the solution curve $S(x, t)$ is monotone in $[x_1(t), x_2(t)]$, we have

$$\begin{aligned} \int_{t_0}^{t_1} \int_{x_1(t)}^{x_2(t)} \frac{\partial S}{\partial t} dx dt &= - \int_{S_1}^{S_2} x(S, t_1) dS \\ &+ \int_{S_1}^{S_2} x(S, t_0) dS. \end{aligned} \quad (5)$$

Consequently, the integration form of (1) is

$$\begin{aligned} & \int_{S_1}^{S_2} x(S, t_1) dS - \int_{S_1}^{S_2} x(S, t_0) dS \\ &= \int_{t_0}^{t_1} [f(S_2) - \epsilon(S_2) S_{x_2}] - [f(S_1) - \epsilon(S_1) S_{x_1}] dt. \end{aligned} \quad (6)$$

The item on the left-hand side of (6) is the variation of the total quantity of the control volume over the time interval $[t_0, t_1]$; $f(S_1) - \epsilon(S_1) S_{x_1}$ and $f(S_2) - \epsilon(S_2) S_{x_2}$ can be interpreted as the left and right boundary flux, respectively. Thus, (6) is actually a natural result of mass conservation principle. It should be emphasized that (6) is exact as it is derived from (1) without any approximation.

Using linear approximation in the FDM manner, we can obtain first-order discrete form of (6) as

$$\begin{aligned} & (x_i^{t_0+\Delta t} - x_i^{t_0})(S_2 - S_1) \\ &= (f(S_2) - \epsilon(S_2) S_{x_2}) \Delta t \\ & - (f(S_1) - \epsilon(S_1) S_{x_1}) \Delta t, \end{aligned} \quad (7)$$

where

$$\begin{aligned} S_2 &= \frac{S_{i+1} + S_i}{2}, \\ S_1 &= \frac{S_i + S_{i-1}}{2}, \\ S_{x_2} &= \frac{S_{i+1} - S_i}{x_{i+1} - x_i}, \\ S_{x_1} &= \frac{S_i - S_{i-1}}{x_i - x_{i-1}}. \end{aligned} \quad (8)$$

If the items on the right-hand side of (7) are the values at t , the discrete equation is explicit; and if they are values at $t + \Delta t$, it is implicit. One may notice that (7) is quite similar to the discrete equations of FDM and can be solved in the same way

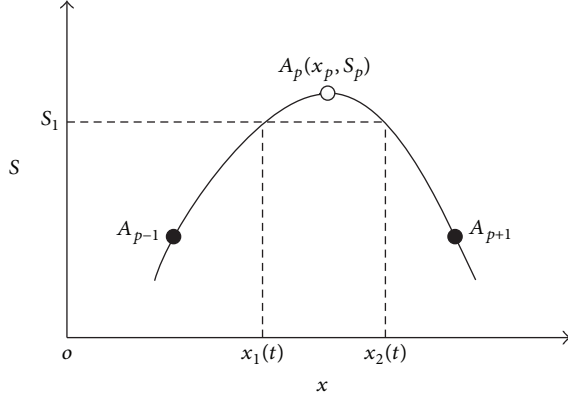


FIGURE 3: The dynamic control volume around an extremum point.

of FDM, for example, Newton's method. Generally speaking, other kinds of discrete equations and higher-order forms can also be obtained in the same manner as FDM.

However, we should emphasize that the unknown in (7) is x_i , not S_i , which is the essential difference between the proposed method and FDM. It means that the movements of the mesh points are tracked while their values are fixed throughout the computation process. When new positions of the mesh points are located, the approximation of the solution is obtained. Moreover, adaptivity is obtained simultaneously as a benefit of the range-discrete strategy.

We should note that though derived in different manners, (7) is similar to that in the method of Fayers and Sheldon [25]. And also, it only fits for monotone solutions in $[x_1(t), x_2(t)]$. To make the range-discrete grid work for nonmonotone solutions, adjustments are needed.

4. Adjustments for the Extremum Point

As has been mentioned in Section 2, a mesh point, for example, A_p in Figure 1 or Figure 3, is set at the extremum if the solution is nonmonotone. For the control volume of such an extremum point, (6) does not fit and adjustments are needed.

The dynamic control volume $[x_1(t), x_2(t)]$ for an extremum mesh point A_p is shown in Figure 3, where $S_1 = S_2 = S_{p-1} + \Delta S/2$. According to Appendix A, The items inside the brackets in (3) for the control volume of an extremum point are

$$\int_{t_0}^{t_1} \int_{x_1(t)}^{x_2(t)} \frac{\partial S}{\partial t} dx dt = \int_{x_1(t_1)}^{x_2(t_1)} (S(x, t + \Delta t) - S_2) dx - \int_{x_1(t_0)}^{x_2(t_0)} (S(x, t) - S_2) dx. \quad (9)$$

So, we have

$$\begin{aligned} & \int_{x_1(t_1)}^{x_2(t_1)} (S(x, t_1) - S_2) dx - \int_{x_1(t_0)}^{x_2(t_0)} (S(x, t_0) - S_2) dx \\ &= \int_{t_0}^{t_1} [-\epsilon(S_2) S_{x_2}] - [-\epsilon(S_1) S_{x_1}] dt. \end{aligned} \quad (10)$$

With an parabolic approximation of the solution curve between $[x_1(t), x_2(t)]$, we obtain

$$S(x, t) = S_p - \frac{4(S_p - S_{p-1})}{(x_{p+1} - x_{p-1})^2} \left(x - \frac{x_{p+1} + x_{p-1}}{2} \right)^2. \quad (11)$$

Consequently, we have

$$\begin{aligned} & \int_{x_1}^{x_2} (S(x, t) - S_2) dx \\ &= \frac{2}{3} \sqrt{\frac{S_p - S_1}{S_{p-1} - S_1}} (S_p - S_1) (x_{p+1} - x_{p-1}), \end{aligned} \quad (12)$$

$$\begin{aligned} & \epsilon(S_2) S_{x_2} - \epsilon(S_1) S_{x_1} \\ &= -8\epsilon(S_1) \sqrt{\frac{S_p - S_1}{S_{p-1} - S_1}} \frac{S_p - S_{p-1}}{x_{p+1} - x_{p-1}}. \end{aligned}$$

Thus, the discrete equation for an extremum point is obtained.

One can conclude from (10) that, with a positive $\epsilon(S)$, left-hand side of (10) always decreases as time goes on. It means that the value of the extremum S_p is approaching S_1 , making the extremum point a special case: its value and position are always changing and the control volume is shrinking.

To avoid too small a control volume, the mesh points A_{p-1} and A_{p+1} will be removed from the range-discrete mesh if $|S_p - S_1|$ is less than a threshold value, for example, $|S_p - S_1| < \Delta S/4$. Then, let $S_1 = S_{p-2} + \Delta S/2$ and a new control volume is formed immediately to continue the computation. In this way, the extremum point in the initial mesh is always an extremum point and represents the movement of the extremum in the solution.

5. Boundary Conditions

5.1. Dirichlet Boundary Condition. A Dirichlet boundary condition, that is, $S(x_d, t) = S_d$, can be used directly in the discrete equation in the same way as FDM. That is, one can consider a discrete point A_k , set at the boundary to provide the boundary information, with its position and value always fixed as $x_k = x_d$ and $S_k = S_d$ during the computing process.

5.2. Moving Boundary Condition. As has been mentioned in Section 2, either endpoint of a constant piece in the solution is treated as a boundary condition. The value of this boundary is fixed, which is quite similar to the Dirichlet boundary condition, but the position of the boundary varies. Thus, we name it a moving boundary condition.

At a moving boundary, we have $S(\lambda(t), t) = S_f$ and $(\epsilon(S)S_x)|_{\lambda(t)} = 0$ (see Appendix B). Thus, it can be involved in the range-discrete mesh by a boundary point A_k with $S_k = S_f$ and $(\epsilon(S)S_x)|_{A_k} = 0$. The boundary condition is not involved in a discrete manner as what was done in [25], but in a more precise manner, making it more promising for high precision.

One can see that the position of the moving boundary point is not really needed in the range-discrete equation.

However, a constant piece in the solution might disappear and the solution on two sides will then interact with each other. To illustrate this, we need to merge the two boundary points into a normal mesh point if their distance is less than a threshold d_{\min} . The position of the boundary point is only needed here and can be interpolated using $S(x) = a_0(x - \lambda)^n$ by two nearby mesh points, where n can be settled using the method illustrated in Appendix B.

As a benefit of such a special boundary condition, the singular point, where the gradient of the solution might be discontinuous or infinite, as indicated in Appendix B, can be maintained by the proposed method. Numerical tests in Section 6 also confirm this.

5.3. Neumann Boundary Condition. Given a Neumann boundary condition $S_x(x_b) = q_b$, a boundary mesh point A_k will also be set. The discrete value of A_k is determined dynamically both by the value of A_i , which is the point nearest the boundary, and by the sign of q_b , that is, $S_k = S_i - \text{sgn}(q_b)\Delta S$ for the left boundary and $S_k = S_i + \text{sgn}(q_b)\Delta S$ for the right boundary. The position of A_k can be calculated by an linear interpolation:

$$q_b = \frac{S_k - S_i}{x_k - x_i} \quad (13)$$

or other higher-order interpolations. As we can see, the position of a Neumann boundary point determined by (13) can be either in or out of the calculation area. So, we design the following rules:

- (1) If x_k is out the calculation area, computing continuous on.
- (2) If x_k is in the calculation area, this boundary point becomes a normal mesh point and a new boundary point will be inserted into the range-discrete mesh.
- (3) If x_i is out of the calculation area, A_i will be removed immediately and the information of A_k is determined by the new nearest boundary mesh point.

6. Numerical Examples

6.1. A Travelling Wave Solution. With $f(S) = S^2/2$ and $\epsilon(S)$ being a constant, we have Burgers' equation from (1):

$$S_t + \left(\frac{1}{2}S^2\right)_x = \epsilon S_{xx}. \quad (14)$$

It is easy to verify that this equation has the travelling wave solution:

$$S(x, t) = \frac{2c\epsilon^{c(ct-x)/\epsilon}}{1 + e^{c(ct-x)/\epsilon}}, \quad (15)$$

where c is the speed of the wave. With $c = 1$, (15) is the solution of (14) with an initial condition $S(x, 0) = 2e^{-x/\epsilon}/(1 + e^{-x/\epsilon})$. Figure 4 and Table 1 show the solutions and error tables at different time using the proposed method when $\epsilon = 10^{-1}, 10^{-2}, 10^{-3}$. It can be seen from Figure 4 that mesh points

are located adaptively according to the spatial gradient. Moreover, the adaptivity follows the movement of the travelling front. As a benefit, with only a few mesh points, the front is solved with good accuracy.

One should notice that, with the diffusive coefficient ϵ decreasing, the front becomes steeper, tending to form a moving shock. While it is hard to maintain the accuracy near the front with the same number of mesh points using FDM, the accuracy of the proposed method for different diffusive coefficients is uniform.

Furthermore, the calculating area of this problem is actually infinite, that is, $x \in [-\infty, +\infty]$. While most numerical methods approach this within a finite area, the proposed method solves this problem in an infinite area simply with two moving boundary conditions: $S(-\infty) = 1, S_x(-\infty) = 0$ and $S(+\infty) = 0, S_x(+\infty) = 0$.

6.2. A Nonmonotone Case. In this numerical example, the solution of Burgers' equation is designed to be nonmonotone to test the numerical method. The initial condition and boundary condition are set to be $S(x, 0) = \sin(\pi x), S(0, t) = 0$ and $S(1, t) = 0$, respectively. According to Caldwell and Smith [30], the solution is

$$S(x, t) = \frac{2\pi\epsilon \sum_{n=1}^{\infty} a_n e^{-n^2\pi^2\epsilon t} n \sin(n\pi x)}{a_0 + \sum_{n=1}^{\infty} a_n e^{-n^2\pi^2\epsilon t} \cos(n\pi x)}, \quad (16)$$

where

$$\begin{aligned} a_0 &= \int_0^1 \exp\{-(2\pi\epsilon)^{-1}[1 - \cos(\pi x)]\} dx, \\ a_n &= 2 \int_0^1 \exp\{-(2\pi\epsilon)^{-1}[1 - \cos(\pi x)]\} \cos(n\pi x) dx \quad (17) \\ &\quad (n = 1, 2, 3, \dots). \end{aligned}$$

The numerical solutions at different times with diffusive coefficients $\epsilon = 10^{-1}, 10^{-2}, 10^{-3}$ are given by Figure 5 and the errors are Table 2. The results also show good performance of the proposed method for nonmonotone solutions. Again, the adaptivity functions well and tracks the front in an accurate manner.

6.3. Nonlinear Diffusive Term. How a nonlinear diffusive term effects the distribution of the front is tested here. Consider Burgers' equation with a nonlinear diffusive term:

$$S_t + \left(\frac{1}{2}S^2\right)_x = (\epsilon(S) S_x)_x \quad (18)$$

with two Dirichlet boundary conditions $S(0, t) = 1, S(1, t) = 0$ and a lamp initial condition, which is $S(0 \leq x \leq 0.2, t = 0) = 1 - 5x$ and $S(0.2 < x \leq 1, t = 0) = 0$. Diffusive coefficients set as $\epsilon(S) = 0.1S^\alpha$ with $\alpha = 0.5, 1, 2$ are tested. Solutions at $t = 0.5$ are shown in Figure 6.

It is shown by Figure 6 that the gradient of the solution with $\alpha = 0.5$ tends to be zero at the front and thus a smooth solution. However, the gradient with $\alpha = 2$ tends to be infinite at the front, resulting in a continuous but not

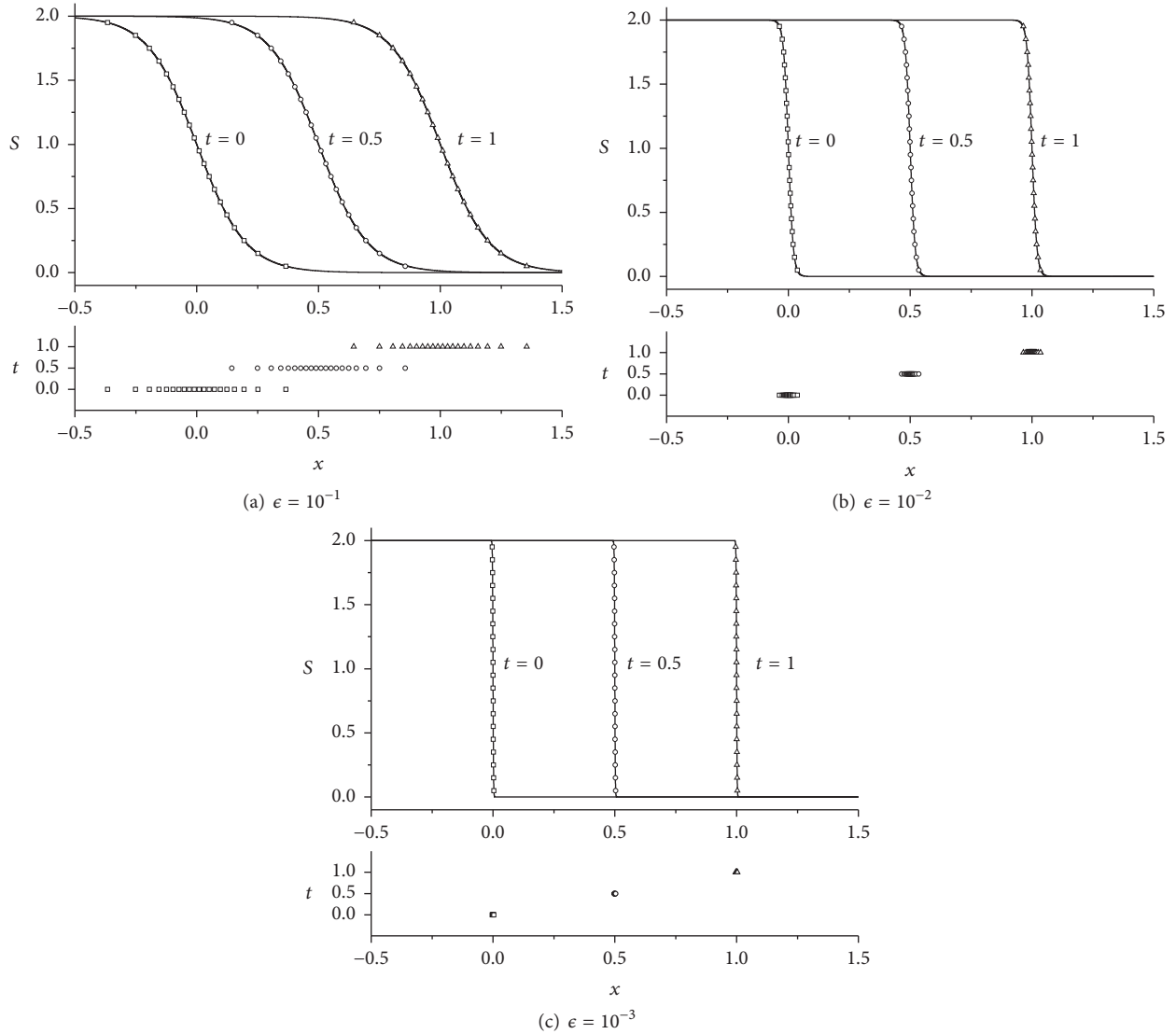


FIGURE 4: Numerical solutions at $t = 0.5$ and $t = 1$ of the travelling wave with different diffusive coefficients. Solid line represents exact solutions and squares, circles, and triangles in S - x figures are numerical solutions. The t - x figures below each S - x figure show the spatial distribution of the mesh points at different time.

TABLE 1: Error table of the numerical solution of Burgers' equation with different diffusive coefficients at different time. N is the number of mesh points.

ϵ	t	errors	$N = 10$	20	40	80	160
10^{-1}	0.5	L^∞ error	$1.00E-02$	$5.23E-03$	$2.70E-03$	$1.37E-03$	$6.95E-04$
		L^1 error	$4.43E-03$	$2.39E-03$	$1.35E-03$	$7.61E-04$	$4.21E-04$
	1.0	L^∞ error	$1.13E-02$	$5.83E-03$	$2.96E-03$	$1.50E-03$	$7.52E-04$
		L^1 error	$5.43E-03$	$2.77E-03$	$1.39E-03$	$7.17E-04$	$3.74E-04$
10^{-2}	0.5	L^∞ error	$1.16E-02$	$5.97E-03$	$3.03E-03$	$1.53E-03$	$7.66E-04$
		L^1 error	$5.64E-04$	$2.94E-04$	$1.50E-04$	$7.59E-05$	$3.82E-05$
	1.0	L^∞ error	$1.16E-02$	$5.97E-03$	$3.03E-03$	$1.53E-03$	$7.66E-04$
		L^1 error	$5.64E-04$	$2.94E-04$	$1.50E-04$	$7.59E-05$	$3.82E-05$
10^{-3}	0.5	L^∞ error	$1.16E-02$	$5.97E-03$	$3.03E-03$	$1.53E-03$	$7.66E-04$
		L^1 error	$5.64E-05$	$2.94E-05$	$1.50E-05$	$7.59E-06$	$3.82E-06$
	1.0	L^∞ error	$1.16E-02$	$5.97E-03$	$3.03E-03$	$1.53E-03$	$7.66E-04$
		L^1 error	$5.64E-05$	$2.94E-05$	$1.50E-05$	$7.59E-06$	$3.82E-06$

TABLE 2: Error table of the numerical solution of the burgers' equation with different diffusive coefficients at different time. N is the number of mesh points.

ϵ	t	errors	$N = 10$	20	40	80	160
10^{-1}	0.5	L^∞ error	$7.95E - 03$	$2.94E - 03$	$1.18E - 03$	$3.64E - 04$	$1.72E - 04$
		L^1 error	$2.83E - 03$	$8.55E - 04$	$2.60E - 04$	$1.04E - 04$	$7.38E - 05$
	1.0	L^∞ error	$1.46E - 02$	$5.16E - 03$	$1.50E - 03$	$5.35E - 04$	$1.26E - 04$
		L^1 error	$5.41E - 03$	$1.60E - 03$	$4.46E - 04$	$1.11E - 04$	$6.53E - 05$
10^{-2}	0.5	L^∞ error	$3.65E - 02$	$7.29E - 03$	$2.39E - 03$	$6.99E - 04$	$4.64E - 04$
		L^1 error	$5.83E - 03$	$1.18E - 03$	$3.28E - 04$	$9.05E - 05$	$4.18E - 05$
	1.0	L^∞ error	$6.16E - 02$	$1.97E - 02$	$9.19E - 03$	$2.93E - 03$	$9.49E - 04$
		L^1 error	$7.38E - 03$	$1.66E - 03$	$6.63E - 04$	$1.95E - 04$	$5.95E - 05$
10^{-3}	0.5	L^∞ error	$2.42E - 02$	$1.10E - 02$	$4.52E - 03$	$1.52E - 03$	$1.49E - 03$
		L^1 error	$5.00E - 03$	$1.46E - 03$	$4.02E - 04$	$9.82E - 05$	$9.71E - 05$
	1.0	L^∞ error	$9.05E - 02$	$4.77E - 02$	$1.68E - 02$	$7.01E - 03$	$2.94E - 03$
		L^1 error	$3.31E - 03$	$1.70E - 03$	$2.07E - 04$	$1.13E - 04$	$6.32E - 05$

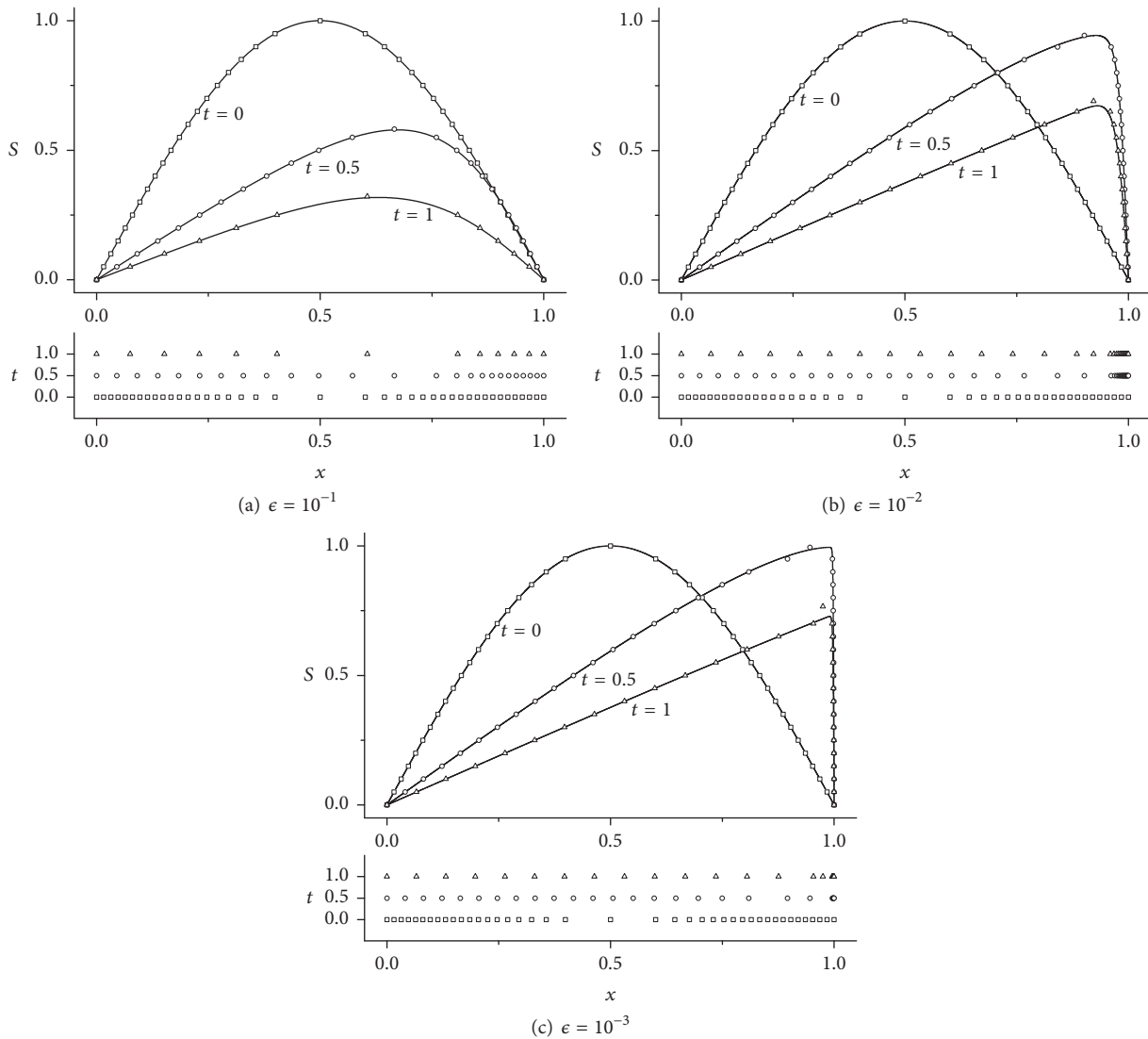


FIGURE 5: Numerical solutions obtained by the proposed method at $t = 0.5$ and $t = 1$ of Burgers' equation with different diffusive coefficients. Solid line represents exact solutions and squares, circles, and triangles in S - x figures are numerical solutions. The t - x figures below each S - x figure show the spatial distribution of the mesh points at different time.

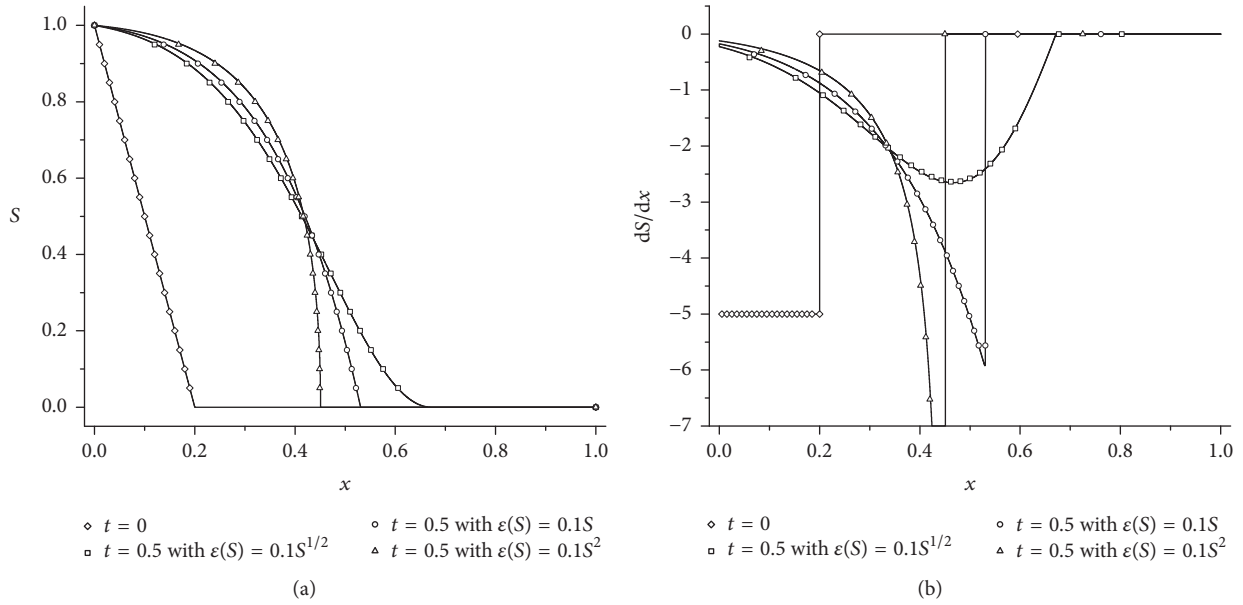


FIGURE 6: Numerical solutions of different nonlinear diffusive coefficients: (a) $S(x)$ and (b) dS/dx .

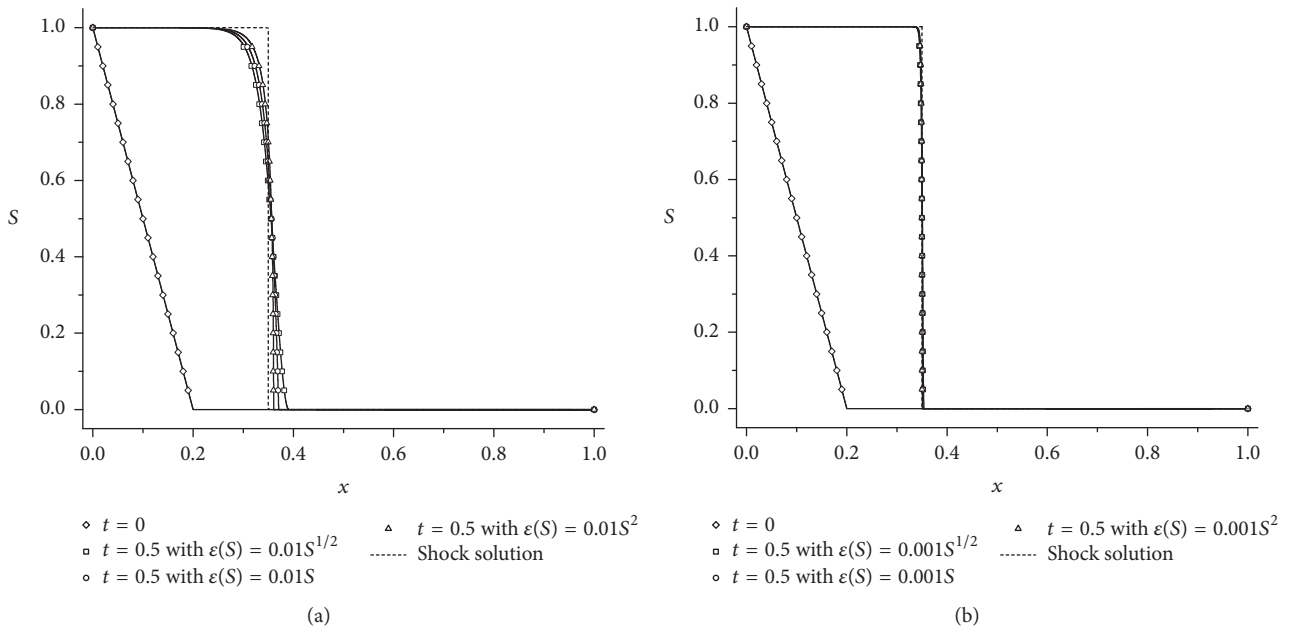


FIGURE 7: Numerical solutions of different nonlinear diffusive coefficients: (a) $\epsilon(S) = 0.01S^\alpha$ and (b) $\epsilon(S) = 0.001S^\alpha$.

smooth solution. As a critical condition, the gradient tends to be a limited value at the front with $\alpha = 1$, which is also a conclusion of Appendix B.

The solutions with diffusive coefficients set as $\epsilon(S) = 0.01S^\alpha$ and $\epsilon(S) = 0.001S^\alpha$ with $\alpha = 0.5, 1, 2$ are shown in Figure 7. With a degenerating diffusive coefficient, the nonlinear term has less impact on the solution, approaching the shock solution of the corresponding hyperbolic equation. With such

a small diffusive coefficient, not only its nonlinearity but also the whole diffusive term can be neglected. If the diffusive term is not so small in contrast to the convective term, its nonlinearity does have a significant influence on the solution.

6.4. Buckley-Leverett Equation. In this example, a two-phase flow problem in porous medium is solved. Considering an infinite horizontal layer, the region $x < 0$ is full of the wetting

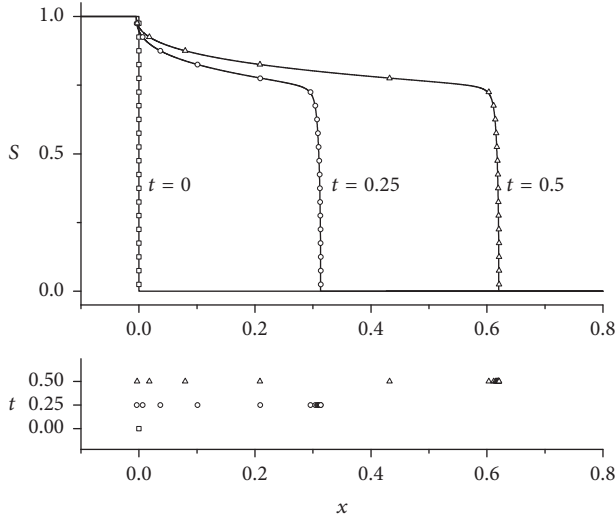


FIGURE 8: Numerical solutions of the Buckley-Leveret equation at $t = 0.25$ and $t = 0.5$. The exact solution shown in solid is obtained by FDM with a fine mesh.

phase, for example, water, and the region $x > 0$ is occupied by a nonwetting phase, for example, oil, initially. The governing equation can be obtained by Buckley-Leverett theory [31]:

$$\phi \frac{\partial S}{\partial t} + \frac{\partial}{\partial x} \left[V(t) f(S) + \frac{KK_{rn}}{\mu_n} f(S) \frac{dP_c}{dS} \frac{\partial S}{\partial x} \right] = 0, \quad (19)$$

where S is the saturation of the wetting phase, $V(t)$ is the total infiltration rate, $P_c(S)$ represents the capillary pressure, and $f(S) = \mu_o K_{rw} / (\mu_n K_{rw} + \mu_w K_{rn})$ is the flux coefficient of the wetting phase. In this example, $V(t) = 1$ and porosity and absolute permeability of the layer are nondimensionalized to be $\phi = 1$ and $K = 1$, respectively. Relative permeability of the wetting phase (w) and the nonwetting phase (n) are $K_{rw} = S^4$ and $K_{rn} = (1 + S)(1 - S)^3$, respectively, and their viscosity is $\mu_w = \mu_n = 1$. The capillary pressure is the J -function $P_c = 0.1S^{-0.5}$.

The convective term is typically nonconvex. Another problem is that the diffusive term is nonlinear, which will cause infinite saturation gradients at the front of each phase. Most methods will smear this singularity out because of their numerical diffusion, no matter how small. With the range-discrete mesh method, this singular feature can be maintained by dealing the front as a moving boundary condition.

The numerical solutions at different time with $\Delta S = 0.05$ are shown in Figure 8. It is obvious that there exists not only a steep front where saturation varies quickly but also two singular points at $S \rightarrow 0$ and $S \rightarrow 1$, where the saturation gradient tends to be infinite. As a benefit of the range-discrete mesh and the moving boundary condition, the steep front is described precisely and two singular points are maintained intactly with only 20 mesh points.

7. Conclusion

Achievements of this paper are summarized as follows:

- (i) Traditional adaptive mesh methods involve complex adaptive operations and introduce numerical dissipation by interpolation.
- (ii) We have developed a self-adaptive numerical method based on uniformly distributed range-discrete mesh for convection-diffusion equation. The governing equation is discretized by integration on the dynamic control volume of each mesh point. The goal of adaptivity and solving the equation are achieved simultaneously by solving the discretized equation, which moves the mesh points but does not change their values.
- (iii) The method was verified against the analytical solution of several numerical examples. Steep fronts were tracked accurately with only a few mesh points. The residual error is found to be independent of the magnitude of diffusion.
- (iv) With a moving boundary condition, singular points at the fronts were maintained by the proposed method. It is found that, despite its magnitude, a nonlinear diffusion coefficient $\epsilon(S) = S^\alpha$ ($\alpha \geq 1$) can produce singularities where the gradient of the solution can be discontinuous or infinite.

In all, the proposed method has shown advantages in solving convection-diffusion equations with high efficiency. The method can serve as a fast numerical tool for a wide range of front propagation problems, such as underground water flow, chemical floods of oil fields, and air pollution problems. On the other hand, it is obvious that, for higher dimensions, the elements in the range-discrete mesh become contour lines or contour planes and the solution can be achieved by tracking their movements. This work is in our next research scope.

Appendix

A. Integration of the Transient Term in (3)

In (3), we have the integration of the transient term over the dynamic control volume $[x_1(t), x_2(t)]$. To understand this term, first, we know

$$\begin{aligned} \frac{\partial}{\partial t} \int_{x_1(t)}^{x_2(t)} S dx &= \int_{x_1(t)}^{x_2(t)} \frac{\partial S}{\partial t} dx + S(x_2(t), t) \frac{dx_2(t)}{dt} \\ &\quad - S(x_1(t), t) \frac{dx_1(t)}{dt} \\ &= \int_{x_1(t)}^{x_2(t)} \frac{\partial S}{\partial t} dx + S_2 \frac{dx_2(t)}{dt} \\ &\quad - S_1 \frac{dx_1(t)}{dt}. \end{aligned} \quad (A.1)$$

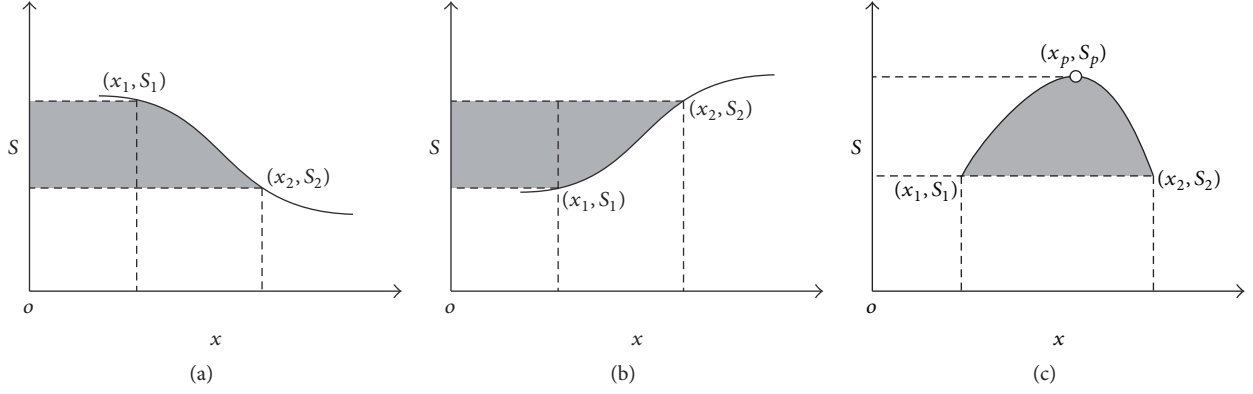


FIGURE 9: Geometric description of the integration.

So, integration of the transient term in (3) is

$$\begin{aligned}
 & \int_{t_0}^{t_1} \int_{x_1(t)}^{x_2(t)} \frac{\partial S}{\partial t} dx dt \\
 &= \int_{t_0}^{t_1} \frac{\partial}{\partial t} \int_{x_1(t)}^{x_2(t)} S dx dt - \int_{t_0}^{t_1} S_2 \frac{dx_2(t)}{dt} dt \\
 & \quad + \int_{t_0}^{t_1} S_1 \frac{dx_1(t)}{dt} dt \\
 &= \int_{x_1(t_1)}^{x_2(t_1)} S dx - \int_{x_1(t_0)}^{x_2(t_0)} S dx \\
 & \quad - S_2 [x_2(t_1) - x_2(t_0)] + S_1 [x_1(t_1) - x_1(t_0)] \\
 &= \left[\int_{x_1(t)}^{x_2(t)} S dx - S_2 x_2(t) + S_1 x_1(t) \right]^{t_1} \\
 & \quad - \left[\int_{x_1(t)}^{x_2(t)} S dx - S_2 x_2(t) + S_1 x_1(t) \right]^{t_0}.
 \end{aligned} \tag{A.2}$$

The items inside the brackets in (A.2) are

$$\begin{aligned}
 & \int_{x_1(t)}^{x_2(t)} S dx - S_2 x_2(t) + S_1 x_1(t) \\
 &= \int_{x_1(t)}^{x_2(t)} S dx - \int_0^{x_2(t)} S_2 dx + \int_0^{x_1(t)} S_1 dx \\
 &= \int_{x_1(t)}^{x_2(t)} S dx - \left(\int_0^{x_1(t)} S_2 dx + \int_{x_1(t)}^{x_2(t)} S_2 dx \right) \\
 & \quad + \int_0^{x_1(t)} S_1 dx \\
 &= \int_0^{x_1(t)} (S_1 - S_2) dx + \int_{x_1(t)}^{x_2(t)} (S(x) - S_2) dx.
 \end{aligned} \tag{A.3}$$

which can be understood according to Figure 9. Consider the following three situations:

- (1) $S = S(x, t)$ is monotone decreasing in $[x_1(t), x_2(t)]$, as shown in Figure 9(a). Then (A.3) is the shaded area shown in Figure 9(a). So, we have

$$\begin{aligned}
 & \int_0^{x_1(t)} (S_1 - S_2) dx + \int_{x_1(t)}^{x_2(t)} (S(x) - S_2) dx \\
 &= - \int_{S_1}^{S_2} x(S, t) dS.
 \end{aligned} \tag{A.4}$$

- (2) $S = S(x, t)$ is monotone increasing in $[x_1(t), x_2(t)]$, as shown in Figure 9(b). Then (A.3) is the shaded negative area shown in Figure 9(b). So, we have

$$\begin{aligned}
 & \int_0^{x_1(t)} (S_1 - S_2) dx + \int_{x_1(t)}^{x_2(t)} (S(x) - S_2) dx \\
 &= - \int_0^{x_1(t)} (S_2 - S_1) dx - \int_{x_1(t)}^{x_2(t)} (S_2 - S(x)) dx \\
 &= - \int_{S_1}^{S_2} x(S, t) dS.
 \end{aligned} \tag{A.5}$$

- (3) $S = S(x, t)$ is nonmonotone in $[x_1(t), x_2(t)]$, as shown in Figure 9(c). As we have $S_1 = S_2$, so

$$\begin{aligned}
 & \int_0^{x_1(t)} (S_1 - S_2) dx + \int_{x_1(t)}^{x_2(t)} (S(x) - S_2) dx \\
 &= \int_{x_1(t)}^{x_2(t)} (S(x) - S_2) dx
 \end{aligned} \tag{A.6}$$

is the shaded area or negative area according to the sign of $S(x) - S_2$.

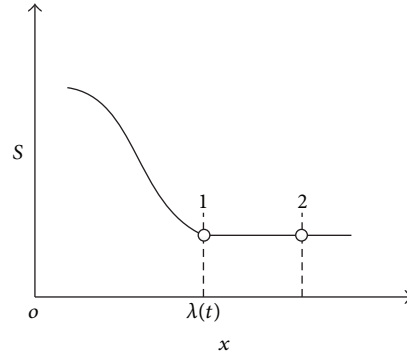


FIGURE 10: The description of a moving boundary condition.

In short, the integration of the transient item is

$$\int_{t_0}^{t_1} \int_{x_1(t)}^{x_2(t)} \frac{\partial S}{\partial t} dx dt = \begin{cases} - \int_{S_1}^{S_2} x(S, t_1) dS + \int_{S_1}^{S_2} x(S, t_0) dS, & \text{for monotone } S(x, t) \\ \int_{x_1(t_1)}^{x_2(t_1)} (S(x, t_1) - S_2) dx - \int_{x_1(t_0)}^{x_2(t_0)} (S(x, t_0) - S_2) dx, & \text{for non-monotone } S(x, t). \end{cases} \quad (\text{A.7})$$

B. The Moving Boundary Condition

Assume that there is a piece of constant solution at time t , a moving boundary condition is formed at either end of the constant piece. In this section, without loss of generality, the constant piece is $x > \lambda(t)$, which means that $S(x \geq \lambda(t), t) = S_C$, and $x = \lambda(t)$ is the so-called moving boundary.

A dynamic control volume $[x_1, x_2]$, where $x_1(t) = \lambda(t)$ and x_2 is an arbitrary point in the constant piece, is chosen as shown in Figure 10. For $S(x \geq \lambda(t), t) = S_C$, we have

$$S(x, t) = S_C, \quad x \in [x_1(t), x_2(t)] \quad (\text{B.1})$$

and also $S_1 = S_2 = S_C$. For this control volume, the integration equation becomes

$$0 = \int_t^{t+\Delta t} \left[\epsilon(S_2) \left(\frac{\partial S}{\partial x} \right) \Big|_{x_2(t)} - \epsilon(S_1) \left(\frac{\partial S}{\partial x} \right) \Big|_{x_1(t)} \right] dt. \quad (\text{B.2})$$

For $x = x_2(t)$, we have $S_x(x_2(t)) = 0$; thus (B.2) becomes

$$\left(\epsilon(S) \frac{\partial S}{\partial x} \right) \Big|_{\lambda(t)} = 0. \quad (\text{B.3})$$

Therefore, (B.3) and $S(\lambda(t)) = S_C$ both hold for the front point $x = \lambda(t)$ and will serve as the boundary condition for range-discrete method.

However, $\lambda(t)$ is not a given condition but rather a result of the solution. It can be calculated by an interpolation as one of the two following cases:

- (1) If $\epsilon(S) \rightarrow \epsilon_0 \neq 0$ when $x \rightarrow \lambda^-$ or $S \rightarrow S_C$: from (B.3), we can conclude that $S_x(\lambda(t)) = 0$. Thus, using the Taylor series, the solution when $x \rightarrow \lambda^-$ is

$$S(x) = S(\lambda) + S_x(\lambda)(\lambda - x) + \frac{1}{2} S_{xx}(\lambda)(\lambda - x)^2 + \frac{1}{6} S_{xxx}(\lambda)(\lambda - x)^3 + \dots \quad (\text{B.4})$$

Dropping the items of order more than 2, we have an approximation as

$$S(x) = S_C + a_0(\lambda - x)^2. \quad (\text{B.5})$$

- (2) If $\epsilon(S) \rightarrow 0$ when $x \rightarrow \lambda^-$ or $S \rightarrow S_C$: an approximation behavior of the diffusive coefficient can be obtained as $\epsilon(S) \rightarrow C_\epsilon(S - S_C)^\alpha$ when $S \rightarrow S_C$. And we assume that the solution when $x \rightarrow \lambda^-$ can be approximated by $S(x) = S_C + a_0(\lambda - x)^n$. n can be calculated using the limitation that the quality flux cannot be infinite, that is, $Q(x)/S(x) < \infty$ when $x \rightarrow \lambda^-$, where

$$Q(x) = f(S(x)) - \epsilon(S(x)) \frac{\partial S(x)}{\partial x}. \quad (\text{B.6})$$

Thus, $\epsilon(S)S_x$ should approach zero at the same speed as $S(x) - S_C$ when $x \rightarrow \lambda^-$. So, we have $S_x(x) = -n(\lambda(t) - x)^{n-1}$, $\epsilon(S) = C_\epsilon a_0^\alpha (\lambda - x)^{\alpha n}$ and finally

$$\epsilon(S)S_x = -nC_\epsilon a_0^\alpha (\lambda - x)^{\alpha n + n - 1}. \quad (\text{B.7})$$

Thus, $\alpha n + n - 1 = n$, and so we have $\alpha = 1/n$. This means that, when $x \rightarrow \lambda^-$,

$$S(x) = S_C + a_0 (\lambda - x)^{1/\alpha}. \quad (\text{B.8})$$

It can be seen from (B.5) that when $\alpha > 1$, the gradient of the solution tends to be infinite when $x \rightarrow \lambda(t)$. The situation when $\alpha = 2$ graphed in Figure 7 shows us an example.

With the information of the two neighboring mesh points known, $\lambda(t)$ can be obtained approximately using (B.5) or (B.8).

Conflicts of Interest

The authors declare that they have no conflicts of interest.

Acknowledgments

This work is supported by the National Natural Science Foundation of China (nos. 11572315 and 11202205) and CNPC-CAS Science and Technology Cooperation Project (no. 2015A-4812).

References

- [1] B. A. Finlayson, *Numerical Methods for Problems with Moving Fronts*, Ravenna Park Publishing, Incorporated, Seattle, WA, USA, 1992.
- [2] L. Debnath, *Nonlinear Partial Differential Equations for Scientists and Engineers*, Birkhäuser Boston, Inc, Boston, MA, USA, 3rd edition, 2011.
- [3] R. E. Ewing and H. Wang, "A summary of numerical methods for time-dependent advection-dominated partial differential equations," *Journal of Computational and Applied Mathematics*, vol. 128, no. 1-2, pp. 423–445, 2001.
- [4] R. J. LeVeque, *Finite Volume Methods for Hyperbolic Problems*, Cambridge Texts in Applied Mathematics, Cambridge University Press, Cambridge, UK, 2002.
- [5] A. Kurganov and E. Tadmor, "New high-resolution central schemes for nonlinear conservation laws and convection-diffusion equations," *Journal of Computational Physics*, vol. 160, no. 1, pp. 241–282, 2000.
- [6] T. Nazir, M. Abbas, A. I. Ismail, A. A. Majid, and A. Rashid, "The numerical solution of advection-diffusion problems using new cubic trigonometric B-splines approach," *Applied Mathematical Modelling. Simulation and Computation for Engineering and Environmental Systems*, vol. 40, no. 7-8, pp. 4586–4611, 2016.
- [7] P. K. Sweby, "High resolution schemes using flux limiters for hyperbolic conservation laws," *SIAM Journal on Numerical Analysis*, vol. 21, no. 5, pp. 995–1011, 1984.
- [8] K. Alhumaizi, "Comparison of finite difference methods for the numerical simulation of reacting flow," *Computers and Chemical Engineering*, vol. 28, no. 9, pp. 1759–1769, 2004.
- [9] C.-W. Shu, "High order weighted essentially nonoscillatory schemes for convection dominated problems," *SIAM Review*, vol. 51, no. 1, pp. 82–126, 2009.
- [10] H. Ding and Y. Zhang, "A new difference scheme with high accuracy and absolute stability for solving convection-diffusion equations," *Journal of Computational and Applied Mathematics*, vol. 230, no. 2, pp. 600–606, 2009.
- [11] H. K. Dahle, M. S. Espedal, and R. E. Ewing, "Characteristic Petrov-Galerkin subdomain methods for convection-diffusion problems," *Computer Methods in Applied Mechanics and Engineering*, vol. 64, pp. 77–86, 1988.
- [12] T. F. Russell and M. A. Celia, "An overview of research on Eulerian-Lagrangian localized adjoint methods (ELLAM)," *Advances in Water Resources*, vol. 25, no. 8-12, pp. 1215–1231, 2002.
- [13] Z. Chen, "Characteristic mixed discontinuous finite element methods for advection-dominated diffusion problems," *Computer Methods in Applied Mechanics and Engineering*, vol. 191, no. 23-24, pp. 2509–2538, 2002.
- [14] M. Seaïd, "An Eulerian-Lagrangian method for coupled parabolic-hyperbolic equations," *Applied Numerical Mathematics*, vol. 59, no. 3-4, pp. 754–768, 2009.
- [15] J. Caldwell, P. Wanless, and A. E. Cook, "Solution of Burgers' equation for large Reynolds number using finite elements with moving nodes," *Applied Mathematical Modelling*, vol. 11, no. 3, pp. 211–214, 1987.
- [16] J. Behrens, A. Iske, and M. Käser, "Adaptive Meshfree Method of Backward Characteristics for Nonlinear Transport Equations," in *Meshfree Methods for Partial Differential Equations SE - 2*, M. Griebel and M. Schweitzer, Eds., vol. 26 of *Lecture Notes in Computational Science and Engineering*, pp. 21–36, Springer Berlin Heidelberg, Berlin, Germany, 2003.
- [17] T. Plewa, T. Linde, and V. G. Weirs, "Adaptive mesh refinement-theory and applications," in *Proceedings of the Chicago Workshop on Adaptive Mesh Refinement Methods*, vol. 41, Chicago, Ill, USA, 2003.
- [18] X.-H. Wang, M. Quintard, and G. Darche, "Adaptive mesh refinement for one-dimensional three-phase flow with phase change in porous media," *Numerical Heat Transfer, Part B: Fundamentals*, vol. 50, no. 3, pp. 231–268, 2006.
- [19] W. Huang and R. D. Russell, *Adaptive Moving Mesh Methods*, Springer Science & Business Media, New York, NY, USA, 2011.
- [20] H. Dong, Z. Qiao, S. Sun, and T. Tang, "Adaptive moving grid methods for two-phase flow in porous media," *Journal of Computational and Applied Mathematics*, vol. 265, pp. 139–150, 2014.
- [21] S. Reboux, B. Schrader, and I. F. Sbalzarini, "A self-organizing Lagrangian particle method for adaptive-resolution advection-diffusion simulations," *Journal of Computational Physics*, vol. 231, no. 9, pp. 3623–3646, 2012.
- [22] C.-C. Chueh, N. Djilali, and W. Bangerth, "An h -adaptive operator splitting method for two-phase flow in 3D heterogeneous porous media," *SIAM Journal on Scientific Computing*, vol. 35, no. 1, pp. B149–B175, 2013.
- [23] O. Angelini, K. Brenner, and D. Hilhorst, "A finite volume method on general meshes for a degenerate parabolic convection-reaction-diffusion equation," *Numerische Mathematik*, vol. 123, no. 2, pp. 219–257, 2013.
- [24] Z. Cao, Z. Liu, X. Wang, A. Shi, H. Luo, and B. Noettinger, "A dissipation-free numerical method to solve one-dimensional hyperbolic flow equations," *International Journal for Numerical Methods in Fluids*.

- [25] F. J. Fayers and J. W. Sheldon, "The effect of capillary pressure and gravity on two-phase fluid flow in a porous medium, petroleum transactions," *AIME*, vol. 216, pp. 147–155, 1959.
- [26] F. Hussain, Y. Cinar, and P. Bedrikovetsky, "A semi-analytical model for two phase immiscible flow in porous media honouring capillary pressure," *Transport in Porous Media*, vol. 92, no. 1, pp. 187–212, 2012.
- [27] I. R. Goumiri, J. H. Prévost, and M. Preisig, "The effect of capillary pressure on the saturation equation of two-phase flow in porous media," *International Journal for Numerical and Analytical Methods in Geomechanics*, vol. 36, no. 3, pp. 352–361, 2012.
- [28] J. Mackenzie, "Uniform convergence analysis of an upwind finite-difference approximation of a convection-diffusion boundary value problem on an adaptive grid," *IMA Journal of Numerical Analysis*, vol. 19, no. 2, pp. 233–249, 1999.
- [29] N. Kopteva and M. Stynes, "A robust adaptive method for a quasi-linear one-dimensional convection-diffusion problem," *SIAM Journal on Numerical Analysis*, vol. 39, no. 4, pp. 1446–1467, 2001.
- [30] J. Caldwell and P. Smith, "Solution of Burgers' equation with a large Reynolds number," *Applied Mathematical Modelling*, vol. 6, no. 5, pp. 381–385, 1982.
- [31] S. E. Buckley and M. C. Leverett, "Mechanism of fluid displacement in sands," *Transactions of the AIME*, vol. 146, no. 1, pp. 107–116, 2013.

Research Article

Finite Element Model for Linear Elastic Thick Shells Using Gradient Recovery Method

Achille Germain Feumo,¹ Robert Nzengwa,² and Joseph Nkongho Anyi³

¹Department of Mathematics, University of Yaounde I, Yaounde, Cameroon

²Department of Civil Engineering, University of Douala, Douala, Cameroon

³Department of Mechanical Engineering, Higher Technical Teachers Training College, University of Buea, P.O. Box 249 Buea Road, Kumba, Cameroon

Correspondence should be addressed to Achille Germain Feumo; achillefeumo@yahoo.com

Received 23 January 2017; Accepted 15 March 2017; Published 14 June 2017

Academic Editor: Mohsen Sheikholeslami

Copyright © 2017 Achille Germain Feumo et al. This is an open access article distributed under the Creative Commons Attribution License, which permits unrestricted use, distribution, and reproduction in any medium, provided the original work is properly cited.

This research purposed a new family of finite elements for spherical thick shell based on Nzengwa-Tagne's model proposed in 1999. The model referred to hereafter as N-T model contains the classical Kirchhoff-Love (K-L) kinematic with additional terms related to the third fundamental form governing strain energy. Transverse shear stresses are computed and C^0 finite element is proposed for numerical implementation. However, using straight line triangular elements does not guarantee a correct computation of stress across common edges of adjacent elements because of gradient jumps. The gradient recovery method known as Polynomial Preserving Recovery (PPR) is used for local interpolation and applied on a hemisphere under diametrically opposite charges. A good agreement of convergence results is observed; numerical results are compared to other results obtained with the classical K-L thin shell theory. Moreover, simulation on increasing values of the ratio of the shell shows impact of the N-T model especially on transverse stresses because of the significant energy contribution due to the third fundamental form tensor present in the kinematics of this model. The analysis of the thickness ratio shows difference between the classical K-L theory and N-T model when the ratio is greater than 0.099.

1. Introduction

N-T's theoretical approach which was mathematically and rigorously deduced from three-dimensional linear elastic curvilinear media through multiple scaling and limit analysis is a more general Kirchhoff-Love (K-L) model. The displacement here is a two-degree polynomial of the thickness parameter z while the strain tensor which is planar contains the change in the third fundamental form in addition to the change of the first and second.

For more than thirty years, numerous articles, books, and theses have addressed the problem of shell. Plates and more generally thin shells represent over 70% of industrial calculations [1, 2]. The mechanical models have been validated by some well-known benchmarks. Some locally stiffened thin shells or more generally thick shells have not received the same development probably because some few existing models do not account for transverse stresses and have not

been mathematically established. Moreover it is well known that transverse stresses can not be neglected as the shell becomes thicker. Without any ad hoc geometrical hypothesis, it was deduced that the strain tensor is planar; that is, $\epsilon_{i3} = 0$ and, as a consequence, the limit displacement reads $u = u_\alpha g^\alpha + u_3 g^3$, with $u_\alpha(x, z) = \xi_\alpha(x) - z\theta_\alpha(x) + z^2\psi_\alpha(x)$, $u_3 = \xi_3(x)$ (where $\{g^1, g^2, g^3\}$ is the three-dimensional contravariant shell basis); the in-plane strain $\epsilon_{\alpha\beta} = e_{\alpha\beta} - zk_{\alpha\beta} + z^2Q_{\alpha\beta}$ and the stresses $\sigma^{\alpha\beta}$ depend on the in-plane strains and σ^{i3} are computed from appropriate differential equations; see [3].

The form of the displacement clearly shows that C^0 finite element is discontinuous across adjacent elements and usually provides inaccurate results at elements boundaries. Some authors indeed proposed different numerical methods: the finite difference method (FDM); finite volume method (FVM); finite element method for various simulations like magnetohydrodynamic (MHD) [4–6]; Curved Triangular

Finite Elements (CTFE) of [7]; a weighted average method to calculate stresses, which provided good results for both interior and boundary elements; and L^2 -projection to also calculate stresses, by considering “discrete smoothing” and least squares fitting at the gauss points. But this last method was limited to one element; consequently, the smoothen stress is still discontinuous across element boundaries. This problem was completely solved 20 years ago, when Sheikholeslami et al. introduced their Superconvergent Patch Recovery (SPR) [8–10], where the discrete least square fitting was performed on an element patch, a set of elements having the same vertex. This SPR method produces a continuous stress field, which is superconvergent under uniform mesh. Soon after, Wiberg et al. incorporated equilibrium and boundary conditions to enhance SPR [11, 12] and discussed strategies to improve the finite element solution u_h itself (other than the stress, which is essentially the gradient of u_h) [12]. Recently, Naga and Zhang and their colleagues proposed an alternative strategy, called Polynomial Preserving Recovery (PPR) [13–17], to recover the gradient. Theoretical analyses revealed that PPR has better superconvergence (over any mesh) properties than SPR and the numerical tests indicated that the a posteriori error estimator based on PPR is as good as or better than that of SPR ([18, 19], remarks: page 323).

In order to validate the N-T model, the program is first tested successfully on the widely known hemisphere under diametrically opposite charges of thin shells. Then thin shell theory of K-L and thick shell theory of N-T are implemented in order to evaluate the impact of thickness ratio. Next, simulations with various values of the characteristic shell parameter (thickness ratio) are implemented in order to reveal the contribution of Gauss curvature (change of the third fundamental form) in the stiffness energy.

In addition to that, Section 2 presents materials and methods: a brief description of the N-T model is presented without all the mathematical development, including gradient recovery method. A variational formulation of the shell equation and the resolution of transverse stresses equations are done. Section 3 is devoted to the discretization of the N-T model. Finite element spaces are next described and also the discretization scheme is layout. All numerical integrations are performed on a reference triangular element using the gradient recovery PPR method. Section 4 is completely devoted to the validation of the finite element model. Finally, results are discussed and concluded.

2. Materials and Methods

2.1. The N-T Model of Thick Shells. Let $\Omega = \{M \in \Omega, \overrightarrow{OM} = \overrightarrow{om} + za^3; -h/2 < z < h/2, m \in S\}$ (S is midsurface, $h > 0$ is the thickness, and x is the coordinate of m in S) denote a shell. We assume the surface S is bounded and sufficiently smooth for all subsequent computations. Let $\{a_1, a_2, a_3\}$ and $\{a^1, a^2, a^3\}$ denote the covariant and contravariant basis of the midsurface and $\{g_1, g_2, g_3\}$ and $\{g^1, g^2, g^3\}$, respectively, the covariant and contravariant basis of the shell. Then

$$g_\alpha = (\delta_\alpha^\tau - zb_\alpha^\tau) a_\tau = (\mu_\alpha^\tau) a_\tau, \quad g_3 = a_3$$

$$g^\alpha = (\mu_\alpha^\tau)^{-1} a^\tau, \quad g^3 = a^3$$

$$d\Omega = (1 - 2zb_\alpha^\alpha + z^2 \det(b_\beta^\alpha)) dzdS = \phi(x, z) dzdS, \quad (1)$$

where $b_\alpha^\rho = a^{\rho\gamma} b_{\gamma\alpha}$ and $b_{\gamma\alpha}$ denote curvature tensor components and $a^{\rho\gamma}$ is the contravariant component of the metric of the midsurface S . The repeated index convention is adopted. Values of Greek indices α, β take range in the set $\{1, 2\}$ while Latin indices i, j take their values in the set $\{1, 2, 3\}$. A vector field can be expressed component wise indifferently in g^i -basis or a^i -basis as follows:

$$v = v_i(x, z) g^i = \bar{v}_i(x, z) a^i,$$

$$v_\alpha = (\mu_\alpha^\tau) \bar{v}_\tau, \quad (2)$$

$$\bar{v}_\alpha = (\mu_\alpha^\tau)^{-1} v_\tau.$$

Then the strain tensor (see [3]) is given by

$$\epsilon_{\alpha\beta}(u) = \frac{1}{2} (u_{\alpha/\beta} + u_{\beta/\alpha})$$

$$= \frac{1}{2} ((\mu_\alpha^\tau) (\nabla_\beta \bar{u}_\tau - b_{\tau\beta} \bar{u}_3) + (\mu_\beta^\tau) (\nabla_\alpha \bar{u}_\tau - b_{\alpha\tau} \bar{u}_3)) \quad (3)$$

$$\epsilon_{3\alpha}(u) = \frac{1}{2} (u_{\alpha/3} + u_{3/\alpha}) = \frac{1}{2} ((\mu_\alpha^\tau) \bar{u}_{\tau,3} + \bar{u}_{3,\alpha} + b_\alpha^\tau \bar{u}_\tau)$$

$$\epsilon_{33}(u) = \bar{u}_{3,3}$$

(/ and ∇ indicate covariant derivation in Ω and S , resp., while $f_{,\alpha} = \partial f / \partial x^\alpha$). The equation $\epsilon_{i3}(u) = 0$ yields the following results:

$$\bar{u}_\alpha = (\mu_\alpha^\tau) \xi_\tau - z \partial_\alpha \xi_3$$

$$\bar{u}_3 = \xi_3 \text{ for } \xi_\alpha, \xi_3 \text{ function of } x = (x_1, x_2), \quad (4)$$

$$u_\alpha = \xi_\alpha - z (\partial_\alpha \xi_3 + 2b_\alpha^\tau \xi_\tau) + z^2 (b_\alpha^\tau b_\tau^\nu \xi_\nu + b_\alpha^\tau \partial_\alpha \xi_3)$$

$$u_3 = \xi_3.$$

The strain tensor now reads

$$\epsilon_{\alpha\beta}(u) = e_{\alpha\beta}(\xi) - zk_{\alpha\beta}(\xi) + z^2 Q_{\alpha\beta}(\xi)$$

$$e_{\alpha\beta}(\xi) = \frac{1}{2} (\nabla_\alpha \xi_\beta + \nabla_\beta \xi_\alpha - 2b_{\alpha\beta} \xi_3)$$

$$k_{\alpha\beta}(\xi) = \nabla_\alpha b_\beta^\nu \xi_\nu + b_\alpha^\nu \nabla_\beta \xi_\nu + b_\beta^\nu \nabla_\alpha \xi_\nu + \nabla_\alpha \nabla_\beta \xi_3$$

$$- b_\alpha^\lambda b_{\lambda\beta} \xi_3 \quad (5)$$

$$Q_{\alpha\beta}(\xi) = \frac{1}{2} [b_\alpha^\nu \nabla_\beta b_\nu^\rho \dot{u}_\rho + b_\alpha^\nu b_\nu^\rho \nabla_\beta \dot{u}_\rho + b_\beta^\nu b_\nu^\rho \nabla_\alpha \dot{u}_\rho$$

$$+ b_\beta^\nu \nabla_\alpha b_\alpha^\rho \dot{u}_\rho + b_\alpha^\nu \nabla_\beta \nabla_\nu \dot{u}_3 + b_\beta^\nu \nabla_\alpha \nabla_\nu \dot{u}_3].$$

Let us recall that $(e_{\alpha\beta})$, $(k_{\alpha\beta})$, and $(Q_{\alpha\beta})$ are, respectively, changes in the first, second, and third fundamental forms tensors, while the displacement

$$u = u_\alpha(x, z) g^\alpha + \xi_3(x) a^3 = \bar{u}_\alpha(x, z) a^\alpha + \xi_3(x) a^3 \quad (6)$$

is a more generalized Kirchhoff-Love displacement [3] and can also be written in Reissner-Mindlin format as follows:

$$\begin{aligned} u &= (\xi_\alpha(x) - z\theta_\alpha(x) + z^2\psi_\alpha(x))g^\alpha + \xi_3(x)a^3 \\ &= (\xi_\alpha(x) + z\beta_\alpha(x))a^\alpha + \xi_3(x)a^3, \end{aligned} \quad (7)$$

where $\beta_\alpha = \xi_{3,\alpha} + 2b_\alpha^\nu \xi_\nu = \theta_\alpha + zb_\alpha^\nu \xi_\nu$ and θ_α are the rotations angles. Strain tensors are miscalculated in some literatures because wrong basis vectors were used. The condition $\epsilon_{i3}(u) = 0$ modifies the constitutive law which, expressed with the Lamé constants, now reads

$$\sigma^{\alpha\beta}(u) = (\bar{\lambda}g^{\gamma\delta}g^{\alpha\beta} + \mu(g^{\alpha\gamma}g^{\delta\beta} + g^{\alpha\delta}g^{\gamma\beta}))\epsilon_{\gamma\delta}(u), \quad (8)$$

where $\bar{\lambda} = 2\lambda\mu/(\lambda + 2\mu)$, or equivalently with Young's modulus E and Poisson's coefficient ν , reads

$$\begin{aligned} \sigma^{\alpha\beta}(u) &= \frac{E}{1-\nu^2} (\nu g^{\gamma\delta}g^{\alpha\beta} + (1-\nu)(g^{\alpha\gamma}g^{\delta\beta} + g^{\alpha\delta}g^{\gamma\beta})) \epsilon_{\gamma\delta}(u) \end{aligned} \quad (9)$$

Consider a shell of thickness h , clamped on a part of its border Γ_0 , subject to volume forces f^α and f^3 and to surface forces \bar{h}^α and \bar{h}^3 on the rest of its border Γ^1 . Suppose the forces are sufficiently smooth; then the transverse stresses are solutions to the differential equations:

$$\begin{aligned} \frac{\partial\sigma^{\alpha 3}}{\partial z} + 2\Gamma_{\lambda 3}^\alpha \sigma^{\lambda 3} + \Gamma_{\lambda 3}^\lambda \sigma^{\alpha 3} &= -(\sigma_{,\beta}^{\alpha\beta} + \Gamma_{\beta\lambda}^\alpha \sigma^{\lambda\beta} - f^\alpha) \\ \sigma^{\alpha 3}\left(-\frac{h}{2}\right) &= -\bar{h}_-^\alpha \\ \sigma^{\alpha 3}\left(+\frac{h}{2}\right) &= \bar{h}_+^\alpha, \end{aligned} \quad (10)$$

where $f^\alpha \in L^2(\Omega)$; $\sigma^{\alpha 3} \in H^1(-h/2, h/2; H^{-1}(S))$ and

$$\begin{aligned} \frac{\partial\sigma^{33}}{\partial z} + \Gamma_{\alpha 3}^\alpha \sigma^{33} &= -(\sigma_{,\alpha}^{3\alpha} + \Gamma_{\alpha\lambda}^3 \sigma^{\lambda\alpha} + \Gamma_{\beta\lambda}^\beta \sigma^{\lambda 3} - f^3) \\ \sigma^{33}\left(-\frac{h}{2}\right) &= -\bar{h}_-^3 \\ \sigma^{33}\left(+\frac{h}{2}\right) &= \bar{h}_+^3, \end{aligned} \quad (11)$$

where $f^3 \in H^1(\Omega)$; $\sigma^{33} \in H^2(-h/2, h/2; H^{-2}(S))$.

The generic point of the sphere is described by

$$\overrightarrow{OM} \begin{cases} X = R \sin(y) \cos(x) \\ Y = R \sin(x) \sin(y) \\ Z = R \cos(y), \end{cases} \quad (12)$$

where x and y are curvilinear coordinates, $0 \leq x \leq 2\Pi$, and $0 \leq y \leq \Pi$; R is the radius of the sphere, and X, Y, Z are the global coordinates.

The covariant and contravariant metric tensors on the middle surface S are defined by

$$\begin{aligned} (a_{\alpha\beta}) &= \begin{bmatrix} R^2 \sin^2(y) & 0 \\ 0 & R^2 \end{bmatrix} \\ (a^{\alpha\beta}) &= \begin{bmatrix} \frac{1}{R^2 \sin^2(y)} & 0 \\ 0 & \frac{1}{R^2} \end{bmatrix}. \end{aligned} \quad (13)$$

The covariant and contravariant curvature tensors on S (second fundamental form) are given by

$$\begin{aligned} (b_{\alpha\beta}) &= \begin{bmatrix} R \sin^2(y) & 0 \\ 0 & R \end{bmatrix}; \\ (b^{\alpha\beta}) &= \begin{bmatrix} \frac{1}{R^3 \sin^2(y)} & 0 \\ 0 & \frac{1}{R^3} \end{bmatrix}; \\ (b_\beta^\alpha) &= \begin{bmatrix} \frac{1}{R} & 0 \\ 0 & \frac{1}{R} \end{bmatrix}. \end{aligned} \quad (14)$$

Let h be the thickness of the sphere; the Christoffel symbols are defined by

$$\begin{aligned} \Gamma_{11}^1 &= \Gamma_{12}^2 = \Gamma_{21}^2 = \Gamma_{22}^2 = \Gamma_{22}^1 = 0; \\ \Gamma_{12}^1 &= \Gamma_{21}^1 = \cotan(y); \\ \Gamma_{11}^2 &= \frac{-1}{2} \sin(2y); \\ \Gamma_{23}^1 &= \Gamma_{13}^2 = \Gamma_{12}^3 = \Gamma_{21}^3 = 0; \\ \Gamma_{13}^1 &= \Gamma_{23}^2 = \frac{1}{h-R}; \\ \Gamma_{11}^3 &= (R-h) \sin^2(y); \\ \Gamma_{22}^3 &= R-h. \end{aligned} \quad (15)$$

2.2. Variational Equations. Let the border of S , $\partial S = \gamma_0 \cup \gamma_1$ be partitioned in two parts and the border of the shell $\partial\Omega = \Gamma_0 \cup \Gamma^1$ with $\Gamma_0 = \gamma_0 \times \{-h/2, h/2\}$, and $\Gamma^1 = \gamma_1 \times \{-h/2, h/2\} \cup \Gamma_- \cup \Gamma_+$. We denote $\Gamma_- = S \times \{-h/2\}$ and $\Gamma_+ = S \times \{h/2\}$. Suppose the shell is clamped on Γ_0 and subject to volume and surface forces as stated above; then the three-dimensional variational equation related to the equilibrium equation reads

$$\begin{aligned} \text{find } u &\in IH_{\Gamma_0}^1 \\ \text{such that: } &\int_{\Omega} (\sigma(u) : \epsilon(v)) d\Omega \\ &= \int_{\Omega} f \cdot v d\Omega + \int_{\Gamma_1} \bar{h} \cdot v dS = L(v) \quad \forall v \in IH_{\Gamma_0}^1, \end{aligned} \quad (16)$$

where $IH_{\Gamma_0}^1(\Omega) = \{u_i \in L^2(\Omega); \nabla_j u_i \in L^2(\Omega) \text{ and } u_i = 0 \text{ on } \Gamma_0\}$ is the Sobolev space and $:$ and \cdot denote, respectively, tensors and vectors scalar products. The variational formulation under Kirchhoff-Love's approach which is given by

$$A_0(u, v) = \frac{Eh}{1-\nu^2} \int_S \left(\{E_u\}^t \left[(1-\nu) ([D_e]_\beta^\alpha)^t [D_e]_\alpha^\beta + \nu ([D_e]_\alpha^\alpha)^t ([D_e]_\beta^\beta) \right] \{E_v\} + \frac{h^2}{12} \{E_u\}^t \cdot \left[(1-\nu) ([D_k]_\beta^\alpha)^t [D_k]_\alpha^\beta + \nu ([D_k]_\alpha^\alpha)^t ([D_k]_\beta^\beta) \right] \cdot \{E_v\} \right) dS = L(v), \quad (17)$$

$$A_1(u, v) = \frac{Eh}{1-\nu^2} \int_S \left(\{E_u\}^t \left[(1-\nu) ([D_e]_\beta^\alpha)^t [D_e]_\alpha^\beta + \nu ([D_e]_\alpha^\alpha)^t ([D_e]_\beta^\beta) \right] \{E_v\} + \frac{h^2}{12} \{E_u\}^t \cdot \left[(1-\nu) ([D_k]_\beta^\alpha)^t [D_k]_\alpha^\beta + \nu ([D_k]_\alpha^\alpha)^t ([D_k]_\beta^\beta) \right] \cdot \{E_v\} + \frac{h^2}{12} \{E_u\}^t \left[(1-\nu) ([D_e]_\beta^\alpha)^t [D_Q]_\alpha^\beta + \nu ([D_e]_\alpha^\alpha)^t ([D_Q]_\beta^\beta) \right] \{E_v\} + \frac{h^2}{12} \{E_u\}^t \left[(1-\nu) ([D_Q]_\beta^\alpha)^t [D_e]_\alpha^\beta + \nu ([D_Q]_\alpha^\alpha)^t ([D_e]_\beta^\beta) \right] \cdot \{E_v\} + \frac{h^4}{80} \{E_u\}^t \left[(1-\nu) ([D_Q]_\beta^\alpha)^t [D_Q]_\alpha^\beta + \nu ([D_Q]_\alpha^\alpha)^t ([D_Q]_\beta^\beta) \right] \cdot \{E_v\} + \frac{h^4}{80} \{E_u\}^t \left[(1-\nu) ([D_Q]_\beta^\alpha)^t [D_Q]_\alpha^\beta + \nu ([D_Q]_\alpha^\alpha)^t ([D_Q]_\beta^\beta) \right] \cdot \{E_v\} \right) dS = L(v) \quad (18)$$

is a truncated thick shell or the best first-order thick shell variational equation under N-T's model; see [3]. It can be observed that this equation has similarities with familiar equations in engineering literature.

Let

$$\begin{aligned} H^1(S) &= \{\varphi \in L^2(S), \nabla_\alpha \varphi \in L^2(S)\} \\ IH^1(S) &= [H^1(S)]^2 \\ IH_{\gamma_0}^1(S) &= \{(\eta_\alpha) \in IH^1(S), \eta_\alpha = 0 \text{ on } \gamma_0\} \\ H^2(S) &= \{\varphi \in H^1(S), \nabla_\alpha \varphi \in H^1(S)\} \\ H_{\gamma_0}^2(S) &= \{\varphi \in H^2(S), \varphi = \partial_\alpha \varphi = 0 \text{ on } \gamma_0\} \\ U_{ad} &= IH_{\gamma_0}^1(S) \times H_{\gamma_0}^2(S). \end{aligned} \quad (19)$$

Nzengwa and Tagne Simo established existence and unicity of solutions of this truncated problem in U_{ad} . We

should remember that the displacement calculated after ξ is

$$\begin{aligned} u_\alpha &= \xi_\alpha - z(\partial_\alpha \xi_3 + 2b_\alpha^\tau \xi_\tau) + z^2(b_\nu^\tau b_\alpha^\nu \xi_\tau + b_\alpha^\tau \partial_\alpha \xi_3) \\ u_3 &= \xi_3 \end{aligned} \quad (20)$$

or in the Nzengwa-Tagne format

$$\begin{aligned} u_\alpha &= \xi_\alpha(x) - z\beta_\alpha(x) + z^2\psi_\alpha(x) \\ u_3 &= \xi_3(x) \end{aligned} \quad (21)$$

which suggests C^0 finite element implementation.

The linearized membrane strain tensor is expressed as follows:

$$\begin{aligned} e_\beta^\alpha(u) &= a^{\alpha\lambda} e_{\beta\lambda}(u) \\ &= \frac{1}{2} a^{\alpha\lambda} (u_{\beta,\lambda} + u_{\lambda,\beta}) - a^{\alpha\lambda} \bar{\Gamma}_{\lambda\beta}^\rho u_\rho - a^{\alpha\lambda} b_{\lambda\beta} u_3. \end{aligned} \quad (22)$$

Using the formulas

$$T_\beta^\alpha(u) = a^{\alpha\lambda} T_{\beta\lambda}(u) = [T]_\beta^\alpha \{E_u\}, \quad (23)$$

we can put (22) in the following form:

$$e_\beta^\alpha(u) = [D_e]_\beta^\alpha \{E_u\}, \quad (24)$$

where

$$\begin{aligned} [E_u]^T &= \left[u_1; \partial_1 u_1; \partial_2 u_1; u_2; \partial_1 u_2; \partial_2 u_2; u_3; -2b_1^1 u_1 \right. \\ &\quad - 2b_1^2 u_2 - \partial_1 u_3; -2b_1^1 \partial_1 u_1 - 2b_1^2 \partial_1 u_2 - 2b_1^1 \partial_2 u_1 \\ &\quad - 2b_1^2 \partial_2 u_2; -2b_2^1 u_1 - 2b_2^2 u_2 - \partial_2 u_3; -2b_2^1 \partial_1 u_1 \\ &\quad - 2b_2^2 \partial_1 u_2; -2b_2^1 \partial_2 u_1 - 2b_2^2 \partial_2 u_2; \bar{b}^1 u_1 + \bar{b}^1 u_2 \\ &\quad + b_1^1 \partial_1 u_3 + b_1^2 \partial_2 u_3; \bar{b}^1 \partial_1 u_1 + \bar{b}^1 \partial_1 u_2; \bar{b}^1 \partial_2 u_1 \\ &\quad + \bar{b}^1 \partial_2 u_2; \bar{b}^2 u_1 + \bar{b}^2 u_2 + b_2^1 \partial_1 u_3 + b_2^2 \partial_2 u_3; \bar{b}^2 u_1 \\ &\quad + \bar{b}^2 u_2 + b_2^1 \partial_1 u_3 + b_2^2 \partial_2 u_3; \bar{b}^2 \partial_1 u_1 + \bar{b}^2 \partial_1 u_2; \bar{b}^2 \partial_2 u_1 \\ &\quad \left. + \bar{b}^2 \partial_2 u_2 \right], \end{aligned} \quad (25)$$

where

$$\begin{aligned} \bar{b}^1 &= b_1^1 b_1^1 + b_2^1 b_1^2, \\ \bar{b}^1 &= b_1^2 b_1^1 + b_2^2 b_1^2, \\ \bar{b}^2 &= b_1^1 b_2^1 + b_2^1 b_2^2, \\ \bar{b}^2 &= b_1^2 b_2^1 + b_2^2 b_2^2; \end{aligned} \quad (26)$$

$$[D_e]^\alpha_\beta = \left[-a^{\alpha\nu}\Gamma_{\beta\nu}^1; a^{\alpha 1}I(\beta, 1); \frac{1}{2}a^{\alpha\lambda}J(\lambda, \beta); \right. \\ \left. -a^{\alpha\lambda}\Gamma_{\beta\lambda}^2; \frac{1}{2}a^{\alpha\lambda}J(\lambda, \beta); a^{\alpha 2}J(\beta, 2); \right. \\ \left. -b_\beta^\alpha; 0; 0; 0; 0; 0; 0; 0; 0; 0; 0; 0 \right]; \quad (27)$$

$$I = \begin{bmatrix} 1 & 0 \\ 0 & 1 \end{bmatrix},$$

$$J = \begin{bmatrix} 0 & 1 \\ 1 & 0 \end{bmatrix}.$$

The linearized part of the change of the curvature tensor of the middle surface is expressed as follows:

$$[D_k]^\alpha_\beta = \left[\frac{1}{2}a^{\alpha\mu} \left(b_{\mu,\beta}^1 + \bar{\Gamma}_{\lambda\beta}^1 b_\mu^\lambda - \bar{\Gamma}_{\mu\beta}^\lambda b_\lambda^1 \right); 0; 0; \frac{1}{2} \right. \\ \cdot a^{\alpha\mu} \left(b_{\mu,\beta}^2 + \bar{\Gamma}_{\lambda\beta}^2 b_\mu^\lambda - \bar{\Gamma}_{\mu\beta}^\lambda b_\lambda^2 \right); 0; 0; b^{\alpha\mu} b_{\mu\beta}; -a^{\alpha\mu} \bar{\Gamma}_{\mu\beta}^1; \\ \left. -I(\alpha, 1) a^{\alpha 1}; \frac{1}{2}J(\alpha, \beta) a^{\alpha\mu}; -a^{\alpha\mu} \bar{\Gamma}_{\mu\beta}^2; \frac{1}{2}J(\alpha, \beta) \right. \\ \left. \cdot a^{\alpha\mu}; I(\alpha, 2) a^{\alpha 2}; 0, 0, 0, 0, 0, 0 \right]. \quad (28)$$

The linearized part of the change of the third fundamental form tensor can be expressed as follows:

$$[D_Q]^\alpha_\beta = \left[a^{\alpha\mu} b_\nu^1 \left(b_{\beta,\mu}^\nu + \bar{\Gamma}_{\gamma\beta}^\nu b_\mu^\gamma - \bar{\Gamma}_{\mu\beta}^\nu b_\gamma^\nu \right); 0; 0; \right. \\ \left. a^{\alpha\mu} b_\nu^2 \left(b_{\beta,\mu}^\nu + \bar{\Gamma}_{\gamma\beta}^\nu b_\mu^\gamma - \bar{\Gamma}_{\mu\beta}^\nu b_\gamma^\nu \right); 0; 0; 0; \right. \\ \left(b_{\beta,\mu}^1 + \bar{\Gamma}_{\gamma\beta}^1 b_\mu^\gamma - \bar{\Gamma}_{\mu\beta}^1 b_\gamma^1 \right); 0; 0; \left(b_{\beta,\mu}^2 + \bar{\Gamma}_{\gamma\beta}^2 b_\mu^\gamma - \bar{\Gamma}_{\mu\beta}^2 b_\gamma^2 \right); \\ \left. 0; 0; -a^{\alpha\mu} \bar{\Gamma}_{\mu\beta}^1; I(\alpha, 1) a^{\alpha 1}; \frac{1}{2}J(\alpha, \beta) a^{\alpha\mu}; -a^{\alpha\mu} \bar{\Gamma}_{\mu\beta}^2; \right. \\ \left. \frac{1}{2}J(\alpha, \beta) a^{\alpha\mu}; I(\alpha, 2) a^{\alpha 2} \right]. \quad (29)$$

2.3. Resolution of the Transverse Stress Ordinary Differential Equation. Using expressions (27), (28), and (29), let $\tau = -4/(h - R)$, Γ_{jk}^i be the three dimension Christoffel symbols, and

$$\bar{\sigma}_0^{13} = \frac{-E}{1 - \nu^2} \left[\left(a^{11} \left(e_1^1 + \nu e_2^2 \right) \right)_{,x^1} + (1 - \nu) \left(a^{11} e_1^2 \right)_{,x^2} \right. \\ \left. + (1 - \nu) \cotan(y) a^{11} e_1^2 \right. \\ \left. + (1 - \nu) \cotan(y) a^{22} e_2^2 \right].$$

$$\bar{\sigma}_1^{13} = \frac{-E}{1 - \nu^2} \left[\left(a^{11} \left(K_1^1 + \nu k_2^2 \right) \right)_{,x^1} \right. \\ \left. + (1 - \nu) \left(a^{11} k_1^2 \right)_{,x^2} + (1 - \nu) \cotan(y) a^{11} k_1^2 \right. \\ \left. + (1 - \nu) \cotan(y) a^{22} k_2^2 \right]$$

$$\bar{\sigma}_2^{13} = \frac{-E}{1 - \nu^2} \left[\left(a^{11} \left(Q_1^1 + \nu Q_2^2 \right) \right)_{,x^1} \right. \\ \left. + (1 - \nu) \left(a^{11} Q_1 \right)_{,x^2} + (1 - \nu) \cotan(y) a^{11} Q_1^2 \right. \\ \left. + (1 - \nu) \cotan(y) a^{22} Q_2^2 \right] \quad (30)$$

Then the first shear stress of (10) is given as follows:

$$\sigma^{13}(x, y, z) = \left\{ -\bar{h}_-^{-1} \exp\left(-\tau\left(z + \frac{h}{2}\right)\right) + \left[1 \right. \right. \\ \left. \left. - \exp\left(-\tau\left(z + \frac{h}{2}\right)\right) \right] \left[\frac{\bar{\sigma}_0^{13}}{\tau} + \frac{\bar{\sigma}_1^{13}}{\tau^2} + 2 \frac{\bar{\sigma}_2^{13}}{\tau^3} \right. \right. \\ \left. \left. + \left(z - \frac{h}{2} \right) \left(-\frac{\bar{\sigma}_1^{13}}{\tau} - 2 \frac{\bar{\sigma}_2^{13}}{\tau^2} \right) + \left(z^2 + \frac{h^2}{4} \right) \frac{\bar{\sigma}_2^{13}}{\tau^3} \right] \right\} \\ \cdot \{E_u\}. \quad (31)$$

In the same way, let

$$\bar{\sigma}_0^{23} = \frac{-E}{1 - \nu^2} \left[(1 - \nu) \left(a^{22} e_{2,x^1}^2 \right) + \left(a^{11} e_1^2 \right)_{,x^2} \right. \\ \left. + \frac{1}{2} \sin(2y) a^{11} \left(e_1^1 + \nu e_2^2 \right) \right] \\ \bar{\sigma}_1^{23} = \frac{-E}{1 - \nu^2} \left[(1 - \nu) \left(a^{22} k_{2,x^1}^2 \right) + \left(a^{11} k_1^2 \right)_{,x^2} \right. \\ \left. + \frac{1}{2} \sin(2y) a^{11} \left(k_1^1 + \nu k_2^2 \right) \right] \quad (32)$$

$$\bar{\sigma}_2^{23} = \frac{-E}{1 - \nu^2} \left[(1 - \nu) \left(a^{22} Q_{2,x^1}^2 \right) + \left(a^{11} Q_1^2 \right)_{,x^2} \right. \\ \left. + \frac{1}{2} \sin(2y) a^{11} \left(Q_1^1 + \nu Q_2^2 \right) \right].$$

The second shear stress (10) is defined as follows:

$$\sigma^{23}(x, y, z) = \left\{ -\bar{h}_-^{-2} \exp\left(-\tau\left(z + \frac{h}{2}\right)\right) + \left[1 \right. \right. \\ \left. \left. - \exp\left(-\tau\left(z + \frac{h}{2}\right)\right) \right] \left[\frac{\bar{\sigma}_0^{23}}{\tau} + \frac{\bar{\sigma}_1^{23}}{\tau^2} + 2 \frac{\bar{\sigma}_2^{23}}{\tau^3} \right. \right. \\ \left. \left. + \left(z - \frac{h}{2} \right) \left(-\frac{\bar{\sigma}_1^{23}}{\tau} - 2 \frac{\bar{\sigma}_2^{23}}{\tau^2} \right) + \left(z^2 + \frac{h^2}{4} \right) \frac{\bar{\sigma}_2^{23}}{\tau^3} \right] \right\} \\ \cdot \{E_u\}. \quad (33)$$

Let

$$\gamma_1 = \frac{\bar{\sigma}_{0,x^1}^{13} + \bar{\sigma}_{0,x^2}^{23}}{\tau} + \frac{\bar{\sigma}_{1,x^1}^{13} + \bar{\sigma}_{1,x^2}^{23}}{\tau^2} + \frac{\bar{\sigma}_{2,x^1}^{13} + \bar{\sigma}_{2,x^2}^{23}}{\tau^3} \\ \gamma_2 = \frac{\bar{\sigma}_{1,x^1}^{13} + \bar{\sigma}_{1,x^2}^{23}}{\tau} + 2 \frac{\left(\bar{\sigma}_{2,x^1}^{13} + \bar{\sigma}_{2,x^2}^{23} \right)}{\tau^2} \\ \gamma_3 = 2 \frac{\left(\bar{\sigma}_{2,x^1}^{13} + \bar{\sigma}_{2,x^2}^{23} \right)}{\tau^3};$$

$$\begin{aligned}
\varsigma &= \frac{2}{h-R} = \Gamma_{13}^1 + \Gamma_{23}^2 \\
\gamma_0 &= \gamma_1 + \frac{h}{2}\gamma_2 - \frac{h^4}{4}\gamma_3 \\
\bar{\gamma}_1 &= \frac{E(h-R)\sin^2(y)}{1-\nu^2}a^{11}(e_1^1 + \nu e_2^2) \\
&\quad - E\frac{\cotan(y)}{1+\nu}a^{11}e_1^2 + \frac{E(h-R)}{1-\nu^2}a^{22}(e_2^2 + \nu e_1^1) \\
\bar{\gamma}_2 &= \frac{E(h-R)\sin^2(y)}{1-\nu^2}a^{11}(k_1^1 + \nu k_2^2) \\
&\quad - E\frac{\cotan(y)}{1+\nu}a^{11}k_1^2 + \frac{E(h-R)}{1-\nu^2}a^{22}(k_2^2 + \nu k_1^1) \\
\bar{\gamma}_3 &= \frac{E(h-R)\sin^2(y)}{1-\nu^2}a^{11}(Q_1^1 + \nu Q_2^2) \\
&\quad - E\frac{\cotan(y)}{1+\nu}a^{11}Q_1^2 \\
&\quad + \frac{E(h-R)}{1-\nu^2}a^{22}(Q_2^2 + \nu Q_1^1).
\end{aligned} \tag{34}$$

Then the third expression of (11) is defined as follows:

$$\begin{aligned}
\sigma^{33}(x, y, z) &= \left\{ \left[\frac{\gamma_0}{\varsigma - \tau} - \gamma_2 \left(\frac{z}{\varsigma - \tau} - \frac{1}{(\varsigma - \tau)^2} \right) \right. \right. \\
&\quad \left. \left. + \gamma_3 \left(\frac{z^2}{\varsigma - \tau} - \frac{2z}{(\varsigma - \tau)^2} + \frac{2}{(\varsigma - \tau)^3} \right) \right] \right. \\
&\quad \cdot \exp\left(-\tau\left(z - \frac{h}{2}\right)\right) + \left[\frac{\bar{\gamma}_1 - \gamma_0}{\varsigma} \right. \\
&\quad \left. + (\gamma_2 - \bar{\gamma}_2) \left(\frac{z}{\varsigma} - \frac{1}{\varsigma^2} \right) \right. \\
&\quad \left. + (\bar{\gamma}_3 - \gamma_3) \left(\frac{z^2}{\varsigma} - \frac{2z}{\varsigma^2} + \frac{2}{\varsigma^3} \right) \right] \\
&\quad \left. + \exp\left(-\tau\left(z - \frac{h}{2}\right)\right) \left[\bar{h}_+^{-3} + \frac{\gamma_0 - \bar{\gamma}_1}{\varsigma} \right. \right. \\
&\quad \left. \left. + (\bar{\gamma}_2 - \gamma_2) \left(\frac{h}{2\varsigma} - \frac{1}{\varsigma^2} \right) \right. \right. \\
&\quad \left. \left. + (\gamma_3 - \bar{\gamma}_3) \left(\frac{h^2}{4\varsigma} - \frac{h}{\varsigma^2} + \frac{2}{\varsigma^3} \right) + \frac{\gamma_0}{\varsigma - \tau} \right. \right. \\
&\quad \left. \left. + \gamma_2 \left(\frac{h}{2(\varsigma - \tau)} - \frac{1}{(\varsigma - \tau)^2} \right) \right. \right. \\
&\quad \left. \left. - \gamma_3 \left(\frac{h^2}{4(\varsigma - \tau)} - \frac{h}{(\varsigma - \tau)^2} + \frac{2}{(\varsigma - \tau)^3} \right) \right] \right\} \{E_u\}.
\end{aligned} \tag{35}$$

2.4. Polynomial Preserving Recovery Method. Let us recall that the linear stress-strain relation does not guarantee smoothness across elements because of gradient jumps since the displacement is only C^0 . The shell is meshed with straight lines triangular elements obtained by linear transformation of a reference 2D triangle. Jumps across elements will be prevented by implementing the gradient recovery methods that we briefly present hereafter. Let u_h be C^0 finite element approximation of the solution u , and let

$$\begin{aligned}
E_1 &= (I, J, K) \\
E_2 &= (I, J, L)
\end{aligned} \tag{36}$$

be two triangular elements with a common node I . We denote

$$\begin{aligned}
U_1 &= (U_h^I, U_h^J, U_h^K), \\
U_2 &= (U_h^I, U_h^J, U_h^L)
\end{aligned} \tag{37}$$

are the vector of nodal values in E_1 and E_2 , respectively. Let N_i be the shape functions matrix; then restriction of u_h in each element reads

$$\begin{aligned}
u_{h|E_1} &= N_1 U_1^t, \\
u_{h|E_2} &= N_2 U_2^t, \\
u'_{h|E_1} &= N'_1 U_1^t, \\
u'_{h|E_2} &= N'_2 U_2^t,
\end{aligned} \tag{38}$$

where N'_i stands for the derivative according to x or y of N_i . At the common node I , the derivative of u_h , $u'_h(I)$, is not necessarily the same in both elements. This means that on a patch including a node I common to different elements the gradient of u_h , ∇u_h , cannot be calculated because of the jump on each part of the patch. Consequently ∇u_h is not a good approximation of ∇u across elements and stress and strain calculated using ∇u cannot be continuous across edges. How to define a unique ∇u_h at a node I common to different elements has been addressed by gradient recovery methods. The idea is to define a local operator G_h such that $G_h u_h(I)$ is unique through any patch and $|G_h u_h - \nabla u|$ has better approximation than $|\nabla u_h - \nabla u|$. Consequently convergence issues of these methods should be considered also. In this analysis we consider the 2D PPR gradient recovery methods which also guarantees a superconvergence property of $G_h u_h$ to ∇u independently of mesh size. The method is described as follows.

Let Z_i be a node where ∇u is to be determined. Let Z_i^j be the nodes of all triangles E_j having Z_i as common vertex. Suppose $u_{h|E_j} \in P_{k+1}$, the set of polynomials of order $k+1$; then the gradient recovery PPR operator consists in defining $p(x) \in P_{k+1}$ such that

$$\sum_{j=1}^n (p(x) - u_h)^2(Z_i^j) = \min_{q(x) \in P_{k+1}} \sum_{j=1}^n (q(x) - u_h)^2(Z_i^j) \tag{39}$$

$$G_h u_h(Z_i) = \nabla p(Z_i).$$

This value also depends on the sampling points chosen. In the 2D case it is proved (cf. [14]) that if $n \geq m = (k+2)(k+3)/2$ and if the sum of two adjacent angles in the mesh is not more than π , then $G_h u_h(Z_i)$ is unique for any Z_i . In this work the angle condition will be implemented in the triangularization. The number m of sampling nodes will be respected as follows:

$$G_h u_h(Z_i) = \nabla p(x_i, y_i) = \nabla \bar{p}(0, 0) \approx \nabla u(x_i, y_i). \quad (40)$$

For the 2D case, three types of nodes can be distinguished: internal nodes, boundary nodes at a corner, and boundary nodes out of a corner.

- (i) For the in-plane displacement u_α ($\alpha = 1, 2$), the existence and uniqueness solution are possible if $(u_1, u_2) \in (H^2(S))^2$; we fit linear polynomial using the same regular pattern:

$$\begin{aligned} P_1(x, y) &= (1, x, y)(a_0, a_1, a_3)^t \\ &= (1, \xi, \varsigma)(\hat{a}_0, \hat{a}_1, \hat{a}_2)^t. \end{aligned} \quad (41)$$

We scale by a factor h with $x = h\xi$ and $y = h\varsigma$, (ξ, ς) with respect to the six derivative values at the barycentric center of each element on the patch. Now we define $e = (1, 1, 1, 1, 1, 1)$, $\hat{a} = (\hat{a}_0, \hat{a}_1, \hat{a}_2) = (a_0, ha_1, ha_3)$, $A = (e, \vec{\xi}, \vec{\varsigma})$, $H = \text{diag}(1, h, h)$.

Let u_α^i be the values of u_α at the nodal points Z_i^i $i = 1, 2, 3, 4, 5, 6$; we denote $\bar{u} = (u_\alpha^i)_{i=1}^6$; we hereby determine \hat{a} so that $A\hat{a} = \bar{b}_h$.

Then, we obtain

$$P_1(x, y) = (1, x, y)H^{-1}(A^t A)^{-1}A^t \bar{b}_h; \quad (42)$$

notice that

$$\begin{aligned} \frac{\partial u_\alpha}{\partial x}(x, y) &= \frac{\partial P_1}{\partial x}(x, y) = (0, 1, 0)H^{-1}(A^t A)^{-1}A^t \bar{b}_h \\ &= [P_1 X_\alpha^1] \bar{b}_h \end{aligned} \quad (43)$$

$$\begin{aligned} \frac{\partial u_\alpha}{\partial y}(x, y) &= \frac{\partial P_1}{\partial y}(x, y) = (0, 0, 1)H^{-1}(A^t A)^{-1}A^t \bar{b}_h \\ &= [P_1 X_\alpha^2] \bar{b}_h. \end{aligned}$$

For the transversal displacement, u_3 , the existence and uniqueness of a gradient recovery solution are possible if $(u_3) \in H^2(S)$; we fit quadratic polynomial using the same regular pattern:

$$\begin{aligned} P_2(x, y) &= (1, x, y, x^2, xy, y^2)(a_1, a_2, a_3, a_4, a_5, a_6)^t \\ &= (1, \xi, \varsigma, \xi^2, \xi\varsigma, \varsigma^2)(\hat{a}_1, \hat{a}_2, \hat{a}_3, \hat{a}_4, \hat{a}_5, \hat{a}_6)^t; \end{aligned} \quad (44)$$

then, we scale by a factor h with $x = h\xi$ and $y = h\varsigma$, (ξ, ς) with respect to the six derivative values at the coordinates nodes of each element on the patch. Let $e = (1, 1, 1, 1, 1, 1)$,

$\hat{a} = (\hat{a}_1, \hat{a}_2, \hat{a}_3, \hat{a}_4, \hat{a}_5, \hat{a}_6) = (a_1, ha_2, ha_3, h^2 a_4, h^2 a_5, h^2 a_6)$ be the vectors of the matrix $B = (e, \vec{\xi}, \vec{\varsigma}, \vec{\xi}^2, \vec{\xi}\vec{\varsigma}, \vec{\varsigma}^2)$ and consider the diagonal matrix $H_1 = \text{diag}(1, h, h, h^2, h^2, h^2)$ and also $\bar{b}_h = (u_{30}, u_{31}, u_{32}, u_{33}, u_{34}, u_{35}, u_{36})$ the approximation vector of u_3 in a nodal point Z_I . Then we fit $P_2(x, y) = (1, x, y, x^2, xy, y^2)H_1^{-1}(B^t B)^{-1}B^t \bar{b}_h$ and obtain the recovered gradient at the patch center point as follows:

$$\begin{aligned} \frac{\partial u_3}{\partial x}(x, y) &= \frac{\partial P_2}{\partial x}(x, y) \\ &= (0, 1, 0, 2x, y, 0)H_1^{-1}(B^t B)^{-1}B^t \bar{b}_h \\ &= [P_2 X_3^1] \bar{b}_h \\ \frac{\partial u_3}{\partial y}(x, y) &= \frac{\partial P_2}{\partial y}(x, y) \\ &= (0, 0, 1, 0, x, 2y)H_1^{-1}(B^t B)^{-1}B^t \bar{b}_h \\ &= [P_2 X_3^2] \bar{b}_h \\ \frac{\partial^2 u_3}{\partial x^2}(x, y) &= \frac{\partial^2 P_2}{\partial x^2}(x, y) \\ &= (0, 1, 0, 2, 0, 0)H_1^{-1}(B^t B)^{-1}B^t \bar{b}_h \\ &= [P_2 X_3^{11}] \bar{b}_h \\ \frac{\partial^2 u_3}{\partial x \partial y}(x, y) &= \frac{\partial^2 P_2}{\partial x \partial y}(x, y) \\ &= (0, 0, 0, 0, 1, 0)H_1^{-1}(B^t B)^{-1}B^t \bar{b}_h \\ &= [P_2 X_3^{12}] \bar{b}_h \\ \frac{\partial^2 u_3}{\partial y^2}(x, y) &= \frac{\partial^2 P_2}{\partial y^2}(x, y) \\ &= (0, 0, 0, 0, 0, 2)H_1^{-1}(B^t B)^{-1}B^t \bar{b}_h \\ &= [P_2 X_3^{22}] \bar{b}_h. \end{aligned} \quad (45)$$

With $G_h u_i$ given at each vertex by the same processes in (43) and (45), we are able to form a recovered gradient field by using the finite element basis functions. Recovering the gradient at a boundary vertex is more delicate. Using efficient strategy computational experiment indicated in [14], to recover the gradient at a vertex $z_I \in \partial S$, we look for the nearest layer of vertices around z_I that contain at least one internal vertex. Let this layer be the n th one and denote the internal vertices in this layer by z_1, z_2, \dots, z_m , where $m \geq 1$. The union of the sampling points used in recovering the gradient at z_1, z_2, \dots, z_m and the mesh nodes in the first n layers around z_I constitute the set of sampling point for recovering the gradient at z_I ; see [15].

3. Discretization of N-T Model

3.1. Finite Element Space. The continuous truncated variational equation (18) is defined in the space U_{ad} . In order to define a finite element space, we begin by recalling the following results. Let T_j be a triangle with nodes $a_1 = (x_1, y_1)$, $a_2 = (x_2, y_2)$, and $a_3 = (x_3, y_3)$. Let P_1 and P_2 be the sets of the first- and second-order polynomials with basis $\{1, x, y\}$ and $\{1, x, y, x^2, y^2, xy\}$, respectively, then $\{\lambda_1, \lambda_2, \lambda_3\}$ and $\{\lambda_1, \lambda_2, \lambda_3, 4\lambda_1\lambda_2, 4\lambda_1\lambda_3, 4\lambda_2\lambda_3\}$ also generate P_1 and P_2 where the barycentric basis functions of the triangle are defined by

$$\begin{aligned} \lambda_1(x, y) &= \frac{1}{2\Delta} [(y_3 - y_2)(x_2 - x) - (x_3 - x_2)(y_2 - y)] \\ \lambda_2(x, y) &= \frac{1}{2\Delta} [(y_1 - y_3)(x_3 - x) - (x_1 - x_3)(y_3 - y)] \\ \lambda_3(x, y) &= \frac{1}{2\Delta} [(y_2 - y_1)(x_1 - x) - (x_2 - x_1)(y_1 - y)] \\ 2\Delta &= 2 \int_{T_j} dx dy = 2 \det \begin{bmatrix} 1 & 1 & 1 \\ x_1 & x_2 & x_3 \\ y_1 & y_2 & y_3 \end{bmatrix} \\ &= (x_3 - x_2)(y_1 - y_2) - (x_1 - x_2)(y_3 - y_2). \end{aligned} \quad (46)$$

Let T_h be a triangularization of the midsurface of the shell and n_h the number of triangles. We denote by

$$\begin{aligned} X_h^1 &= \left\{ v_h \in C^0(\bar{S}), v_{h|T_j} \in P_1(T_j), \forall T_j, j = 1, \dots, n_h \right\} \end{aligned} \quad (47)$$

the subspace of dimension N_h (which is the number of nodes) and

$$\begin{aligned} X_h^2 &= \left\{ v_h \in C^0(\bar{S}), v_{h|T_j} \in P_2(T_j), \forall T_j, j = 1, \dots, n_h, \nabla v_h = G_h v_h = \nabla P_2 \right\}; \end{aligned} \quad (48)$$

\bar{S} is the closure of S , the subspace of dimension N_h^2 which is the number of unisolvent points (nodes and edge mid points).

The space $U_{\text{ad}} = (H_0^1(S))^2 \times H_0^2(S)$ is approximated with the finite element space of dimension $3N = 2N_h + N_h^2$

$$\mathcal{U}_h = X_h^1 \times X_h^1 \times X_h^2. \quad (49)$$

3.2. The Discrete Scheme. Let T_h be a triangularization of the shell's midsurface S and $T_j \in T_h$ be a triangle of vertices

a_1, a_2, a_3 and midedges a_4, a_5, a_6 . Let $\eta^h \in \mathcal{U}_h$ as defined above. Then

$$\begin{aligned} \eta_\alpha^h(x, y)|_{T_j} &\in P_1, \quad \alpha = 1, 2; \quad 1 \leq j \leq n_h, \\ \eta_3^h(x, y)|_{T_j} &\in P_2, \quad 1 \leq j \leq n_h. \end{aligned} \quad (50)$$

By using the barycentric polynomials and writing $\lambda_4 = \lambda_1, 1 \leq l \leq 2; 1 \leq \alpha, \beta \leq 2$, and $1 \leq j \leq n_h$,

$$\begin{aligned} \eta_\alpha^h(x, y)|_{T_j} &= \sum_{k=1}^3 \eta_\alpha^h(a_k) \lambda_k(x, y) = \sum_{k=1}^3 \bar{\eta}_\alpha^k \lambda_k(x, y) \\ \eta_3^h(x, y)|_{T_j} &= \sum_{k=1}^3 \eta_3^h(a_k) \lambda_k(x, y) \\ &\quad + \sum_{k=4}^6 \eta_3^h(a_k) \lambda_{k-3}(x, y) \lambda_{k-2}(x, y) \\ &= \sum_{k=1}^3 \bar{\eta}_3^k \lambda_k(x, y) \\ &\quad + \sum_{k=4}^6 \bar{\eta}_3^k \lambda_{k-3}(x, y) \lambda_{k-2}(x, y) \end{aligned} \quad (51)$$

$$\partial_\alpha \eta_l^h(x, y)|_{T_j} = \sum_{k=1}^3 \partial_\alpha \eta_3^h(a_k) \lambda_k(x, y),$$

$$\partial_\alpha \eta_l^h(a_k) = G_h(\eta_l^h)(a_k)$$

$$\partial_{\alpha\beta}^2 \eta_3^h(x, y)|_{T_j} = \sum_{k=1}^3 \partial_{\alpha\beta}^2 \eta_3^h(a_k) \lambda_k(x, y),$$

$$\partial_{\alpha\beta}^2 \eta_3^h(a_k) = G_h(\partial_\alpha \eta_3^h)(a_k).$$

In the above formula, G_h is the gradient operator and $\bar{\eta}_3^4, \bar{\eta}_3^5$, and $\bar{\eta}_3^6$ are, respectively, the unknown values of η_3 in the midedges a_1a_2, a_1a_3 , and a_2a_3 . Let

(i) $[P_\nu I_\alpha^\beta] = [P_\nu X_\alpha^\beta]$ and $[P_2 I_\alpha^{\alpha\beta}] = [P_2 X_\alpha^{\alpha\beta}]$ the coefficient of the approximation of the gradient when the vertex is internal of the mesh,

(ii) $[P_\nu C_\alpha^\beta] = [P_\nu X_\alpha^\beta]$ and $[P_2 C_\alpha^{\alpha\beta}] = [P_2 X_\alpha^{\alpha\beta}]$ the coefficient of the approximation of the gradient when the vertex is in the boundary at the corner of the mesh,

(iii) $[P_\nu M_\alpha^\beta] = [P_\nu X_\alpha^\beta]$ and $[P_2 M_\alpha^{\alpha\beta}] = [P_2 X_\alpha^{\alpha\beta}]$ the coefficient of the approximation of the gradient when the vertex is in the boundary not at the corner of the mesh.

Exploiting the above, let us take linear element on uniform triangular mesh of a regular pattern; we hereby investigate the case of the element where all three nodes are internal of the mesh; the matrices deduced from the discretization of the gradient are given as follows:

$$\begin{aligned}
 [A_1] &= \begin{bmatrix} \lambda_1(x_1, y_1) & 0 & 0 & 0 & 0 & 0 & 0 \\ 0 & \lambda_2(x_1 + h, y_1) & 0 & 0 & 0 & 0 & 0 \\ 0 & 0 & 0 & 0 & 0 & 0 & \lambda_3(x_1, y_1 - h) \end{bmatrix}^t \\
 [A_2] &= \begin{bmatrix} 0 & 0 & 0 & 0 & \lambda_1(x_2 - h, y_2) & 0 & 0 \\ \lambda_2(x_2, y_2) & 0 & 0 & 0 & 0 & 0 & 0 \\ 0 & 0 & 0 & 0 & 0 & \lambda_3(x_2 - h, y_2 - h) & 0 \end{bmatrix}^t \\
 [A_3] &= \begin{bmatrix} 0 & 0 & 0 & \lambda_1(x_3, y_3 + h) & 0 & 0 & 0 \\ 0 & 0 & \lambda_2(x_3 + h, y_3 + h) & 0 & 0 & 0 & 0 \\ \lambda_3(x_3, y_3) & 0 & 0 & 0 & 0 & 0 & 0 \end{bmatrix}^t.
 \end{aligned} \tag{52}$$

When we return to energy function with $m = 0, 1$, we have

$$\begin{aligned}
 A_m(\bar{u}, \bar{v}) &= \int_S (E_u^T C_g^m E_v) dS \\
 &= \sum_{j=1}^{n_h} \sum_{k=1}^3 \int_{T_j} \left([E_{\bar{u}_k}^{T_j}]^t C_g^m [E_{\bar{v}_k}^{T_j}] \right) dx dy.
 \end{aligned} \tag{53}$$

Using (43), (45), and (51) in which all three nodes of the triangular element are internal, let $i = 1, 2, 3$; $\alpha, \beta = 1, 2$ and we consider

$$\begin{aligned}
 \alpha_i &= \lambda_i(x, y) \\
 \rho_k &= 4\lambda_{k-3}(x, y) \lambda_{k-2}(x, y), \quad k = 4, 5, 6
 \end{aligned}$$

$$\begin{aligned}
 \beta_i^\alpha &= [P_1 I_i^\alpha] [A_1](:, i) + [P_1 I_i^\alpha] [A_2](:, i) \\
 &\quad + [P_1 I_i^\alpha] [A_3](:, i) \\
 \gamma_i^\alpha &= [P_2 I_3^\alpha] [A_1](:, i) + [P_2 I_3^\alpha] [A_2](:, i) \\
 &\quad + [P_2 I_3^\alpha] [A_3](:, i) \\
 \tau_i^{\alpha\beta} &= [P_2 I_3^{\alpha\beta}] [A_1](:, i) + [P_2 I_3^{\alpha\beta}] [A_2](:, i) \\
 &\quad + [P_2 I_3^{\alpha\beta}] [A_3](:, i).
 \end{aligned} \tag{54}$$

Then the deformation vector can be written as $\{E_u^{T_j}\} = [B^{T_j}] \{d_u^{T_j}\}$ where

$$\begin{aligned}
 & [B^{T_j}]^t \\
 &= \begin{bmatrix} \alpha_1 & \alpha_2 & \alpha_3 & 0 & 0 & 0 & 0 & 0 & 0 & 0 & 0 & 0 & 0 \\ \beta_1^1 & \beta_2^1 & \beta_3^1 & 0 & 0 & 0 & 0 & 0 & 0 & 0 & 0 & 0 & 0 \\ \beta_1^2 & \beta_2^2 & \beta_3^2 & 0 & 0 & 0 & 0 & 0 & 0 & 0 & 0 & 0 & 0 \\ 0 & 0 & 0 & \alpha_1 & \alpha_2 & \alpha_3 & 0 & 0 & 0 & 0 & 0 & 0 & 0 \\ 0 & 0 & 0 & \beta_1^1 & \beta_2^1 & \beta_3^1 & 0 & 0 & 0 & 0 & 0 & 0 & 0 \\ 0 & 0 & 0 & \beta_1^2 & \beta_2^2 & \beta_3^2 & 0 & 0 & 0 & 0 & 0 & 0 & 0 \\ 0 & 0 & 0 & 0 & 0 & 0 & \alpha_1 & \alpha_2 & \alpha_3 & \rho_4 & \rho_5 & \rho_6 & 0 \\ -2b_1^1 \alpha_1 & -2b_1^1 \alpha_2 & -2b_1^1 \alpha_3 & -2b_1^2 \alpha_1 & -2b_1^2 \alpha_2 & -2b_1^2 \alpha_3 & -\gamma_1^1 & -\gamma_2^1 & -\gamma_3^1 & 0 & 0 & 0 & 0 \\ -2b_1^1 \beta_1^1 & -2b_1^1 \beta_2^1 & -2b_1^1 \beta_3^1 & -2b_1^2 \beta_1^1 & -2b_1^2 \beta_2^1 & -2b_1^2 \beta_3^1 & -\tau_1^{11} & -\tau_2^{11} & -\tau_3^{11} & 0 & 0 & 0 & 0 \\ -2b_1^1 \beta_1^2 & -2b_1^1 \beta_2^2 & -2b_1^1 \beta_3^2 & -2b_1^2 \beta_1^2 & -2b_1^2 \beta_2^2 & -2b_1^2 \beta_3^2 & -\tau_1^{12} & -\tau_2^{12} & -\tau_3^{12} & 0 & 0 & 0 & 0 \\ -2b_2^1 \alpha_1 & -2b_2^1 \alpha_2 & -2b_2^1 \alpha_3 & -2b_2^2 \alpha_1 & -2b_2^2 \alpha_2 & -2b_2^2 \alpha_3 & -\gamma_1^2 & -\gamma_2^2 & -\gamma_3^2 & 0 & 0 & 0 & 0 \\ -2b_2^1 \beta_1^1 & -2b_2^1 \beta_2^1 & -2b_2^1 \beta_3^1 & -2b_2^2 \beta_1^1 & -2b_2^2 \beta_2^1 & -2b_2^2 \beta_3^1 & -\tau_1^{12} & -\tau_2^{12} & -\tau_3^{12} & 0 & 0 & 0 & 0 \\ -2b_2^1 \beta_1^2 & -2b_2^1 \beta_2^2 & -2b_2^1 \beta_3^2 & -2b_2^2 \beta_1^2 & -2b_2^2 \beta_2^2 & -2b_2^2 \beta_3^2 & -\tau_1^{22} & -\tau_2^{22} & -\tau_3^{22} & 0 & 0 & 0 & 0 \\ \bar{b}^{-1} \alpha_1 & \bar{b}^{-1} \alpha_2 & \bar{b}^{-1} \alpha_3 & \bar{b}^{-1} \alpha_1 & \bar{b}^{-1} \alpha_2 & \bar{b}^{-1} \alpha_3 & b_1^1 \gamma_1^1 + b_1^2 \gamma_1^2 & b_1^1 \gamma_2^1 + b_1^2 \gamma_2^2 & b_1^1 \gamma_3^1 + b_1^2 \gamma_3^2 & 0 & 0 & 0 & 0 \\ \bar{b}^{-1} \beta_1^1 & \bar{b}^{-1} \beta_2^1 & \bar{b}^{-1} \beta_3^1 & \bar{b}^{-1} \beta_1^1 & \bar{b}^{-1} \beta_2^1 & \bar{b}^{-1} \beta_3^1 & b_1^1 \tau_1^{11} + b_1^2 \tau_1^{12} & b_1^1 \tau_2^{11} + b_1^2 \tau_2^{12} & b_1^1 \tau_3^{11} + b_1^2 \tau_3^{12} & 0 & 0 & 0 & 0 \\ \bar{b}^{-1} \beta_1^2 & \bar{b}^{-1} \beta_2^2 & \bar{b}^{-1} \beta_3^2 & \bar{b}^{-1} \beta_1^2 & \bar{b}^{-1} \beta_2^2 & \bar{b}^{-1} \beta_3^2 & b_1^1 \tau_1^{12} + b_1^2 \tau_1^{22} & b_1^1 \tau_2^{12} + b_1^2 \tau_2^{22} & b_1^1 \tau_3^{12} + b_1^2 \tau_3^{22} & 0 & 0 & 0 & 0 \\ \bar{b}^{-2} \alpha_1 & \bar{b}^{-2} \alpha_2 & \bar{b}^{-2} \alpha_3 & \bar{b}^{-2} \alpha_1 & \bar{b}^{-2} \alpha_2 & \bar{b}^{-2} \alpha_3 & b_2^1 \gamma_1^1 + b_2^2 \gamma_1^2 & b_2^1 \gamma_2^1 + b_2^2 \gamma_2^2 & b_2^1 \gamma_3^1 + b_2^2 \gamma_3^2 & 0 & 0 & 0 & 0 \\ \bar{b}^{-2} \beta_1^1 & \bar{b}^{-2} \beta_2^1 & \bar{b}^{-2} \beta_3^1 & \bar{b}^{-2} \beta_1^1 & \bar{b}^{-2} \beta_2^1 & \bar{b}^{-2} \beta_3^1 & b_2^1 \tau_1^{11} + b_2^2 \tau_1^{12} & b_2^1 \tau_2^{11} + b_2^2 \tau_2^{12} & b_2^1 \tau_3^{11} + b_2^2 \tau_3^{12} & 0 & 0 & 0 & 0 \\ \bar{b}^{-2} \beta_1^2 & \bar{b}^{-2} \beta_2^2 & \bar{b}^{-2} \beta_3^2 & \bar{b}^{-2} \beta_1^2 & \bar{b}^{-2} \beta_2^2 & \bar{b}^{-2} \beta_3^2 & b_2^1 \tau_1^{12} + b_2^2 \tau_1^{22} & b_2^1 \tau_2^{12} + b_2^2 \tau_2^{22} & b_2^1 \tau_3^{12} + b_2^2 \tau_3^{22} & 0 & 0 & 0 & 0 \end{bmatrix},
 \end{aligned} \tag{55}$$

$$\{d_u^{T_j}\} = [\bar{u}_1^{j1}, \bar{u}_1^{j2}, \bar{u}_1^{j3}, \bar{u}_2^{j1}, \bar{u}_2^{j2}, \bar{u}_2^{j3}, \bar{u}_3^{j1}, \bar{u}_3^{j2}, \bar{u}_3^{j3}, \bar{u}_3^{j4}, \bar{u}_3^{j5}, \bar{u}_3^{j6}]^t. \tag{56}$$

3.3. *Stiffness Matrix.* Using local element, stiffness matrix can be expressed as follows:

$$[K_0^j] = \int_{T_j} \left([B^{T_j}]^t C_g^0 [B^{T_j}] \right) dx dy; \quad 1 \leq j \leq N_h \quad (57)$$

$$[K_1^j] = \int_{T_j} \left([B^{T_j}]^t C_g^1 [B^{T_j}] \right) dx dy; \quad 1 \leq j \leq N_h,$$

where

$$\begin{aligned} C_g^0 &= \frac{Eh}{1-\nu^2} (1-\nu) ([D_e]_\beta^\alpha)^t ([D_e]_\alpha^\beta) \\ &+ \frac{Eh}{1-\nu^2} \nu ([D_e]_\alpha^\alpha)^t ([D_e]_\lambda^\lambda) \\ &+ \frac{Eh^3}{12(1-\nu^2)} (1-\nu) ([D_k]_\beta^\alpha)^t ([D_k]_\alpha^\beta) \\ &+ \frac{Eh^3}{12(1-\nu^2)} \nu ([D_k]_\alpha^\alpha)^t ([D_k]_\lambda^\lambda) \\ C_g^1 &= \frac{Eh}{1-\nu^2} (1-\nu) ([D_e]_\beta^\alpha)^t ([D_e]_\alpha^\beta) \\ &+ \frac{Eh}{1-\nu^2} \nu ([D_e]_\alpha^\alpha)^t ([D_e]_\lambda^\lambda) \\ &+ \frac{Eh^3}{12(1-\nu^2)} (1-\nu) ([D_k]_\beta^\alpha)^t ([D_k]_\alpha^\beta) \\ &+ \frac{Eh^3}{12(1-\nu^2)} \nu ([D_k]_\alpha^\alpha)^t ([D_k]_\lambda^\lambda) \\ &+ \frac{Eh^3}{12(1-\nu^2)} (1-\nu) ([D_Q]_\beta^\alpha)^t ([D_e]_\alpha^\beta) \\ &+ \frac{Eh^3}{12(1-\nu^2)} \nu ([D_Q]_\alpha^\alpha)^t ([D_k]_\lambda^\lambda) \\ &+ \frac{Eh^3}{12(1-\nu^2)} (1-\nu) ([D_e]_\beta^\alpha)^t ([D_Q]_\alpha^\beta) \\ &+ \frac{Eh^3}{12(1-\nu^2)} \nu ([D_e]_\alpha^\alpha)^t ([D_Q]_\lambda^\lambda) \\ &+ \frac{Eh^5}{80(1-\nu^2)} (1-\nu) ([D_Q]_\beta^\alpha)^t ([D_Q]_\alpha^\beta) \\ &+ \frac{Eh^5}{80(1-\nu^2)} \nu ([D_Q]_\alpha^\alpha)^t ([D_Q]_\lambda^\lambda) \end{aligned} \quad (58)$$

is the generalized 19×19 behavior matrix.

Let $F_0(x, y) = ([B^{T_j}]^t C_g^0 [B^{T_j}])$ and $F_1(x, y) = ([B^{T_j}]^t C_g^1 [B^{T_j}])$; then we have

$$\begin{aligned} [K_0^j] &= \int_{T_j} F_0(x, y) dx dy; \quad 1 \leq j \leq N_h \\ &= \frac{1}{3} F_0 \left(\frac{2}{3} x_1 + \frac{1}{6} x_2 + \frac{1}{6} x_3, \frac{2}{3} y_1 + \frac{1}{6} y_2 + \frac{1}{6} y_3 \right) \\ &+ \frac{1}{3} F_0 \left(\frac{1}{6} x_1 + \frac{2}{3} x_2 + \frac{1}{6} x_3, \frac{1}{6} y_1 + \frac{2}{3} y_2 + \frac{1}{6} y_3 \right) \\ &+ \frac{1}{3} F_0 \left(\frac{1}{6} x_1 + \frac{1}{6} x_2 + \frac{2}{3} x_3, \frac{1}{6} y_1 + \frac{1}{6} y_2 + \frac{2}{3} y_3 \right) \end{aligned} \quad (59)$$

$$\begin{aligned} [K_1^j] &= \int_{T_j} F_1(x, y) dx dy; \quad 1 \leq j \leq N_h \\ &= \frac{1}{3} F_1 \left(\frac{2}{3} x_1 + \frac{1}{6} x_2 + \frac{1}{6} x_3, \frac{2}{3} y_1 + \frac{1}{6} y_2 + \frac{1}{6} y_3 \right) \\ &+ \frac{1}{3} F_1 \left(\frac{1}{6} x_1 + \frac{2}{3} x_2 + \frac{1}{6} x_3, \frac{1}{6} y_1 + \frac{2}{3} y_2 + \frac{1}{6} y_3 \right) \\ &+ \frac{1}{3} F_1 \left(\frac{1}{6} x_1 + \frac{1}{6} x_2 + \frac{2}{3} x_3, \frac{1}{6} y_1 + \frac{1}{6} y_2 + \frac{2}{3} y_3 \right). \end{aligned}$$

Using (18) the second member of the variational equation is written as follows:

$$\begin{aligned} L(\dot{v}) &= \sum_{j=1}^N \int_{T_j} \left\{ d_v^{T_j} \right\}^t [B^{T_j}]^t [P] |J|^{T_j} dS \\ &+ \oint_{\omega_1}^{\omega_2} \left\{ d_v^{T_j} \right\}^t [B^{T_j}]^t [G] |J_*|^{T_j} d\zeta \quad (60) \\ &= \sum_{j=1}^{n_h} \left\{ d_v^{T_j} \right\} [f^j], \end{aligned}$$

where $[f^j] = [F_1^{j1}, F_1^{j2}, F_1^{j3}, F_2^{j1}, F_2^{j2}, F_2^{j3}, F_3^{j1}, F_3^{j2}, F_3^{j3}, F_3^{j4}, F_3^{j5}, F_3^{j6}]^T$ and $\{d_v^{T_j}\}$ is defined as in (56); here $|J_*|$ is the determinant of the Jacobian which toggles between the linear element $d\zeta$ of curve $\phi(\gamma_1)$ to real element dy . These formulas take into account the load spread over the entire surface and average load at the edges.

4. Validation Tests of Our Finite Element

The aim of this study is to investigate the accuracy of N-T thick shells theory for linear elastic shell by using Spherical Shell Finite Element (SSFE). We lay our investigation on a well-known benchmark as hemisphere under diametrically opposite charges given in Figure 1 used to evaluate the performance of a shell element. The computed deformed limit surface of a quarter of the hemisphere is shown in Figure 2 plotted with the Matlab R2015a tools and the displacement convergence results are shown in Figure 3 and Table 1.

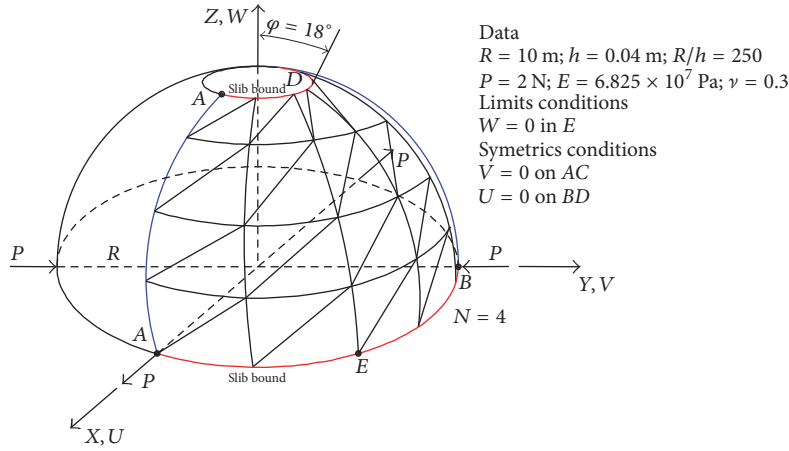


FIGURE 1: Hemisphere shell benchmark.

TABLE 1: Table of results of displacement at point A for the hemisphere.

Thickness = 0.04 and force = 0.5 N sol_ref = reference solution ($U_A * 10^3$)						
N	DKT12	DKT18	SKLFE	SFE3 (cmc)	SSFE	sol_ref
2	121	87	—	4.1	—	94
3	—	—	1.6	—	1.61	94
4	108	94	10.2	28	10.21	94
6	102	94	52.3	63	52.3	94
8	99	93	73.8	77	73.8	94
10	98	93	81.56	82	81.55	94
12	96	93	86.3	84	86.32	94
15			88.4	86	88.4	94
20			86.5	87	86.52	94

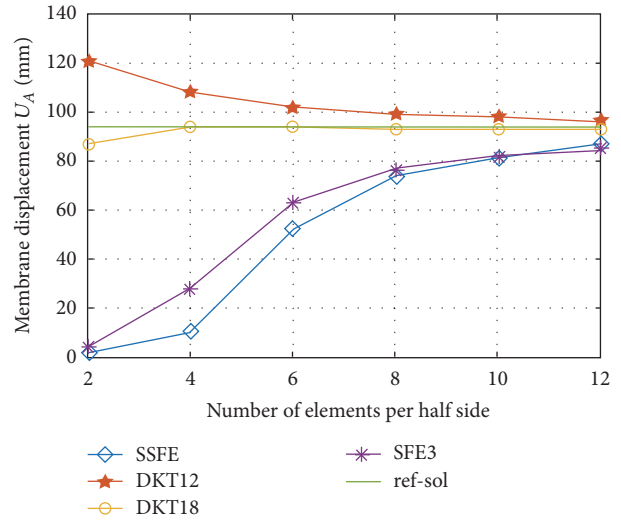


FIGURE 3: Convergence in the hemisphere.

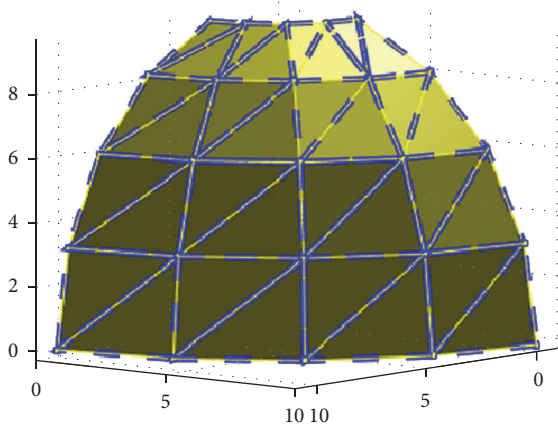


FIGURE 2: Deformed configuration of one quarter of the hemisphere.

We monitor the displacement in load point A presented in Figure 1.

Here, the case study is that of a thin shell of hemisphere subjected to four opposite diametrically concentrated loads at the base proposed by Macneal and Harder [20] which

is a standard test. This benchmark is usually used to verify the absence of membrane locking and good representation of rigid bodies motion. The hemisphere undergoes large rotations around the normal of the middle surface. Deformations of inextensible bending membrane are also important and this problem is therefore an excellent test to examine the ability of a shell element to represent the rigid and inextensible modes. The geometrical and mechanical characteristics are indicated for $h/R = 0.004$, the radius $R = 10 \text{ m}$, the thickness $h = 0.04 \text{ m}$, the angle subtended by the north pole of the hemisphere is $\theta = 18^\circ$, Young's modulus is $E = 6.825e + 7 \text{ Pa}$, Poisson's ratio is $\nu = 0.3$, and the diametrically opposite loads at points A and B are 0.5 N. The limits conditions $W = 0$ in the slab bound E and the symmetric conditions are given by $V = 0$ on the edge bound AC and $U = 0$ on the edge bound BD.

4.1. Convergence. A reference solution presented in [20] provides for displacement in the direction of the loads as follows: $U_A = V_B = 0.094 \text{ m}$. Only 1/4 of the hemisphere

TABLE 2: Deviation of both Reissner-Mindlin (R-M) and N-T thick shell according to the scaling of the ratio h/R .

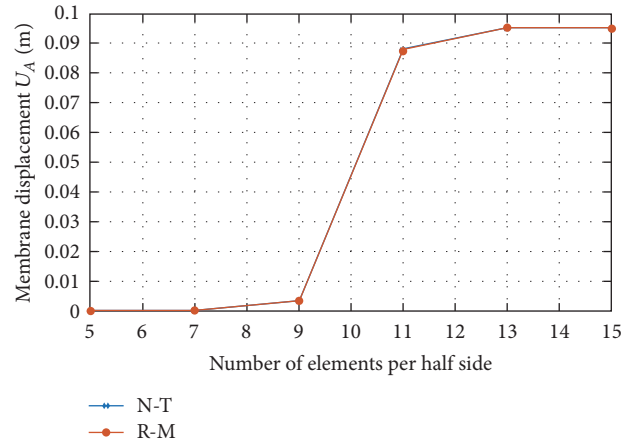
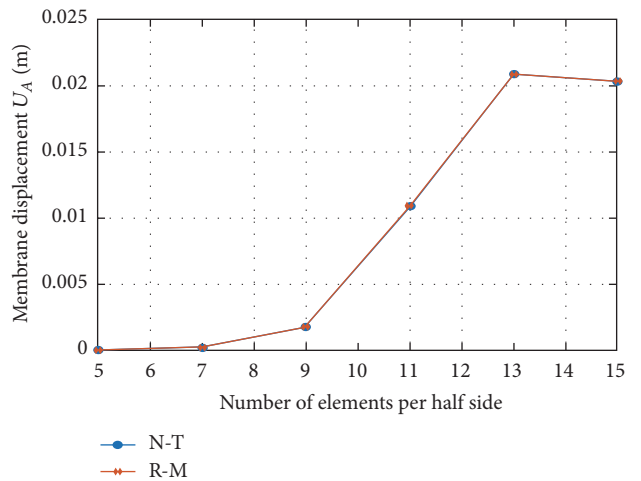
Ratio h/R	Theory	Mesh					
		5×5	7×7	9×9	11×11	13×13	15×15
0.006	R-M	$1.77 * 10^{-5}$	$3.91 * 10^{-4}$	0.0035	0.088	0.0954	0.0950
	N-T	$1.77 * 10^{-5}$	$3.91 * 10^{-4}$	0.0035	0.0877	0.0954	0.0950
0.099	R-M	$1.14 * 10^{-5}$	$2.64 * 10^{-4}$	0.0018	0.0109	0.0209	0.0204
	N-T	$1.14 * 10^{-5}$	$2.64 * 10^{-4}$	0.0018	0.0110	0.0209	0.0204
0.12	R-M	$2.91 * 10^{-6}$	$8.76 * 10^{-6}$	$4.52 * 10^{-3}$	$1.07 * 10^{-2}$	$2.76 * 10^{-2}$	$2.47 * 10^{-2}$
	N-T	$4.67 * 10^{-6}$	$9.72 * 10^{-6}$	$3.52 * 10^{-3}$	$9.90 * 10^{-3}$	$2.67 * 10^{-2}$	$2.47 * 10^{-2}$
0.15	R-M	$1.07 * 10^{-6}$	$1.20 * 10^{-5}$	$4.67 * 10^{-4}$	$5.02 * 10^{-3}$	$1.57 * 10^{-2}$	$1.39 * 10^{-2}$
	N-T	$3.03 * 10^{-6}$	$4.21 * 10^{-6}$	$1.79 * 10^{-4}$	$2.35 * 10^{-3}$	$1.36 * 10^{-2}$	$1.17 * 10^{-2}$
0.175	R-M	$1.23 * 10^{-6}$	$2.87 * 10^{-6}$	$3.20 * 10^{-4}$	$3.22 * 10^{-3}$	$9.41 * 10^{-3}$	$8.96 * 10^{-3}$
	N-T	$8.20 * 10^{-7}$	$1.02 * 10^{-6}$	$2.30 * 10^{-4}$	$3.41 * 10^{-4}$	$7.12 * 10^{-3}$	$6.89 * 10^{-3}$
0.2	R-M	$5.36 * 10^{-7}$	$3.51 * 10^{-6}$	$4.89 * 10^{-4}$	$2.89 * 10^{-3}$	$5.88 * 10^{-3}$	$5.52 * 10^{-3}$
	N-T	$4.01 * 10^{-7}$	$3.10 * 10^{-6}$	$3.71 * 10^{-4}$	$2.49 * 10^{-4}$	$5.57 * 10^{-3}$	$5.23 * 10^{-3}$

is discretized because of the symmetry of loads and the geometry. Both Kirchhoff-Love shell theory and N-T shell theory are computed using SSFE model and the respective results are analysed, compared with DKT12 and DKT18 proposed in [21] and SFE3 [22] then commented. Table 1 shows the displacement results at point A and Figure 3 perfectly describes their variation and the rate of convergence. The convergence properties of the method are clearly shown from Figure 3 and Table 1. Then SSFE converge as well as both the semifinite element (SFE) and Discrete Kirchhoff Triangle (DKT) elements for the membrane displacement at load point A.

4.2. Scaling and Deviation. Scaling of the ratio $2\chi = h/R$ given in Table 2 is proceeded on the range of the following values 0.006, 0.099, 0.12, 0.15, 0.175, and 0.2 of the spherical shell. Notice that the radius R is constant while the thickness varies with the ratio. We observe in Tables 1 and 2 and Figure 3 that, for the thickness ratio $0 < 2\chi < 0.099$, the membrane displacement in load point A is the same for both K-L and N-T models. When the ratio $2\chi = h/R$ is greater or equal to 0.099, the displacement computed for inextensible bending membrane from spherical equation of K-L and N-T is not the same. This means that, above $2\chi \approx 1/10$, both K-L and N-T approaches are different for all values of the thickness ratio.

We investigate now the deviation between K-L and N-T displacements in load point A. With the variation of thickness ratio $2\chi = 0.06, 0.099, 0.12, 0.15, 0.175$, and 0.2 , the results plotted in Table 2 and Figures 4–7 clearly show that the deviation of displacement is encountered at the specified values of 2χ above. This deviation increases with the number of meshes at the load point A. We also observe that the deviation increases with thickness ratio.

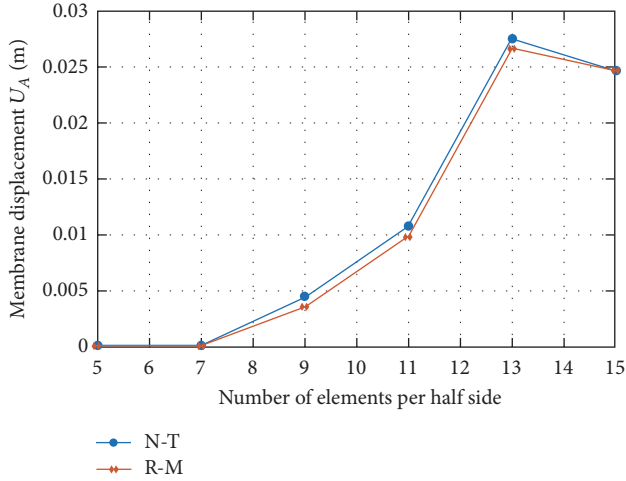
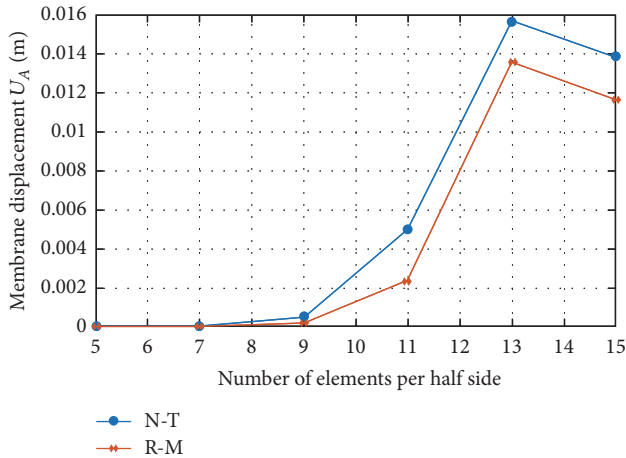
4.3. Impact of the Transverse Stresses. Surveys of various shear stresses in linear elastic thick shells can be found in the works of [3] where they are mathematically substantiated. We have obtained good convergence results for thin shells with the half side element $N = 12$ and a pressure in the load point $P_A = 0.53$ Pa for a spherical shell. For the thickness coordinate

FIGURE 4: Variation of membrane displacement U_A at A for the thickness ratio $2\chi = h/R = 0.006$.FIGURE 5: Variation of membrane displacement U_A at A for the thickness ratio $2\chi = h/R = 0.099$.

$z \in [-h/2, +h/2]$, where $h = 1.2$ m, the numerical results of the transverse shear stresses through the thickness are computed (see Table 3).

TABLE 3: Transverse shear stresses of a thick spherical shell under load point A convergence analysis.

z	-0.6	-0.466	-0.2	0.066	0.2	0.467	0.6
σ^{13} (Pa)	0	0.005	0.001	0.019	0.021	0.025	0.259
σ^{23} (Pa)	0	0.007	0.018	0.026	0.028	0.034	0.035
σ^{33} (Pa)	1.6×10^{-14}	-0.132	0.309	-0.417	-0.455	-0.514	-0.533


 FIGURE 6: Variation of membrane displacement U_A at A for the thickness ratio $2\chi = h/R = 0.12$.

 FIGURE 7: Variation of membrane displacement U_A at A for the thickness ratio $2\chi = h/R = 0.15$.

After shear stresses investigation, we observe that they satisfy tangential stress-free boundary conditions at bottom to top surfaces of the panel. These results show predicting ability of SSFE finite element based on N-T's model. It also appears that the shear stresses vary through the thickness as compared to 3D thick shell equations. We can also appreciate that transverse shear stresses σ^{13} and σ^{23} are not negligible in thick shells.

4.4. Discussion. C^0 finite element discretization of the first-order N-T model applied the PPR method to solve problems of gradient discontinuities across edges of triangular elements

during interpolation. The displacement is two-degree polynomial of the thickness ratio χ while the membrane strain tensor contains the change in the third fundamental form.

The convergence of SSFE has been clearly established and this element uses 12 degrees of freedom per triangular element which is robust and less greedy (in terms of memory) than DKT12, DKT18, and SFE that are based on the Kirchhoff-Love (thin shells) and Reissner-Mindlin (thick shells) approaches which neglect the third fundamental form in their shell kinematic equations [23]. The constitutive law through the strain tensor contains the change of third fundamental form $Q_{\alpha\beta}$ as shown in the tables; the thickness ratio χ impacts the behavior of the shell because of the significant energy contribution due to $Q_{\alpha\beta}$ as the ratio increases unlike the K-L classical model [3].

Recall that, in (17), we see that total deformation energy due to K-L and R-M models contains membrane deformation energy E_{ee} and bending deformation energy E_{kk} ; that is, $E^{R-M} = E_{ee} + E_{kk}$. Equation (18) shows that the total deformation energy due to N-T model contains additional terms: coupled membrane and Gaussian bending (E_{eQ}, E_{Qe}) and Gaussian deformation energy E_{QQ} . Then $E^{N-T} = E^{R-M} + E_{QQ} + E_{eQ} + E_{Qe}$.

Where $E_{ee} = E(h/R)\alpha_{ee}$, $E_{kk} = E(h/R)(h/R)^2\alpha_{kk}$, $E_{QQ} = 10^{-1}E(h/R)(h/R)^4\alpha_{QQ}$, and $E_{eQ} = E_{Qe} = 10^{-1}E(h/R)(h/R)^2\alpha_{eQ}$, which represents the portion of energy contribution, α_{ee} , α_{kk} , and α_{eQ} are constants which do not depend on h/R .

As we mentioned above, when the thickness ratio 2χ is greater than 0.098, this additional energy (E_{eQ}, E_{Qe}) influences global deformation energy and shows the difference between N-T and R-M models applied to the spherical thick shells.

The investigation of the variation of the thickness ratio h/R for certain values $0 < 2\chi < 0.099$ proves that the Kirchhoff-Love, Reissner-Mindlin, and N-T classical models have the same contribution of total deformation energy. The additional terms containing the change of the third fundamental form do not have here any influence. The energies E_{eQ} and E_{QQ} disappear in the global deformation energy when $2\chi < 0.1$ or $\chi^2 < 0.01$ because they are inversely proportional, respectively, to 10^4 and 10^8 . In this case $E^{N-T} = E^{R-M}$. But if the thickness ratio is $0.099 \leq h/R < 1$, displacement results encountered for both models are different because E_{eQ} and E_{QQ} do not disappear in the global deformation energy. The consequence is that they enhance global deformation energy and improve the rigidity of the shell structure. Moreover, N-T's model brings us real facilitation to determine the distribution of transverse shear stresses through the thickness.

5. Conclusion

The finite element SSFE using the PPR method for the spherical shell described in this paper for C^0 finite element triangularization has given accurate results and is skilled to design thicker shells. It has proved to be faster and uses less memory than other well-known methods used in the different benchmarks. The N-T model handles spherical thin and thick shell properly because it clearly shows how the change of the third fundamental form enhances the total deformation energy when the ratio χ becomes greater.

Transverse stresses which have been predicted by the 2D governing equations of N-T model were calculated numerically and correctly. Structural engineers can therefore design more accurately spherical thick shells.

Disclosure

Achille Germain Feumo is the corresponding author, Robert Nzengwa is co-first author, and Joseph Nkongho Anyi is co-second author.

Conflicts of Interest

The authors declare that they have no conflicts of interest regarding this research article.

References

- [1] E. Reisner, "The effect of transverse shear deformation on the bending of elastic plates," *Journal of Applied Mechanics*, vol. 12, pp. A-69–A-77, 1945.
- [2] M. Bernadou and P. Mato Eiroa, "Approximation de Problèmes linéaires de coques minces par une méthode d'éléments finis de type DKT," Rapport de Recherche, Institut National de Recherche en Informatique et en Automatique, Sophia Antipolis, France, 1987.
- [3] R. Nzengwa and B. H. Tagne Simo, "A two-dimensional model for linear elastic thick shells," *International Journal of Solids and Structures*, vol. 36, no. 34, pp. 5141–5176, 1999.
- [4] M. Sheikholeslami, "Numerical simulation of magnetic nanofluid natural convection in porous media," *Physics Letters A*, vol. 381, no. 5, pp. 494–503, 2017.
- [5] M. Sheikholeslami, P. Rana, and S. Soleimani, "Numerical study of MHD natural convection liquid metal flow and heat transfer in a wavy enclosure using CVFEM," *Heat Transfer Research*, vol. 48, no. 2, pp. 121–138, 2017.
- [6] M. Sheikholeslami and H. B. Rokni, "Numerical modeling of nanofluid natural convection in a semi annulus in existence of Lorentz force," *Computer Methods in Applied Mechanics and Engineering*, vol. 317, pp. 419–430, 2017.
- [7] J. Nkongho Anyi, R. Nzengwa, J. Chills Amba, and C. V. Abbe Ngayihi, "Approximation of linear elastic shells by curved triangular finite elements based on elastic thick shells theory," *Mathematical Problems in Engineering*, vol. 2016, Article ID 8936075, 12 pages, 2016.
- [8] M. Sheikholeslami, M. Gorji-Bandpy, and D. D. Ganji, "Investigation of nanofluid flow and heat transfer in presence of magnetic field using KKL model," *Arabian Journal for Science and Engineering*, vol. 39, no. 6, pp. 5007–5016, 2014.
- [9] O. C. Zienkiewicz and J. Z. Zhu, "The superconvergent patch recovery and a posteriori error estimates. Part 1: the recovery technique," *International Journal for Numerical Methods in Engineering*, vol. 33, no. 7, pp. 1331–1364, 1992.
- [10] O. C. Zienkiewicz and J. Z. Zhu, "The superconvergent patch recovery and a posteriori error estimates. Part 2: error estimates and adaptivity," *International Journal for Numerical Methods in Engineering*, vol. 33, no. 7, pp. 1365–1382, 1992.
- [11] N.-E. Wiberg and F. Abdulwahab, "Patch recovery based on superconvergent derivatives and equilibrium," *International Journal for Numerical Methods in Engineering*, vol. 36, no. 16, pp. 2703–2724, 1993.
- [12] N.-E. Wiberg, F. Abdulwahab, and S. Ziukas, "Enhanced superconvergent patch recovery incorporating equilibrium and boundary conditions," *International Journal for Numerical Methods in Engineering*, vol. 37, no. 20, pp. 3417–3440, 1994.
- [13] A. Naga and Z. Zhang, "The polynomial-preserving recovery for higher order finite element methods in 2D and 3D," *Discrete and Continuous Dynamical Systems. Series B. A Journal Bridging Mathematics and Sciences*, vol. 5, no. 3, pp. 769–798, 2005.
- [14] A. Naga and Z. Zhang, "A posteriori error estimates based on the polynomial preserving recovery," *SIAM Journal on Numerical Analysis*, vol. 42, no. 4, pp. 1780–1800, 2004.
- [15] Z. Zhang and A. Naga, "A new finite element gradient recovery method: superconvergence property," *SIAM Journal on Scientific Computing*, vol. 26, no. 4, pp. 1192–1213, 2005.
- [16] Z. Zhang and J. Zhu, "Analysis of the superconvergent patch recovery technique and a posteriori error estimator in the finite element method. I," *Computer Methods in Applied Mechanics and Engineering*, vol. 123, no. 1-4, pp. 173–187, 1995.
- [17] Z. Zhang, "Polynomial preserving recovery for anisotropic and irregular grids," *Journal of Computational Mathematics*, vol. 22, no. 2, pp. 331–340, 2004.
- [18] Z. Zhang, "Polynomial preserving gradient recovery and a posteriori estimate for bilinear element on irregular quadrilaterals," *International Journal of Numerical Analysis and Modeling*, vol. 1, no. 1, pp. 1–24, 2004.
- [19] Z. Zhang, "Recovery techniques in finite element methods," in *Adaptive Computations: Theory and Algorithms*, T. Tang and J. Xu, Eds., pp. 297–365, Science Press, Beijing, China, 2007.
- [20] R. H. Macneal and R. L. Harder, "A proposed standard set of problems to test finite element accuracy," *Finite Elements in Analysis and Design*, vol. 1, no. 1, pp. 3–20, 1985.
- [21] Bernadou, "Methodes d'éléments finis pour les problèmes de coques minces. Edition Masson," Recherches en mathématiques Appliquées, Paris.
- [22] H. Laurent, *Etude en grande transformation d'une nouvelle famille d'éléments finis coque triangulaire à trois degrés de liberté par noeud. Application à la simulation numérique de l'emboutissage [Ph.D. thesis]*, Thèse présentée à l'Université de Maine, 1996.
- [23] E. Carrera, S. Brischetto, M. Cinefra, and M. Soave, "Effects of thickness stretching in functionally graded plates and shells," *Composites Part B: Engineering*, vol. 42, no. 2, pp. 123–133, 2011.

Research Article

Global Attractor of Thermoelastic Coupled Beam Equations with Structural Damping

Peirong Shi,¹ Danxia Wang,² and Weiyi Chen¹

¹Mechanics College, Taiyuan University of Technology, Taiyuan 030024, China

²Department of Mathematics, Taiyuan University of Technology, Taiyuan 030024, China

Correspondence should be addressed to Danxia Wang; danxia.wang@163.com

Received 17 November 2016; Accepted 21 December 2016; Published 22 March 2017

Academic Editor: Rahmat Ellahi

Copyright © 2017 Peirong Shi et al. This is an open access article distributed under the Creative Commons Attribution License, which permits unrestricted use, distribution, and reproduction in any medium, provided the original work is properly cited.

In this paper, we study the existence of a global attractor for a class of n -dimension thermoelastic coupled beam equations with structural damping $u_{tt} + \Delta^2 u + \Delta^2 u_t - [\sigma(\int_{\Omega} (\nabla u)^2 dx) + \phi(\int_{\Omega} \nabla u \nabla u_t dx)] \Delta u + f_1(u) + g(u_t) + \nu \Delta \theta = q(x)$, in $\Omega \times R^+$, and $\theta_t - \Delta \theta + f_2(\theta) - \nu \Delta u_t = 0$. Here Ω is a bounded domain of R^N , and $\sigma(\cdot)$ and $\phi(\cdot)$ are both continuous nonnegative nonlinear real functions and q is a static load. The source terms $f_1(u)$ and $f_2(\theta)$ and nonlinear external damping $g(u_t)$ are essentially $|u|^\rho u$, $|\theta|^\theta$, and $|u_t|^\tau u_t$ respectively.

1. Introduction

This problem is based on the equation

$$u_{tt} + u_{xxxx} - \left(\alpha + \beta \int_0^L u_x^2 dx \right) u_{xx} = 0, \quad (1)$$

which was proposed by Woinowsky-Krieger [1] as a model for vibrating beam with hinged ends.

Without thermal effects, Ball [2] studied the initial-boundary value problem of more general beam equation

$$u_{tt} + u_{xxxx} - M \left(\int_0^L u_x^2 dx \right) u_{xx} = 0 \quad (2)$$

subjected to homogeneous boundary condition. Ma and Narciso [3] proved the existence of global solutions and the existence of a global attractor for the Kirchhoff-type beam equation

$$\begin{aligned} u_{tt} + \Delta^2 u - M \left(\int_{\Omega} (\nabla u)^2 dx \right) \Delta u + f(u) + g(u_t) \\ = h(x), \end{aligned} \quad (3)$$

without structural damping, subjected to the conditions

$$u = \frac{\partial u}{\partial \nu} = 0 \quad \text{on } \partial \Omega \times R^+. \quad (4)$$

In fact, the plate equations without thermal effects were studied by several authors; we quote, for instance, [4–8].

In the following we also make some comments about previous works for the long-time dynamics of thermoelastic coupled beam system with thermal effects.

Giorgi et al. [9] studied a class of one-dimensional thermoelastic coupled beam equations

$$\begin{aligned} u_{tt} + \Delta^2 u - \left(\beta + \|\nabla u\|_{L^2(0,l)}^2 \right) \Delta u - \Delta u_{tt} + f(u) + \Delta \theta \\ = f, \\ \theta_t - \Delta \theta - \Delta u_t = g \end{aligned} \quad (5)$$

and gave the existence and uniqueness of global weak solution and the existence of global attractor under Dirichlet boundary conditions. Barbosa and Ma [10] studied the long-time behavior for a class of two-dimension thermoelastic coupled beam equation

$$\begin{aligned} u_{tt} + \Delta^2 u - M \left(\int_{\Omega} |\nabla u|^2 dx \right) \Delta u - \Delta u_{tt} + f(u) + \nu \Delta \theta \\ = h(x), \end{aligned} \quad (6)$$

$$\theta_t - \omega \Delta \theta - (1 - \omega) \int_0^t k(t-s) \Delta \theta ds - \nu \Delta u_t = 0$$

subjected to the conditions

$$\begin{aligned} u &= \Delta u = 0, \\ \theta &= 0. \end{aligned} \quad (7)$$

In addition, we also refer the reader to [11–15] and the references therein.

A mathematical problem is the nonlinear n -dimension thermoelastic coupled beam equations with structural damping which arise from the model of the nonlinear vibration beam with Fourier thermal conduction law:

$$u_{tt} + \Delta^2 u + \Delta^2 u_t - \left[\sigma \left(\int_{\Omega} (\nabla u)^2 dx \right) + \phi \left(\int_{\Omega} \nabla u \nabla u_t dx \right) \right] \Delta u \quad (8)$$

$$+ f_1(u) + g(u_t) + \nu \Delta \theta = q(x), \quad \text{in } \Omega \times R^+,$$

$$\theta_t - \Delta \theta + f_2(\theta) - \nu \Delta u_t = 0 \quad (9)$$

with the initial conditions

$$\begin{aligned} u(x, 0) &= u^0(x), \\ u_t(x, 0) &= u^1(x), \\ \theta(x, 0) &= \theta^0(x) \end{aligned} \quad (10)$$

and the boundary conditions

$$\begin{aligned} u|_{\partial\Omega} &= \frac{\partial u}{\partial \nu} \Big|_{\partial\Omega} = 0, \\ \theta|_{\partial\Omega} &= 0. \end{aligned} \quad (11)$$

To our best knowledge, the existence of global attractor for thermoelastic coupled beam equations was not considered in the presence of nonlinear structure damping. Here the unknown function $u(x, t)$ is the elevation of the surface of beam; $u^0(x)$ and $u^1(x)$ are the given initial value functions; the subscript t denotes derivative with respect to t and the assumptions on nonlinear functions $\sigma(\cdot)$, $\phi(\cdot)$, $f_1(\cdot)$, $f_2(\cdot)$, $g(\cdot)$, and the external force function $q(x)$ will be specified later.

Our fundamental assumptions on $\sigma(\cdot)$, $\phi(\cdot)$, $f_1(\cdot)$, $f_2(\cdot)$, $g(\cdot)$, and $q(x)$ are given as follows.

Assumption 1. We assume that $\sigma(\cdot) \in C^1(R)$ satisfying

$$\sigma(z)z \geq \tilde{\sigma}(z) \geq 0, \quad \forall z \geq 0, \quad (12)$$

where $\tilde{\sigma}(z) = \int_0^z \sigma(s)ds$. This condition is promptly satisfied if $\sigma(\cdot)$ is nondecreasing with $\sigma(0) = 0$.

Assumption 2. We also assume that $\phi(\cdot) \in C^1(R)$ satisfying $\phi(0) = 0$ and $\phi(\cdot)$ is nondecreasing and

$$\phi(s) \geq 0, \quad \forall s \in R^+. \quad (13)$$

Assumption 3. The function $f_1(\cdot) : R \rightarrow R$ is of class $C^1(R)$ and satisfies $f_1(0) = 0$, and there exist constants k and $\rho \geq 0$ such that

$$|f_1(u) - f_1(v)| \leq k_1(1 + |u|^\rho + |v|^\rho)|u - v|, \quad (14)$$

$$\forall u, v \in R,$$

$$-a_0 \leq \hat{f}_1(u) \leq \frac{1}{2}f_1(u)u + a_1, \quad (15)$$

where $\hat{f}_1(z) = \int_0^z f_1(s)ds$.

Assumption 4. The function $f_2(\cdot) : R \rightarrow R$ is of class $C^1(R)$ and satisfies $f_2(0) = 0$, and there exist constants k_2 , k_3 and $\varrho \geq 0$ such that

$$|f_2(\theta) - f_2(\bar{\theta})| \leq k_2(1 + |\theta|^\varrho + |\bar{\theta}|^\varrho)|\theta - \bar{\theta}|, \quad (16)$$

$$\forall \theta, \bar{\theta} \in R,$$

$$(f_2(\theta) - f_2(\bar{\theta}))(\theta - \bar{\theta}) \geq k_3(\theta - \bar{\theta})^{\varrho+2}, \quad (17)$$

$$\forall \theta, \bar{\theta} \in R.$$

Assumption 5. The function $g(\cdot) : R \rightarrow R$ is of class $C^1(R)$ and satisfies $g(0) = 0$, and there exist constants k_4 , k_5 and $r \geq 0$ such that

$$(g(u) - g(v))(u - v) \geq k_4|u - v|^{r+2}, \quad \forall u, v \in R, \quad (18)$$

$$|g(u) - g(v)| \leq k_5(1 + |u|^r + |v|^r)|u - v|, \quad (19)$$

$$\forall u, v \in R.$$

Assumption 6. $q(x) \in L^2(\Omega)$.

Under the above assumptions, we prove the existence of global solutions and the existence of a global attractor of extensible beam equation system (8)–(11). And the paper is organized as follows. In Section 2, we introduce some Sobolev spaces. In Section 3, we discuss the existence and uniqueness of global strong solution and weak solution. In Sections 4 and 5, we establish the result of the existence of a global attractor.

2. Basic Spaces

Our analysis is based on the following Sobolev spaces. Let

$$U = \{\theta \in H^2(\Omega) \cap L^2(\Omega); \theta|_{\partial\Omega} = 0\}. \quad (20)$$

Then for regular solutions we consider the phase space

$$H_1 = H^4(\Omega) \cap H_0^2(\Omega) \times H^4(\Omega) \cap H_0^2(\Omega) \times U. \quad (21)$$

In the case of weak solutions we consider the phase space

$$H_0 = H_0^2(\Omega) \times L^2(\Omega) \times L^2(\Omega). \quad (22)$$

In H_0 we adopt the norm defined by

$$\|(u, v, \theta)\|_{H_0}^2 = \|\Delta u\|^2 + \|v\|^2 + \|\theta\|^2. \quad (23)$$

3. The Existence of Global Solutions

Firstly, using the classical Galerkin method, we can establish the existence and uniqueness of regular solution to problem (8)–(11). We state it as follows.

Theorem 7. *Under assumptions (H_1) – (H_6) , for any initial data $(u^0, u^1, \theta^0) \in H_1$, then problem (8)–(11) has a unique regular solution (u, θ) with*

$$\begin{aligned} u &\in L^\infty(R^+, H^4(\Omega) \cap H_0^2(\Omega)), \\ u_t &\in L^\infty(R^+, H^4(\Omega) \cap H_0^2(\Omega)), \\ u_{tt} &\in L^\infty(R^+, L^2(\Omega)), \\ \theta &\in L^\infty(R^+, U), \\ \theta_t &\in L^\infty(R^+, L^2(\Omega)). \end{aligned} \quad (24)$$

Proof. Let us consider the variational problem associated with (8)–(11): find $(u(t), \theta(t)) \in H^4(\Omega) \cap H_0^2(\Omega) \times U$ such that

$$\begin{aligned} &\int_{\Omega} u_{tt} \omega \, dx + \int_{\Omega} \Delta u \Delta \omega \, dx + \int_{\Omega} \Delta u_t \Delta \omega \, dx \\ &+ \sigma (\|\nabla u\|^2) \int_{\Omega} \nabla u \nabla \omega \, dx \\ &+ \phi \left(\int_{\Omega} \nabla u_t \nabla \omega \, dx \right) \int_{\Omega} \nabla u_t \nabla \omega \, dx \\ &+ \int_{\Omega} f_1(u) \omega \, dx + \int_{\Omega} g(u_t) \omega \, dx \\ &+ \nu \int_{\Omega} \Delta \theta \omega \, dx = \int_{\Omega} q(x) \omega \, dx, \\ &\int_{\Omega} \theta_t \bar{\omega} \, dx - \int_{\Omega} \Delta \theta \bar{\omega} \, dx + \int_{\Omega} f_2(\theta) \bar{\omega} \, dx \\ &- \nu \int_{\Omega} \Delta u_t \bar{\omega} \, dx = 0 \end{aligned} \quad (25)$$

for all $\omega \in H_0^2(\Omega)$ and $\bar{\omega} \in U$. This is done with the Galerkin approximation method which is standard. Here we denote the approximate solution by $(u^m(t), \theta^m(t))$. We can get the theorem by proving the existence of approximation solution, the estimate of approximation solution, convergence, and uniqueness. In the following we give the estimates of approximation solution and the proof of uniqueness of solution.

Estimate 1. In the first approximate equation and the second approximate equation of (25), respectively putting $\omega = u_t^m(t)$ and $\bar{\omega} = \theta^m(t)$ and making a computation of addition and considering $\hat{\sigma}(z) = \int_0^z \sigma(s) ds$ and $\hat{f}_1(z) = \int_0^z f_1(s) ds$, by

using Schwarz inequality, and then integrating from 0 to $t < t_m$, we see that

$$\begin{aligned} &\|u_t^m\|^2 + \|\Delta u^m\|^2 + \hat{\sigma}(\|\nabla u^m\|^2) + \int_{\Omega} \hat{f}_1(u^m) \, dx \\ &+ \|\theta^m\|^2 + \int_0^t \|\Delta u_t^m\|^2 \, dt + 2 \int_0^t \|\nabla \theta^m\|^2 \, dt \\ &+ 2 \int_0^t \phi \left(\int_{\Omega} \nabla u \nabla u_t \, dx \right) \int_{\Omega} \nabla u \nabla u_t \, dx \, ds \\ &+ 2 \int_0^t \int_{\Omega} g(u_t^m) u_t^m \, dx \, ds \\ &+ 2 \int_0^t \int_{\Omega} f_2(\theta^m) \theta^m \, dx \, ds \\ &\leq \frac{1}{\lambda_1} \int_0^t \|q(x)\|^2 \, ds + \|u_t^m(0)\|^2 + \|\Delta u^m(0)\|^2 \\ &+ \hat{\sigma}(\|\nabla u^m(0)\|^2) + \int_{\Omega} \hat{f}_1(u^m(0)) \, dx \\ &+ \|\theta^m(0)\|^2 \end{aligned} \quad (26)$$

independent of m and t , where λ_1 is the same as λ_1 of (47). Taking into account assumptions (13), (17), and (18) of $\phi(\cdot)$, $f_2(\cdot)$, and $g(\cdot)$ and Assumption 6, we see that there exists $M_1 > 0$ depending only on T such that

$$\begin{aligned} &\|u_t^m\|^2 + \|\Delta u^m\|^2 + \hat{\sigma}(\|\nabla u^m\|^2) + \int_{\Omega} \hat{f}_1(u^m) \, dx \\ &+ \|\theta^m\|^2 \leq M_1 \end{aligned} \quad (27)$$

for all $t \in [0, T]$ and for all $m \in N$.

Estimate 2. In the first approximate equation and the second approximate equation of (25), respectively, putting $\omega = \Delta^2 u_t^m(t)$ and $\bar{\omega} = \Delta \theta^m(t)$ and making a computation of addition by using Schwarz inequality and Young inequality and considering the assumptions of $\sigma(\cdot)$, $\phi(\cdot)$, $f_1(\cdot)$, $g(\cdot)$, $f_2(\cdot)$, and $q(\cdot)$, we see that there exists $M_2 > 0$ depending only on T such that

$$\|\Delta u_t^m\|^2 + \|\Delta^2 u^m\|^2 + \|\nabla \theta^m\|^2 \leq M_2 \quad (28)$$

for all $t \in [0, T]$ and for all $m \in N$.

Estimate 3. In the first approximate equation and the second approximate equation of (25), respectively integrating by parts with $\omega = u_{tt}^m(0)$ and $\bar{\omega} = \theta_t^m(0)$ with $t = 0$ and using Schwarz inequality and Young inequality, we see that there exists $M_3, M_4 > 0$ depending only on T such that

$$\begin{aligned} &\|u_{tt}^m(0)\|^2 \leq M_3, \\ &\|\theta_t^m(0)\|^2 \leq M_4 \end{aligned} \quad (29)$$

for all $t \in [0, T]$ and for all $m \in N$.

Estimate 4. Let us fix $t, \xi > 0$ such that $\xi < T - t$. Respectively taking the difference of the first approximate equation and the second approximate equation of (25) with $t = t + \xi$ and $t = t$ and respectively replacing ω by $u_t^m(t + \xi) - u_t^m(t)$ and $\bar{\omega}$ by $\theta^m(t + \xi) - \theta^m(t)$, we can find constants $M_5, M_6 > 0$, depending only on T , such that

$$\begin{aligned} \|u_{tt}^m\|^2 + \|\Delta u_t^m\|^2 &\leq M_5, \\ \|\theta_t^m\|^2 &\leq M_6, \\ \forall m \in N, \forall t \in [0, T]. \end{aligned} \quad (30)$$

Estimate 5. Taking the scalar product in H with $\omega = \Delta \theta^m$ for the second approximate equation of (25), after a computation we can find a constant $M_7 > 0$, depending only on T such that

$$\|\Delta \theta^m\|^2 \leq M_7, \quad \forall m \in N, \forall t \in [0, T]. \quad (31)$$

With the estimates 1-2 and 4-5, we can get the necessary compactness in order to pass approximate equation of (25) to the limit. Then it is a matter of routine to conclude the existence of global solutions in $[0, T]$.

Uniqueness. Let $(u, \theta), (v, \bar{\theta})$ be two solutions of (8)–(11) with the same initial data. Then writing $p = u - v, \vartheta = \theta - \bar{\theta}$ and taking the difference (25) with $u = u, \theta = \theta$ and $u = v, \theta = \bar{\theta}$ and respectively replacing $\omega, \bar{\omega}$ by p_t, ϑ and then making a computation of addition, we have

$$\begin{aligned} \frac{1}{2} \frac{d}{dt} [\|p_t\|^2 + \|\Delta p\|^2 + \|\vartheta\|^2] + \|\Delta p_t\|^2 + \|\Delta \vartheta\|^2 + J_1 \\ + J_2 + \int_{\Omega} [f_1(u) - f_1(v)] p_t dx \\ + \int_{\Omega} [g(u_t) - g(v_t)] p_t dx \\ + \int_{\Omega} [f_2(\theta) - f_2(\bar{\theta})] \vartheta_t dx = 0, \end{aligned} \quad (32)$$

where $J_1 = \int_{\Omega} [\sigma(\int_{\Omega} (\nabla u)^2 dx) \Delta u - \sigma(\int_{\Omega} (\nabla v)^2 dx) \Delta v] p_t dx$ and $J_2 = \int_{\Omega} [\phi(\int_{\Omega} \nabla u \nabla u_t dx) \Delta u - \phi(\int_{\Omega} \nabla v \nabla v_t dx) \Delta v] p_t dx$. Using Mean Value Theorem and the Young inequalities combined with the estimates 1-2 and 4-5, we deduce that for some constant $M_8 > 0$,

$$\begin{aligned} \frac{d}{dt} (\|p_t\|^2 + \|\Delta p\|^2 + \|\vartheta\|^2) \\ \leq M_8 (\|p_t\|^2 + \|\Delta p\|^2 + \|\vartheta\|^2), \quad \forall t \in (0, T). \end{aligned} \quad (33)$$

Then from Gronwall's Lemma we see that $u = v, \theta = \bar{\theta}$. The proof of Theorem 7 is completed. \square

Theorem 8. *Under the assumptions of Theorem 7, if the initial data $(u^0, u^1, \theta^0) \in H_0$, there exists a unique weak solution of problem (8)–(11) which depends continuously on initial data with respect to the norm of H_0 .*

Proof. By using density arguments, we can obtain the existence of a weak solution in H_0 .

Let us consider $\{u^0, u^1, \theta^0\} \in \overline{H_1}$. Since H_1 is dense in H_0 , then there exists $\{u_{\mu}^0, u_{\mu}^1, \theta_{\mu}^0\} \subset H_1$, such that

$$\begin{aligned} u_{\mu}^0 &\longrightarrow u^0 \quad \text{in } H_0^2(\Omega); \\ u_{\mu}^1 &\longrightarrow u^1 \quad \text{in } L^2(\Omega); \\ \theta_{\mu}^0 &\longrightarrow \theta^0 \quad \text{in } L^2(\Omega). \end{aligned} \quad (34)$$

We observe that for each $\mu \in N$, there exists (u_{μ}, θ_{μ}) , smooth solution of the initial-boundary value problem (8)–(11) which satisfies

$$\begin{aligned} u_{tt\mu} + \Delta^2 u_{\mu} + \Delta^2 u_{t\mu} \\ - \left[\sigma \left(\int_{\Omega} (\nabla u_{\mu})^2 dx \right) + \phi \left(\int_{\Omega} \nabla u_{\mu} \nabla u_{t\mu} dx \right) \right] \Delta u_{\mu} \\ + f_1(u_{\mu}) + g(u_{t\mu}) + \nu \Delta \theta_{\mu} = q(x), \end{aligned} \quad (35)$$

$$\theta_{t\mu} - \Delta \theta_{\mu} + f_2(\theta_{\mu}) - \nu \Delta u_{t\mu} = 0.$$

Respectively multiplying the first equation in (35) by u_{μ} and multiplying the second equation in (35) by θ_{μ} and integrating over Ω and taking the sum and then considering the arguments used in the estimate of the existence of solution, we obtain

$$\|u_{t\mu}\|^2 + \|\Delta u_{\mu}\|^2 + \|\theta_{\mu}\|^2 \leq C_0, \quad (36)$$

where C_0 is a positive constant independent of $\mu \in N$.

Defining $Z_{\mu, \sigma} = u_{\mu} - u_{\sigma}, \bar{Z}_{\mu, \sigma} = \theta_{\mu} - \bar{\theta}_{\mu} : \mu, \sigma \in N$, following the steps already used in the uniqueness of regular solution for (8)–(11), and considering the convergence given in (34), we deduce that there exists (u, θ) such that

$$\begin{aligned} u_{\mu} &\longrightarrow u \quad \text{strongly in } C([0, T]; H_0^2(\Omega)), \\ u_{t\mu} &\longrightarrow u_t \quad \text{strongly in } C([0, T]; L^2(\Omega)), \\ \theta_{\mu} &\longrightarrow \theta \quad \text{strongly in } C([0, T]; L^2(\Omega)). \end{aligned} \quad (37)$$

From the above convergence, we can pass to the limit using standard arguments in order to obtain

$$\begin{aligned} u_{tt\mu} + \Delta^2 u_{\mu} + \Delta^2 u_{t\mu} \\ - \left[\sigma \left(\int_{\Omega} (\nabla u_{\mu})^2 dx \right) + \phi \left(\int_{\Omega} \nabla u_{\mu} \nabla u_{t\mu} dx \right) \right] \Delta u_{\mu} \\ + f_1(u_{\mu}) + g(u_{t\mu}) + \nu \Delta \theta_{\mu} = q(x), \\ \theta_{t\mu} - \Delta \theta_{\mu} + f_2(\theta_{\mu}) - \nu \Delta u_{t\mu} = 0. \end{aligned} \quad (38)$$

Theorem 8 is proved. \square

Remark 9. In both cases

$$\|u_t\|^2 + \|\Delta u\|^2 + \|u\|_{\rho+2}^{\rho+2} + \|\theta\|^2 \leq C, \quad (39)$$

where C is a constant depending on the initial data in different expression.

In addition, in this paper, C denotes different constant in different expression.

Remark 10. Theorem 8 implies that problem (8)–(11) defines a nonlinear C_0 -semigroup $S(t)$ on H_0 . Indeed, let us set $S(t)(u^0, u^1, \theta^0) = (u(t), u_t(t), \theta(t))$, where u is the unique solution corresponding to initial data $(u^0, u^1, \theta^0) \in H_0$. Moreover, the operator $S(t)$ defined in H_0 meets the usual semigroup properties

$$\begin{aligned} S(t, \tau) &= S(t)S(\tau), \quad \forall t, \tau \in R, \\ S(0) &= I. \end{aligned} \quad (40)$$

To prove the main result, we need the following Lemma 11 of Nakao and Lemma 12

Lemma 11 (see [16]). *Let $\varphi(t)$ be a nonnegative continuous function defined on $[0, T)$, $1 < T \leq \infty$, which satisfies*

$$\begin{aligned} \sup_{t \leq s \leq t+1} \varphi(s)^{1+\eta} &\leq M_0 (\varphi(t) - \varphi(t+1)) + M_1, \\ 0 &\leq t \leq T-1, \end{aligned} \quad (41)$$

where M_0, M_1, η are positive constants. Then we have

$$\begin{aligned} \varphi(t) &\leq \left(M_0^{-1} \eta (t-1)^+ + \left(\sup_{0 \leq s \leq 1} \varphi(s) \right)^{-\eta} \right)^{-1/\eta} \\ &+ M_1^{1/(\eta+1)}, \quad 0 \leq t \leq T. \end{aligned} \quad (42)$$

Lemma 12 (see [17]). *Assume that for any bounded positive invariant set $B \subset H$ and for any $\varepsilon > 0$, there exists $T = T(\varepsilon, B)$ such that*

$$d(S(T)x, S(T)y) \leq \varepsilon + \omega_T(x, y), \quad \forall x, y \in B, \quad (43)$$

where $\omega_T : H \times H \rightarrow R$ satisfies for any sequence $\{z_n\} \subset B$

$$\liminf_{m \rightarrow \infty} \liminf_{n \rightarrow \infty} \omega_T(z_n, z_m) = 0. \quad (44)$$

Then $S(t)$ is asymptotically smooth.

4. The Existence of Absorbing Set

The main result of an absorbing set reads as follows.

Theorem 13. *Assume the hypotheses of Theorem 8; then the corresponding semigroup $S(t)$ of problem (8)–(11) has an absorbing set \mathbb{B} in H_0 .*

Proof. Now we show that semigroup $S(t)$ has as absorbing set \mathbb{B} in H_0 . Firstly, we can calculate the total energy functional

$$\begin{aligned} E(t) &= \frac{1}{2} \{ \|u_t\|^2 + \|\Delta u\|^2 + \widehat{\sigma}(\|\nabla u\|^2) + \|\theta\|^2 \} \\ &+ \int_{\Omega} \widehat{f}_1(u) dx - \int_{\Omega} qu(t) dx. \end{aligned} \quad (45)$$

Let us fix an arbitrary bounded set $B \subset H_0$ and consider the solutions of problem (8)–(11) given by $(u(t), u_t(t), \theta(t)) =$

$S(t)(u^0, u^1, \theta^0)$ with $(u^0, u^1, \theta^0) \in B$. Our analysis is based on the modified energy function

$$\widetilde{E}(t) = E(t) + a_0 |\Omega| + \frac{1}{\lambda_1} \|q\|^2, \quad (46)$$

where $\lambda_1 > 0$ is the first eigenvalue of the operator Δ in $H_0^2(\Omega)$; that is, λ_1 satisfies

$$\|u\|^2 \leq \frac{1}{\lambda_1} \|\Delta u\|^2, \quad \forall u \in H_0^2(\Omega). \quad (47)$$

□

It is easy to see that $\widetilde{E}(t)$ dominates $\|(u(t), u_t(t), \theta(t))\|_{H_0}^2$ and $\widetilde{E}(t) \geq (1/4)\|\Delta u(t)\|^2$. By multiplying (8) by u and integrating over Ω , we have

$$\begin{aligned} \|\Delta u\|^2 &= - \left[\sigma \left(\int_{\Omega} |\nabla u|^2 dx \right) + \phi \left(\int_{\Omega} \nabla u \nabla u_t dx \right) \right] \|\nabla u\|^2 \\ &- \int_{\Omega} f_1(u) u dx + \|u_t\|^2 - \frac{d}{dt} (u_t, u) \\ &- \int_{\Omega} g(u_t) u dx + \int_{\Omega} qu(t) dx - \int_{\Omega} \Delta u \Delta u_t dx \\ &+ \nu \int_{\Omega} \nabla \theta \nabla u dx. \end{aligned} \quad (48)$$

Inserting (48) into $\widetilde{E}(t)$, we obtain

$$\begin{aligned} \widetilde{E}(t) &= \|u_t\|^2 \\ &+ \frac{1}{2} \left[\widehat{\sigma} \left(\int_{\Omega} |\nabla u|^2 dx \right) - \sigma \left(\int_{\Omega} |\nabla u|^2 dx \right) \right] \|\nabla u\|^2 \\ &- \frac{1}{2} \phi \left(\int_{\Omega} \nabla u \nabla u_t dx \right) \|\nabla u\|^2 + \frac{1}{2} \|\theta\|^2 \\ &- \frac{1}{2} \int_{\Omega} \Delta u \Delta u_t dx + \int_{\Omega} \left(\widehat{f}_1(u) - \frac{1}{2} f_1(u) \right) dx \\ &- \frac{1}{2} \frac{d}{dt} \int_{\Omega} u_t u dx - \frac{1}{2} \int_{\Omega} g(u_t) u dx \\ &+ \frac{\nu}{2} \int_{\Omega} \nabla \theta \nabla u dx + a_0 |\Omega| + \frac{1}{\lambda_1} \|q\|^2 \\ &- \frac{1}{2} \int_{\Omega} qu(t) dx. \end{aligned} \quad (49)$$

Considering (12) and (15) and integrating from t_1 to t_2 (49), we obtain that

$$\begin{aligned} &\int_{t_1}^{t_2} \widetilde{E}(t) ds \\ &\leq \int_{t_1}^{t_2} \|u_t\|^2 ds - \frac{1}{2} \int_{t_1}^{t_2} \phi \left(\int_{\Omega} \nabla u \nabla u_t dx \right) \|\nabla u\|^2 ds \end{aligned}$$

$$\begin{aligned}
& + \frac{1}{2} \int_{t_1}^{t_2} \|\theta\|^2 ds - \frac{1}{2} \int_{t_1}^{t_2} \int_{\Omega} \Delta u \Delta u_t dx ds \\
& - \frac{1}{2} \left(\int_{\Omega} u_t(t_2) u(t_2) dx - \int_{\Omega} u_t(t_1) u(t_1) dx \right) \\
& - \frac{1}{2} \int_{t_1}^{t_2} \int_{\Omega} g(u_t) u dx ds \\
& + \frac{\nu}{2} \int_{t_1}^{t_2} \int_{\Omega} \nabla \theta \nabla u ds dx + (a_0 + a_1) |\Omega| \\
& + \frac{1}{\lambda_1} \|q\|^2 + \frac{1}{2} \int_{t_1}^{t_2} \int_{\Omega} qu(t) dx ds,
\end{aligned} \tag{50}$$

where $t_1, t_2 \in [t, t+1]$.

Now let us begin to estimate the right hand side of (50) to use the above Lemma 11 of Nakao.

First, by multiplying (8) by u_t and multiplying (9) by θ and integrating over Ω and then taking the sum, we have

$$\begin{aligned}
& \frac{d}{dt} E(t) + \|\Delta u_t\|^2 + \|\nabla \theta\|^2 \\
& = - \int_{\Omega} g(u_t) u_t dx \\
& \quad - \phi \left(\int_{\Omega} \nabla u \nabla u_t dx \right) \int_{\Omega} \nabla u \nabla u_t dx \\
& \quad - \int_{\Omega} f_2(\theta) \theta dx.
\end{aligned} \tag{51}$$

Then integrating from t to $t+1$, we get

$$\begin{aligned}
& E(t+1) - E(t) + \int_t^{t+1} \|\Delta u_t\|^2 ds + \int_t^{t+1} \|\nabla \theta\|^2 ds \\
& = - \int_t^{t+1} \int_{\Omega} g(u_t) u_t dx ds \\
& \quad - \int_t^{t+1} \phi \left(\int_{\Omega} \nabla u \nabla u_t dx \right) \int_{\Omega} \nabla u \nabla u_t dx ds \\
& \quad - \int_t^{t+1} \int_{\Omega} f_2(\theta) \theta dx ds.
\end{aligned} \tag{52}$$

Taking into account assumptions (13), (17), and (18) of $\phi(\cdot)$, $f_2(\cdot)$, and $g(\cdot)$, we have

$$E(t) \geq E(t+1). \tag{53}$$

Then we define an auxiliary function $I^2(t)$ by putting

$$I^2(t) = E(t) - E(t+1) \geq 0. \tag{54}$$

Thus it is obvious that

$$\int_t^{t+1} \|\Delta u_t\|^2 \leq I^2(t), \tag{55}$$

$$\int_t^{t+1} \|\nabla \theta\|^2 \leq I^2(t). \tag{56}$$

Noting that $r/(r+2) + 2/(r+2) = 1$ and using twice Holder inequalities and considering assumption (18) of $g(\cdot)$, we have

$$\begin{aligned}
& \int_t^{t+1} \|u_t\|^2 ds \\
& \leq |\Omega|^{r/(r+2)} \left(\int_t^{t+1} \int_{\Omega} |u_t|^{(r+2)} dx ds \right)^{2/(r+2)} \\
& \leq |\Omega|^{r/(r+2)} \frac{1}{k_4} \left(\int_t^{t+1} \int_{\Omega} g(u_t) u_t dx ds \right)^{2/(r+2)} \\
& \leq |\Omega|^{r/(r+2)} \frac{1}{k_4} I(t)^{4/(r+2)}.
\end{aligned} \tag{57}$$

Using the Mean Value Theorem with $\phi(0) = 0$ and considering the estimate of (39) and then using Young inequality combined with (55), we have

$$\begin{aligned}
& \frac{1}{2} \int_{t_1}^{t_2} \phi \left(\int_{\Omega} \nabla u \nabla u_t dx \right) \|\nabla u\|^2 ds \\
& = \frac{1}{2} \int_{t_1}^{t_2} \phi'(\xi_1) \int_{\Omega} \nabla u \nabla u_t dx \|\nabla u\|^2 ds \\
& \leq \frac{1}{2} \int_{t_1}^{t_2} C \|\Delta u_t\| \|\Delta u\| ds \\
& \leq \frac{C}{4\eta} \int_{t_1}^{t_2} \|\Delta u_t\|^2 ds + \frac{\eta}{4} \int_{t_1}^{t_2} \|\Delta u\|^2 ds \\
& \leq \frac{C}{4\eta} \int_{t_1}^{t_2} \|\Delta u_t\|^2 ds + \eta \sup_{t \leq s \leq t+1} \bar{E}(s) \\
& \leq \frac{C}{4\eta} I^2(t) + \eta \sup_{t \leq s \leq t+1} \bar{E}(s),
\end{aligned} \tag{58}$$

where ξ_1 is among 0 and $\int_{\Omega} \nabla u \nabla u_t dx$.

Since $\|\theta\|^2 \leq (1/\lambda_2) \|\nabla \theta\|^2$, $\forall \theta \in H_0^1$, from (56) we obtain

$$\frac{1}{2} \int_{t_1}^{t_2} \|\theta\|^2 ds \leq \frac{1}{2\lambda_2} I^2(t), \tag{59}$$

where λ_2 is the first eigenvalue of the operator ∇ in $H_0^1(\Omega)$.

Using Young inequality, we get

$$\begin{aligned}
& \frac{1}{2} \int_{t_1}^{t_2} \int_{\Omega} \Delta u \Delta u_t ds \leq \frac{1}{4\eta} \int_{t_1}^{t_2} \|\Delta u_t\|^2 ds \\
& \quad + \frac{\eta}{4} \int_{t_1}^{t_2} \|\Delta u\|^2 ds \\
& \leq \frac{1}{4\eta} I(t)^2 + \eta \sup_{t \leq s \leq t+1} \bar{E}(s).
\end{aligned} \tag{60}$$

Since (57), in view of the Mean Value Theorem for integral, there exist number $t_1 \in [t, t + 1/4]$ and number $t_2 \in [t + 3/4, t + 1]$ such that

$$\begin{aligned} \|u_t(t_1)\|^2 &\leq |\Omega|^{r/(r+2)} \frac{4}{k_4} I(t)^{4/(r+2)}, \\ \|u_t(t_2)\|^2 &\leq |\Omega|^{r/(r+2)} \frac{4}{k_4} I(t)^{4/(r+2)}. \end{aligned} \tag{61}$$

Thus from Schwarz inequality combined with (47) and (61), we have

$$\begin{aligned} &\frac{1}{2} \left(\int_{\Omega} u_t(t_2) u(t_2) dx - \int_{\Omega} u_t(t_1) u(t_1) dx \right) \\ &\leq \frac{1}{2\sqrt{\lambda_1}} (\|u_t(t_2)\| \|\Delta u(t_2)\| + \|u_t(t_1)\| \|\Delta u(t_1)\|) \\ &\leq \frac{2}{\sqrt{\lambda_1} \sqrt{k_4}} |\Omega|^{r/2(r+2)} I(t)^{2/(r+2)} \sup_{t \leq s \leq t+1} \|\Delta u\| \\ &\leq \frac{((2/\sqrt{\lambda_1} \sqrt{k_4}) |\Omega|^{r/2(r+2)})^2}{\eta} I(t)^{4/(r+2)} \\ &\quad + \eta \sup_{t \leq s \leq t+1} \tilde{E}(s). \end{aligned} \tag{62}$$

Considering assumption (19) of $g(\cdot)$ and using Young inequality and Holder inequality with $(r + 1)/(r + 2) + 1/(r + 2) = 1$, then from (47) and (57), we have

$$\begin{aligned} &\frac{1}{2} \int_{t_1}^{t_2} \int_{\Omega} g(u_t) u dx ds \leq \frac{k_5}{2} \int_{t_1}^{t_2} \int_{\Omega} (1 + |u_t|^r) |u_t| u dx ds \\ &\leq \frac{k_5^2}{4\eta\lambda_1} \int_t^{t+1} \int_{\Omega} u_t(s)^2 dx ds + \frac{\eta\lambda_1}{4} \int_t^{t+1} \int_{\Omega} u(s)^2 dx ds \\ &\quad + \frac{k_5}{2} \int_{t_1}^{t_2} |u_t|^{r+1} u dx ds \leq \frac{k_5^2}{4\eta\lambda_1} \int_t^{t+1} \int_{\Omega} u_t(s)^2 dx ds + \frac{\eta\lambda_1}{4} \\ &\quad \cdot \int_t^{t+1} \int_{\Omega} u(s)^2 dx ds + \frac{k_5}{2} \\ &\quad \cdot \int_t^{t+1} \left(\int_{\Omega} |u_t|^{r+2} dx \right)^{(r+1)/(r+2)} \left(\int_{\Omega} u^{r+2} dx \right)^{1/(r+2)} ds \\ &\leq \frac{k_5^2}{4\eta\lambda_1} \int_t^{t+1} \int_{\Omega} u_t(s)^2 dx ds + \frac{\eta\lambda_1}{4} \int_t^{t+1} \int_{\Omega} u(s)^2 dx ds \\ &\quad + \frac{k_5}{2} \left\{ \int_t^{t+1} \left[\left(\int_{\Omega} u_t^{r+2} dx \right)^{(r+1)/(r+2)} \right]^{(r+2)/(r+1)} ds \right\}^{(r+1)/(r+2)} \\ &\quad \cdot \left\{ \int_t^{t+1} \left[\left(\int_{\Omega} u^{r+2} dx \right)^{1/(r+2)} \right]^{r+2} ds \right\}^{1/(r+2)} = \frac{k_5^2}{4\eta\lambda_1} \\ &\quad \cdot \int_t^{t+1} \int_{\Omega} u_t(s)^2 dx ds + \frac{\eta\lambda_1}{4} \int_t^{t+1} \int_{\Omega} u(s)^2 dx ds \\ &\quad + \frac{k_5}{2} \left(\int_t^{t+1} \int_{\Omega} u_t^{r+2} dx ds \right)^{(r+1)/(r+2)} \end{aligned}$$

$$\begin{aligned} &\cdot \left(\int_t^{t+1} \int_{\Omega} u^{r+2} dx ds \right)^{1/(r+2)} \leq \frac{k_5^2}{4\eta\lambda_1} |\Omega|^{r/(r+2)} \frac{1}{k_4} I(t)^{4/(r+2)} \\ &\quad + \eta \sup_{t \leq s \leq t+1} \tilde{E}(s) + \frac{k_5 \mu}{2k_4} I(t)^{2(r+1)/(r+2)} \sup_{t \leq s \leq t+1} \|\Delta u\| \\ &\leq \frac{k_5^2}{4\eta\lambda_1} |\Omega|^{r/(r+2)} \frac{1}{k_4} I(t)^{4/(r+2)} + \eta \sup_{t \leq s \leq t+1} \tilde{E}(s) + \frac{k_5^2 \mu^2}{4\eta k_4^2} \\ &\quad \cdot I(t)^{4(r+1)/(r+2)} + \eta \sup_{t \leq s \leq t+1} \tilde{E}(s). \end{aligned} \tag{63}$$

Also by Young inequality, we have

$$\begin{aligned} &\frac{\nu}{2} \int_{t_1}^{t_2} \int_{\Omega} \nabla \theta \nabla u dx ds \leq \frac{\nu}{2} \int_{t_1}^{t_2} \|\nabla \theta\| \|\nabla u\| ds \\ &\leq \int_{t_1}^{t_2} \frac{\nu^2}{4\eta\lambda_3} \|\nabla \theta\|^2 ds \\ &\quad + \int_{t_1}^{t_2} \frac{\eta\lambda_3}{4} \|\nabla u\|^2 ds \\ &\leq \frac{\nu^2}{4\eta\lambda_3} I^2(t) + \eta \sup_{t \leq s \leq t+1} \tilde{E}(s), \end{aligned} \tag{64}$$

where $\lambda_3 > 0$ is the first eigenvalue of the operator ∇ in $H_0^1(\Omega)$; that is, λ_3 satisfies

$$\|\nabla u\|^2 \leq \frac{1}{\lambda_3} \|\Delta u\|^2, \quad \forall u \in H_0^1(\Omega). \tag{65}$$

Finally using Young inequality again, we get that

$$\frac{1}{2} \int_{t_1}^{t_2} \int_{\Omega} qu(t) dx ds \leq \frac{1}{4\eta\lambda_1} \|q\|^2 + \eta \sup_{t \leq s \leq t+1} \tilde{E}(s). \tag{66}$$

Inserting (57)–(60) and (62), (63), (64), and (66) into (50), we obtain

$$\begin{aligned} &\int_{t_1}^{t_2} \tilde{E}(s) ds \leq \left[\left(|\Omega|^{r/(r+2)} \frac{1}{k_4} \right. \right. \\ &\quad + \frac{((2/\sqrt{\lambda_1} \sqrt{k_4}) |\Omega|^{r/2(r+2)})^2}{\eta} \\ &\quad + \frac{k_5^2}{4\eta\lambda_1} |\Omega|^{r/(r+2)} \frac{1}{k_4} \Big) I(t)^{4/(r+2)} + \left(\frac{C}{4\eta} + \frac{1}{2\lambda_2} \right. \\ &\quad + \frac{1}{4\eta} + \frac{\nu^2}{4\eta\lambda_3} \Big) I(t)^2 + \left. \left(\frac{k_5^2 \mu^2}{4\eta k_4^2} \right) I(t)^{4(r+1)/(r+2)} \right] \\ &\quad + 6\eta \sup_{t \leq s \leq t+1} \tilde{E}(s) + (a_0 + a_1) |\Omega| + \left(\frac{1}{\lambda_1} + \frac{1}{4\eta\lambda_1} \right) \\ &\quad \cdot \|q\|^2. \end{aligned} \tag{67}$$

For the left hand side of (67), we use the Mean Value Theorem; then there exists number $\tau \in [t_1, t_2]$ such that

$$\int_{t_1}^{t_2} \tilde{E}(s) ds \geq \frac{1}{2} \tilde{E}(t+1) = \frac{1}{2} (\tilde{E}(t) - I(t)^2). \quad (68)$$

So we conclude that

$$\tilde{E}(t) \leq I(t)^2 + 2 \int_{t_1}^{t_2} \tilde{E}(s) ds. \quad (69)$$

Inserting (67) into (69), we obtain that

$$\begin{aligned} \tilde{E}(t) \leq & 2 \left[\left(|\Omega|^{r/(r+2)} \frac{1}{k_4} \right. \right. \\ & + \frac{((2/\sqrt{\lambda_1} \sqrt{k_4}) |\Omega|^{r/2(r+2)})^2}{\eta} \\ & + \left. \frac{k_5^2}{8\eta\lambda_1} |\Omega|^{r/(r+2)} \frac{1}{k_4} \right) I(t)^{4/(r+2)} + \left(1 + \frac{C}{4\eta} \right. \\ & + \left. \frac{1}{2\lambda_2} + \frac{1}{4\eta} + \frac{\nu^2}{4\eta\lambda_3} \right) I(t)^2 + \left(\frac{k_5^2 \mu^2}{4\eta k_4^2} \right) \\ & \cdot I(t)^{4(r+1)/(r+2)} \left. \right] + 12\eta \sup_{t \leq s \leq t+1} \tilde{E}(s) + (a_0 + a_1) |\Omega| \\ & + 2 \left(\frac{1}{\lambda_1} + \frac{1}{4\eta\lambda_1} \right) \|q\|^2. \end{aligned} \quad (70)$$

Letting $0 < \eta < 1/12$ and noting that $I(t)^{2r/(r+2)}$ and $I(t)^{4r/(r+2)}$ are bounded with estimate (39), then from (70), we get

$$\begin{aligned} \tilde{E}(t) \leq & \frac{2}{1-12\eta} I(t)^{4/(r+2)} \left[\left(|\Omega|^{r/(r+2)} \frac{1}{k_4} \right. \right. \\ & + \frac{((2/\sqrt{\lambda_1} \sqrt{k_4}) |\Omega|^{r/2(r+2)})^2}{\eta} \\ & + \left. \frac{k_5^2}{4\eta\lambda_1} |\Omega|^{r/(r+2)} \frac{1}{k_4} \right) + \left(1 + \frac{C}{4\eta} + \frac{1}{2\lambda_2} + \frac{1}{4\eta} \right. \\ & + \left. \frac{\nu^2}{4\eta\lambda_3} \right) C + \frac{k_5^2 \mu^2}{4\eta k_4^2} C \left. \right] + \frac{1}{1-12\eta} (a_0 + a_1) |\Omega| \\ & + \frac{2}{1-12\eta} \left(\frac{1}{\lambda_1} + \frac{1}{4\eta\lambda_1} \right) \|q\|^2, \end{aligned} \quad (71)$$

where C is a constant which depends on B .

Set

$$\begin{aligned} C_1 = & \frac{2}{1-12\eta} \left[\left(|\Omega|^{r/(r+2)} \frac{1}{k_4} \right. \right. \\ & + \frac{((2/\sqrt{\lambda_1} \sqrt{k_4}) |\Omega|^{r/2(r+2)})^2}{\eta} \\ & + \left. \frac{k_5^2}{4\eta\lambda_1} |\Omega|^{r/(r+2)} \frac{1}{k_4} \right) + \left(1 + \frac{C}{4\eta} + \frac{1}{2\lambda_2} + \frac{1}{4\eta} \right. \\ & + \left. \frac{\nu^2}{4\eta\lambda_3} \right) C + \frac{k_5^2 \mu^2}{4\eta k_4^2} C \left. \right]; \end{aligned} \quad (72)$$

then (70) can be rewritten as

$$\begin{aligned} \tilde{E}(t)^{1+r/2} \leq & C_1 (\tilde{E}(t) - \tilde{E}(t+1)) \\ & + \left[\frac{2}{1-12\eta} (a_0 + a_1) |\Omega| \right. \\ & + \left. \frac{2}{1-12\eta} \left(\frac{1}{\lambda_1} + \frac{1}{4\eta\lambda_1} \right) \|q\|^2 \right]^{1+r/2}. \end{aligned} \quad (73)$$

Using Nakao's Lemma II, we conclude that

$$\begin{aligned} \tilde{E}(t) \leq & \left(C_1^{-1} \frac{r}{2} (t-1)^+ + \tilde{E}(0)^{-r/2} \right)^{-2/r} \\ & + \frac{1}{1-12\eta} (a_0 + a_1) |\Omega| \\ & + \frac{2}{1-12\eta} \left(\frac{1}{\lambda_1} + \frac{1}{4\eta\lambda_1} \right) \|q\|^2. \end{aligned} \quad (74)$$

As $r \rightarrow \infty$, the first term of the right side of (74) goes to zero; thus, with $\tilde{E}(t)$, we conclude

$$\begin{aligned} \mathbb{B} = & \left\{ (u, v, \theta) \in H_0 \mid \|\Delta u\|^2 + \|v\|^2 + \|\theta\|^2 \right. \\ & \leq \frac{8}{1-12\eta} (a_0 + a_1) |\Omega| \\ & \left. + \frac{8}{1-12\eta} \left(\frac{1}{\lambda_1} + \frac{1}{4\eta\lambda_1} \right) \|q\|^2 \right\} \end{aligned} \quad (75)$$

is an absorbing set for $S(t)$ in H_0 .

5. The Existence of a Global Attractor

The main result of a global attractor reads as follows.

Theorem 14. *Assume the hypotheses of Theorem 8; then the corresponding semigroup $S(t)$ of problem (8)–(11) is asymptotic compactness.*

Proof. We are going to apply Lemmas 11 and 12 to prove the asymptotic smooth. Given initial data (u^0, u^1, θ^0) and

$(v^0, v^1, \tilde{\theta}^0)$ in a bounded invariant set $B \subset H_0$, let $(u, \theta), (v, \tilde{\theta})$ be the corresponding weak solutions of problem (8)–(11). Then the differences $w = u - v, \vartheta = \theta - \tilde{\theta}$ are the weak solutions of

$$\begin{aligned} w_{tt} + \Delta^2 w + \Delta^2 w_t + \nu \Delta \vartheta + \Delta g \\ = \sigma (\|\nabla u\|^2) \Delta u - \sigma (\|\nabla v\|^2) \Delta v + \Delta \phi - \Delta f_1, \\ \vartheta_t - \Delta \vartheta + \Delta f_2 - \nu \Delta w_t = 0, \\ w = \frac{\partial w}{\partial \nu} = 0, \\ \vartheta = 0, \\ w(0) = u^0 - v^0, \\ w_t(0) = u^1 - v^1, \\ \vartheta(0) = \theta^0 - \tilde{\theta}_0, \end{aligned} \quad (76)$$

where

$$\begin{aligned} \Delta \phi &= \phi \left(\int_{\Omega} \nabla u \nabla u_t dx \right) \Delta u - \phi \left(\int_{\Omega} \nabla v \nabla v_t dx \right) \Delta v, \\ \Delta g &= g(u_t) - g(v_t), \\ \Delta f_1 &= f_1(u) - f_1(v), \\ \Delta f_2 &= f_2(\theta) - f_2(\tilde{\theta}). \end{aligned} \quad (77)$$

Let us define

$$E_w(t) = \|w_t\|^2 + \|\Delta w\|^2 + \sigma (\|\nabla u\|^2) \|\nabla w\|^2 + \|\vartheta\|^2. \quad (78)$$

As before, by density, we can assume formally that w is sufficiently regular. Then, multiplying the first equation in (76) by w_t and integrating over Ω and multiplying the second equation in (76) by ϑ and integrating over Ω and then taking the sum, we get

$$\begin{aligned} \frac{1}{2} \frac{d}{dt} E_w(t) + \|\Delta w_t\|^2 + \|\nabla \vartheta\|^2 + \int_{\Omega} \Delta g w_t dx \\ + \int_{\Omega} \Delta f_2 \vartheta dx \\ = -\sigma' (\|\nabla u\|^2) \|\nabla w\|^2 \int_{\Omega} \Delta u u_t dx \\ + \Delta \sigma \int_{\Omega} \Delta v w_t dx + \int_{\Omega} \Delta \phi w_t dx - \int_{\Omega} \Delta f_1 w_t dx, \end{aligned} \quad (79)$$

where

$$\Delta \sigma = \sigma (\|\nabla u\|^2) - \sigma (\|\nabla v\|^2). \quad (80)$$

Let us estimate the right hand side of (79).

Considering the continuity of $\sigma'(\cdot)$ and estimate (39)

$$-\sigma' (\|\nabla u\|^2) \|\nabla w\|^2 \leq C \|\nabla w\|^2, \quad (81)$$

Applying the Mean Value Theorem combined with estimate (39), by Young inequality, we get

$$\Delta \sigma \int_{\Omega} \Delta v w_t dx \leq C \|\nabla w\|^{(r+2)/(r+1)} + \frac{k_4}{4} \|w_t\|_{r+2}^{r+2}. \quad (82)$$

Also use the Mean Value Theorem combined with estimate (39) and Young inequality to get

$$\begin{aligned} \int_{\Omega} \Delta \phi w_t dx &= \int_{\Omega} \phi \left(\int_{\Omega} \nabla u \nabla u_t dx \right) \Delta w w_t dx \\ &- \int_{\Omega} \left[\phi \left(\int_{\Omega} \nabla u \nabla u_t dx \right) - \phi \left(\int_{\Omega} \nabla v \nabla v_t dx \right) \right] \\ &\cdot \Delta v w_t dx = \int_{\Omega} \phi'(\xi_2) \int_{\Omega} \nabla u \nabla u_t dx \Delta w w_t dx \\ &- \int_{\Omega} \phi'(\xi_3) \int_{\Omega} \nabla v \nabla v_t dx \Delta v w_t dx \leq C \|w\| \|\Delta w_t\| \\ &+ C \|w\| \|\Delta w_t\| \|w_t\| \leq \frac{1}{4} \|\Delta w_t\|^2 + C^2 \|w\|^2 \\ &+ \frac{1}{4} \|\Delta w_t\|^2 + C^2 \|w\|^2 \|w_t\|^2 \leq \frac{1}{4} \|\Delta w_t\|^2 \\ &+ C^2 \|\nabla w\|^2 + C^2 \|w\|^2 \|w_t\|_{r+2}^2 \leq \frac{1}{4} \|\Delta w_t\|^2 \\ &+ C^2 \|\nabla w\|^2 + \frac{C^4}{k_3} \|w\|^{2((r+2)/r)} + \frac{k_3}{4} \|w_t\|_{r+2}^{r+2}, \end{aligned} \quad (83)$$

where ξ_2 is among 0 and $\int_{\Omega} \nabla u \nabla u_t dx$, and ξ_3 is among $\int_{\Omega} \nabla u \nabla u_t dx$ and $\int_{\Omega} \nabla v \nabla v_t dx$.

By the Holder inequality, Minkowski inequality combined with the estimate of (39), and Young inequality, we obtain

$$\int_{\Omega} \Delta f_1 w_t dx \leq C \|\nabla w\|^{(r+2)/(r+1)} + \frac{k_4}{4} \|w_t\|_{r+2}^{r+2}. \quad (84)$$

On the other hand, considering assumptions (17) and (18) of $f_2(\cdot)$ and $g(\cdot)$,

$$\begin{aligned} \int_{\Omega} \Delta f_2 \vartheta dx &\geq k_3 \|\vartheta\|_{q+2}^{q+2}, \\ \int_{\Omega} \Delta g w_t dx &\geq k_4 \|w_t\|_{r+2}^{r+2}. \end{aligned} \quad (85)$$

Thus by inserting (81)–(85) into (79), we get that

$$\begin{aligned} \frac{1}{2} \frac{d}{dt} E_w(t) + \frac{1}{4} \|\Delta w_t\|^2 + \|\nabla \vartheta\|^2 + \frac{k_4}{4} \|w_t\|_{r+2}^{r+2} \\ + k_3 \|\vartheta\|_{q+2}^{q+2} \\ \leq C (\|\nabla w\|^2 + \|\nabla w\|^{(r+2)/(r+1)} + \|\nabla w\|^{2((r+2)/r)}). \end{aligned} \quad (86)$$

Then integrating from t to $t + 1$ and defining an auxiliary function $F^2(t)$, we get

$$\begin{aligned} & \frac{1}{4} \int_t^{t+1} \|\Delta w_t\|^2 ds + \int_t^{t+1} \|\nabla \vartheta\|^2 ds + \frac{k_4}{4} \\ & \cdot \int_t^{t+1} \|w_t\|_{r+2}^{r+2} ds + k_3 \int_t^{t+1} \|\vartheta\|_{q+2}^{q+2} ds \leq E_w(t) \\ & - E_w(t+1) + C \int_t^{t+1} (\|\nabla w\|^2 + \|\nabla w\|^{(r+2)/(r+1)} \\ & + \|\nabla w\|^{2(2(r+2)/r)}) ds = F(t)^2. \end{aligned} \quad (87)$$

It is obvious that

$$E_w(t+1) \geq E_t(t), \quad (88)$$

$$\frac{1}{4} \int_t^{t+1} \|\Delta w_t\|^2 ds \leq F(t)^2, \quad (89)$$

$$\int_t^{t+1} \|\nabla \vartheta\|^2 ds \leq F(t)^2,$$

$$\frac{k_4}{4} \int_t^{t+1} \|w_t\|_{r+2}^{r+2} ds \leq F(t)^2, \quad (90)$$

$$k_3 \int_t^{t+1} \|\vartheta\|_{q+2}^{q+2} ds \leq F(t)^2.$$

Then by multiplying first equation in (76) by w and integrating over Ω again, we obtain that

$$\begin{aligned} \|\Delta w\|^2 + \sigma (\|\nabla u\|^2) \|\nabla w\|^2 &= -\frac{d}{dt} \int_{\Omega} w_t w dx + \|w_t\|^2 \\ &- \int_{\Omega} \Delta^2 w_t w dx + \Delta \sigma \int_{\Omega} \Delta v w dx - \int_{\Omega} \Delta f_1 w dx \\ &- \int_{\Omega} \Delta g w dx \\ &+ \int_{\Omega} \left[\phi \left(\int_{\Omega} \nabla u \nabla u_t dx \right) - \phi \left(\int_{\Omega} \nabla v \nabla v_t dx \right) \right] \\ &\cdot \Delta v w dx - \phi \left(\int_{\Omega} \nabla u \nabla u_t dx \right) \|\nabla w\|^2 \\ &- \nu \int_{\Omega} \vartheta \Delta w dx. \end{aligned} \quad (91)$$

Integrating from t_1 to t_2 , we get

$$\begin{aligned} & \int_{t_1}^{t_2} (\|\Delta w\|^2 + \sigma (\|\nabla u\|^2) \|\nabla w\|^2) ds = \int_{\Omega} w_t(t_2) \\ & \cdot w(t_2) dx - \int_{\Omega} w_t(t_1) w(t_1) dx \\ & + \int_{t_1}^{t_2} \|w_t\|^2 dt - \int_{t_1}^{t_2} \int_{\Omega} \Delta w_t \Delta w dx ds \end{aligned}$$

$$\begin{aligned} & + \int_{t_1}^{t_2} \Delta \sigma \int_{\Omega} \Delta v w dx ds - \int_{t_1}^{t_2} \int_{\Omega} \Delta f_1 w dx ds \\ & - \int_{t_1}^{t_2} \int_{\Omega} \Delta g w dx ds \\ & + \int_{t_1}^{t_2} \int_{\Omega} \left[\phi \left(\int_{\Omega} \nabla u \nabla u_t dx \right) - \phi \left(\int_{\Omega} \nabla v \nabla v_t dx \right) \right] \\ & \cdot \Delta v w dx ds - \int_{t_1}^{t_2} \phi \left(\int_{\Omega} \nabla u \nabla u_t dx \right) \|\nabla w\|^2 ds \\ & + \nu \int_{t_1}^{t_2} \int_{\Omega} \nabla \vartheta \nabla w dx ds. \end{aligned} \quad (92)$$

Now let us estimate the right hand side of (92). Firstly, from the first inequality of (90), by holder inequality we infer that

$$\begin{aligned} \int_t^{t+1} \|w_t\|^2 ds &= \int_t^{t+1} \int_{\Omega} |w_t|^2 dx ds \\ &\leq |\Omega|^{r/(r+2)} \left(\int_t^{t+1} \int_{\Omega} |w_t|^{2(r+2)/2} dx ds \right)^{2/(r+2)} \\ &\leq CF(t)^{4/(r+2)}; \end{aligned} \quad (93)$$

thus there exists $t_1 \in [t, t + 1/4]$ and $t_2 \in [t + 3/4, t + 1]$ such that

$$\begin{aligned} \|w_t(t_1)\|^2 &\leq CF^{4/(r+2)}(t), \\ \|w_t(t_2)\|^2 &\leq CF^{4/(r+2)}(t); \end{aligned} \quad (94)$$

then we can deduce that

$$\begin{aligned} & \int_{\Omega} w_t(t_2) w(t_2) dx - \int_{\Omega} w_t(t_1) w(t_1) dx \\ & \leq CF(t)^{4/(r+2)} + \frac{1}{8} \sup_{t \leq \sigma \leq t+1} E_w(\sigma). \end{aligned} \quad (95)$$

Use Schwarz inequality combined with the estimate of (39) and Holder inequality to obtain

$$\begin{aligned} & \int_{t_1}^{t_2} \int_{\Omega} \Delta w_t \Delta w dx ds \leq C \int_{t_1}^{t_2} \|\Delta w_t\| ds \\ & \leq C \left(\int_{t_1}^{t_2} 1 ds \right)^{1/2} \left(\int_{t_1}^{t_2} \|\Delta w_t\|^2 ds \right)^{1/2} \leq CF(t). \end{aligned} \quad (96)$$

Apply the Mean Value Theorem combined with estimate (39) to get

$$\int_{t_1}^{t_2} \Delta \sigma \int_{\Omega} \Delta v w dx ds \leq C \int_{t_1}^{t_2} \|\nabla w\|^2 ds. \quad (97)$$

Assumption (14) of $f(\cdot)$ and the estimate of (39) imply that

$$\int_{t_1}^{t_2} \int_{\Omega} \Delta f_1 w dx ds \leq C \int_{t_1}^{t_2} \|\nabla w\|^2 ds. \quad (98)$$

Also from assumption (19) of $g(\cdot)$ and the estimate of (39) combined with (94), we have

$$\begin{aligned} \int_{t_1}^{t_2} \int_{\Omega} \Delta g w \, dx \, ds &\leq C \int_{t_1}^{t_2} \|w_t\| \|\Delta w\| \, ds \\ &\leq CF(t)^{4/(r+2)} + \frac{1}{8} \sup_{t \leq \sigma \leq t+1} E_w(\sigma). \end{aligned} \quad (99)$$

Using the Mean Value Theorem and considering the assumption of $\phi(\cdot)$ and the estimate of (39), we have

$$\begin{aligned} \int_{t_1}^{t_2} \int_{\Omega} \left[\phi \left(\int_{\Omega} \nabla u \nabla u_t \, dx \right) - \phi \left(\int_{\Omega} \nabla v \nabla v_t \, dx \right) \right] \\ \cdot \Delta v w \, dx \, ds &= \int_{t_1}^{t_2} \phi'(\xi_4) \int_{\Omega} \nabla w \nabla v_t \, dx \\ &\cdot \int_{\Omega} \Delta v w \, dx \, ds \leq C \int_{t_1}^{t_2} \|w\| \|w_t\| \, ds \\ &\leq C \int_{t_1}^{t_2} \|\nabla w\|^2 \, ds + C \int_{t_1}^{t_2} \|w_t\|^2 \, ds, \end{aligned} \quad (100)$$

$$\int_{t_1}^{t_2} \phi \left(\int_{\Omega} \nabla u \nabla u_t \, dx \right) \|\nabla w\|^2 \, ds \leq C \int_{t_1}^{t_2} \|\nabla w\|^2 \, ds, \quad (101)$$

where ξ_4 is among $\int_{\Omega} \nabla u \nabla u_t \, dx$ and $\int_{\Omega} \nabla v \nabla v_t \, dx$. Finally, use Young inequality to get

$$\begin{aligned} \nu \int_{t_1}^{t_2} \int_{\Omega} \nabla \vartheta \nabla w \, dx \, ds &\leq \frac{\nu^2}{2} \int_{t_1}^{t_2} \|\nabla \vartheta\|^2 \\ &+ \frac{1}{2} \int_{t_1}^{t_2} \|\nabla w\|^2 \, ds. \end{aligned} \quad (102)$$

By inserting (93) and (95)–(102) into (92), we obtain that

$$\begin{aligned} \int_{t_1}^{t_2} \left[\|\Delta w\|^2 + \sigma \left(\|\nabla u\|^2 \right) \|\nabla w\|^2 \right] \, ds \\ \leq 3C \int_{t_1}^{t_2} \|\nabla w\|^2 \, ds + 2C \int_{t_1}^{t_2} \|w_t\|^2 \, ds \\ + C \int_{t_1}^{t_2} \|\nabla \vartheta\|^2 \, ds + 2CF(t)^{4/(r+2)} \\ + \frac{1}{4} \sup_{t \leq \sigma \leq t+1} E_w(\sigma) + CF(t). \end{aligned} \quad (103)$$

Considering (89) and (93), from (103), we have

$$\begin{aligned} \int_{t_1}^{t_2} \left[\|\Delta w\|^2 + \sigma \left(\|\nabla u\|^2 \right) \|\nabla w\|^2 \right] \, ds \\ \leq 3C \int_t^{t+1} \|\nabla w\| \, ds + CF(t) + CF^2(t) \\ + 4CF(t)^{4/(r+2)} + \frac{1}{4} \sup_{t \leq \sigma \leq t+1} E_w(\sigma). \end{aligned} \quad (104)$$

Using Holder inequality with $1/(\varrho + 2) + (\varrho + 1)/(\varrho + 2) = 1$,

$$\begin{aligned} \int_{t_1}^{t_2} \|\vartheta\|^2 \, ds &\leq C \int_{t_1}^{t_2} \|\vartheta\|_{\varrho+2} \, ds \\ &\leq C \left(\int_{t_1}^{t_2} 1^{(\varrho+2)/(\varrho+2)} \, ds \right)^{(\varrho+1)/(\varrho+2)} \int_{t_1}^{t_2} \|\vartheta\|_{\varrho+2}^{\varrho+2} \, ds \\ &\leq C \int_{t_1}^{t_2} \|\vartheta\|_{\varrho+2}^{\varrho+2} \, ds \leq CF^2(t). \end{aligned} \quad (105)$$

Then from the definition of $E_w(t)$ and (93), (104), and (105), we obtain that

$$\begin{aligned} \int_{t_1}^{t_2} E_w(s) \, ds &\leq 5CF(t)^{4/(r+2)} + 2CF^2(t) + CF(t) \\ &+ \frac{1}{4} \sup_{t \leq \sigma \leq t+1} E_w(\sigma) \\ &+ 3C \int_t^{t+1} \|\nabla w\| \, ds. \end{aligned} \quad (106)$$

For (106), by using Mean Value theorem, there exists $t^* \in [t_1, t_2]$ such that

$$\begin{aligned} E_w(t^*) &\leq 10CF(t)^{4/(r+2)} + 2CF(t) + 4CF^2(t) \\ &+ \frac{1}{2} \sup_{t \leq \sigma \leq t+1} E_w(\sigma) + 6C \int_t^{t+1} \|\nabla w\| \, ds. \end{aligned} \quad (107)$$

From (87), we see that

$$E_w(t) \leq E_w(t+1) + F^2(t). \quad (108)$$

Let $E_w = \sup_{t \leq \sigma \leq t+1} E_w(\sigma)$ with $\tau \in [t, t+1]$; then integrate (86) over $[t, \tau]$ and over $[t^*, t+1]$ to have

$$\begin{aligned} \sup_{t \leq \sigma \leq t+1} E_w(\sigma) &\leq E_w(\tau) \\ &\leq E_w(t+1) + F^2(t) \\ &+ C \int_t^{t+1} \left(\|\nabla w\|^2 + \|\nabla w\|^{2(r+2)/r} \right) \, ds \\ &\leq E_w(t^*) + F^2(t) \\ &+ C \int_t^{t+1} \left(\|\nabla w\|^2 + \|\nabla w\|^{2(r+2)/r} \right) \, ds. \end{aligned} \quad (109)$$

Inserting (107) into (109), we obtain

$$\begin{aligned} \sup_{t \leq \sigma \leq t+1} E_w(\sigma) &\leq 10CF(t)^{4/(r+2)} + 2CF(t) + 4CF^2(t) \\ &+ \frac{1}{2} \sup_{t \leq \sigma \leq t+1} E_w(\sigma) + 6C \int_t^{t+1} \|\nabla w\| \, ds \\ &+ F^2(t) \\ &+ C \int_t^{t+1} \left(\|\nabla w\|^2 + \|\nabla w\|^{2(r+2)/r} \right) \, ds. \end{aligned} \quad (110)$$

Therefore from the boundary of $1 + F(t)^{(1-4/(r+2))} + F(t)^{2-4/(r+2)}$, we have

$$\begin{aligned} & \sup_{t \leq \sigma \leq t+1} E_w(\sigma) \\ & \leq CF(t)^{4/(r+2)} \\ & + C \int_t^{t+1} (\|\nabla w\| + \|\nabla w\|^2 + \|\nabla w\|^{2(r+2)/r}) ds. \end{aligned} \tag{111}$$

Therefore

$$\begin{aligned} & \sup_{t \leq \sigma \leq t+1} E_w(\sigma)^{1+r/2} \leq C(E_w(t) - E_w(t+1)) \\ & + C \sup_{0 \leq \sigma \leq T} \int_{\sigma}^{\sigma+1} (\|\nabla w\| + \|\nabla w\|^2 + \|\nabla w\|^{2(r+2)/r}) ds. \end{aligned} \tag{112}$$

From Nakao's Lemma 11, there exists $C_B > 0$ and $C_T > 0$ such that

$$\begin{aligned} E_w(t) & \leq C_B [(t-1)^+]^{-2/r} + C_T \left(\sup_{0 \leq \sigma \leq T} \int_{\sigma}^{\sigma+1} (\|\nabla w\| \right. \\ & \left. + \|\nabla w\|^2 + \|\nabla w\|^{2(r+2)/r}) ds \right)^{2/(r+2)}, \end{aligned} \tag{113}$$

$$0 \leq t \leq T.$$

From the definition of $E_w(t)$, we have

$$\begin{aligned} & \|(w, w_t, \vartheta)\|_{H_0} \leq C_B [(t-1)^+]^{-2/r} \\ & + C_T \left(\sup_{0 \leq \sigma \leq T} \int_{\sigma}^{\sigma+1} (\|\nabla w\| + \|\nabla w\|^2 \right. \\ & \left. + \|\nabla w\|^{2(r+2)/r}) ds \right)^{2/(r+2)}. \end{aligned} \tag{114}$$

Given $\varepsilon > 0$, we choose T large such that

$$C_B [(t-1)^+]^{-2/r} \leq \varepsilon, \tag{115}$$

and define $\omega_T : H_0 \times H_0 \rightarrow R$ as

$$\begin{aligned} & \omega_T \left((u^0, u^1, \theta^0), (v^0, v^1, \tilde{\theta}^0) \right) \\ & = C_T \left(\sup_{\sigma} \int_{\sigma}^{\sigma+1} (\|\nabla w\| + \|\nabla w\|^2 \right. \\ & \left. + \|\nabla w\|^{2(r+2)/r}) ds \right)^{2/(r+2)}. \end{aligned} \tag{116}$$

Then from (114)–(116), we get

$$\begin{aligned} & \|S(T)(u^0, u^1, \theta^0) - S(T)(v^0, v^1, \tilde{\theta}^0)\|_{H_0} \\ & \leq \varepsilon + \omega_T \left((u^0, u^1, \theta^0), (v^0, v^1, \tilde{\theta}^0) \right) \end{aligned} \tag{117}$$

for all $(u^0, u^1, \theta^0), (v^0, v^1, \tilde{\theta}^0) \in B$.

Let $(u_n^0, u_n^1, \theta_n^0)$ be a given sequence of initial data in B . Then the corresponding sequence (u_n, u_{tn}, θ_n) of solutions of the problem (8)–(11) is uniformly bounded in H_0 , because B is bounded and positively invariant. So $\{u_n\}$ is bounded in $C([0, \infty), H_0^2(\Omega)) \cap C^1([0, \infty), L^2(\Omega))$. Since $H_0^2(\Omega) \hookrightarrow H_0^1(\Omega)$ compactly, there exists a subsequence u_{nk} which converges strongly in $C([0, T], H_0^1(\Omega))$. Therefore

$$\begin{aligned} & \lim_{k \rightarrow \infty} \lim_{l \rightarrow \infty} \int_0^T (\|\nabla u_{nk}(s) - \nabla u_{nl}(s)\| \\ & + \|\nabla u_{nk}(s) - \nabla u_{nl}(s)\|^2 \\ & + \|\nabla u_{nk}(s) - \nabla u_{nl}(s)\|^{2(r+2)/r}) ds = 0, \end{aligned} \tag{118}$$

$$\lim_{k \rightarrow \infty} \lim_{l \rightarrow \infty} \omega_T \left((u_{nk}^0, u_{nk}^1, \theta_{nk}^0), (u_{nl}^0, u_{nl}^1, \theta_{nl}^0) \right) = 0.$$

So $S(t)$ is asymptotically smooth in H_0 . That is, Lemma 12 holds. Thus Theorem 14 is proved. \square

In view of Theorems 13 and 14, we have the following.

Theorem 15. *The corresponding semigroup $S(t)$ of problem (8)–(11) has a compact global attractor in the phase space H_0 .*

Competing Interests

The authors declare that they have no competing interests.

Acknowledgments

The project is supported by the National Natural Science Foundation of China (Grant nos. 11172194 and 11401420), the Natural Science Foundation of Shanxi Province, China (Grant no. 2015011006 and Grant no. 2014011005-4).

References

- [1] S. Woinowsky-Krieger, “The effect of an axial force on the vibration of hinged bars,” *Journal of applied Mechanics*, vol. 17, pp. 35–36, 1950.
- [2] J. M. Ball, “Initial-boundary value problems for an extensible beam,” *Journal of Mathematical Analysis and Applications*, vol. 42, pp. 61–90, 1973.
- [3] T. F. Ma and V. Narciso, “Global attractor for a model of extensible beam with nonlinear damping and source terms,” *Nonlinear Analysis. Theory, Methods & Applications*, vol. 73, no. 10, pp. 3402–3412, 2010.
- [4] A. F. Pazoto and G. P. Menzala, “Uniform stabilization of a nonlinear beam model with thermal effects and nonlinear boundary dissipation,” *Funkcialaj Ekvacioj. Serio Internacia*, vol. 43, no. 2, pp. 339–360, 2000.
- [5] T. F. Ma, “Boundary stabilization for a non-linear beam on elastic bearings,” *Mathematical Methods in the Applied Sciences*, vol. 24, no. 8, pp. 583–594, 2001.
- [6] T. F. Ma, V. Narciso, and M. L. Pelicer, “Long-time behavior of a model of extensible beams with nonlinear boundary dissipations,” *Journal of Mathematical Analysis and Applications*, vol. 396, no. 2, pp. 694–703, 2012.

- [7] Z. Yang, "On an extensible beam equation with nonlinear damping and source terms," *Journal of Differential Equations*, vol. 254, no. 9, pp. 3903–3927, 2013.
- [8] D. Wang, J. Zhang, Y. Wang, and S. Zhang, "Attractor of beam equation with structural damping under nonlinear boundary conditions," *Mathematical Problems in Engineering*, vol. 2015, Article ID 857920, 10 pages, 2015.
- [9] C. Giorgi, M. G. Naso, V. Pata, and M. Potomkin, "Global attractors for the extensible thermoelastic beam system," *Journal of Differential Equations*, vol. 246, no. 9, pp. 3496–3517, 2009.
- [10] A. R. A. Barbosa and T. F. Ma, "Long-time dynamics of an extensible plate equation with thermal memory," *Journal of Mathematical Analysis and Applications*, vol. 416, no. 1, pp. 143–165, 2014.
- [11] C. Giorgi and M. G. Naso, "Modeling and steady state analysis of the extensible thermoelastic beam," *Mathematical and Computer Modelling*, vol. 53, no. 5-6, pp. 896–908, 2011.
- [12] L. H. Fatori and T. F. Ma, "A thermoelastic system of memory type in noncylindrical domains," *Applied Mathematics and Computation*, vol. 200, no. 2, pp. 583–589, 2008.
- [13] M. Marin, "On existence and uniqueness in thermoelasticity of micropolar bodies," *Comptes Rendus de l'Académie des Sciences, Paris, Serie II*, vol. 321, no. 12, pp. 475–480, 1995.
- [14] M. Marin, "Some basic theorems in elastostatics of micropolar materials with voids," *Journal of Computational and Applied Mathematics*, vol. 70, no. 1, pp. 115–126, 1996.
- [15] M. Marin and C. Marinescu, "Thermoelasticity of initially stressed bodies, asymptotic equipartition of energies," *International Journal of Engineering Science*, vol. 36, no. 1, pp. 73–86, 1998.
- [16] M. Nakao, "Global attractors for nonlinear wave equations with nonlinear dissipative terms," *Journal of Differential Equations*, vol. 227, no. 1, pp. 204–229, 2006.
- [17] I. Chueshov and I. Lasiecka, "Long-time behavior of second order evolution equations with nonlinear damping," *Memoirs of the American Mathematical Society*, vol. 195, no. 912, 2008.

Research Article

Frequency Equation of Flexural Vibrating Cantilever Beam Considering the Rotary Inertial Moment of an Attached Mass

Binghui Wang,¹ Zhihua Wang,² and Xi Zuo³

¹*School of Architecture and Civil Engineering, Jiangsu University of Science and Technology, 2 Mengxi Road, Zhenjiang, Jiangsu, China*

²*Institute of Geotechnical Engineering, Nanjing Tech University, 200 North Zhongshan Road, Nanjing, China*

³*Institute of Architectural Engineering, Jinling Institute of Technology, Nanjing, China*

Correspondence should be addressed to Zhihua Wang; wzhnjut@163.com

Received 13 December 2016; Accepted 5 February 2017; Published 22 February 2017

Academic Editor: Rahmat Ellahi

Copyright © 2017 Binghui Wang et al. This is an open access article distributed under the Creative Commons Attribution License, which permits unrestricted use, distribution, and reproduction in any medium, provided the original work is properly cited.

The major goal of this paper is to address the derivation of the frequency equation of flexural vibrating cantilever beam considering the bending moment generated by an additional mass at the free end of beam, not just the shear force. It is a transcendental equation with two unambiguous physical meaning parameters. And the influence of the two parameters on the characteristics of frequency and shape mode was made. The results show that the inertial moment of the mass has the significant effect on the natural frequency and the shape mode. And it is more reasonable using this frequency equation to analyze vibration and measure modulus.

1. Introduction

The cantilever beam is a simple structure, and it is an important simplified model for many engineering problem in the fields of mechanical engineering, civil engineering, and so forth. However, there is a vast number of papers concerned with the determination of the eigenfrequencies of the cantilever beam subject to various boundary conditions, which can be found in the classic book [1]. And more and more issues of cantilever beam with complicated boundary conditions [2] or external load conditions [3, 4] have been studied by theoretical deduction [5] or numerical method [6], or it is application to determine Young's modulus [7].

The cantilever beam model is also used in geotechnical earthquake engineering as a simplified model [8] for the ground responses due to earthquake. It is also a basic principle of measuring the soil's dynamic shear modulus which is an indispensable parameter for analyzing the earthquake response of site caused by far-field ground. The apparatus used to obtain the dynamic shear modulus is well known as resonant column apparatus. The soil column, installed in this apparatus, is driven by electromagnetic force at free end [9] producing its torsional vibration. If flexural vibration

of the soil column occurs, the dynamic Young modulus can be obtained, which is also an important parameter for dynamic analysis of site suffered by near-field ground motion. Essentially, the frequency equation of flexural vibrating cantilever beam with an additional mass is needed. However, the vibrating frequency and shape mode of soil column are effected by not only the shear force but also the moment force, generated by the motion of the additional mass attached at the free end of the soil column. So the influence of these two forces on the vibrating of soil column must be discussed. Cascante et al. [10] derived a frequency equation of this vibrational problem using Rayleigh's method assuming that the mode shape is a third-order polynomial. Laura [11] derived the frequency equation of a cantilever beam attaching an additional mass, which is considered as shear force acted on the free end of beam but did not consider the moment force generated by the mass. And recently, Gürgöze [12–14] studies the eigenfrequencies of a cantilever beam carrying a tip mass or spring-mass.

The paper tried to derive the frequency equation of the cantilever beam in order to obtain more accurate solution for the soil column and to analyze the frequency characteristics

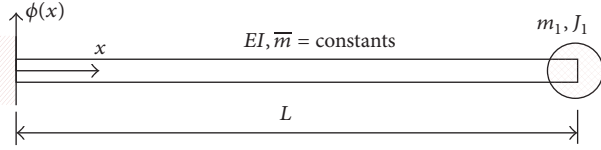


FIGURE 1: Diagram of the cantilever beam with an additional mass.

of this system effected by the bending moment generated by the additional mass.

2. Flexural Motion Equation of Cantilever Beam with an Additional Mass

The flexural cantilever beam to be considered is the straight, uniform beam with an additional rigid mass attached by fixed connection. The significant physical properties of this beam are assumed to be the flexural stiffness EI and the mass per unit length \bar{m} , both of which are constant along the span L . The transverse displacement response $y(x, t)$ is a function of position and time. The free vibration equation of motion for the system as shown in Figure 1 is easily formulated by directly expressing the equilibrium of all forces acting on the differential segment of beam. And it becomes [15]

$$EI \frac{\partial^4 y(x, t)}{\partial x^4} + \bar{m} \frac{\partial^2 y(x, t)}{\partial t^2} = 0. \quad (1)$$

Since EI and \bar{m} are constant, one form of solution of this equation can be obtained by separation of variables using

$$y(x, t) = \phi(x) Y(t) \quad (2)$$

which indicates that the free vibration motion is of a specific shape $\phi(x)$ having a time-dependent amplitude $Y(t)$. Substituting this equation into (1) can yield two ordinary differential equations.

$$\begin{aligned} \ddot{Y}(t) + \omega^2 Y(t) &= 0, \\ \phi''''(x) - \beta^4 \phi(x) &= 0 \end{aligned} \quad (3)$$

in which $\beta^4 = \omega^2 \bar{m} / EI$, and ω is the circular frequency. These equations have the solution separately as follows:

$$Y(t) = B_1 \sin(\omega t) + B_2 \cos(\omega t), \quad (4)$$

$$\phi(x) = A_1 \cos \beta x + A_2 \sin \beta x + A_3 \text{ch} \beta x + A_4 \text{sh} \beta x \quad (5)$$

in which constants B_1 and B_2 depend upon the initial displacement and velocity conditions; and real constants A_i must be evaluated so as to satisfy the known boundary conditions at the ends of the beam.

The cantilever beam considered has a fixed end, so its two known boundary conditions are

$$\begin{aligned} \phi(0) &= 0, \\ \phi'(0) &= 0. \end{aligned} \quad (6)$$

Making use of (5) and its first partial derivative with respect to x , from (6) one obtains $A_3 = -A_1$ and $A_4 = -A_2$, So (5) becomes

$$\phi(x) = A_1 (\cos \beta x - \text{ch} \beta x) + A_2 (\sin \beta x - \text{sh} \beta x). \quad (7)$$

An additional rigid mass m_1 having a rotary mass moment of inertia J_1 is attached by fixed connection to its free end as also shown in Figure 2. These internal force components are along with the translational and rotary inertial force components $m_1 \omega^2 \phi(L)$ and $J_1 \omega^2 \phi'(L)$, respectively. So the force and moment equilibrium of the additional mass requires the boundary conditions

$$\begin{aligned} M(L) &= EI \phi''(L) = -\omega^2 \phi'(L) J_1, \\ V(L) &= EI \phi'''(L) = -\omega^2 \phi(L) m_1. \end{aligned} \quad (8)$$

Making use of (5) and its first, second, and third partial derivative with respect to x and substituting them into (8) yield

$$\begin{bmatrix} \beta^2 (\cos \beta L + \text{ch} \beta L) + \frac{\omega^2 J_1}{EI} \beta (\sin \beta L + \text{sh} \beta L) & \beta^2 (\sin \beta L + \text{sh} \beta L) - \frac{\omega^2 J_1}{EI} \beta (\cos \beta L - \text{ch} \beta L) \\ \beta^3 (\sin \beta L - \text{sh} \beta L) + \frac{\omega^2 m_1}{EI} (\cos \beta L - \text{ch} \beta L) & -\beta^3 (\cos \beta L + \text{ch} \beta L) + \frac{\omega^2 m_1}{EI} (\sin \beta L - \text{sh} \beta L) \end{bmatrix} \begin{Bmatrix} A_1 \\ A_2 \end{Bmatrix} = \begin{Bmatrix} 0 \\ 0 \end{Bmatrix}. \quad (9)$$

For coefficients A_1 and A_2 to be nonzero, the determinant of the square matrix in this equation must equal zero, thus giving the frequency equation

$$\begin{aligned} & \left[\beta^2 (\cos \beta L + \text{ch} \beta L) + \frac{\omega^2 J_1}{EI} \beta (\sin \beta L + \text{sh} \beta L) \right] \\ & \cdot \left[-\beta^3 (\cos \beta L + \text{ch} \beta L) + \frac{\omega^2 m_1}{EI} (\sin \beta L - \text{sh} \beta L) \right] \end{aligned}$$

$$- \left[\beta^2 (\sin \beta L + \text{sh} \beta L) - \frac{\omega^2 J_1}{EI} \beta (\cos \beta L - \text{ch} \beta L) \right]$$

$$\cdot \left[\beta^3 (\sin \beta L - \text{sh} \beta L) + \frac{\omega^2 m_1}{EI} (\cos \beta L - \text{ch} \beta L) \right]$$

$$= 0$$

$$(10)$$

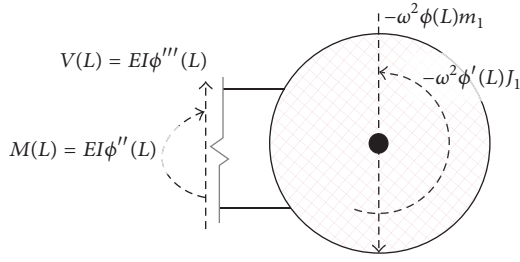


FIGURE 2: Diagram of force equilibrium analysis at the free end.

which can reduce to the following form making use of $\omega^2/EI = \beta^4/\bar{m}$

$$\begin{aligned} & \frac{J_1 m_1}{\bar{m}^2} \beta^4 (1 - \cos \beta L \operatorname{ch} \beta L) \\ & + \frac{m_1}{\bar{m}} \beta (\sin \beta L \operatorname{ch} \beta L - \cos \beta L \operatorname{sh} \beta L) \\ & = \frac{J_1}{\bar{m}} \beta^3 (\sin \beta L \operatorname{ch} \beta L + \cos \beta L \operatorname{sh} \beta L) \\ & + (1 + \cos \beta L \operatorname{ch} \beta L). \end{aligned} \quad (11)$$

Setting

$$z = \beta L = \sqrt[4]{\frac{\omega^2 \bar{m}}{EI}} L \quad (12)$$

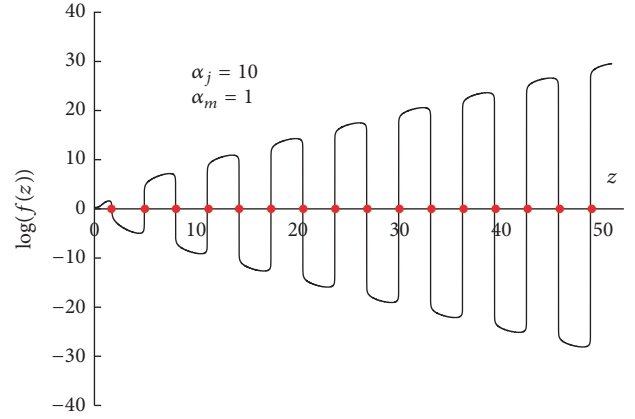
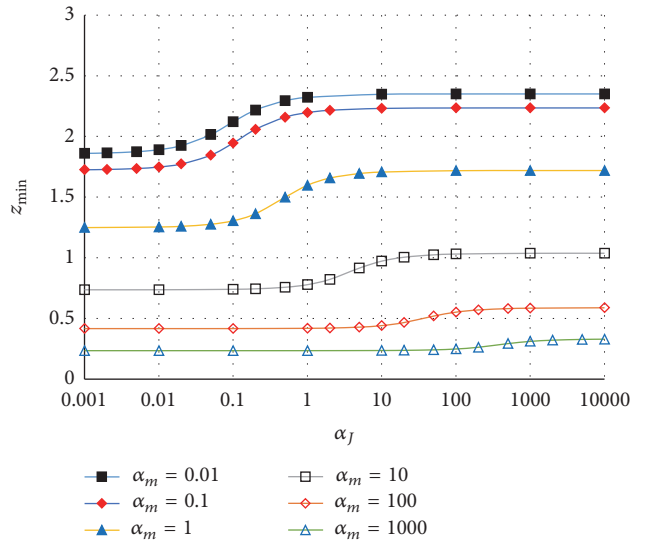
is a power function of the frequency of the flexural vibrating cantilever beam. And setting $\alpha_j = J_1/\bar{m}L^3 = J_1/m_T L^2$ is a ratio of the rotary mass moment of inertia for the additional mass and for a rigid mass of m_T having a rotary arm length of L ; and $\alpha_m = m_1/\bar{m}L = m_1/m_T$ is a ratio of the mass between the additional mass and the cantilever beam. So the frequency equation becomes

$$\begin{aligned} & \alpha_j \alpha_m z^4 (1 - \cos z \operatorname{ch} z) + \alpha_m z (\sin z \operatorname{ch} z - \cos z \operatorname{sh} z) \\ & = \alpha_j z^3 (\sin z \operatorname{ch} z + \cos z \operatorname{sh} z) + (1 + \cos z \operatorname{ch} z). \end{aligned} \quad (13)$$

This frequency equation is a transcendental equation that contained two parameters with unambiguous physical meaning. The solution of this equation, which is the frequency of the system of the flexural vibrating cantilever beam, can be only obtained by numerical method for now.

3. Solution of the Frequency Equation

In order to solve the frequency equation, the term of the right side of (13) can be moved to the left side, and then suppose the left side equals $f(z, \alpha_j, \alpha_m)$. And $f = 0$ is equivalent to (13). Suppose the parameters α_j and α_m are constant, and then the relationship between $f(z)$ and z can be calculated and drawn as shown in Figure 3, in which the parameters $\alpha_j = 10$ and $\alpha_m = 1$. However, the value of $f(z)$ rises abruptly. So the y -axis alters to $\log f(z)$ in order to show the curve is up and down across the x -axis obviously. The intersection points of


 FIGURE 3: Relationship between $f(z)$ and z .

 FIGURE 4: Varied z with α_j .

the curve and x -axis as marked in Figure 3 with circle points are the roots of the equation $f(z) = 0$, where its approximate roots can be obtained using numerical methods for solving system of nonlinear equations, such as method of bisection and Newton's method.

For a specific system, where the α_j and α_m are determined, the solution of the frequency equation (13) can be obtained. And the roots of the parameter z are varied with the parameters α_j and α_m . Figures 4 and 5 show their effects. With the increment of the parameter α_j , the root z is increased identically with a sigmoid function as shown in Figure 4. It means that the frequency of the system will increase if the rotary mass moment of inertia for the additional mass is increased. And the rate of the increment is larger around $\alpha_j = \alpha_m$ than others. For example, the increment of z at the range of $\alpha_j = 0.1 \sim 10$ is fastest while $\alpha_m = 1$. With the increment of the parameter α_m , the root z is decreasing, as shown in Figure 5, which means that the frequency of the system will decrease with the additional mass increasing.

TABLE 1: The first five natural frequencies of the cantilever beam considering the bending moment.

Frequency number (i)	Nondimensional natural frequency $\omega_i' = \sqrt{EI/\bar{m}L^4}z_i$									$\omega_i'*$ $\alpha_m = 1$ (ref [11])
	$\alpha_m = 100$ $\alpha_j = 1$	$\alpha_m = 10$ $\alpha_j = 1$	$\alpha_m = 1$ $\alpha_j = 100$	$\alpha_m = 1$ $\alpha_j = 10$	$\alpha_m = 1$ $\alpha_j = 1$	$\alpha_m = 1$ $\alpha_j = 0.1$	$\alpha_m = 1$ $\alpha_j = 0.01$	$\alpha_m = 1$ $\alpha_j = 0.001$	$\alpha_m = 1$ $\alpha_j = 0$	
1	0.1749603	0.6054297	2.950242	2.91158	2.55044	1.70226	1.571098	1.55867	1.557298	1.557298
2	22.30366	22.47413	23.93841	23.93129	23.86031	23.17405	19.13831	16.57872	16.25009	16.25009
3	61.66046	61.83822	63.43232	63.42955	63.40190	63.1286	60.72695	53.50208	50.89584	50.89584
4	120.90684	121.0850	122.7265	122.7251	122.71062	122.5668	121.2014	113.2826	105.1983	105.1983
5	199.86943	200.0480	201.7208	201.71991	201.71107	201.6229	200.7639	194.2422	179.2320	179.2320

*Notes. The values of this column were calculated by authors using the frequency equation from [11]. And the results were carefully checked by comparing the values of z_i (using the character y_i in this reference).

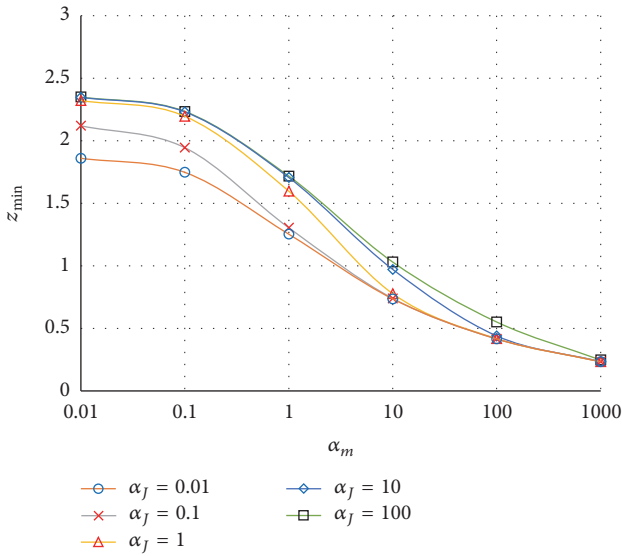


FIGURE 5: Varied z with α_m .

4. Natural Frequencies and Shape Modes Characteristics

The natural frequency ω_i of the flexural vibration of cantilever beam considering the bending moment generated by the attached mass can be calculated using the transformation of (12). Table 1 lists the results of the first five natural frequencies of this system with the varied parameters values α_j and α_m . The natural frequency increases with the parameter α_m decreasing, which means the quality of the additional mass reduction compared to that of the cantilever beam. This is consistent with the result of others [7, 16]. And the frequency also increases with the increment of the rotary mass moment of inertia for the additional mass compared to the beam, which is defined as the parameter α_j . In order to make comparisons, the results of frequencies when the parameters $\alpha_j = 0$ and $\alpha_m = 1$ are also listed, which means the free end of beam has no moment force generated by the additional mass. As expected, these natural frequency values are the same as that obtained from [11], in which only the shear force is considered generated by the attached mass. And the larger

value of α_j causes the higher frequency of the cantilever beam as shown in Table 1.

However, the interval between the two frequencies for α_j equal to zero and for α_j unequal to zero is considerable, especially that between the two higher frequency numbers. So the ignored rotary mass moment of inertia may be too ideal for engineering problem and cause obviously error.

The vibration shape mode can also be obtained by substituting the ratio of A_1 and A_2 into the shape equation (7). And Figure 6(a) shows the first four mode shapes of the cantilever beam considering the moment force with the parameters $\alpha_m = 1$ and $\alpha_j = 10$. The first four mode shapes of the cantilever beam are shown without considering the moment force in [11]. It is clearly shown that the vibration shape is effected by the moment force from the additional mass significantly. However, the existence of the additional mass restrains the development of displacement at the free end of beam.

In order to analyze the influence of α_j on the mode shape, the 3rd to 5th mode shapes of considering the moment force with $\alpha_m = 1$ and $\alpha_j = 0.001$ and without considering situation are given, as shown in Figure 6(b). Even if the parameter α_j is of very small value, the 5th mode shape of these two situations has obviously divergence, though the smaller the serial number of mode shape is, the less obvious the divergence becomes.

5. Conclusion

The frequency equation of cantilever beam with an additional mass exciting flexural vibration was derived considering the rotary inertial moment of inertia of an attached mass, including the shear force. It is a transcendental equation, and it contains two parameters with unambiguous physical meaning, which can be defined as the ratio of rotary mass moment of inertia and the ratio of the mass, respectively.

These two parameters effect both the natural frequency and the shape mode of the beam. As the ratio of rotary mass moment of inertia increases, the natural frequency climbs. Even a little increment of the ratio may cause higher variance between considering and not considering the rotary mass moment of inertia, especially for the high natural frequency. And the ratio of the rotary mass moment of inertia also

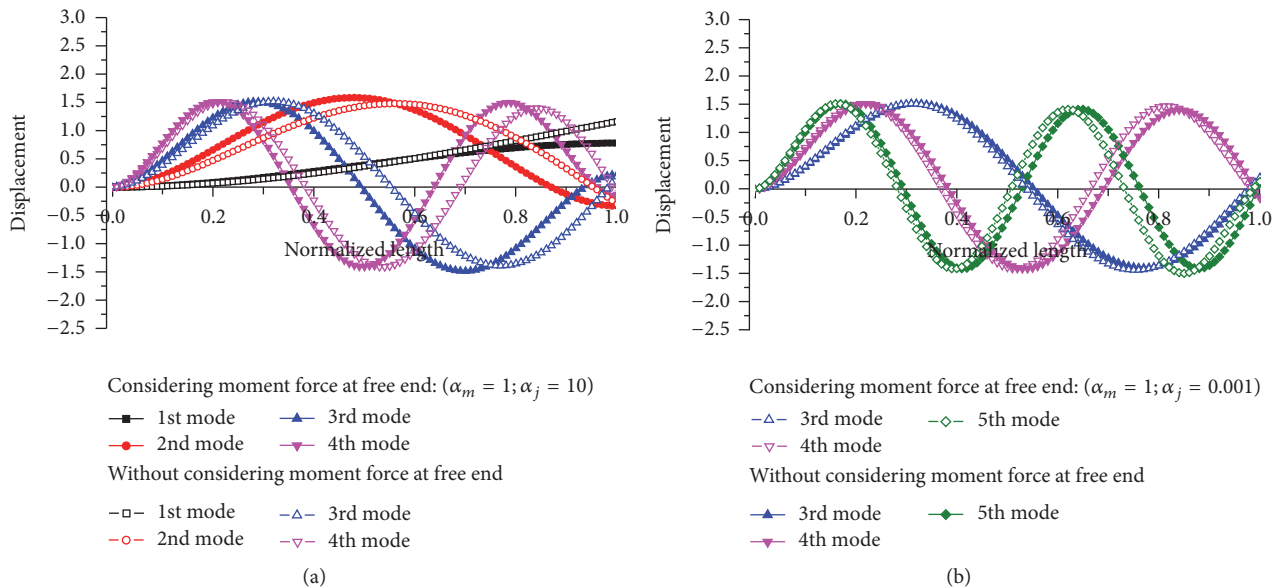


FIGURE 6: The first five mode shapes of considering the moment force with $\alpha_m = 1$ and $\alpha_j = 10$ and without considering situation (a) and the 3rd to 5th mode shapes of considering the moment force with $\alpha_m = 1$ and $\alpha_j = 0.001$ and without considering situation (b).

effects the mode shape of this system. The higher the serial number of mode shape investigated is, the more obvious the divergence becomes.

Competing Interests

There are no competing interests regarding this paper.

Acknowledgments

This paper is supported by National Science Foundation of China (NSFC 51309121) and Natural Science Foundation of Jiangsu Province (BK20130463).

References

- [1] S. S. Rao, *Mechanical Vibrations*, Pearson Education, Upper Saddle River, NJ, USA, 4th edition, 2004.
- [2] Y. K. Rudavskii and I. A. Vikovich, "Forced flexural-and-torsional vibrations of a cantilever beam of constant cross section," *International Applied Mechanics*, vol. 43, no. 8, pp. 912–923, 2007.
- [3] D. Zhou and T. Ji, "Estimation of dynamic characteristics of a spring-mass-beam system," *Shock and Vibration*, vol. 14, no. 4, pp. 271–282, 2007.
- [4] D. Zhou and T. Ji, "Dynamic characteristics of a beam and distributed spring-mass system," *International Journal of Solids and Structures*, vol. 43, no. 18-19, pp. 5555–5569, 2006.
- [5] C. A. Rossit and P. A. A. Laura, "Free vibrations of a cantilever beam with a spring-mass system attached to the free end," *Ocean Engineering*, vol. 28, no. 7, pp. 933–939, 2001.
- [6] J. R. Banerjee, "Free vibration of beams carrying spring-mass systems—a dynamic stiffness approach," *Computers and Structures*, vol. 104-105, pp. 21–26, 2012.
- [7] R. M. Digilov and H. Abramovich, "Flexural vibration test of a beam elastically restrained at one end: a new approach for Young's modulus determination," *Advances in Materials Science and Engineering*, vol. 2013, Article ID 329530, 6 pages, 2013.
- [8] M. I. Idriss and B. H. Seed, "Seismic response of horizontal soil layers," *Journal of the Soil Mechanics and Foundation Division, American Society of Civil Engineers*, vol. 94, no. 4, pp. 1003–1031, 1968.
- [9] V. P. Drnevich, *Resonant-Column Testing—Problems and Solutions*, ASTM, Denver, Colo, USA, 1978.
- [10] G. Cascante, C. Santamarina, and N. Yassir, "Flexural excitation in a standard torsional-resonant column device," *Canadian Geotechnical Journal*, vol. 35, no. 3, pp. 478–490, 1998.
- [11] P. A. A. Laura, J. L. Pombo, and E. A. Susemihl, "A note on the vibrations of a clamped-free beam with a mass at the free end," *Journal of Sound & Vibration*, vol. 37, no. 2, pp. 161–168, 1974.
- [12] M. Gürgöze, "On the representation of a cantilevered beam carrying a tip mass by an equivalent spring-mass system," *Journal of Sound and Vibration*, vol. 282, no. 1-2, pp. 538–542, 2005.
- [13] M. Gürgöze, "On the eigenfrequencies of a cantilever beam carrying a tip spring-mass system with mass of the helical spring considered," *Journal of Sound and Vibration*, vol. 282, no. 3-5, pp. 1221–1230, 2005.
- [14] M. Gürgöze, "On the eigenfrequencies of a cantilever beam with attached tip mass and a spring-mass system," *Journal of Sound and Vibration*, vol. 190, no. 2, pp. 149–162, 1996.
- [15] R. Clough and J. Penzien, *Dynamics of Structures*, McGraw-Hill, 1993.
- [16] L. E. Monterrubio, "Free vibration of shallow shells using the Rayleigh—Ritz method and penalty parameters," *Proceedings of the Institution of Mechanical Engineers, Part C: Journal of Mechanical Engineering Science*, vol. 223, no. 10, pp. 2263–2272, 2009.

Research Article

Unsteady Bioconvection Squeezing Flow in a Horizontal Channel with Chemical Reaction and Magnetic Field Effects

Qingkai Zhao,¹ Hang Xu,¹ and Longbin Tao²

¹*Collaborative Innovation Center for Advanced Ship and Deep-Sea Exploration (CISSE), State Key Lab of Ocean Engineering, School of Naval Architecture, Ocean and Civil Engineering, Shanghai Jiao Tong University, Shanghai 200240, China*

²*School of Marine Science and Technology, Newcastle University, Newcastle NE17RU, UK*

Correspondence should be addressed to Hang Xu; hangxu@sjtu.edu.cn

Received 22 November 2016; Revised 29 December 2016; Accepted 4 January 2017; Published 24 January 2017

Academic Editor: Mohsen Sheikholeslami

Copyright © 2017 Qingkai Zhao et al. This is an open access article distributed under the Creative Commons Attribution License, which permits unrestricted use, distribution, and reproduction in any medium, provided the original work is properly cited.

The time-dependent mixed bioconvection flow of an electrically conducting fluid between two infinite parallel plates in the presence of a magnetic field and a first-order chemical reaction is investigated. The fully coupled nonlinear systems describing the total mass, momentum, thermal energy, mass diffusion, and microorganisms equations are reduced to a set of ordinary differential equations via a set of new similarity transformations. The detailed analysis illustrating the influences of various physical parameters such as the magnetic, squeezing, and chemical reaction parameters and the Schmidt and Prandtl numbers on the distributions of temperature and microorganisms as well as the skin friction and the Nusselt number is presented. The conclusion is drawn that the flow field, temperature, and chemical reaction profiles are significantly influenced by magnetic parameter, heat generation/absorption parameter, and chemical parameter. Some examples of potential applications of such bioconvection could be found in pharmaceutical industry, microfluidic devices, microbial enhanced oil recovery, modeling oil, and gas-bearing sedimentary basins.

1. Introduction

The unsteady squeezing channel flow, caused by the moving boundary under the influence of external normal stresses or vertical velocities, is often encountered in fabrication of hydrodynamical machines, accelerators, compression and injection moulding, lubrication equipment, and polymer processing and so on. Since Stefan [1] initiated the investigation of squeezing flow by using the lubrication approximation, many researchers successively considered squeezing flow problems for various geometrical configurations in many different ways. Moore [2] concluded that the Stefan equation [1] is inadequate to describe the molecular mechanism of viscosity of squeezing flows; instead, he indicated that the influences such as surface finish, viscoelastic liquids, elastomeric surfaces, and molecular effects also need to be considered partially or entirely based on the degree of complexity of problems. P. S. Gupta and A. S. Gupta [3] noticed that the unsteady squeezing channel flow problem could be simplified significantly via similarity variables in the

case that the distance between the paralleled plates varies as the square root of a linear function of time. Duwairi et al. [4] considered the heat transfer effects on the unsteady squeezing channel flow, in which case they assumed that the paralleled walls are heated uniformly by a constant temperature. The unsteady squeezing flow problems were further investigated by different researchers with consideration of various physical problems and computational techniques, such as Verma [5], Mustafa et al. [6], and Hayat et al. [7].

It is known that a large amount of microorganisms are suspended in appropriate aqueous environments, such as oceans and rivers, puddles, and droplets. Their behaviours govern the dynamics of many of these interactions with fluid mechanics. The hydrodynamic characteristics of single-celled microorganisms which are motile and self-propelled were firstly studied by Pedley et al. [8] and Pedley and Kessler [9]. Pedley's theory [8] was then adopted by Kuznetsov [10] to consider the thermal bioconvection, in which a macroscopic convective motion was induced in a fluid layer by the combined effect of density stratification caused by

the upswimming of oxytactic microorganisms and heating from below. Kuznetsov [11] then investigated the influences of nanoparticles on the behaviours of gyrotactic microorganisms and concluded that nanoparticles can be either stabilizing or destabilizing the density of microorganisms, depending on whether the basic nanoparticle distribution is bottom-heavy or top-heavy. His idea was confirmed by Xu and Pop [12] via an analysis of a mixed bioconvection nanofluid flow over a stretching flat sheet with uniform free stream with an improved nanofluid model proposed by Kuznetsov and Nield [13]. The novel behaviours of thermo-bioconvection in nanofluids were further investigated by Xu and Pop [14] and Raees et al. [15].

Physically, magnetic fields can induce currents in a moving electrically conductive fluid, which in turn polarizes the fluid and reciprocally changes the magnetic field itself. Such fluid was named as magnetohydrodynamics (MHD) by Alfvén [16]. Since MHD flows have been found to be very useful in heat and mass transfer progresses in many industrial procedures such as polymer extrusion, drawing of copper wires, continuous stretching of plastic films and artificial fibers, hot rolling, wire drawing, glass-fiber, metal extrusion, and metal spinning, many studies [17–27] have been done towards understandings of their transport mechanisms and novel applications. It is worth mentioning that Khan and Makinde [28] conducted an investigation about the magnetic effect on bioconvection of a nanofluid along a vertical stretching sheet. They concluded that the ratio of convective to conductive heat transfer across (normal to) the boundary decreases with the magnetic parameter increasing, while the density number of the motile microorganisms decreases with magnetic parameter enlarging. Their work indicates that the MHD flow could be used to alter the distributions of microorganisms in potential applications such as removal of microorganisms attached in a water tank.

In this paper, we shall consider an unsteady bioconvection squeezing flow in a horizontal channel in the presence of both chemical reaction and magnetic effect. In a flowing fluid that contains heat transfer, mass transfer, and chemical reactions, the flow velocity is always to affect partially the transport of reactants, products, and heat and hence influences the overall mass and heat transfer rates. An analysis for accurate estimates of the transport effects upon the performance of processes with combined chemical reaction and magnetic effect in a combined flow regime is thus very desirable. As far as we know, no such study has been available in the literature. This study attempts to meet such a need.

2. Mathematical Descriptions

Consider the unsteady MHD flow of an electrically conducting fluid containing motile microorganisms between two infinite parallel plates in the presence of a first-order chemical reaction. As shown in Figure 1, the coordinate system is chosen such that the x -axis is along the lower plate and y -axis is perpendicular to the main flow direction, respectively. It is assumed that the two plates are placed at the distance $y = h(t) = [\nu(1 - at)/b]^{1/2}$ while the upper plate is moving towards or away from the lower stationary plate with the

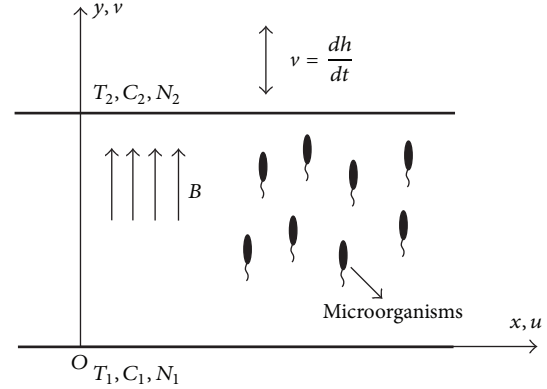


FIGURE 1: Physical model and coordinate system.

velocity $v(t) = dh/dt$. Here, a and b are positive numbers, ν is the kinematic viscosity, and t denotes the time. Obviously, it is known that $1 - at$ must be greater than zero, which indicates that a must be less than $1/t$. Physically, when $a = 0$, it means that the two plates are fixed. As $0 < a < 1/t$, it shows that the upper plate is squeezed to the lower one. While as $a < 0$, it indicates the upper plate moves away from the lower plate. It is also assumed that the lower and upper plates are maintained, respectively, at the constant temperatures T_1 and T_2 , constant concentration of microorganisms N_1 and N_2 , and constant chemical reaction concentrations C_1 and C_2 . The time-varying magnetic field of strength $B(t)$ is imposed along the y -axis. Based on the above assumptions, the conservation equations for total mass, momentum, thermal energy, mass diffusion, and microorganisms equations are expressed by

$$\nabla \cdot \mathbf{V} = 0,$$

$$\frac{\partial \mathbf{V}}{\partial t} + (\mathbf{V} \cdot \nabla) \mathbf{V} = -\frac{1}{\rho} \nabla p + \nu \nabla^2 \mathbf{V} + \frac{1}{\rho} (\mathbf{J} \times \mathbf{B}),$$

$$\frac{\partial T}{\partial t} + \mathbf{V} \cdot \nabla T = \alpha \nabla^2 T + \frac{Q_s(t)}{\rho c_p} (T - T_0), \quad (1)$$

$$\frac{\partial C}{\partial t} + \mathbf{V} \cdot \nabla C = D \nabla^2 C - K(t) (C - C_0),$$

$$\frac{\partial N}{\partial t} = -\nabla \cdot \mathbf{j},$$

where \mathbf{V} is the velocity vector, \mathbf{J} is the electric current density in the fluid, \mathbf{B} is the magnetic induction, ρ is the fluid density, p is the pressure, ν is the kinematic viscosity of the fluid, T is the temperature, T_0 is the reference temperature, α is the thermal diffusivity, $Q_s(t)$ is the volumetric rate of heat generation/absorption, C is the concentration of the chemical reaction, C_0 is the reference concentration, D is the mass diffusivity, $K(t)$ is the reaction rate, N is the concentration of motile microorganism, and \mathbf{j} is the flux of microorganisms.

It is assumed that the magnetic Reynolds number is small ($\ll 1$) so that the induced magnetic field can be omitted. It is also assumed that the heating due to the plates and the chemical reaction is weak so that microorganisms can survive

and their gyrotactic behaviour can keep unchanged. With those assumptions, we can expand (1) into the following forms:

$$\begin{aligned} \frac{\partial \xi}{\partial t} + u \frac{\partial \xi}{\partial x} + v \frac{\partial \xi}{\partial y} &= \nu \left(\frac{\partial^2 \xi}{\partial x^2} + \frac{\partial^2 \xi}{\partial y^2} \right) + \frac{\sigma B^2(t) u}{\rho}, \\ \frac{\partial T}{\partial t} + u \frac{\partial T}{\partial x} + v \frac{\partial T}{\partial y} &= \alpha \left(\frac{\partial^2 T}{\partial x^2} + \frac{\partial^2 T}{\partial y^2} \right) + \frac{Q_s(t)}{\rho c_p} (T - T_0), \\ \frac{\partial C}{\partial t} + u \frac{\partial C}{\partial x} + v \frac{\partial C}{\partial y} &= D \left(\frac{\partial^2 C}{\partial x^2} + \frac{\partial^2 C}{\partial y^2} \right) - K(t) (C - C_0), \\ \frac{\partial N}{\partial t} + u \frac{\partial N}{\partial x} + v \frac{\partial N}{\partial y} + \frac{\partial}{\partial x} (N\bar{v}) + \frac{\partial}{\partial y} (N\bar{v}) &= D_n \left(\frac{\partial^2 N}{\partial x^2} + \frac{\partial^2 N}{\partial y^2} \right), \end{aligned} \quad (2)$$

subject to the boundary conditions

$$\begin{aligned} u &= 0, \\ v &= 0, \\ T &= T_1, \\ C &= C_1, \\ N &= N_1 \\ &\text{at } y = 0, \\ u &= 0, \\ v &= \frac{dh}{dt}, \\ T &= T_2, \\ C &= C_2, \\ N &= N_2 \\ &\text{at } y = h(t), \end{aligned} \quad (3)$$

where u and v are the velocity components in the x - and y -directions defined by $u = \partial\psi/\partial y$ and $v = -\partial\psi/\partial x$ with ψ being the stream function, $\xi = -\nabla^2\psi$ is the vorticity function, N is the density of motile microorganisms, $\bar{v} = [b_c W_c / (C_1 - C_0)] \partial C / \partial y$ is the average swimming velocity vector of the oxytactic microorganisms with b_c being the chemotaxis constant and W_c being the maximum cell swimming speed, and D_n is the diffusivity of microorganisms.

We then introduce the following similarity transformations and nondimensional quantities:

$$\begin{aligned} \psi(x, y) &= \left(\frac{b\nu}{1-at} \right)^{1/2} x f(\eta), \\ u &= \frac{bx}{1-at} f'(\eta), \\ v &= - \left(\frac{b\nu}{1-at} \right)^{1/2} f(\eta), \\ \eta &= \left(\frac{b}{\nu(1-at)} \right)^{1/2} y, \\ \theta(\eta) &= \frac{T - T_0}{T_1 - T_0}, \\ \phi(\eta) &= \frac{C - C_0}{C_1 - C_0}, \\ w(\eta) &= \frac{N}{N_1}. \end{aligned} \quad (4)$$

In view of (4), (2) can be reduced to the following nondimensional form:

$$f''''(\eta) - Mf'(\eta) - 3\beta f''(\eta) - \beta\eta f''''(\eta) - f'(\eta) f''(\eta) + f(\eta) f''''(\eta) = 0, \quad (5)$$

$$\frac{1}{Pr} \theta''(\eta) + Q\theta(\eta) - \beta\eta\theta'(\eta) + f(\eta)\theta'(\eta) = 0, \quad (6)$$

$$\frac{1}{LePr} \phi''(\eta) - K_0\phi(\eta) - \beta\eta\phi'(\eta) + f(\eta)\phi'(\eta) = 0, \quad (7)$$

$$w''(\eta) - Sc\beta\eta w'(\eta) + Sc f(\eta) w'(\eta) - Pe w(\eta) \phi''(\eta) - Pe \phi'(\eta) w'(\eta) = 0. \quad (8)$$

subject to the following boundary conditions:

$$\begin{aligned} f'(0) &= 0, \\ f(0) &= 0, \\ \theta(0) &= 1, \\ \phi(0) &= 1, \\ w(0) &= 1, \\ f'(1) &= 0, \\ f(1) &= \beta, \\ \theta(1) &= \delta_\theta, \\ \phi(1) &= \delta_\phi, \\ w(1) &= \delta_w, \end{aligned} \quad (9)$$

where M is the magnetic field parameter, β is the squeezing parameter, Pr is the Prandtl number, Q is the heat generation/absorption parameter, Le is the Lewis number, K_0 is the

chemical reaction parameter, Sc is the Schmidt number, Pe is the bioconvection Péclet number, and δ_θ , δ_ϕ , and δ_w are constants, which are defined by

$$\begin{aligned} M &= \frac{\sigma}{\nu\rho} B_0^2, \\ \beta &= \frac{a}{2b}, \\ Pr &= \frac{\nu}{\alpha}, \\ Q &= \frac{Q_0}{\rho c_p}, \\ Le &= \frac{\alpha}{D}, \\ K_0 &= \left(\frac{b}{1-at} \right)^{-1} K(t), \\ Sc &= \frac{\nu}{D_n}, \\ Pe &= \frac{b_c W_c}{D_n}, \\ \delta_\theta &= \frac{T_2 - T_0}{T_1 - T_0}, \\ \delta_\phi &= \frac{C_2 - C_0}{C_1 - C_0}, \\ \delta_w &= \frac{N_2}{N_1}. \end{aligned} \quad (10)$$

In above equation $B_0 = (b/\nu(1-at))^{-3/4} B(t)$ is a reference magnetic field parameter, $Q_0 = (b/(1-at))^{-1} Q_s(t)$ is a reference heat generation/absorption parameter, and K_0 is the chemical reaction parameter.

Practical interests of this problem are the local skin friction C_{fx} , the local Nusselt number Nu_x , the local wall mass flux Sh_x , and the local wall motile microorganisms flux Q_x , which are defined by

$$\begin{aligned} C_{fx} &= \frac{\tau_w}{(1/2)\rho U_x^2}, \\ Nu_x &= \frac{xq_w}{k(T_1 - T_0)}, \\ Sh_x &= \frac{xj_w}{D(C_1 - C_0)}, \\ Q_x &= \frac{xh_w}{D_n(N_1 - N_0)}, \end{aligned} \quad (11)$$

where

$$\begin{aligned} \tau_w &= \mu \left(\frac{\partial u}{\partial y} \right)_{y=0}, \\ q_w &= -k \left(\frac{\partial T}{\partial y} \right)_{y=0}, \end{aligned}$$

$$\begin{aligned} j_w &= -D \left(\frac{\partial C}{\partial y} \right)_{y=0}, \\ h_w &= -D_n \left(\frac{\partial N}{\partial y} \right)_{y=0}. \end{aligned} \quad (12)$$

Without loss of generality, we set $N_0 = 0$. Substituting (12) into (11), we obtain

$$\begin{aligned} Re_x^{1/2} C_{fx} &= 2f''(0), \\ Re_x^{-1/2} Nu_x &= -\theta'(0), \\ Re_x^{-1/2} Sh_x &= -\phi'(0), \\ Re_x^{-1/2} Q_x &= -w'(0), \end{aligned} \quad (13)$$

where $Re_x = U_w x / \nu$ is the local Reynolds number.

3. Results and Discussion

Equations (5)–(8) and their boundary conditions (9) are solved numerically for various values of the parameters using the shooting method along with fourth-order Runge-Kutta scheme. In the computation, the value of the step size $\Delta\eta$ between 0.001 and 0.01 was used, in order that the numerical values obtained are mesh independent. In addition, we choose $\delta_\theta = 1/2$, $\delta_\phi = 0$, and $\delta_w = 1$ for all considered cases, which are not against physical requirements. Further, to check the accuracy of the results, we compare them with those given by the BVPh2.0 programme (which is based on the homotopy analysis methods technique). Here, the initial approximations $f_0(\eta)$, $\theta_0(\eta)$, $\phi_0(\eta)$, and $w_0(\eta)$ are chosen based on (9) as below:

$$\begin{aligned} f_0(\eta) &= 3\beta\eta^2 - 2\beta\eta^3, \\ \theta_0(\eta) &= 1 + (\delta_\theta - 1)\eta, \\ \phi_0(\eta) &= 1 + (\delta_\phi - 1)\eta, \\ w_0(\eta) &= 1 + (\delta_w - 1)\eta. \end{aligned} \quad (14)$$

The auxiliary linear operator are chosen as:

$$\begin{aligned} L[f(\eta)] &= \frac{\partial^4 f(\eta)}{\partial \eta^4}, \\ L[\theta(\eta)] &= \frac{\partial^2 \theta(\eta)}{\partial \eta^2}, \\ L[\phi(\eta)] &= \frac{\partial^2 \phi(\eta)}{\partial \eta^2}, \\ L[w(\eta)] &= \frac{\partial^2 w(\eta)}{\partial \eta^2}. \end{aligned} \quad (15)$$

Through calculation and comparison, excellent agreement is found, as shown in Figure 2.

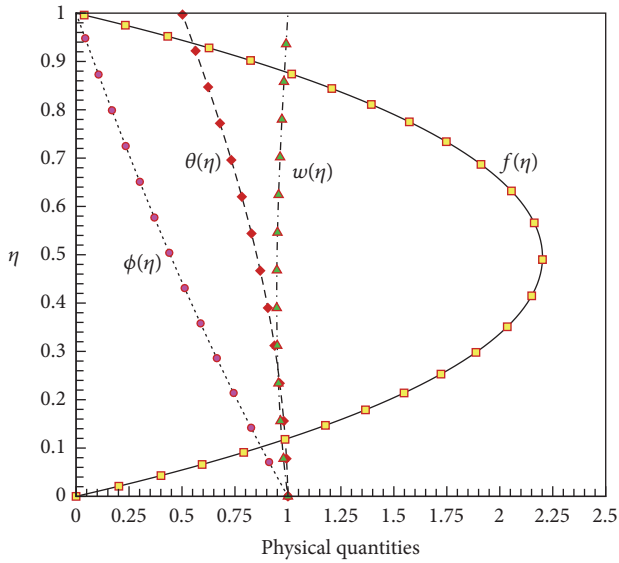


FIGURE 2: Comparison of the BVPh2.0 programme results and the numerical results for $\beta = 1.5, Q = 1, K_0 = 1,$ and $Pr = Le = Sc = Pe = 1,$ where symbols are numerical results and lines are BVPh2.0 programme results.

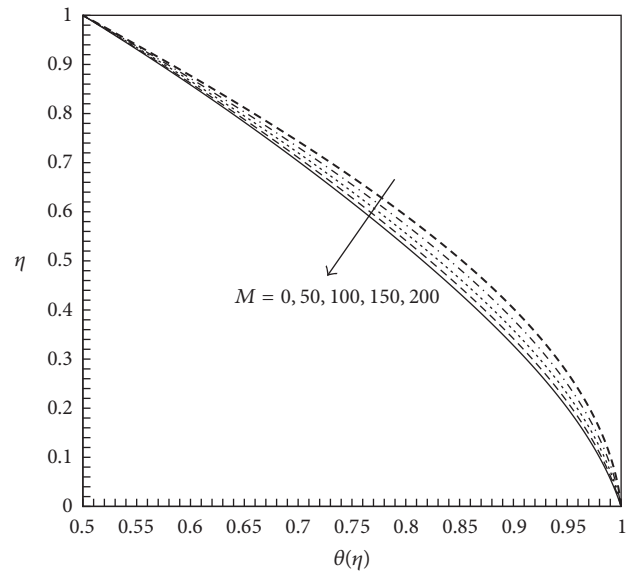


FIGURE 4: Variation of $\theta(\eta)$ with η for various M in the case of $\beta = 1.5, Q = 1, K_0 = 1,$ and $Pr = Le = Sc = Pe = 1.$

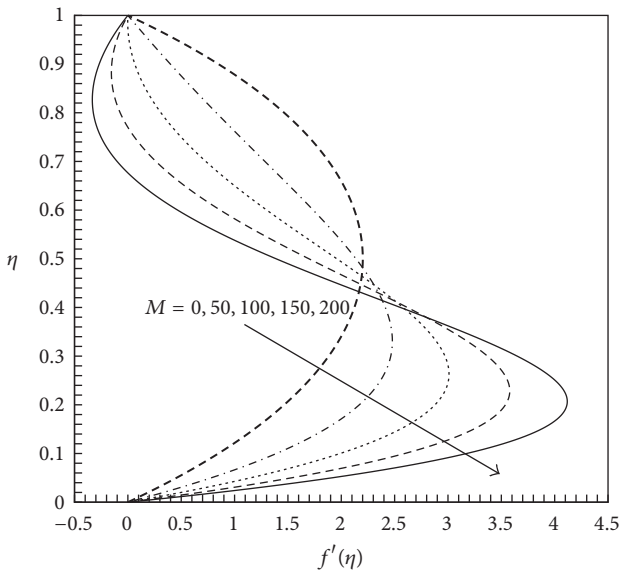


FIGURE 3: Variation of $f'(\eta)$ with η for various M in the case of $\beta = 1.5, Q = 1, K_0 = 1,$ and $Pr = Le = Sc = Pe = 1.$

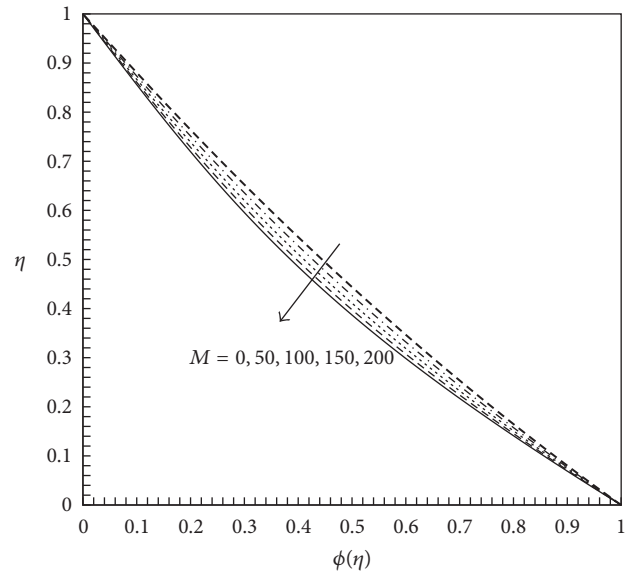


FIGURE 5: Variation of $\phi(\eta)$ with η for various M in the case of $\beta = 1.5, Q = 1, K_0 = 1,$ and $Pr = Le = Sc = Pe = 1.$

We first consider the influence of the magnetic parameter M on variations of various profiles. It is shown in Figure 3 that $f'(\eta)$ develops rapidly with M evolving, the enlargement of M causes the enhancement of the flow velocity in the vicinity of the lower plate but the reduction of the flow velocity on the other side. This is due to the fact that the enhanced Lorentz force imparts additional momentum into the squeezing channel, which accelerates the flow motion in the lower part of the channel. Synchronously the flow near the upper plate is retarded owing to the nonslip boundary. It is found in Figure 4 that the temperature profiles decrease

continuously as M increases. The reason is that the enhanced Lorentz force increases the thermal boundary-layer thickness in the channel. Particularly, we notice that the temperature profiles near the lower plate reduce a bit more quickly than that near the upper plate, which is due to the fact that the flow velocity in the vicinity of the lower plate is higher than that near the upper plate. As shown in Figure 5, the influence of the magnetic parameter M on the concentration of chemical reaction $\phi(\eta)$ is similar to that on the temperature profiles $\theta(\eta)$; that is to say, the larger the value of M , the lower the profile $\phi(\eta)$. Physically, this variation is mainly caused by the mass transportation induced by the enhanced Lorentz

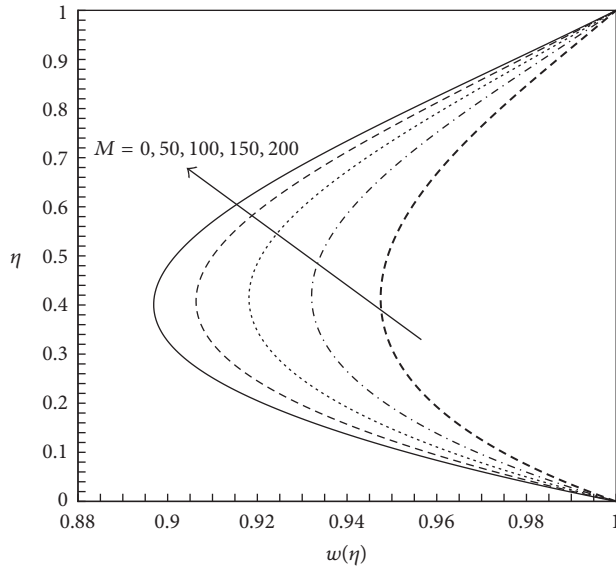


FIGURE 6: Variation of $w(\eta)$ with η for various values of parameter M in the case of $\beta = 1.5$, $Q = 1$, $K_0 = 1$, and $\text{Pr} = \text{Le} = \text{Sc} = \text{Pe} = 1$.

force. It is illustrated in Figure 6 that M has obvious effect on variation of the motile density of the microorganisms $w(\eta)$. $w(\eta)$ decreases as M enlarges, since the increase of M accelerates the fluid motion, which is helpful to alter the distributions of microorganisms.

We next consider the effects of the chemical reaction parameter K_0 and the heat generation/absorption parameter Q on various profiles. In view of (5), (6), and (7), it is readily found that $f(\eta)$ and $\theta(\eta)$ are uncoupled with $\phi(\eta)$; that is to say, the variation of $\phi(\eta)$ due to the evolution of K_0 does not affect the velocity and temperature distributions at all. Therefore, we need only to consider the influence of K_0 on $\phi(\eta)$ and $w(\eta)$. As shown in Figure 7, the increase of K_0 causes the decrease of $\phi(\eta)$. Physically, K_0 is related to the chemical reaction rate. The larger this value is, the faster the reaction rate is. As a result, the concentration of the chemical species is reduced as K_0 evolves. It is illustrated in Figure 8 that the density of motile microorganisms $w(\eta)$ reduces as K_0 enlarges. This is due to the fact that the enhancement of K_0 reduces the concentration of chemical species, which leads to the decrease of the density of motile microorganisms. Similarly, it is found from (5)–(8) that the heat generation/absorption parameter Q is only associated with $\theta(\eta)$ via the reduced energy equation (8) and $\theta(\eta)$ has no relation with any other functions. We therefore only need to consider its influence on the temperature distribution. As shown in Figures 9 and 10, for $Q > 0$, corresponding to the heat source generation case, $\theta(\eta)$ increase rapidly with Q increasing. On the other hand, for $Q < 0$, corresponding to the heat source absorption case, $\theta(\eta)$ reduces rapidly with Q decreasing. In other words, the heat generation/absorption parameter Q has a great influence on the temperature.

We now discuss the effects of various physical parameters on physically important quantities. It is known that M and δ_θ can affect the local Nusselt number $\text{Re}_x^{-1/2}\text{Nu}_x$, according to

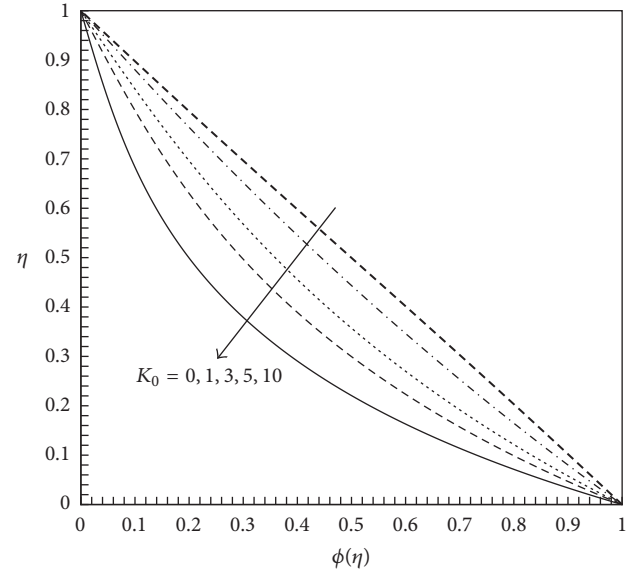


FIGURE 7: Variation of $\phi(\eta)$ with η for various values of K_0 in the case of $\beta = 1.5$, $Q = 1$, $M = 1$, and $\text{Pr} = \text{Le} = \text{Sc} = \text{Pe} = 1$.

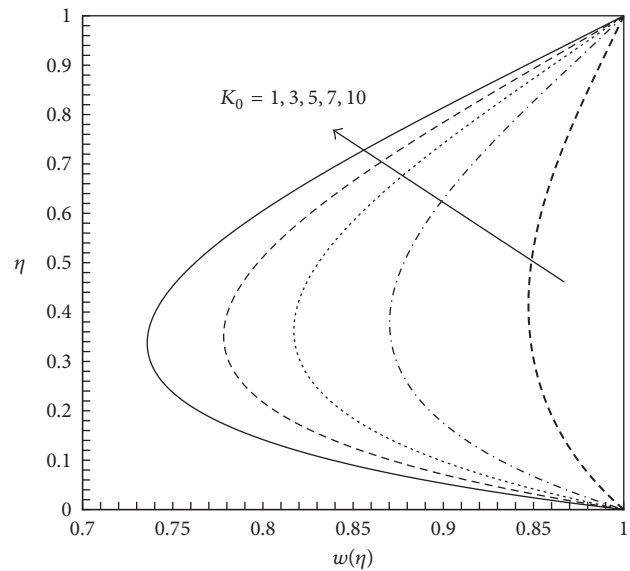


FIGURE 8: Variation of $w(\eta)$ with η for various values of K_0 in the case of $\beta = 1.5$, $Q = 1$, $M = 1$, and $\text{Pr} = \text{Le} = \text{Sc} = \text{Pe} = 1$.

(6) and its boundary condition (9) for temperature distribution on the upper plate. As shown in Table 1, the local Nusselt number increases gradually as the magnetic parameter M enlarges. This is due to the fact that the increase of M means more additional momentum caused by the enhanced Lorentz force is imparted into the sneezing channel. As a result, the fluid flow is accelerated and the temperature difference between this plate and the reference value is increased. Similarly, we know that M and δ_ϕ take effects on the local wall mass flux $\text{Re}_x^{-1/2}\text{Sh}_x$. It is seen in Table 2 that the local wall mass flux increases continuously as M enlarges. This trend indicates that the magnetic parameter plays a role on

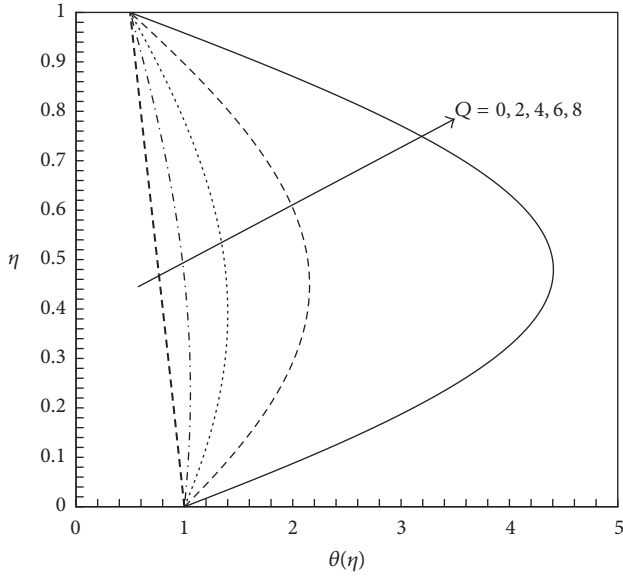


FIGURE 9: Variation of $\theta(\eta)$ with η for various positive values of Q in the case of $\beta = 1.5$, $M = 1$, $K_0 = 1$, and $\text{Pr} = \text{Le} = \text{Sc} = \text{Pe} = 1$.

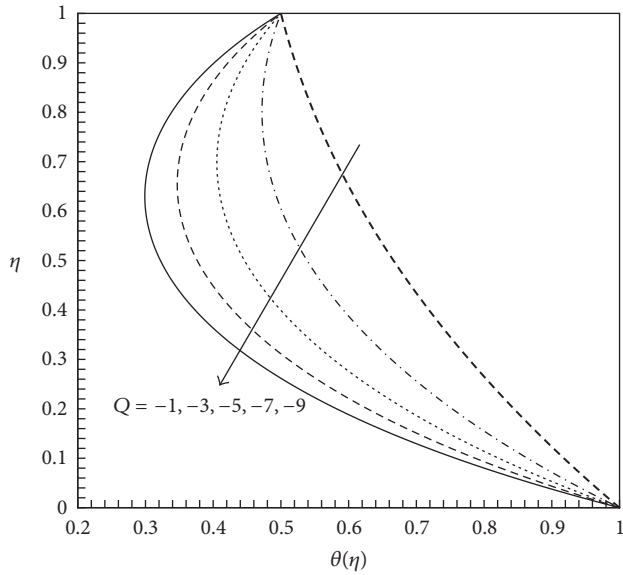


FIGURE 10: Variation of $\theta(\eta)$ with η for various negative values of Q in the case of $\beta = 1.5$, $M = 1$, $K_0 = 1$, and $\text{Pr} = \text{Le} = \text{Sc} = \text{Pe} = 1$.

variation of the nanoparticles distribution. When M is fixed, it is found in this table that the local wall mass flux reduces gradually as δ_ϕ evolves.

In practical application, It is interesting to give some approximate formulae for calculating those physical quantities. For instance, by regression analysis, we obtain the estimated formulae for various physical quantities as functions of M and/or K_0 in the case of $Q = \text{Pr} = \text{Le} = \text{Sc} = \text{Pe} = 1$ and $\beta = 1.5$,

$$\begin{aligned} \text{Re}_x^{1/2} C_{fx} &= 9.035322 + 0.177944M, \\ \text{Re}_x^{-1/2} \text{Nu}_x &= 0.04904 + 0.00524M, \end{aligned}$$

TABLE 1: The local Nusselt number $\text{Re}_x^{-1/2} \text{Nu}_x$ for various values of parameters δ_θ and M in the case of $\delta_\phi = 0$, $\delta_w = 1$, $Q = K_0 = \text{Pr} = \text{Le} = \text{Sc} = \text{Pe} = 1$, and $\beta = 1.5$.

δ_θ	$M = 0$	$M = 50$	$M = 100$	$M = 200$
0	0.62504	0.68927	0.75182	0.85656
0.2	0.39363	0.44398	0.49285	0.57423
0.4	0.16221	0.19868	0.23388	0.29191
0.6	-0.06921	-0.04661	-0.02509	0.00959
0.8	-0.30062	-0.29191	-0.28406	-0.27273
1	-0.53204	-0.53721	-0.54303	-0.55505

TABLE 2: For different M , the values of the local wall flux $\text{Re}_x^{-1/2} \text{Sh}_x$ for various values of parameter δ_ϕ in the case of $\delta_\theta = 0.5$, $\delta_w = 1$, $Q = K_0 = \text{Pr} = \text{Le} = \text{Sc} = \text{Pe} = 1$, and $\beta = 1.5$.

δ_ϕ	$M = 0$	$M = 50$	$M = 100$	$M = 200$
0	1.28437	1.33808	1.39126	1.48271
0.2	1.11792	1.16167	1.20508	1.28000
0.4	0.95147	0.98525	1.01890	1.07729
0.6	0.78501	0.80883	0.83271	0.87459
0.8	0.61856	0.63242	0.64653	0.67188
1	0.45210	0.45600	0.46035	0.46918

$$\begin{aligned} \text{Re}_x^{-1/2} \text{Sh}_x &= 1.1097864 + 0.0081446M \\ &\quad + 0.20924432K_0, \\ \text{Re}_x^{-1/2} Q_x &= 0.1403712 + 0.00089064M \\ &\quad + 0.22188504K_0. \end{aligned} \tag{16}$$

Similarly, we are able to give the estimated formulae by linear regression for other physical parameters. For instance, we are able to obtain the approximate expressions regarding δ_θ , δ_ϕ and δ_w by defining

$$P_{hQ} = B_0 + B_1 \delta_\theta + B_2 \delta_\phi + B_3 \delta_w, \tag{17}$$

where P_{hQ} can be replaced by various quantities including the local Nusselt number, the local wall mass flux, and the local wall motile microorganisms. When the value of δ_θ , δ_ϕ , and δ_w are, respectively, taken as 0, 0.4, 0.8, 1.2, 1.6, an 2, the coefficients B_1 , B_2 , and B_3 can be computed by linear regression, as shown in Tables 3–5. Note that here we set $Q = \text{Pr} = \text{Le} = \text{Sc} = \text{Pe} = K_0 = 1$ and $\beta = 1.5$.

4. Conclusions

The unsteady squeezing flow of an incompressible viscous fluid with suspension of small motile microorganisms between two infinite parallel plates in the presence of both chemical reaction and magnetic effect has been studied. The governing equations embody the total mass, momentum, thermal energy, and mass diffusion and microorganisms are reduced to a set of nonlinear ordinary differential equations via a set of similarity transformations. The effects of the

TABLE 3: Linear regression coefficients and the maximum relative error ϵ for the local Nusselt number $Re_x^{-1/2}Nu_x$.

M	B_0 (y-intercept)	B_1	B_2	B_3	ϵ
0	0.6250	-1.1571	0	0	$5.64E-07$
50	0.6893	-1.2265	0	0	$5E-07$
100	0.7518	-1.2949	0	0	$1.57E-16$
200	0.8566	-1.4116	0	0	$5E-07$
500	0.9942	-1.5765	0	0	$5E-07$

TABLE 4: Linear regression coefficients and the maximum relative error ϵ for the local wall flux $Re_x^{-1/2}Sh_x$.

M	B_0 (y-intercept)	B_1	B_2	B_3	ϵ
0	1.2844	0	-0.8323	0	$5.39E-07$
50	1.3381	0	-0.8821	0	$4.59E-07$
100	1.3913	0	-0.9309	0	$5.82E-07$
200	1.4827	0	-1.0135	0	$5.39E-07$
500	1.6144	0	-1.1258	0	$5.12E-07$

TABLE 5: Linear regression coefficients and the maximum relative error ϵ for the local wall motile microorganisms flux $Re_x^{-1/2}Q_x$.

M	B_0 (y-intercept)	B_1	B_2	B_3	ϵ
0	1.3019	0	0.1535	-1.0013	0.0401
50	1.4114	0	0.1082	-1.0534	0.0407
100	1.5201	0	0.0628	-1.1044	0.0411
200	1.7075	0	-0.0158	-1.1907	0.0419
500	1.9784	0	-0.1263	-1.3083	0.0431

various parameters on the distributions of velocity, temperature, chemical reaction concentration, and density of motile microorganisms, as well as the important physical quantities, have been examined in detail. The major contributions can be summarized as follows:

- (i) This problem solved by two methods and the results obtained by numerical methods have good agreement with the analytical solution.
- (ii) The magnetic parameter M takes actions on each profile since it imparts additional momentum into the squeezing channel. The increase of M leads to the enhancement of the velocity profile, but causes the decrease of the profiles of the temperature, the chemical reaction concentration, and the motile density of microorganisms. In short, the magnetic field can be used to control the flow characteristics.
- (iii) The chemical parameter K_0 plays a role in the chemical reaction concentration and motile density of microorganisms profiles. The increase of K_0 causes the decrease of both profiles.
- (iv) The heat generation/absorption parameter Q is critical for the profiles of the temperature. The temperature is found to increase as we go from strong absorption to strong generation of heat.

- (v) The estimated expressions for physical quantities of practical interests are given by linear regression for a range of parameters.

Competing Interests

The authors declare that no potential competing financial interests with others exist.

Authors' Contributions

Hang Xu and Qingkai Zhao conceived the work that led to the submission. Qingkai Zhao prepared figures. Hang Xu played an important role in interpreting the results. Longbin Tao drafted and revised the manuscript. All authors reviewed the manuscript and approved the final version.

Acknowledgments

The second author would like to acknowledge the program for New Century Excellent Talents in University (Grant no. NCET-12-0347) for its financial support.

References

- [1] J. Stefan, "Versuche über die scheinbare adhesion," *Akademie der Wissenschaften in Wien, Math.-Naturw.*, vol. 69, pp. 713–721, 1874.
- [2] D. F. Moore, "A review of squeeze films," *Wear*, vol. 8, no. 4, pp. 245–263, 1965.
- [3] P. S. Gupta and A. S. Gupta, "Squeezing flow between parallel plates," *Wear*, vol. 45, no. 2, pp. 177–185, 1977.
- [4] H. M. Duwairi, B. Tashtoush, and R. A. Damseh, "On heat transfer effects of a viscous fluid squeezed and extruded between two parallel plates," *Heat and Mass Transfer*, vol. 41, no. 2, pp. 112–117, 2004.
- [5] R. L. Verma, "A numerical solution for squeezing flow between parallel channels," *Wear*, vol. 72, no. 1, pp. 89–95, 1981.
- [6] M. Mustafa, T. Hayat, and S. Obaidat, "On heat and mass transfer in the unsteady squeezing flow between parallel plates," *Meccanica*, vol. 47, no. 7, pp. 1581–1589, 2012.
- [7] T. Hayat, A. Qayyum, F. Alsaadi, M. Awais, and A. M. Dobaie, "Thermal radiation effects in squeezing flow of a Jeffery fluid," *European Physical Journal Plus*, vol. 128, no. 8, pp. 85–91, 2013.
- [8] T. J. Pedley, N. A. Hill, and J. O. Kessler, "The growth of bioconvection patterns in a uniform suspension of gyrotactic micro-organisms," *Journal of Fluid Mechanics*, vol. 195, pp. 223–237, 1988.
- [9] T. J. Pedley and J. O. Kessler, "Hydrodynamic phenomena in suspensions of swimming microorganisms," *Annual Review of Fluid Mechanics*, vol. 24, pp. 313–358, 1992.
- [10] A. V. Kuznetsov, "The onset of bioconvection in a suspension of gyrotactic microorganisms in a fluid layer of finite depth heated from below," *International Communications in Heat and Mass Transfer*, vol. 32, no. 5, pp. 574–582, 2005.
- [11] A. V. Kuznetsov, "The onset of nanofluid bioconvection in a suspension containing both nanoparticles and gyrotactic microorganisms," *International Communications in Heat and Mass Transfer*, vol. 37, no. 10, pp. 1421–1425, 2010.

- [12] H. Xu and I. Pop, "Mixed convection flow of a nanofluid over a stretching surface with uniform free stream in the presence of both nanoparticles and gyrotactic microorganisms," *International Journal of Heat and Mass Transfer*, vol. 75, pp. 610–623, 2014.
- [13] A. V. Kuznetsov and D. A. Nield, "The Cheng-Minkowycz problem for natural convective boundary layer flow in a porous medium saturated by a nanofluid: a revised model," *International Journal of Heat and Mass Transfer*, vol. 65, pp. 682–685, 2013.
- [14] H. Xu and I. Pop, "Fully developed mixed convection flow in a horizontal channel filled by a nanofluid containing both nanoparticles and gyrotactic microorganisms," *European Journal of Mechanics. B. Fluids*, vol. 46, pp. 37–45, 2014.
- [15] A. Raees, H. Xu, and S.-J. Liao, "Unsteady mixed nano-bioconvection flow in a horizontal channel with its upper plate expanding or contracting," *International Journal of Heat and Mass Transfer*, vol. 86, pp. 174–182, 2015.
- [16] H. Alfvén, "Existence of electromagnetic-hydrodynamic waves," *Nature*, vol. 150, no. 3805, pp. 405–406, 1942.
- [17] A. Chakrabarti and A. S. Gupta, "Hydromagnetic flow and heat transfer over a stretching sheet," *Q Appl Math*, vol. 37, no. 1, pp. 73–78, 1979.
- [18] K. Vajravelu and A. Hadjinicolaou, "Convective heat transfer in an electrically conducting fluid at a stretching surface with uniform free stream," *International Journal of Engineering Science*, vol. 35, no. 12-13, pp. 1237–1244, 1997.
- [19] H. A. Attia and N. A. Kotb, "MHD flow between two parallel plates with heat transfer," *Acta Mechanica*, vol. 117, pp. 215–220, 1996.
- [20] K. A. Helmy, "HMD unsteady free convection flow past AA vertical porous plate," *Zeitschrift für Angewandte Mathematik und Mechanik*, vol. 78, no. 4, pp. 255–270, 1998.
- [21] W. I. Thacker, L. T. Watson, and S. Kishore Kumar, "Magneto-hydrodynamic free convection from a disk rotating in a vertical plane," *Applied Mathematical Modelling*, vol. 14, no. 10, pp. 527–535, 1990.
- [22] H. A. Attia, "Unsteady MHD flow and heat transfer of dusty fluid between parallel plates with variable physical properties," *Applied Mathematical Modelling*, vol. 26, no. 9, pp. 863–875, 2002.
- [23] H. S. Takhar, A. J. Chamkha, and G. Nath, "Flow and mass transfer on a stretching sheet with a magnetic field and chemically reactive species," *International Journal of Engineering Science*, vol. 38, no. 12, pp. 1303–1314, 2000.
- [24] Z. G. Makukula, P. Sibanda, S. S. Motsa, and S. Shateyi, "On new numerical techniques for the MHD flow past a shrinking sheet with heat and mass transfer in the presence of a chemical reaction," *Mathematical Problems in Engineering*, vol. 2011, Article ID 489217, 19 pages, 2011.
- [25] A. Zeeshan, R. Ellahi, and M. Hassan, "Magneto-hydrodynamic flow of water/ethylene glycol based nanofluids with natural convection through a porous medium," *European Physical Journal Plus*, vol. 129, no. 261, 2014.
- [26] M. Bhatti, A. Zeeshan, and R. Ellahi, "Simultaneous effects of coagulation and variable magnetic field on peristaltically induced motion of Jeffrey nanofluid containing gyrotactic microorganism," *Microvascular Research*, vol. 110, pp. 32–42, 2017.
- [27] R. Ellahi, M. Hassan, and A. Zeeshan, "Study of natural convection mhd nanofluid by means of single and multi-walled carbon nanotubes suspended in a salt-water solution," *IEEE Transactions on Nanotechnology*, vol. 14, no. 4, pp. 726–734, 2015.
- [28] W. A. Khan and O. D. Makinde, "MHD nanofluid bioconvection due to gyrotactic microorganisms over a convectively heat stretching sheet," *International Journal of Thermal Sciences*, vol. 81, no. 1, pp. 118–124, 2014.

Research Article

Level-of-Service Based Hierarchical Feedback Control Method of Network-Wide Pedestrian Flow

Zhe Zhang,^{1,2} Limin Jia,^{1,2,3} and Yong Qin^{1,2,3}

¹Traffic and Transportation School, Beijing Jiaotong University, Beijing 100044, China

²State Key Laboratory of Rail Traffic Control and Safety, Beijing Jiaotong University, Beijing 100044, China

³Beijing Research Center of Urban Traffic Information Sensing and Service Technologies, Beijing Jiaotong University, Beijing 100044, China

Correspondence should be addressed to Limin Jia; jialm@vip.sina.com

Received 3 November 2016; Accepted 28 November 2016

Academic Editor: Mohsen Sheikholeslami

Copyright © 2016 Zhe Zhang et al. This is an open access article distributed under the Creative Commons Attribution License, which permits unrestricted use, distribution, and reproduction in any medium, provided the original work is properly cited.

Pedestrian flow control is usually used to manage the crowd motion in public facilities to avoid congestion. We propose a network-wide pedestrian flow model based on the modified cell transmission model which describes the link flow as ordinary differential equations. The network flow control model (NFCM) is proposed to limit the number of pedestrians in a network according to the level-of-service requirements; however, the NFCM cannot ensure the uniform link density which is a premise of using NFCM. As a solution, the link flow control model (LFCM) is proposed to adjust the walking speed of pedestrians to realize the uniform link density. The NFCM provides the inputs for the LFCM and the LFCM compensates the deficiency of NFCM. Both NFCM and LFCM control the pedestrian flow in a cooperative way, and thus they form the hierarchical feedback control model (HFCM) of network-wide pedestrian flow. At last, the proposed HFCM is applied to control the crowd of a hall and the comparison of the simulation results in the controlled and uncontrolled scenarios shows that the proposed HFCM has the capability to suggest the optimal link inflows and walking speeds in real time to meet the LOS requirement.

1. Introduction

1.1. Background. Many public facilities including complex buildings, transportation stations, football stadiums, commercial malls, and other types of facilities have been suffering from very high levels of crowd congestion in peak hours, especially when large public gatherings are held in these facilities [1–3]. A lot of potential risks will increase due to the high level of pedestrian density [4], and the overcrowded situation decreases the overall welfare of pedestrians [5, 6]. Because of the high cost and long period of walking facility reconstruction, facility managers prefer to use some organization strategies to control pedestrian flow [7, 8], such as limiting the inflow of facilities [9] and limiting the walking space by using handrails [10].

From the viewpoint of pedestrians, poor execution of crowd flow control strategy in facilities can put the pedestrians in crowded situation which may reduce the comfort level or cause public accidents including crowd crush, injuries,

and fatalities. From the viewpoint of managers, overcrowded pedestrian flow can lead to excessive use of facility capacity, which creates a poor public environment which may destroy the customer experience and contributes towards a lower level of service in turn. The optimal pedestrian flow control strategy is to transport most pedestrians while the security and level of service (LOS) are accepted [9]. Furthermore, the pedestrian flow control strategy is produced based on the managers' experience for now. The absence of a pedestrian flow control system tends to result in overcrowded facilities because of the stochastic nature of traffic demand and behavior. Therefore, intelligent control of pedestrian flow in public facilities is exigently needed.

Further, a video surveillance system has been built [11] in public facilities to enhance the level of safety management; at the same time, it realizes the real-time acquisition of pedestrian density and walking speed [12]. However, the pedestrian flow data captured by videos or sensors is still not used scientifically for pedestrian flow control, and thus the

main objective of this paper is to introduce a pedestrian flow control model to provide crucial support towards meeting the LOS requirement of pedestrians in everyday operation. A literature review is provided and the contributions of the paper are discussed in the next section.

1.2. Related Literature. Many methods supporting pedestrian flow control and crowd management have been proposed. The majority of these works can be broadly categorized as performance-based method, network-based model, and control theory-based model.

The performance-based method is to evaluate the traffic performance of pedestrian network after simulating the pedestrian flow under self-defined scenarios. With regard to the method, a hybrid Petri nets-based model has been proposed to evaluate the effect of the network layout or design of railway transit station on the crowd safety [13], and a system dynamics based tool has been developed to evaluate the effect of facility allocation plans on the waiting time of passengers [14]. A state-dependent queuing model has been proposed to evaluate the width of corridor on the designed LOS [15], which is based on the standard from [16]. Microscopic crowd simulation models such as agent-based model [17], cellular automata model [10], social force model [18], and lattice gas model [19] have been used to evaluate the performance of walking facilities under different scenarios, and these works can give some suggestions about how to design the facility layout or how to influence the pedestrians' behavior to improve the LOS or service capacity. Models listed in the above works are mainly developed to analyze the effect of network layout and design on the efficiency of pedestrian movement and they cannot provide feasible strategies for managing the crowd directly before simulating the pedestrian flow. These methods have obvious limitations, especially when a large number of crowd control or network optimization plans are required. Furthermore, the success of the above methods is dependent on a limited number of crowd control plans. A large number of crowd management plans may result in a complicated and time-consuming evaluation process, which may lead to the impossible realization of the real-time pedestrian flow control.

The network-based models usually determine optimal routes to which pedestrians should be guided within an existing physical environment and the optimal service and capacity allocation plan of facilities. With regard to the network-based model, an $M/G/C/C$ state-dependent queuing network-based model was also proposed to find the optimal width of corridors to minimize the blocking probability of pedestrian network [20]. A network-based facility allocation model for optimizing passenger flows within a hub has been proposed to reduce the transit delays and improve the LOS of hub facilities [21]. In order to support efficient crowd movement in a network, a network optimization-based approach for crowd management has been proposed to compute the optimal width of corridors and the feasible network configuration to realize the optimal network performance under the budget constraints [22]. However, it is infeasible to increase facility capacities or build new service facilities due to the high cost and long period of reconstruction. Passenger

flow control strategies can relieve some demand pressure on the downstream facility by adjusting the passenger inflow of subway stations, and thus a queue-network-based passenger flow control model was proposed by [9] to solve the severe congestion problem in subway stations, and a pedestrian flow optimization method based on $M/G/C/C$ queue network was also developed to maximize the pedestrian flow rate in evacuation network [23]; however, the queue-network-based control model can only control the inflow of network and has little ability to suggest the real-time optimal inflow of various facilities and the optimal velocities before modification.

The performance-based models and network-based models examine the pedestrians flow in networks from a simulation and analysis point of view, which may be not suitable for real-time and intelligent implementation. The control theory-based models including sliding mode control and feedback control have been proposed to control pedestrian flow based on the real-time state information. The feedback control models have been proposed to support the smooth evacuation in rooms [24, 25], corridors [26], and networks [27] based on the linear or nonlinear ordinary differential equation model (ODE) and hyperbolic partial differential equations (PDEs). Sliding mode control is also used to control the crowd evacuation [28] and avoid the congestion in bottleneck of corridors [29] based on PDEs.

To the best of our knowledge, there is little research to bridge the pedestrian flow control and the LOS requirement. Few studies have performed a real-time control of network-wide pedestrian flow to satisfy the LOS requirement. The real-time crowd control methods described in the previous works are designed mainly for use in crowd evacuation. However, they do not provide strategies for controlling the network-wide pedestrian flow in everyday operation. Accurate determination of the optimal pedestrian flow control to meet LOS requirement has been rare. This study provides a basis for addressing these issues.

1.3. Contributions. We define pedestrian flow control as the rational administration of the pedestrian movement and traffic demand to generate adequate performance of pedestrian network to balance the benefits of pedestrians and managers. The present research demonstrates a cell transmission based network-wide pedestrian flow model and a hierarchical feedback control model to find the optimal pedestrian flow control plan based on the LOS requirement. The proposed research contributes to the state-of-the-art related pedestrian flow control research in three ways:

- (1) The links in the pedestrian network are taken as the minimal analytical units, and a network-wide pedestrian flow model has been proposed in a macroscopic sense, wherein ordinary differential equations (ODEs) for each link are obtained based on the modified cell transmission model. The collection of these ODEs is used scientifically to define the state-space model of the network-wide pedestrian flow, and this modeling approach leads to the easier development of pedestrian flow control algorithm.

- (2) A hierarchical feedback control model (HFCM) of pedestrian flow is developed to improve the LOS of pedestrian network, which is a rare try to link the pedestrian flow control with LOS and service capacity requirements. The service capacity of pedestrian network is maximized under the limits of LOS in the control process. The above control objective balances the benefits of managers and pedestrians. Therefore, the proposed control model can meet the demand of pedestrians and managers at the same time.
- (3) The network flow control model (NFCM) can suggest the optimal link inflows to satisfy the LOS but cannot ensure the uniform link density, which is the premise of using this model. Therefore, a link flow control model (LFCM) is proposed firstly to realize the uniform density in links such that the NFCM controls the network-wide flow state more precisely. Therefore, the NFCM and LFCM control the network-wide pedestrian flow in a cooperative way and constitute our HFCM.

The rest of the paper is organized as follows. Section 2 builds the network-wide pedestrian flow model by which the pedestrian flow in the network is simulated. Section 3 describes the methodology used to control the network-wide pedestrian flow based on the LOS requirements. Section 4 describes the results of an experiment and a case study that were carried out to verify the effectiveness of the proposed control method. Finally, conclusions and directions for future studies are made.

2. Network-Wide Pedestrian Flow Model

The microscopic models are best suited for generating more accurate and detailed description of pedestrians flow modeling and route choice characteristic, but unsuitable for network flow simulation due to more complex structure data input, more computing time, and developing efforts required. Therefore, in this paper, the pedestrian flow is simulated by a macroscopic model which is similar to the vehicular traffic flow model [30] because the macroscopic models can give us a big-picture averaged view of the network-wide pedestrian flow state. In this section, an analytical model for simulating network-wide pedestrian flow is proposed and described as the collection of ordinary differential equations (ODEs). The inputs of the ODEs are generated by the cell transmission model (CTM) proposed by Daganzo [31] and the modified CTM (MCTM) proposed by Muñoz et al. [32].

Let $G = (N, A)$ be a directed pedestrian network defined by a set N of nodes and a set A of directed links. The links denote the walking facilities with holding capacity such as corridors and stairways and the nodes denote the source node and sink node of each link. We call the current pedestrian density and maximum pedestrian density of link the link density and maximum link density, respectively. Similarly, we call the current walking speed and maximum walking speed of link the link speed and maximum link speed, respectively. Let ρ_a and ρ_a^m be the current and maximum link density of link a , respectively. The link density can be observed or

calculated by probes such as sensors and videos. It can be obtained that $0 \leq \rho_a \leq \rho_a^m$. Let v_a and v_a^m be the link speed and maximum link speed of link a , respectively. It can be obtained that $0 \leq v_a \leq v_a^m$. According to the relationship between speed and density, the link speed v_a can be described as follows:

$$v_a = v_a^m f\left(\frac{\rho_a}{\rho_a^m}\right), \quad (1)$$

where $f(\cdot)$ is a decreasing function and $f(0) = 1$ and $f(1) = 0$. Equation (1) ensures that the pedestrians can walk at the free speed when there are a small number of pedestrians in link a and they stop walking when the number of pedestrians in link a has reached the holding capacity. Let L_a and W_a be the length and width of link a ; the hydrodynamic pedestrian flow in link a q_a can be described as the following equation:

$$q_a = W_a \rho_a v_a^m f\left(\frac{\rho_a}{\rho_a^m}\right). \quad (2)$$

Let q_a^{in} and q_a^{out} be the current inflow and outflow of link a , respectively. Using the mass conservation law, the derivation of link density with respect to time $\dot{\rho}_a$ can be described as the following ODE:

$$\dot{\rho}_a = \frac{q_a^{\text{in}} - q_a^{\text{out}}}{L_a W_a}. \quad (3)$$

In order to simulate the pedestrian flow in uncontrolled scenario, the value of q_a^{in} and q_a^{out} should be determined. In uncontrolled scenario, because of the urgent willingness of arriving at destinations, pedestrians want to enter and leave the links at the maximum inflow q_a^{min} and outflow q_a^{mout} . The cell transmission model [31] (CTM) is used in this paper to determine the value of q_a^{min} and q_a^{mout} . The CTM is proposed by Daganzo for approximating the Lighthill and Whitham (1955) and Richards (1956) [30] hydrodynamic traffic flow model (LWR model):

$$\frac{\partial \rho(x, t)}{\partial t} + \frac{\partial q(x, t)}{\partial x} = 0, \quad (4)$$

where $\rho(x, t)$ denotes the density at place x and time t and $q(x, t)$ is the traffic flow. The CTM divides the links into many cells with the same length and simulates the traffic flow by defining the flow between cells [31]. Compared to the CTM, the modified cell transmission model (MCTM) proposed by Muñoz et al. [32], which discretizes the LWR model (or its simplified version) in both time and space, was shown to be computationally efficient and easy to analyze many important traffic phenomena, such as queue buildup and dissipation [33]. In MCTM, the nonuniform cell lengths are acceptable. Also, the pedestrian CTM has been developed to simulate the pedestrian flow in public facilities and the accuracy results about LOS [34] can be obtained [35]; the CTM was also used to control the vehicular-pedestrian mixed flows in the evacuation zone [36]. All above works indicate that the CTM can simulate the traffic flow in roadway network as well as the pedestrian flow in the network of corridors. By taking each

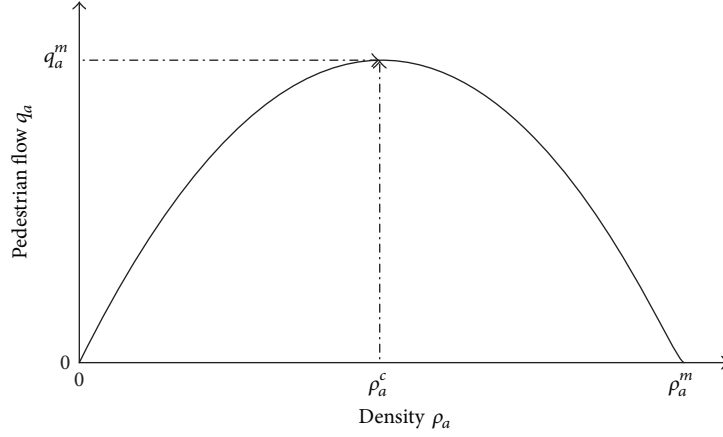


FIGURE 1: Pedestrian fundamental diagram: an example.

link in the pedestrian network as a cell in MCTM, we can use the MCTM and pedestrian flow fundamental diagram to simulate the network-wide pedestrian flow. Within a link of pedestrian network, pedestrians are assumed to be homogeneously distributed, and their movements are not modeled explicitly.

The hydrodynamic outflow capacity (HOC) can be defined as the maximum number of pedestrians leaving links per unit time and the hydrodynamic inflow capacity (HIC) can be defined as the maximum number of pedestrians entering links per unit time according to the fundamental diagram [34]. In the pedestrian flow fundamental diagram, as shown in Figure 1, there is a critical density ρ_a^c to maximize the pedestrian flow in link a q_a and it divides the link density domain into two regimes. For the link density $\rho_a \leq \rho_a^c$, the increase in link density leads to increased hydrodynamic flow and is thus denoted as the free-flow regime. On the contrary, the congested regime comprises the values of link density ρ_a greater than ρ_a^c , as an increase in link density in this domain leads to a decrease in hydrodynamic flow. According to the fundamental diagram, if the link density $\rho_a \leq \rho_a^c$, the HOC of link a q_a^{hoc} is equal to the hydrodynamic flow in link a ; if the link density $\rho_a > \rho_a^c$, the HOC of link a q_a^{hoc} is equal to the maximum hydrodynamic flow in link a q_a^m ; that is,

$$q_a^{\text{hoc}} = \begin{cases} q_a, & \text{if } \rho_a \leq \rho_a^c, \\ q_a^m, & \text{otherwise.} \end{cases} \quad (5)$$

Similarly, if the density of the downstream link b $\rho_b \leq \rho_b^c$, the HIC of link b q_b^{hic} is equal to the maximum hydrodynamic flow in link b q_b^m ; if the link density $\rho_b > \rho_b^c$, the HIC of link b q_b^{hic} is equal to the hydrodynamic flow in link b q_b ; that is,

$$q_b^{\text{hic}} = \begin{cases} q_b^m, & \text{if } \rho_b \leq \rho_b^c \\ q_b, & \text{otherwise.} \end{cases} \quad (6)$$

As in the MCTM proposed by Muñoz et al. [32], a sending and receiving capacity is defined for each link, representing the maximum number of pedestrians who can leave and enter

a link per unit time, respectively. The sending capacity of link a is determined by the minimum value between the number of pedestrians in link a N_a and the HOC of link a q_a^{hoc} ; that is,

$$S_a = \min \{N_a, q_a^{\text{hoc}}\}. \quad (7)$$

The receiving capacity of downstream link b R_b is determined by the minimum value between the available holding capacity of link b M_b and the HIC of link b q_b^{hic} ; the available holding capacity of link b C_b is the difference between the holding capacity of link b C_b and the number of pedestrians in link b N_b at time t ; that is, $M_b = C_b - N_b$. Therefore,

$$R_b = \min \{M_b, q_b^{\text{hic}}\}. \quad (8)$$

The maximum outflow of link a is determined by the sending capacity of link a and the receiving capacity of downstream link b R_b ; that is,

$$q_a^{\text{mout}} = \min \{S_a, R_b\}. \quad (9)$$

The above equation describes the pedestrian flow between two interconnected links in series topology, as indicated by Figure 2(a). In the pedestrian network, there are also merge and split topologies [37], as indicated by Figures 2(b) and 2(c). Tampère et al. [38] established the split model and merge model of traffic flow based on Daganzo's merge and split models [31] and the merge distribution schemes of Jin and Zhang [39] and of Ni and Leonard II [40]. The link outflow can be got by maximizing the total flow in the merge and split node.

For the merge topology as indicated by Figure 2(b), the merge flow can be determined by solving the following linear programming problem:

$$\max \quad q^{\text{mout}} = q_a^{\text{mout}} + q_b^{\text{mout}} \quad (10)$$

$$\text{s.t.} \quad q_a^{\text{mout}} \leq S_a$$

$$q_b^{\text{mout}} \leq S_b \quad (11)$$

$$q_a^{\text{mout}} + q_b^{\text{mout}} \leq R_c.$$

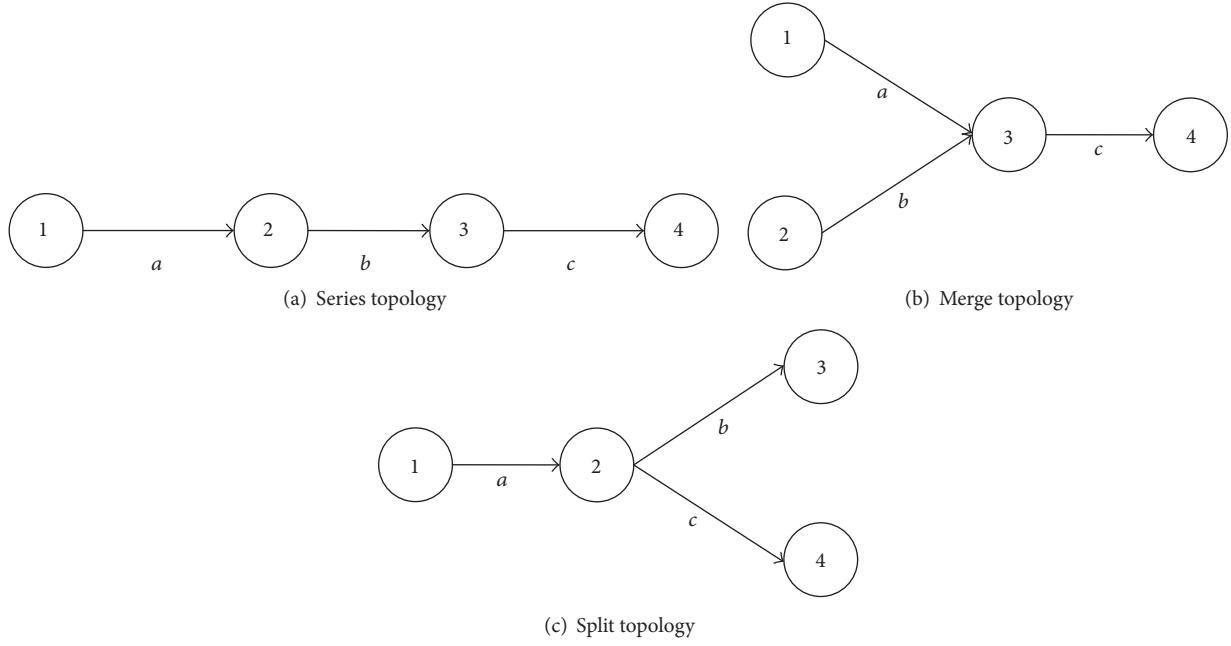


FIGURE 2: Series, merge, and split topology in pedestrian network.

As can be seen from (11), the objective function $q^{mout} = \min\{S_a + S_b, R_c\}$. All pedestrians in link a and link b can enter the link c if the sending capacity of incoming links a and b does not exceed the receiving capacity of link c R_c ; otherwise, the receiving capacity of link c R_c is allocated proportionally to the two incoming links. A level of reduction α has been introduced to represent the proportion of the sending capacity of links a and b being transferred to link c when the receiving capacity of link c R_c cannot handle the incoming pedestrians flow $S_a + S_b$:

$$\alpha = \frac{R_c}{S_a + S_b}. \quad (12)$$

The pedestrian flow from link a to link c q_a^{mout} and the pedestrian flow from link b to link c q_b^{mout} can be described as follows:

$$\begin{aligned} q_a^{mout} &= \min\{1, \alpha\} S_a, \\ q_b^{mout} &= \min\{1, \alpha\} S_b. \end{aligned} \quad (13)$$

For the split topology as indicated by Figure 2(c), let P_b and P_c be the transfer probability from link a to link b and link c , respectively, and the flow constraints can be described as follows:

$$\begin{aligned} q_a^{mout} &= q_{ab}^{mout} + q_{ac}^{mout} \leq S_a, \\ q_{ab}^{mout} &= P_b q_a^{mout} \leq R_b, \\ q_{ac}^{mout} &= P_c q_a^{mout} \leq R_c. \end{aligned} \quad (14)$$

Based on (10) and (15), the maximum outflow of link a can be described as follows:

$$q_a^{mout} = \min \left\{ S_a, \frac{R_b}{P_b}, \frac{R_c}{P_c} \right\}. \quad (15)$$

Then, the pedestrian flow from link a to link b and links c q_{ab}^{mout} and q_{ac}^{mout} can be described as follows:

$$\begin{aligned} q_{ab}^{mout} &= \min\{1, \alpha_1, \alpha_2\} P_b S_a, \\ q_{ac}^{mout} &= \min\{1, \alpha_1, \alpha_2\} P_c S_a, \end{aligned} \quad (16)$$

where α_1 and α_2 are defined as follows:

$$\begin{aligned} \alpha_1 &= \frac{R_b}{P_b S_a} \\ \alpha_2 &= \frac{R_c}{P_c S_a}. \end{aligned} \quad (17)$$

According to the inflow and outflow characteristics of links, the links in the pedestrian network $G = (N, A)$ are divided into four groups: the link group without inflow and with outflow at time t $A_o(t)$, the link group with inflow and outflow at time t $A_d(t)$, the link group with inflow and without outflow at time t $A_i(t)$, and the link group without inflow and outflow at time t $A_e(t)$. The link a can belong to different link group at different time t . The four link groups in the pedestrian network $G = (N, A)$ can be described as follows:

$$\begin{aligned} A_o(t) &= \{a \mid q_a^{\min} = 0, q_a^{mout} > 0\}, \\ A_d(t) &= \{a \mid q_a^{\min} > 0, q_a^{mout} > 0\}, \\ A_i(t) &= \{a \mid q_a^{\min} > 0, q_a^{mout} = 0\}, \\ A_e(t) &= \{a \mid q_a^{\min} = 0, q_a^{mout} = 0\}. \end{aligned} \quad (18)$$

The link a may belong to different link groups at different time t because the link inflow and outflow are time-dependent variable.

3. Pedestrian Flow Control Model

When the capacity of pedestrian network cannot satisfy the traffic demand, crowd congestion will occur. In order to deal with the congestion and improve the LOS of pedestrian network, the control measures such as limiting the pedestrian inflow or the variable speed limiting will be conducted with design and usage of devices, such as speakers and video displays, to guide the pedestrians [41]. In this section, a hierarchical feedback control model (HFCM) of network-wide pedestrian flow is proposed to satisfy the LOS requirements. The proposed HFCM comprises two models: network flow control model (NFCM) and link flow control model (LFCM). The NFCM produces the inflow and outflow control plan of each link to satisfy the LOS requirement and the LFCM produces the walking speed control plan which realizes uniform link density after receiving the control inputs from the NFCM.

3.1. Network Flow Control Model. In peak hours, there is a conflict between the management objective of network managers and the satisfaction of pedestrians. First, network managers will control the pedestrian inflow of each link if the LOS of links becomes lower. However, the pedestrian flow control measures may increase the delay time of pedestrians and reduce their satisfaction. In order to measure the LOS of links, the link densities are usually considered [42]. On the other hand, pedestrians want to spend less time in walking to destination [43, 44].

If the targets of network managers and pedestrians are achieved at the same time, the density of the objective LOS, which can maximize the link flow, can be considered as the objective density value of pedestrian flow control because the objective density balances the profits of managers and passengers. Let $[\rho_a^l, \rho_a^u]$ be the density domain for the required LOS of link a ; according to the fundamental diagram of pedestrian flow as indicated by Figure 1, the objective density of link a ρ_a^t can be described as follows:

$$\rho_a^t = \begin{cases} \rho_a^u, & \text{if } \rho_a^u \leq \rho_a^c, \\ \rho_a^c, & \text{if } \rho_a^l \leq \rho_a^c \leq \rho_a^u, \\ \rho_a^l, & \text{if } \rho_a^l \geq \rho_a^c. \end{cases} \quad (19)$$

If the LOS of links is lower than the required LOS, the control measures should be taken to achieve the convergence of the link density ρ_a to the objective density ρ_a^t for the link $a \in A_d(t) \cup A_i(t)$, to achieve the convergence of the link density ρ_a to the 0 for the link $a \in A_o(t)$, and to maximize the number of pedestrians served by the network per unit time Q_s while realizing the two above objectives. The link $a \in A_e(t)$ has no inflow and outflow and thus can be deleted from the network at time t , which reduces the computing time of the proposed control algorithm. Let the binary variable σ_a denote the link with or without inflow, $\sigma_a = 1$ denote the link $a \in A_d(t) \cup A_i(t)$, and $\sigma_a = 0$ denote the link $a \in A_o(t)$. The exponential convergence of link densities to the objective

densities can be realized if the derivation of link density with respect to time $\dot{\rho}_a$ satisfies the following equation:

$$\dot{\rho}_a = -k_a (\rho_a - \sigma \rho_a^t), \quad (20)$$

where k_a is the control gain and is greater than zero. Substituting (3) into (20), the following equation can be obtained:

$$\frac{q_a^{\text{in}} - q_a^{\text{out}}}{L_a W_a} = -k_a (\rho_a - \sigma \rho_a^t). \quad (21)$$

The controlled inputs of the network flow control model are the inflow and outflow of links q_a^{in} and q_a^{out} . Therefore, (21) represents the feedback linearization of the system of state-space equation (3) [27] and denotes the equation constraints on the control inputs q_a^{in} and q_a^{out} .

As described in Section 2, the maximum value of the inflow and outflow of links occurs in uncontrolled pedestrian flow; therefore, the inflow and outflow of links q_a^{in} and q_a^{out} are greater than or equal to zero and lower than or equal to the maximum inflow and outflow in uncontrolled pedestrian flows q_a^{min} and q_a^{mout} . All in all, the bound constraint of the control inputs can be described as follows:

$$\begin{aligned} 0 &\leq q_a^{\text{in}} \leq q_a^{\text{min}} \\ 0 &\leq q_a^{\text{out}} \leq q_a^{\text{mout}}. \end{aligned} \quad (22)$$

From the analysis of control objective, the number of pedestrians served by the network per unit time Q_s (service capacity) should be maximized in the control process. The service capacity Q_s is equal to maximizing the number of pedestrians leaving the network per unit time. Let Q_e be the number of pedestrians entering the network per unit time; the following equation can be got by adding (21) of each link in the pedestrian network:

$$Q_e - Q_s = \sum_{a \in A} -k_a (\rho_a - \sigma \rho_a^t). \quad (23)$$

Then, $Q_e = Q_s + \sum_{a \in A} -k_a (\rho_a - \sigma \rho_a^t)$; because the second part of the right hand of this equation is a variable independent of control inputs, maximizing service capacity Q_s is equal to maximizing the number of pedestrians entering the network per unit time Q_e ; that is, $\max Q_s \cong \max Q_e$.

At every time instant, the control inputs satisfying the equation constraint (21) and bound constraint (22) should be solved to maximize the number of pedestrians entering the network per unit time Q_e . The equation constraint (21) is linear and the number of pedestrians entering the network per unit time Q_e is also the linear sum of the inflows of

source links in pedestrian network. Therefore, the network-wide pedestrian flow control model can be described as the following linear programming problem (LP):

$$\max Q_e \quad (24)$$

$$\begin{aligned} \text{s.t. } & \frac{q_a^{\text{in}} - q_a^{\text{out}}}{l_a W_a} = -k_a (\rho_a - \sigma \rho_a^t) \\ & 0 \leq q_a^{\text{in}} \leq q_a^{\text{min}} \\ & 0 \leq q_a^{\text{out}} \leq q_a^{\text{mout}}. \end{aligned} \quad (25)$$

The large control gain k_a may make the above LP problem become infeasible. In order to select the proper control gains, we can define a high value k_h as the initial control gain of the LP problem, and then we can get the infeasible solution $q_s = (q_a^{\text{in}}, q_a^{\text{out}}, \dots)$ which is greater than the upper bounds of the control input $q^u = [q_a^{\text{min}}, q_a^{\text{mout}}, \dots]$. Let the scaling factor $\mu = \max(q_s/q^u)$, and then the proper control gain $k_a = k_h/\mu$, which will make the LP problem become feasible.

3.2. Link Flow Control Model. The pedestrians are assumed to be homogeneously distributed all the time in NFCM. However, the NFCM may lead to the nonuniform link density because the minimal control unit of NFCM is the links of pedestrian network. Therefore, the link flow control model is proposed in this section to realize the uniform link density with the control inputs from the NFCM $q_s = (q_a^{\text{in}}, q_a^{\text{out}}, \dots)$. The solution to the LP problem has given the details about the inflow and outflow of link a $q_a^{\text{in}}, q_a^{\text{out}}$. We divide the unidirectional links into n sections with the same length l_a . Let q_a^i and ρ_a^i be the inflow and density of link section i , respectively. Similarly, let $\dot{\rho}_a^i$ be the derivation of section density with respect to time and $\dot{\rho}_a^i$ can be formulated as

$$\begin{aligned} \dot{\rho}_a^1 &= \frac{q_a^{\text{in}} - q_a^2}{l_a W_a}, \\ \dot{\rho}_a^i &= \frac{q_a^i - q_a^{i+1}}{l_a W_a}, \quad \text{for } 1 < i < n, \\ \dot{\rho}_a^n &= \frac{q_a^n - q_a^{\text{out}}}{l_a W_a}. \end{aligned} \quad (26)$$

The inflow of section i q_a^i can be described as $q_a^i = \rho_a^{i-1} v_a^i f(\rho_a^{i-1}/\rho_a^m)$ if the section density is assumed to be uniform [26]. v_a^i is the controlled walking speed of pedestrians in section i and $0 \leq v_a^i \leq v_a^f$. Equation (26) can be formulated as follows:

$$\begin{aligned} \dot{\rho}_a^1 &= \frac{q_a^{\text{in}} - W_a \rho_a^1 v_a^1 f(\rho_a^1/\rho_a^m)}{l_a W_a}, \\ \dot{\rho}_a^i &= \frac{W_a \rho_a^{i-1} v_a^{i-1} f(\rho_a^{i-1}/\rho_a^m) - W_a \rho_a^i v_a^i f(\rho_a^i/\rho_a^m)}{l_a W_a}, \end{aligned} \quad (27)$$

for $1 < i < n$,

$$\dot{\rho}_a^n = \frac{W_a \rho_a^{n-1} v_a^{n-1} f(\rho_a^{n-1}/\rho_a^m) - q_a^{\text{out}}}{l_a W_a}.$$

If the link density is nonuniform, the link flow control measures should be applied to realize the density difference between link sections D^i to zero; for link a , the density difference D_a^i can be described as follows:

$$D_a^i = \rho_a^i - \rho_a^{i+1} = 0. \quad (28)$$

The exponential convergence of density difference between sections to zero can be realized if the derivation of section density difference with respect to time \dot{D}_a^i satisfies the following equation:

$$\dot{D}_a^i = -k_a^i D_a^i, \quad (29)$$

where k_a^i is the control gains of the link flow control model. Substituting (27) into (29), we can obtain the following equations:

$$\begin{aligned} & \frac{(q_a^{\text{in}} - W_a \rho_a^1 v_a^1 f(\rho_a^1/\rho_a^m)) - (W_a \rho_a^1 v_a^1 f(\rho_a^1/\rho_a^m) - W_a \rho_a^2 v_a^2 f(\rho_a^2/\rho_a^m))}{l_a W_a} = -k_a^1 (\rho_a^1 - \rho_a^2), \\ & \frac{(W_a \rho_a^{i-1} v_a^{i-1} f(\rho_a^{i-1}/\rho_a^m) - W_a \rho_a^i v_a^i f(\rho_a^i/\rho_a^m)) - (W_a \rho_a^i v_a^i f(\rho_a^i/\rho_a^m) - W_a \rho_a^{i+1} v_a^{i+1} f(\rho_a^{i+1}/\rho_a^m))}{l_a W_a} = -k_a^i (\rho_a^i - \rho_a^{i+1}), \end{aligned} \quad (30)$$

$1 < i < n - 1$,

$$\frac{(W_a \rho_a^{n-2} v_a^{n-2} f(\rho_a^{n-2}/\rho_a^m) - W_a \rho_a^{n-1} v_a^{n-1} f(\rho_a^{n-1}/\rho_a^m)) - (W_a \rho_a^{n-1} v_a^{n-1} f(\rho_a^{n-1}/\rho_a^m) - q_a^{\text{out}})}{l_a W_a} = -k_a^{n-1} (\rho_a^{n-1} - \rho_a^n).$$

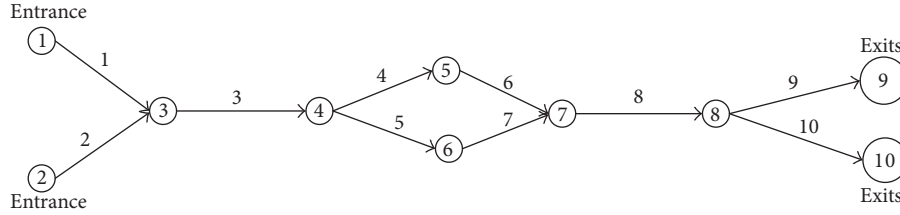


FIGURE 3: Pedestrian network description.

TABLE 1: Network information.

Link	Length (m)	Width (m)	Free walking speed v_a^m (m/s)	Jam density ρ_a^m (peds/m ²)	Initial density (peds/m ²)
1	50	2.5	1.5	3.8	1
2	50	2.5	1.5	3.8	2
3	50	5	1.5	3.8	3
4	50	2.5	1.5	3.8	2.5
5	50	2.5	1.5	3.8	1.5
6	50	2.5	1.5	3.8	0.5
7	50	2.5	1.5	3.8	0.1
8	50	5	1.5	3.8	1.2
9	50	2	1.5	3.8	0.5
10	50	2	1.5	3.8	1.1

At present, in (30), all variables except the walking speed v_a^j are known. The variables q_a^{in} and q_a^{out} can be produced by the NFCM and the section densities ρ_a^i can be observed and analyzed by the sensors. The walking speed v_a^i , $i = 1, 2, \dots, n-1$, should be adjusted to achieve the uniform link density. There are $n-1$ unknown variables to be determined by solving $n-1$ linear equations, and thus (30) can be easily solved to realize the link flow control objective.

From the physical viewpoint, the network controlled by the NFCM comprises the links which are controlled by LFCM. From the model viewpoint, the LFCM needs the link inflow values produced by the NFCM and the premise of using NFCM is ensured by the LFCM. The feedback control theory is used by the NFCM and LFCM. Therefore, the NFCM and LFCM can be regarded as a hierarchical feedback control model (HFCM) of network-wide pedestrian flow.

4. Numerical Example: Pedestrian Flow Control in a Hall

4.1. Network Description and Model Development. To investigate the efficiency of the proposed pedestrian flow control model, we consider a real college university hall in Beijing as a test platform of our control model. The hall is used as a place for important events such as visiting and learning the railway devices and students meetings. The network description of the hall is depicted in Figure 3. The network consists of 10 nodes, 10 links, 2 entrances, and 2 exits. Two divergence and two merge topologies exist in the hall, which makes the selected network general. The network information including the lengths and widths of corridors is listed in Table 1.

For the pedestrian fundamental diagram of links, the Greenshield model [45], which is recommended in the Society of Fire Protection Engineers (SFPE) handbook [46] and [47], is adopted in this paper and can be described as follows:

$$v_a = v_a^m \left(1 - \frac{\rho_a}{\rho_a^m} \right). \quad (31)$$

The data including free walking speed, jam density, and initial densities of all links in pedestrian network are also listed in Table 1. The LOS evaluation standard comes from [16], which is designed to evaluate the LOS of walking facilities in transportation terminals. The LOS standard and the fundamental diagram of pedestrian flow are depicted in Figure 4.

Assume that a large crowd is visiting and has to pass through the hall. There are 4 OD pairs in the network. The corresponding OD demand of the pedestrian network is listed in Table 2. There are two routes to be chosen for each OD, and the route choice probability is equal to 0.5.

The purpose of this case study is to evaluate the LOS of links during traffic rush hours and the performance of the proposed pedestrian flow control model. Under uncontrolled scenario, the pedestrian flow model in the hall is developed based on the description in Section 2 and then the LOS evaluation results can be obtained and will determine the control decision. If the control is required to improve the LOS of pedestrian network, the pedestrian flow control model is developed based on the description in Section 3 and utilized to provide the control plan for network managers. All computational experiments were conducted in a PC with CPU 2.93 GHz, under Windows XP operating system.

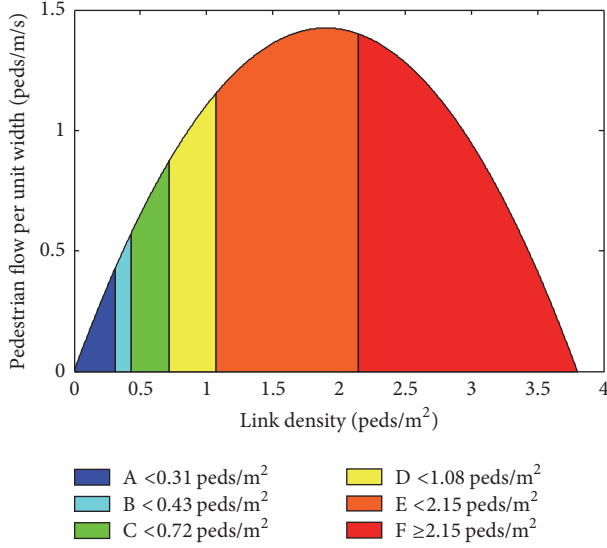


FIGURE 4: Pedestrian flow fundamental diagram and LOS.

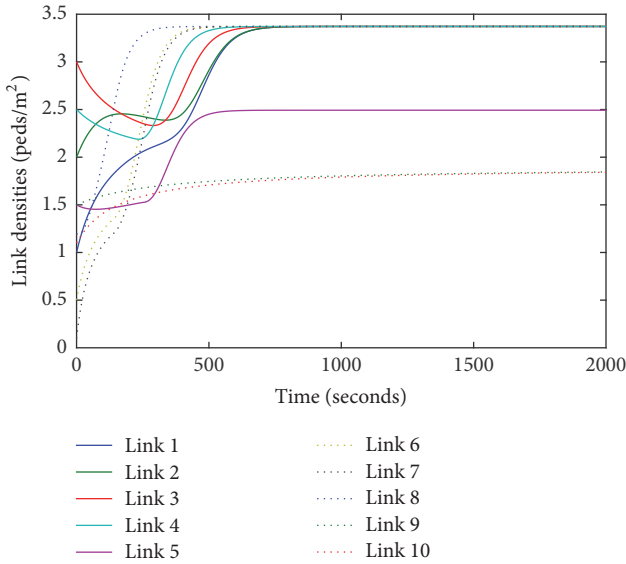


FIGURE 5: Link densities in uncontrolled flow case.

4.2. *Model Results and Discussion.* Under the self-defined demand scenario, the pedestrian flow in the example network was simulated and the link densities at different time are depicted in Figure 5.

The final link densities can be obtained from the simulation in uncontrolled flow case and the corresponding LOS is evaluated based on the LOS standard as indicated by Figure 4 and the results have been listed in Table 3. The LOS of links 1 to 8 is F while the LOS of links 8 and 9 is E, as shown in Table 3. The results show that the network traffic performs so seriously that the pedestrian flow control is required to improve the LOS of the network.

The control objective of LOS is assumed to be E and D, respectively, and the corresponding objective densities are 1.9 peds/m² and 1.08 peds/m² based on (19). The pedestrian

TABLE 2: OD demand of the pedestrian network.

Node	9	10
1	3 peds/s	2 peds/s
2	2 peds/s	3 peds/s

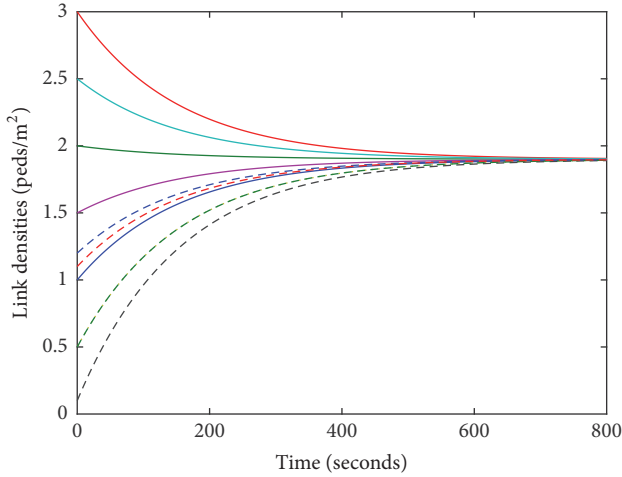
TABLE 3: LOS of links in uncontrolled flow case.

Link	Final densities (peds/m ²)	LOS
1	3.37	F
2	3.37	F
3	3.37	F
4	3.37	F
5	2.49	F
6	3.37	F
7	3.37	F
8	3.37	F
9	1.85	E
10	1.84	E

flow control model is established based on the description in Section 3. The control gains are chosen from a wide range of gain values. If the value of the control gains k_a is too low, then the control objective cannot be realized in a short time. However, if the value of k_a is too high, the gain scaling procedure should be done to search the proper gain value repeatedly to ensure the feasibility of (25) and (26), which will lead to additional computing cost and may not realize the real-time control. We have run simulations for a wide range of gain values and found the control gains $k_a = 0.0065$, $a = 1, 2, 3, \dots, 10$, for LOS E and $k_a = 0.0028$, $a = 1, 2, 3, \dots, 10$, for LOS D to be a good tradeoff between high and low gains. The computing time of the pedestrian flow control model ranges from 5.06 s to 5.28 s, which indicates that the proposed control algorithm can produce the control plan of pedestrian flow in a very short time.

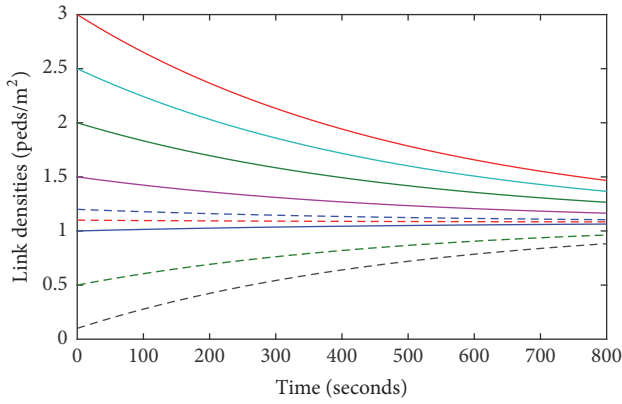
As the result of the network flow control, the link densities converged to the objective densities 1.9 peds/m² and 1.08 peds/m², which makes the network performance meet the LOS E and LOS D, as indicated by Figure 6. The LOS E-oriented control spends less time than the LOS D-oriented control making the link densities converge to the objective density because larger control gains can result in quicker convergence based on (21) and the control gains of LOS D-oriented control $k_a = 0.0028$ are much lower than LOS E $k_a = 0.0065$. Based on the control gain selection results of LOS E and LOS D, it can be seen that the LOS D-oriented control needs much more control works than LOS E because the LOS D requires lower density level than LOS E.

The link inflows controlled by NFCM are depicted in Figure 7. In order to realize the objective LOS E, the inflows of links 3 and 8 converged to the steady value of 2.8598 peds/s while the inflows of the other links converged to the steady value of 1.4327 peds/s, as indicated by Figure 7(a). In order to realize the objective LOS D, the inflows of links 3 and 8 converged to the steady value of 2.3192 peds/s while the



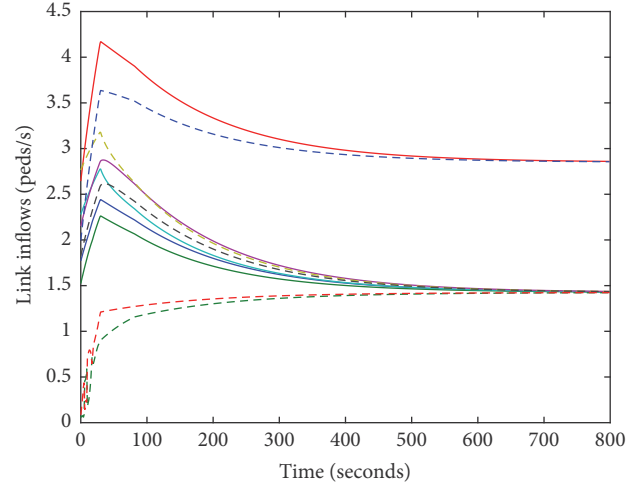
Link 1 (solid blue), Link 2 (solid green), Link 3 (solid red), Link 4 (solid cyan), Link 5 (solid magenta), Link 6 (dotted yellow), Link 7 (dashed black), Link 8 (dashed blue), Link 9 (dashed green), Link 10 (dashed red)

(a) Link densities controlled for LOS E



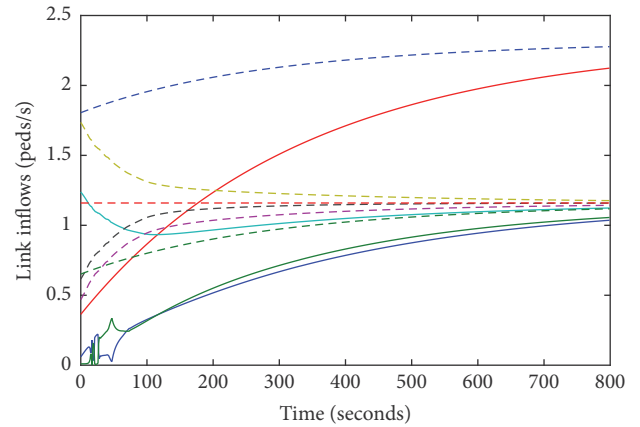
(b) Link densities controlled for LOS D

FIGURE 6: Link densities controlled for LOS E and LOS D.



q_1^{in} (solid blue), q_2^{in} (solid green), q_3^{in} (solid red), q_4^{in} (solid cyan), q_5^{in} (solid magenta), q_6^{in} (dashed yellow), q_7^{in} (dashed black), q_8^{in} (dashed blue), q_9^{in} (dashed green), q_{10}^{in} (dashed red)

(a) Link inflows controlled for LOS E



(b) Link inflows controlled for LOS D

FIGURE 7: Link inflows controlled for LOS E and LOS D.

inflows of the other links converged to the steady value of 1.1596 peds/s, as indicated by Figure 7(b).

In order to prove the necessity of LFCM in the network-wide pedestrian flow control, link 1 is selected and divided into 5 sections, as shown in Figure 8. In the NFCM, the pedestrians are assumed to be homogeneously distributed and the link density is uniform. However, the real fact is that the section densities of link are not the same all the time if only the NFCM is established.

With regard to the LOS E-oriented NFCM, the section densities of link 1 controlled only by NFCM are depicted in Figure 9(a), and the section densities are not equal all the time with only NFCM. For example, the final density values of sections s1, s2, s3, s4, and s5 are 0.4310 peds/m², 0.4312 peds/m², 1.8736 peds/m², 3.3703 peds/m², and 3.3704 peds/m², respectively. Although the average density of 5 sections is equal to the objective density 1.9 peds/m², the pedestrians are not to

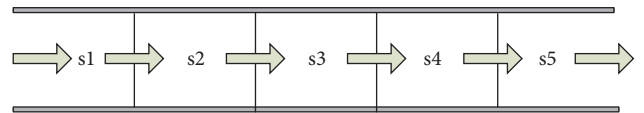


FIGURE 8: 5 sections of link 1.

be homogeneously distributed in link 1, which is inconsistent with the assumption of NFCM.

With regard to the LOS D-oriented NFCM, a similar phenomenon can be seen from Figure 10(a); the section density values of link 1 are not equal all the time with only NFCM. For example, the final density values of sections s1, s2, s3, s4, and s5 are 0.299 peds/m², 0.298 peds/m², 0.297 peds/m², 0.961 peds/m², and 3.502 peds/m², respectively. Although the average density of 5 sections is equal to the objective density

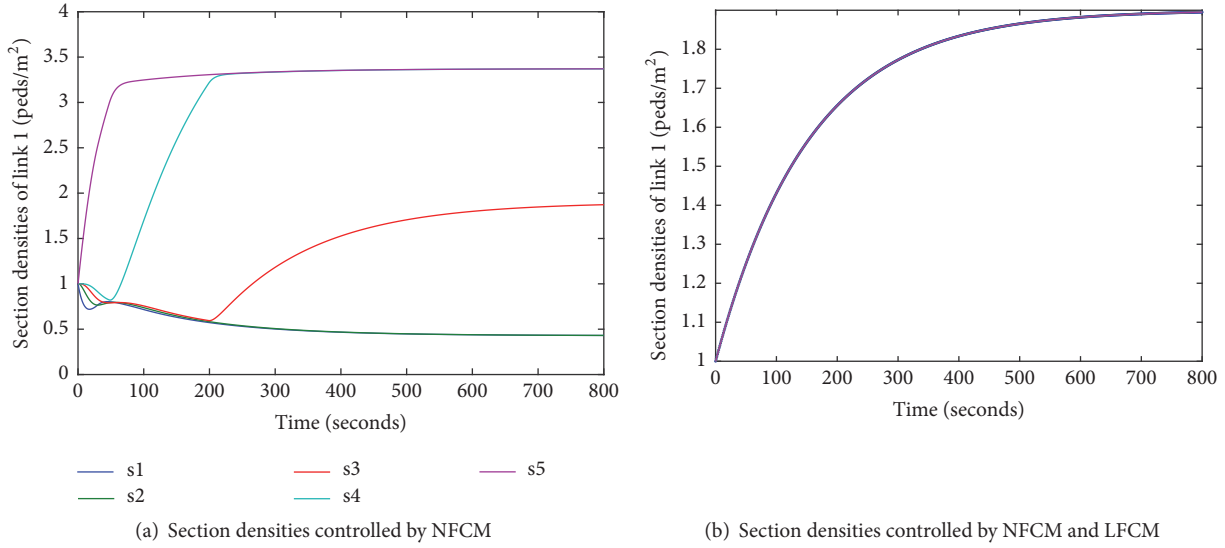


FIGURE 9: Section densities controlled for LOS E.

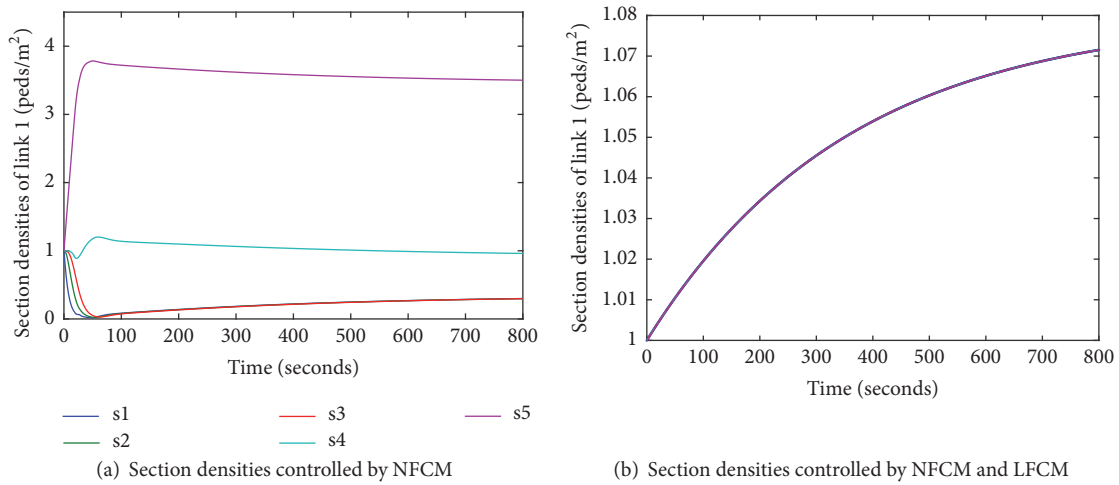


FIGURE 10: Section densities controlled for LOS D.

1.08 peds/m², the pedestrians are not to be homogeneously distributed in link 1, which is also inconsistent with the assumption of NFCM. Therefore, the proposed LFCM is required to ensure the NFCM's feasibility.

In the LOS E-oriented LFCM, the control gains $K_1^i = 0.001$ for $i = 1, 2, \dots, 5$. Figure 9(b) shows the section densities of link 1 at different time after the control plan produced by LFCM is executed. The curves of section density of link 1 overlapped in Figure 9(b), which indicates that the time-dependent values of section densities are equal and the uniform link density of NFCM is ensured by the LFCM. The controlled walking speeds of pedestrians in link 1, v_1^1, v_1^2, v_1^3 , and v_1^4 , are depicted in Figure 11(a). The walking speed has converged to the steady value of 0.6 m/s, which describes the speed control strategy for LOS E-oriented link flow control in detail.

In the LOS D-oriented LFCM, the control gains $K_1^i = 0.001$ for $i = 1, 2, \dots, 5$. Figure 10(b) shows the section densities of link 1 at different time after the LFCM is executed. The curves of section density of link 1 overlapped in Figure 10(b), which indicates that the time-dependent section densities are equal and the uniform link density is realized by the LFCM. The controlled walking speeds in link 1, v_1^1, v_1^2, v_1^3 , and v_1^4 , are also depicted in Figure 11(b). The walking speeds are also converging to the steady value of 0.6 m/s, which describes the speed control strategy for LOS D-oriented link flow control in detail. Therefore, the LFCM can realize the uniform link density and thus ensure the NFCM's feasibility; at the same time, the LFCM can realize the full and even use of link capacity.

All in all, the hierarchical feedback control model (HFCM), which integrates NFCM and the LFCM, can make

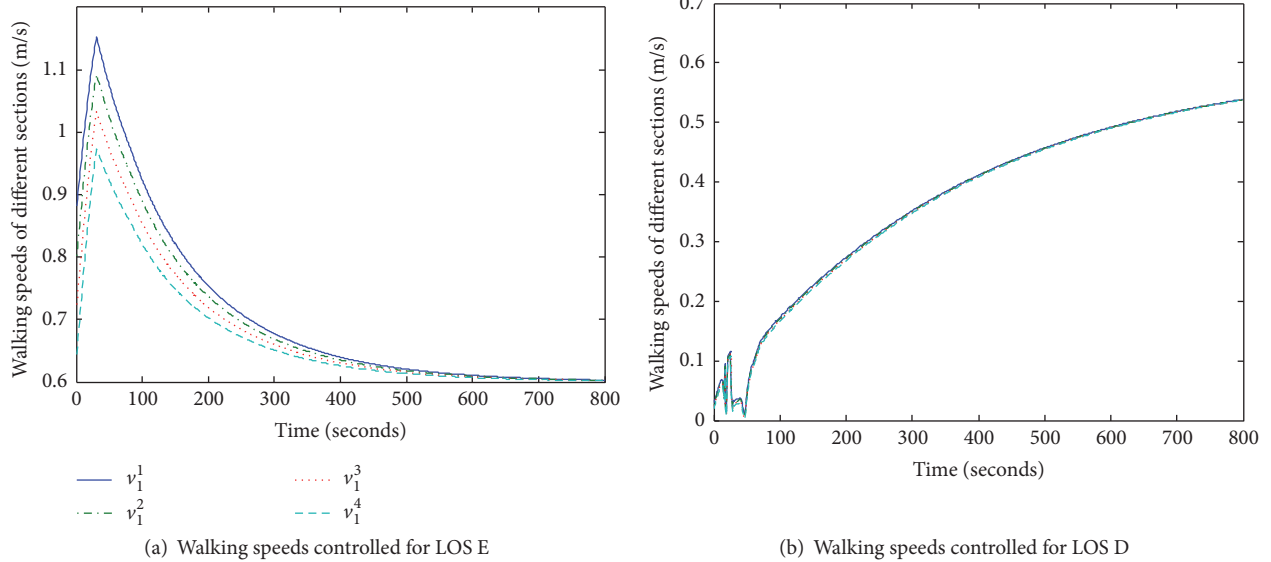


FIGURE 11: Walking speeds controlled by LFCM.

the pedestrian network meet the objective LOS requirement by controlling the link inflows and adjusting the walking speed of pedestrians.

5. Conclusion and Extension

In order to realize the real-time control of pedestrian flow in network and provide crucial support for the LOS-based crowd management, this paper presented a hierarchical feedback control model (HFCM) of network-wide pedestrian flow.

First, this paper presents a cell transmission based network-wide pedestrian flow model by taking the links as the minimum analytical units. It realizes a holistic assessment of the network performance in order to support the decision-making about pedestrian flow control, as it provides us with a big-picture averaged view of the network-wide pedestrian flow state. Based on the conservation of mass, the collection of ODEs is used to represent the state-space equations of network-wide pedestrian flow and that makes the establishment of pedestrian flow control model easier than the PDE-based model. Additionally, the proposed pedestrian flow model can be easily adapted to a wide spectrum of public facility configurations, as the flow model for different topologies has been developed in this paper and the numerical example also proved its flexibility in achieving pedestrian flow simulation in general network.

Secondly, the network flow control model (NFCM) is firstly proposed to find the optimal link inflows to ensure the number of pedestrians in the link satisfies the LOS requirement. In order to realize the uniform link density and make full and even use of the link capacity, the link flow control model (LFCM) has been proposed to adjust the walking speed of pedestrians by dividing the link into many sections. The LFCM uses the link inflows from the NFCM and the premise of using NFCM is ensured by the LFCM

in turn. The two models control the pedestrian flow in a cooperative way and are integrated as the HFCM of network-wide pedestrian flow.

Finally, the proposed HFCM is applied to control the pedestrian flow in a hall and the model results show that the HFCM can find the optimal control plan to trade off the benefits of pedestrians and managers. The higher LOS requirement needs much more control works, which is also consistent with the reality. The HFCM can be regarded as a general control model for network-wide crowd management. The computing time of the proposed model is about 5 seconds which indicates that the control plan can be generated in real time.

The proposed control algorithm utilizes the pedestrian density data to compute the optimal inflows and walking speeds and thus it depends on the real-time capture of link densities, which can be realized by the videos or sensors. Therefore, the proposed control model can be integrated with the intelligent devices such as videos, sensors [48], and wireless communication network to realize the LOS-based intelligent control of network-wide pedestrian flow.

Future research includes the comparison of the results obtained by the proposed pedestrian flow control model against both actual data and the outcomes of other software packages that have been used to simulate the pedestrian flow under control, for example, Anylogic and Legion. Moreover, there is opportunity for model enhancements towards

- (1) the extension of the proposed control model to address the control of multidirectional pedestrian flow in a more general network with much more kinds of facilities such as stairs, walkways, escalators, and slopes;
- (2) the extension of the proposed model to address the pedestrian flow control with accounting for the presence of uncertainties, such as the uncertain link

capacity and traffic demand, the error between the inflow control plan and the actual controlled link inflow, and the pedestrians' willingness to obey the control command;

- (3) the extension of the proposed model to address the flow control with accounting for the dynamic route choice behavior of pedestrians in the control process;
- (4) the extension of the proposed control model to address the regulation of traffic flow in freeway networks which is controlled by the traffic signal lights and speed limiting.

Competing Interests

The authors declare no competing interests.

Authors' Contributions

Zhe Zhang analyzed the previous studies about pedestrian flow control and built the pedestrian flow model and the control model. Limin Jia gave suggestions and helped complete and wrote the manuscript.

Acknowledgments

The research was supported by the Fundamental Research Funds for the Central Universities (no. 2016YJS075) and the National Natural Science Foundation of China (no. 71171015).

References

- [1] E. Ben-Elia and D. Ettema, "Rewarding rush-hour avoidance: a study of commuters' travel behavior," *Transportation Research Part A: Policy and Practice*, vol. 45, no. 7, pp. 567–582, 2011.
- [2] X.-Y. Xu, J. Liu, H.-Y. Li, and J.-Q. Hu, "Analysis of subway station capacity with the use of queueing theory," *Transportation Research Part C: Emerging Technologies*, vol. 38, pp. 28–43, 2014.
- [3] J. van den Heuvel, A. Voskamp, W. Daamen, and S. P. Hoogenboom, "Using bluetooth to estimate the impact of congestion on pedestrian route choice at train stations," in *Traffic and Granular Flow '13*, pp. 73–82, Springer International, 2015.
- [4] C. Shi, M. Zhong, X. Nong, L. He, J. Shi, and G. Feng, "Modeling and safety strategy of passenger evacuation in a metro station in China," *Safety Science*, vol. 50, no. 5, pp. 1319–1332, 2012.
- [5] J. Y. S. Lee, P. K. Goh, and W. H. K. Lam, "New level-of-service standard for signalized crosswalks with bi-directional pedestrian flows," *Journal of Transportation Engineering*, vol. 131, no. 12, pp. 957–960, 2005.
- [6] K. M. Kim, S.-P. Hong, S.-J. Ko, and D. Kim, "Does crowding affect the path choice of metro passengers?" *Transportation Research Part A: Policy and Practice*, vol. 77, pp. 292–304, 2015.
- [7] F. Delgado, J. C. Muñoz, R. Giesen, and A. Cipriano, "Real-time control of buses in a transit corridor based on vehicle holding and boarding limits," *Transportation Research Record: Journal of the Transportation Research Board*, vol. 2090, pp. 59–67, 2009.
- [8] F. Delgado, J. C. Munoz, and R. Giesen, "How much can holding and/or limiting boarding improve transit performance?" *Transportation Research Part B: Methodological*, vol. 46, no. 9, pp. 1202–1217, 2012.
- [9] X.-Y. Xu, J. Liu, H.-Y. Li, and M. Jiang, "Capacity-oriented passenger flow control under uncertain demand: algorithm development and real-world case study," *Transportation Research Part E: Logistics and Transportation Review*, vol. 87, pp. 130–148, 2016.
- [10] S. Seriani and R. Fernandez, "Pedestrian traffic management of boarding and alighting in metro stations," *Transportation Research Part C: Emerging Technologies*, vol. 53, pp. 76–92, 2015.
- [11] C. Norris, M. McCahill, and D. Wood, "The growth of CCTV: a global perspective on the international diffusion of video surveillance in publicly accessible space," *Surveillance & Society*, vol. 2, no. 2-3, 2002.
- [12] C. Kim, D. K. Kim, S. Y. Kho, S. Kang, and K. Chung, "Dynamically determining the toll plaza capacity by monitoring approaching traffic conditions in real-time," *Applied Sciences*, vol. 6, no. 3, p. 87, 2016.
- [13] F. Kaakai, S. Hayat, and A. El Moudni, "A hybrid Petri nets-based simulation model for evaluating the design of railway transit stations," *Simulation Modelling Practice and Theory*, vol. 15, no. 8, pp. 935–969, 2007.
- [14] I. E. Manataki and K. G. Zografos, "A generic system dynamics based tool for airport terminal performance analysis," *Transportation Research Part C: Emerging Technologies*, vol. 17, no. 4, pp. 428–443, 2009.
- [15] L. Hu, Y. Jiang, J. Zhu, and Y. Chen, "A PH/PH(n)/C/C state-dependent queueing model for metro station corridor width design," *European Journal of Operational Research*, vol. 240, no. 1, pp. 109–126, 2015.
- [16] A. R. Danaher, *Transit Capacity and Quality of Service Manual*, Transportation Research Circular, 2003.
- [17] G. Hoy, E. Morrow, and A. Shalaby, "Use of agent-based crowd simulation to investigate the performance of large-scale intermodal facilities," *Transportation Research Record: Journal of the Transportation Research Board*, vol. 2540, pp. 20–29, 2016.
- [18] D. Helbing, I. Farkas, and T. Vicsek, "Simulating dynamical features of escape panic," *Nature*, vol. 407, no. 6803, pp. 487–490, 2000.
- [19] K. Takimoto, Y. Tajima, and T. Nagatani, "Effect of partition line on jamming transition in pedestrian counter flow," *Physica A: Statistical Mechanics and Its Applications*, vol. 308, no. 1–4, pp. 460–470, 2002.
- [20] F. R. B. Cruz, J. M. Smith, and D. C. Queiroz, "Service and capacity allocation in M/G/c/c state-dependent queueing networks," *Computers & Operations Research*, vol. 32, no. 6, pp. 1545–1563, 2005.
- [21] M. E. O'Kelly, "Routing traffic at hub facilities," *Networks and Spatial Economics*, vol. 10, no. 2, pp. 173–191, 2010.
- [22] L. Feng and E. Miller-Hooks, "A network optimization-based approach for crowd management in large public gatherings," *Transportation Research Part C: Emerging Technologies*, vol. 42, pp. 182–199, 2014.
- [23] R. Khalid, M. A. Baten, M. K. M. Nawawi, and N. Ishak, "Analyzing and optimizing pedestrian flow through a topological network based on M/G/C/C and network flow approaches," *Journal of Advanced Transportation*, vol. 50, no. 1, pp. 96–119, 2016.
- [24] P. Kachroo, S. J. Al-Nasur, S. A. Wadoo, and A. Shende, *Pedestrian Dynamics: Feedback Control of Crowd Evacuation*, Springer Science & Business Media, 2008.
- [25] S. A. Wadoo and P. Kachroo, "Feedback control of crowd evacuation in one dimension," *IEEE Transactions on Intelligent Transportation Systems*, vol. 11, no. 1, pp. 182–193, 2010.

- [26] A. Shende, M. P. Singh, and P. Kachroo, "Optimization-based feedback control for pedestrian evacuation from an exit corridor," *IEEE Transactions on Intelligent Transportation Systems*, vol. 12, no. 4, pp. 1167–1176, 2011.
- [27] A. Shende, M. P. Singh, and P. Kachroo, "Optimal feedback flow rates for pedestrian evacuation in a network of corridors," *IEEE Transactions on Intelligent Transportation Systems*, vol. 14, no. 3, pp. 1053–1066, 2013.
- [28] G.-X. Zeng and Y. Xue, "Application of the quasi-sliding-mode control to traffic bottleneck in pedestrian channel," *Acta Physica Sinica*, vol. 1, article 58, 2011.
- [29] S. A. Wadoo, "Sliding mode control of crowd dynamics," *IEEE Transactions on Control Systems Technology*, vol. 21, no. 3, pp. 1008–1015, 2013.
- [30] M. J. Lighthill and G. B. Whitham, "On kinematic waves. II. A theory of traffic flow on long crowded roads," *Proceedings of the Royal Society. London. A. Mathematical, Physical and Engineering Sciences*, vol. 229, pp. 317–345, 1955.
- [31] C. F. Daganzo, "The cell transmission model, part II: network traffic," *Transportation Research Part B: Methodological*, vol. 29, no. 2, pp. 79–93, 1995.
- [32] L. Muñoz, X. Sun, R. Horowitz, and L. Alvarez, "Traffic density estimation with the cell transmission model," in *Proceedings of the IEEE American Control Conference*, vol. 5, pp. 3750–3755, 2003.
- [33] A. Sumalee, R. X. Zhong, T. L. Pan, and W. Y. Szeto, "Stochastic cell transmission model (SCTM): a stochastic dynamic traffic model for traffic state surveillance and assignment," *Transportation Research Part B: Methodological*, vol. 45, no. 3, pp. 507–533, 2011.
- [34] F. S. Hänseler, M. Bierlaire, B. Farooq, and T. Mühlematter, "A macroscopic loading model for time-varying pedestrian flows in public walking areas," *Transportation Research Part B: Methodological*, vol. 69, pp. 60–80, 2014.
- [35] M. Asano, A. Sumalee, M. Kuwahara, and S. Tanaka, "Dynamic cell transmission-based pedestrian model with multidirectional flows and strategic route choices," *Transportation Research Record*, no. 2039, pp. 42–49, 2007.
- [36] X. Zhang and G.-L. Chang, "Optimal control strategies with an extended cell transmission model for massive vehicular-pedestrian mixed flows in the evacuation zone," *Journal of Advanced Transportation*, vol. 48, no. 8, pp. 1030–1050, 2014.
- [37] F. R. B. Cruz, J. MacGregor Smith, and R. O. Medeiros, "An M/G/C/C state-dependent network simulation model," *Computers & Operations Research*, vol. 32, no. 4, pp. 919–941, 2005.
- [38] C. M. J. Tampère, R. Corthout, D. Cattrysse, and L. H. Immers, "A generic class of first order node models for dynamic macroscopic simulation of traffic flows," *Transportation Research Part B: Methodological*, vol. 45, no. 1, pp. 289–309, 2011.
- [39] W. L. Jin and H. M. Zhang, "On the distribution schemes for determining flows through a merge," *Transportation Research Part B: Methodological*, vol. 37, no. 6, pp. 521–540, 2003.
- [40] D. Ni and J. D. Leonard II, "A simplified kinematic wave model at a merge bottleneck," *Applied Mathematical Modelling*, vol. 29, no. 11, pp. 1054–1072, 2005.
- [41] M. Campanella, R. Halliday, S. Hoogendoorn, and W. Daamen, "Managing large flows in metro stations: the new year celebration in copacabana," *IEEE Intelligent Transportation Systems Magazine*, vol. 7, no. 1, pp. 103–113, 2015.
- [42] J. Fruin, *Designing for Pedestrians*, Public Transportation United States, 1992.
- [43] S. P. Hoogendoorn and P. H. L. Bovy, "Pedestrian route-choice and activity scheduling theory and models," *Transportation Research Part B: Methodological*, vol. 38, no. 2, pp. 169–190, 2004.
- [44] Z. Liu, S. Wang, W. Chen, and Y. Zheng, "Willingness to board: a novel concept for modeling queuing up passengers," *Transportation Research Part B: Methodological*, vol. 90, pp. 70–82, 2016.
- [45] B. D. Greenshields, W. S. Channing, H. H. Miller et al., "A study of traffic capacity," in *Proceedings of the 14th Annual Meeting of the Highway Research Board*, Washington, DC, USA, 1935.
- [46] M. J. Hurley, D. T. Gottuk, J. R. Hall et al., "SFPE handbook of fire protection engineering," in *Industrial Safety and Environmental Protection*, vol. 29, pp. 487–500, 2016.
- [47] S. Al-nasur and P. Kachroo, "A microscopic-to-macroscopic crowd dynamic model," in *Proceedings of the IEEE Intelligent Transportation Systems Conference (ITSC '06)*, pp. 606–611, Toronto, Canada, September 2006.
- [48] T.-J. Ho and M.-J. Chung, "Information-aided smart schemes for vehicle flow detection enhancements of traffic microwave radar detectors," *Applied Sciences*, vol. 6, no. 7, article 196, 2016.